Universidade de Aveiro Departamento de Química
2019

**Maria José
Peixoto
De Sousa**

Estratégias Biomiméticas usando a técnica Camada-a-Camada para Aplicações Biomédicas e Engenharia de Tecidos

Biomimetic Strategies using Layer-by-Layer towards Biomedical and Tissue Engineering Applications

Universidade de Aveiro Departamento de Química
2019

Maria José
Peixoto
De Sousa

Estratégias Biomiméticas usando a técnica Camada-a-Camada para Aplicações Biomédicas e Engenharia de Tecidos

Biomimetic Strategies using Layer-by-Layer towards Biomedical and Tissue Engineering Applications

Tese apresentada à Universidade de Aveiro para cumprimento dos requisitos necessários à obtenção do grau de Doutor em Química, realizada sob a orientação científica do Doutor João Filipe Colardelle da Luz Mano, Professor Catedrático do Departamento de Química da Universidade de Aveiro.

Apoio financeiro da FCT e do FSE no âmbito do III Quadro Comunitário de Apoio (Bolsa de Doutoramento SFRH/BD/97606/2013).

o júri

Presidente

Prof. Doutor José Joaquim Cristino Teixeira Dias
Professor Catedrático da Universidade de Aveiro

Prof. Doutor José Luís Gómez Ribelles
Professor Catedrático da Universidade Politécnica de Valência

Prof. Doutor Ilídio Joaquim Sobreira Correia
Professor Associado com Agregação da Universidade da Beira Interior

Prof. Doutora Natália Maria Araújo Alves
Professor Auxiliar da Universidade do Minho

Prof. Doutor Armando Jorge Domingues Silvestre
Professor Catedrático da Universidade de Aveiro

Prof. Doutor João Filipe Colardelle da Luz Mano
Professor Catedrático da Universidade de Aveiro

Agradecimentos

All over my PhD, several people have contributed to the accomplishment of this thesis, professionally and personally. In the next paragraphs I will try to express my gratitude to them.

Firstly, I want to acknowledge my supervisor Prof. João Mano, without whom all this work would not be possible. Thank you for accepting me on your group and for providing me all the tools and means to perform my scientific work and evolve as a scientist. Since my master year until today, Professor João always gave me an important guidance, attention and confidence that made this journey easier. His constant and positive encouragement, ideas, enthusiastic and creative spirit were truly inspiring and motivating. Also, I would like to acknowledge the opportunity to be a part of the COMPASS Research Group, for making possible not only the development of my PhD work, but the whole experience of starting in a new place and contributing for the progress of the group. It was not an easy journey, yet a very rewarding experience. My sincere gratitude, Professor.

I want to acknowledge the 3B's Research Group and the University of Minho, where I started this hardworking journey and that gave me tools, equipment, infra-structures and knowledge indispensable for my individual and collective progress.

I also want to acknowledge CICECO, the Chemistry Department and the University of Aveiro for accepting and offering me the opportunity of working in a such recognized institute and university.

I would like to acknowledge Dra. Sylvia Nürnberger. I really appreciate the opportunity to have gone to Austria and have worked on the Medical University and Hospital of Vienna. Thank you, Dra. Sylvia, for the support and enlightening guidance, patience and knowledge, kindness and motivation. Thank you to my lab colleagues there, especially Marian for his help.

My sincere acknowledge to Sofia Caridade who directly contributed with her specific expertise to the work presented in this thesis.

(cont.)

A huge thanks to the whole team of COMPASS Research Group for all the valuable discussions, shared knowledge and especially for all the moments shared inside and outside the labs, for being the best labmates. My special thanks are directed to Texugos, I will never forget your support and friendship. A special thanks to Margarida, the best labmate, PhDmate and roommate that I could ever have. Thank you, Margarida, thank you Texugos. I cannot obviously forget all the persons that I was finding and working during all these last years, that directly and indirectly contributed for my PhD, in the different places that I worked: 3B's Research Group, COMPASS Research Group, CICECO and Ludwig Boltzmann Institute for Experimental and Clinical Traumatology. All of you made my journey even better, easier and funnier.

To the Portuguese Foundation for Science and Technology for the financial support through a PhD grant with the reference SFRH/BD/97606/2013.

Then, to my "3B's family", persons that I started to share my workspace and I rapidly shared my friendship, thank you.

To my "Berdadeiros" family, thank you: I am glad and pleased to have people that I can trust and share my life. The family that I choose.

Thank you to my high-school friends that no matter the distance or the differences they always encourage me to keep going.

The deepest gratitude goes to my family. Thanks for all unconditional love, patience and emotional support. Thank you to my mother and sister to be always on my side when I most needed, even in the moments that I seemed like a crazy person. Thank you to my nephews that were the best gifts that I could ever receive.

Lastly, thank you to my father, that is the main responsible for my resilience and motivation. The education and values that you taught me, made me who I am today. I hope that I could make you proud.

palavras-chave

Camada-a-Camada, revestimentos multicamada, membranas, polipéptidos como-elastina, polissacarídeos, responsividade a estímulos, memória de forma, matriz extracelular, topografia com padrão, alinhamento celular, diferenciação celular, catecol, adesividade, cicatrização de ferida, cartilagem articular, engenharia de tecidos, aplicações biomédicas.

Resumo

O desenvolvimento de um revestimento ou material cujas propriedades físico-química, mecânicas ou biológicas podem ser modificadas de acordo com as propriedades do tecido alvo, tem ganho cada vez mais importância, nomeadamente para fins biomédicos e de engenharia de tecidos e medicina regenerativa. Durante os últimos anos, diferentes estratégias biomiméticas têm contribuído significativamente para o progresso destas áreas. Estas são possíveis de implementar a diferentes níveis: imitar formas e funções existentes na natureza ou mimetizar processos e sistemas naturais. Na presente tese, a técnica camada-a-camada (LbL) foi usada como uma ferramenta biomimética para modificar superfícies ou produzir membranas com base em múltiplas camadas de polieletrólitos. A crescente utilização desta técnica, concretamente na área biomédica, prende-se com a possibilidade de funcionalizar ou produzir biomateriais aliada à capacidade de incorporar uma gama alargada de blocos de construção. Aqui, diferentes polímeros sintéticos e naturais têm sido usados para construir estruturas multicamada; no entanto, a generalidade dos polímeros sintéticos não apresenta naturalmente locais de ligação e adesão celular. Para contornar este obstáculo, algumas modificações químicas aos polímeros sintéticos têm sido sugeridas e novos compostos têm sido desenvolvidos, inspirados na composição de sistemas naturais. Por exemplo, polipéptidos tipo-elastina (ELPs) são uma classe de polímeros inspirados na natureza, que apresentam propriedades não-imunogénicas e biocompatíveis, podendo ser geneticamente programados conforme desejado. A sua composição baseia-se na repetição de pequenos péptidos também presentes na elastina humana, com a possibilidade também de incorporar outras sequências bioativas especificas, como o tripéptido Arginina-Glicina-Ácido Aspártico (RGD), reconhecido por promover a adesão celular. Para esta tese foram produzidos ELPs, que mais tarde foram funcionalizados com grupos azida e alquino para introduzir a reatividade necessária para uma reação 1,3-dipolar de ciclo-adição se realizar em condições biocompatíveis, sem produtos tóxicos resultantes e em curtos tempos de reação. Esta reação foi realizada sob a técnica LbL, mas conduzida por interações covalentes ao invés de electroestáticas, para atuar como revestimento biomédico. Estes polímeros são ainda reconhecidos pela sua temperatura de transição (Tt) em solução aquosa, relacionada com uma reorganização conformacional da cadeia polimérica. Abaixo da Tt as suas cadeias poliméricas são solúveis, mas acima de Tt formam-se micro-agregados; este é um processo reversível que confere propriedades responsivas aos revestimentos. Nos seguintes capítulos, diferentes polissacarídeos como quitosano (CHT), alginato (ALG), sulfato de condroitina (CS) ou ácido hialurónico (HA), foram usados para produzir membranas multicamadas conduzidas maioritariamente via interações electroestáticas. Esta abordagem tem ganho cada vez mais importância para desenvolver materiais com funcionalidade bioquímica, biocompatibilidade e para mimetizar algumas interações observadas na matriz extracelular (ECM).

(cont.)

Ao longo desta tese foram usadas membranas multicamada de CHT/CS; estes materiais revelaram algumas propriedades muito particulares, quando comparadas com outros sistemas de multicamada, como a sua elasticidade e taxas de degradação mais rápidas. No entanto, a baixa rigidez e maiores taxas de hidratação, que muitas vezes impedem a adesão celular, surgem frequentemente associados a sistemas multicamada compostos somente por polissacarídeos. Para contornar este obstáculo, as membranas multicamada de CHT/CS foram reticuladas com genipina. De notar que este composto é de origem natural, sendo extraído da fruta da gardénia; a pós-modificação das membranas com genipina resultou na melhoria das propriedades mecânicas e biocompatibilidade, e ainda, no aumentando das propriedades bio-adesivas. Na realidade, a possibilidade de modular as propriedades destes sistemas multicamada por reticulação química pode ser conseguida logo durante a adsorção de cada camada ou no fim do processo. Características dos biomateriais como a morfologia, espessura, taxas de adsorção de água ou biodegradação, propriedades mecânicas e biológicas podem ser moduladas ajustando certos parâmetros de reticulação (por exemplo, agente de reticulação, concentração ou tempo de reação). Para além do mais, estudos de memória de forma destas membranas multicamada mostraram resultados promissores, considerando o seu uso para fins biomédicos. As propriedades mecânicas destes sistemas foram melhoradas combinando as ligações electroestáticas já existentes com ligações covalentes conferidas pela reticulação química, dando origem a uma rede polimérica multicamada, mas interpenetrada. Na continuação deste trabalho foi possível criar uma topografia com padrão bem organizado na superfície das membranas, alterando somente o material onde efetuamos a deposição das multicamadas. Esta estratégia visou mimetizar a topografia da ECM de diferentes tecidos, como o osso, a pele ou os nervos, criando canais alinhados na superfície do material. Usando este tipo de materiais multicamada padronizados foi possível modular funções e comportamentos celulares como o alinhamento ou a diferenciação. Em seguida, inspirados pela composição das proteínas que conferem adesividade aos mexilhões, foram produzidas membranas multicamada contendo HA modificado com dopamina (DN). A presença de DN ao longo da espessura das membranas multicamada parece ter contribuído para uma melhor e maior força de adesão, quando comparadas com as membranas controlo (membranas multicamada CHT/HA e CHT/ALG). Para além do mais, os testes *in vitro* resultaram em uma significante melhoria da adesão celular às membranas contendo DN. Esta estratégia mostrou ser promissora para diferentes aplicações biomédicas e de engenharia de tecidos, particularmente para a regeneração de tecido ósseo e a cicatrização de feridas da pele. Combinando diferentes estratégias e conceitos biomiméticos, foi também possível recriar um sistema complexo associado à cartilagem articular e concretamente a doenças como a osteoartrite. Assim sendo, na última parte desta tese, estas membranas multicamada com propriedades adesivas foram utilizadas como veículo para transportar células estaminais humanas do tecido adiposo (hASCs) para o local onde a cartilagem se encontra danificada. A presença deste tipo de células tem sido utilizada como tratamento para cartilagem danificada. Aqui, hASCs aderiram temporariamente às membranas multicamada, e foram assim transportadas diretamente para discos de cartilagem humana danificada, permitindo a criação de uma ponte celular entre as membranas e a superfície da cartilagem. Desta forma, estas células começaram a proliferar na superfície da cartilagem começando a migrar para os defeitos (em profundidade), segregando fatores capazes de ajudar na reparação da cartilagem. No geral, o trabalho desenvolvido para a presente tese mostra a grande versatilidade da técnica LbL, que proporciona os meios necessários para desenvolver uma gama alargada de materiais, estratégias e soluções muito necessárias e promissoras para aplicações biomédicas e de engenharia de tecidos e medicina regenerativa.

keywords

Layer-by-layer, multilayer coatings, freestanding membranes, elastin-like polypeptides, polyssacharides, stimuli-responsive; shape-memory, extracellular matrix, patterned topography, cellular allignment, cellular differentiation, adhesiveness, wound healing, articular cartilage, tissue engineering, biomedical applications.

abstract

The development of a suitable coating or material, which physico-chemical, mechanical or biological properties, that can be tailored according the features of the target tissue, has been gaining increased importance in biomedical and tissue engineering and regenerative medicine (TERM) fields. Biomimetic strategies have contributed significantly for the progress of biomedical field during the last years. This is possible to be achieved at different levels: imitating Nature form or function and mimicking natural processes and systems are the most used biomimetic approaches. In this thesis, Layer-by-Layer (LbL) methodology was used as a hierarchical biomimetic tool to modify surfaces and to produce freestanding membranes based on polyelectrolyte multilayers (PEMs). The possibility to functionalize or engineer biomaterials combined with the ability to incorporate a wide range of building blocks, makes LbL a powerful processing technique in the biomedical field. Synthetic polymers have been used to construct PEMs for biomedical and TERM applications; however, they lack often on adhesive cues for cell attachment and tissue growth. To overcome such issue, biomimetic synthetic polymers have been developed. Elastin-like polypeptides (ELPs) are a class of nature-inspired polymers, nonimmunogenic, genetically encodable and biocompatible. These materials are based on the repetition of short peptides considered to be building blocks in natural elastin and can include specific bioactive sequences, as the tripeptide Arginine-Glycine-Aspartame (RGD) known by promoting cell adhesion. For the first work of this thesis, ELPs were functionalized with azide and alkyne groups to introduce the reactivity required to carry out the 1,3-dipolar cycloaddition under mild biocompatible conditions, with no toxic by-products and in short reaction times. This reaction was done by means of a LbL assembly, driven by covalent interactions instead of being driven by electrostatic interactions, obtaining a bioactive and biomimetic multilayer coating. Moreover, these polymers are characterized by a critical temperature, known as the transition temperature in aqueous solution (Tt), which is related with a conformational reorganization. Thus, below Tt the polymer chains were soluble in water and above Tt they formed nano- and micro-aggregates becoming insoluble in a reversible process, making these coatings stimuli-responsive. In the following chapters, several polysaccharides as chitosan (CHT), alginate (ALG), hyaluronic acid (HA) or chondroitin sulfate (CS) were used to produce freestanding structured membranes through LbL processes, mainly driven by electrostatic interactions. The use of PEMs containing biopolymers are particularly appealing to coat and develop multilayered structures with biochemical functionalities, biocompatibility, and to mimic the interactions observed in native extracellular matrix (ECM).

(cont.)

CHI/CS multilayers were used throughout the thesis, revealing some unique properties, when compared with other polysaccharide-based multilayers, such as their elasticity and degradation rate. However, natural origin polymer-based multilayers present low stiffness and higher hydration rates, which hinder cell adhesion. To overcome this, the CHT/CS multilayers were crosslinked with genipin. This is also a natural product, that is extracted from gardenia fruits and presents the ability to improve the mechanical properties, while preserves the biocompatibility and even enhances the cell adhesive properties. The ability to tailor the multilayers properties can be applied during their assembly or post-assembly. Upon adjusting cross-linking parameters (e.g., cross-linker concentration and reaction time) the morphology, thickness, water uptake, rate of biodegradation, mechanical properties and cell adhesive properties can be tuned. Studies of shape-memory of these multilayered films, presented promising results regarding their use in biomedical applications. The mechanical properties of the multilayers can be further improved combining covalent and ionic crosslinking, which gives rise to a full interpenetrating polymer network. More interesting, it was possible to create a well-organized patterned topography at the surface of the freestanding multilayered membrane, just by using a different underlying substrate. This strategy envisaged to mimic the topography of the ECM of some tissues, as bone, skin or nerves, creating grooves on the material's surface at nanoscale. Using this approach, it was possible to control some cellular functions and behavior as alignment and differentiation. Further in this thesis and inspired by the composition of the adhesive proteins in mussels, freestanding multilayered membranes containing dopamine-modified hyaluronic acid (HA-DN) were produced. The presence of DN along with the thickness of the membranes presented better lap-shear adhesion strength than the control membranes (hyaluronic acid and alginate films – two polysaccharides often regarded as good natural adhesives – were assembled together). Moreover, *in vitro* tests showed an enhanced cell adhesion for the membranes containing HA-DN and ability to use such kind of membranes for different biomedical and TERM applications, particularly for bone regeneration and skin wound healing. Combining different biomimetic concepts, it was also possible to recreate the complex environment of osteoarthritic articular cartilage by preparing human circular discs of superficially damaged articular cartilage from human samples. Herein, the adhesive freestanding multilayered membranes were used as a vehicle to deliver human adipose stem cells (hASCs) to help to repair the damaged cartilage. hASCs temporarily adhered to the adhesive LbL-based membranes, and were transported to the cartilage discs, creating a bridge of cells between the membranes and the surface of the cartilage. The cells started to migrate into the defects of the cartilage, proliferating and secreting factors capable of repairing the cartilage. Overall, the developed work in this thesis shows that LbL is a very versatile technique that provides the means to develop a wide range of solutions to be useful in biomedical and TERM applications.

List of publications during this PhD work

Scientific papers in international journals:

✓ Biomimetic click assembled multilayer coatings exhibiting responsive properties
MP Sousa, IG de Torre, MB Oliveira, JC Rodríguez-Cabello, JF Mano
Materials Today Chemistry 4, 150-163, 2017

✓ Elastic chitosan/chondroitin sulfate multilayer membranes
MP Sousa, F Cleymand, JF Mano
Biomedical Materials 11 (3), 035008, 2016

✓ Control of cell alignment and morphology by redesigning ECM-mimetic nanotopography on multilayer membranes
MP Sousa, SG Caridade, JF Mano
Advanced Healthcare Materials 6 (15), 2017

✓ Cell adhesive bioinspired and catechol-based multilayer freestanding membranes for bone tissue engineering
MP Sousa, JF Mano
Biomimetics 2 (4), 2017

✓ Bioinspired multilayer membranes as potential adhesive patches for skin wound healing
MP Sousa, AI Neto, TR Correia, SP Miguel, M Matsusaki, IJ Correia, JF Mano
Biomaterials science; 2018

✓ Multilayered membranes with tuned well arrays to be used as regenerative patches
NI Martins, MP Sousa, CA Custódio, VC Pinto, PJ Sousa, G Minas, F Cleymand, JF Mano
Acta Biomaterialia 57, 313-323, 2017

✓ High performance free-standing films by layer-by-layer assembly of graphene flakes and ribbons with natural polymers
D Moura, SG Caridade, MP Sousa, E Cunha, HC Rocha, JF Mano, NA Alves
Journal of Materials Chemistry B 4 (47), 7718-7730, 2016

✓ Antibacterial bioadhesive layer-by-layer coatings for orthopedic applications
AL Carvalho, AC Vale, MP Sousa, AM Barbosa, E Torrado, JF Mano, NA Alves
Journal of Materials Chemistry B 4 (32), 5385-5393, 2016

✓ Nanoengineering hybrid supramolecular multilayered biomaterials using polysaccharides and self-assembling peptide amphiphiles
J Borges, MP Sousa, G Cinar, SG Caridade, MO Guler, JF Mano
Advanced Functional Materials 27 (17), 2017

✓ Biomedical films of graphene nanoribbons and nanoflakes with natural polymers
M Silva, SG Caridade, AC Vale, E Cunha, MP Sousa, JF Mano, MC Paiva, NM Alves
RSC Advances 7 (44), 27578-27594, 2017

✓ Nanostructured Biopolymer/Few-Layer Graphene Freestanding Films with Enhanced Mechanical and Electrical Properties
C Silva, SG Caridade, E Cunha, MP Sousa, H Rocha, JF Mano, MC Paiva, NM Alves
Macromolecular Materials and Engineering 303 (4), 1700316; 2018

Scientific papers in submission process:

- ✓ Surface micro and nanoengineering: Applications of Layer-by-Layer technology as a versatile tool to control the cellular behavior

MP Sousa, E Arab-Tehrany, F Cleymand, JF Mano

- ✓ Dopamine-containing self-adhesive membranes as a delivery device of therapeutic stem cells for cartilage repair

MP Sousa, M. Fürsatz, H. Lee JF. Mano, S. Nürnberger

Journal Covers:

- ✓ Cell alignment: Control of cell alignment and morphology by redesigning ECM-mimetic nanotopography on multilayer membranes

MP Sousa, SG Caridade, JF Mano
Inside back cover of Advanced Healthcare Materials 6 (15), 2017

- ✓ Biomaterials: Nanoengineering hybrid supramolecular multilayered biomaterials using polysaccharides and self-assembling peptide amphiphiles

J Borges, MP Sousa, G Cinar, SG Caridade, MO Guler, JF Mano
Inside Back Cover of Advanced Functional Materials 27 (17), 2017

- ✓ Macromol. Mater. Eng. 4/2018

C Silva, SG Caridade, E Cunha, MP Sousa, H Rocha, JF Mano, MC Paiva, NM Alves
Picture Front Cover of Macromolecular Materials and Engineering 303 (4), 1870014, 2018

Oral communications in scientific meetings:

- ✓ Free-standing multilayered membranes from renewable polymers, towards tissue engineering applications

MP Sousa, F Cleymand, JF Mano
253rd American Chemical Society National Meeting & Exposition, CELL division, San Francisco, CA, 2017

Main posters communications in scientific meetings:

- ✓ Production of an elastin-based free-standing membrane, using a simple multilayer assembly approach

TERM STEM 2014; Porto

- ✓ Production of Elastic Chitosan/Chondroitin Sulphate Multilayer Films Regeneration

Tissue Engineering Part A, vol. 21(Supp. 1), S352, 2015
4th TERMIS World Congress, Boston, Massachusetts

- ✓ Freestanding Multilayered Membranes patterned with Micro-Reservoirs as potential Regenerative Paths

Tissue Engineering Part A 23, S55-S55; 2017
TERMIS-Americas Conference & Exhibition Charlotte

- ✓ Catechol-based freestanding multilayer membranes as an adhesive and functional scaffold to treat superficial cartilage damage

5th TERMIS World Congress 2018

Table of Contents

List of figures

Chapter I

Chapter II

Chapter III

Chapter IV

Chapter V

Chapter VI

Chapter VII

Chapter VIII

Chapter IX

List of tables

Chapter II

Chapter III

Chapter VIII

Abbreviations

A
AFM Atomic Force Microscopy
ALG Alginate
ANOVA Analysis of Variance
ASCs Adipose Stem Cells

B
BL Bilayers
BMP-6 Bone Morphogenetic Protein-6
BSA Bovine Serum Albumin

C
CA Cellulose Acetate
CAD Computer Assisted Design
CD Compact Disk
CHT Chitosan
CL Crosslinked
COL Collagen
CS Chondroitin Sulphate

D
Da Dalton
DAPI 4′,6-diamidino-2-phenylindole dihydrochloride
DMAEMA Dimethyl aminoethyl methacrylate
DMA Dynamic mechanical analysis
DMEM Dulbecco's modified Eagle's medium
DMSO Dimethyl sulfoxide
DN dopamine
DOPA dihydroxyphenylalanine
DPBS Dulbecco's Phosphate-Buffered Saline
dsDNA Double stranded DNA

E
E Young's modulus
ECs Endothelial cells
ECM Extracellular matrix
EDC 1-Ethyl-3-(3-dimethylaminopropyl)carbodiimide
EF Elongation Factor
ELP Elastin-like Polypeptide
ELR Elastin-like Recombinamer
EDS Energy-dispersive X-ray spectroscopy

F
FAs Focal Adhesions
FBS Fetal bovine serum
FN Fibronectin
FITC Fluorescein-5(6)-isothiocyanate
FTIR Fourier transform infrared
FMM Freestanding multilayer membrane
FS Freestanding

G
G Genipin

H
hASCs Human adipose-derived stem cells
HA Hyaluronic Acid
HA-DN Conjugated of Hyaluronic Acid modified with Dopamine
HApNPs Hydroxyapatite nanoparticles
HEMA Hydroxyethyl methacrylate
HDFs Human Dermal Fibroblasts
HMDS Hexamethyldisilazane
H&E Hematoxylin and Eosin stain

I
ITS Insulin-Transferrin-Selenium

L
L929 Mouse lung fibroblasts cell line
LbL Layer-by-Layer
LCST Lower Critical Solution Temperature

M
MAPs Mussel Adhesive Proteins
M3T3-E1 Murine osteoblastic cell line
MTS (3-(4,5-dimethylthiazol-2-yl)-5-(3-carboxymethoxyphenyl)-2-(4-sulfophenyl)-2H-tetrazolium)
MSCs Mesenchymal stem cells
MWCO Molecular weight cut-off

N
NMR Nuclear Magnetic Resonance
NMPs Nuclear Matrix Proteins

O
OA Osteoarthritis
OD Optical density
OS Osteopontin

P
PAA Poly (acrylic acid)
PAH Poly(allylamine hydrochloride)
PAM Polyacrylamide
PAT Patterned
PBS Phosphate buffered saline
PCL Poly(ε-caprolactone)
PDADMAC Poly(diallyldimethylammonium chloride)
PEM Polyelectrolyte multilayer
PDMS Polydimethylsiloxane
PLL Poly(L-lysine)s
PP Polypropylene
PS Polystyrene
PSS Poly(styrenesulfonate)

Q
QCM-D Quartz Crystal Microbalance with Dissipation monitoring

R
RFP Red Fluorescent Protein
RGD Arginine-glycine-aspartate
RT Room temperature

S
SAMs Self-assembled monolayers
SD Standard Deviation
SEM Scanning electron microscopy

T
TCPS Tissue Culture Polystyrene Substrate
TERM Tissue Engineering and Regenerative Medicine
TERT-1 Telomerase reverse transcriptase
TGF-β3 Transforming growth factor beta-3
TL tetralayers

U
UV Ultraviolet

V
VIS Visible

W
WCA Water Contact Angle

2D two-Dimensional
3D three-Dimensional
β-GP β-glycerolphosphate

I. General Introduction

Abstract

This first chapter corresponds to the general introduction of this thesis. Here, it is possible to find a briefly contextualization of the problems and the respective strategies that were designed throughout this thesis.

1. Biomimetic strategies to produce multifunctional materials for biomedical and tissue engineering applications

Biomimetics is a kind of recent multidisciplinary concept that takes inspiration from Nature to develop new materials, processes, systems and strategies towards different science fields [1]. In this thesis, we are particularly concerned with biomedical and tissue engineering needs. Motivated by the innumerous successfully cases of nature lessons translation into science progress, more and different biomimetic strategies should be exploited to develop novel functional and effective materials and technologies. Among others, superhydrophobic surfaces [2], reversible-adhesive materials [3], high-mechanical strength fibers [4], self-healing mechanism [5] or biological self-assembly [6] are some biomimetic examples already reported in literature.

Conventional strategies in biomedical field involved the use of metals [7], ceramics [8] or synthetic polymers [9] that were processed and usually modified on their surface according with clinical requirement [10]. Problems with long-term biocompatibility, degradation products and implantation increased the need of new strategies [9]. Also, the progress of tissue engineering and regenerative medicine field brings the need of new approaches to address the need of recreating in some extent the native process of tissue repairing and regeneration. We believe that applying Nature principles, materials and processes can be a changeover from conventional strategies, towards biomedical and tissue engineering ends. Therefore, the aim of this thesis was the design different biomimetic strategies to produce multifunctional materials and technologies, capable of responding to different clinical needs and potentially to be bring new insights for these fields.

Looking at nature, tissues are organized in very complex structures with different degrees of arrangements, ranging from a nano- to a micro-organization, being a combination of small units assembled over the several scales [11]. Therefore, to construct biomimetic structures can be faced as a bottom-up approach assembly; in this context we hypothesize that layer-by-layer (LbL) assembly can be an adequate tool to process and engineer hierarchical organized biomimetic materials suitable for biomedical and tissue engineering applications. This technique is based on the sequential and alternate deposition of complementary materials, usually by means of electrostatic interactions [12]. Even thought, other driven forces have been suggested, as covalent bonds or hydrophobic interactions [13]. Hence, throughout this thesis, different biomimetic strategies were combined with LbL technology to produce biomimetic multifunctional multilayered materials.

From literature, different methods were nowadays employed to direct materials for biomedical and tissue engineering and in some extent to modulate the cellular behavior when in contact with material’s surface. Three main approaches were selected to design the different strategies presented in this thesis – see Figure I-1. Therefore, LbL assembly was combined with the presence of bio-based or functional materials, the presence of bio-recognition molecules, as RGD moiety, other bioactive motifs or growth factor, and the presence of physical or mechanical cues, as shaped topographical features, areas of different elastic and stiff or different surface energy, towards different applications.

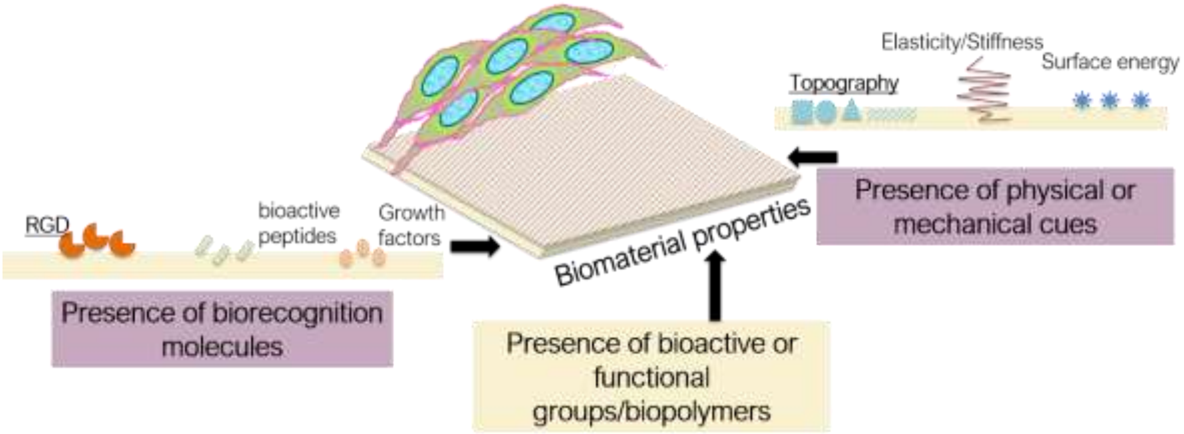

Figure I-1. Schematic representation of the different methodologies that were integrated with the LbL technique, to design the biomimetic strategies suggested in the experimental part of this PhD thesis.

Elastin-like polypeptides (ELPs) are synthetic polymers that have their origin in the repeating sequences found in the mammalian elastic protein, the elastin, a vital component of the extracellular matrix (ECM) and that exhibit a set of properties that places them in an excellent position for biomedical and tissue engineering applications [14]. ELPs can be modified to virtually include any desired peptide sequence [14]; we investigated the ability of constructing a multilayered film modifying ELPs with azide and alkyne groups, providing them capacity of interact through cycloaddition click chemistry reactions, creating covalent bonds [15].

Besides they are synthetically obtained, these materials are bioinspired; for instance, ELPs have similar mechanical properties of nature elastin, being biocompatible and with potential to self-assemble and respond to changes of the environment or under physiological conditions [14]. Their characteristic inverse temperature phase transition makes ELPs to be soluble below this temperature and undergo an aqueous demixing phase transition above this value – reversibility property [16]. It provides ELPs the ability of responding at temperature and other stimulus, being recognized as smart polymers [16]. Therefore, we designed multilayered coatings composed of these interesting biomimetic polymers to produce stimuli-responsive coatings capable of creating a kind of a controlled microenvironment to study cell-materials interactions or to act as a drug delivery system. The success of implantable medical systems is highly determined by the response they prompt to the surrounding *in vivo* environment [17]. In this sense, we investigated the ability of modifying ELPs with arginylglycylaspartic acid (RGD) moieties, reported as promoting cell adhesion [18]. The potential and effectiveness of these multifunctional biomimetic coatings were exploited in Chapter IV.

From 2-dimensional (2D) to 3-dimensional (3D), LbL assembly has been reported in the form of nanostructured coatings [19], membranes [20], capsules [21]or porous scaffolds [22]. Using LbL technique, if the film is deposited on a low surface energy substrate, it can further be removed in mild conditions, leading a freestanding membrane without the need for a post-processing step [20, 23]. Among the others, we believe that freestanding membranes are a quite simple model where it is possible to have more control over materials’ properties and that can be integrated in a bottom-up route, creating more complex systems. Therefore, in the next chapters of this thesis, freestanding multilayered membranes were produced towards different ends.

Surfaces aspects related to biomaterials have received a great attention from scientific field [24]. Natural polymers, as chitosan (CHT), alginate (ALG), chondroitin sulfate (CS) or hyaluronic acid (HA) present some similarities with ECM and in some cases, specific sites for cell binding [24b]. The polycationic nature of chitosan makes this polymer well-suitable for LbL processes [25]. CS is an important ECM component, that plays an important role in maintaining cell functions [26]; their anionic nature allows the combination with CHT to produce freestanding multilayered membranes. We hypothesize that when crosslinking these multilayers with genipin, it would be possible to tailor their swelling, mechanical and biological properties (Chapter V). This could be applied in a diversity of biomedical applications.

Besides the significance of both chemical and biochemical compounds that are exposed on the materials’ surface, it is also central to consider the influence of topography, particularly at the nanoscale, on cell behavior and functions [27]. Distinct topographies can be found in Nature and these may lead to peculiar behaviors, as exploited in Chapter II. Herein, it is possible to find an overview of the different methodologies existing to produce physical patterned LbL-based materials and their application to modulate distinct cellular functions.

In fact, in the experimental part of this thesis, we designed an LbL approach to obtain nanoengineered multilayered freestanding membranes (Chapter VI). Taking advantage of a patterned template, we investigated the ability to construct patterned substrates and the influence of the presence of nanogrooved cues to modulate the cellular behavior.

The ultimate strategy of employing biomimetic principles for the progress of biomedical and tissue engineering fields was to develop materials that could mimic the adhesive behavior of mussels [28]. The catechol component of DOPA is the main responsible for the strong adhesion of mussels to rocks, even in a wet environment [28]. Catechol chemistry has been increasingly investigated in the last years [28-29], exploiting the adhesion to different wet organic and inorganic substrates. For that, different materials have been modified with DOPA derivates [30]. To confer adhesive properties, HA will be modified with dopamine (DN) following a procedure already reported and well-stablished in our research group [30c]. DN is an analogue of the non-cationic amino acid 3,4-dihydroxy-L-alanine (DOPA), that is usually in high amounts in mussel adhesive proteins [30c]. We hypothesize that using such interesting conjugated combined with other polysaccharides within a LbL methodology could result in increased mechanical adhesive properties as well as in enhanced cytocompatible materials. In Chapter VII, we investigated the potential of applying LbL-based freestanding membranes, composed of alternate nanolayers of CHT and HA-DN for bone tissue engineering. For that, we evaluated the ability to adhere freestanding membranes as a patch on bone defects and their osteophilic properties.

Also wound healing processes could be favored with the application of such kind of adhesive systems. Therefore, we investigate the feasibility and effectiveness of using the previous multilayered system to act as a patch to promote wound healing. In this work, besides *in vitro* also *in vivo* experiments were performed (Chapter VIII).

The last experimental work of this thesis merged all the previous strategies described for this thesis. employing biomaterials, LbL, topographical features, adhesiveness and therapeutic cells for articular cartilage repair. Herein, the potential to functionalize freestanding ultrathin multilayer membranes with adipose-stem cells (ASCs) to treat superficial cartilage damages and early stages of osteoarthritis was evaluated. The idea behind materials to be applied for damaged articular cartilage was that it might protect the cartilage surface, shield the tissue from degradative influences from the synovial space (enzymes, inflammatory factors and so on) and reduce additional mechanical damage *in vivo* by reduced fiction while movement. To use ASCs functionalized freestanding multilayered membranes could result in the improvement of the patient’s life quality as these cells are already reported by supporting cartilage tissue repair by reduction of inflammation and/or stimulate chondrogenic differentiation [31]. Adhesiveness and the presence of topographical cues were crucial to determine the potential of the construct. HA-DN, CHT and ALG were combined to produce nanostructured freestanding membranes and it could result in biochemical cues and adhesive properties to this system. Note, that the adhesive properties would be essential to fix the material to the area to treat. Additionally, we also investigated the influence of the presence of nanotopographical features on the performance of the construct and, consequently, on the potential to repair and form cartilage tissue. Besides *in vitro*, also *in situ* tests were performed using human damaged cartilage samples.

Overall, we truly believe that the present thesis highlights the importance of LbL assembly as a building block strategy for biomedical and tissue engineering ends, and the ability to integrate other important biomimetic strategies within LbL. As a result, increasingly complexity can be achieved in a simpler way.

2. References

1. Bhushan, B., Biomimetics: lessons from nature–an overview. *Philosophical Transactions of the Royal Society A: Mathematical, Physical and Engineering Sciences* **2009,** *367* (1893), 1445-1486.
2. Oliveira, M. B.; Mano, J. F., Biomimetic Superhydrophobic Surfaces In *Handbook of Biomimetics and Bioinspiration*, 2014; pp 153-180.
3. Northen, M. T.; Greiner, C.; Arzt, E.; Turner, K. L., A Gecko-Inspired Reversible Adhesive. *Advanced Materials* **2008,** *20* (20), 3905-3909.
4. Susan, L.; Bojun, L.; Zuwei, M.; He, W.; Casey, C.; Seeram, R., Biomimetic electrospun nanofibers for tissue regeneration. *Biomedical Materials* **2006,** *1* (3), R45.
5. Diesendruck, C. E.; Sottos, N. R.; Moore, J. S.; White, S. R., Biomimetic Self-Healing. *Angewandte Chemie International Edition* **2015,** *54* (36), 10428-10447.
6. Zhao, Y.; Sakai, F.; Su, L.; Liu, Y.; Wei, K.; Chen, G.; Jiang, M., Progressive Macromolecular Self-Assembly: From Biomimetic Chemistry to Bio-Inspired Materials. *Advanced Materials* **2013,** *25* (37), 5215-5256.
7. Hermawan, H.; Ramdan, D.; Djuansjah, J., *Metals for Biomedical Applications*. 2011; p 411-430.
8. Treccani, L.; Yvonne Klein, T.; Meder, F.; Pardun, K.; Rezwan, K., Functionalized ceramics for biomedical, biotechnological and environmental applications. *Acta Biomaterialia* **2013,** *9* (7), 7115-7150.
9. Gunatillake, P. A.; Adhikari, R., Biodegradable synthetic polymers for tissue engineering. *European cells & materials* **2003,** *5*, 1-16; discussion 16.
10. Ratner, B. D., Surface Modification of Polymers for Biomedical Applications: Chemical, Biological, and Surface Analytical Challenges. In *Surface Modification of Polymeric Biomaterials*, Ratner, B. D.; Castner, D. G., Eds. Springer US: Boston, MA, 1997; pp 1-9.
11. Isenberg, B. C.; Wong, J. Y., Building structure into engineered tissues. *Materials Today* **2006,** *9* (12), 54-60.
12. (a) Silva, T. H.; Duarte, A. R.; Moreira-Silva, J.; Mano, J. F.; Reis, R. L., Biomaterials from Marine-Origin Biopolymers. In *Biomimetic Approaches for Biomaterials Development*, 2012; (b) Younes, I.; Rinaudo, M., Chitin and chitosan preparation from marine sources. Structure, properties and applications. *Marine drugs* **2015,** *13* (3), 1133-1174.
13. Borges, J.; Mano, J. F., Molecular Interactions Driving the Layer-by-Layer Assembly of Multilayers. *Chemical Reviews* **2014,** *114* (18), 8883-8942.
14. Rodriguez-Cabello, J.; Ribeiro, A.; Reguera, J.; Girotti, A.; Testera, A., 14 - Elastin-like systems for tissue engineering. In *Natural-Based Polymers for Biomedical Applications*, Reis, R. L.; Neves, N. M.; Mano, J. F.; Gomes, M. E.; Marques, A. P.; Azevedo, H. S., Eds. Woodhead Publishing: 2008; pp 374-395.
15. (a) Teeuwen, R. L. M.; van Berkel, S. S.; van Dulmen, T. H. H.; Schoffelen, S.; Meeuwissen, S. A.; Zuilhof, H.; de Wolf, F. A.; van Hest, J. C. M., "Clickable" elastins: elastin-like polypeptides functionalized with azide or alkyne groups. *Chemical Communications* **2009,** (27), 4022-4024; (b) Testera, A.; Girotti, A.; González, I.; bullet, T.; Quintanilla, L.; Santos, M.; Matilde, b.; bullet, A.; Rodríguez-Cabello, J., *Biocompatible elastin-like click gels: design, synthesis and characterization*. 2015; Vol. 26.
16. (a) Costa, R. R.; Custódio, C. A.; Testera, A. M.; Arias, F. J.; Rodríguez-Cabello, J. C.; Alves, N. M.; Mano, J. F., Stimuli-Responsive Thin Coatings Using Elastin-Like Polymers for Biomedical Applications. *Advanced Functional Materials* **2009,** *19* (20), 3210-3218; (b) Shang, Y.; Yan, Y.; Hou, X., *Stimuli responsive elastin-like polypeptides and applications in medicine and biotechnology*. 2013; Vol. 25.
17. Joung, Y.-H., Development of implantable medical devices: from an engineering perspective. *International neurourology journal* **2013,** *17* (3), 98-106.
18. Ruoslahti, E.; Pierschbacher, M., New perspectives in cell adhesion: RGD and integrins. *Science* **1987,** *238* (4826), 491-497.
19. Couto, D. S.; Alves, N. M.; Mano, J. F., Nanostructured Multilayer Coatings Combining Chitosan with Bioactive Glass Nanoparticles. *Journal of Nanoscience and Nanotechnology* **2009,** *9* (3), 1741-1748.

20. Silva, J. M.; Duarte, A. R. C.; Caridade, S. G.; Picart, C.; Reis, R. L.; Mano, J. F., Tailored freestanding multilayered membranes based on chitosan and alginate. *Biomacromolecules* **2014,** *15* (10), 3817-3826.
21. Correia, C.; Reis, R. L.; Mano, J. F., *Multilayered Hierarchical Capsules Providing Cell Adhesion Sites*. 2013; Vol. 14.
22. Silva, J. M.; Georgi, N.; Costa, R.; Sher, P.; Reis, R. L.; Van Blitterswijk, C. A.; Karperien, M.; Mano, J. F., Nanostructured 3D Constructs Based on Chitosan and Chondroitin Sulphate Multilayers for Cartilage Tissue Engineering. *PLOS ONE* **2013,** *8* (2), e55451.
23. Caridade, S. G.; Monge, C.; Gilde, F.; Boudou, T.; Mano, J. F.; Picart, C., Free-standing polyelectrolyte membranes made of chitosan and alginate. *Biomacromolecules* **2013,** *14* (5), 1653-1660.
24. (a) Castner, D. G.; Ratner, B. D., Biomedical surface science: Foundations to frontiers. *Surface Science* **2002,** *500* (1), 28-60; (b) Sell, S. A.; Wolfe, P. S.; Garg, K.; McCool, J. M.; Rodriguez, I. A.; Bowlin, G. L., The Use of Natural Polymers in Tissue Engineering: A Focus on Electrospun Extracellular Matrix Analogues. *Polymers* **2010,** *2* (4), 522.
25. (a) Pavinatto, F. J.; Caseli, L.; Oliveira, O. N., Chitosan in Nanostructured Thin Films. *Biomacromolecules* **2010,** *11* (8), 1897-1908; (b) Croisier, F.; Jérôme, C., Chitosan-based biomaterials for tissue engineering. *European Polymer Journal* **2013,** *49* (4), 780-792.
26. Scott, R. A.; Panitch, A., Glycosaminoglycans in biomedicine. *Wiley interdisciplinary reviews. Nanomedicine and nanobiotechnology* **2013,** *5* (4), 388-398.
27. (a) Curtis, A.; Wilkinson, C., Topographical control of cells. *Biomaterials* **1997,** *18* (24), 1573-83; (b) Yim, E. K. F.; Darling, E. M.; Kulangara, K.; Guilak, F.; Leong, K. W., Nanotopography-induced changes in focal adhesions, cytoskeletal organization, and mechanical properties of human mesenchymal stem cells. *Biomaterials* **2010,** *31* (6), 1299-1306.
28. Lee, B. P.; Messersmith, P. B.; Israelachvili, J. N.; Waite, J. H., Mussel-Inspired Adhesives and Coatings. *Annual review of materials research* **2011,** *41*, 99-132.
29. Oh, Y. J.; Cho, I. H.; Lee, H.; Park, K.-J.; Lee, H.; Park, S. Y., Bio-inspired catechol chemistry: a new way to develop a re-moldable and injectable coacervate hydrogel. *Chemical Communications* **2012,** *48* (97), 11895-11897.
30. (a) Lee, B. P.; Dalsin, J. L.; Messersmith, P. B., Synthesis and Gelation of DOPA-Modified Poly(ethylene glycol) Hydrogels. *Biomacromolecules* **2002,** *3* (5), 1038-1047; (b) Wang, X.; Jiang, Z.; Shi, J.; Zhang, C.; Zhang, W.; Wu, H., Dopamine-Modified Alginate Beads Reinforced by Cross-Linking via Titanium Coordination or Self-Polymerization and Its Application in Enzyme Immobilization. *Industrial & Engineering Chemistry Research* **2013,** *52* (42), 14828-14836; (c) Neto, A. I.; Cibrão, A. C.; Correia, C. R.; Carvalho, R. R.; Luz, G. M.; Ferrer, G. G.; Botelho, G.; Picart, C.; Alves, N. M.; Mano, J. F., Nanostructured Polymeric Coatings Based on Chitosan and Dopamine-Modified Hyaluronic Acid for Biomedical Applications. *Small* **2014,** *10* (12), 2459-2469.
31. (a) Anderson, J. A.; Little, D.; Toth, A. P.; Moorman, C. T., 3rd; Tucker, B. S.; Ciccotti, M. G.; Guilak, F., Stem cell therapies for knee cartilage repair: the current status of preclinical and clinical studies. *The American journal of sports medicine* **2014,** *42* (9), 2253-2261; (b) Gu, X.; Li, C.; Yin, F.; Yang, G., Adipose-derived stem cells in articular cartilage regeneration: current concepts and optimization strategies. *Histology and histopathology* **2018,** *33* (7), 639-653.

II. Surface micro and nanoengineering: Applications of Layer-by-Layer technology as a versatile tool to control the cellular behavior[*]

Abstract

Extracellular matrix (ECM) cues have been widely investigated for their impact on cellular behavior. Among mechanics, physics, chemistry and topography, different ECM properties have been discovered as important parameters to modulate cell functions, including cell adhesion, morphology or migration, activating mechanotransduction pathways that can influence gene expression, proliferation or even differentiation. Particularly, ECM topography has been gaining more and more interest based on the solid evidences that these physical cues can really tailor cell behavior. We overview bottom-up and top-down approaches reported to produce materials capable of mimicking the ECM topography and being applied for biomedical purposes. Moreover, we highlight the increasing motivation of using layer-by-layer (LbL) technique to reproduce these topographical cues. LbL assembly is a simple and versatile methodology used to coat materials with a nanoscale fidelity to the geometry of the template or to produce multilayer thin films composed of polymers, proteins, colloids, or even cells. Different geometries, sizes or shapes can imply different behaviors: effects on the cell adhesion, proliferation, morphology, alignment, migration, gene expression and even differentiation are discussed. Finally, we conclude with an overview of the importance of LbL assembly to produce defined topographical cues on materials against other techniques, highlighting the potential of micro- and nanoengineered materials to modulate the cell function and fate.

Keywords: Extracellular matrix; microfabrication; nanofabrication; pattern; topography; cell behaviour; cell functions and fate.

---

[*] This chapter is based on the following publication: Sousa M. P.; Arab-Tehrany E.; Cleymand F.; Mano J. F., Surface micro and nanoengineering: Applications of Layer-by-Layer technology as a versatile tool to control the cellular behaviour, **2019** (in submission process).

1. Introduction

Conventional LbL assembly is usually based on the sequential and alternatively assembly of oppositely charged solutions onto a substrate [1]. More recently, other less traditional thin multilayer film deposition approaches, often denominated as unconventional LbL approaches have been arising [2]. Among other, coordination-driven films and certain cellular multilayer films, as well as inkjet deposition driven LbL are examples of unconventional LbL methodologies [2b]. Numerous reviews have focused on the driving forces or the materials used for LbL methodologies [3], or on the production and application of 2-dimensional (2D) or 3-dimensional (3D) LbL materials [4]; even though, a review focusing on LbL methodology to fabricate micro and nanoengineered materials is still lacking. Micro- and nanomaterials have been reported in literature by their many advantages over macroscale counterparts. Different industries, from electronics to information technology, environmental, food safety, energy, homeland security and even to medical field, have been exploring micro and nanoengineered materials [5]. In the medical field, that is especially focused in this review, micro- and nanotechnologies are involved in a number of different therapeutics, since drug delivery systems [6] to improved vaccines delivery [7], regenerative medicine and tissue engineering [8].

In biomedical and tissue engineering applications, biomaterials/scaffolds function plays a pivotal part on the development of efficient strategies. One of them can be to mimic essential structural and compositional aspects of the extracellular matrix (ECM), that comprises a mesh network composed of proteins and bioactive agents where the cells are confined into [8b, 9]. The ECM provides structural and mechanical support and modulates central cellular functions, since it presents features across multiple scales capable of interacting with cells and inducing intracellular signalling pathways [9b]. Some differences have been noted between the different tissues at the ECM level; for instance, vessels are composed of amorphous sheets intermittently laden with pits, meshes and grooves [10]; on the other hand, muscle tissue is made up of many muscle bundles, straight and parallel aligned, that are composed at the microscale of hundreds of aligned fibers, organized in packaged myofibril, that are composed of thousands of aligned contractile nanofilaments [11].

Hence different micro- and nanofabrication techniques have been suggested to reproduce some ECM features, fabricating or modifying biomaterials/scaffolds for biomedical and tissue engineering applications. We decided to focus this review specifically on the use of LbL assembly to control physical properties of the material, often reported as a strategy to modulate the cellular behaviour. Among all, the versatility, less expensive character and ability to use a wide range of materials make LbL an interesting technique to exploit for micro and nanoengineering biomaterials. In this review, we also discuss the use of other micro and nanofabrication techniques in combination with LbL to produce surface patterned materials for biomedical and tissue engineering applications.

2. ECM topography

Each tissue of the human body presents specific surface topographical structures from the nano to the microscale. Since tissues have different functions and are exposed to different stimuli and environments, they can be organized in different categories: protective tissues (e.g. skin), electro-active tissues (e.g. heart or neurons), shear-stress sensitive tissues (e.g. blood vessels) and mechano-sensitive tissues (bone or tendon) [8a]. Nowadays, Tissue Engineering and Regenerative Medicine (TERM) has been exploring the complex multi-dimensional and hierarchical organization of tissues, focusing on the interactions between cells and their extracellular environment, pursuing an ideal ECM substitute [12]. Mimicking ECM properties has been recognized as an effective strategy to generate higher levels of complexity of tissue engineering constructs [13], increasing the chances of success. Concretely, surface topography is one of the most relevant properties of the material to control cell behavior and tissue development [14].

Typical tissues sizes are in the range of hundreds to thousands of microns, single cells sizes are typically tens of microns and many subcellular elements like filopodia or transmembrane proteins sizes are at the nanometer scale – see Figure II-1 [15]. Therefore, it is clearly understandable that besides cells respond to microscale patterned surfaces, they are also able to respond to nanoscale features on the materials' surface [14a]. ECM provides an array of interwoven proteins that can provide regulatory topographical cues, depending on the source tissue [16]. Playing with the surface topography at different length scales is crucial to control material-cell interactions, ECM remodeling and cytoskeleton rearrangement, being able to trigger specific cellular responses.

Therefore, the development of patterned scaffolds can tailor cell-substrate interactions [17], providing and stimulating specific biological recognition pathways to control the cytoskeletal organization of the cells [18]. Living systems are hierarchical organized. Single cells are the basic unit of living organisms, and still composed of smaller elements that are imperial to keep cells functional; for instance, cells are composed of lysosomes that break down macromolecules and destroy foreign invaders. Cells are combined in tissues, which are groups of similar cells performing the same function. Analogously, LbL assembly offers the possibility to control at different length scales the hierarchical organization of the developed materials, as shown in Figure II-1.

Therefore, LbL assemblies have been used as nano and microfabrication techniques, to produce multi-dimensional materials that can trigger specific cell response and be applied for different type of tissues. This review firstly addresses the most relevant nano- and microfabrication techniques, that combined with LbL technique, simplifies the process of mimicking the complexity of the tissues. Further in the review, we discuss how LbL-based patterned materials can trigger different cellular responses, highlighting the importance of physical cues on the surface of materials to control specific functions of different cell types.

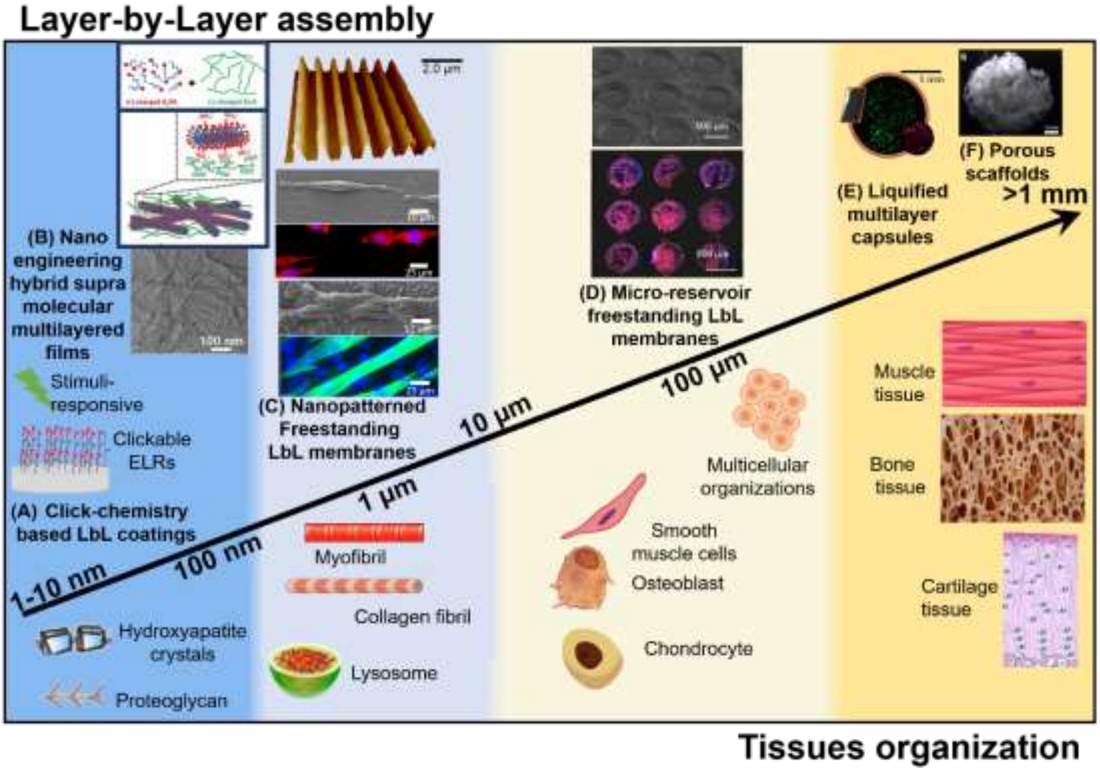

Figure II-1. Multiscale hierarchy of different representative tissues. The creation of the macroscopic-scale tissues requests a suitable architecture ranging from nanometer- to micrometer-scale elements, up to millimeters. For instance, actin-myosin molecular motors are organized as overlapping structures that are assembled forming myofibrils. Cardiomyocytes are organized into aligned sheets composed of myofibrils, creating the myocardium tissue. LbL assembly is a versatile technique capable of creating multiscale materials, hierarchically organized. Some examples of LbL-based materials applied for biomedical and tissue engineering fields are here represented, according with the working range size: (A) click-chemistry-based LbL coatings, enabling the assembly at [19], (B) nanoengineering hybrid supramolecular multilayer films [20], (C) nanopatterned freestanding LbL-based membranes [21], (D) micro-reservoir freestanding LbL-based membranes [22], (E) liquified multilayered capsules [23] and (F) porous scaffolds [24].

3. Fabrication techniques to obtain micro and nano patterned surfaces

Progresses in surface patterning of materials at micro- and nanoscales opened new knowledge about material-cell interactions. Several methodologies have been reported to produce ordered or randomly structured surface topographical features, at different length scales. Bottom-up approaches can be used with different polymers, being a cost-effective way to create well-organized topographies [25]. On the other hand, top-down approaches usually involve the application of external stimuli like heat, UV-exposure or pressure to produce thin polymer films with specific geometries [25]. Advanced micro and nanofabrication techniques have been developed with increased resolution and precision, being often combined with different deposition techniques [25]. Among all, LbL assembly has been suggested as an interesting adjunct to different micro and nanofabrication strategies, offering a hierarchical control of the construction of the multilayer film.

LbL technique was firstly described in 1991, in a work made by Hong and Decher [1a], as a facile and versatile bottom-up method to create multilayer films. Note that besides electrostatic-driven deposition of cationic and anionic microparticles had been already suggested in the middle of 1960's year by Kirkland [26] and Iler [27], it were Hong and Decher that many years later refreshed this mechanism and developed a simple approach based on alternating electrostatic deposition of a wide range of polycation and polyanion species onto a substrate and named it LbL [1a]. Initially, LbL was suggested to coat substrates with bioactive species, offering higher control and versatility compared to other deposition and modification techniques: from polymers, to colloids, to proteins, to bioactive molecules and even to cells, different materials have been used, depending on the purpose [4c, 28]. By playing with different raw materials (composition), their concentration and adsorption time, the solvent composition or even the type or shape of the underlying substrate, LbL methodology have some control of physicochemical, morphological, mechanical and even biological properties of the film [29]. This technology has been mainly suggested to assemble multilayered films through electrostatic interactions, but, in the last years other type of driving forces have been also proposed, such as covalent, hydrogen or even click chemistry [30]. Therefore, LbL can be use with a wide range of materials as colloids, synthetic and natural polymers, proteins, growth factors, cells or even DNA.

By carefully combining bottom-up and top-down techniques with selected materials, LbL films can be effectively patterned with a sub- micrometer resolution. The use of this technology can simplify both lateral and vertical patterning at micro- and nanoscale, allowing the development of patterned materials for numerous applications, particularly for biomedical and tissue engineering applications. Lithography [31], inkjet [32] printing and simple stacking of bio-based materials [33] were some techniques already used together with LbL technique, to produce patterned materials. The patterning step can be previous or posterior to the LbL assembly, and the final product can be a simple coating or a freestanding material, highlighting the versatility of this technique.

In this section, we firstly introduce micro- and nanofabrication techniques that can be used in combination with LbL assembly, discussing the basic concept of the technology, some of the advantages and limitations of each one and the ability to be combined with LbL. A schematic representation of some of these micro- and nanofabrication techniques is presented in Figure II-2, as well as the respective comparison in terms of resolution with natural systems.

3.1. Bottom-up approaches

3.1.1. Electrospinning

Electrospinning consists in the application of a high electric field between a charged polymer solution and a counter electrode, forcing the solution to pass through a small diameter syringe nozzle, creating a fiber [34]. The resulting electrospun fiber mats are characterized usually by large surface areas, with varying levels of porosity [34b]. Depending on the purpose, aligned fibers or random non-woven mesh fibers can be produced using this technique, with several centimeters down to tens of nanometers; aligned or random fibers have been found to mimic natural tissues architecture [35]. To create align structures using an electrospinning methodology, alternative collectors should be designed.

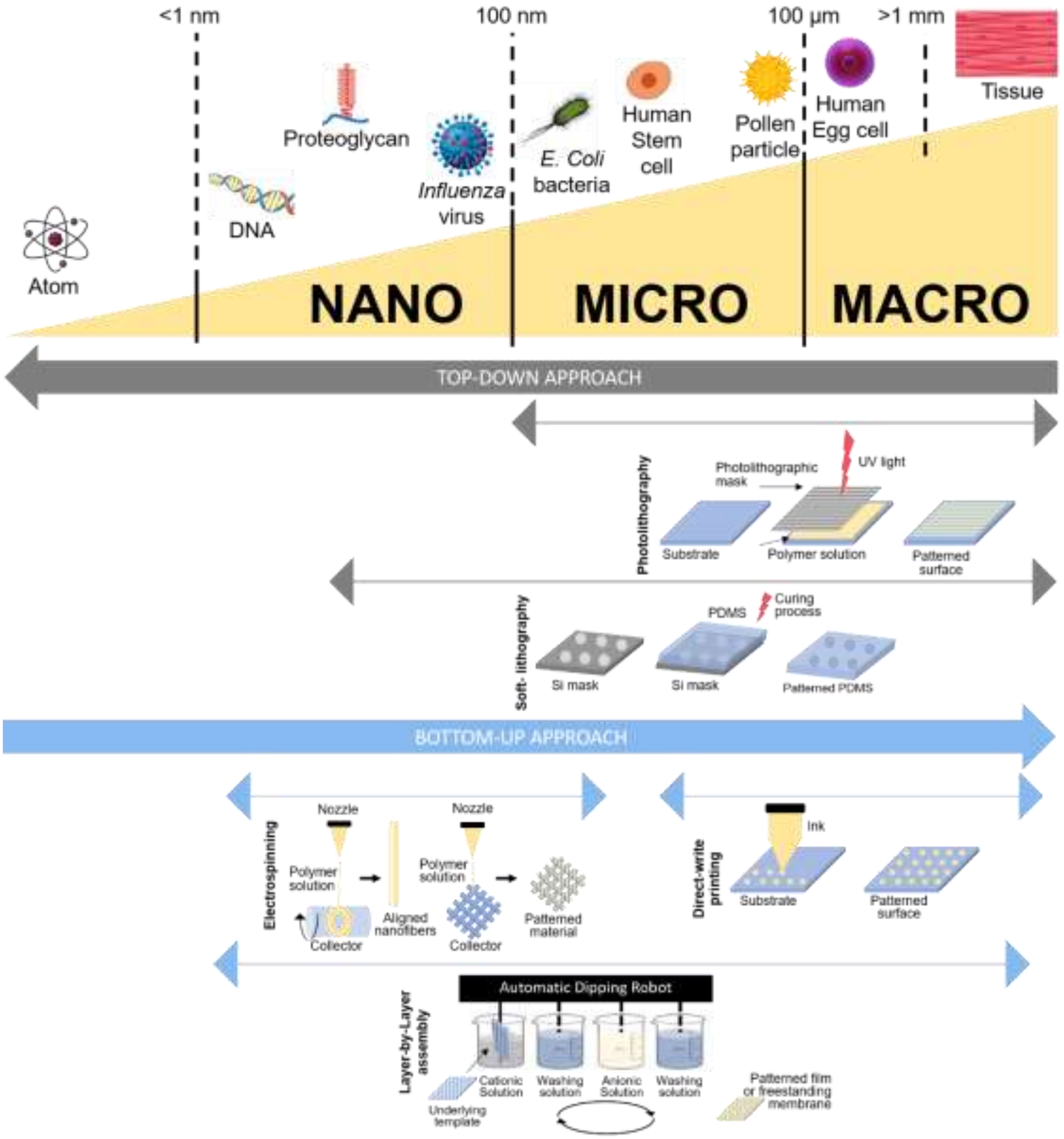

Figure II-2. Living systems are organized in different levels, with increasing complexity. The most representative micro– and nanofabrication methods are represented in terms of range resolution and compared with natural systems at different scales of organizational levels. LbL appears as a promising technique to create micro and nanoengineered materials due to its low cost, versatility and remarkable ability to produce structured materials from nanometer to macrometer length scales. To ensure the fabrication of a well-defined pattern, LbL technique is usually combined with other techniques, such as soft-lithography or direct-write/inkjet printing.

For instance, a hemispherical non-conductive device with a metal pin in the center and a cooper wire around could be used as a collector to originate organized nanofibrous matrix. Kim *et. al.* [36] fabricated a 3D hemispherical and transparent nanofibrous scaffold using this strategy, where the fibers were radially aligned. Such kind of materials could be useful for the treatment of ocular tissues, guiding the direction of collagen and cell action filament in the ECM. Another template collectors can result as a stainless-steel mesh; Yazhou [37] fabricated electrospun nanofibers meshes composed of biodegradable poly (ε-caprolactone) (ε-PCL), with well-organized architecture and pattern. Higher proliferation rates were found for patterned ε-PCL electrospun nanofibers when culture with MC3T3-E1 cells, where they grew and elongated along the fibers orientation. However, for biomedical and TERM applications sometimes it is necessary to modify the surface of those electrospun nanofibers. A possibility is to coat the surface of the material with cytophilic polyelectrolyte multilayers, immobilizing ECM proteins as collagen (COL) on the surface of the fibers. Chitosan (CHT) and collagen type I (COL I) were assembly together using LbL to create a biomimetic coating on nanofibrous matrices fabricated by electrospinning of PCL and cellulose acetate (CA) together [38]. Also, isotropic and anisotropic electrospun poly(ε-caprolactone) (PCL)/cellulose nanofibers were modified with the LbL deposition of chondroitin sulphate (CS) and COLI to engineer functional vascular structures [39]. In fact, the development of a LbL-structured nanofibrous mats improved the vascularization *in vivo*, up-regulating the expression of specific ECM proteins, which indicates the potential of the material to restore the structure and function of wounded skin or to be used as implantable vascular grafts.

Other bioinspired systems can benefit with the combination of electrospinning and LbL techniques. For example, biomimetic superhydrophobic surfaces can be produced by modifying electrospun nanofibrous membranes with LbL structured films; titanium dioxide (TiO_2) nanoparticles and poly(acrylic acid) (PAA) were deposited above nanofibrous membranes to imitate the rough surface of nanosized grooves along the silver ragwort leaf fibre axis [40].

The simplicity of the technique, the ability to control the process and the easiness to scale-up make electrospinning a very attractive technique to produce micro to nanofibers from a wide range of biodegradable polymers. LbL can be an advantageous complement to electrospinning to obtain biomimetic nanopatterned materials.

3.1.2. Colloidal particles

The need of inexpensive, relatively fast and efficient processes to produce highly precise patterns at the nanometer scale is still a challenge in nanofabrication field [41]. Different methodologies can be employed to produce colloidal particles, such as suspension-, emulsion-, dispersion-, and precipitation-based polymerization [41]. The chosen methodology depends on the selected material, usually silica [42] or polystyrene (PS) [43]. Adjusting the environmental conditions, colloidal particles can be used as building blocks to form colloidal nanostructured surfaces, particularly by a self-assembly process [41, 44]. As that, bottom-up approaches based on bioinspired self-assembly have been reported, with colloidal particles being assembled and organized into more complex architectures [41].

LbL assembly can be combined, in different ways, with colloidal particles to produce micro- or nanopatterned surfaces. These particles can be coated with different polyelectrolytes to produce stable multilayer micro- or nanostructures [45]. Other strategies can be envisaged using colloidal templates: Caruso and Moehwald [46] suggested the using of colloidal particles as substrates for nano-scaled LbL assemblies. Here, the size of these micro-templates ranges from tens of nanometers to sub-millimeters. Hollow capsules of the multilayered assemblies can be obtained by selective dissolution of the core, creating a kind of microreactors. In fact, crystalline arrays of silica colloidal particles can also be used as porous templates to produce three-dimensional ordered macroporous (3DOM) materials, commonly referred as inverse opals [47]. These structures are a result of the removal of the template following LbL deposition.

The LbL assembly of colloidal particles can also represent a patterning strategy, being driven by electrostatic interactions and hydrogen bonding [48]. Colloidal particles could be selectively deposited on patterned films creating colloidal-containing microporous multilayered films [49]. Further, LbL deposition of colloidal nanoparticles on a patterned LbL film was used as a versatile way to obtain composite colloidal structures capable of being adapted to different shaped patterned surfaces [50].

3.1.3. Phase-separation

Phase-separation technique comprehends the immiscibility of two specific polymers capable to induce a spontaneous polymer de-mixing, creating nano- or microtopographical features [51]. Few studies were still reported combining phase separation with LbL assembly [49, 52]. Being an easy to perform and control technique, phase separation can allow the patterning of non-ordered features [53]. Therefore, LbL films prepared from weak polyelectrolytes can be deposited on the top of the porous phase-separation based substrate [54]. When a porous substrate is used, a very rapid deposition of polyelectrolytes can result in the formation of an LBL film that lays above the porous substrate, but not covering the walls of the pores. This results in a micropattern LbL structure [52, 54]. On the other hand, under specific stimuli LbL films exposed to a phase-separation process can result in the formation of microporous multilayer membranes. For instance, poly(acrylic acid) (PAA) and poly(allylamine) (PAH) multilayered films when immersed into acid solutions (pH ≈ 2.4) experimented an irreversible transformation in terms of film's morphology, resulting in a patterned structure at the microscale length [49].

3.1.4. Direct-write/inkjet printing

Direct-write/inkjet printing take advantage of a nozzle or a printing head to spatially deposit inorganic or organic small molecules, proteins, nuclei acids or even cells onto specific areas of a certain surface [55]. In this context, direct-write or inkjet printing can be useful as a post- processing technique to complement LbL. Different polymeric inks have been suggested to patterned materials; for instance, a novel polymeric ink composed of physically entangled poly(acrylamide) (PAM) chains in a photopolymerizable acrylamide solution could be directly patterned in air by a combination of direct-write assembly and in situ photocuring above an already formed multilayered film [56]. The major advantage of this ink is that it can be used in a wide range of surface chemistries. This combined technology enables to create microstructure features in both planar and 3D forms of LbL systems that could be applied as optical sensors, stimuli-responsive soft materials or structures for TERM. Also, ink-jet based LbL assembly was already suggested to create a diversity of features on the multiple self-regulating deposition spots of a potential biological surface [57]. By alternating solution droplets from ink reservoirs that were filled with positively or negatively charged materials, the authors produced multilayered nanofilms [57]. Using such technology, it is possible to specify size, shape, and materials for each desired spot.

Direct write printing can be combined with LbL manufacture, being considered a simple and powerful strategy to obtain complex structures. Well-defined micropatterned features with nanometer thickness and microscopic lateral dimensions are a result of this combining LbL assembly and direct write printing, respectively [32, 58]. Nowadays, higher lateral resolution has been pursued using this combined strategy, particularly by reducing the nozzle dimension and limiting the droplet spreading on highly hydrophobic surface. For instance, microscale pH responsive poly(vinylpyrrolidone)/poly(methacrylic acid) (PVPON/ PMAA) LbL were directly printed with dots, that diameter decreased from 100µm to 40µm with the number of bilayers ranging from 2 to 10, inducing an increasing of the thicknesses from 50 to 500 nm [59].

3.1.5. Nano-and microcontact printing

Nano- and microcontact printing is based on the pattern transfer from a template to a specific material surface [60]. The fabrication of organic and inorganic microscale patterned surfaces have increasingly interest in medical and electronics applications. For instance, Yang and Choi [61] suggested a versatile method to create silica patterns under mild conditions: poly(diallyl dimethyl ammonium chloride) (PDADMA)/ sodium polystyrene sulfonate (PSS) were deposited above patterned surfaces, obtained by microcontact printing. Biomimetic silicification occurred at PDADMA/PSS-presenting areas. This method is not restricted to silica and can be extended to other inorganic materials. LbL technique enables that all the processes can be made under mild conditions and aqueous solutions.

3.2. Top-down approaches

3.2.1. Lithographic techniques

Photolithography is a widely and well-known micro and nanofabrication technique, that was mainly developed in the microelectronic industry but rapidly applied in other fields. Briefly, in this technique there is a photoreactive material that is coated onto a substrate, typically a Si wafer. Using a mask with micro or nanoscale features, previously designed on a computer-aided assisted (CAD) software, it is possible just expose selective areas of the photoreactive material. Therefore, upon ultraviolet light (UV) exposure, the photoreactive material can polymerize, degrade or crosslink with the unwanted parts of the material being dissolved in an organic solvent [62]. The resulting patterning can be used as that or can act as a master. Different resolutions can be achieved with this technique, depending on the wavelength of the UV-light and the type of mask used, ranging from about 5 nm [63] to thousands of microns [64]. Nowadays, photolithographic technique has been increasingly applied for biomedical and TERM purposes and used in numerous investigations about the influence of nano- and micro-scale topographical features on the cellular behaviour. For instance, Qi *et. al.* [60] used photolithography to fabricate patterned Si wafers with different topographical features: linear, circular and dots micropatterns with different sizes were compared considering their ability to enhance neuronal differentiation. Photolithography can be used alone, being the patterned wafers the testing surface, or combining with other deposition techniques, as LbL. In biomedical and tissue engineering photolithography and LbL were combined to investigate how cells react to different micropatterned polymeric films [31] Lithography offers he ability to create precise and even complex two-dimensional (2D) or three-dimensional (3D) structures at nano- and microscales. In turn, LbL enables to play with a wide range of materials and quite precise reproduction of the shaped-structures presented designed by topography. Their combination results in a very versatile strategy to produce patterned biomaterials. Overall, photolithography-assisted LbL allows the formation higher resolution templates where polyelectrolytes can be deposited, creating complex patterns that, depending on the chosen materials, could be applied for biomedical and TERM purposes. The LbL-based multilayers can be a part of the systems together with the underlying template or can be detached, originating a self-supported material.

Soft lithography represents a family of micro and nanofabrication techniques that take advantage of a soft and flexible elastomer material, often polydimethylsiloxane (PDMS) to create a micro to sub-microscale features onto a material's surface [65]. Being an advanced lithographic methodology, this technique also involves the production of a master template that is used to emboss the structures onto the elastomer. Although, soft lithography can overcome the limitations of photolithography with curved or non-planar surfaces [62b]. Patterned PDMS can be used within other techniques as micromodeling, nano- and microcontact printing, embossing, microfluidics and LbL. Combining soft-lithography with LbL can occur in different ways: printing, molding or embossing the PDMS structure on the surface of the multilayer film material or constructing a LbL-based system above the patterned PDMS substrate. For instance, polyelectrolyte multilayers presenting an array of microgrooves were already produced by layer-by-layer assembly on patterned PDMS molds and compared with polyelectrolyte complexes prepared in the same conditions [66]. For biomedical and tissue engineering applications, microstructured PDMS substrates can be functionalized with ECM components; poly(L-lysine) (PLL)/ hyaluronic acid (HA) LbL films were deposited above microstructured PDMS templates to investigate muscle cell alignment and differentiation[67]. Freestanding LbL membranes can be obtained [22], as a result of the combination of soft lithography with LbL assembly of CHT and ALG; in the end, these patterned membranes were easily detached from the PDMS template, creating an unique platform for medical applications.

3.2.2. Microfluidics

A microfluidic substrate offers a set of fluidic unit operations, prepared to be easily combined with a well-defined microscale design. This platforms are typically used for miniaturization, automation and parallelization of biochemical processes, using the resulting channels to deliver a specific solution to restricted areas of the substrate [68]. The elementary microfluidic unit is a microvalve, that is usually composed of a planar glass substrate and an elastomeric layer containing the fluidic microchannels [69]. One of the advantages of this technology is the fact that two or more streams of laminar flow can be generated, connected and managed, providing a unique technology to pattern cells and their environments [68, 70].

Polymer microscale materials patterned with grooved microstructures can be produced using a microfluidic system. In this context, Kang *et. al.* [71] reported the fabrication of alginate microfibers patterned with grooved microstructures, by introducing a sheath fluid with a high-speed flow rate. Grooves could be engraved on the surfaces of the flat fibers in the longitudinal direction, with effective control over the number and dimensions of micrometer-scale. The effectiveness of the technique was confirmed by SEM observation. Microfluidics can be also used to pattern 3D monolithic microscale structures made of multiple type of materials inside a microchannel. Briefly, the authors [72] used confocal scanning or conventional fluorescence microscopy to polymerize selected regions of a photocurable material, and microfluidics to automate the delivery of a series of washes and photocurable reagents. Upon completion of these cycles, it was possible to produce aligned 3D microstructures with different geometries, size scales (up to 1 mm^2), and materials.

Mimicking 3D chemical and particularly spatial architecture and composition of native tissues is still a challenge for microfluidics. As that, LbL can be combined with microfluidics, resulting in a powerful tool to study how spatial features can control different function of cells. Biopolymer solutions have been employed for the creation of 3-D patterns inside channels. For instance, a capillary flow -based microfluidic device was suggested to produce different multilayer films, creating a kind of high-throughput system of LbL films. The resulting LbL-coated microfluidic platform has a great potential to study the behaviour of the cells [73].

4. LbL assembly to obtain micro- and nanopatterned surfaces

Until now, there are many reviews on LbL technology [2b, 4c, 28b, 30, 74] focusing not only on the chosen materials or the driving forces of the deposition but also on the control of the film properties or on their specific applications. Instead, this review focuses on LbL approaches to produce multilayer films with a defined topography at micro- or nanoscale- see Figure II-3 for some schematic examples. As already referred, patterned multilayers can be created by constructing the multilayers above a pre-patterned substrate, fabricated using the abovementioned techniques, or by modification of an already prepared LbL-based material [21-22]. The pattern is engraved in the multilayer film during or after the deposition of the polymeric chains, with a sub-micrometer fidelity. The LbL assembly of 3D bio-based materials above patterned substrates can be capable of creating 3D complex architectures, composed of different type of cells and ECM proteins [33].

The ability to control vertically and horizontally different properties of the film makes patterned LbL films excellent substrates to apply in optoelectronic [75], drug screening [76] or even tissue engineering [77] fields. Therefore, to be able to combine the ability to tailor the properties of the film with the possibility of having a patterned topography, some variations have been applied to conventional LbL using flat underlying substrates[78]. An overview of the fabrication, characterization and properties of patterned LbL films is now presented.

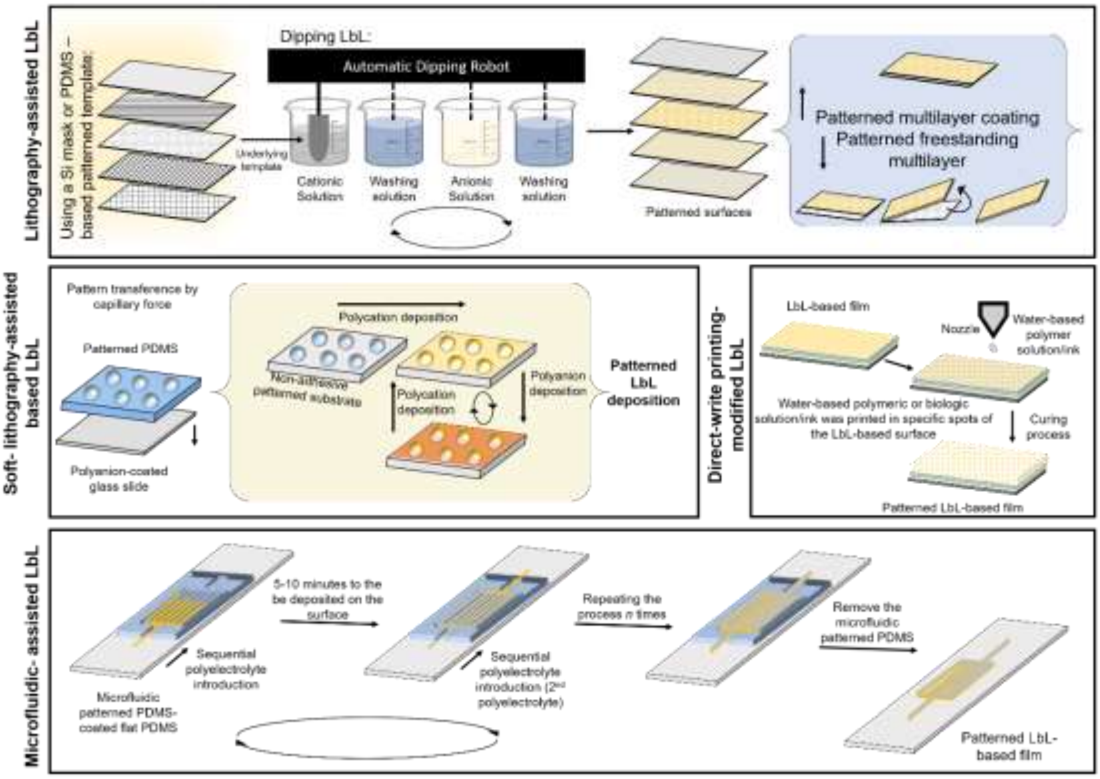

Figure II-3. Examples of LbL-based strategies to produce multilayer patterned materials. These strategies range from conventional (dipping LbL) to non-conventional LbL approaches and are representative of the existent LbL-based methodologies to fabricate nano- or microengineered materials. Conventional dipping LbL assembly can be performed with already patterned underlying substrates (made by lithographic techniques or bought as that). In the end the LbL film can be used as a freestanding material/membrane or a coating. A soft-lithography based LbL strategy can derivate from the polyelectrolyte deposition above patterned PDMS substrate: different ECM proteins can be deposited above the patterning material to produce a biologically-inspired system. Direct-write and inkjet printing can be directly used to pattern LbL-based films. Microfluidic PDMS can be used with different polyelectrolytes to create a patterned LbL film, that resembles the channel path.

4.1. Micropatterning strategies using the LbL assembly

Microfabrication methodologies are a standard strategy in the electronic industry, but also for biomedical and tissue engineering fields, especially to investigate how the surrounding environment influences cell processes. The microscale structures can be built within the bulk of the material or just on the surface of the substrate, using techniques as photolithography, soft lithography or film deposition. As refereed in the previous section, LbL has been combining with other techniques to obtain micropatterned structures.

In this context, different approaches can be trailed. A micropatterned LbL system can be attained by depositing a LbL nanolayers above a micropatterned substrate or by modifying a LbL film with microscale features. For instance, using a microfluidic device, it is possible to generate gradients of biochemical and physical cues on PEM films. Hyaluronan (HA) and poly(L-lysine) (PLL) nanolayers were deposited above a glass slide [79]. This system was placed in contact with a PDMS microfluidic device containing straight and parallel microchannels to spatially modify the polyelectrolyte multilayer with specific biomolecules (see Figure II-4A). After that, the PDMS microfluidic device removed and it resulted in a PEM film with a micro-gradient of the biomolecule of interest. LbL technique can also be used to construct a multilayer system above a micropatterned substrate, that can be further removed. Figure II-4B represents a LbL approach to fabricate sculptured multilayer film. Lin *et. al.* [80] firstly produced a sacrificial micropatterned substrate, made of PS, by using capillary transfer microprinting technique. Then, the LbL film was fabricated above this substrate and in the end the process the polystyrene material was released by dissolution, obtaining a square micropatterned LbL membrane. The most usual strategy to produce micropatterned LbL structures is based on the combination of lithographic substrates followed by LbL deposition. Another strategy is represented in Figure II-4C, where a glass substrate was firstly with a pre-layer of self-assembled polyelectrolytes [81]. Then, a photoresist pattern was placed right above and the LbL technique was employed to construct a gelatin-fibronectin film. Finally, a liftoff approach was performed to remove the photo-resist and obtain the microfabricated multilayer film. Chien *et. al.* [82] produced LbL multilayer films composed of PAA/PAM with interwoven PAA conjugated with 4-azidoaniline. Covering the film with a photo mask and applying a UV irradiation, the uncovered areas were crosslinked, and the covered areas were then rinsed away with alkaline water; this resulted in a micropatterned surface (see Figure II4-D). Also, self-assembly monolayers (SAMs) have been reported to fabricate micropatterned materials: [83] SAMs functionalized with specific end groups (with the ability of promoting or preventing adsorption) were selectively attached to a metal oxide surface. Then, during the LbL assembling specific areas promoted adsorption of the polyions while the remaining areas prevent adsorption. This resulted in a micropatterned thin multilayer film (see Figure II-4E).

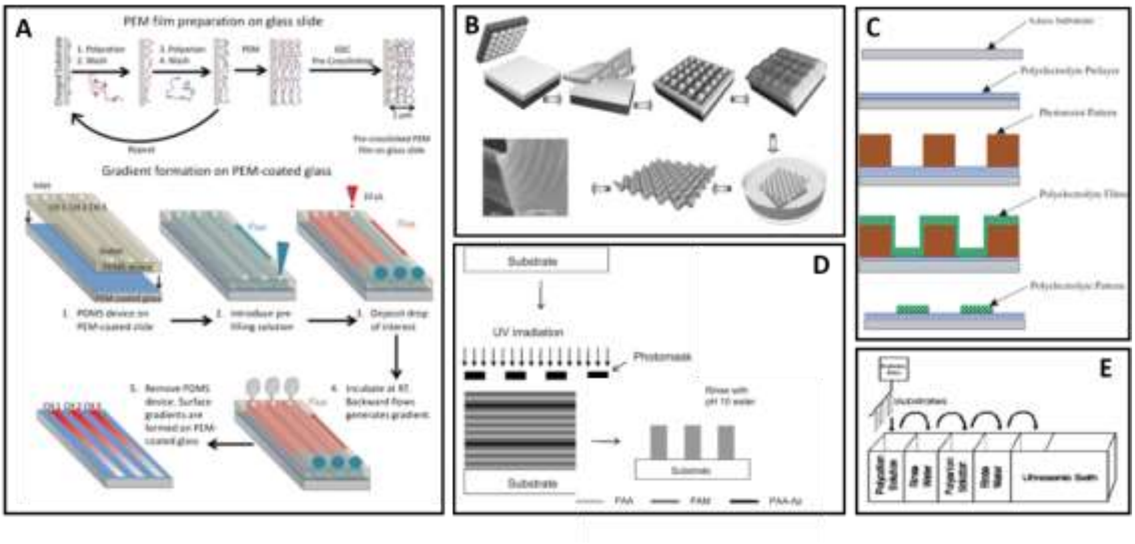

Figure II-4. Schematic representation of some examples of microfabrication methodologies to produce patterned LbL-based materials. A) Polyelectrolyte multilayer (PEM) film construction on a glass slide and the formation of a surface gradient of biomolecules on PEM films [79]. B) Fabrication of sculptured LbL films by combining microstamping and sacrificial templates and scanning electron microscopy (SEM) image of the freely suspended LbL film with a square pattern [80]. C) Self-assembling of PEM on a glass substrate after lithography [81] D) Micropatterned polyelectrolyte multilayer after UV exposure films. Deposition of PEM films on amino-glass, followed by UV exposure [82]. E) Cycles of the LbL process using an adapted slide stainer, producing as result a film with one polyion pair [83].

Table II-1 resumes some of the most important works reporting LbL assisted methodologies to obtain patterned surfaces at the microscale level.

Table II-1. Literature survey of some of the existent works on microscale patterned materials, produced by single or combined LbL technique, highlighting the type of features, the respective dimensions and the used materials

Feature type	***Dimensions***			***Material***
	Width/ Diameter	**Gap/ spacing**	**Depth/ height**	
Organized fiber mesh	200µm	400µm	-----------	PCL scaffold coated with modified hydroxyapatite nanoparticles and collagen type I [84]
Pillars	1.25-9µm	18µm	2.5µm	$(PDAC/SPS)_{10}$ coated PDMS [77]
Grooves	6.5/69µm	3.5/ 43µm	1.29-0.109µm	Glass slides coated with PAA/PAH multilayer films, that were then imprinted [85]
Tuned well arrays	500µm	200µm	38µm	Freestanding $(CHT/ALG)_{100}$ multilayers patterned with tuned well arrays and crosslinked with genipin [22]
Stripes	------------	------------	---------	Patterned multilayer films $(DAR/PAA)_{10}$ [86]
Stripes/ Circles	~50µm/ 300µm	~50µm/ 200µm	----------	UV-irradiated $(PAA/PAM)_{10}$ films with different PAA–Az densities [82]
Different features	1-100µm	------------	---------	$(CHT/SWNT)_n$ and $(CHT/AuNP)_n$ LBL film deposited above glass slides [75]
Ridges	~6µm	~4 µm	0.05-0.5µm	$(SPS/PDAC)_n$ multilayer films above COOH SAM surface [83]
Stripes/ Nano particles	5µm/ 78 and 150 nm	------------	----------	Patterns of multiple types of nanoparticles on one 4-inch Si wafer coated with $[(PDDA/PSS)_2\ (PDDA/\ PS)]$ LbL film [87]
Circles holes	100µm	------------	0.06µm	Patterned cell culture on HA/collagen glass surface [88]
Cylindrical holes	15-150µm	------------	----------	HA/PLL layering approach to pattern co-cultures [33]
Ridges	2.5µm	------------	0.160 µm	(MPS/PPV) sculptured LbL films [80]
Squares	20µm	~80µm	----------	sPLA2/gelatin, sPLA2/PLL and sPLA2/BSA substrates coated with $(PDDA/PSS)_3$multilayer films [89]
Stripes	80/100 µm	240/300 µm	0.06/ 0.15µm	Patterned substrates coated with different LbL film combinations: $(PSS/PDDA)_5$, $(PSS/PDDA)_{10}$; $(CS/PEI)_4/CS$, $(CS/PEI)_9/CS$; $(PSS/PEI)_5$, $(PSS/PEI)_{10}$; $(PSS/Collagen)_5$, $(PSS/Collagen)_{10}$; $(PSS/PEI)_4/PSS$, $(PSS/PEI)_9/PSS$ [90]
Different features	Until 25 µm	------------	0.007-0.127 nm	sADH patterns on a PEM (10.5 PDAC/SPS bilayers) coated glass substrates [76]
Stripes/ Squares	60/80/ 100µm	------------	---------	$(PSS/TR\text{-}PAH)_2/(gelatin/TR\text{-}PAH)_4$/gelatin and $(PSS/FITCPAH)_5$/fibronectin patterned substrates [81]
Stripes	25/50/ 150µm µm	------------	0.03-0.2µm	Micropatterned PEM $(PAH/PSS)_5$ and $(pARG/DXS)_5$ coated glass [91]
Grooves	5/10/30/ 100µm	5/10/30/ 100µm	4µm	Micropatterned PDMS coated by a $(PLL/HA)_{12}$-PLL multilayer film [67]
Pyramids	Base 250µm	------------	900µm	Microneedle arrays coated with DNA-carrying $(PS/SPS)_n$-(Poly-1/Cy3-pLUC) $_n$PEMs films [92]

4.2. Nanopatterning strategies using the LbL assembly

With the progress of technology, the search of increasingly controlling size and miniaturization triggered the development of nanofabrication techniques, which integrates the production of materials, components or features down to the nanoscale. Nowadays, advances on nanofabrication relies on the scalability, controllability and reliability of even smaller features. The different nanofabrication methods are usually classified into bottom-up and top-down approaches. For the bottom-up, nanoscale materials are constructed from atomic or molecular units that can grow or be self-assemble into more complex structures [93]. This usually relies on deposition methodologies and molecular self-assembly processes. On the other hand, for the top-down approach, nanoscale structures are constructed through the controlled removal of materials from larger or bulk solids, often produced by lithographic techniques or chemical-based processes. Micro to nanoscale patterned surfaces can be also produced by combining lithographic and LbL technologies, with the ability of integrating different type of materials; different resolution can result from using different materials. Multilayers composed of chitosan, single-walled nanotube (SWNT) and gold nanoparticles were assembled above glass slides (Figure II-5A1) [75]; then, direct-write maskless lithography was used to produce for instance prototypal concentric spiral pattern from the multilayer film nanocomposite – see Figure II-5A2. The authors reported that gold nanoparticle-based films had better accuracy and higher resolution in direct-write patterning than SWNT films, probably due to the granular morphology rather than fibrous nature of the SWNT.

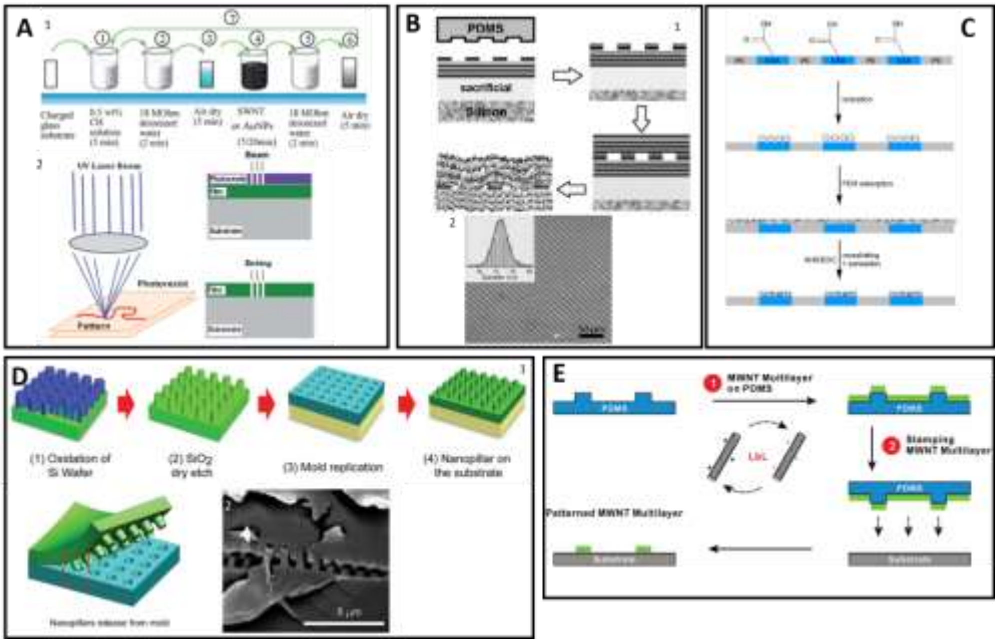

Figure II-5. Schematic representation of some examples of nanofabrication methodologies already reported in literature to produce patterned LbL-based materials. A1) LbL composite synthesis using CHT and SWNTs, considering that the assembly of the gold nanoparticles multilayers followed the same basis [75]. A2) Direct-write (maskless) lithography and patterning process [75]. B1) Polymer-on-polymer stamping fabrication of a nanomembrane containing patterned gold nanoparticle arrays using a PDMS stamp [94]. B2) Large-area SEM image of gold nanoparticle arrays on a PAH/PSS on a Si substrate, with a diameter histogram of gold nanoparticles in the inset [94]. C) PAH/PAA multilayer patterning on cross-section surfaces of PEM films [95]. D1) Si master-template formation and double replication to construct nanopillars on the target substrate [96]. D2) SEM image of the cross-section between the nanopillars and the mold displaying spontaneous detachment of the nanopillars from the mold walls after curing [96]. E) MWNT multilayer pattern transfer process: LbL assembled MWNT multilayer directly on top of patterned PDMS was stamped onto the receiving substrate [97].

Table II-2 resumes some of the few works reporting LbL assisted methodologies to obtain patterned surfaces at the nanoscale level.

Table II-2. Literature survey of some of the existent works on nanoscale patterned materials, produced by single or combined LbL technique, highlighting the type of features, the respective dimensions and the used materials

Feature type	***Dimensions***			***Material***
	Width/ Diameter	**Gap/ Spacing**	**Depth/ height**	
CNTs-based matrix	1710nm	--------------	----------------	Free-standing matrix based on $[(PEI/MWNTs)_5(PEI/PSS)]_n$ [98]
Grooves	Ranging between 650-850nm	~500nm	Ranging between 200-500nm	Nanogrooved freestanding (CHT/CS) multilayer membrane [99]
Columns	150nm	--------------	1-2µm	PEM-assisted fabrication of non-periodic silicon nanocolumn substrates [100]
Fibers	392-541nm	--------------	----------------	Biomimetic nanofibrous matrices via co-electrospinning of PCL/CA coated with CHT and type Ⅰ collagen multilayer film [101]
Stripes	500 nm	--------------	----------------	PEMs of PAA/PAH deposited onto nanostriped surfaces, generated using the cross-section surfaces of EAA/LLDPE multilayers [95]

5. Applications in the biomedical and TERM fields

The first evidence of cell response to topographic features appeared in 1911, resulting from the experiments of Harrison *et. al.* [102]; it was found that cells grown within the fibers of a spider's web. Almost 100 years after, Curtis [103] reported that cells are for sure sensitive to topographical sub-millimeter features. Different nano- to micro-sized geometrical features presented on material surface's topography were investigated as capable of inducing specific cell responses. Notwithstanding, different cell types can give different responses to similar stimuli [14b, 104], as discussed along the next sections.

Micro and nanopatterned LbL-based surfaces have been nowadays suggested for biomedical and TERM purposes and can overcome some drawbacks presented by other fabrication techniques, as already discussed above. In this review, more than discussing the different approaches to obtain lateral patterned surface engineering using LbL approaches, we also highlight possible cellular responses to such kind of surfaces.

Different cellular response can result from these micro or/and nano topographical stimuli: surface micrometric topography are generally related with cellular adhesion, morphology, migration and organization while nanoscale patterned substrates are more prone to influence cell functions, as proliferation, differentiation, alignment or gene expression [105]. Parameters like the patterning features' dimensions, thickness, shape or repeating space as well as the presence or not of specific immobilized molecules are responsible of affecting the cellular response.

Cell adhesion is the first cellular event that responds to microenvironmental cues, guiding action and microtubule networks assembly and orienting the construction of cell internal architecture and establishing cell polarity [106]. Consequently, the resulting spatial organization regulates cell growth and differentiation and the intercellular coordination propagates spatial information to influence the mechanical and functional activity of the tissue [106-107]. Figure II-6 shows some examples of LbL-based methodologies to produce micropatterned surfaces, particularly for biomedical and TERM applications. Figure II-6A represents an investigation reported by Picart *et. al.* [67], where it was suggested the engineering of muscle tissue using microstructured polyelectrolyte multilayer films made by a LbL methodology. A PDMS substrate with a biomimetic PEM coating composed of PLL and hyaluronic acid (PLL/HA) was suggested for skeletal muscle tissue engineering; different widths of microgrooves (5, 10, 30, and 100 µm) were tested to guide skeletal muscle cell differentiation into myotubes. Different grooves' width may result in differentiated cell behavior. Particularly for this example, authors found, for all the grooves' width, favorable conditions for both the formation of parallel-oriented myotubes and their maturation. As observed by fluorescence images in Figure II-6A, the myoblasts were all pre-aligned to the grooves before their differentiation, with the highest aspect ratio and orientation of nuclei for the 5 and 10 µm grooves width. Overall, the authors showed that the combination of the LbL coating with the PDMS could be a powerful tool to muscle tissue engineering where alignment and orientation must be of extreme importance. Other geometries have been suggested, but with different purposes; for instance, Li *et. al.* [81] fabricated gelatin/fibronectin (FN)-coated micropatterns with different geometries to study how rat aorta smooth muscle cells (RASMCs) responded. The spreading of the cells depended on the geometry of the pattern features; as shown in Figure II-6B, groove/strip features constrained cell growth beyond the patterning while square patterns could not do that over time and confluence.

Microfabricated surfaces have been gaining more importance for TERM field since such kind of substrates allow to reconstruct better tissue-like environment for *in vitro* assays than classic cell culture methods; it has been reported as an efficient strategy to study the response of a cell to environmental cues. Moreover, it also can act as a multiple reservoir for different bioactive agents, like cells growth factor or even drugs. In this way, Martins *et. al.* [22] developed a technology that involves the use of a patterned PDMS substrate and consequent LbL assembly of CHT and ALG to obtain a freestanding multilayer membrane with a tuned array of micro-wells, that can inclusive works as a one-side porous material- see Figure II-6C. Cultured osteoblast-like cells tended to migrate to the wells (fluorescence image of Figure II-6C). This concept has real potential to produce patches able to delivery specific bioagents or as cell carrier patches for regenerative medicine. Other investigations have been done with this purpose: Chien. *et. al.* [82] also combined LbL assembly and photolithography to produce PAA conjugated with 4-azidoaniline was interwoven in PAA/PAM multilayer films, where after UV exposure through a photomask, the uncovered areas were crosslinked and the cover areas were rinsed away by alkaline water, creating the micropatterns – see Figure II-6D1. The cellular adhesion was then limited to the base substrate (cytophilic), but by modifying the surface chemistry of the substrate with bioactive agents the authors could switch the cell behavior. Figure II-6D shows the formation of a cell co-culture system of C3A hepatocytes (Figure II-6D2) and L929 cells (Figure II-6D3), that has been reported to promote liver functions. This methodology could be included in a highly flexible system to produce micropatterned PEM films for controlling cellular distribution, adhesion and grow. Similar methodologies were reported [33]: for instance, LbL deposition of polyelectrolyte solutions above HA micropatterns was used to immobilize cells and proteins to glass substrates. Figure II-6E1 represents the optical image of HA pattern on a glass substrate, before washing, Figure II-6E2 shows the fluorescence image after FN adsorption, that was preferential on the glass circular areas. After FN adsorption, the fibroblasts adhered on the FN-treated patterns- see Figure II-6E3. The potentiality and versatility of this technique was shown through patterning different cell types, as embryonic stem cells (ECs) (Figure II-6E4), or even co-culture systems. Therefore, micropatterned surfaces have been successfully used to create controlled cellular co-cultures for cell–cell interaction studies and tissue engineering applications.

Overall, diverse studies have demonstrated that micropatterned materials either corresponding to surface chemistry or topography changes, can affect cell adhesion, proliferation, differentiation, and gene expression.

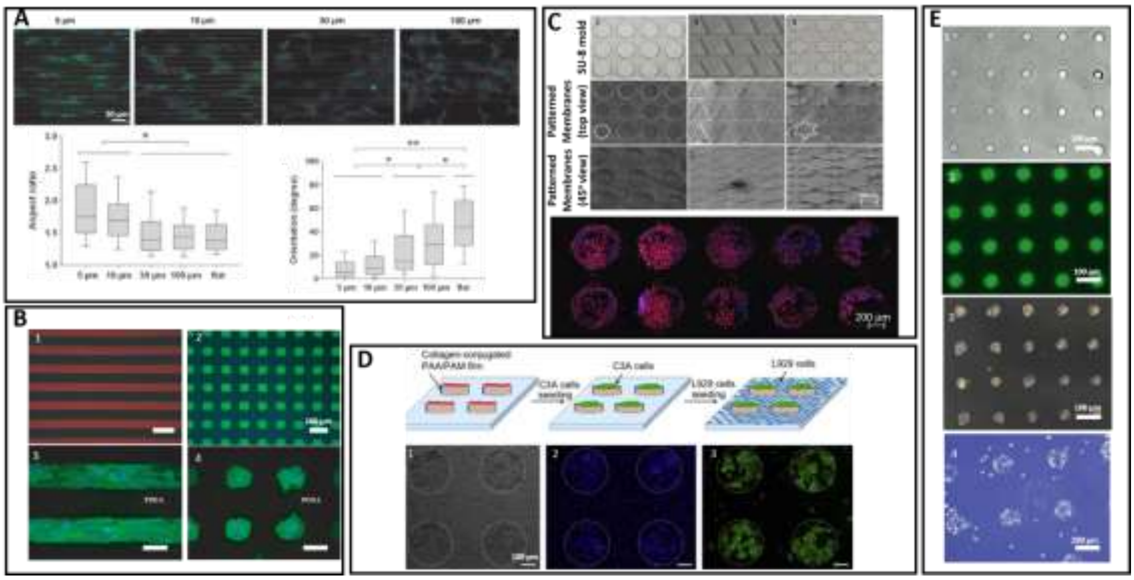

Figure II.6. Using LbL-based methodologies to produce microscale patterned materials to control cellular behavior. A) Nuclei staining (Hoechst) and vinculin immunostaining of cells grown out of the micropatterns of increasing width, scale bar 50 mm. Aspect ratio of nuclei (length over width of the equivalent ellipse) as a function of the width of the micropatterns and orientation of nuclei with considering to the main axis of the micropatterns (*p < 0.05, **p < 0.001) 67. Fluorescence images of thin film patterns after liftoff B1) (PSS/TR-PAH)$_2$/(gelatin/TR-PAH)$_4$/gelatin and B2) (PSS/FITCPAH)$_5$/fibronectin. SMCs cultured on fibronectin-coated patterns after 2 days [81]; B3) strip pattern and B4) square pattern [81]. C) Top-view images of the SU-8 molds obtained by UV photolithography, the second and third row correspond to SEM images (top-view and 45° tilted view) of the freestanding (CHT/ALG)$_{100}$ membranes produced by LbL using the PDMS templates produced using the above molds wells; triangles and stars. Note that the white drawings highlight the geometric feature of the obtained pattern. Global aspect of a patterned and crosslinked (CHT/ALG)$_{100}$ /fibronectin membrane upon 7 days of culture [22]. D) Procedure for seeding of C3A cells and L929 cells on the micropatterned PAA/PAM multilayer film for co-culture. C3A cells were first inoculated in a serum-free medium and attached on the collagen-immobilized PEM regions. After unattached cells were rinsed away, L929 cells were seeded at serum-contained condition [82]. After 3 days of culture, D1) cell morphology was observed by phase contrast microscope, D2) cell nuclei were stained with DAPI, and D3) albumin synthesis in C3A cells was visualized by immuno-fluorescent staining. The diameter of circles was 300 mm and the distance between circles was 200 mm. E1) Optical image of an HA pattern on a glass substrate prior to washing [33]. E2) Fluorescent image of fibronectin adsorption on the surface of an HA pattern [33]. E3) Fibroblast adhesion on the surface of FN-coated HA pattern. E4) Murine embryonic stem cells adhesion on the surface of FN-coated HA pattern [33].

Nanopatterning is already a well-established concept in tissue engineering field, but it can still progress in the next years in both fundamental mechanistic understanding or in technological developments. Cells recognize and attach to the extracellular environment through cell receptors, which are organized at the nanoscale scale [108]. The most known cell adhesion receptors are the group of the integrins, that have approximately 10 nm in diameter; these units cluster to form Focal Adhesions (FAs), needed to stablish strong cell adhesion as well as intracellular signaling pathways, and that usually are between 10 and 200 nm [108-109]. Therefore, nanopatterned surfaces have been developed to mimic ECM and concretely to modulate the cell-adhesion event. Most part of cell investigations using nanopatterned materials have been reported similar geometries as grooves, columns or pits. Each kind of geometry is used with different purposes, and depending also on the sizes, it can influence cell events as cell adhesion and proliferation, morphology or even differentiation. Indeed, the presence of the patterning features can increase or decrease cell adhesion, influence alignment within the pattern direction, or even alter genotypic expression. Until now, very few works reported the production of nanopatterned materials obtained using a technology-assisted LbL, to modulate cell behavior. For instance, Lee *et. al.* [100] fabricated vertical Si nanocolumns arrays (vSNAs) materials using a combined methodology of LbL and sphere lithography. To allow large scale fabrication of vSNAs, the authors decided to use an adherent Si surface that can strongly hold individual masks in a non-periodic pattern but not in a non-closed packing- see Figure II-7A1. Si surfaces were coated with PAH and poly-(sodium 4-styrenesulfonate) (PSS) adhesive films using a LbL technique, and these films were then easily removed by gas-phase etching without really affecting vSNAs. Another interesting fact is that the nanocolumn geometric factors, such as the diameter, height, density, and spatial patterning, could be fully controlled in an independent manner- see Figure II-7A2. As result, the authors demonstrated that cells adhered differently to these LbL-modified patterned surfaces (Figure II-7A3 shows the vSNAs surface and II.7A4 the flat one), with smaller cell area and uninterrupted motility on the vSNAs surface. Additionally, the Live-Dead images on the inset of Figure II-7A3 and II-7A4 show that both patterned and flat surfaces supported viable neuronal cell culture. Also, the fabrication of nanogrooved LbL-based materials were reported: Sousa *et. al.* [99] used a LbL technology to produce freestanding multilayer membranes made of CHT and chondroitin sulfate (CS), using an optical media substrate as mold. The SEM and Atomic Force Microscopy (AFM) images presented in Figure II-7B1 and II-7B2 represent the freestanding multilayer membranes when crosslinked with genipin; even when crosslinked the patterning was maintained. Figure II-7B3 and II.7B4 show the fluorescence images corresponding to the culture of L929 fibroblasts and C2C12 myoblasts on the multilayer membranes, respectively. Both type of cells seemed to have similar behaviors: more cells adhered to the crosslinked membranes and patterned surfaces seemed to present more elongated cells since the first day of culture.

5.1. Engineering the micro- and nanoscale topography to modulate the cellular adhesion and proliferation

Adherent cells need to anchor to the surface to grow and proliferate on the material, otherwise they can enter in a quiescence or apoptotic phases [110]. Different LbL-based material's properties have been investigated by influencing cellular adhesion [111]. Surface topography has been gaining special attention. The process of cellular adhesion involves three main phases. Firstly, the cells adhere to the material's surface through specific cell membrane receptors forming the FAs. Then, more and bigger FAs sites are created, and the cells start to spread all over the surface and orient themselves according with the material's topography. Consequently, the cells start to proliferate, divide and multiplicate. Note that the formed FAs are composed of proteins, which are involved in a direct physical connection of the cell membrane with the nuclear membrane or in an indirect signaling pathway via activation of kinases [112]. In fact, either via direct or indirect signaling, the integrins are the point of entry for transmitting information from surface properties, concretely topographical features, to the nucleus. Once FAs sites are created, cells start exploiting their surroundings through filopodia [112-113]. If filopodia can fix appropriately on a topographical feature of the surface using wide FAs, bigger cell protrusions are produced; as a result, the cells extend or migrate in this direction [113b, 114]. On the other hand, if cells encounter an obstacle the extension of filopodia is limited and protrusions are significantly smaller [114-115]. After adhesion and proliferation, cells can maintain the acquired shape and conformation due to the pre-stressed state that creates an equilibrium between the tension of microfilaments and the compression of the microtubules of the cell cytoskeleton [113a].

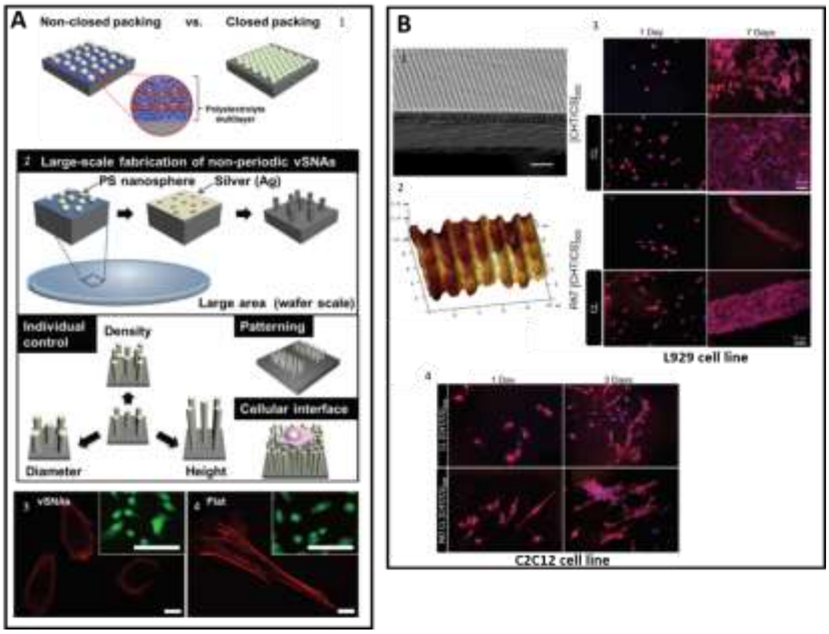

Figure II-7. Using LbL-based methodologies to produce nanoscale patterned materials to control cellular behavior. A1) Schematic of randomized non-close packed nanosphere lithography using polyelectrolyte-multilayers compared with the conventional close-packed nanosphere lithography [100]. A2) Schematic of the vSNA preparation employing non-close packed nanospheres, demonstrating large-scale fabrication, independent control over the nanocolumn geometry, array patterning, and cellular interface applications [100]. Laser confocal fluorescence microscopy images of actin-labelled fibroblasts on the A3) vSNA and the A4) flat substrates with inset images of the Live/Dead assay results (scale bars: 10 μm, inset 100 μm) [100]. B1) SEM images of the cross-section of the patterned [CHT/CS]$_{300}$ multilayer membranes. The scale bars represent 5 μm 21. B2) Atomic force microscopy (AFM) image of the patterned crosslinked [CHT/CS]$_{300}$ multilayer membranes in liquid [21]. Representative images of B3) L929 fibroblasts and B4) C2C12 myoblasts, over the different membranes. DAPI–phalloidin fluorescence assay culture on flat and nanopatterned [CHT/CS]$_{300}$ membranes, with or without crosslinking [21]. Cells nuclei are stained in blue by DAPI and F-actin filaments are stained in red by phalloidin.

Kidambi *et. al.* [77] investigated the influence of the topography of the materials' surface on cell adhesion and proliferation: PDMS surfaces were produced with circle-shaped patterns with different diameters but fixed height of 2.5 µm. These materials were coated with $(PDAC/SPS)_{10}$ polyelectrolyte multilayers, with SPS as the topmost surface, maintaining for all the conditions the same surface chemistry properties. Different cell lines were tested with such kind of materials; primary hepatocytes, 3T3 fibroblasts and HeLa cells had similar behavior in terms of cell adhesion, as observed in Figure II-8A. After 8 hours, it was observed a decreasing of cell number with increasing of the diameter of the circle features. Considering the proliferation rate of these cells when cultured above these materials, the authors reported a linear increase over time in the number of 3T3 fibroblasts and HeLa cells for TCPS, PEM-coated PDMS, P1, P2, and P3 (smaller diameters). The proliferation rate was much lower on the P6 and P9 surfaces, being very close to zero for the P9 surface as well as for uncoated PDMS surfaces (see cells number for 8, 24 hours and 3 days in Figure II-8A). In turn, Mohammed *et. al.* [89] reported a versatile method based on the combination of LbL and photolithography, to fabricate micropatterns of bioactive nanofilm coatings. These surfaces contained secreted phospholipase A2 ($sPLA_2$), a known membrane-active enzyme for neurons, for direct comparison with gelatin PLL, or bovine serum albumin (BSA) and were tested with neuronal cells. Figure II-8B1 and II-8B2 show the merged images of phase contrast fluorescence images of the FITC-labelled $sPLA_2$ nanofilm micropatterns at 1 day of culture while Figure II-8B3 presents a merged image of cells plated onto TRITC-BSA nanofilms. It could be observed that the cells attached specifically to the square patterns. The authors estimated that approximately 70% of the $sPLA_2$ squares are occupied while a little adhesion is observed on non-$sPLA_2$ surfaces. The high binding affinity to the squares patterns makes cells crowd onto the surface and then appear to go beyond the pattern boundaries. Different geometries were fabricated, to investigate their influence on cellular adhesion and proliferation. Naturally having columns areas will originate different cellular responses than grooves, squares or even circles. Khademhosseini *et. al.* [33] used LbL deposition above HA micropatterns to pattern cellular co-cultures of hepatocytes or embryonic stem cells (ES) with fibroblasts. The percentage of fibroblasts seeded that were adhered after 6 hours is represented in Figure II-8C. Cells really adhered to PLL-treated HA patterns and the % of cells seeded that adhered after 6 hours was significantly higher than HA micropatterns: indeed, PLL treatment was considered a switching agent, with the ability of reversing the cytophobic character of the HA surface to cytophilic.

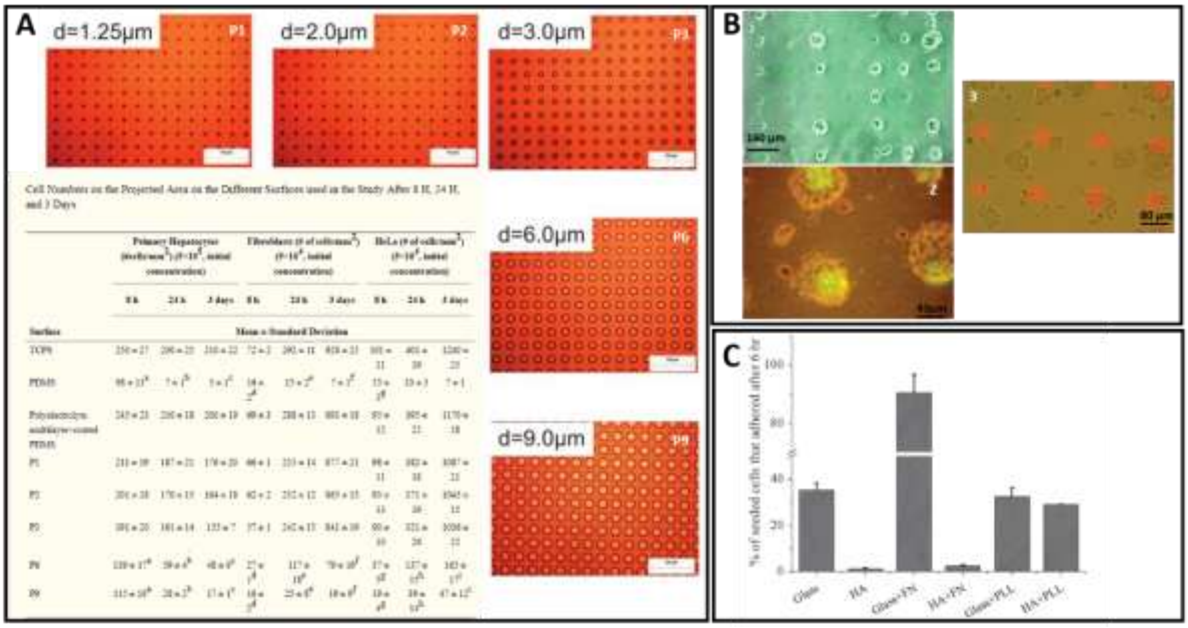

Figure II-8. A) Phase contrast microscope images of circle patterns on PDMS surfaces of varying diameters. All the patterns have constant pitch distance (center to center) of 18 mm and height of 2.5 mm (scale bar, 50 mm). Cell number per projected area of the different surfaces used in the study, determined after 8 hours, 24 hours and 3 days of culture [77]. Specific attachment of neurons to FITC-labeled sPLA2 nanofilm micropatterns. In all images, green squares are FITC-labeled sPLA2 nanofilm micropatterns, and cells are at 1 day *in vitro*: merged images of B1) and B2) phase and FITC-labeled sPLA2 nanofilm micropatterns and B3) of cells plated onto TRITC-BSA nanofilms [89]. C) Adhesion of NIH-3T3 cells on various surfaces. Cells did not adhere to HA or HA coated surfaces that were FN treated. In contrast, cells adhered to PLL treated HA surfaces at similar levels as PLL treated glass surfaces, indicating that PLL can be used to switch the surface properties of HA [33].

5.2. Engineering the micro- and nanoscale topography to modulate the cellular morphology

After adhering cells start to adapt to the topographical features of the material surface, because of the formation of FAs sites to the material. The FAs conformation is dependent on geometry, distribution and dimensions of the topographical features [116] and can result in changes cell morphology [117], shape [117b, 118], alignment [119] and even cell differentiation [117b, 120]. Different cells respond differently to topography and different topographical features and sizes generate different reactions from cell to cell type [16b]. However, usually, cell types as fibroblasts [21], stem cells [121], smooth muscular [122], endothelial [123], epithelial [124] or Schwann cells [125] respond similar to grooved geometries, with cells starting to align and elongate with the direction of the patterning. In this way, Lu *et. al.* [85] used a room-temperature imprinting method to produce patterned PAA/PAH multilayer films with line structures of different lateral size and vertical height. While nonpatterned PAA/PAH multilayer films are cytophilic toward NIH/3T3 and HeLa cells, the potential for cells adhering to the patterned PAA/PAH multilayer films depended on the lateral size and the vertical height of the patterned features. Figure II-9A shows phase contrast microscopic images of NIH/3T3 fibroblasts after 5 days in culture on various imprinted PAA/PAH films with fixed line structures of 6.5 μm line/3.5 μm space but different vertical heights. The first image (Figure II-9A1) corresponds to the $(PAA/PAH)_{20}$ films with a line height of 1.29 μm and, as observed, almost no cell adhesion or spreading occurred. When the authors decreased the line height to 687 nm (Figure II-9A2), some fibroblasts adhered on the surface and acquired elongated morphologies, becoming the films more cytophilic. This positive effect of decreasing vertical height was confirmed when the height decreased to 107 nm (Figure II-9A3); cells exhibited more elongated morphology than in the other cases.

Depending on topographical properties as geometry, different morphological effects can result from the cell-material topography interaction; for instance, the presence of pits or posts on the surface of the material usually results in reduced stretching of the cells. The overall impact of this morphological observation depends on the cell type. Lee *et. al.* [100] fabricated vertical Si nanocolumns materials using a combined methodology of LbL and sphere lithography, where nanocolumn geometric factors, such as the diameter, height, density, and spatial patterning, could be fully controlled in an independent manner. The authors demonstrated that cells adhered differently to these LbL-modified patterned surfaces (Figure II-9B1 shows the patterned surface and II-9B2 the flat one); minimal cell penetration was observed on the nanocolumn patterned surface while a really stretched morphology was found for the flat surface. Interestingly, fibroblasts seeded above the patterned material presented a rounder morphology and a smaller cell area than fibroblasts seeded above the non-patterned surfaces – see Figure II-9B3. In turn, a method based on the combination of lithography and LbL was designed to fabricate freestanding micro and nanostructured matrixes. The complex architecture is composed of successive layers of intercrossed carbon nanotubes that self-assemble into orderly structures [98]. Preliminary studies of cells (human osteosarcoma cell line CAL-72) interaction with the MWNTs freestanding materials were performed. Figure II-9C1 and II-9C2 represent the SEM images corresponding to osteoblast-like cells cultured above the nanostructured substrates: cells seemed to spread all over the surface, forming very extended stress elongations, which is a signal that they really sense the topography of the material.

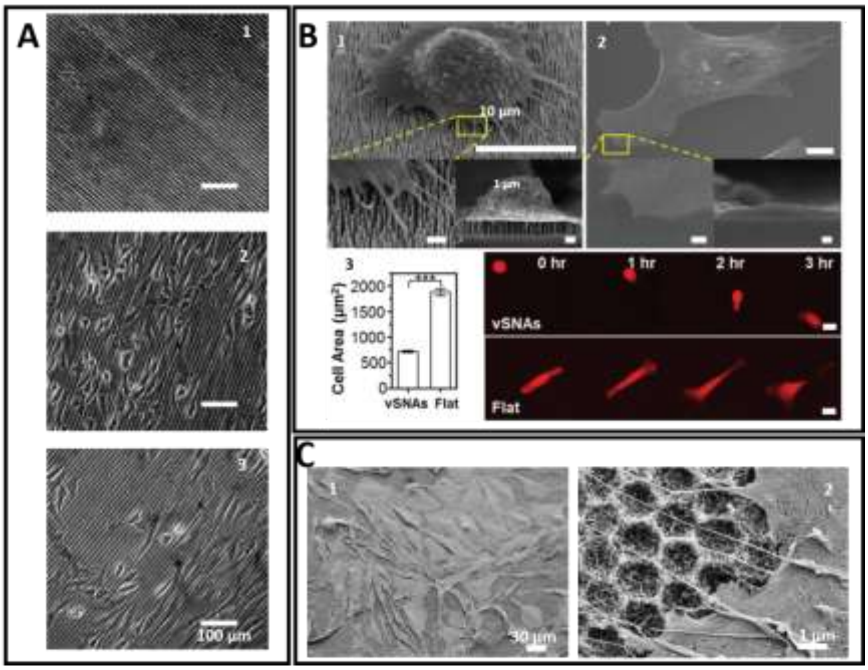

Figure II-9. Phase contrast microscope images of NIH/3T3 fibroblasts after 5 days in culture on various imprinted PAA/PAH films with line structures of 6.5-µm-line/3.5-µm-space: A1) imprinted (PAA/PAH)$_{20}$ films with a line height of 1.29 µm, A2) imprinted (PAA/PAH)$_{7}$ multilayers with a line height of ~107 nm and A3) imprinted (PAA/PAH)$_{15}$ multilayers with a line height of ~687 nm. 45°tilted and cross-sectional [85]. SEM images of fibroblasts cultured on the B1) vSNA and B2) flat substrates [100]. B3) Cell spreading areas of fibroblasts cultured on 4 different substrates for each set of conditions (***p< 0.0001, n = 217 for the vSNAs and 181 for the flat) [100]. A series of time-lapse fluorescence images of fibroblasts transiently expressing CAG-mRFP on the vSNA and the flat substrates with 1-hour intervals (scale bar: 20 µm). C1) SEM image of human osteoblast cells cultured onto a nanostructured substrate and C2) a higher magnification image of cells in contact with a nanotopography surface [98].

5.3. Engineering the micro- and nanoscale topography to modulate the cellular alignment

Another cellular event that has been related with the topography of the material's surface is the alignment of the cells to the substrate axis. This can happen when the topography is anisotropic, and it can be at micro or/and nanoscale. Briefly, cells are inhibited in their spreading by an obstacle, and follow the edge feature to elongate and go into the groove direction. The elongation of the cell can induce the deformation of the nucleus and the rearrangement of the DNA chromatin inside [18a]. From fibroblasts, to myoblasts or even cardiomyocytes, the alignment is essential to their function.

When cultured on micro or/and nanogrooved surfaces with regular spacing, the cells move along with the long axis of the ridges/grooves; here, factors as width, depth and type of material play an important key for cellular alignment [116]. Generally, cell alignment is favored by increasing depth sizes and decreasing grooves/ridges width sizes [104b, 126]. However, this trend can be undone depending on materials composition, cell type or culture conditions. Sousa *et. al.* [21] produced nanogrooved freestanding multilayered membranes capable of inducing cellular alignment. The presence of grooves of about 800 nm width and 400 nm depth allowed L929 cells to move in a direction of the pattern axis- see the comparison between patterned and non-patterned freestanding membranes through SEM imaging of the cell-material interaction in Figure II-10A. This fact is based on the theory that cells make a projection in one direction depending on the shape and type of features it encountered; for micro and nanopatterned surfaces, the alignment phenomenon is expected in the direction with less topographic and mechanic obstruction. Additionally, for the patterned substrate, the cells distributed in the range from −30° to 20° and ≈71% of cells were aligned with the pattern direction (angle between −10°and 10°)- see Figure II-10A, corresponding to the fibroblast's orientation with respect to the groove direction. C2C12 is an animal cell line often used as a model for skeletal muscle differentiation; for that, the alignment of myotubes is an essential step. Palamà *et. al*. [127] reported the production of biomimetic microstructured surfaces, combining a double-sheet PDMS and LbL methodology, to promote cellular adhesion and differentiation of parallel arrays of mature C2C12 myoblasts. Figure II-10B shows the fluorescence images of C2C12 cells when seeded above the PDMS microstructured substrates without coatings, coated with FN or coated with LbL multilayers. The cells were stained with phalloidin. The white arrows in the images indicate the direction of the pattern and the entire situation the cells seemed to align in the direction of the arrows, adopting a more spindle-shaped morphology in the conditions where patterned surfaces were coated. The micropatterned PDMS surfaces coated with LbL $(DXS/PRM)_3$ multilayers presented the higher percentage of elongated cells (elongated cells were defined as those with elongation factor higher than 1.3). The combination of patterned PDMS with a biomimetic PEM film composed of PLL and HA was also suggested for skeletal muscle tissue engineering [67]: the successful deposition of the LbL film above the PDMS surface is shown in Figure II-10C. Different sizes of grooves' width (5, 10, 30 and 100 µm) were tested to have an idea on the effect of the size; the orientation of the nuclei was strongly dependent of the width of the grooves. For smaller features as the 5 and the 10 µm, the tilting angle was less than 10°- graph of Figure II-10C- which means that the nuclei were almost parallel to the patterning direction. The authors believe that the spatial constrains led to the nuclei deformation and the respective alignment with patterning features direction.

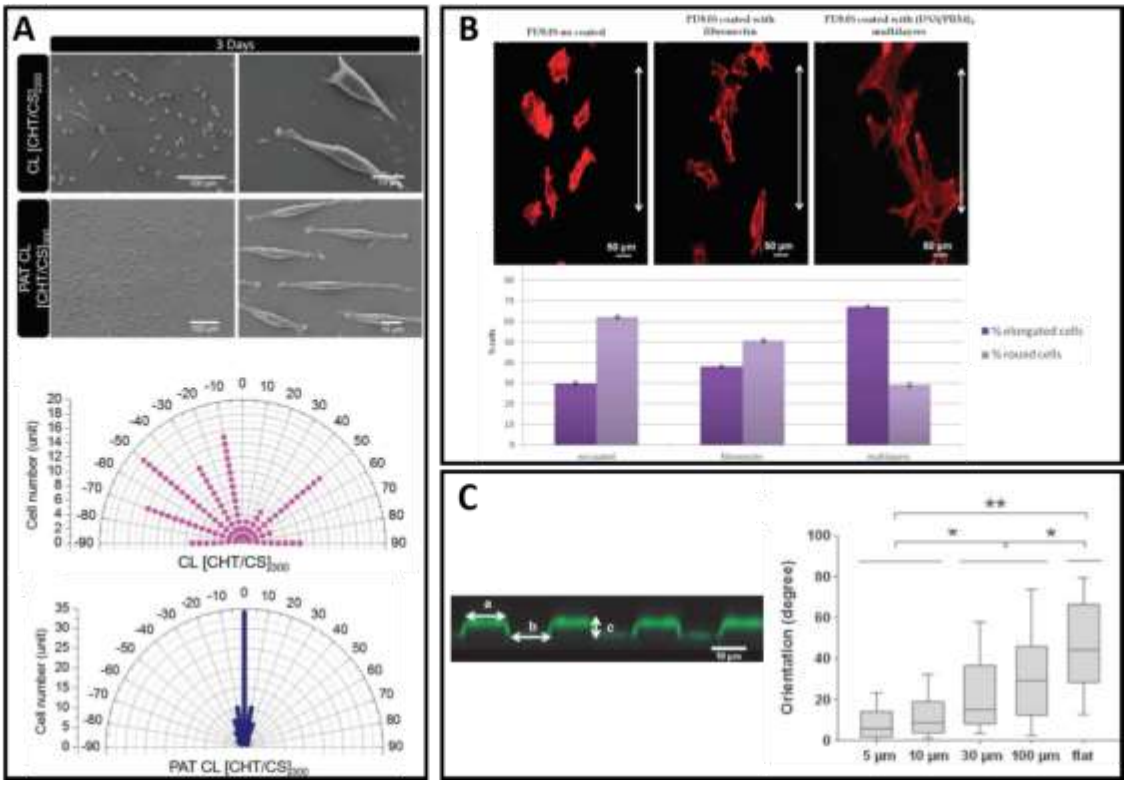

Figure II-10. A) SEM observation at 3 days of culture above crosslinked flat and nanopatterned crosslinked [CHT/CS]$_{300}$ membranes. Polar graphical representation of cellular alignment for crosslinked [CHT/CS]$_{300}$ and patterned crosslinked [CHT/CS]$_{300}$ [21]. B) Fluorescent images of C2C12 cells were seeded on substrates not coated, coated with fibronectin and coated with polyelectrolyte multilayers under static conditions and stained with fluorescent phalloidin (red) after 1 day [127]. The white arrows indicate the directions of the patterns. Percentage of elongated and round cells on substrates no coating, coating with fibronectin and coating with multilayers under static conditions [127]. Note that cell elongation was defined as the ratio between the length and breadth of each cells. Elongated cells presented cells elongations higher than 1.3, while round cells presented cells elongations lower than 1.3. C) Confocal laser scanning microscopy cross-section of the 10 mm wide micropattern coated by a (PLL/HA)$_{12}$-PLLFITC film [67]. The dimensions a and b correspond to the width of the ridge and the groove (a = b). The dimension c characterizes the height of the pattern. Here, $c = 4$ mm. Orientation of nuclei with respect to the main axis of the micropatterns (*$p < 0.05$, **$p < 0.001$).

5.4. Engineering the micro- and nanoscale topography to modulate the cellular migration

After adhered to the surface, cells' cytoskeleton is pre-stressed allowing cells to move on the material's surface depending on their micro or/and nanotopography. This movement can be investigated through migration studies [128]. Cell migration plays an important role in physiological and healing processes, thus efforts have been done to investigate its response on the presence of topographical features [128-129]. Understanding this complex mechanism is still a challenge. Nevertheless, it is known that cell migration results from different integrated processes, existing two modes of single cell migration: one that it is characterized by an elongated morphology and strong adhesion (e.g. fibroblasts) and the other characterized by dynamic focal complexes and high ability of deformability (e.g. lymphocytes) [130]. Despite different cell types have specific migration mechanism, general events are shared in response to topographical cues [130-131]. Firstly, the migrating cell alters its morphology and intracellular organization, where polarized cells present a fan-shaped protrusion at the leading edge and traction at the rear. FAs were established making cells create stable connection with the material's surface. Then cell motility, that moves the cell body forward, is generated by the attachment of actin stress fibres to FAs. This results in the formation of new adhesion at the leading edge, being the rear edge disassembled [130-131]. While single cell motility involves usually this combination of cell processes, collective cell migration must coordinate with the ECM microenvironment, retaining cell-to-cell contacts [129-130, 132]. Both migration processes play a key role on regulation, formation, and organization of tissues [128].

Martins *et. al.* [22] suggested a new concept of producing flexible freestanding CHT/ALG multilayer membranes featuring well arrays and forming a pore-like environment to accommodate cells. The presence of geometrical cues led cells to migrate and start to adhere in the border of the wells and proliferate to the center direction- see Figure II-11A. An easy and versatile technique was designed for cell patterning, based on a photolithography assisted-LbL technology [82]. Micropatterned multilayer films composed of PAA conjugated with 4-azidoaniline interwoven in PAA/PAM were also produced. Surface topography can serve as physical guidance and migration for the cells - see Figure II-11B. Khademhosseini *et. al.* [33] developed a novel method to pattern cell co-cultures, using LbL deposition of polyelectrolytes: HA micropatterns were used to immobilize cells and proteins to glass surfaces and PLL to switch the cell repulsive character of the HA layer to cell adherent. Figure II-11C1 shows the interaction between embryonic stem cells (ES) (in red) and NIH-3T3 (in green) in patterned co-cultures of circular fibronectin (FN): fluorescent images confirmed that NIH-3T3 cells were restricted to the HA-coated regions and were not seeded on top of ES cells as indicated by the lack of yellow regions on the aggregates. The circle-shaped micropattern allowed the different type of cells to not migrate into the surrounding regions. The versatility of this methodology was validated by reversing the order of the cell seeding (ES in green and NIH-3T3 in red), as shown in Figure II-11C2.

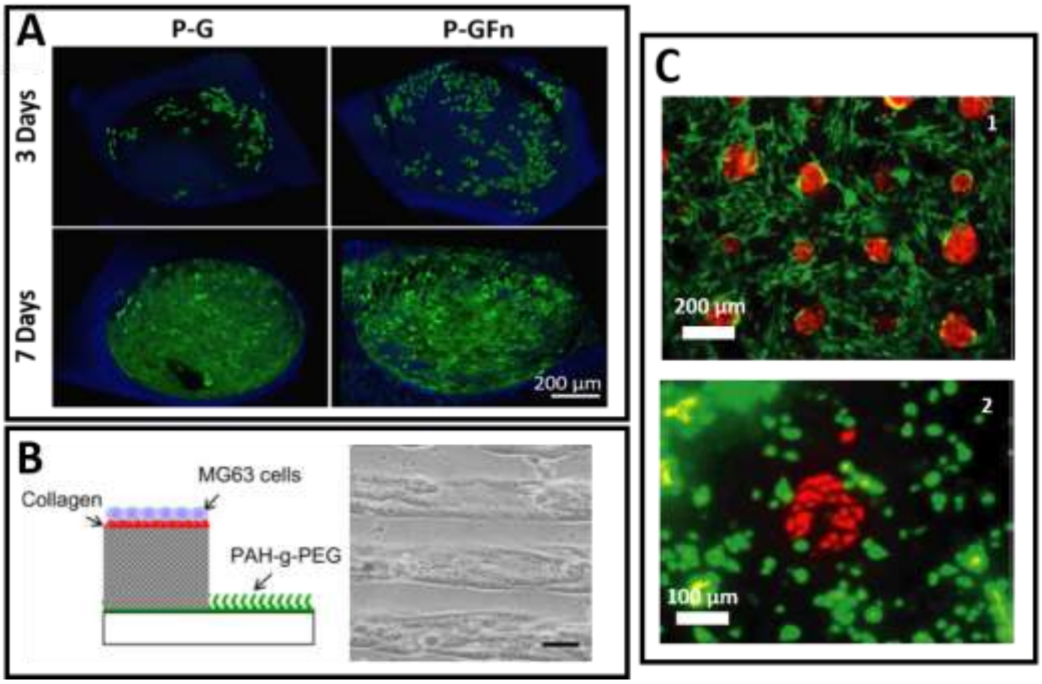

Figure II-11. A) Representative images obtained by confocal microscopy of the well region of the patterned crosslinked membrane and the patterned crosslinked membrane coated with fibronectin [22]. The cells nuclei were stained blue by DAPI and F-actin filaments in green by phalloidin. B) MG63 cells were then seeded on the micropatterned PEM film: microscopic image of MG63 cells cultured on the 10-bilayer micropatterned PEM film with 60/30 mm-wide stripes for 5 days (scale bar = 50 mm) [82]. C) Fluorescent images of patterned co-cultures of ES cells (red) with NIH-3T3 fibroblasts (green) after C1) 1 day and C2) the reversal in the order of cell seeding in which NIH-3T3 fibroblasts (red) were initially seeded followed by ES cells as the secondary cells [33]. This methodology is independent from the type of cell initially seeded.

5.5. Engineering the micro- and nanoscale topography to modulate the genetic expression and cellular differentiation

Topography can also tailor the gene expression profiles of different cell types. The presence of topographical features in the surface of materials can be responsible for changes in the cytoskeleton of the cell, leading to fluctuations on the stress levels imparted on the nucleus. This can disturb organelle and DNA organization and distribution, resulting in the most on the alteration of cell function. One possible explanation for the transduction of cell morphology information into gene expression is based on the mechanical forces transmitted via direct linking of the cell cytoskeleton to the nucleus (mechanotransduction) [133]. Herein, nuclear matrix proteins (NMPs) have an important role in gene expression as it can induce alterations in DNA and interact with gene promoter sequences [133-134].

The impact of surface's topography on cell function can be used to drive the important process of cellular differentiation of stem cells to a desired lineage [117b]. This fact, can be intrinsically correlated with gene expression, as undifferentiated cells express different genes than differentiated cells [117b, 135]. In the last years, some works [120, 136] have been reporting that the presence of topographical features on the material's surface could be responsible to direct their differentiation, even without any other inductive external factor.

Mesenchymal Stem Cells (MSCs) are a kind of non-differentiated type of cells, that can be isolated from bone marrow or adipose tissue and include a subpopulation of cells that can differentiated towards different tissues like osteocytes or chondrocytes for instance. Considering the relevance of MSCs in TERM, recent investigations have been focusing on driving MSCs differentiation through the presence of specific topographical features on the material's surface. Different studies [137] have reported the commitment of MSCs to adipogenic, neuronal or myogenic phenotypes, when in presence of a grooved surface, particularly when the groove size is less than 500 nm. In the other hand, this kind of topographical features can influence negatively the osteogenic differentiation of MSCs: grooved surfaces can be responsible for cellular alignment, which in turns can reduce osteogenesis [138]. Contrarily to anisotropic surfaces, the effect of isotropic patterning features is often inconsistent and difficult to conclude about: it depends always on the cell type, cell culture conditions or materials' properties. However, there are some evidences that the presence of deep pits tends to enhance osteogenesis [139]. Therefore, Kim *et. al.* [84] suggested a LbL-coated microstructure scaffold for bone tissue engineering: the combination of surface topographical cues and chemistry of the hydroxyapatite nanoparticles (HApNPs)/collagen multilayer coating could mimic the natural ECM to some extent. In fact, during osteogenic induction of the seeded MSCs, the (alkaline phosphatase) ALP activity increased overall with time and the number of deposited layers (see Figure II-12A), suggesting that the (HApNPs)/COL multilayer coated- microstructured scaffold could improve matrix intracellular signaling that is directly connected to the osteogenic activity. Furthermore, the quantitative real-time (RT) -PCR analysis was realized for conventional expressed osteoblast-related genes as bone sialo protein-II (BSP), bone morphogenetic protein-2 (BMP2), osteopontin (OP), and osteocalcin (OC)- see Figure II-12A. The authors found that, for the 20 bilayers condition, there are an up-regulation of three markers, corroborating the results of ALP activity. TiO_2 nanotube (TNT) arrays were also suggested as drug nanoreservoirs for loading of bone morphogenetic protein 2 (BMP2) and coating with (gelatin/chitosan) multilayer films [140]. The presence of BMP2-loaded and multilayer-coated TNT array substrates could stimulate motogenic responses of MSCs and promote their osteoblast differentiation - see Figure II-12B.

C2C12 cells have ability to differentiate into myotubes (myogenic differentiation) or osteocytes (osteogenic differentiation). A simple methodology only based on LbL and composed of natural polymers (CHT/CS) was suggested to produce a material which topography of the nanopatterned design along the XY plane is combined with the nanostructure organization along the Z axis [21]. The differentiation of C2C12 into myotubes was influenced by the presence of nanogrooves and the resultant strong cellular alignment (see Figure II-12C). Therefore, micro- and nanoscale anisotropic and isotropic topographies can induce strong morphological changes in FAs, cytoskeletal or cellular level, depending on the features' size. This originate changes in gene expression, opening space to modulate cell differentiation into a specific lineage.

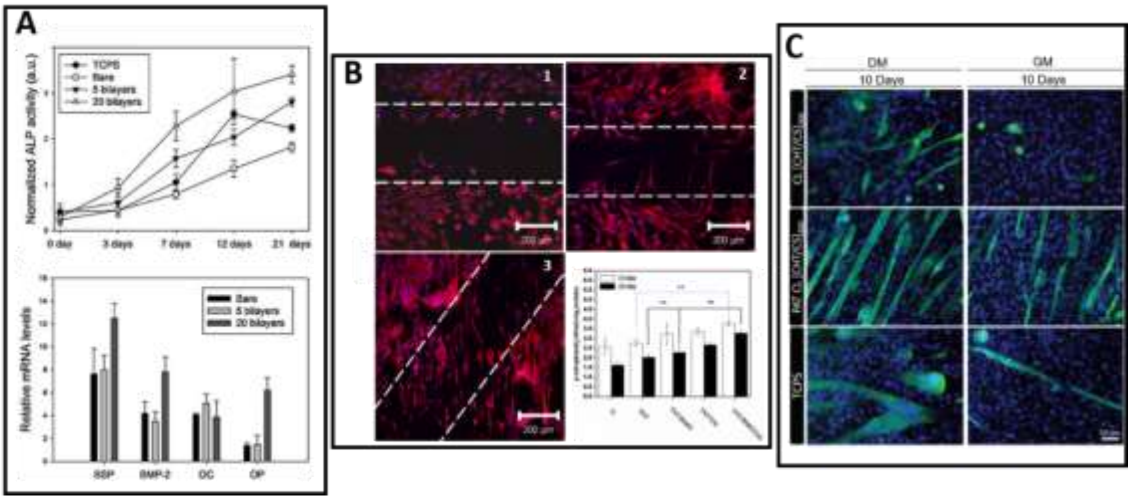

Figure II-12. A) ALP activity and relative mRNA expression during culture of hMSCs on various substrates in an osteoinduction medium [84]. Motogenic responses of MSCs adhered to different substrates after culture for 48 h [140]: B1) bare TNT arrays (110 nm); B2) Gel/Chi multilayer-coated TNT arrays (TNT/LbL); and B3) Gel/Chi multilayer-coated, BMP2-loaded TNT arrays (TNT/BMP2/LbL). ALP activity of MSCs adhered to different substrates after culture for 10 and 20 days (error bars represent means ± SD for n = 6, $p < 0.01$) [140]. C) Immunofluorescence with troponin T (green myotubes) and DAPI (blue nuclei) at 10 days of culture. Images are representative of crosslinked flat and nanopatterned CHT/CS membranes and tissue culture polystyrene (TCPS), using differentiation medium (DM) and normal growth medium (GM) (the scale bar is representative for all images) [21].

From the overview of the experimental evidences, it is obvious that each type of cell responds in a different way to different topographical cues, including geometry, shape and size. Table S II-1 resumes research works already reported in literature regarding the use of micro- or nanoscale patterned surfaces, obtained through LbL-based methodologies, to tailor the cellular behavior and fate.

6. Future perspective

In this review, different methodologies were described to produce micro and nanostructured multilayered coatings and materials; indeed, LbL-based approaches were emphasized as being more cost-effective, versatile, simpler and easier to perform than the other possible techniques, allowing the use organic and non-meltable materials. The main goal related with the development of those kind of materials was to apply for biomedical and TERM field: micro- and nanopatterned materials have been suggested to mimic, with higher similarity, the features presented by tissues' ECM. In the last decade, a big effort has been directed to investigate the cell's response on 2D or 3D material that presented specific micro- and/or nanotopographical features. Cell functions as adhesion, proliferation, migration, alignment, gene expression or differentiation can be modulated by using patterned surfaces. Feature size seems to be one of the most determining parameters to tailor the cellular behavior; notwithstanding, the optimal feature size can be different according with the cell type, the material and the shape of the feature.

Nanotopographical features can be relevant since they match the size of normal cellular sensing domains and microtopographical features are important to determine functions, such as migration and confinement.

The significance of the existence of nano- and/or microtopographical features will be helpful to design suitable materials and surfaces to apply for biomaterials science and TERM. With the future of technological developments, we expect that such topographic features engraved over LbL multilayers could be transposed into the 3D microenvironment and accommodated the more complex and hierarchical structures. More work will be also necessary to develop smart and adaptable materials, where nano/microtopography could change overtime as result of specific physicochemical or biological stimuli.

7. References

1. (a) Decher, G.; Hong, J.-D., Buildup of ultrathin multilayer films by a self-assembly process, 1 consecutive adsorption of anionic and cationic bipolar amphiphiles on charged surfaces. *Makromolekulare Chemie. Macromolecular Symposia* **1991,** *46* (1), 321-327; (b) Decher, G., Fuzzy Nanoassemblies: Toward Layered Polymeric Multicomposites. *Science* **1997,** *277* (5330), 1232-1237.
2. (a) Zhang, X.; Chen, H.; Zhang, H., Layer-by-layer assembly: from conventional to unconventional methods. *Chemical Communications* **2007,** (14), 1395-1405; (b) Richardson, J. J.; Cui, J.; Björnmalm, M.; Braunger, J. A.; Ejima, H.; Caruso, F., Innovation in Layer-by-Layer Assembly. *Chemical Reviews* **2016,** *116* (23), 14828-14867.
3. (a) Kotov, N. A., Layer-by-layer self-assembly: The contribution of hydrophobic interactions. *Nanostructured Materials* **1999,** *12* (5), 789-796; (b) Bergbreiter, D. E.; Liao, K.-S., Covalent layer-by-layer assembly—an effective, forgiving way to construct functional robust ultrathin films and nanocomposites. *Soft Matter* **2009,** *5* (1), 23-28.
4. (a) Jiang, C.; Tsukruk, V. V., Freestanding Nanostructures via Layer-by-Layer Assembly. *Advanced Materials* **2006,** *18* (7), 829-840; (b) Boudou, T.; Crouzier, T.; Ren, K.; Blin, G.; Picart, C., Multiple Functionalities of Polyelectrolyte Multilayer Films: New Biomedical Applications. *Advanced Materials* **2010,** *22* (4), 441-467; (c) Costa, R. R.; Mano, J. F., Polyelectrolyte multilayered assemblies in biomedical technologies. *Chemical Society Reviews* **2014,** *43* (10), 3453-3479.
5. Pan, T.; Wang, W., From Cleanroom to Desktop: Emerging Micro-Nanofabrication Technology for Biomedical Applications. *Annals of Biomedical Engineering* **2011,** *39* (2), 600-620.
6. Kam, K. R.; Desai, T. A., Nano- and microfabrication for overcoming drug delivery challenges. *Journal of Materials Chemistry B* **2013,** *1* (14), 1878-1884.
7. Ferreira, S. A.; Gama, F. M.; Vilanova, M., Polymeric nanogels as vaccine delivery systems. *Nanomedicine: Nanotechnology, Biology and Medicine* **2013,** *9* (2), 159-173.
8. (a) Kim, H. N.; Jiao, A.; Hwang, N. S.; Kim, M. S.; Kang, D. H.; Kim, D.-H.; Suh, K.-Y., Nanotopography-guided tissue engineering and regenerative medicine. *Advanced Drug Delivery Reviews* **2013,** *65* (4), 536-558; (b) Custódio, C. A.; Reis, R. L.; Mano, J. F., Engineering Biomolecular Microenvironments for Cell Instructive Biomaterials. *Advanced Healthcare Materials* **2014,** *3* (6), 797-810.
9. (a) Wade, R. J.; Burdick, J. A., Engineering ECM signals into biomaterials. *Materials Today* **2012,** *15* (10), 454-459; (b) Kyburz, K. A.; Anseth, K. S., Synthetic Mimics of the Extracellular Matrix: How Simple is Complex Enough? *Annals of Biomedical Engineering* **2015,** *43* (3), 489-500; (c) Silva, J. M.; Reis, R. L.; Mano, J. F., Biomimetic Extracellular Environment Based on Natural Origin Polyelectrolyte Multilayers. *Small* **2016,** *12* (32), 4308-42.
10. Wagenseil, J. E.; Mecham, R. P., Vascular Extracellular Matrix and Arterial Mechanics. *Physiological Reviews* **2009,** *89* (3), 957-989.
11. Meyer, G. A.; Lieber, R. L., Elucidation of extracellular matrix mechanics from muscle fibers and fiber bundles. *Journal of Biomechanics* **2011,** *44* (4), 771-773.
12. Mano, J. F., Designing biomaterials for tissue engineering based on the deconstruction of the native cellular environment. *Materials Letters* **2015,** *141*, 198-202.
13. (a) Kelleher, C. M.; Vacanti, J. P., Engineering extracellular matrix through nanotechnology. *Journal of The Royal Society Interface* **2010,** *7* (Suppl 6), S717-S729; (b) Atala, A.; Kasper, F. K.; Mikos, A. G., Engineering complex tissues. *Science translational medicine* **2012,** *4* (160), 160rv12.
14. (a) Norman, J. J.; Desai, T. A., Methods for Fabrication of Nanoscale Topography for Tissue Engineering Scaffolds. *Annals of Biomedical Engineering* **2006,** *34* (1), 89-101; (b) Bettinger, C. J.; Langer, R.; Borenstein, J. T., Engineering Substrate Topography at the Micro- and Nanoscale to Control Cell Function. *Angewandte Chemie International Edition* **2009,** *48* (30), 5406-5415.
15. (a) Kanchanawong, P.; Shtengel, G.; Pasapera, A. M.; Ramko, E. B.; Davidson, M. W.; Hess, H. F.; Waterman, C. M., Nanoscale architecture of integrin-based cell adhesions. *Nature* **2010,** *468*, 580; (b) Singh, A. V.; Patil, R.; Thombre, D. K.; Gade, W. N., Micro-nanopatterning as tool to study the role of physicochemical properties on cell–surface interactions. *Journal of Biomedical Materials Research Part A* **2013,** *101* (10), 3019-3032.
16. (a) von der Mark, K.; Park, J.; Bauer, S.; Schmuki, P., Nanoscale engineering of biomimetic surfaces: cues from the extracellular matrix. *Cell and Tissue Research* **2009,** *339* (1), 131; (b) Janson, I. A.; Putnam, A. J., Extracellular matrix elasticity and topography: Material-based cues that affect cell function via conserved mechanisms. *Journal of Biomedical Materials Research Part A* **2015,** *103* (3), 1246-1258.

17. (a) Curtis, A. S.; Wilkinson, C. D., Reactions of cells to topography. *Journal of biomaterials science. Polymer edition* **1998,** *9* (12), 1313-29; (b) Flemming, R. G.; Murphy, C. J.; Abrams, G. A.; Goodman, S. L.; Nealey, P. F., Effects of synthetic micro- and nano-structured surfaces on cell behavior. *Biomaterials* **1999,** *20* (6), 573-88; (c) Sardella, E.; Favia, P.; Gristina, R.; Nardulli, M.; d'Agostino, R., Plasma-Aided Micro- and Nanopatterning Processes for Biomedical Applications. *Plasma Processes and Polymers* **2006,** *3* (6-7), 456-469.
18. (a) Dalby, M. J.; Riehle, M. O.; Yarwood, S. J.; Wilkinson, C. D. W.; Curtis, A. S. G., Nucleus alignment and cell signaling in fibroblasts: response to a micro-grooved topography. *Experimental Cell Research* **2003,** *284* (2), 272-280; (b) Sarkar, S.; Lee, G. Y.; Wong, J. Y.; Desai, T. A., Development and characterization of a porous micro-patterned scaffold for vascular tissue engineering applications. *Biomaterials* **2006,** *27* (27), 4775-4782.
19. Sousa, M. P.; Gonzalez de Torre, I.; Oliveira, M. B.; Rodríguez-Cabello, J. C.; Mano, J. F., Biomimetic click assembled multilayer coatings exhibiting responsive properties. *Materials Today Chemistry* **2017,** *4*, 150-163.
20. Borges, J.; Sousa, M. P.; Cinar, G.; Caridade, S. G.; Guler, M. O.; Mano, J. F., Nanoengineering Hybrid Supramolecular Multilayered Biomaterials Using Polysaccharides and Self-Assembling Peptide Amphiphiles. *Advanced Functional Materials* **2017,** *27* (17), 1605122.
21. Sousa, M. P.; Caridade, S. G.; Mano, J. F., Control of Cell Alignment and Morphology by Redesigning ECM-Mimetic Nanotopography on Multilayer Membranes. *Advanced Healthcare Materials* **2017,** *6* (15), 1601462.
22. Martins, N. I.; Sousa, M. P.; Custódio, C. A.; Pinto, V. C.; Sousa, P. J.; Minas, G.; Cleymand, F.; Mano, J. F., Multilayered membranes with tuned well arrays to be used as regenerative patches. *Acta Biomaterialia* **2017**.
23. Correia, C. R.; Sher, P.; Reis, R. L.; Mano, J. F., Liquified chitosan–alginate multilayer capsules incorporating poly(l-lactic acid) microparticles as cell carriers. *Soft Matter* **2013,** *9* (7), 2125-2130.
24. Silva, J. M.; Georgi, N.; Costa, R.; Sher, P.; Reis, R. L.; Van Blitterswijk, C. A.; Karperien, M.; Mano, J. F., Nanostructured 3D Constructs Based on Chitosan and Chondroitin Sulphate Multilayers for Cartilage Tissue Engineering. *PLOS ONE* **2013,** *8* (2), e55451.
25. Qian, T.; Wang, Y., Micro/nano-fabrication technologies for cell biology. *Medical & biological engineering & computing* **2010,** *48* (10), 1023-1032.
26. Kirkland, J. J., Porous Thin-Layer Modified Glass Bead Supports for Gas Liquid Chromatography. *Analytical Chemistry* **1965,** *37* (12), 1458-1461.
27. Iler, R. K., Multilayers of colloidal particles. *Journal of Colloid and Interface Science* **1966,** *21* (6), 569-594.
28. (a) Keeney, M.; Jiang, X. Y.; Yamane, M.; Lee, M.; Goodman, S.; Yang, F., Nanocoating for biomolecule delivery using layer-by-layer self-assembly. *Journal of materials chemistry. B, Materials for biology and medicine* **2015,** *3* (45), 8757-8770; (b) Oliveira, M. B.; Hatami, J.; Mano, J. F., Coating Strategies Using Layer-by-layer Deposition for Cell Encapsulation. *Chemistry, an Asian journal* **2016,** *11* (12), 1753-64.
29. (a) Picart, C., Polyelectrolyte multilayer films: from physico-chemical properties to the control of cellular processes. *Current medicinal chemistry* **2008,** *15* (7), 685-97; (b) Silva, J. M.; Duarte, A. R.; Caridade, S. G.; Picart, C.; Reis, R. L.; Mano, J. F., Tailored Freestanding Multilayered Membranes Based on Chitosan and Alginate. *Biomacromolecules* **2014,** *15* (10), 3817-3826.
30. Borges, J.; Mano, J. F., Molecular Interactions Driving the Layer-by-Layer Assembly of Multilayers. *Chemical Reviews* **2014,** *114* (18), 8883-8942.
31. Shaikh Mohammed, J.; DeCoster, M. A.; McShane, M. J., Fabrication of Interdigitated Micropatterns of Self-Assembled Polymer Nanofilms Containing Cell-Adhesive Materials. *Langmuir* **2006,** *22* (6), 2738-2746.
32. Andres, C. M.; Kotov, N. A., Inkjet Deposition of Layer-by-Layer Assembled Films. *Journal of the American Chemical Society* **2010,** *132* (41), 14496-14502.
33. Khademhosseini, A.; Suh, K. Y.; Yang, J. M.; Eng, G.; Yeh, J.; Levenberg, S.; Langer, R., Layer-by-layer deposition of hyaluronic acid and poly-l-lysine for patterned cell co-cultures. *Biomaterials* **2004,** *25* (17), 3583-3592.
34. (a) Reneker, D. H.; Yarin, A. L., Electrospinning jets and polymer nanofibers. *Polymer* **2008,** *49* (10), 2387-2425; (b) Bhardwaj, N.; Kundu, S. C., Electrospinning: A fascinating fiber fabrication technique. *Biotechnology Advances* **2010,** *28* (3), 325-347; (c) Kenry; Lim, C. T., Nanofiber technology: current status and emerging developments. *Progress in Polymer Science* **2017,** *70*, 1-17.

35. (a) Teo, W. E.; Ramakrishna, S., A review on electrospinning design and nanofibre assemblies. *Nanotechnology* **2006,** *17* (14), R89; (b) Sell, S.; Barnes, C.; Smith, M.; McClure, M.; Madurantakam, P.; Grant, J.; McManus, M.; Bowlin, G., Extracellular matrix regenerated: tissue engineering via electrospun biomimetic nanofibers. *Polymer International* **2007,** *56* (11), 1349-1360; (c) Xie, J.; Li, X.; Lipner, J.; Manning, C. N.; Schwartz, A. G.; Thomopoulos, S.; Xia, Y., "Aligned-to-random" nanofiber scaffolds for mimicking the structure of the tendon-to-bone insertion site. *Nanoscale* **2010,** *2* (6), 923-926.
36. Kim, J. I.; Kim, J. Y.; Park, C. H., Fabrication of transparent hemispherical 3D nanofibrous scaffolds with radially aligned patterns via a novel electrospinning method. *Scientific Reports* **2018,** *8* (1), 3424.
37. Yazhou, W.; Guixue, W.; Liang, C.; Hao, L.; Tieying, Y.; Bochu, W.; James, C. M. L.; Qingsong, Y., Electrospun nanofiber meshes with tailored architectures and patterns as potential tissue-engineering scaffolds. *Biofabrication* **2009,** *1* (1), 015001.
38. Huang, R.; Li, W.; Lv, X.; Lei, Z.; Bian, Y.; Deng, H.; Wang, H.; Li, J.; Li, X., Biomimetic LBL structured nanofibrous matrices assembled by chitosan/collagen for promoting wound healing. *Biomaterials* **2015,** *53*, 58-75.
39. Cui, L.; Li, J.; Long, Y.; Hu, M.; Li, J.; Lei, Z.; Wang, H.; Huang, R.; Li, X., Vascularization of LBL structured nanofibrous matrices with endothelial cells for tissue regeneration. *RSC Advances* **2017,** *7* (19), 11462-11477.
40. Tasuku, O.; Bin, D.; Yuji, S.; Seimei, S., Super-hydrophobic surfaces of layer-by-layer structured film-coated electrospun nanofibrous membranes. *Nanotechnology* **2007,** *18* (16), 165607.
41. van Dommelen, R.; Fanzio, P.; Sasso, L., *Surface self-assembly of colloidal crystals for micro- and nano-patterning*. 2017; Vol. 251.
42. Hyde, E. D. E. R.; Seyfaee, A.; Neville, F.; Moreno-Atanasio, R., Colloidal Silica Particle Synthesis and Future Industrial Manufacturing Pathways: A Review. *Industrial & Engineering Chemistry Research* **2016,** *55* (33), 8891-8913.
43. Kaewsaneha, C.; Tangboriboonrat, P.; Polpanich, D.; Eissa, M.; Elaissari, A., Janus Colloidal Particles: Preparation, Properties, and Biomedical Applications. *ACS Applied Materials & Interfaces* **2013,** *5* (6), 1857-1869.
44. Trujillo, N. J.; Baxamusa, S. H.; Gleason, K. K., Grafted Functional Polymer Nanostructures Patterned Bottom-Up by Colloidal Lithography and Initiated Chemical Vapor Deposition (iCVD). *Chemistry of Materials* **2009,** *21* (4), 742-750.
45. (a) Sukhorukov, G.; Donath, E.; Lichtenfeld, H.; Knippel, E.; Knippel, M.; Budde, A.; Moehwald, H., *Layer-by-layer self-Assembly of polyelectrolytes onto colloidal particles*. 1998; Vol. 137, p 253-266; (b) Coustet, M.; Irigoyen, J.; Garcia, T. A.; Murray, R. A.; Romero, G.; Susana Cortizo, M.; Knoll, W.; Azzaroni, O.; Moya, S. E., Layer-by-layer assembly of polymersomes and polyelectrolytes on planar surfaces and microsized colloidal particles. *J Colloid Interface Sci* **2014,** *421*, 132-40.
46. Caruso, F.; Caruso, R. A.; Mohwald, H., Nanoengineering of inorganic and hybrid hollow spheres by colloidal templating. *Science* **1998,** *282* (5391), 1111-4.
47. Wang, Y.; Caruso, F., Macroporous Zeolitic Membrane Bioreactors. *Advanced Functional Materials* **2004,** *14* (10), 1012-1018.
48. McGorty, R.; Fung, J.; Kaz, D.; Manoharan, V. N., Colloidal self-assembly at an interface. *Materials Today* **2010,** *13* (6), 34-42.
49. Mendelsohn, J. D.; Barrett, C. J.; Chan, V. V.; Pal, A. J.; Mayes, A. M.; Rubner, M. F., Fabrication of Microporous Thin Films from Polyelectrolyte Multilayers. *Langmuir* **2000,** *16* (11), 5017-5023.
50. Zheng, H.; Lee, I.; Rubner, M. F.; Hammond, P. T., Two Component Particle Arrays on Patterned Polyelectrolyte Multilayer Templates. *Advanced Materials* **2002,** *14* (8), 569-572.
51. Liu, X.; Ma, P. X., Phase separation, pore structure, and properties of nanofibrous gelatin scaffolds. *Biomaterials* **2009,** *30* (25), 4094-103.
52. Kumar, S. K.; Hong, J. D., Photoresponsive ion gating function of an azobenzene polyelectrolyte multilayer spin-self-assembled on a nanoporous support. *Langmuir* **2008,** *24* (8), 4190-3.
53. Zhao, J.; Han, W.; Chen, H.; Tu, M.; Zeng, R.; Shi, Y.; Cha, Z.; Zhou, C., Preparation, structure and crystallinity of chitosan nano-fibers by a solid–liquid phase separation technique. *Carbohydrate Polymers* **2011,** *83* (4), 1541-1546.
54. Tokarev, I.; Minko, S., Multiresponsive, Hierarchically Structured Membranes: New, Challenging, Biomimetic Materials for Biosensors, Controlled Release, Biochemical Gates, and Nanoreactors. *Advanced Materials* **2009,** *21* (2), 241-247.
55. (a) Arnold, C. B.; Serra, P.; Piqué, A., Laser direct-write techniques for printing of complex materials. *Mrs Bulletin* **2007,** *32* (1), 23-31; (b) Zhang, Y.; Liu, C.; Whalley, D. In *Direct-write techniques*

for maskless production of microelectronics: A review of current state-of-the-art technologies, 2009 International Conference on Electronic Packaging Technology & High Density Packaging, 10-13 Aug. 2009; 2009; pp 497-503.
56. Barry, R. A.; Shepherd, R. F.; Hanson, J. N.; Nuzzo, R. G.; Wiltzius, P.; Lewis, J. A., Direct-Write Assembly of 3D Hydrogel Scaffolds for Guided Cell Growth. *Advanced Materials* **2009,** *21* (23), 2407-2410.
57. Choi, M.; Park, H. H.; Choi, D.; Han, U.; Park, T. H.; Lee, H.; Park, J.; Hong, J., Multilayer Nanofilms via Inkjet Printing for Stabilizing Growth Factor and Designing Desired Cell Developments. *Advanced Healthcare Materials* **2017,** *6* (14), 1700216.
58. Yang, S. Y.; Rubner, M. F., Micropatterning of Polymer Thin Films with pH-Sensitive and Cross-linkable Hydrogen-Bonded Polyelectrolyte Multilayers. *Journal of the American Chemical Society* **2002,** *124* (10), 2100-2101.
59. Suntivich, R.; Shchepelina, O.; Choi, I.; Tsukruk, V. V., Inkjet-Assisted Layer-by-Layer Printing of Encapsulated Arrays. *ACS Applied Materials & Interfaces* **2012,** *4* (6), 3102-3110.
60. (a) Alom Ruiz, S.; Chen, C. S., Microcontact printing: A tool to pattern. *Soft Matter* **2007,** *3* (2), 168-177; (b) Gu, J.; Xiao, X.; Takulapalli, B. R.; Morrison, M. E.; Zhang, P.; Zenhausern, F., A new approach to fabricating high density nanoarrays by nanocontact printing. *Journal of Vacuum Science & Technology B: Microelectronics and Nanometer Structures Processing, Measurement, and Phenomena* **2008,** *26* (6), 1860-1865.
61. Yang, S. H.; Choi, I. S., Bio-Inspired Silicification on Patterned Surfaces Generated by Microcontact Printing and Layer-by-Layer Self-Assembly. *Chemistry – An Asian Journal* **2009,** *4* (3), 382-385.
62. (a) Desai, T. A., Micro- and nanoscale structures for tissue engineering constructs. *Medical Engineering and Physics* **2000,** *22* (9), 595-606; (b) Tran, K. T. M.; Nguyen, T. D., Lithography-based methods to manufacture biomaterials at small scales. *Journal of Science: Advanced Materials and Devices* **2017,** *2* (1), 1-14.
63. Choi, Y.-K.; Zhu, J.; Grunes, J.; Bokor, J.; Somorjai, G. A., Fabrication of Sub-10-nm Silicon Nanowire Arrays by Size Reduction Lithography. *The Journal of Physical Chemistry B* **2003,** *107* (15), 3340-3343.
64. Pinto, V.; Sousa, P.; Cardoso, V.; Minas, G., Optimized SU-8 Processing for Low-Cost Microstructures Fabrication without Cleanroom Facilities. *Micromachines* **2014,** *5* (3), 738.
65. Qin, D.; Xia, Y.; Whitesides, G. M., Soft lithography for micro- and nanoscale patterning. *Nature Protocols* **2010,** *5*, 491.
66. Gai, M.; Frueh, J.; Kudryavtseva, V. L.; Mao, R.; Kiryukhin, M. V.; Sukhorukov, G. B., Patterned Microstructure Fabrication: Polyelectrolyte Complexes vs Polyelectrolyte Multilayers. *Scientific Reports* **2016,** *6*, 37000.
67. Monge, C.; Ren, K.; Berton, K.; Guillot, R.; Peyrade, D.; Picart, C., Engineering Muscle Tissues on Microstructured Polyelectrolyte Multilayer Films. *Tissue Engineering. Part A* **2012,** *18* (15-16), 1664-1676.
68. Velve-Casquillas, G.; Le Berre, M.; Piel, M.; Tran, P. T., Microfluidic tools for cell biological research. *Nano today* **2010,** *5* (1), 28-47.
69. Mark, D.; Haeberle, S.; Roth, G.; von Stetten, F.; Zengerle, R., Microfluidic lab-on-a-chip platforms: requirements, characteristics and applications. *Chemical Society Reviews* **2010,** *39* (3), 1153-1182.
70. Zhen, C.; Yu, Z.; Wei, W.; Zhihong, L. In *Microfluidic patterning of nanoparticle monolayer: Mechanism analysis and noncontinuously patterning approach*, 2009 4th IEEE International Conference on Nano/Micro Engineered and Molecular Systems, 5-8 Jan. 2009; 2009; pp 818-821.
71. Kang, E.; Choi, Y. Y.; Chae, S.-K.; Moon, J.-H.; Chang, J.-Y.; Lee, S.-H., Microfluidic Spinning of Flat Alginate Fibers with Grooves for Cell-Aligning Scaffolds. *Advanced Materials* **2012,** *24* (31), 4271-4277.
72. Cheung, Y. K.; Gillette, B. M.; Zhong, M.; Ramcharan, S.; Sia, S. K., Direct patterning of composite biocompatible microstructures using microfluidics. *Lab on a Chip* **2007,** *7* (5), 574-579.
73. Castleberry, S. A.; Li, W.; Deng, D.; Mayner, S.; Hammond, P. T., Capillary Flow Layer-by-Layer: A Microfluidic Platform for the High-Throughput Assembly and Screening of Nanolayered Film Libraries. *ACS Nano* **2014,** *8* (7), 6580-6589.
74. Hammond, P. T., Building biomedical materials layer-by-layer. *Materials Today* **2012,** *15* (5), 196-206.

75. Bai, Y.; Ho, S.; Kotov, N. A., Direct-write maskless lithography of LBL nanocomposite films and its prospects for MEMS technologies. *Nanoscale* **2012,** *4* (15), 4393-4398.
76. Kohli, N.; Worden, R. M.; Lee, I., Direct transfer of preformed patterned bio-nanocomposite films on polyelectrolyte multilayer templates. *Macromol Biosci* **2007,** *7* (6), 789-97.
77. Kidambi, S.; Udpa, N.; Schroeder, S. A.; Findlan, R.; Lee, I.; Chan, C., Cell Adhesion on Polyelectrolyte Multilayer Coated Polydimethylsiloxane Surfaces with Varying Topographies. *Tissue Engineering* **2007,** *13* (8), 2105-2117.
78. (a) Jiang, X.; Hammond, P. T., Selective Deposition in Layer-by-Layer Assembly: Functional Graft Copolymers as Molecular Templates. *Langmuir* **2000,** *16* (22), 8501-8509; (b) Jiang, X.-P.; Clark, S. L.; Hammond, P. T., Side-by-Side Directed Multilayer Patterning Using Surface Templates. *Advanced Materials* **2001,** *13* (22), 1669-1673; (c) Park, J.; Hammond, P. T., Multilayer Transfer Printing for Polyelectrolyte Multilayer Patterning: Direct Transfer of Layer-by-Layer Assembled Micropatterned Thin Films. *Advanced Materials* **2004,** *16* (6), 520-525.
79. Almodovar, J.; Crouzier, T.; Selimovic, S.; Boudou, T.; Khademhosseini, A.; Picart, C., Gradients of physical and biochemical cues on polyelectrolyte multilayer films generated via microfluidics. *Lab Chip* **2013,** *13* (8), 1562-70.
80. Lin, Y.-H.; Jiang, C.; Xu, J.; Lin, Z.; Tsukruk, V. V., Sculptured Layer-by-Layer Films. *Advanced Materials* **2007,** *19* (22), 3827-3832.
81. Li, M.; Cui, T.; Mills, D. K.; Lvov, Y. M.; McShane, M. J., Comparison of selective attachment and growth of smooth muscle cells on gelatin- and fibronectin-coated micropatterns. *J Nanosci Nanotechnol* **2005,** *5* (11), 1809-15.
82. Chien, H.-W.; Chang, T.-Y.; Tsai, W.-B., Spatial control of cellular adhesion using photo-crosslinked micropatterned polyelectrolyte multilayer films. *Biomaterials* **2009,** *30* (12), 2209-2218.
83. Clark, S. L.; Hammond, P. T., Engineering the Microfabrication of Layer-by-Layer Thin Films. *Advanced Materials* **1998,** *10* (18), 1515-1519.
84. Kim, T. G.; Park, S.-H.; Chung, H. J.; Yang, D.-Y.; Park, T. G., Microstructured scaffold coated with hydroxyapatite/collagen nanocomposite multilayer for enhanced osteogenic induction of human mesenchymal stem cells. *Journal of Materials Chemistry* **2010,** *20* (40), 8927-8933.
85. Lu, Y.; Sun, J.; Shen, J., Cell adhesion properties of patterned poly(acrylic acid)/poly(allylamine hydrochloride) multilayer films created by room-temperature imprinting technique. *Langmuir* **2008,** *24* (15), 8050-5.
86. Shi, F.; Wang, Z.; Zhao, N.; Zhang, X., Patterned Polyelectrolyte Multilayer: Surface Modification for Enhancing Selective Adsorption. *Langmuir* **2005,** *21* (4), 1599-1602.
87. Hua, F.; Shi, J.; Lvov, Y.; Cui, T., Patterning of Layer-by-Layer Self-Assembled Multiple Types of Nanoparticle Thin Films by Lithographic Technique. *Nano Letters* **2002,** *2* (11), 1219-1222.
88. Fukuda, J.; Khademhosseini, A.; Yeh, J.; Eng, G.; Cheng, J.; Farokhzad, O. C.; Langer, R., Micropatterned cell co-cultures using layer-by-layer deposition of extracellular matrix components. *Biomaterials* **2006,** *27* (8), 1479-86.
89. Shaikh Mohammed, J.; DeCoster, M. A.; McShane, M. J., Micropatterning of Nanoengineered Surfaces to Study Neuronal Cell Attachment *in Vitro*. *Biomacromolecules* **2004,** *5* (5), 1745-1755.
90. Shaik, J.; Shaikh Mohammed, J.; McShane, M. J.; Mills, D. K., Chondrocyte Behavior on Micropatterns Fabricated Using Layer-by-Layer Lift-Off: Morphological Analysis. *Journal of Medical Engineering* **2013,** *2013*, 12.
91. Palamà, I. E.; D'Amone, S.; Coluccia, A. M. L.; Gigli, G., Micropatterned polyelectrolyte nanofilms promote alignment and myogenic differentiation of C2C12 cells in standard growth media. *Biotechnology and Bioengineering* **2013,** *110* (2), 586-596.
92. DeMuth, P. C.; Su, X.; Samuel, R. E.; Hammond, P. T.; Irvine, D. J., Nano-Layered Microneedles for Transcutaneous Delivery of Polymer Nanoparticles and Plasmid DNA. *Advanced Materials* **2010,** *22* (43), 4851-4856.
93. Neto, A. I.; Levkin, P. A.; Mano, J. F., Patterned superhydrophobic surfaces to process and characterize biomaterials and 3D cell culture. *Materials Horizons* **2018,** *5* (3), 379-393.
94. Jiang, C.; Tsukruk, V. V., Organized arrays of nanostructures in freely suspended nanomembranes. *Soft Matter* **2005,** *1* (5), 334-337.
95. Zhang, C.; Hirt, D. E., Layer-by-layer self-assembly of polyelectrolyte multilayers on cross-section surfaces of multilayer polymer films: A step toward nano-patterning flexible substrates. *Polymer* **2007,** *48* (23), 6748-6754.

96. Lee, K. G.; Choi, B. G.; Kim, B. I.; Shyu, T.; Oh, M. S.; Im, S. G.; Chang, S.-J.; Lee, T. J.; Kotov, N. A.; Lee, S. J., Scalable Nanopillar Arrays with Layer-by-Layer Patterned Overt and Covert Images. *Advanced Materials* **2014,** *26* (35), 6119-6124.

97. Kim, B.-S.; Lee, S. W.; Yoon, H.; Strano, M. S.; Shao-Horn, Y.; Hammond, P. T., Pattern Transfer Printing of Multiwalled Carbon Nanotube Multilayers and Application in Biosensors. *Chemistry of Materials* **2010,** *22* (16), 4791-4797.

98. Firkowska, I.; Giannona, S.; Rojas-Chapana, J.; Giersig, M., Qualitative Evaluation of the Response of Human Osteoblast Cells to Nanotopography Surface Based on Carbon Nanotubes. **2006**.

99. Sousa, M. P.; Caridade, S. G.; Mano, J. F., Control of Cell Alignment and Morphology by Redesigning ECM-Mimetic Nanotopography on Multilayer Membranes. *Advanced Healthcare Materials* **2017,** *6* (15), 1601462.

100. Lee, S.; Kim, D.; Kim, S. M.; Kim, J. A.; Kim, T.; Kim, D. Y.; Yoon, M. H., Polyelectrolyte multilayer-assisted fabrication of non-periodic silicon nanocolumn substrates for cellular interface applications. *Nanoscale* **2015,** *7* (35), 14627-35.

101. Huang, R.; Li, W. Z.; Lv, X. X.; Lei, Z. J.; Bian, Y. Q.; Deng, H. B.; Wang, H. J.; Li, J. Q.; Li, X. Y., Biomimetic LBL structured nanofibrous matrices assembled by chitosan/collagen for promoting wound healing. *Biomaterials* **2015,** *53*, 58-75.

102. Harrison, R. G., On the stereotropism of embryonic cells. *Science* **1911,** *34* (870), 279-81.

103. Clark, P.; Connolly, P.; Curtis, A. S.; Dow, J. A.; Wilkinson, C. D., Topographical control of cell behaviour. I. Simple step cues. *Development* **1987,** *99* (3), 439-448.

104. (a) Georges, P. C.; Janmey, P. A., Cell type-specific response to growth on soft materials. *Journal of applied physiology (Bethesda, Md. : 1985)* **2005,** *98* (4), 1547-53; (b) Biela, S. A.; Su, Y.; Spatz, J. P.; Kemkemer, R., Different sensitivity of human endothelial cells, smooth muscle cells and fibroblasts to topography in the nano-micro range. *Acta Biomater* **2009,** *5* (7), 2460-6.

105. Jeon, H.; Simon, C. G.; Kim, G., A mini-review: Cell response to microscale, nanoscale, and hierarchical patterning of surface structure. *Journal of Biomedical Materials Research Part B: Applied Biomaterials* **2014,** *102* (7), 1580-1594.

106. Cretel, E.; Pierres, A.; Benoliel, A.-M.; Bongrand, P., How Cells feel their environment: a focus on early dynamic events. *Cellular and Molecular Bioengineering* **2008,** *1* (1), 5-14.

107. Thery, M., Micropatterning as a tool to decipher cell morphogenesis and functions. *Journal of cell science* **2010,** *123* (Pt 24), 4201-13.

108. Cavalcanti-Adam, E. A.; Volberg, T.; Micoulet, A.; Kessler, H.; Geiger, B.; Spatz, J. P., Cell Spreading and Focal Adhesion Dynamics Are Regulated by Spacing of Integrin Ligands. *Biophysical Journal* **2007,** *92* (8), 2964-2974.

109. Diener, A.; Nebe, B.; Lüthen, F.; Becker, P.; Beck, U.; Neumann, H. G.; Rychly, J., Control of focal adhesion dynamics by material surface characteristics. *Biomaterials* **2005,** *26* (4), 383-392.

110. Duval, K.; Grover, H.; Han, L.-H.; Mou, Y.; Pegoraro, A. F.; Fredberg, J.; Chen, Z., Modeling Physiological Events in 2D vs. 3D Cell Culture. *Physiology* **2017,** *32* (4), 266-277.

111. (a) Aurore, S.; Ludovic, R.; Gregory, F.; Jean-Claude, V.; Catherine, P., Elasticity, biodegradability and cell adhesive properties of chitosan/hyaluronan multilayer films. *Biomedical Materials* **2007,** *2* (1), S45; (b) Pozos Vázquez, C.; Boudou, T.; Dulong, V.; Nicolas, C.; Picart, C.; Glinel, K., Variation of Polyelectrolyte Film Stiffness by Photo-Cross-Linking: A New Way To Control Cell Adhesion. *Langmuir* **2009,** *25* (6), 3556-3563; (c) Correia, C. R.; Pirraco, R. P.; Cerqueira, M. T.; Marques, A. P.; Reis, R. L.; Mano, J. F., Semipermeable Capsules Wrapping a Multifunctional and Self-regulated Co-culture Microenvironment for Osteogenic Differentiation. *Scientific Reports* **2016,** *6*, 21883; (d) Sousa, M. P.; Neto, A. I.; Correia, T. R.; Miguel, S. P.; Matsusaki, M.; Correia, I. J.; Mano, J. F., Bioinspired multilayer membranes as potential adhesive patches for skin wound healing. *Biomaterials Science* **2018,** *6* (7), 1962-1975.

112. Anh Tuan, N.; Sharvari, R. S.; Evelyn, K. F. Y., From nano to micro: topographical scale and its impact on cell adhesion, morphology and contact guidance. *Journal of Physics: Condensed Matter* **2016,** *28* (18), 183001.

113. (a) Parsons, J. T.; Horwitz, A. R.; Schwartz, M. A., Cell adhesion: integrating cytoskeletal dynamics and cellular tension. *Nature reviews. Molecular cell biology* **2010,** *11* (9), 633-643; (b) Albuschies, J.; Vogel, V., The role of filopodia in the recognition of nanotopographies. *Scientific Reports* **2013,** *3*, 1658.

114. Ventre, M.; Natale, C. F.; Rianna, C.; Netti, P. A., Topographic cell instructive patterns to control cell adhesion, polarization and migration. *Journal of the Royal Society Interface* **2014,** *11* (100), 20140687.

115. Lee, J. W.; Lee, K. B.; Jeon, H. S.; Park, H. K., Effects of surface nano-topography on human osteoblast filopodia. *Analytical sciences : the international journal of the Japan Society for Analytical Chemistry* **2011,** *27* (4), 369.

116. Ventre, M.; Causa, F.; Netti, P. A., Determinants of cell–material crosstalk at the interface: towards engineering of cell instructive materials. *Journal of The Royal Society Interface* **2012,** *9* (74), 2017-2032.

117. (a) Lenhert, S.; Meier, M. B.; Meyer, U.; Chi, L.; Wiesmann, H. P., Osteoblast alignment, elongation and migration on grooved polystyrene surfaces patterned by Langmuir-Blodgett lithography. *Biomaterials* **2005,** *26* (5), 563-70; (b) Abagnale, G.; Sechi, A.; Steger, M.; Zhou, Q.; Kuo, C.-C.; Aydin, G.; Schalla, C.; Müller-Newen, G.; Zenke, M.; Costa, I. G.; van Rijn, P.; Gillner, A.; Wagner, W., Surface Topography Guides Morphology and Spatial Patterning of Induced Pluripotent Stem Cell Colonies. *Stem Cell Reports* **2017,** *9* (2), 654-666.

118. Malheiro, V.; Lehner, F.; Dinca, V.; Hoffmann, P.; Maniura-Weber, K., Convex and concave micro-structured silicone controls the shape, but not the polarization state of human macrophages. *Biomaterials Science* **2016,** *4* (11), 1562-1573.

119. (a) Karuri, N. W.; Liliensiek, S.; Teixeira, A. I.; Abrams, G.; Campbell, S.; Nealey, P. F.; Murphy, C. J., Biological length scale topography enhances cell-substratum adhesion of human corneal epithelial cells. *Journal of cell science* **2004,** *117* (Pt 15), 3153-3164; (b) Peterbauer, T.; Yakunin, S.; Siegel, J.; Hering, S.; Fahrner, M.; Romanin, C.; Heitz, J., Dynamics of Spreading and Alignment of Cells Cultured *In Vitro* on a Grooved Polymer Surface. *Journal of Nanomaterials* **2011,** *2011*, 10.

120. McNamara, L. E.; McMurray, R. J.; Biggs, M. J.; Kantawong, F.; Oreffo, R. O.; Dalby, M. J., Nanotopographical control of stem cell differentiation. *Journal of tissue engineering* **2010,** *2010*, 120623.

121. Hwang, Y.; Seo, T.; Hariri, S.; Choi, C.; Varghese, S., Matrix Topographical Cue-Mediated Myogenic Differentiation of Human Embryonic Stem Cell Derivatives. *Polymers* **2017,** *9* (11), 580.

122. Agrawal, A.; Lee, B. H.; Irvine, S. A.; An, J.; Bhuthalingam, R.; Singh, V.; Low, K. Y.; Chua, C. K.; Venkatraman, S. S., Smooth Muscle Cell Alignment and Phenotype Control by Melt Spun Polycaprolactone Fibers for Seeding of Tissue Engineered Blood Vessels. *International Journal of Biomaterials* **2015,** *2015*, 434876.

123. Vandrangi, P.; Gott, S. C.; Kozaka, R.; Rodgers, V. G. J.; Rao, M. P., Comparative Endothelial Cell Response on Topographically Patterned Titanium and Silicon Substrates with Micrometer to Sub-Micrometer Feature Sizes. *PLOS ONE* **2014,** *9* (10), e111465.

124. Teixeira, A. I.; Abrams, G. A.; Bertics, P. J.; Murphy, C. J.; Nealey, P. F., Epithelial contact guidance on well-defined micro- and nanostructured substrates. *Journal of cell science* **2003,** *116* (10), 1881-1892.

125. Hsu, S. H.; Chen, C. Y.; Lu, P. S.; Lai, C. S.; Chen, C. J., Oriented Schwann cell growth on microgrooved surfaces. *Biotechnol Bioeng* **2005,** *92* (5), 579-88.

126. Li, J.; McNally, H.; Shi, R., Enhanced neurite alignment on micro-patterned poly-L-lactic acid films. *Journal of biomedical materials research. Part A* **2008,** *87* (2), 392-404.

127. Palamà, I. E.; Coluccia, A. M. L.; Gigli, G.; Riehle, M., Modulation of alignment and differentiation of skeletal myoblasts by biomimetic materials. *Integrative Biology* **2012,** *4* (10), 1299-1309.

128. Trepat, X.; Chen, Z.; Jacobson, K., Cell Migration. *Comprehensive Physiology* **2012,** *2* (4), 2369-2392.

129. George, M.; Bullo, F.; Campàs, O., Connecting individual to collective cell migration. *Scientific Reports* **2017,** *7* (1), 9720.

130. Horwitz, R.; Webb, D., Cell migration. *Current Biology* **2003,** *13* (19), R756-R759.

131. Ngalim, S. H.; Magenau, A.; Le Saux, G.; Gooding, J. J.; Gaus, K., How Do Cells Make Decisions: Engineering Micro- and Nanoenvironments for Cell Migration. *Journal of Oncology* **2010,** *2010*.

132. Mak, M.; Spill, F.; Kamm, R. D.; Zaman, M. H., Single-Cell Migration in Complex Microenvironments: Mechanics and Signaling Dynamics. *Journal of Biomechanical Engineering* **2016,** *138* (2), 0210041-0210048.

133. Jansen, K. A.; Atherton, P.; Ballestrem, C., Mechanotransduction at the cell-matrix interface. *Seminars in Cell & Developmental Biology* **2017,** *71*, 75-83.

134. le Digabel, J.; Ghibaudo, M.; Trichet, L.; Richert, A.; Ladoux, B., Microfabricated substrates as a tool to study cell mechanotransduction. *Med Biol Eng Comput* **2010,** *48* (10), 965-76.

135. Massumi, M.; Abasi, M.; Babaloo, H.; Terraf, P.; Safi, M.; Saeed, M.; Barzin, J.; Zandi, M.; Soleimani, M., The effect of topography on differentiation fates of matrigel-coated mouse embryonic stem cells cultured on PLGA nanofibrous scaffolds. *Tissue Eng Part A* **2012,** *18* (5-6), 609-20.

136. (a) Kilian, K. A.; Bugarija, B.; Lahn, B. T.; Mrksich, M., Geometric cues for directing the differentiation of mesenchymal stem cells. *Proceedings of the National Academy of Sciences* **2010,** *107* (11), 4872-4877; (b) Newman, P.; Galeano Niño, J. L.; Graney, P.; Razal, J. M.; Minett, A. I.; Ribas, J.; Ovalle-Robles, R.; Biro, M.; Zreiqat, H., Relationship between nanotopographical alignment and stem cell fate with live imaging and shape analysis. *Scientific Reports* **2016,** *6*, 37909.
137. (a) Wang, P. Y.; Li, W. T.; Yu, J.; Tsai, W. B., Modulation of osteogenic, adipogenic and myogenic differentiation of mesenchymal stem cells by submicron grooved topography. *Journal of materials science. Materials in medicine* **2012,** *23* (12), 3015-28; (b) Prabhakaran, M. P.; Vatankhah, E.; Kai, D.; Ramakrishna, S., Methods for Nano/Micropatterning of Substrates: Toward Stem Cells Differentiation. *International Journal of Polymeric Materials and Polymeric Biomaterials* **2015,** *64* (7), 338-353.
138. Kirmizidis, G.; Birch, M. A., Microfabricated grooved substrates influence cell-cell communication and osteoblast differentiation *in vitro*. *Tissue Eng Part A* **2009,** *15* (6), 1427-36.
139. Davison, M. J.; McMurray, R. J.; Smith, C.-A.; Dalby, M. J.; Meek, R. M. D., Nanopit-induced osteoprogenitor cell differentiation: The effect of nanopit depth. *Journal of tissue engineering* **2016,** *7*, 2041731416652778.
140. Hu, Y.; Cai, K.; Luo, Z.; Xu, D.; Xie, D.; Huang, Y.; Yang, W.; Liu, P., TiO2 nanotubes as drug nanoreservoirs for the regulation of mobility and differentiation of mesenchymal stem cells. *Acta Biomater* **2012,** *8* (1), 439-48.

8. Supplementary Information

Table S II-1. Literature survey of some of the existent works on modulating the cellular functions and fate using micro- and nanoscale patterned materials, produced by single or combined LbL technique. The type of features, the respective dimensions, the tested cell type and the respective biological responses are described

Feature type	Dimensions			Cell type	Cell behaviour
	Width/ D	Gap/ Spacing	Depth/ Height		
Organized fiber mesh	200µm	400µm		hMSCs	Enhanced cell adhesion, proliferation and ALP activity (when in osteogenic medium) [1]
CNTs-based matrix	1.7µm	----------	----------	Human osteosarcoma cell line CAL-72	Excellent adhesion and spreading, coating the matrix surface very densely; stress elongation formation [2]
Pillars	1.25-9µm	18µm	2.5µm	NIH 3T3 fibroblast and HeLa cell lines	Differences in the features sizes influenced the attachment and growth of the cells; in general, smaller features ‘diameter meant higher proliferation [3]
Grooves	6.5/69µm	3.5/43µm	1.29-0.109µm	NIH 3T3 fibroblast and HeLa cell lines	By either increasing the lateral size of the patters to 69µm-line/43µm-space or decreasing the height of the imprinted lines to ~107 nm, the imprinted PAA/PAH multilayer films become cytophilic [4]
Tuned well arrays	500µm	200µm	38µm	SaOs-2 human osteoblast-like cells	The cells migrated specifically to the wells; the increasing surface area allowed higher rates of proliferation as well as better cellular distribution over the substrates [5]
Grooves	Ranging between 650-850nm	~500nm	Ranging between 200-500nm	Mouse L929 fibroblast and C2C12 myoblast cell line	For L929 fibroblast: the nanotopography could induce significantly cell orientation. For C2C12 myoblast: it was possible to observe the alignment and myogenic differentiation on nanopatterned membranes, even in absence of special differentiation medium [6]
Columns	150nm	----------	1-2µm	Fibroblasts (NIH/3T3) and primary neuronal cell line	The topography supported the viable culture of primary neuronal cells and proliferating fibroblasts, which show a smaller cell area and uninterrupted motility [7]
Fibers	392-541nm	-----------	----------	Normal human dermal fibroblasts (NHDFs)	Accelerated cell migration, relatively higher cell attachment, proliferation, spreading and migration of cells tested were observed on LBL structured nanofibrous matrices in comparison to the unmodified ones [8]
Stripes/Circles	~50µm/ 300µm	~50µm/ 200µm	----------	PC-12, MG-63, C3A and L929 cells	The topography could control cellular spatial attachment and growth
Circles holes	100µm	-----------	0.06µm	Murine embryonic stem cells, AML12 hepatocytes and NIH-3T3 fibroblasts	The pattern afforded high biological affinity and no cytotoxicity [9]

Cylindrical holes	15-150µm	-----------	----------	Murine embryonic stem cells, AML12 hepatocytes and NIH-3T3 fibroblasts	This is a versatile approach to generate patterned co-cultures irrespective of the primary cell seeding and relative adhesion of the seeded cells [10]
Circles holes	-----------	-----------	60µm	L929 cells	The seeding of L929 cells onto the LbL coating leads to a highly selective adhesion of cells; they spread well within twelve hours over the imprints [11]
Squares	20µm	~80µm	----------	Primary neuronal cell line	sPLA2 has potential as a neuronal binding target. This technique offers the potential for production of a wide array of biological test systems, including comparison chips with different materials, different size and shapes of the micropatterns, and utility with different cell models [12]
Stripes	80/100 µm	240/300 µm	0.06/0.15µm	Canine chondrocytes (CnC)	CnC exhibited preferential attachment on micropatterns of PEI, PSS, collagen, and CS multilayer nanofilms [13]
Stripes/ squares	60/80/ 100µm	-----------	-------------	Smooth muscle cells (SMCs)	The SMCs depends on the shape of the gelatin patterns: strip patterns have more power to limit the cells to only grow on gelatin-coated surface, while square patterns do not. Fibronectin attract all the cells to grow on its surface no matter the shape of the patterns [14]
Stripes	25/50/ 150µm µm	-----------	0.03-0.2µm	C2C12 cell line	Patterned substrates consisting of cell-repellant and cell-adhesive regions have been used for the spatial control of cell attachment *in vitro*; their parallel alignment was essential for their fusion into myotubes [15]
Grooves	5/10/30/ 100µm	5/10/30/ 100µm	4µm	C2C12 cell line	The substrate can serve as an inductive template for *in vivo* muscle tissue regeneration; it drives the development, alignment, and further fusion of cells after implantation [16]

References

1. Kim, T. G.; Park, S.-H.; Chung, H. J.; Yang, D.-Y.; Park, T. G., Microstructured scaffold coated with hydroxyapatite/collagen nanocomposite multilayer for enhanced osteogenic induction of human mesenchymal stem cells. *Journal of Materials Chemistry* **2010,** *20* (40), 8927-8933.
2. Firkowska, I.; Giannona, S.; Rojas-Chapana, J.; Giersig, M., Qualitative Evaluation of the Response of Human Osteoblast Cells to Nanotopography Surface Based on Carbon Nanotubes. **2006**.
3. Kidambi, S.; Udpa, N.; Schroeder, S. A.; Findlan, R.; Lee, I.; Chan, C., Cell Adhesion on Polyelectrolyte Multilayer Coated Polydimethylsiloxane Surfaces with Varying Topographies. *Tissue Engineering* **2007,** *13* (8), 2105-2117.
4. Lu, Y.; Sun, J.; Shen, J., Cell adhesion properties of patterned poly(acrylic acid)/poly(allylamine hydrochloride) multilayer films created by room-temperature imprinting technique. *Langmuir* **2008,** *24* (15), 8050-5.
5. Martins, N. I.; Sousa, M. P.; Custódio, C. A.; Pinto, V. C.; Sousa, P. J.; Minas, G.; Cleymand, F.; Mano, J. F., Multilayered membranes with tuned well arrays to be used as regenerative patches. *Acta Biomaterialia* **2017**.
6. Sousa, M. P.; Caridade, S. G.; Mano, J. F., Control of Cell Alignment and Morphology by Redesigning ECM-Mimetic Nanotopography on Multilayer Membranes. *Advanced Healthcare Materials* **2017,** *6* (15), 1601462.
7. Lee, S.; Kim, D.; Kim, S. M.; Kim, J. A.; Kim, T.; Kim, D. Y.; Yoon, M. H., Polyelectrolyte multilayer-assisted fabrication of non-periodic silicon nanocolumn substrates for cellular interface applications. *Nanoscale* **2015,** *7* (35), 14627-35.

8. Huang, R.; Li, W. Z.; Lv, X. X.; Lei, Z. J.; Bian, Y. Q.; Deng, H. B.; Wang, H. J.; Li, J. Q.; Li, X. Y., Biomimetic LBL structured nanofibrous matrices assembled by chitosan/collagen for promoting wound healing. *Biomaterials* **2015,** *53*, 58-75.
9. Fukuda, J.; Khademhosseini, A.; Yeh, J.; Eng, G.; Cheng, J.; Farokhzad, O. C.; Langer, R., Micropatterned cell co-cultures using layer-by-layer deposition of extracellular matrix components. *Biomaterials* **2006,** *27* (8), 1479-86.
10. Khademhosseini, A.; Suh, K. Y.; Yang, J. M.; Eng, G.; Yeh, J.; Levenberg, S.; Langer, R., Layer-by-layer deposition of hyaluronic acid and poly-l-lysine for patterned cell co-cultures. *Biomaterials* **2004,** *25* (17), 3583-3592.
11. Madaboosi, N.; Uhlig, K.; Schmidt, S.; Jäger, M. S.; Möhwald, H.; Duschl, C.; Volodkin, D. V., Microfluidics meets soft layer-by-layer films: selective cell growth in 3D polymer architectures. *Lab on a Chip* **2012,** *12* (8), 1434-1436.
12. Shaikh Mohammed, J.; DeCoster, M. A.; McShane, M. J., Micropatterning of Nanoengineered Surfaces to Study Neuronal Cell Attachment *in Vitro*. *Biomacromolecules* **2004,** *5* (5), 1745-1755.
13. Shaik, J.; Shaikh Mohammed, J.; McShane, M. J.; Mills, D. K., Chondrocyte Behavior on Micropatterns Fabricated Using Layer-by-Layer Lift-Off: Morphological Analysis. *Journal of Medical Engineering* **2013,** *2013*, 12.
14. Li, M.; Cui, T.; Mills, D. K.; Lvov, Y. M.; McShane, M. J., Comparison of selective attachment and growth of smooth muscle cells on gelatin- and fibronectin-coated micropatterns. *J Nanosci Nanotechnol* **2005,** *5* (11), 1809-15.
15. Palamà, I. E.; D'Amone, S.; Coluccia, A. M. L.; Gigli, G., Micropatterned polyelectrolyte nanofilms promote alignment and myogenic differentiation of C2C12 cells in standard growth media. *Biotechnology and Bioengineering* **2013,** *110* (2), 586-596.
16. Monge, C.; Ren, K.; Berton, K.; Guillot, R.; Peyrade, D.; Picart, C., Engineering Muscle Tissues on Microstructured Polyelectrolyte Multilayer Films. *Tissue Engineering. Part A* **2012,** *18* (15-16), 1664-1676.

III. Materials and Methods

Abstract

In this Chapter, it is possible to obtain a detailed description of the used materials, the produced films and the properties and explanation of the techniques used to obtain the results described in this thesis.

The present chapter describes and details the materials, methodologies and techniques used to produce thin multilayered films and modify them towards biomedical and TE strategies. Multilayered films were produced by the layer-by-layer adsorption of different polysaccharides, as CHT, CS, HA and ALG. Moreover, by playing with biomimetic elastin-like-polypeptides (ELPs) it was possible to perceive the versatility of the LbL assembly, being driven by click chemistry instead electrostatic forces. In addition, a biomimetic mussel foot protein, dopamine (DN) was chemically bounded to HA conferring adhesive properties. Overall, tailoring the composition, the driven forces of the deposition, as well as the underlying substrate or the physical or chemical modification of the LbL-based film, can influence the cellular behaviour. Therefore, different types of cells were tested, namely L929 fibroblasts and C2C12 myoblasts, MC3T3-E1 pre-osteoblasts, human dermal fibroblasts (HDFs) and adipose stem cells (ASCs). The different multilayered systems were tested *in vitro, in vivo* and *in situ* as materials for biomedical and tissue engineering applications.

1. Materials

Several strategies to produce materials for biomedical and tissue engineering purposes, researchers have been focusing on mimicking compounds, systems or phenomena presented in the nature [1]. These strategies can be denominated as biomimetic approaches.

Synthetic polymers have been extensively used during the last decades for biomedical and tissue engineering purposes, resulting generally in highly mechanical stable materials, with good shape control and low variability [1c]. Oppositely, polysaccharides have been increasingly used during the last decades due to the high chemical similarity to the composition of the ECM, the higher rates of biodegradation and the presence of more cell-recognition sites [1b]. Elastin-like polypeptides (ELPs) are a class of synthetic materials but still a sophisticated example of biomimetic materials, being inspired in native elastin to confer smart functionalities to biomaterials [1b]. Therefore, we started selecting ELPs to produce multilayered systems, investigating their biological potential in combination with LbL assembly.

While ELPs materials must be designed to mimic native elastin, natural polymers can offer similarities with ECM in a natural way. Thus, we study the proficiencies of using polysaccharides to produce the multilayered systems, specifically CHT; CS, HA and ALG.

The detailed specifications of the different materials are provided below, as well as the reasoning behind their selection.

1.1. Elastin-like polypeptides (ELPs)

ELPs are a class of genetically-engineered materials that besides present the same basic structure as native elastin, it can also exhibit specific amino acid length and any desired peptide sequence and respective stimuli-responsiveness under external factor as temperature, light, pH or even ionic strength [1b, 2]. In fact, elastin is an essential ECM protein that confers elasticity to different mammalian tissues like skin, connective tissues, arteries, lungs or bladder. Indeed, elastin is responsible for the ability of tissues stretch and relax more than a billion of times during life [3].

In chapter IV, ELPs were used to construct the multilayer films/coatings. Bioproduction conditions, purification protocols and chemical modifications were adapted from de Torre *et. al.* [1b]. Two distinct ELPs were produced, differing just in their amino acid sequence and respective bioactivity. Generally, ELPs were obtained by the induction of gene expression from a stock of recombinant *Escherichia coli* strains containing the desired expressing gene [2, 4]. These methodologies will be detailed further in this chapter. Briefly, specific bioactive moieties were introduced in the polypeptide sequence to confer cell adhesive or anti-adhesive properties to the resulting multilayer system. The presence of the arginine-glycine-aspartic acid (RGD) tripeptide determined their adhesive character. Moreover, these ELPs were designed to react between them, through a catalyst free click technology, in which specific interactions are a result from Huisgen 1,3-dipolar cycloaddition of azides and alkynes – click chemistry reaction.

The schematic representation of the designed ELPs and respective click-chemistry reaction is presented in Figure III-1.

Figure III-1. Chemical scheme representing the click chemistry reaction, that results from the Huisgen 1,3-dipolar cycloaddition of azides and alkynes.

1.2. Chitosan

CHT is a linear polysaccharide composed of randomly distributed N -D-glucosamine and N-acetyl-D-glucosamine, linked by β-(1-4) glycosidic bonds [1b] – see Figure III-2. This interesting polymer is a result of the partial deacetylation of chitin, that is found in the exoskeleton of shellfish (e.g. shrimp and crabs), fungi cellular wall, cephalopod endoskeleton and the cuticles of insects [5]. This process happens in the solid state, under alkaline conditions or through enzymatic hydrolysis in the presence of a chitin deacetylase [5a]. Basically, it results from a process called N-deacetylation, where the acetyl functional groups of chitin are removed; when the degree of deacetylation is bigger than 50%, the compound is designated as chitosan [6]. In acidic solutions, CHT acquires a positive charge which favors its solubility due to electrostatic repulsions [6c]. CHT undergoes a conformational transition when in aqueous solution at its pKa (depends on the molecular weight and deacetylation degree, but usually is reported in the range of $6.1<pH<7$) [7]. This means that below pH the amine groups of CHT are protonated while at higher pH they are deprotonated.

During the last decades, several studies [8] have been reporting the biocompatibility of CHT, being nowadays widely used for biomedical and tissue engineering applications, to produce 2D to 3D materials.

In chapters V, VI, VII, VIII and IX, CHT was used as the positive polyelectrolyte to produce the respective multilayer systems, through LbL assembly. For all of this works we used medium molecular weight CHT, with a degree of deacetylation of 80% (Sigma Aldrich, MKBB0566), after purifying through a re-precipitation process. Briefly, CHT was dissolved as purchased in a 2%(v/v) of acetic acid solution at a 1% (w/v) concentration. This solution was maintained stirring overnight at room temperature, until all the CHT powder was dissolved. The impurities were then removed by three filtration cycles using a nylon mesh filter. CHT was precipitated by the addition of 1 M NaOH, always keeping the mixture stirring, and then washed with distilled water until achieve a neutral pH. The final steps involved the de-hydration of the resulting mixture, by washing with ethanol–water mixtures with increasing ethanol content (30–95% (v/v)). Finally, the resulting CHT material was freeze dried and kept at RT under a dry environment until use:

1.3. Chondroitin sulphate

CS is a linear, complex, sulphated unbranched polysaccharide belonging to the class of macromolecules known as glycosaminoglycans (GAGs) [9]. It is composed of repeating dissacharide units of D-glucuronic acid and N-acetylgalactosamine linked by β-(1→3) bonds [10]. Like other polysaccharides, CS derives from animal sources by extraction and purification processes [11]. The animal sources generally used are chicken, porcine, bovine and cartilaginous fish such as sharks and skate [12]. Therefore, CS is considered a heterogeneous polysaccharide in terms of charge densities, having sulfate groups in varying amounts and being linked in different positions, different molecular masses, polydispersivity, chemical properties, biological and pharmacological activities [13]. For bone and cartilaginous tissues, this molecule is an important structural component [13]. The tightly packed and highly charged sulfate groups of CS generate electrostatic repulsion that provides much of the resistance of cartilage and bone to compression and also cooperates in the shock absorbing capacity of aggrecans [14]. Consequently, this polysaccharide with anionic nature enables efficient interaction with cationic molecules to form interesting structures. However, the major drawback of chondroitin sulfate is the high solubility in water, which limits its use alone in the solid state for biomedical applications, being frequently cross-linked or combined with other polymers, such as chitosan, hyaluronic acid, PVA, PLGA, or gelatin [15].

In chapters V and VI, CS was used as the negative-charged polyelectrolyte to produce the respective multilayer systems, through LbL assembly. In both chapter, CS was used as reveived: chondroitin sulfate A sodium salt from bovine trachea.

1.4. Hyaluronic acid

HA is a linear, anionic and a naturally ocurring non-sulfated polyssacharide, also belonging to the class of macromolecules known as GAGs [16]. It is composed of repeating and alternating dissacharide units of D-glucuronic acid and N-acetyl-D-glucosamine, linked by β-(1→3) bonds [16-17] (Figure III-2). HA is an essential component of the human ECM and as that it is an attractive material for biomedical and tissue engineering applications [18]. Like other polysaccharides, HA derives can be found in marine environment, either on the cartilaginous or on vitreous tissues of different fish. Moreover, it can be produced in large scales through microbial fermentation, from strains of certain bacteria [19].

HA has been widely studied for a extensive range of biomedical and tissue engineering applications, resulting already in different commercially available products [20]. Nevertheless, depending on the size of the molecule different results were obtained. For instace, larger molecules of HA (Mw>10^7 Da) are reported to use for spacefilling, antiangiogenic and immunosuppressive ends while smaller molecules of HA are reported as antiapoptotic [20]. In cartilage,HA have an important structural role for the ECM, forming an aggregation centre for aggrecan [21]. These aggregates have highly Mw and are surrounded within a collagenous framework [22]. In the skin, the primary protecting barrier between the inner body and the hostile action of the outside environment, HA plays a role of collecting the free radicals generated by the UV rays, which could result in cell oxidative stress and might damage their genetic material [23].

In Chapters VII, VIII and IX HA was used alone or chemical modified with DN moieties. HA was used as reveived: high molecular weight hyaluronic acid sodium salt (1.5-1.8 x 10^6 Da) from Streptococcus equi (Chapter VII and VIII) and low molecular weight (8-10 x 10^4 Da) hyaluronic acid sodium salt (Chapter IX). For the work reported in the Chapter IX, it was more essencial to have a material with antiapoptotic properties rather than with space filling properties for instance.

1.5. Alginate

ALG is an naturally occurring anionic polymer, usually extracted from brown algae, by treatment with aquous alkali solutions [22b, 24]. In their chemical structure, ALG is a linear unbranched polymers composed by homopolymeric blocks of consecutive or alternating opolymeric blocks of (1-4)-linked β-D-mannuronate and its C-5 epimer α-L-guluronate (G) residues, covalently linked together in different sequences or blocks [25]- see Figure III-2. Their relative amount is dependent on the origin of the ALG [26].

Unlike the other biopolymers, in mammals, ALG is not naturally broken down by means of an enzymatic action, having low rates of biodegradation [27]. Moreover, this polymer lacks on mammalian cell adhesive ligands, which are central to control material-cell interactions [7b]. Howerver, due to ALG biocompatibility, low toxicity and low cost this anionic polymer has been widely used, being frequently combined with other materials or modified with adhesive moieties to apply for biomedical and tissue engineering applications [10a, 28].

ALG has been extensively used in the form of a hydrogel due to their mild gelation conditions and easy preparation by ionotropic gelation with calcium ions [29]. Althout in Chapter VII, VIII and IX, ALG is used as a negatively-charged polyelectrolyte to produce multilayer membranes based on electrostatic interactions, being combined with other polymers more prone to establish cell-material interactions. Herein, ALG was used as received: Sodium alginate from brown algae.

1.6. Genipin

Genipin is a natural crosslinking agent, obtained by hydrolyze of geniposide, and extracted from the fruits of the plant Gardenia jasminoides Ellis [29b]- see the chemical structure in Figure III-2. In fact, this compound is traditionally used in Chinese medicine to attenuate the symptomes of Type-2 diabetes, headache, inflammation and hepatic disorders, among others. Regarding their crosslinking ability, genipin can naturally crosslink collagen, gelatin, proteins and chitosan [30]. Therefore, in combination with genipin's biocompability and ability to materialize stable products, genipin has been reported in the last decades for biomedical applications [30]. Furthermore, the degradation of this product has been described as slower than other popular crosslinker agents like glutaraldehyde, being more efficient to crosslink polymers containing amino-groups [31].

In Chapter V and VII, genipin is used to crosslink CHT. The mechanism of genipin-CHT crosslinking comprehends the nucleophilic attack by primary amino group of CHT engaged at C-3 carbon atom in genipin, steered to the formation of a heterocyclic compound of genipin that is coupled to the glucosamine residue in CHT which develops the crosslinking.

1.7. Dopamine

DOPA (3,4-dihydroxyphenylalanine) is a specific amino acid and catechol-containing compound, widely known as presented in mussels foot proteins [31].. It has been reported that DOPA is the critical element responsible for the mussels' ability of forming strong adhesive interaction with various organic and inorganic substrates, when in a wet environment [32]. Therefore, using DOPA or its derivates as 3,4-dihydroxyphenethylamine (dopamine, DN) has been one of the strategies to modify solid surfaces or to produce polymeric conjugates capable of mimicking the adhesive character of mussels [32-33].

In chapter VII, VIII and IX, dopamine was used to modify the backbone of HA to confer increasing adhesive properties. Dopamine was purchased as Dopamine hydrochloride - the chemical structure of dopamine is represented in Figure III-2.

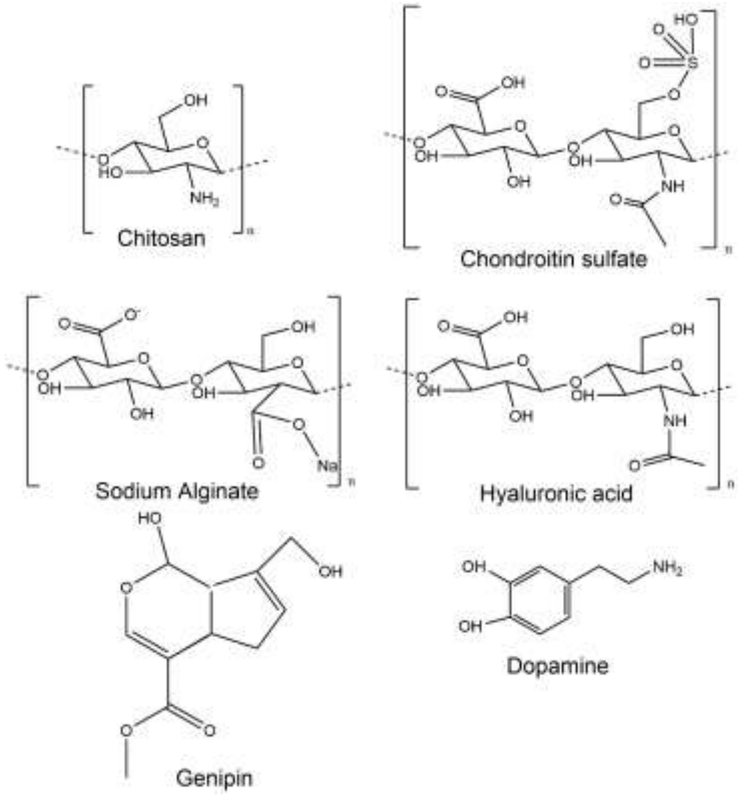

Figure III-2. Schematic representation of the chemical structures of the different biopolymers and natural molecules used in this thesis.

2. Cell sources/types

2.1. L929 cell line

L929 are mouse fibroblast cells that have been used confirm the *in vitro* non-cytotoxicity of the developed material, as recoomended by the ISO 10993-5[33a], as well as to characterize the cells-material interaction in terms of adhesion, proliferation and morphology of the cells [10a, 34]. L929 cell line consists in fibroblasts derived from the connective tissue of mouse and was obtained from the European Collection of Cell Cultures (ECACC). L929 cell line was used in the work reported in Chapters V and VI.~

2.2. C2C12 cell line

C2C12 are mouse myoblast cells that derived from satellite cells. This cell line was obtained from the European Collection of Cell Cultures (ECACC). These cells spontaneously differentiate in culture when in appropriate medium conditions, providing researchers an *in vitro* tool for studying muscle cell proliferation and differentiation [10b, 35]. Myoblasts in culture are able to exhibit all of the features of myogenesis, including proliferation, migration, fusion, myotube formation and contraction. C2C12 cells grow in a medium containing 10% of serum until confluence, while these same cell lines, while in media containing 2% horse serum, these cells fuse and form myotubes [36]. C2C12 cell line was used in the work reported in Chapters IV and VI.

2.3. MC3T3-E1

MC3T3-E1 cell line is a pre-osteoblastic murine cell line that was obtained from the European Collection of Cell Cultures (ECACC). These cells have been used as a model of osteoblastic activity since they exhibit the ability of matrix mineralization and differentiation into osteoblasts or osteocytes [12]. In tissue culture polystyrene and in basal media, MC3T3-E1 cells have basal ALP activity and basal extracellular matrix mineralization [13]. In osteoconductive medium (includes ascorbic acid and β-glycerophosphate), the cell line shows a increased production of mineralized collagenous matrix, as compared to base levels [13]. MC3T3-E1 cell line was used in the work reported in Chapter VII.

2.4. HDFs

Human dermal fibroblasts were obtained from the European Collection of Cell Cultures (ECACC). These cells are responsible for producing the extracellular matrix forming the connective tissue of the skin, and play a crucial role during wound healing [14a]. These cells have been used as a model to study many aspects of cell physiology, and have been utilized in dozens of research publications, particularly those related to skin biology and reprogramming/induced pluripotency studies [14b, 15a]. HDFs cell line was used in the work reported in Chapter VIII.

2.5. hASCs/TERT1

Human adipose derived stem cells (hASCs) are multipotent stem cells that can be easily obtained from adipose tissue harvested by liposuction surgeries, with low site associated morbidity [15b]. A considerably large amount of hASCs can be obtained, as opposed to other stem cell sources (e.g. bone marrow aspirates) [15b]. Human ASCs transduced using human telomerase reverse transcriptase (TERT) are immortalized cells, characterized by an unlimited growth while maintaining expression of cell type specific markers and functions such as typical fibroblastoid morphology and adherent growth [16]. Besides expressing mesenchymal stem cells as CD73, CD90 or CD105, these cells do not express CD34 [16]. Adipogenic, chondrogenic or osteonic differentiation can achived using these kind of cells, being also reported with immunomodulatory properties [17]. In this thesis, the used ASC/TERT1 cell line was kindly provided by Evercyte. These cells were used in the work reported in Chapter VIII.

3. Materials processing

3.1. ELP expression, purification and modification

ELPs are a family of geneticaly engineeered polypeptides that can exhibit specific amino acid length and sequence [18a]. In Chapter IV, ELPs were used as the main constituints of the multilayered coatings. As already referred above, the designed polymers have the ability to interact in another way than the conventional ionic forces; in fact, the developed ELPs can intereact one with other through click chemistry, creating a thin coating much more stable.

Expression conditions and purification protocols to produce the desired ELPs were already descried Meyer and Chilkoti [18b] and Girotti *et. al.*[19]. Briefly, ELPs were obtained by the induced gene expression from a stock of recombinant Escherichia coli strains containing the desired expressing gene.the bioproduced polymers was purified by a series of centrifugations under and above its transition temperature. After that, the ELPs were dialyzed against MilliQ water and lyophilized. Two ELRs were employed: the VKVx24 and the HRGD6. The first corresponds to a structural polymer with no bioactive sequence, with the amino acid sequence MESLLP VG VPGVG [VPGKG(VPGVG)$_5$]$_{23}$ VPGKG VPGVG VPGVG VPGVG VPGV. The second one corresponds to a polymer containing a well-known adhesion sequence (RGD), with the following amino acid sequence MGSSHHHHHHSSGLVPRGSHMESLLP [(VPGIG)$_2$(VPGKG)(VPGIG)$_2$]$_2$ AVTGRGDSPASS[(VPGIG)$_2$(VPGKG)(VPGIG)$_2$]$_2$. The purity and molecular weight of these ELPs were confirmed by different techniques. The resultant polymers were then chemically modified at their lysine amino acids ti bear the reactive groups needed for click chemistry reaction. Therefore, the developed ELPs were chemically modified by the transformation of the amine group present in the lateral chain of the lysine residue to bear the groups to be used in the click chemistry reaction: the azide-bearing ELPs and the cyclooctyne-modified ELPs. The chemical reaction between azide and cyclooctyne is represented in Figure III-1.

3.2. Modification of HA with Dopamine

In Chapter VII, VIII and IX HA was modified with DN moieties through carbodiimide chemistry, using a 1- ethyl-3-(3'-dimethyl aminopropyl) carbodiimide (EDC) as an activation agent of carboxyl groups on HA chain. Briefly, 1 g of HA was dissolved in 100 mL of PBS solution and pH was adjusted to 5.5 using 1 N HCl solution. Then the HA solution was purged with nitrogen for 30 minutes the solution was transferred for an In the solution, 388.1 mg (2.5 mmol) of EDC (N-(3-Dimethylaminopropyl)-N'-ethylcarbodiimide hydrochloride, MW of 191.70 g.mol^{-1}, Sigma-Aldrich) and 474.1 mg (2.5 mmol) of dopamine hydrochloride (Dopamine hydrochloride, Light sensitive, MW of 189.64 g.mol^{-1}, Sigma-Aldrich) was added and pH of the reaction solution was maintained at 5.5 for 3 hours with 1.0 N HCl and 1.0 N NaOH. Unreacted chemicals and urea byproducts were removed by extensive dialysis.Afterwards, the HA-DN conjugate was freeze dried and stored at -20°C until use. The scheme of this procedure is presented in Figure III-3.

The presence of DN in the conjugated HA-DN was confirmed using different techniques; Ultraviolet (UV) spectrophotometry and proton nuclear magnetic resonance (^{1}H-NMR). These techniques are detailed in the next sub-section.

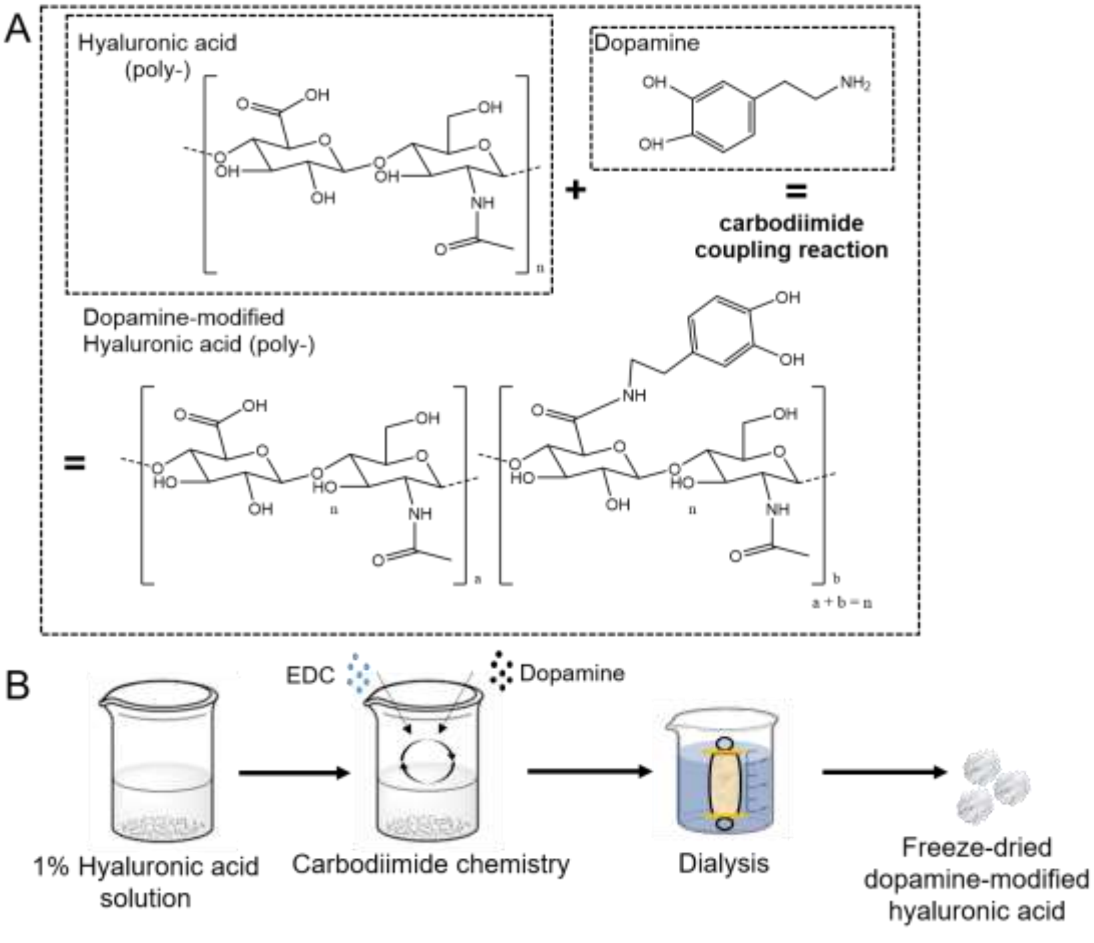

Figure III-3. Schematic representation of the synthesis of the conjugated HA-DN: A), the chemical structures of the HA, DN and the conjugated HA-DN and B) the experimental procedure involved.

3.3. Materials characterization

3.3.1. Determination of the zeta potential

The charge exhibited by each polymer in aqueous solution was determined by the measurement of zeta (ζ)-potentials using a ZetaSizer equipment, based on the laser Doppler electrophoresis. When a solid surface is in contact with an aqueous solution, an interfacial charge forms and causes a reorganization of the free ions in the solution to produce a thin region of non-zero net charge density near the interface [20]. The organization of the charges at the solid-liquid interface and the balancing counter-ions in the liquid is usually referred to as the electrical double layer [20]. This region consists in a thin layer of counter-ions immediately next to the charged solid surface, called the compact layer, or Stern layer. The counter-ions in the compact layer are permanent due to the strong electrostatic attraction, while counter-ions outside the compact layer are variable. This last part of the electrical double layer is called the diffuse layer. The ζ-potential is the electrostatic potential at the boundary dividing the compact layer and the diffuse layer [20-21].This potential may depend on factors as the polymer concentration, pH and ionic strength. Thus, solutions of each different polymeric material were prepared to measure the ζ-potential: For the work reported in Chapter IV we studied the conditions in which the developed coatings are placed after their construction, to determine their behavior. Regarding the work developed in Chapter V and VIII we focused on the conditions that would be used afterwards for the construction of the LbL films. Aqueous solutions of each ingredient were tested all the times at 25ºC.

3.3.2. Determination of the degree of substitution of the HA-DN conjugate

As above referred, UV spectrophotometry and proton nuclear magnetic resonance (^{1}H-NMR) were performed to determine the degree of substitution of the DN in the conjugate.

Ultraviolet visible spectrophotometry was used to confirm if the modification of HA with catechol groups was successful, measuring the absorbance between 200 and 400 nm. UV-Visible spectrophotometry involves measuring the amount of ultraviolet or visible radiation absorbed by a substance in solution. For the work reported in Chapters VII, VIII and IX, the absorbance of distinct solutions of dopamine (ranging concentrations of 0.05 mM to 1 mM) was measured with the purpose to calculate the degree of dopamine substitution. It was noticed that an excitation band appears at approximately 280 nm for dopamine [21b]. The real degree of dopamine substitution in each case was obtained by following the UV excitation band centered at 280 nm and upon comparison with a standard curve obtained for distinct concentrations of free dopamine in solution. Using the measured absorbance of the conjugates and the equation obtained from the standard curve, the relative concentration of dopamine units was determined.

In the other hand, **hydrogen-1 nuclear magnetic resonance (^{1}H-NMR)** spectra were recorded for a sample of HA-DN. NMR is a common technique used to determine the structure of unknown organic structures, by applying a nuclear magnetic resonance with respect to hydrogen-1 nuclei within the molecules of a substance [22a]. Among other, using this technique we can determine the number of protons in a molecule and the different types of hydrogen atoms. Thus, for the work developed in Chapters VII, VIII and IX, and with the purpose to calculate the degree of dopamine substitution, dopamine, non-modified hyaluronic acid and the produced conjugate were dissolved in deuterated water (D2O), at final concentrations of 1 mg.mL^{-1}. An aliquot of this solution was placed in a 5 mm NMR tube and the spectrum recorded at 60 ºC. The final spectra of ^{1}H-NMR result were obtained at 298 K and 300 MHz. Note that the new N-H linkage formed in the conjugate could not be detected by ^{1}H-NMR as this conjugate is only soluble in water; in this solvent the NH linkage interchange with water, therefore no new signal appears.

3.3.3. Monitoring the growth of the multilayered film

Firstly, to determine the capacity of producing multilayered films using a specific combination of parameters as type of polymer, concentrations, time of depositions and washing steps, pH and temperature, a **quartz-crystal microbalance with dissipation monitoring (QCM-D)** (Q-Sense) was used. This technique can detect adsorbed surface density changes in the order of ng.cm^{-2} and determine the viscoelastic properties of the resulting surface, *in situ* [22b, 23]. Briefly, a sensor is composed of a thin AT-cut quartz disk sandwiched between a pair of electrodes. Quartz allows exploiting the piezoelectric which makes it possible to convert an electric AC voltage across its electrodes into mechanical signal, exciting the quartz to oscillation at a fundamental frequency of 5 MHz [22b]. Therefore, the use of quartz sensors for QCM requires their coating with an electrode material, usually gold [24]. Briefly, an AT-cut quartz crystal is excited at its fundamental frequency (5 MHz) and at several overtones: 1, 3, 5, 7, 9, 11 and 13, corresponding respectively to 5, 15, 25, 35, 45, 55 and 65 MHz. When a polymer layer is deposited onto the sensor crystal, the frequency decreases (Δf). If the film is thin and rigid, the decrease in frequency (ΔF) is proportional to the mass of the film. However, usually when using biopolymers, the adsorbed film is not rigid, making this relation not valid. Notwithstanding, the ΔD monitoring gives an indirect indication of the film's viscoelastic properties; increased ΔD represents a shift to the construction of a higher viscosity component and damping properties characteristic of soft polymeric LbL films. In fact, this dampening is responsible for the oscillation of the crystal, known as ΔD.

In Chapter IV, V, VI, VII and VIII the *in situ* monitorization of the adsorption of different polymeric layers was investigated onto gold-coated quartz, that were previously cleaned by immersing in acetone, absolute ethanol and 2-propanol. For all the chapters, the adsorption took place at RT, using solutions at 0.15 M NaCl. Each polyelectrolyte layer was flushed sequentially into the chamber, where the sensor is immobilized, at a constant flow rate (between 25-50 mL.min^{-1}), being each adsorption step separated by a rinsing step with 0.15 M NaCl. Table III.1 represents the pairs of polymers and the respective chosen parameters used to perform the QCM-D monitoring.

Table III-1. QCM-D parameters chosen for each one of the works developed in each chapter of this thesis

Chapter	Materials	[C] (mg.mL^{-1})	Driven force	Nº of cycles	T (°C) / pH
C. IV	ELPs	0.5/0.5	Covalent	4 BL	RT / 7
C. V	CHT/CS	1/1	Electrostatic	8 BL	RT / 5.5
C. VI	CHT/CS	1/1	Electrostatic	10 BL	RT / 5.5
C. VII	CHT/HA or HA-DN	1/0.5	Electrostatic	4 TL	RT / 5.5
C. VIII	CHT/ALG CHT/HA or HA-DN	1/1 and 1/0.5	Electrostatic	2TL	RT / 5.5

More than giving an indication of the viscoelasticity of the resulting film, QCM-D data analysis is used to estimate some physical properties of the films, as the thickness, viscosity and elastic shear modulus. Therefore, based on the Voigt viscoelastic model, which is integrated into the QTools software (Q-Sense), it was possible to estimate the thickness of the films from the Equation III.1 and IIII.2. Iterations of the model were performed using at least three overtones. The model requires three parameters, namely solvent density, solvent viscosity and film density, to be fixed. The solvent viscosity repeat as desired was therefore fixed at 0.001 Pa·s (same as water) and the film density at 1200 kg.m^{-3} (often assumed to return the lowest calculation error).

$$\Delta f \approx \frac{1}{2\pi\rho_0 h_0}\left[\frac{\eta_l}{\delta_l}+\sum_{j=n}\left(\rho_j h_j\omega-2h_j\left\{\frac{\eta_l}{\delta_l}\right\}^2\frac{2\eta_j\omega^2}{\mu_j^2+\omega^2\eta_j^2}\right)\right] \quad \text{Equation III.1}$$

$$\Delta f \approx \frac{1}{2\pi f\rho_0 h_0}\left[\frac{\eta_l}{\delta_l}+\sum_{j=n}\left(2h_j\left\{\frac{\eta_l}{\delta_l}\right\}^2\frac{\mu_j\omega}{\mu_j^2+\omega^2\eta_j^2}\right)\right] \quad \text{Equation III.2}$$

In these equations, *j* corresponds to the total number of thin viscoelastic layers, ρ_0 and h_0 are the density and thickness of the quartz crystal, η_l is the viscosity of the bulk liquid, δ_l is the viscous penetration depth of the shear wave in the bulk liquid, ρ_l is the density of liquid, μ is the elastic shear modulus of an overlayer and ω is the angular frequency of the oscillation. The thickness, density, viscosity and elastic shear modulus of the adsorbed layer are represented by h_j, ρ_j, η_j *and* μ_j, respectively.

3.4. Layer -by-layer assembly

LbL is a simple and versatile technology, widely used to fabricate nanostructured films for biomedical and tissue engineering applications [25]. This technology offers the opportunity to control and tailor the surface's properties at micro and nanoscale level, working with a wide range of materials like synthetic polymers, biopolymers, cells or particles [26]. Moreover, LbL assembly represents a bottom-up approach, meaning that starts from the smaller particles to build-up increasingly bigger structures [27]. Among other LbL assembly can result in different shaped-structures, from simple coatings [7b] to freestanding multilayer membranes [10a], to capsules [28a], to tubes [28b], and even to porous scaffolds [29a]. Moreover, typically LbL assembly is based on a simple and alternated deposition of polycationic and polyanionic materials above an underlying substrate [29b]-see Figure III-4. Conventional LbL assembly is exploited in the Chapter V, VI, VII, VIII and IX; for all of those works LbL assembly was performed above inert substrates, making possible the detachment of the multilayered membrane in the end of the process. Notwithstanding, other driven forces can be used to construct a LbL-based film [29b]. In the Chapter IV, LbL assembly was demanded by a click chemistry reaction azide-alkyne cycloaddition- see Figure III-1.

Table III.2 details the pairs of polymers and the respective chosen parameters used to perform the LbL assembly and consequently to produce freestanding multilayered membranes. The construction of the multilayered films was assisted by an in-house developed dipping robot that allowed the automated assembly of each layer in a programmed manner- see Figure III-4C. Due to the sensitivity and size of the underlying substrate, the multilayered film was constructed manually for the work developed in the Chapter IV.

Table III-2. LbL construction parameters, for each one of the works developed in each chapter of this thesis

Chapter	Materials	[C] (mg.mL^{-1})	Driven force	Nº of cycles	T (°C) / pH	Underlying substrate
C. IV	ELPs	0.5/0.5	Covalent	4 BL	RT / 7	Glass
C. V	CHT/CS	2/2	Electrostatic	250 BL	RT / 5.5	PP
C. VI	CHT/CS	2/2	Electrostatic	300 BL	RT / 5.5	PP and PC
C. VII	CHT/HA or HA-DN	2/1	Electrostatic	200 BL	RT / 5.5	PP
C. VIII	CHT/ALG CHT/HA or HA-DN	2/2 and 2/1	Electrostatic	100 TL	RT / 5.5	PP
C. IX	CHT/ALG CHT/HA or HA-DN	2/2 and 2/1	Electrostatic	100 TL	RT / 5.5	PP and PC

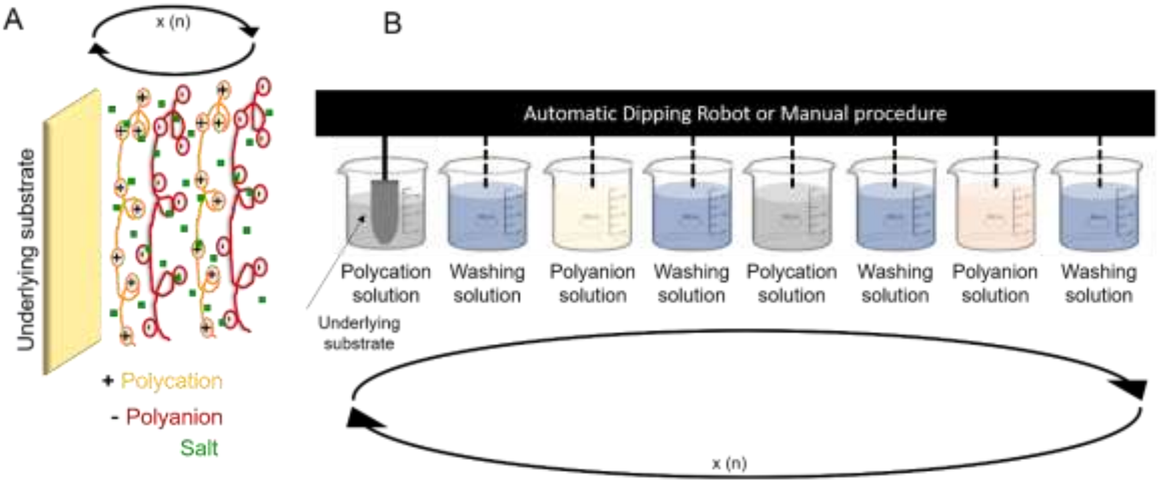

Figure III-4. Schematic representation of A) the LbL assembly driven by electrostatic interactions and B) experimental procedure using an automatic dipping robot or just manually. C) QR-code for a video of an automatic dipping robot at work.

3.5. Crosslinking reaction with genipin (G)

To reinforce the mechanical properties, genipin was chemically incorporated in the freestanding multilayer membranes (Chapter V and VI) and compared with the original ones. The reaction mechanism of genipin with the multilayer membrane was based on the spontaneous formation of crosslinks with primary amine groups of CHT [30]. Briefly, there is a faster reaction where genipin is attacked by a primary amine of CHT resulting in the formation of a heterocyclic compound of genipin linked to the glucosamine residue in CHT [30]. Then, there is a second and slower reaction with a nucleophilic substitution of the ester group of genipin to form a secondary amide link with CHT [30].

Therefore, genipin solutions (1 and 2 mg.mL^{-1}) were prepared in an optimized mixture of 1:4 DMSO/0.15 M NaCl. The dried freestanding membranes were immersed in those solutions for 12 hours at RT. In the end, the reaction was stopped using absolute ethanol a couple of times to remove the excess of genipin of the samples, and then dried at RT. Genipin is photosensitive, therefore all the steps involved were protect from light sources.

4. Characterization of the developed LbL systems

4.1. Physico-chemical characterization

4.1.1. Fourier transform infrared spectroscopy (FTIR)

The analysis of the different membranes (crosslinking and not crosslinked), and the respective natural polysaccharides was performed using a spectrophotometer (Chapter V). The samples were accessed using a membrane holder instrument, by the averaging 34 individual scans over the range 4400 cm^{-1} to 400 cm^{-1}. Using the same parameters but preparing in potassium bromide (KBr) discs, it was possible to obtain the FTIR spectrums for pure CHT and CS.

4.1.2. Scanning electron microscopy (SEM) and energy dispersive X-ray spectroscopy (EDS)

SEM and EDS were used to characterize the physico-chemical properties of the multilayer systems. SEM is an electron microscope that produces images of a sample by scanning it with a focused beam of electrons [31]. The electrons interact with atoms in the sample, producing various signals that can be detected and that contain information about the sample's surface topography and composition [31]. The membrane morphology of the different LbL-based films was visualized by SEM (Chapter IV, V, VI, VII, VIII, IX). Additionally, SEM was also used to visualize the cells morphology adhered on the surface micro- and nanostructure (Chapter IV, VI, IX). Moreover, the elemental chemical composition was investigated by EDS (Chapter VII). Briefly, the samples were dehydrated using sequential ethanol series, namely 30%, 50%, 60%, 70%, 80%, 90%, 96% and 100% v/v, 5 to 15 min each. Prior to SEM visualization EDS analysis was performed. Then, samples were gold-coated using a sputter coater.

4.1.3. Atomic force microscopy (AFM)

AFM is an excellent tool to study the morphology and the topography at micro- and nanoscales of diverse materials' surface [32]. This equipment has the advantage of imaging almost any type of surface, including polymers, ceramics, composites, glass, and biological samples [32]. In AFM, a sharp probing tip is raster-scanned over a surface using a feedback loop to adjust parameters needed to image a surface, being the atomic forces used to map the tip-sample interactions [32].

AFM measurements were performed in the LbL-coated cover glass (Chapter IX) or directly on membranes (Chapter VI). The surface topography of dry and wet films was analyzed and the root mean square (Rq) and the average roughness (Ra) were determined. The Ra is the mean height as calculated over the entire measured length/area. The Rq is a function that takes the square of the measures. The Rq roughness of a surface is like the Ra, with the only difference being the mean squared absolute values of surface roughness profile. Additionally, the AFM imaging was used to measure specific micro- or nanostructures of the surfaces.

4.1.4. Water Contact Angle and wettability

The wettability of the materials' surface is defined by the physico-chemical characteristics of the LbL-based films [33]. Generally, the wettability of the films is affected by the existence of micro- and nanorough surfaces, being higher for low-energy surfaces (lower water contact angles (WCA)) and lower for high-energy surfaces (higher WCA) [33a]. The WCA of a liquid drop on a solid surface is the angle at which a liquid/vapor interface meets a solid surface [34]. Physically, it can be defined by the mechanical equilibrium of the drop under the action of three interfacial tensions and allows to quantify the wettability of a solid surface [34]. A goniometer was used as the measurement tool to determine the WCA. The values were obtained by the sessile drop method, using always ultrapure water and the fixed drop volume for 3 µl. This technique was employed to determine the effects of temperature or pH fluctuations on the physicochemical properties of the LbL coatings (Chapter IV).

4.1.5. Water uptake ability

To investigate the water uptake ability, samples of known weight (dried weight, w_d) were immersed in a phosphate buffered saline (PBS) at pH=7.4 up to 3 days and 37°C (Chapter V, VIII and IX). The swollen membranes were removed at predetermined time points and instantly weighted with an analytical balance, always after the removal of the water excess using filter paper. The water uptake was calculated using Equation III.3, where w_d and w_w represents the weights of dried and wetted membranes, respectively. For each condition, at least 5 samples were considered.

$$Water\ uptake\ (\%) = \frac{w_w - w_d}{w_d} \times 100 \qquad \text{Equation III.3}$$

4.1.6. Biodegradation

Degradation studies were performed to determine de biodegradation degree of the freestanding multilayer membranes made of CHT and CS, when implemented in a similar environment to the human body (Chapter V). As already referred in the materials section, natural polymers are usually biodegradable an it can happen by different routes when inside the human body. The enzymatic via seems to be the most impactful; there are different enzymes responsible for the degradation of biopolymers. CHT and CS were usually degraded under the action of lysosome and hyaluronidase, respectively. Therefore, the freestanding multilayer membranes were placed in PBS, at pH=7.4 (control), and in an enzymatic solution composed by 0.13 mg.mL^{-1} of lysosome and 0.33 mg.mL^{-1} of hyaluronidase in PBS with sodium azide (NaN_3), at pH=7.11; all experiments were put in a shaking water bath at 37 °C. The medium was replaced every 3 days and at predetermined time points (3, 7, 14 and 30 days), the membranes were removed from the solutions and washed with distilled water to remove the excess of salts. Then, the membranes were dried at constant temperature and weighted. The percentage of weight loss (w_L) of the membranes for the different conditions was determined following Equation III.4, with w_i being the initial dry weight of the membrane and w_f being the weight of the dry membrane after each predetermined time point. Thus, the percentage of weight retaining (WR) was calculated using Equation III.5, using the result of Equation III.4.

$$WL(\%) == \frac{w_i - w_f}{w_i} \times 100 \qquad \text{Equation III.4}$$

$$WR\ (\%) = 100 - WL \qquad \text{Equation III.5}$$

4.2. Mechanical properties

To investigate the mechanical properties of the different developed materials and the influence of being or not being chemical crosslinked (Chapter V), the presence of a different topographies (Chapter VI) and the presence of adhesive functional groups (Chapters VII, VIII and IX).

4.2.1. Static mechanical assays

Therefore, uniaxial tensile tests were performed on rectangular membranes using a mechanical testing equipment. Different parameters were evaluated, according with the application. For the work developed in Chapter V, 40×5mm^2 rectangles PEM membranes were tested in wet condition. A micrometer was used to measure both the thickness and the width of the samples. Before starting the test, the samples were immersed in PBS until equilibrium was reached, about 3 hours later. The tensile assays were made at a crosshead speed of 1mm.min^{-1} and room temperature, with a gauge length of 10 mm. The presented results are representative of at least five specimens and the Young's Modulus values were determined from the initial slope of the stress-strain curves. In the Chapter VII, 30×5mm^2 rectangles PEM membranes were tested in wet condition. The tensile assays were made at a crosshead speed of 1mm/min^{-1} and room temperature, with a gauge length of 10 mm.

4.2.2. Dynamic Mechanical Analysis (DMA)

Dynamic Mechanical analysis (DMA) apparatus was used to investigate the mechanical/viscoelastic properties of the FS multilayered membranes in the Chapter VI. The testing procedure consists in applying an oscillatory force to the sample and the consequent response analysis of the sample to that force. It allows obtaining data about the mechanical properties of materials (elastic modulus, viscous modulus and damping capability), as a function of time, temperature and frequency. Briefly, the membranes were cut with ≈ 8 mm width. Prior to the DMA assays, samples were soaked overnight, in a PBS solution, to reach the swelling equilibrium. The geometry of the samples was then measured accurately for each sample where the thickness was determined in three different regions of each sample using a micrometer. The measurements were carried out at 37°C during which the membranes were immersed in a PBS solution placed in a Teflon® reservoir. Membranes were clamped in the DMA apparatus with a gauge length of 10 mm and immersed in the PBS bath. After equilibration at 37°C, the DMA spectra were obtained during a frequency scan between 0.2 and 20 Hz. The experiments were performed under constant strain amplitude (50 µm) and a static pre-load of 1 N was applied during the tests to keep the sample tight. At least three specimens were tested for each condition with the same experimental settings.

4.2.3. Adhesiveness evaluation

To evaluate the adhesiveness character of the membranes, different approaches were envisaged using a mechanical testing apparatus – see Figure III-5. In Chapter VII, we followed a standard test method for shear strength of single-lap-joint adhesively bonded metal specimens by tension loading ASTM D1002 [37] (ASTM International, West Conshohocken, Pennsylvania, United States of America) with slightly modifications. All the adhesion experiments were conducted at 25 °C, at a cross-head speed of 5 $mm.min^{-1}$ and using a 1.0 kN static load cell. The lap shear adhesion specimens were squares (20 mm × 20 mm) of freestanding membranes that were incubated at 37 °C and equilibrated in a 50% humidity atmosphere prior to testing. Briefly, the samples were put between two glass slides and left in contact overnight. Then, the systems were stressed until enough force was applied to trigger their detachment and pull them apart, using the Instron apparatus. The lap shear bonding strength was then determined from the maximum of the force–deformation curve obtained. The average and standard deviations were determined using the results from five samples. While lap shear strength gives a quantitative idea of the adhesive properties of the membranes, other nonconventional test was made to observe the bio-adhesiveness potential of these systems. Briefly, the multilayered membranes were put in contact with a clean surface of porcine bone tissue in a 50% humidity-controlled environment at 37 °C. Then, the freestanding membranes were pulled out of the bone with tweezers. This process was recorded by a video camera. On the other hand, in Chapter VIII, the adhesive properties of the produced freestanding membranes were evaluated using a single lap shear adhesion strength test adapted also from ASTM D1002. Rectangular samples (30 x 10 mm^2) were cut and overlapped in pairs with an overlapping area of 5 x 10 mm^2. Samples were then hydrated with a PBS solution and placed between firmly tight glass slides, overnight and at 37 °C. After that, the glass slides were removed, and the samples were tested using a mechanical testing equipment, with each grip pulled the extremity of one of the overlapped samples. A tensile speed of 5 $mm.min^{-1}$ was used until sufficient stress was applied for membrane detachment. The resulting stress-strain curves allowed to determine the adhesion strength of the developed freestanding membranes.

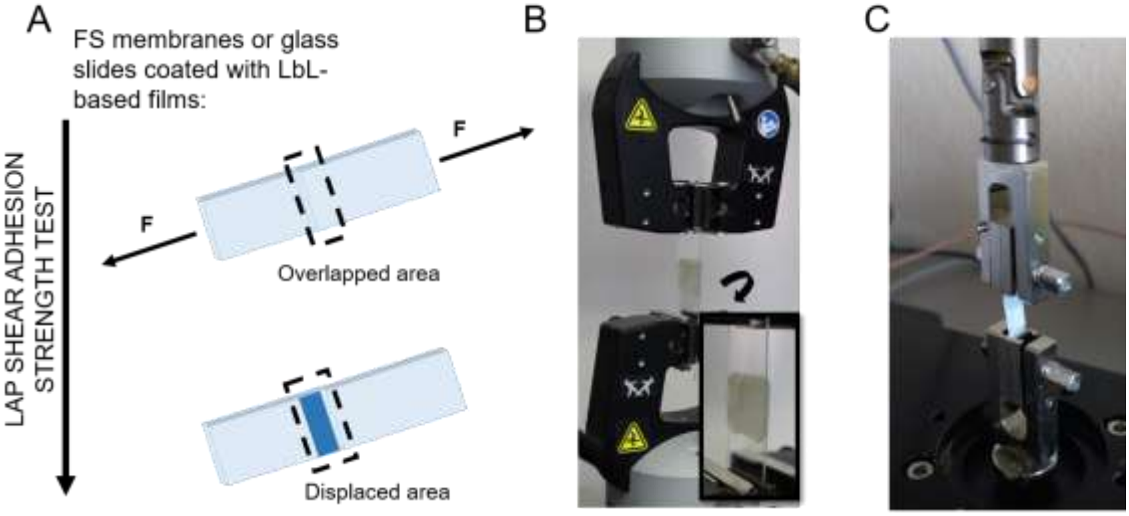

Figure III-5. A) Experimental setup for the measurement of the lap shear adhesive strength. Mounting configuration used for the works of B) Chapter VII and C) VIII.

4.3. Bioactive and functional properties

Biomedical and TE applications increasingly claim for materials exhibiting bioactive properties.

4.3.1. Stimuli-responsiveness ability

In Chapter IV stimuli-responsiveness ability was evaluated through different techniques, that were already described above. Briefly, taking advantage of the responsive properties that have been reported for ELPs, we decided to investigate if these properties would be transposed for the nanocoatings. Therefore, the film's growth, the morphology and the wettability of the ELP-based nanocoating were evaluated by changing temperature and pH. SEM was used to investigate the morphology of the resulting multilayer-coated surfaces, produced at RT. These samples were observed after overnight incubations at different temperatures: 4°C, RT and 37°C. Prior to observation the samples were dried and coated with platinum using a sputter coater. Then, we investigated the influence of the temperature and the pH on their wettability. The WCA of cleaned glass coverslips and ELP-based coatings, produced at RT, were investigated firstly at RT and then for repeating cycles of temperatures of 37°C and 4°C. This was possible using a liquid temperature control unit, which could be coupled with goniometer system and linked to a temperature-controlled bath system. This system allowed a protective atmosphere to surround the sample working area, maintaining temperature and humidity homogeneously distributed over working area. The cycle temperatures were continuously repeated 10 times to evaluate the reversibility of the temperature responsiveness of elastin-coated surfaces. The pH responsiveness of the surfaces was also investigated. WCA measurements were made after sample immersion at working pH 7. Then, the elastin-based surfaces were submitted to sequential immersions on different pH solutions, wherein after each 60-minute immersion the samples were withdraw and the WCA measured. Basically, acid and alkaline sodium acetate solutions were prepared at a 150mM concentration; the samples were sequentially and continuously immersed in solutions with pH values of 4, 10, 3, 11, 2 and 12. Lastly, QCM-D analysis was performed to investigate the influence in situ of acidic and alkaline cascades after the film construction. The procedure described for the build-up kinetics construction was repeated. After the film build-up, the elastin multilayers were flushed with acidic or alkaline sodium acetate solutions, where the pH was adjusted using appropriated volumes of NaOH (0.5M) and acetic acid (2%(v/v)). These solutions were injected into the system for 30 minutes, followed by a short injection with a sodium acetate solution at pH 7 to evaluate the reversibility of the process. The influence of the pH on the elastin multilayers was evaluated by varying the pH in a cyclic way in an acidic range (pH 4, pH 3 and pH 2) and, also, in an alkaline range (pH 10, pH 11 and pH 12). The respective frequency and dissipation changes were recorded in real time.

4.3.2. Shape-memory ability

All the produced freestanding films presented a flat shape, but due to the elastic behavior associated to polysaccharide-based freestanding membranes and their ability to uptake water, the initial shape can be deformed, through an external action. This can be described as a shape-memory phenomenon, triggered by hydration. Therefore, in the Chapter V, membranes were cut in 40 mm x 8 mm rectangles and were then hydrated in PBS, until equilibrium was reached, about 3 hours after. With the help of a rod, the wetted membrane was rolled around, dehydrated with ethanol 100% to fix the shape, to induce the extraction of water molecules, and then allowed to dry. The membrane was carefully removed from the rod, to verify the maintenance of the resulting temporary shape. Rehydration was the next step, and the samples were again immersed in PBS to recover the initial and permanent flat shape. These transformations were observed and recorded by photography. The representative scheme of the procedure is presented in Figure III-6.

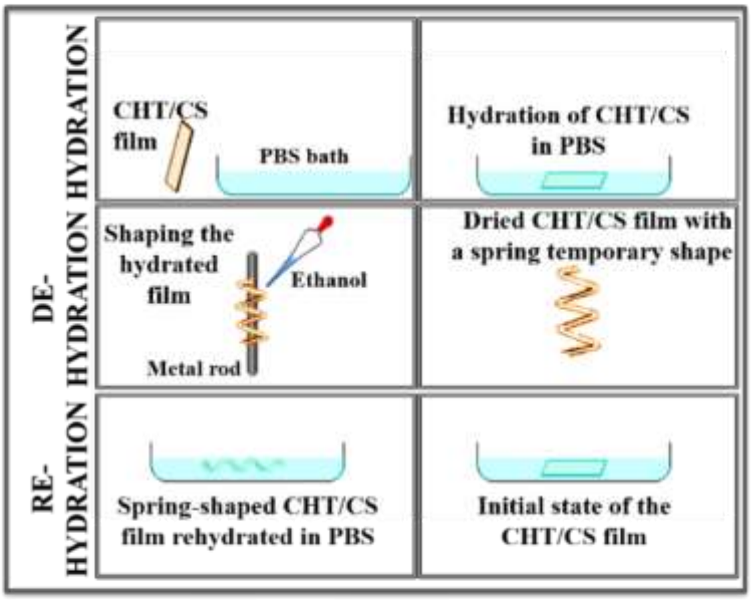

Figure III-6. Schematic representation of the experimental procedure related with the shape-memory test. After hydrating the membrane with PBS, the sample was shaped like a spring and tested to maintain this shape under the action of ethanol. To test the reversibility of the process, the membrane was immersed again in PBS.

4.3.3. Bactericidal activity

In the Chapter VIII, the bactericidal activity was evaluated for the developed freestanding membranes. Therefore, Staphylococcus aureus was used as model of a gram-positive bacterium, whereas Escherichia coli used as model of a gram-negative bacterium. To do that, both strains of bacteria (1 × 10^8 Colony-forming unit (CFU) mL^{-1}) were grown in sterilized LB (Lysogeny broth) and incubated for 4h at 37°C. 200 µL of the bacterial suspension were placed on the LB agar growth plates and spread uniformly using a sterile cotton swab. The different sides of the membranes were placed on the top of the inoculated agar plates and incubated overnight at 37°C. To determine the biofilm formation at the membranes surface' and the bacterial growth, SEM images were acquired.

4.4. *In vitro* biological performance

The *in vitro* cellular response to materials is essential to evaluate their biocompatibility and bioactivity. Using more specific or general cell types, we investigated if any harmful reaction was triggered upon interaction with a living organism, and, if not we studied important cellular functions upon cell-material interactions. Therefore, in this thesis, different cell types and models were used to evaluate the *in vitro* biological performance of each developed materials described in each chapter: L929 fibroblasts (Chapters V and VI), C2C12 myoblasts (Chapters IV and VI), MC3T3-E1 pre-osteoblasts (Chapter VII), HDFs (Chapter VIII) and hASCs (Chapter IX).Considering each type of cell, developed material and application, different methodologies were employed to evaluate the cell-materials interactions.

4.4.1. 3-(4,5-dimethylthiazol-2-yl)-5-(3-carboxymethoxyphenyl)-2-(4-sulphofenyl)-2H-tetrazolium (MTS) assay

The MTS assay was used to test the cytotoxicity and the viability of cells, upon interaction with materials. This metabolic activity assay is based on the bio-reduction ability of mitochondrial dehydrogenase enzymes present in viable cells to convert the MTS compound into a cell culture soluble brown formazan product [35]. Specific cell types, that were above mentioned, were cultured above the LbL-based films and incubated at 37°C and 5% CO_2, using adequate culture media according with the cell type. At different pre-determined periods, MTS assay was performed protected from light, as it is photosensitive. Briefly, the culture medium was removed and serum-free DMEM containing MTS solution with a dilution ratio of 1:5 was added to each well. Samples were then incubated in the dark at 37°C and 5% CO_2 for 3 hours. Then, 100 µL of each well (in triplicate) was transferred to a 96-well plate and the amount of formazan product was measured by absorbance at a wavelength of 490 nm using a multiwall spectrophotometer (Chapter IV, V, VI and VIII).

4.4.2. Alamar Blue ® assay

The alamarBlue® assay was also used to investigate the cytotoxicity by analyzing their metabolic activity (Chapter VII). MC3T3-E1 were cultured above the LbL-based films and incubated at 37°C and 5% CO_2, using adequate culture media. At different pre-determined periods, alamarBlue® assay was performed protected from light, as it is photosensitive. Briefly, the culture medium was removed and supplemented α-MEM containing 10% (v/v) of alamarBlue solution was added to each well. The samples were then incubated in the dark, overnight, at 37 °C and 5% CO_2. After 12 h, 100 µL of each well (in triplicate) was transferred to a 96-well plate. The absorbance was monitored at 570 nm and 600 nm, using a microplate reader.

4.4.3. DNA quantification assay

The DNA quantification assay was used to quantify the number of the cells as well to evaluate the cellular adhesion, viability and proliferation. Specific cell types, that were above mentioned, were cultured above the LbL-based films and incubated at 37°C and 5% CO_2, using adequate culture media according with the cell type. At different pre-determined periods each well was washed with Dulbecco's phosphate-buffered saline (DPBS) and 1 mL of ultrapure sterile water was added. Upon mixing, contents were transferred to Eppendorf tubes, which were then placed in a shaking water bath at 37°C for 1 h. Ultimately, the tubes were immediately stored at -80°C until use. Quantification of total DNA was determined after cell lysis, according to the manufacturer's description. After transferring each solution to a 96-well white opaque plate (in triplicate), the plate was incubated at RT protected from light for 10 min. The standard curve for DNA analysis was generated with provided DNA from the assay kit. Fluorescence was read at excitation of 485/20 nm and emission of 528/20 nm using a multiwall spectrophotometer (Chapter IV, V, VI, VII and VIII).

4.4.4. Cell quantification by trypsin detachment

Briefly, the sterile membranes (A=4cm^2) were placed in poly-HEMA coated 12-well culture plates and the same number of cells.mm^2 was dropped right above each membrane and incubated at 37°C, for 3 days. After 1 and 3 days, 3 samples per condition were taken and the cells adhered on each on were detached using trypsin and counted using an automatic cell counter equipment.

4.4.5. Cellular Morphology

The morphology of the different cell types when adhering and proliferating above the LbL-based systems was visualized over the time. Specific cell types, that were above mentioned, were cultured above the LbL-based films and incubated at 37°C and 5% CO_2, using adequate culture media according with the cell type. After pre-determined times, the samples were washed with DPBS and fixed at RT in formalin solution. After that, samples were kept in DPBS until using. In this thesis, two different experimental methodologies were employed to visualize and evaluate the morphology of cells upon interaction with material's surface: SEM and immunofluorescence staining.

Regarding the **SEM observation**, samples were dehydrated in an increasing gradient series of ethanol. After gold sputtering, samples were visualized by SEM (Chapter VI and IX).

Before the **immunofluorescence staining** cells were permeabilized through immersion in a triton solution, followed by a blocking step in a bovine serum albumin (BSA) solution. Then, after washing with DPBS the cells were incubated in the dark a phalloidin solution for at least 30 minutes, to stain the cytoskeleton of cells. For cell nuclei staining, cells were incubated in the dark in a 4,6-diamino-2-phenyindole dilactate (DAPI) solution in DPBS. Samples were observed using an inverted Fluorescence Inverted Microscope (Chapter IV, V, VI, VII, VIII and IX). Moreover, after 5 days of culture adherent cells were labelled with an immunofluorescence antibody to vinculin (Chapter VI). Basically, cell seeded membranes were fixed with formalin, permeabilized with triton solution for 5 minutes and the non-specific binding sites were blocked with of BSA solution for 1 hour. The samples were incubated at 4°C overnight with the primary antibody vinculin and then incubated with secondary donkey antibody anti-mouse Alexa Fluor 488 during 1 hour at RT, in the dark. Finally, the cells were incubated with DAPI at RT for 15 minutes. Prior to fluorescence microscopy, the samples were washed several times, and left in PBS overnight. Microscopic images were obtained using the transmitted and reflected light microscope.

For the work reported in Chapter IX, different methodologies were used to **SEM and fluorescence observations**. Briefly, the sterile membranes were cut in circles of 8 mm diameter (A superficial=0.5 cm^2) and put inside each well of the poly-HEMA coated 48-well culture plates. A cell suspension was dropped gently and right above the membrane surface. The cells were incubated at 37°C for 7 days, changing the medium every 2-3 days. Taking advantage of using RFP-ASC/TERT1, that were already labelled with a red fluorescein, live fluorescence images of the cells were taken for each condition, using an optical and fluorescence microscope. For SEM imaging, the RFP-ASC/TERT1 seeded-membranes were fixed after 5 days of culture. Therefore, the samples were incubated with a formalin solution for 1 hour and then washed with DPBS three times. Then the samples were dehydrated following a sequence of incubations in ethanol solutions, where the concentration gradually increased until being 100% ethanol. In the end, the samples were chemically dried with hexamethyldisilazane (HMDS). When HDMS was totally evaporated, the samples were coated with gold and examined with the SEM equipment.

4.4.6. Morphometric parameters

From morphology observation some **morphometric parameters** could be measured or calculated. Averaged cell perimeter and area, elongation factor (EF) and circularity were determined using the Image J® software (National Institutes of Health, Bethesda, MD, USA) (Chapter VI and IX). Moreover, using the fluorescence imaging just for the DAPI also nuclei elongation and orientation were calculated (Chapter VI). Therefore, Cells area, perimeter, circularity and EF were determined after 3 days of culture. The cell EF corresponds to the longest cell axis divided by the maximal length perpendicular to this long axis [36]. The alignment was determined using information obtained by SEM or fluorescence images, where images shown both the cells adhered on the membranes and the nanopatterning; the patterning orientation was rotated to be equal to 0°. Additionally, also the cells angle distribution was determined using the Image J® software analyzing 5 images per condition, relatively to the day 3 of culture (where cells were suitably grown and dispersed to measure these parameters). The orientation analysis of the nucleus of individual cells adhered on FS membranes was assessed from fluorescent images. Image J® was used define the boundary of the nuclei, to determine the orientation of the nucleus of the individual cells relative to the preferential direction (assumed as the patterning direction). Nuclei included for analysis had to be fully contained within the border of the image. The nuclei EF was obtained by dividing the longest nucleus axis by the maximal length perpendicular to this long axis. The orientation of the nuclei was based on the angle between the major axis of the object and the long axis of the underlying topography (defined as 0°). Nuclei were considered aligned for an orientation angle between 10° and -10°. Five images were analyzed for each condition. Representative fluorescent images of the nuclei of the cells were presented for each condition.

4.4.7. Cellular differentiation

Cell differentiation was investigated in different chapters, using cell types with such ability. Therefore, in the Chapter IV and VI, myogenic differentiation was studied using murine C2C12 cells, osteoblastic differentiation was inspected using MC3T3-E1 cells and chondrogenic differentiation was considered using ASCs. Specific culture media were used to support differentiation and different methodologies and markers were used to detect the potential of differentiation. These experimental details will be briefly described below.

To evaluate the potential of the developed coatings to allow **myogenic differentiation** (Chapters IV and VI), C2C12 cells were seeded above the samples and incubated at 37°C and 5% CO_2 in DMEM culture medium. When 90% of confluence was achieved, the culture medium was exchanged by differentiation medium, composed of DMEM supplemented with 2% of horse serum and 1% of antibiotics/antimycotics, to induce cell differentiation. Basal culture medium was used to investigate the cellular differentiation potential when in presence of a patterned material's surface (Chapter VI). After one week, the cells were stained by an immunocytochemistry protocol to identify troponin T-positive cells. After fixing the cells with formalin, the samples were washed and permeabilized with a Triton x100 solution and blocked with a BSA solution. After washing with DPBS, the samples were incubated overnight at 4 °C with the mouse troponin T antibody and after this time the samples were washed and incubated with the secondary antibody anti-mouse Alexa Fluor 488 during 1 hour at RT. Then the cells were incubated with DAPI to counterstain the nuclei. The samples were then extensively washed with DPBS to remove the excess of fluorescence probes. A transmitted and reflected light microscope was used to image the stained cells. From fluorescence microscopic observation, different morphometric parameters related with the myogenic differentiation could be determined; fusion index and average number of troponin T-positive myotubes per area were determined using ImageJ tools. A cell containing

3 or more nuclei was considered a myotube. The fusion index was calculated, as the ratio of the nuclei number within the troponin T-positive myotubes versus the total number of nuclei in the same area. Also, the average of myotubes area, perimeter, length and elongation factor were determined using ImageJ tools. The elongation factor describes to what extent the equimomental ellipse is lengthened or stretched out.

To evaluate **the osteogenic differentiation** potential of the FS multilayered membranes developed in Chapter VII, cells were cultured with MC3T3-E1 in basal growth medium, at 37 °C and 5% of CO_2. After five days in basal conditions, the medium was changed for osteogenic medium (α-MEM containing 10% FBS, 10 mM β-glycerolphosphate disodium salt hydrate, and 50 $\mu g.mL^{-1}$ L-ascorbic acid). The differentiation medium was changed every three days. Then, intracellular osteopontin expression was evaluated as it has been reported as a marker for osteogenic differentiation. After 14 days in differentiation medium, the samples were fixed in formalin solution in DPBS. Following the fixation step, the fixed samples were permeabilized with a Triton X-100 solution in DPBS solution for 10 min and then blocked with a fetal bovine serum (FBS) solution in DPBS solution for 60 min. Then, the samples were examined for protein expression visualization using a mouse antibody against osteopontin by incubation overnight, at 4 °C. Subsequently, the samples were treated with the corresponding secondary antibody anti-mouse Alexa Fluor 647 for 1 h, at RT and consequently with rhodamine phalloidin and DAPI for 45 min and 15 min, respectively. Between each step the samples were extensively washed. Afterwards, the cell morphology was observed using fluorescence microscopy.

4.5. *In vivo* biological performance

For Chapter VIII, animal experiments were performed according to the protocol approved by the Ethics Committee of Centro Hospitalar Cova da Beira (approval number 24/2009) and the guidelines set forth in the National Institute for the care and use of laboratory animals. To perform the in vivo assays, a total of 10 Wistar rats (4-6 weeks) weighing between 100- 150 g were used. Animals were separated into three groups: group 1, wounds were treated with control membrane; group 2, wounds were covered HA-DN-containing membrane; whereas in the group 3, used as positive control, wounds were covered with serum physiologic solution. During the study, animals were kept in separate cages and were fed with commercial rat food and water ad libitum. Animals were sacrificed after 10 and 21 days. Hematoxylin and Eosin (H&E) staining analysis was used to evaluate the local and systemic immune response of different membranes, tissue specimens were obtained from each wound area by sharp dissection at days 10 and 21. Skin tissue samples were obtained by necropsy, formalin fixed, and paraffin embedded for histological processing. Sections of 3 µm were obtained from each sample using a cryostat microtome and then stained with hematoxylin and eosin (H&E) or with Toluidine blue. Subsequently, samples were visualized using a light microscope with a specific image analysis software. Skin fragments without membrane were used as control. Other tissue samples such as brain, lung, liver, spleen and kidney, were also obtained by necropsy and analyzed to check for any morphological.

4.6. *In situ* biological assays

In chapter IX, we designed an *in situ* experimental methodology that allowed testing superficial cartilage under a more controlled environment than in vivo, but in the natural place.

4.6.1. Preparation of the damaged cartilage plug chips

Damaged cartilage plug chips were prepared of human samples and using with the approval of the Ethics Committee of General Hospital of Vienna and the guidelines set forth in the National Institute for Health. Human hip joints were used as the source for cartilage plug chips. Just hip joint samples with visible signs of damaging were considered for this study; therefore, parameters like color, roughness and redness were taken in account. Firstly, the cartilage areas of interest were cut from the hip joint with the help of a scalper. With the careful of maintaining always the sample hydrated, 8 mm chip diameter were then made using an appropriate manual biopsy punch. Subsequently the chips were kept into a sterile solution of DPBS containing 10% of antibiotics at 4°C and used in the day after. The representative scheme of the procedure is presented in Figure III-7.

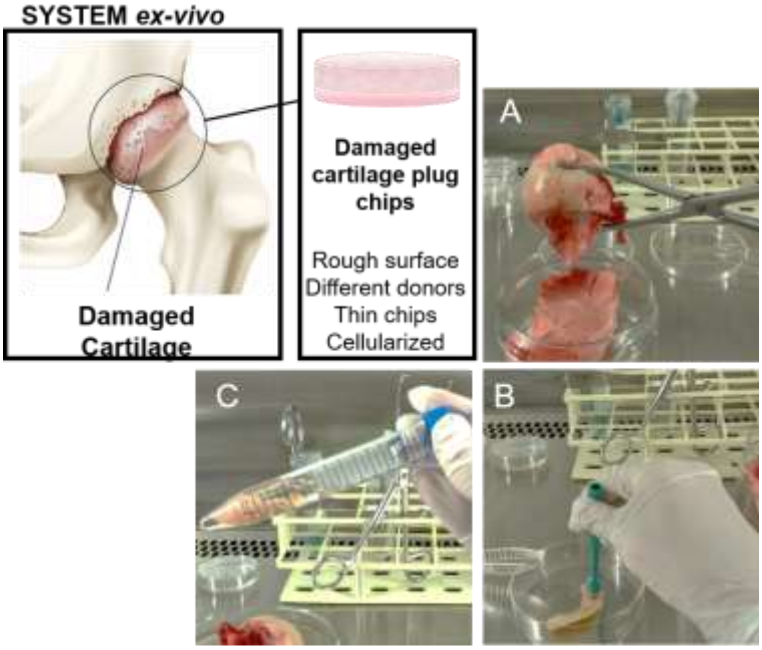

Figure III-7. Schematic representation and photographs of the system created to test the potentiality of the material to delivery ASCs, to treat damaged articular cartilage: A) human femoral head sample; B) Removal of the damaged cartilage layer to make 8 mm discs; C) Overnight incubation of the prepared discs in a DPBS solution containing 10% of antibiotics at 4°C.

4.6.2. System composed of RFP-ASC/TERT1 seeded membranes and damaged cartilage plug chip in basal medium

To test the membranes with the damaged human cartilage plug, a very similar procedure used for adhesion and viability tests was used. Briefly, the sterile membranes were cut in circles of 8 mm put inside each well of the sterile poly-HEMA coated 48-well culture plates. A cell suspension of RFP-ASCs was dropped gently and right above the membrane surface. The cells were then incubated at 37°C, overnight. In the day after, RFP-ASC/TERT1 seeded-membranes were put directly above the damaged surface of the human cartilage chips, with the RFP-ASC/TERT1 side facing the cartilage surface. Then this system was transferred in one-piece to the poly-HEMA coated 48-well culture plates, upside down (membrane in contact with the bottom and the chip right above). Each well/system was cultured in basal ASC differentiation medium, supplemented with 100 mM of dexamethasone. The medium was changed every 2-3 days and the culture was maintained for 3 weeks.

Live imaging of the interaction between RFP-ASC/TER1 seeded membranes and the damaged cartilage chip. The interaction between RFP-ASC/TERT1 seeded membranes and the damaged cartilage chip was live recorded after 3 days, 1 week and 2 weeks of culture, using a confocal microscopy equipment.

Cross-section observation of the RFP-ASC/TERT1 seeded membranes and the damaged cartilage chip. After 2 weeks of culture, the samples were fixed with paraformaldehyde 4% solution during overnight, under automatic agitation. In the day after, the samples were washed with DPBS 3 times and then transversally cut in 2 sections. These sections were placed in a glass slide with the cross section turned down; fluorescence images of the cross-section were using the confocal microscopy.

Histological sections preparation: Azan staining analysis. After 3 weeks of culture, other samples were fixed with formalin 4% solution during overnight, under automatic agitation. Next day, the samples were washed under continuous tap water for 1 hour and then put in ethanol 30% for another hour under automatic agitation. In the end the samples were kept in ethanol 70% until use. To evaluate histologically the impact of the ASCs-seeded membranes on the structure of cartilage, sections of the formalin-fixed samples were prepared for Azan trichrome staining. Briefly, the formalin-fixed sections dehydrated with ascending alcohol series. Samples were fixed in 4% neutral buffered formalin, washed in PBS and dehydrated with a graded series of alcohol. Then, samples were embedded in paraffin and sectioned with 3-4 µm thickness with a rotatory microtome. Sections were stained with Azan. Subsequently, samples were visualized using a light microscope with a specific image analysis software. Cartilage fragments without membrane were used as control. Other tissue samples such as brain, lung, liver, spleen and kidney, were also obtained by necropsy and analyzed to check for any morphological.

4.6.3. System composed of RFP-ASC/TERT1 seeded membranes and damaged cartilage plug chip in differentiation medium.

To test the differentiation potential of these membranes when implemented above the cartilage superficial defect, we culture the system ASCs-seeded membranes and damaged cartilage plug chip in differentiation medium. Briefly, the sterile membranes were cut in circles of 8 mm put inside each well. A cell suspension of RFP-ASC/TERT1 was seeded above the membranes and incubated at 37°C, overnight. In the day after, RFP-ASC/TERT1 seeded-membranes were put directly above the damaged surface of the human cartilage chips, with the RFP-ASC/TERT1 side facing the cartilage surface. Then this system was transferred in one-piece to the well plate, upside down (membrane in contact with the bottom and the chip right above). Each well/system was cultured in ASC differentiation medium, supplemented with 100 mM of dexamethasone and low-dose of transforming growth factor- beta 3 (TGF-β3) and bone morphogenetic protein 6 (BMP-6). The medium was changed every 2 days and the culture was maintained for 5 weeks.

To evaluate the chondrogenic potential of these cells when in contact with the damaged cartilage chips and incubated in a TGF-β3/BMP-6 supplemented medium, immunohistochemistry and histological analysis were done. Therefore, sections of the formalin-fixed samples were prepared. Briefly, the formalin-fixed sections dehydrated with ascending alcohol series. Thereafter, they were embedded in paraffin and sectioned with 3-4 µm thickness with a rotatory microtome. Sections were immunolabelled against collagen type II. Subsequently, samples were visualized using a light microscope with a specific image analysis software. Cartilage fragments without membrane were used as control. Other tissue samples such as brain, lung, liver, spleen and kidney, were also obtained by necropsy and analyzed to check for any morphological.

5. References

1. (a) Papakonstantinou, E.; Roth, M.; Karakiulakis, G., Hyaluronic acid: A key molecule in skin aging. *Dermato-endocrinology* **2012,** *4* (3), 253-258; (b) Lee, K. Y.; Mooney, D. J., Alginate: properties and biomedical applications. *Progress in polymer science* **2012,** *37* (1), 106-126; (c) Silva, T. H.; Duarte, A. R.; Moreira-Silva, J.; Mano, J. F.; Reis, R. L., Biomaterials from Marine-Origin Biopolymers. In *Biomimetic Approaches for Biomaterials Development*, 2012.

2. Szekalska, M.; Puci; #x142; owska, A.; Szyma; #x144; ska, E.; Ciosek, P.; Winnicka, K., Alginate: Current Use and Future Perspectives in Pharmaceutical and Biomedical Applications. *International Journal of Polymer Science* **2016,** *2016*, 17.

3. Sun, J.; Tan, H., Alginate-Based Biomaterials for Regenerative Medicine Applications. *Materials (Basel, Switzerland)* **2013,** *6* (4), 1285-1309.

4. Kuo, C. K.; Ma, P. X., Ionically crosslinked alginate hydrogels as scaffolds for tissue engineering: Part 1. Structure, gelation rate and mechanical properties. *Biomaterials* **2001,** *22* (6), 511-521.

5. (a) Balamurugan, M.; Rajesh, S.; Manogaran, E., 'Genipin' – The Natural Water Soluble Cross-linking Agent and Its Importance in the Modified Drug Delivery Systems: An Overview. *Current Drug Delivery* **2014,** *11* (1), 139-145; (b) Wang, C.; Lau, T. T.; Loh, W. L.; Su, K.; Wang, D.-A., Cytocompatibility study of a natural biomaterial crosslinker—Genipin with therapeutic model cells. *Journal of Biomedical Materials Research Part B: Applied Biomaterials* **2011,** *97B* (1), 58-65.

6. (a) Wang, M.; Da, L.; Xie, Y.; Xie, H., Application of genipin for modification of natural biomaterials as a crosslinking agent. *Zhongguo xiu fu chong jian wai ke za zhi = Zhongguo xiufu chongjian waike zazhi = Chinese journal of reparative and reconstructive surgery* **2013,** *27* (5), 580-5; (b) Slusarewicz, P.; Zhu, K.; Hedman, T., Kinetic analysis of genipin degradation in aqueous solution. *Natural product communications* **2010,** *5* (12), 1853-8; (c) Lee, H.; Dellatore, S. M.; Miller, W. M.; Messersmith, P. B., Mussel-Inspired Surface Chemistry for Multifunctional Coatings. *Science* **2007,** *318* (5849), 426-430.

7. (a) Moulay, S., Dopa/Catechol-Tethered Polymers: Bioadhesives and Biomimetic Adhesive Materials. *Polymer Reviews* **2014,** *54* (3), 436-513; (b) Neto, A. I.; Cibrao, A. C.; Correia, C. R.; Carvalho, R. R.; Luz, G. M.; Ferrer, G. G.; Botelho, G.; Picart, C.; Alves, N. M.; Mano, J. F., Nanostructured polymeric coatings based on chitosan and dopamine-modified hyaluronic acid for biomedical applications. *Small* **2014,** *10* (12), 2459-69.

8. (a) Liu, Y.; Meng, H.; Konst, S.; Sarmiento, R.; Rajachar, R.; Lee, B. P., Injectable Dopamine-Modified Poly(ethylene glycol) Nanocomposite Hydrogel with Enhanced Adhesive Property and Bioactivity. *ACS Applied Materials & Interfaces* **2014,** *6* (19), 16982-16992; (b) Madhurakkat Perikamana, S. K.; Lee, J.; Lee, Y. B.; Shin, Y. M.; Lee, E. J.; Mikos, A. G.; Shin, H., Materials from Mussel-Inspired Chemistry for Cell and Tissue Engineering Applications. *Biomacromolecules* **2015,** *16* (9), 2541-2555; (c) ISO, *Biological Evaluation of Medical Devices – Part 5: Tests for In Vitro Cytotoxicity*. 2009; p 10993-10995.

9. Zange, R.; Kissel, T., Comparative *in vitro* biocompatibility testing of polycyanoacrylates and poly(d,l-lactide-co-glycolide) using different mouse fibroblast (L929) biocompatibility test models. *European Journal of Pharmaceutics and Biopharmaceutics* **1997,** *44* (2), 149-157.

10. (a) Silva, J. M.; Duarte, A. R. C.; Caridade, S. G.; Picart, C.; Reis, R. L.; Mano, J. F., Tailored freestanding multilayered membranes based on chitosan and alginate. *Biomacromolecules* **2014,** *15* (10), 3817-3826; (b) McMahon, D. K.; Anderson, P. A.; Nassar, R.; Bunting, J. B.; Saba, Z.; Oakeley, A. E.; Malouf, N. N., C2C12 cells: biophysical, biochemical, and immunocytochemical properties. *American Journal of Physiology-Cell Physiology* **1994,** *266* (6), C1795-C1802.

11. Lawson, M. A.; Purslow, P. P., Differentiation of Myoblasts in Serum-Free Media: Effects of Modified Media Are Cell Line-Specific. *Cells Tissues Organs* **2000,** *167* (2-3), 130-137.

12. Quarles, L. D.; Yohay, D. A.; Lever, L. W.; Caton, R.; Wenstrup, R. J., Distinct proliferative and differentiated stages of murine MC3T3-E1 cells in culture: An *in vitro* model of osteoblast development. *Journal of Bone and Mineral Research* **1992,** *7* (6), 683-692.

13. Franceschi, R. T.; Iyer, B. S., Relationship between collagen synthesis and expression of the osteoblast phenotype in MC3T3-E1 cells. *Journal of Bone and Mineral Research* **1992,** *7* (2), 235-246.

14. (a) Tracy, L. E.; Minasian, R. A.; Caterson, E. J., Extracellular Matrix and Dermal Fibroblast Function in the Healing Wound. *Advances in wound care* **2016,** *5* (3), 119-136; (b) Chang, H. Y.; Chi, J.-T.; Dudoit, S.; Bondre, C.; van de Rijn, M.; Botstein, D.; Brown, P. O., Diversity, topographic

differentiation, and positional memory in human fibroblasts. *Proceedings of the National Academy of Sciences* **2002,** *99* (20), 12877-12882.

15. (a) Tigges, J.; Krutmann, J.; Fritsche, E.; Haendeler, J.; Schaal, H.; Fischer, J. W.; Kalfalah, F.; Reinke, H.; Reifenberger, G.; Stühler, K.; Ventura, N.; Gundermann, S.; Boukamp, P.; Boege, F., The hallmarks of fibroblast ageing. *Mechanisms of Ageing and Development* **2014,** *138*, 26-44; (b) Cheng, K.-H.; Kuo, T.-L.; Kuo, K.-K.; Hsiao, C.-C., Human adipose-derived stem cells: Isolation, characterization and current application in regeneration medicine. *Genomic Medicine, Biomarkers, and Health Sciences* **2011,** *3* (2), 53-62.

16. Balducci, L.; Blasi, A.; Saldarelli, M.; Soleti, A.; Pessina, A.; Bonomi, A.; Coccè, V.; Dossena, M.; Tosetti, V.; Ceserani, V.; Navone, S. E.; Falchetti, M. L.; Parati, E. A.; Alessandri, G., Immortalization of human adipose-derived stromal cells: production of cell lines with high growth rate, mesenchymal marker expression and capability to secrete high levels of angiogenic factors. *Stem Cell Research & Therapy* **2014,** *5* (3), 63.

17. Leto Barone, A. A.; Khalifian, S.; Lee, W. P. A.; Brandacher, G., Immunomodulatory Effects of Adipose-Derived Stem Cells: Fact or Fiction? *BioMed Research International* **2013,** *2013*, 8.

18. (a) Costa, R. R.; Martín, L.; Mano, J. F.; Rodríguez-Cabello, J. C., Elastin-Like Macromolecules. In *Biomimetic Approaches for Biomaterials Development*, 2012; (b) Meyer, D. E.; Chilkoti, A., Purification of recombinant proteins by fusion with thermally-responsive polypeptides. *Nature biotechnology* **1999,** *17* (11), 1112-5.

19. Girotti, A.; Fernández-Colino, A.; López, I. M.; Rodríguez-Cabello, J. C.; Arias, F. J., Elastin-like recombinamers: Biosynthetic strategies and biotechnological applications. *Biotechnology Journal* **2011,** *6* (10), 1174-1186.

20. Park, S.-J.; Seo, M.-K., Chapter 3 - Solid-Liquid Interface. In *Interface Science and Technology*, Park, S.-J.; Seo, M.-K., Eds. Elsevier: 2011; Vol. 18, pp 147-252.

21. (a) Gumustas, M.; Sengel-Turk, C. T.; Gumustas, A.; Ozkan, S. A.; Uslu, B., Chapter 5 - Effect of Polymer-Based Nanoparticles on the Assay of Antimicrobial Drug Delivery Systems. In *Multifunctional Systems for Combined Delivery, Biosensing and Diagnostics*, Grumezescu, A. M., Ed. Elsevier: 2017; pp 67-108; (b) El-Zohry, A. M.; Hashem, E. Y., Environmental Method to Determine Dopamine and Ascorbic Acid Simultaneously via Derivative Spectrophotometry. *Journal of Spectroscopy* **2013,** *2013*, 7.

22. (a) Fan, T. W. M.; Lane, A. N., Applications of NMR spectroscopy to systems biochemistry. *Progress in nuclear magnetic resonance spectroscopy* **2016,** *92-93*, 18-53; (b) Marx, K. A., Quartz Crystal Microbalance: A Useful Tool for Studying Thin Polymer Films and Complex Biomolecular Systems at the Solution−Surface Interface. *Biomacromolecules* **2003,** *4* (5), 1099-1120.

23. Alves, N. M.; Picart, C.; Mano, J. F., Self Assembling and Crosslinking of Polyelectrolyte Multilayer Films of Chitosan and Alginate Studied by QCM and IR Spectroscopy. *Macromolecular Bioscience* **2009,** *9* (8), 776-785.

24. **!!! INVALID CITATION !!!**

25. (a) Tang, Z.; Wang, Y.; Podsiadlo, P.; Kotov, N. A., Biomedical Applications of Layer-by-Layer Assembly: From Biomimetics to Tissue Engineering. *Advanced Materials* **2007,** *19* (7), 906-906; (b) Gentile, P.; Carmagnola, I.; Nardo, T.; Chiono, V., Layer-by-layer assembly for biomedical applications in the last decade. *Nanotechnology* **2015,** *26* (42), 422001.

26. Costa, R. R.; Mano, J. F., Polyelectrolyte multilayered assemblies in biomedical technologies. *Chemical Society Reviews* **2014,** *43* (10), 3453-3479.

27. Ariga, K.; Hill, J. P.; Ji, Q., Layer-by-layer assembly as a versatile bottom-up nanofabrication technique for exploratory research and realistic application. *Physical Chemistry Chemical Physics* **2007,** *9* (19), 2319-2340.

28. (a) Correia, C. R.; Pirraco, R. P.; Cerqueira, M. T.; Marques, A. P.; Reis, R. L.; Mano, J. F., Semipermeable Capsules Wrapping a Multifunctional and Self-regulated Co-culture Microenvironment for Osteogenic Differentiation. *Scientific Reports* **2016,** *6*, 21883; (b) Silva, J. M.; Duarte, A. R. C.; Custódio, C. A.; Sher, P.; Neto, A. I.; Pinho, A. C. M.; Fonseca, J.; Reis, R. L.; Mano, J. F., Nanostructured Hollow Tubes Based on Chitosan and Alginate Multilayers. *Advanced Healthcare Materials* **2014,** *3* (3), 433-440.

29. (a) Sher, P.; Custódio, C. A.; Mano, J. F., Layer-By-Layer Technique for Producing Porous Nanostructured 3D Constructs Using Moldable Freeform Assembly of Spherical Templates. *Small* **2010,** *6* (23), 2644-2648; (b) Borges, J.; Mano, J. F., Molecular Interactions Driving the Layer-by-Layer Assembly of Multilayers. *Chemical Reviews* **2014,** *114* (18), 8883-8942.

30. Butler, M. F.; Ng, Y.-F.; Pudney, P. D. A., Mechanism and kinetics of the crosslinking reaction between biopolymers containing primary amine groups and genipin. *Journal of Polymer Science Part A: Polymer Chemistry* **2003,** *41* (24), 3941-3953.
31. Vernon-Parry, K. D., Scanning electron microscopy: an introduction. *III-Vs Review* **2000,** *13* (4), 40-44.
32. Franz, C.; Puech, P. H., *Atomic Force Microscopy: A Versatile Tool for Studying Cell Morphology, Adhesion and Mechanics*. 2008; Vol. 1, p 289-300.
33. (a) De Bartolo, L.; Morelli, S.; Bader, A.; Drioli, E., Evaluation of cell behaviour related to physico-chemical properties of polymeric membranes to be used in bioartificial organs. *Biomaterials* **2002,** *23* (12), 2485-2497; (b) Seo, J.; Lutkenhaus, J. L.; Kim, J.; Hammond, P. T.; Char, K., Effect of the Layer-by-Layer (LbL) Deposition Method on the Surface Morphology and Wetting Behavior of Hydrophobically Modified PEO and PAA LbL Films. *Langmuir* **2008,** *24* (15), 7995-8000.
34. Yuan, Y.; Lee, T. R., Contact Angle and Wetting Properties. In *Surface Science Techniques*, Bracco, G.; Holst, B., Eds. Springer Berlin Heidelberg: Berlin, Heidelberg, 2013; pp 3-34.
35. Berridge, M. V.; Herst, P. M.; Tan, A. S., Tetrazolium dyes as tools in cell biology: New insights into their cellular reduction. In *Biotechnology Annual Review*, Elsevier: 2005; Vol. 11, pp 127-152.
36. Yim, E. K. F.; Reano, R. M.; Pang, S. W.; Yee, A. F.; Chen, C. S.; Leong, K. W., Nanopattern-induced changes in morphology and motility of smooth muscle cells. *Biomaterials* **2005,** *26* (26), 5405-5413.
37. ASTM, *ASTM D 1002 Standard Test Method for Apparent Shear Strength of Single-lap Joint Adhesively Bonded Metal Specimens*. ASTM: 2005.

IV. Biomimetic click assembled multilayer coatings exhibiting responsive properties*

Abstract

Stimuli-responsive polymers can change their physico-chemical properties in a dynamic way, to respond to variations on the surrounding environment. These materials have gained increasingly importance for different areas, such as drug delivery, biosensors, microelectronic systems and also for the design and modification of biomaterials to apply on tissue engineering field. In the last years, different strategies have been envisaged for the development of stimuli-responsive biomaterials. Layer-by-layer (LbL) is a promising and versatile technique to modify biomaterials' surfaces and has allowed tailoring interactions with cells. In this study, LbL is used to construct biomimetic stimuli-responsive coatings using elastin-like recombinamers (ELRs). The recombinant nature of ELRs provides the ability to introduce specific bioactive sequences and to tune their physicochemical properties, making them attractive for biomedical and biological applications. By using complementary clickable ELRs, we were able to construct multilayer coatings stabilized by covalent bonds, resulting from the Huisgen 1,3-dipolar cycloaddition of azides and alkynes. Herein, we exploited the switchable properties of the ELRs-based coatings which are dependent on lower critical solution temperature (LCST) transition. Above LCST, the polymers collapsed, and nanostructured precipitates were observed on the surface´s morphology, increasing the water contact angle. Also, the influence of pH on prompting reversible responses on coatings was evaluated. Finally, *in vitro* cell studies using a C2C12 myoblastic cell line were performed to perceive the importance of having bioactive domains within these coatings. The effect of RGD incorporation is clearly noted not only in terms of adhesion and proliferation but also in terms of myoblast differentiation.

Keywords: elastin-like recombinamers; click chemistry; layer-by-layer; stimuli-responsive; myogenic differentiation.

---

[*] This Chapter is based on the following publication: Sousa, M. P.; Gonzalez de Torre, I.; Oliveira, M. B.; Rodríguez-Cabello, J. C.; Mano, J. F., Biomimetic click assembled multilayer coatings exhibiting responsive properties. *Materials Today Chemistry* **2017,** *4*, 150-163.

1. Introduction

Scientists have been increasingly applying efforts to imitate materials, systems or elements present in Nature, in the pursue of solutions for some healthcare concerns. Particular focus has been given to bioinspired systems; for instance, a basic process of living systems is the ability to respond or adapt to different stimuli [1]. In these adaptation processes, different length scales can be considered; from molecular interactions triggering a cascade of cellular events like cell signaling, endocytosis and exocytosis, to macroscopic interactions with external stimuli like temperature, prompting cascades of nervous signals transmitted to the brain and causing a physiological response [2].

Therefore, developing polymeric materials capable of responding to environmental changes represents a challenge with high impact. Different stimuli, such as temperature, pH, chemical composition, mechanical forces or even light or magnetic abilities, can trigger morphological, chemical and physical changes on polymeric materials, [2-3]. A diversity of architectures, from 2-dimensional to 3-dimensional, has been suggested to develop stimuli-responsive systems. Examples include thin films [4], membranes [5], nanoparticles [6], gels or even capsules [6a].A wide-range of techniques has been employed to produce such kind of architectures, and LbL appeared as one of the strongest candidates to fabricate structures with distinct geometries [7]. It is an inexpensive and versatile tool for biomaterials surface modification and has allowed tailoring cell-material interactions [8]. Intermolecular interactions are in the base of LbL methodology, with electrostatic forces assuming a major role [9]; typical LbL is mainly based on the deposition of oppositely charged polyelectrolytes. However, also non-electrostatic forces can be involved [10]; van der Waals, hydrogen, coordination and covalent bonds are some of them. In recent years, significant increase of stability has been reported when considering covalent bonds as the major player on the LbL construction [11]. For instance, Seo J. *et al.* [12] developed multifunctional polymer multilayer thin films with good physicochemical stability using the LbL deposition based on covalent bonds between activated esters and amine groups. Other strategies based on covalent interactions have been suggested. Click chemistry based LbL was reported to produce ultrathin films on silica particles, developing pH-responsive click capsules [13]. Herein, we take advantage of a catalyst-free click technology, in which specific interactions are a result from Huisgen 1,3-dipolar cycloaddition of azides and alkynes [14].

Nowadays, polymeric materials have been the most studied class to produce LbL nanostructured assemblies, either being of synthetic or natural origin [7]. Polysaccharides [15], proteins [16] and even DNA [17] have been explored. Using LbL methodology, Costa R. *et al.* [16a] produced responsive thin multilayer coatings based on electrostatic interactions assembly of chitosan and elastin-like recombinamers (ELRs). Recombinant elastin has been reported as biocompatible, with mechanical properties comparable to those of native human elastin and with a thermosensitive behavior dependent of their lower critical solution temperature (LCST) [16a, 18].

In this study, we propose the production of stable thin coatings to be used in biomedicine, combining ELRs with LbL technology and click chemistry. Taking advantage of recombinant technologies, different

ELRs were synthetized. This technology allows to introduce specific bioactive moieties and tailor physicochemical and bioactive properties of the polymers, making them attractive for biomedical and tissue engineering proposes. Therefore, we investigate the responsive abilities of these coatings and the influence of having the arginine-glycine-aspartic acid (RGD) motif on the chemical structure of the coatings. The presence of RGD tripeptide has gained particular interesting due to its well-known support to cellular adhesion [16a, 19].

We hypothesize that the presence of RGD motifs on the surface of the films can be of extreme relevance to apply those kinds of films towards tissue engineering strategies or in the design of new microenvironments for cell culture.

2. Experimental section

2.1. Materials

The bioproduction, purification and chemical modification of the different clickable ELRs (cyclooctyne- and azide-modified ELRs) can be found elsewhere [20]. Low glucose Dulbecco's modified Eagle's medium (DMEM) without phenol red and sodium bicarbonate and DMEM with phenol red were purchased as powder from Sigma-Aldrich, as well as the sodium bicarbonate, sodium acetate trihydrate, PBS tablets, 4′,6-Diamidine-2′-phenylindole dihydrochloride (DAPI), Phalloidin–Tetramethylrhodamine B isothiocyanate, Triton x100 and bovine serum albumin (BSA). Sodium hydroxide (NaOH) was purchased from Fisher Scientific and glacial acetic acid from VWR. The glass coverslips (13 mm diameter) were provided by Agar Scientific (UK). Fetal bovine serum (FBS), penicillin-streptomycin, Alexa Fluor 488, and DPBS (PBS without calcium and magnesium) were supplied by Life Technologies. CellTiter 96® Aqueous One Solution was purchased from Promega, horse serum (New Zealand origin) from Invitrogen and skeletal muscle troponin T antibody from Acris Antibodies.

2.2. Bioproduction of the ELRs

Genetic engineering techniques were used to synthetize the ELRs of interest, following a procedure already described elsewhere [20]. The obtained ELRs were purified, dialyzed and then lyophilized. In the end, two ELRs were used: the ELR HRGD6, which contains the adhesion sequence RGD and the ELR VKVx24, which contains a similar structure to the first one but without the bioactive sequence. To allow the click chemistry reaction, reactive groups were required; for that, the bio-produced ELRs were chemically modified at their lysine amino acids by transformation of the ε-amine group present in the lateral chain of the lysine residue. This process was achieved with a relatively mild and easy-to-perform reactions. A diazo transfer reaction to amines was performed on the two different ELRs, in order to introduce azides directly at the lysine positions of proteins, following a methodology described before [20]. The resulting azide conversion was in the order of 70-90% of substitution and the two working ELRs were, thus, chemically modified: VKV-N_3 and RGD-N_3. Also alkyne cyclooctyne groups were introduced at the lysine positions of proteins with a substitution degree in the order of 60%, following a procedure already described [20]. From cyclooctyne modification we obtained the clickable ELRs: VKV-cyclo.

2.3. Size distribution and Zeta potential measurement of the polymeric solutions

The modified ELRs solutions were prepared in serum-free DMEM without phenol red at 0.5 mg.mL^{-1}. After that, the solutions were maintained overnight at different temperatures: 4°C, room temperature (RT, 20°C) and 37°C. The single size distribution of the prepared solutions was then measured through dynamic light scattering (DLS), using a Nano-ZS equipment from Malvern (United Kingdom). The measurements were made in the equipment at 4°C, RT and 37°C, accordingly to the different overnight incubations.

ELR solutions were prepared at same concentrations, and their pH was adjusted to 6.5, 7.0 or 7.5 using NaOH 1 M and acetic acid 1% (v/v). The zeta (ζ)-potential of the different solutions were also determined using a Nano-ZS equipment from Malvern.

2.4. Build-up kinetics construction

A quartz crystal microbalance with dissipation monitoring system (QCM-D, Q-Sense, Sweden) was used to follow up the absorption of the ELRs above crystal gold-coated crystals. ELRs solutions were prepared at concentrations of 0.5 mg.mL^{-1} in serum-free DMEM without phenol red, pH of 7. This water-based solvent was used as washing solution. The multilayer construction of combinations of (i) VKV-cyclo with RGD-N_3 and (ii) VKV-cyclo with VKV-N_3 was investigated for the deposition of 4 bilayers. Each polymer solution was pumped during 20 minutes with washing steps between each layer (15 minutes). The working temperature was defined as RT and the flow rate as 50 µl.min^{-1}. The thickness of the multilayer films was estimated based on the Voigt model [21], using the Q-tools software (Q-Sense, Sweden).

2.5. Assembly of ELRs clickable multilayers

Glass coverslips were cleaned with 5-minute cycles of acetone, ethanol and isopropanol (all from Sigma-Aldrich) in a ultrasonication bath and activated using an UV-Ozone Cleaner (ProCleaner 220, Bioforce Nanoscience) for 10 minutes. The polymer solutions were prepared at concentrations of 0.5 mg.mL^{-1} in serum-free DMEM without phenol red and sodium bicarbonate, pH of 7. Different formulations were produced; the combination of VKV-cyclo with RGD-N_3 and VKV-cyclo with VKV-N_3. For both, we started adsorbing the cyclooctyne-modified ELR for 20 minutes, followed by a washing step with serum-free DMEM. Then the click reaction was completed introducing the azide-modified polymers, through the immersion of the surfaces in the RGD-N_3 or VKV-N_3, again for 20 minutes and then a quick washing step. The process was repeated four times, at RT, in order to form a 4-bilayer elastin-based film. Note that, in between each incubation time, the solutions were maintained at 4°C. In the end, two click assembled multilayer coatings were obtained: i) ((VKV- cyclo/RGD- $N_3)_4$ and ii) (VKV-cyclo/VKV- $N_3)_4$.

2.5.1. Fluorescence microscopy

Fluorescence microscopy was used to investigate the effectiveness of the coating process. The addition of fluorescent probes to ELRs was described elsewhere [20]. Acetylene Fluor 488 was added to azide modified ELRs, providing them with fluorescence. Labelled ELRs were used to construct the ELR-based multilayers at RT, instead of using the non-fluorescent forms. After 4 bilayers, the $(\text{VKV-cyclo/RGD-}N_3)_4$ and $(\text{VKV-cyclo/VKV-}N_3)_4$ films were dried at RT, protected from light and visualized under transmitted and reflected light microscope with apotome 2 (Axio Imager Z1m, Zeiss, Germany).

2.5.2. AFM

Atomic force microscopy (AFM) was used to investigate the topography of the multilayer-coated surfaces. These studies were performed using AFM equipment (Dimension Icon, Bruker, USA) operated in a tapping mode at a frequency of 1 Hz. The samples were immersed in PBS for 30 minutes and their topography was evaluated at RT, with an analyzed area of 5 x 5 μm^2. Coatings performed with 1 bilayer and 4 bilayers of $(\text{VKV- cyclo/RGD-}N_3)$ and $(\text{VKV-cyclo/VKV-}N_3)$ coatings were imaged. Values of arithmetic averaged roughness (R_a) surface were determined analyzing 5 samples of each condition.

2.6. Stimuli-responsive properties investigation

2.6.1. SEM

Scanning electron microscopy (SEM) was used to investigate the morphology of the resulting multilayer-coated surfaces. Surface micrographs were obtained using a high-resolution field emission SEM with focused ion beam (Auriga Compact, Zeiss, Germany). $(\text{VKV-cyclo/RGD-}N_3)_4$ and $(\text{VKV-cyclo/VKV-}N_3)_4$ coatings, produced at RT, were observed after overnight incubations at different temperatures: 4°C, RT and 37°C. Prior to observation the samples were dried and coated with platinum using a sputter coater (EM ACE 600, Leica, Austria).

2.6.2. WCA

The water contact angle (WCA) of the elastin-coated surfaces was investigated to study the influence of the temperature and the pH on their wettability. The WCA values were measured using a OCA20 system (DataPhysics, Germany). WCA of cleaned glass coverslips, $(\text{VKV-cyclo/RGD-}N_3)_4$ and $(\text{VKV-cyclo/VKV-}N_3)_4$ coatings, obtained at RT, were investigated firstly at RT and then for repeating cycles of temperatures of 37°C and 4°C. This was possible using a liquid temperature control unit (TFC 100, DataPhysics, Germany), which could be coupled with OCA20 system and linked to a temperature-controlled bath system. This system allowed a protective atmosphere to surround the sample working area, maintaining temperature and humidity homogeneously distributed over working area. The cycle temperatures were continuously repeated 10 times to evaluate the reversibility of the temperature responsiveness of elastin-coated surfaces.

The pH responsiveness of the surfaces was also investigated. WCA measurements were made after sample immersion at working pH 7. Then, the elastin-based surfaces were submitted to sequential immersions on different pH solutions, wherein after each 60-minute immersion the samples were withdraw and the WCA measured. Basically, acid and alkaline sodium acetate solutions were prepared at a 150mM concentration; the samples were sequentially and continuously immersed in solutions with pH values of 4, 10, 3, 11, 2 and 12.

2.6.3. Cascade of pH effect after film construction

QCM-D analysis was performed to investigate the influence *in situ* of acidic and alkaline cascades after the film construction. The procedure described for the build-up kinetics construction was repeated. After the film build-up, the elastin multilayers were flushed with acidic or alkaline sodium acetate solutions, where the pH was adjusted using appropriated volumes of NaOH (0.5M) and acetic acid (2%(v/v)). These solutions were injected into the system for 30 minutes, followed by a short injection with a sodium acetate solution at pH 7 to evaluate the reversibility of the process. The influence of the pH on the elastin multilayers was evaluated by varying the pH in a cyclic way in an acidic range (pH 4, pH 3 and pH 2) and, also, in an alkaline range (pH 10, pH 11 and pH 12). The respective frequency and dissipation changes were recorded in real time.

2.7. Cellular *in vitro* studies

Cell studies were performed onto elastin-coated surfaces (surface area around 133 mm^2) using C2C12 myoblast cell line (ATCC, CRL-1772). This cell line is a mouse myoblast cell line which has already been well-characterized on literature [22], presenting some interesting features; these cells can rapidly differentiate into myotubes, expressing different characteristic muscle proteins and being a well-known model to study *in vitro* cell differentiation. Tissue culture polystyrene surfaces (TCPS) were used as positive control and clean and activated glass coverslips as reference control. The cells were cultured at passages 5, 6 and 7 on 150 cm^3 flasks and maintained in culture with DMEM with phenol red supplemented with 10% fetal bovine serum (FBS) and 1% penicillin/streptomycin, until achieving 65/70% confluence. Then, the cells were enzymatically detached from the flasks using TrypleExpress (Life Technologies ™) and seeded on the surfaces at a density of 2.0 x 10^4 cells per sample, by dropping 200 µl of the cell suspension right above the samples. The samples were incubated at 37°C and 5% CO_2. After 3 hours, 1 mL of culture medium was added to each sample. The cells coated on the samples were analyzed at different time points, using the methodologies described below.

2.7.1. Cellular metabolic activity

C2C12 were seeded on 13 mm diameter circular glass coverslips uncoated and coated with modified ELRs and incubated for 1, 2 and 5 days. The respective metabolic activity was evaluated using MTS (3-(4,5-dimethylthiazol-2-yl)-5-(3-carboxymethoxyphenyl)-2-(4-sulfophenyl)-2H-tetrazolium) reagent (Promega), according with the manufacturer's instructions. The cells adhered to the elastin-based coatings were washed with sterile DPBS and incubated with 500 µl of a 4:1 mixture of serum-free DMEM and MTS reagent. The samples were incubated at 37°C and 5% CO_2 for 3 hours and, after this time, the absorbance was read at 490 nm using a microplate reader (Synergy HT, BioTek). The blank values of absorbance for the materials incubated without cells were subtracted to the absorbance values when in presence of the cells.

2.7.2. Cellular proliferation

Cell proliferation assay was performed using a double stranded DNA (dsDNA) quantification kit (Picogreen®, Invitrogen). C2C12 cells seeded above the elastin-coated surfaces and incubated for 1, 2 and 5 days of culture were washed twice with DPBS and transferred into Eppendorf tubes containing 1 mL of ultra-pure water. The samples were left to incubate for 1 h at 37ºC and 5% CO_2 humidified atmosphere and then frozen at -80ºC until analysis. For the DNA quantification, the samples were thawed and sonicated for 20 min. The DNA standards were prepared at concentrations 0 $\mu l.mL^{-1}$, 0.2 $\mu l.mL^{-1}$, 0.5 $\mu l.mL^{-1}$, 1 $\mu l.mL^{-1}$ and 1.5 $\mu l.mL^{-1}$. The reacting reagent, TE buffer and the samples were added in triplicate to a 96-well opaque plate (Falcon). The fluorescence was measured using a microplate reader, with an excitation wavelength of 480 nm and an emission wavelength of 528 nm. For each sample, the DNA concentration was calculated using a standard curve that relates DNA concentration with fluorescence intensity.

2.7.3. Cellular Morphology

At 1, 2 and 5 days of cell culture, C2C12 cells seeded on the elastin-coated and TCPS were washed with DPBS and then fixed with formalin 10% ((v/v) in DPBS) during 30 minutes at 4°C. The fixed samples were then stained with rhodamine phalloidin (1:200 in DPBS) for cellular F-actin, and DAPI (1:1000 in DPBS) for cell nuclei. A transmitted and reflected light microscope with apotome 2 (Axio Imager Z1m, Zeiss, Germany) was used to image the stained cells.

2.7.4. Myogenic Differentiation

To evaluate the potential of the developed coatings to allow myogenic differentiation, C2C12 cells were seeded at 1.5 x 10^4 cells per sample on the ELR-coated and uncoated glass coverslips, following the same procedure described before. The cells were maintained at 37°C and 5% CO_2 in DMEM culture medium. When 90% of confluence was achieved, the culture medium was exchanged by differentiation medium, composed of DMEM supplemented with 2% of horse serum and 1% of antibiotics/antimicotics, to induce cell differentiation. After one week, the cells were stained by an immunocytochemistry protocol to identify troponin T-positive cells. After fixing the cells with formalin 10% (v/v), the samples were washed and permeabilized with 1% Triton x100 ((v/v) in DPBS) and blocked with 0.1% of BSA. After washing with DPBS, the samples were incubated overnight at 4 °C with the mouse troponin T antibody (1:100 in DPBS) and after this time the samples were washed and incubated with the secondary antibody anti-mouse Alexa Fluor 488 (1:800 in DPBS) during 1 hour at RT. Then the cells were incubated with DAPI (1:1000 in DPBS) to counterstain the nuclei. The samples were then extensively washed with DPBS to remove the excess of fluorescence probes. A transmitted and reflected light microscope with apotome 2 was used to image the stained cells.

2.7.5. Morphometric parameters

Different morphometric parameters can be determined from the immunofluorescence images; fusion index and average number of troponin T-positive myotubes per area were determined using ImageJ (National Institute of Health, USA) tools. A cell containing 3 or more nuclei was considered a myotube. The fusion index was calculated, as the ratio of the nuclei number within the troponin T-positive myotubes versus the total number of nuclei in the same area. Also, the average of myotubes area, perimeter, length and elongation factor were determined using ImageJ tools. The elongation factor describes to what extent the equimomental ellipse is lengthened or stretched out [23].

2.8. Statistical analysis

Unless referred, all quantitative results were obtained in triplicated and considered as mean ± standard deviation (SD). Statistical analysis was done with the help of GraphPad 6.0 software, using the one –way analysis of variance (ANOVA) with Bonferroni post-test multiple comparison; differences were considered statistically significant with a p value less than 0.05, 0.01 and 0.001.

3. Results and Discussion

3.1. Size distribution and zeta potential measurements

ELRs have been explored for biomedical applications [24] due, not only to the ability of tailoring amino acid contents, mechanical stiffness and degradation ratio, but also its thermoresponsive properties. The proposed ELRs were obtained using genetic engineering in *E. choli*; whose bioproduction, purification and modification are well established [25]; the proton nuclear magnetic resonance (NMR), the Fourier transform infrared spectroscopy (FTIR) and the differential scanning calorimetry (DSC) spectra were collected for each modified ELR (VKV-cyclo, RGD-N_3 and VKV-N_3) [20]. For the present investigation, DCS results had particular interest since these materials could present different behaviors below and above LCST This important parameter was already investigated for these modified ELRs, using water as solvent [20]. The cyclooctyne modified VKV (VKV-cyclo) presented LCST around 15°C; the azide modified RGD (RGD-N3) and VKV (VKV-N3) showed LCST around 21°C and 24°C, respectively [20]. Besides we used a water-based solvent, DMEM is composed of salts, which can slightly change the LCST values. Nonetheless we used these values as reference. Size and zeta potential measurements were carried out to perceive if some changes in ELR aggregates size or net charge happen with temperature or pH variation.

Size measurements of the structures in solution were carried out for each ELR – see Figure IV-1A. These measurements were made at 4°C, which is far below the reported LCST, RT, which is close to LCST, and 37°C, which is far above LCST. At 4°C, moderate polydispersity was found for VKV-cyclo (Pdi=0.5±0.05), RGD-N_3 (Pdi=0.5±0.06) and VKV-N_3 (Pdi=0.6±0.15). The size distribution of VKV-cyclo was about 128 ± 59.6 nm; similar size distributions were obtained for RGD-N_3 and VKV-N_3 (150 ± 80.1

nm and 208 ± 15.9 nm, respectively). At RT, ELRs polydispersion slightly increased (Pdi=0.6±0.18 for VKV-cyclo). The single size distribution of the different ELRs also increased; the single size distribution for VKV-cyclo was about 320±125.6 nm while for azide-modified ELRs was about 425±82.8 nm for RGD-N_3 and 258±45.4 nm for VKV-N_3. At 37°C, we observed a significant increase on the size distribution of the different ELRs, with heterogeneous diameters found (Pdi=0.5±0.04 for VKV-cyclo). VKV-cyclo presents a single size distribution of 938±61.8 nm and a little bit lower values were obtained for azide-modified ELRs (671±144.4 nm for RGD-N_3 and 610±40.6 nm for VKV-N_3). The obtained results are consistent with the solubility in water-based solvents of the ELRs below LCST and their precipitation above the LCST. As described above, modified ELRs have a LCST close to RT. We believe that at RT occurs the transition phenomenon and the polymers start to collapse. Even so, and as we were working in the transition temperature range, the phase separation was not clearly visible yet and there was no significant differences on the size distribution results when compared with the ones obtained at 4°C. Below LCST, at 4 °C, the ELRs solutions are hydrated and dispersed in the solvent, mainly in a linear form, while above LCST (37 °C) the polymer solutions started to precipitate in a folded globular organization with higher diameters [20, 26].

To perceive the best pH to construct the clickable elastin-based coatings, the ζ-potentials of the different ELRs in solution were determined for different pH values, at RT - see Figure IV-1B. For RGD-N_3 and VKV-N_3 solutions, the decrease of pH implied the protonation of the solution. Besides the nature of ELRs being essentially hydrophobic, the proposed ELRs were designed to contain lysine residues, which have positively charged amine groups [16a, 27]. At pH below 7.0, the RGD-N_3 solution presented a ζ-potential of 3.1±0.23 mV, being protonated and, naturally, positively charged. At higher pH values, the amine groups started to deprotonate, and the ζ-potential decreased to -2.0±0.15 mv. When pH was equal to 7.0, RGD-N_3 solution charge was closer to 0 (ζ-potential= 0.7±0.13 mv). The ζ-potential of VKV-N_3 solutions presented similar behavior to RGD-N_3 solutions, at the different pH. Although the solutions were differently charged at pH 6.5 and 7.5, the differences between the respective ζ-potentials were not significant. Overall, at pH 7.0 the ζ-potentials of the different azide solutions were closer to 0 and we hypothesize that the different ELRs were almost discharged. For this reason, we decided to construct the coatings at pH 7.0 to minimize the effect of electrostatic interactions on the construction of the LbL-based coatings.

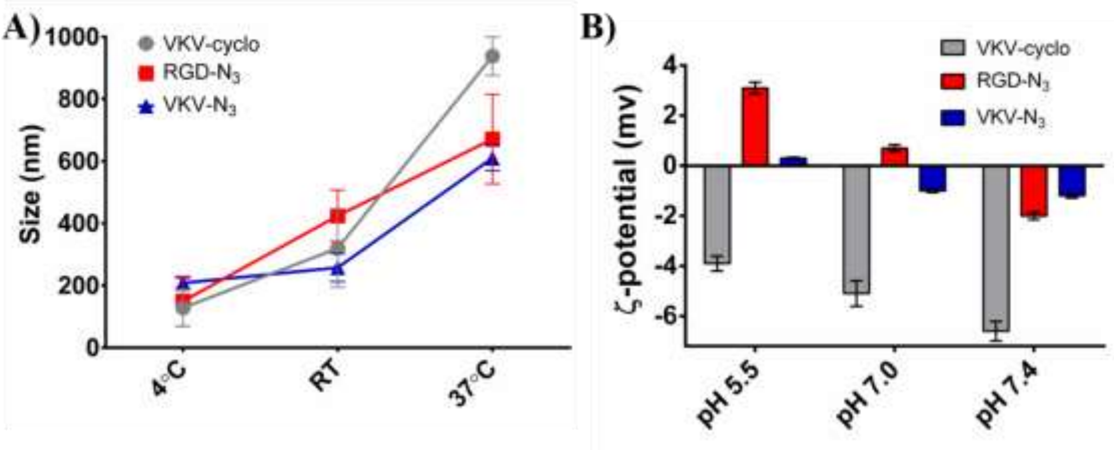

Figure IV-1. Effect of temperature on A) zeta sizer and B) zeta potential of VKV-cyclo, RGD-N_3 and VKV-N_3 solutions (0.05%(w/v)).

3.2. Build-up kinetics construction

After optimizing the working pH and temperature, the build-up of the elastin-based multilayers was assessed using QCM-D monitoring. Figure IV-2A and IV-2B represents the frequency (Δf_n) and dissipation (ΔD_n) variations at third overtone (n=3) above a gold crystal, when flushed by the different ELRs solutions. These variations were monitored accordingly to the time of depositions. Two constructions were evaluated: the one containing the VKV-cyclo and the RGD-N_3 (see Figure IV-2A) and the other one containing the VKV-cyclo and the VKV-N_3 (see Figure IV-2B). The first six minutes correspond to the establishment of the baseline. In both graphs, the next 20 minutes show the deposition of the VKV-cyclo and the subsequent washing until removing the excess of polymer, which was not adsorbed at the surface. The following 20 minutes correspond to the RGD-N_3 or the VKV-N_3 adsorptions. For both cases, Δf_3 decreased with time; this observation can be related with the time of deposition/adsorption of the polymers above the surface of the gold crystal. On the other hand, ΔD_3 increased with time indicating that elastin-based films did not present a rigid behavior and started to dissipate energy. In fact, this non-rigid/viscoelastic behavior is common for macromolecular systems [28]. The subsequent steps show the same trend: the ELRs deposition was strong for the first layers but it decreased for the next ones. Within the multilayer's construction, Δf_3 resultant of washing steps became smaller, showing that ELRs were strongly linked and formed a stable coating for the LbL build-up. As already referred above, at pH 7.0 both azide ELRs showed close to neutral zeta potential, and we hypothesize that there is no surface charge overcompensation by the formation of polycation–polyanion pairs. Therefore, we can consider the covalent bonding resulting from the click reaction (azide-alkyne cycloaddition) as the main force involved in the LbL construction. Four bilayers were constructed, with good indications of the effectiveness of the click chemistry reaction. A chemical scheme of this reaction is presented in Figure IV-2C, where alkyne group links to azide group by means of a cycloaddition reaction, being the basis of the ELR-based film build-up. The first layer of VKV-cyclo was adsorbed to the substrates, allowing the further construction of the remaining layers through covalent linkage between cyclooctyne and azide groups, under mild aqueous conditions. Caruso's research group [29] used cycloaddition chemistry to build-up LbL multilayer systems by dipping different inert substrates into poly(acrylic acid) copolymerized with azide or alkyne groups. They further took advantage of this technology to fabricate pH responsive capsules that can serve as a versatile platform for further functionalization [13]. Other advantages were reported using such technology: producing high stable films, with no need of post cross-linking processes and with the possibility of incorporation of a wide range of functionalized materials [11b, 30].

Other information could be attained from the QCM-D data. The estimated thickness of the elastin-based coatings was calculated based on the Voigt Model, using an appropriated software. The estimated thickness after each deposition was plotted over the number of layers. For both constructions (VKV-cyclo/RDG-N_3)$_n$ and (VKV-cyclo/VKV-N_3)$_n$ (where *n* represents the number of bilayers), the film growth showed a non-linear behavior - see Figure IV-2D and IV-2E, respectively. We used a non-linear regression to generate a mathematical model which fits both (VKV-cyclo/RDG- N_3)$_n$ and (VKV-cyclo/VKV- N_3)$_n$ thickness growth. After 4 bilayers, the (VKV-cyclo/RDG-N_3)$_4$ has an estimated thickness of 598±8.5 nm, while the [VKV-cyclo/VKV- N_3]$_4$ presented an estimated thickness of 586±91.2 nm. Taken a hyperbolic model as base, we hypothesize that after reaching the double of bilayers (16 layers), (VKV-cyclo/RDG- N_3)$_4$ will present an estimated thickness around 739 nm while (VKV-cyclo/VKV- N_3)$_4$ will exhibit an estimated thickness of approximately 636 nm. Interestingly, after 16 bilayers we will observe a decrease of the rate of the thickness growth. Therefore, we assume that after a certain number of layers the film growth achieved a plateau. Comparing the proposed modified ELR-based films with other ELR-based systems already reported in literature based on electrostatic interactions [16a], we believe that covalent interactions allow the deposition of higher amounts of polymer and, thus, the construction of thicker films with less number of bilayers. Moreover, comparing our clickable based multilayer system with other covalent-driven systems [13, 31] we are able to produce thicker films, which means that we can control more precisely the final thickness of the system.

3.3. Elastin-based films production and characterization

The same procedure as the one described for QCM-D build-up was implemented over cleaned and activated glass coverslips, at RT. The solutions were maintained at 4°C, until use, as well as during the incubation steps, to avoid the collapse process of ELRs in solution

The fluorescence images of the 4 bilayers coatings are presented in Figure IV-3A. Following the intensity of the fluorescence of Acetylene Fluor 488 (absorption at 501 nm and emission at 525 nm), it could be observed quite uniform distribution of the intensity on (VKV-cyclo/RGD-N_3)$_4$ films, in red, and (VKV-cyclo/VKV-N_3)$_4$ films, in blue. The surfaces of the glass coverslips were visibly covered by a thin film. This observation was shared for both (VKV-cyclo/RDG-N_3)$_4$ and (VKV-cyclo/VKV-N_3)$_4$ coatings. This result is in accordance with the observations retained from QCM-D monitoring, where 4 bilayer systems were constructed with success.

Additionally, the topography of 1 bilayer and 4 bilayers of (VKV-cyclo/RDG-N_3) and (VKV-cyclo/VKV-N_3) systems processed and maintained at RT were evaluated under AFM observation- see Figure IV-3B.

As we worked at a temperature close to LCST nano-sized polymer agglomerates can be clearly observed on the surface of the coatings, resulting from the collapse of adjacent ELRs chains. For both 1 bilayer systems, a high density of irregularities was perceived and the films presented higher values of roughness (R_a=22±5.0 nm for (VKV-cyclo/RDG-N_3) and R_a=22±9.8 nm for (VKV-cyclo/VKV-N_3)) when compared with other related reported systems [29, 32]. No significant differences were detected between the roughness of (VKV-cyclo/RDG-N_3)$_4$ and (VKV-cyclo/VKV-N_3)$_4$ films. Moreover, the roughness significantly increased with the increasing number of bilayers with R_a=72±55.5 nm for (VKV-cyclo/RDG-N_3)$_4$, which could be a result of an increasing of mass adsorbed on the surface of the glass coverslips. This observation was already reported in literature for other LbL systems [33]. Nonetheless, this increase of roughness was smaller for (VKV-cyclo/VKV-N_3)$_4$, with R_a=25.4±14.0 nm. QCM-D results are in accordance with AFM observation since rough surfaces induce larger hydrodynamic thicknesses [33a], as the ones estimated based on the Voigt Model.

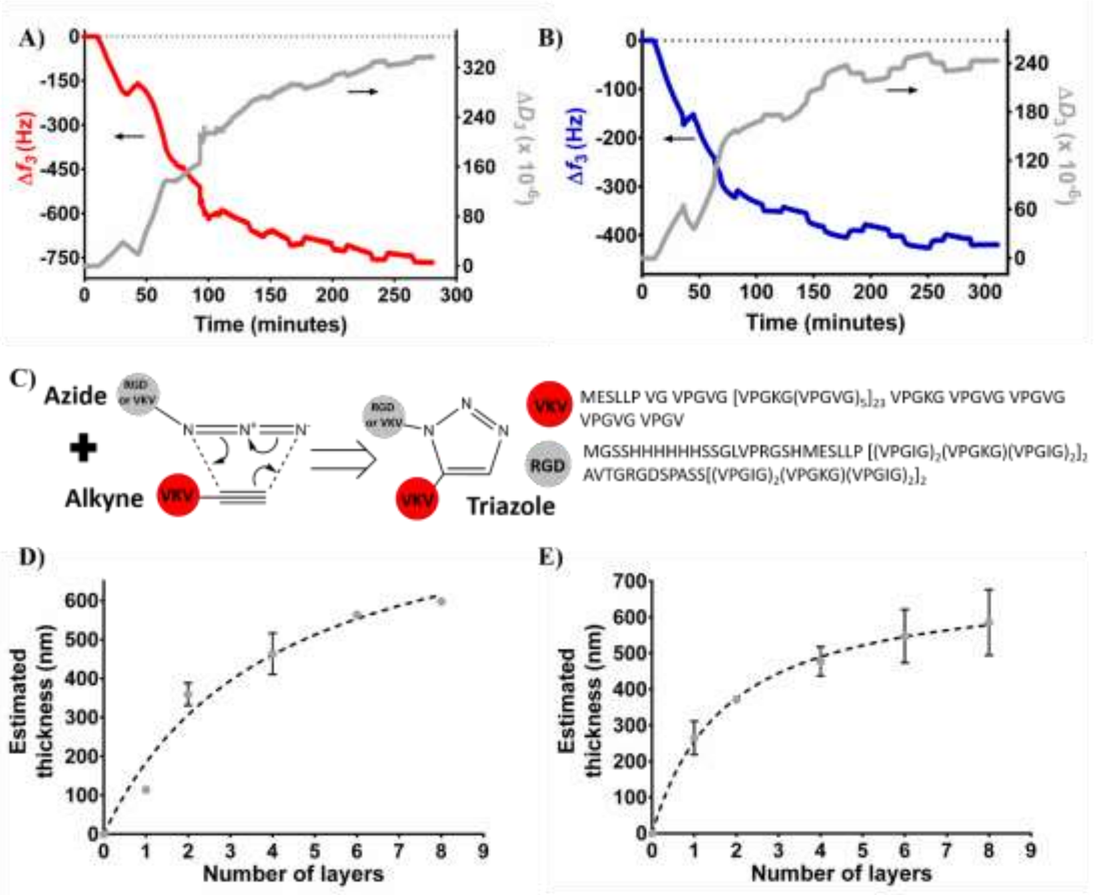

Figure IV-2. Build-up assessment of ELR-based films. QCM-D monitoring of normalized frequency (Δf_n) and dissipation (ΔD_n) obtained at the third overtone, to assess the build-up of A) (VKV-cyclo /RGD-N_3)$_4$ and B) (VKV-cyclo/VKV-N_3)$_4$ films. C) Chemical scheme representing the click chemistry reaction, that results from the Huisgen 1,3-dipolar cycloaddition of azides and alkynes. Cumulative thickness evolution and thickness increase for 4 bilayers, estimated using the Voigt model for D) (VKV-cyclo/RGD-N_3)$_4$ film and E) (VKV-cyclo/VKV-N_3)$_4$ films. The cumulative thicknesses follow non-linear growth model.

3.4. Stimuli-responsiveness properties

We investigated the ability of the (VKV-cyclo/RDG-N_3)$_4$ and (VKV-cyclo/VKV-N_3)$_4$ coatings to respond to changes in the medium such as pH and temperature, which are parameters that influence the adsorption of proteins at solid/liquid interface [34], among other physicochemical processes. This ability has been gaining importance and different works have been reported towards tissue engineering [35], sensors [36] and drug release systems [37].

After drying, (VKV-cyclo/RDG-N_3)$_4$ and (VKV-cyclo/VKV-N_3)$_4$ surfaces were maintained at RT. SEM images were used to evaluate the morphology of the coatings- see Figure IV-4. At RT, both coatings seem to be well distributed over the glass coverslips, even though with some small precipitated polymer. This result was already expected since we constructed and maintained the coatings at a temperature close to LCST. Other conditions were evaluated to study the response to temperature. For that, after constructing the films, at RT, onto glass coverslips the drying process was made at different temperatures: 4°C, RT and 37°C. Some morphological differences are noticed on SEM images; with the significant increase of the temperature above LCST (37°C) the morphology of (VKV-cyclo/RDG-N_3)$_4$ and (VKV-cyclo/VKV-N_3)$_4$ films seem less homogeneous with small aggregated polymer precipitates adhered all over the glass surfaces and even some salt precipitation. Working at 4°C, below LCST, the morphology of the coatings seems to be uniformly distributed on the surfaces, with less rough topography. These morphological changes are related with the thermosensitive behavior of these polymers, which are dependent of their LCST [4b, 38], even after the film construction.

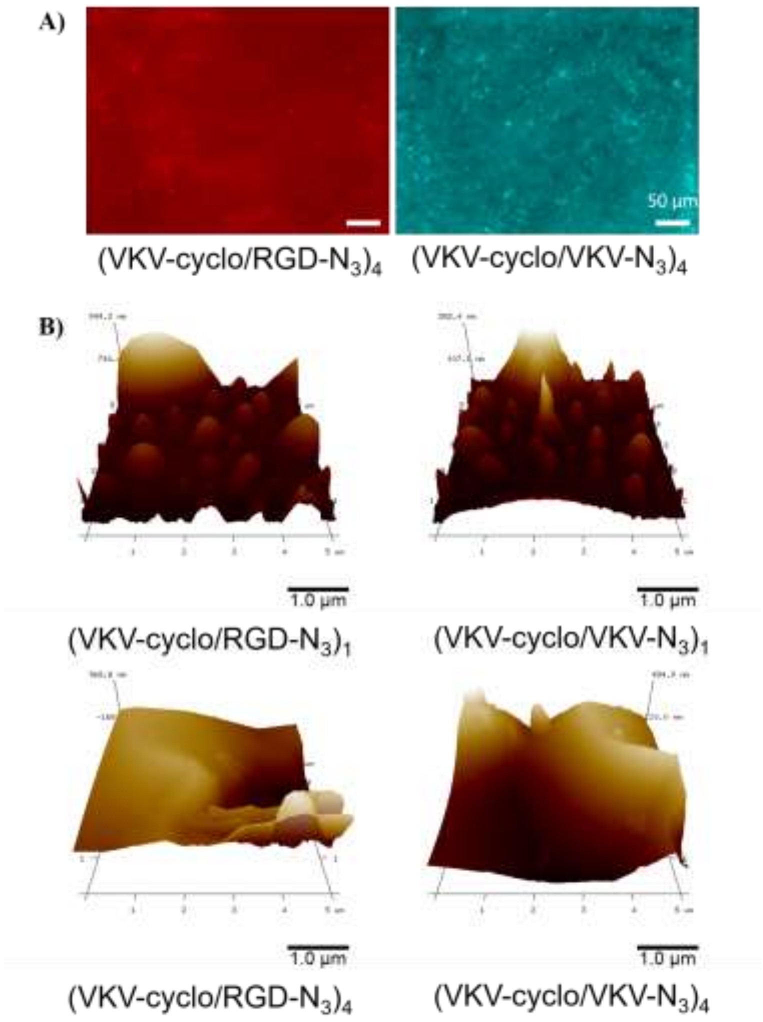

Figure IV-3. A) Fluorescence images of (VKV-N_3/RGD-cyclo)$_4$ and (VKV-N_3/VKV-cyclo)$_4$ coatings (azide-modified ELRS were labelled with Acetylene Fluor 488, before LbL construction). The coatings were produced and dried at RT. The scale bar is representative for both images. B) AFM images of (VKV-N_3/RGD-cyclo)$_1$ and (VKV-N_3/VKV-cyclo)$_1$ and (VKV-N_3/RGD-cyclo)$_4$ and (VKV-N_3/VKV-cyclo)$_4$ coatings.

WCA measurements assess the effect of temperature and pH on the wettability of the (VKV-cyclo/RDG-N_3)$_4$ and (VKV-cyclo/VKV-N_3)$_4$ coatings. To investigate the temperature effect, the WCA measurements were made under controlled temperature and humidity - see Figure IV-5A. At RT, (VKV-cyclo/RDG-N_3)$_4$ and (VKV-cyclo/VKV-N_3)$_4$ coatings presented WCA values of 94±8.1° and 84±7.3°, respectively. These values are closed to the threshold of hydrophobicity (WCA>90°). Therefore, we assumed that at RT the coatings have a moderate hydrophobic nature. The WCA of the uncoated glass slides is 59±1.6°. The effectiveness of the coatings was also confirmed by the differences in the WCA, comparing the pre- and the post-coating values. By varying the temperature from 37°C to 4°C in repeating cycles, we observed switchable values of WCA. Higher values of WCA were observed when the samples were incubated at 37°C (above the LCST); on the contrary, at temperature below LCST (4°C) the WCA values were consistently lower. For instance, in the last cycle, the WCA at 37°C was 110±11.5° for (VKV-cyclo/RDG-N_3) films and 110±12.5° for (VKV-cyclo/VKV-N_3)$_4$. On the other hand, for the last cycle at 4°C the WCA value was about 59±14.1° for (VKV-cyclo/RDG-N_3)$_4$ films and 69±6.7° for (VKV-cyclo/VKV-N_3)$_4$. The images acquired for the calculation of WCA during these temperature cycles are also depicted – see Figure IV-5B. These observations can be a result of temperature and individual properties of the modified ELRs. The three ELRs employed in the film's construction showed similar physicochemical characteristics; the competition between intra and intermolecular hydrogen bonding above and below the LCST confers a thermosensitive nature to each individual ELR. When temperature was above LCST, the conformation of the ELRs chains started to collapse excluding water and adopting a type-II β-turns stabilized by intramolecular electrostatics forces between different groups within the polymer chains. Two consequences could derive from this phenomenon: the interaction between hydrophilic carboxyl and amine groups and water molecules became more difficult and rounded polymer nano-precipitates were observed all over the surface. The presence of the nano-precipitates impelled the increase of the roughness of the coatings. Based on Cassie and Baxter model [39], which describes the entrapment of air-pockets between the grooves and the liquid droplet, we could extrapolate what happens to WCA with the presence of rougher surfaces. With the polymer collapse process, ELRs chains fold and the coatings became rougher; when a droplet is dispensed in a rough surface, the volume of water infiltrated in the nanostructure decrease and the volume of water on the surface increase; this phenomenon resulted in the increase of WCA values. While working at temperatures below LCST, the hydrophilic groups could easily interact with the water molecules, forming water clathrates surrounding the backbone of the ELR. Besides that, as already observed, at 4°C the surfaces became smoother, with the absence of collapse structures on their surface morphology. The combination of these two effects results on more hydrophilic films. Moreover, playing with temperature below and above LCST could also promote the reconfiguration of the hydrophobic domains: above LCST the hydrophobic chains could be exposed to the outside of the films, decreasing the surface affinity to water. The results exposed a strong dependency on temperature indicating the ability to produce smart coatings with switchable wettability using these recombinant materials [3b]. Both (VKV-cyclo /RDG-N_3)$_4$ and (VKV-cyclo/VKV-N_3)$_4$ coatings presented an apparent WCA switchability upon temperature fluctuations. ELRs are well-known as protein-based polymers which present a phase transition in solution above a critical temperature [40]. Responsive polyelectrolyte coatings including ELRs were reported before [4b]. However, contrasting with these results, we obtained elastin-based coatings that present a hydrophobic behavior above LCST and a hydrophilic behavior below LCST. Our thermo-responsive system can be interesting for tissue engineering field where, for example, modified surfaces with PNIPAAm have been broadly reported [35, 41] to produce cell sheets based on similar hydrophilic-to-hydrophobic reversible effect of temperature on wettability.

To investigate the effect of the pH, ELRs-coated surfaces were immersed in sodium acetate solutions at different extreme acidic and alkaline pH values, fixing temperature the temperature at RT. WCA measurements – see Figure IV-5C - were performed after incubations of at least 1 hour and a small step for drying of 30 seconds. The representative images of the WCA for the different conditions is shown in Figure IV-5D. At pH 7, (VKV-cyclo/RDG-N_3)$_4$ presented a WCA value of 94±8.1° and (VKV-cyclo/VKV-N_3)$_4$ coatings presented a WCA of 84±7.3°. Some deviations from the initial WCA were obtained; for (VKV-cyclo/RDG-N_3)$_4$ and (VKV-cyclo/VKV-N_3)$_4$ films, both acidic and alkaline pathways meant a more hydrophilic behavior. This could be understood by the isoelectric point; as already suggested by the ζ-potential measurements; close to pH 7, the electrostatic charges were almost neutralized. For (VKV-cyclo/RGD-N_3)$_4$ coatings on acidic or alkaline environments no significant differences were found in the WCA presented at acidic or alkaline routes, but a slightly increase on hydrophilicity was detected at acidic pH. Indeed, at pH 2, (VKV-cyclo/RDG-N_3)$_4$ films exhibited a significantly more hydrophilic behavior. At extreme acidic pH, amine groups were protonated, and positive electrostatic forces came to be dominant: the ELRs chains expanded and the films became more hydrophilic. Despite that, for (VKV-cyclo/VKV-N_3)$_4$ coatings on acidic or alkaline environments, slightly higher WCA values were obtained at acidic pH values. This could be related to the balance between charged amine and acids being different from (VKV-cyclo/RDG-N_3)$_4$ films; probably, for (VKV-cyclo/VKV-N_3)$_4$ there was a higher content of charged acid groups at lower pH.

Overall, results can be explained by the balance between hydrophobic interactions and charged repulsion [42], and the respective competition between protonation and deprotonation at alkaline and acidic pH value. When environment conditions like pH change, the ELR-based films, which contain ionizable amine and acid groups, are capable of accepting or donating protons. Therefore, altering the pH can lead to changes on the degree of ionization and, subsequently, on the hydrodynamic volume of the ELRs chains [43]. In literature, different wettable behaviors of ELRs-modified surfaces can be found [4b, 16a, 44]. This variability is linked with the ability to introduce different genetically modified sequences, charges and molecular weight, that can alter the folding behavior at the surfaces [45].

To a better understanding of the pH effect on the stability of the systems immediately after the films construction, we also performed QCM-D monitoring studies. After the construction of both (VKV-cyclo/RDG-N_3)$_4$ and (VKV-cyclo/VKV-N_3)$_4$ systems, the resulting multilayers were flushed with a cyclic cascade of acidic and alkaline sodium acetate solutions, separately. QCM-D results show the build-up of four bilayers and their response to changes in pH in terms of Δf and ΔD - see Figure IV-6. For all cases, we took as reference the initial working pH 7. QCM-D data showing (VKV-cyclo/RDG-N_3)$_4$ and (VKV-cyclo/VKV-N_3)$_4$ multilayers flushed with cyclic alkaline cascade of solutions is presented in Figure IV-6A and IV-6B, respectively. For both cases, a decrease of Δf_3 upon flushing the film with a solution at pH 10 was observed; the decrease in Δf_3 was reversible when the pH returned to 7. Naturally, ΔD_3 increased and Δf_3 decreased when the coating was flushed with the alkaline solutions. When (VKV-cyclo/RGD-N_3)$_4$ multilayers were flushed with pH 11 and pH 12, Δf_3 decreased with partially reversibility when pH returned to 7. On the other hand, when (VKV-cyclo/VKV-N_3)$_4$ multilayers were flushed with the solution with pH 11 and pH 12, the Δf_3 abruptly decreased with no reversibility. The same happened to ΔD_3, which showed a great increase. Therefore, at the pH 11 and 12, the changes in Δf_3 and ΔD_3 seemed to be irreversible and could indicate that (VKV-cyclo/VKV-N_3)$_4$ multilayers started to loose structural integrity [46].

Figure IV-6C shows the QCM-D data of the (VKV-cyclo/RDG-N_3)$_4$ multilayers when flushed with a cyclic acidic cascade of solutions. It can be observed an abrupt decrease of Δf_3 when the film is flushed with solutions at pH 4; the decrease in Δf_3 was irreversible when the pH returned to 7. At pH 3 and pH 2, there was no changes on Δf_3. Figure IV-6D presents the QCM-D results for (VKV-cyclo/VKV-N_3)$_4$ multilayers when flushed with an acidic cascade of solutions. For solutions with pHs 4 and 3, the behavior of the film was similar to the one obtained for (VKV-cyclo/RDG-N_3)$_4$ multilayers at pH 4. Notwithstanding, when (VKV-cyclo/VKV-N_3)$_4$ films were flushed with the solution at pH 2, the decrease on the Δf_3 was very abrupt and higher than the others. The same happens with ΔD_3, which exhibited a sudden increase. At this extreme acidic pH, the changes in Δf_3 and ΔD_3 seemed to be irreversible and could indicate some loss of multilayer's structural integrity. The stability and integrity of these smart coatings seemed to be maintained in a wide-range of pH values, being (VKV-cyclo/VKV-N_3)$_4$ films more susceptible at extreme pH (2 and 12).

Overall, properties like morphology, topography, wettability and degradability of the produced ELR-based films can be modulated through different stimuli, including temperature and pH.

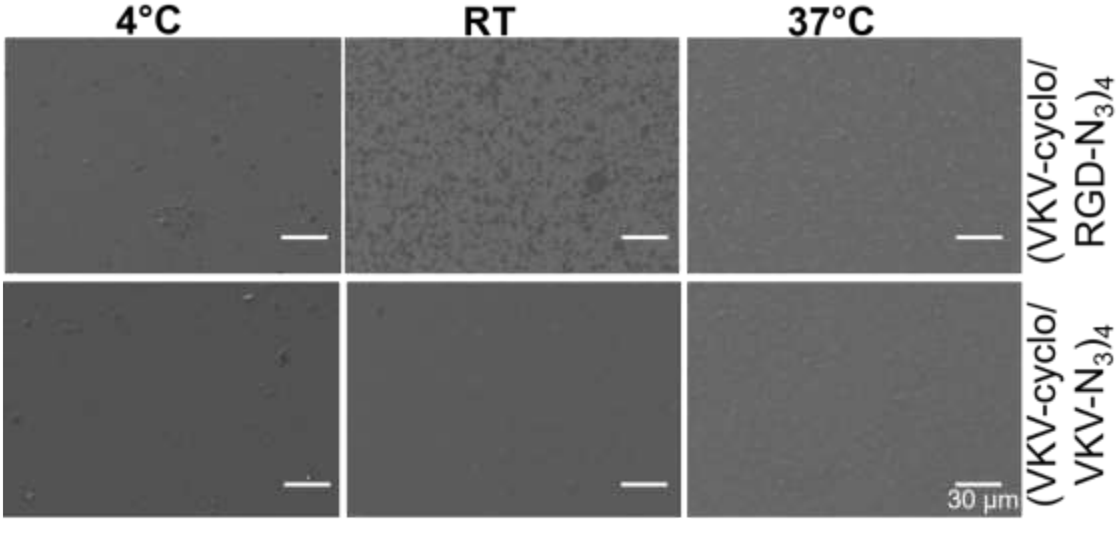

Figure IV-4. SEM images of (VKV-N_3/RGD-cyclo)$_4$ and (VKV-N_3/VKV-cyclo)$_4$, subjected to incubation at different temperatures. The coatings were produced at RT and then stored at 4°C, RT and 37°C, overnight. The scale bar is representative for all images.

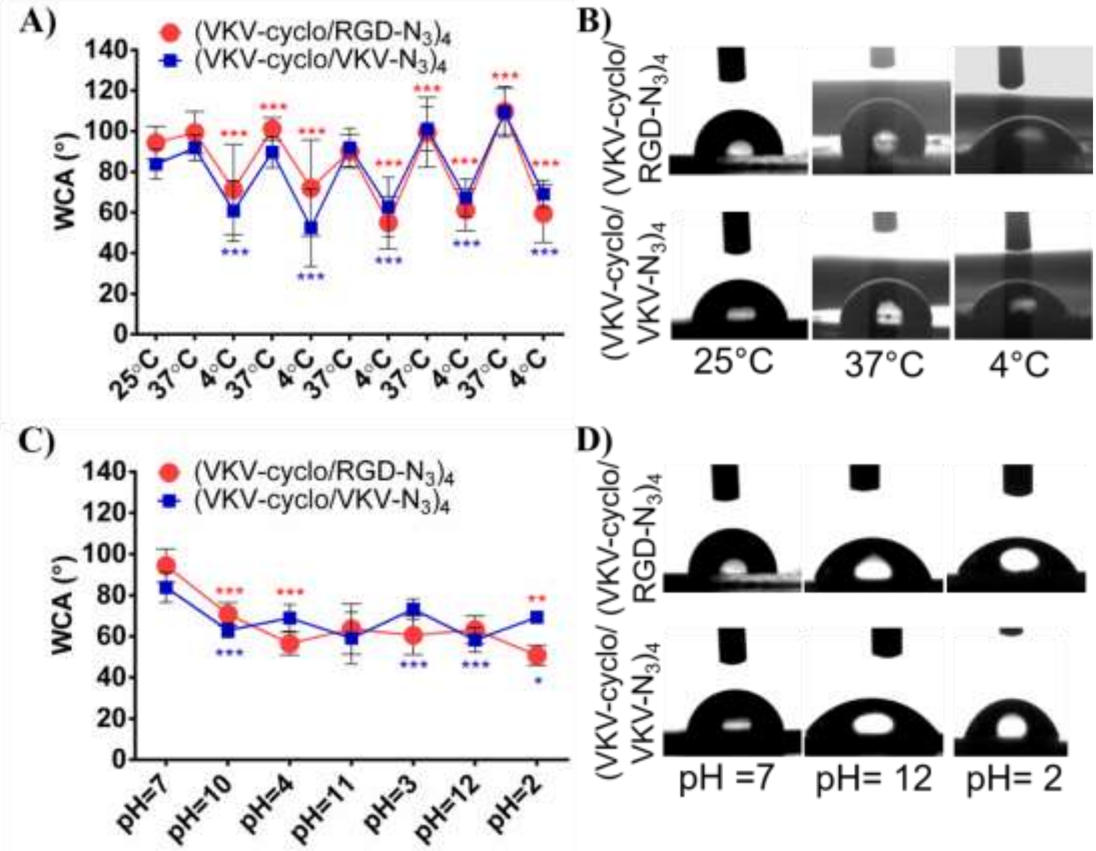

Figure IV-5. A) Temperature dependences of WCA for the different ELR-based films and B) the respective representative pictures for temperature of 25°C, 37°C and 4°C. C) pH dependences of WCA for the different ELR-based films and D) the respective representative photographs for pH=7, 12 and 2. Each WCA shown on A) and C) were statistical significant from the previous one, for $p < 0.05$ (*), $p < 0.01$ (**) and $p < 0.001$.

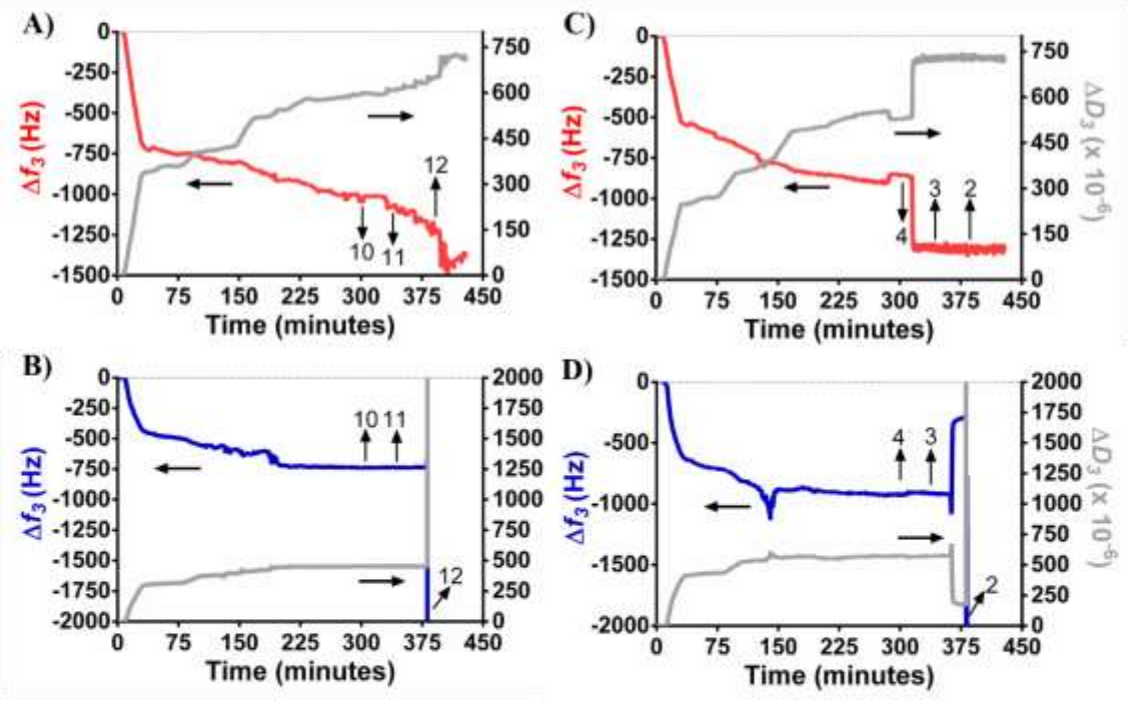

Figure IV-6. Build-up assessment of the effect of a cascade of pHs on ELR-based films. QCM-D monitoring of normalized frequency (Δf_n) and dissipation (ΔD_n) obtained at the third overtone of A) (VKV-cyclo /RGD-N$_3$)$_4$ film flushed with alkaline pH, B) (VKV-cyclo/VKV-N$_3$)$_4$ film flushed with alkaline pHs, C) (VKV-cyclo /RGD-N$_3$)$_4$ film flushed with acidic pHs and D) (VKV-cyclo/VKV-N$_3$)$_4$ film flushed with acidic pH.

3.5. *In vitro* cellular response

ELR-coated films were cultured with C2C12 cells, in order to evaluate their biomedical and tissue engineering potential. Adhesion, viability and proliferation are important parameters that depend on the interaction between material and cells [47]; MTS assay was used to determine the metabolic activity of C2C12 adhered on the samples - see Figure IV-7A. After 2 days of culture some differences started to be noticed, with C2C12 cultured on (VKV-cyclo/RDG-N_3)$_4$ films presenting significantly higher values of absorbance and, thus, higher metabolic activity. This trend was maintained and even amplified after 5 days of culture. The total amount of dsDNA on the samples was also investigated- see Figure IV-7B. In the first day of culture significant differences were found between the (VKV-cyclo/RDG-N_3)$_4$ and (VKV-cyclo/VKV-N_3)$_4$ coatings, with significant higher C2C12 density above the surfaces coated with (VKV-cyclo/RDG-N_3)$_4$ films. This result was also observed after 2 and 5 days of culture, being in accordance with the results obtained for metabolic activity. As expected, the presence of the RGD motif seemed to influence positively the cellular performance, including adhesion and proliferation, on the ELRs-coated film [16a, 19b, 48]. For instance, Picart, C. *et al.* [48] previously suggested the functionalization of polyelectrolyte multilayer films with RGD motifs in order to enhance primary human osteoblasts adhesion. We also investigated the morphology of C2C12, analyzing the F-actin expression of cells adhered to the (VKV-cyclo/RGD-N_3)$_4$ and (VKV-cyclo/VKV-N_3)$_4$ coatings (see Figure IV-7C). Some differences were observed on C2C12 morphology and density as a function of culturing time. As observed in Figure IV-7C, cell density on (VKV-cyclo/RGD-N_3)$_4$ films increased with the time of culture; these results match the DNA quantification and MTS results. In the first day of culture, adhered myoblasts already acquired the star-like shape, which is characteristic of C2C12 cells [22]. This phenotype could be observed more clearly on cells adhered to (VKV-cyclo/RGD-N_3)$_4$ surfaces. At 2 days of culture, myoblasts continued to proliferate and, naturally, started to fuse one with each other, creating a kind of cellular network [49]. This phenomenon was observed for both (VKV-cyclo/RGD-N_3)$_4$ and (VKV-cyclo/VKV-N_3)$_4$ surfaces, with cells being better distributed for (VKV-cyclo/RGD-N_3)$_4$ coatings and more clustered in (VKV-cyclo/VKV-N_3)$_4$ surfaces. At 5 days of culture, the cells occupied the entire area, forming an organized cellular monolayer above the (VKV-cyclo/RGD-N_3)$_4$ surface. The cells adhered to (VKV-cyclo/VKV-N_3)$_4$ films had a similar behavior but, as the rate of proliferation was visibly slower, after 5 days of culture cell-free areas could still be found on the (VKV-cyclo/VKV-N_3)$_4$ coatings. TCPS were used as positive control and, in fact, cell morphology on (VKV-cyclo/RGD-N_3)$_4$ coatings was comparable to cell morphology on TCPS surfaces.

C2C12 differentiation was investigated by the expression of the skeletal muscle protein Troponin T. For that, we performed an immunocytochemistry assay after culturing cells above the ELRs-coated surfaces during 5 days in differentiation medium- see Figure IV-8A. Some differences were observed between Troponin-T positive cells adhered to (VKV-cyclo /RGD- N_3)$_4$ and (VKV-cyclo/VKV-N_3)$_4$ films. Visually, it is possible to observe more troponin T expression on the cells adhered to (VKV-cyclo/RGD-N_3)$_4$ films, with more multinucleated myotubes than on (VKV-cyclo/VKV-N_3)$_4$ films or even on TCPS. To conclude quantitatively about the myogenic differentiation on the ELR-based films, some parameters were calculated. Significant differences were observed between the fusion index of C2C12 adhered to the different films. The cells seeded on (VKV-cyclo/RGD-N_3)$_4$ films presented higher fusion index percentage than the cells seeded on (VKV-cyclo/VKV-N_3)$_4$ - see Figure IV-8B. Also, the number of myotubes per area was significantly higher for (VKV-cyclo/RGD-N_3)$_4$ films - see Figure IV-8C. These results together could be an evidence that myogenic differentiation of C2C12 cells was stimulated by the presence of RGD motifs on material’s surface. This fact is supported by some examples found in the literature [50], which related the presence of the RGD sequence to the promotion cellular attachment and differentiation. Different morphometric parameters were also calculated from immunofluorescence images to assess the effect of RGD on myotube formation. The average area (Figure IV-8D), perimeter (Figure IV-8E) and length (Figure IV-8F) of myotubes were similar and very dispersed, either adhering on (VKV-cyclo/RGD-N_3)$_4$ or (VKV-cyclo/VKV-N_3)$_4$. No significant differences were found between the myotubes elongation factor of C2C12 adhered to (VKV-cyclo/RGD-N_3)$_4$ or (VKV-cyclo/VKV-N_3)$_4$ – see Figure IV-8G. Myogenic differentiation seemed to be favored by the presence of RGD motif, but the morphology of the formed myotubes was quite similar on (VKV-cyclo/RGD-N_3)$_4$ and (VKV-cyclo/VKV-N_3)$_4$ coatings.

Independently of the surface energy and wettability changes of the coatings when subjected to different temperature and pH, cell seeding was performed and maintained at 37º C; at this temperature, the surfaces of both (VKV-cyclo/RGD-N_3)$_4$ and (VKV-cyclo/cyclo-N_3)$_4$ coatings were moderately hydrophobic. Therefore, we hypothesize that the enhanced cell adhesion, activity and even differentiation above the (VKV-cyclo/RGD-N_3)$_4$ was mainly related with chemistry of the surface by the presence of the bioactive sequence RGD and in this specific case was not related with parameters like surface energy, wettability and charge.

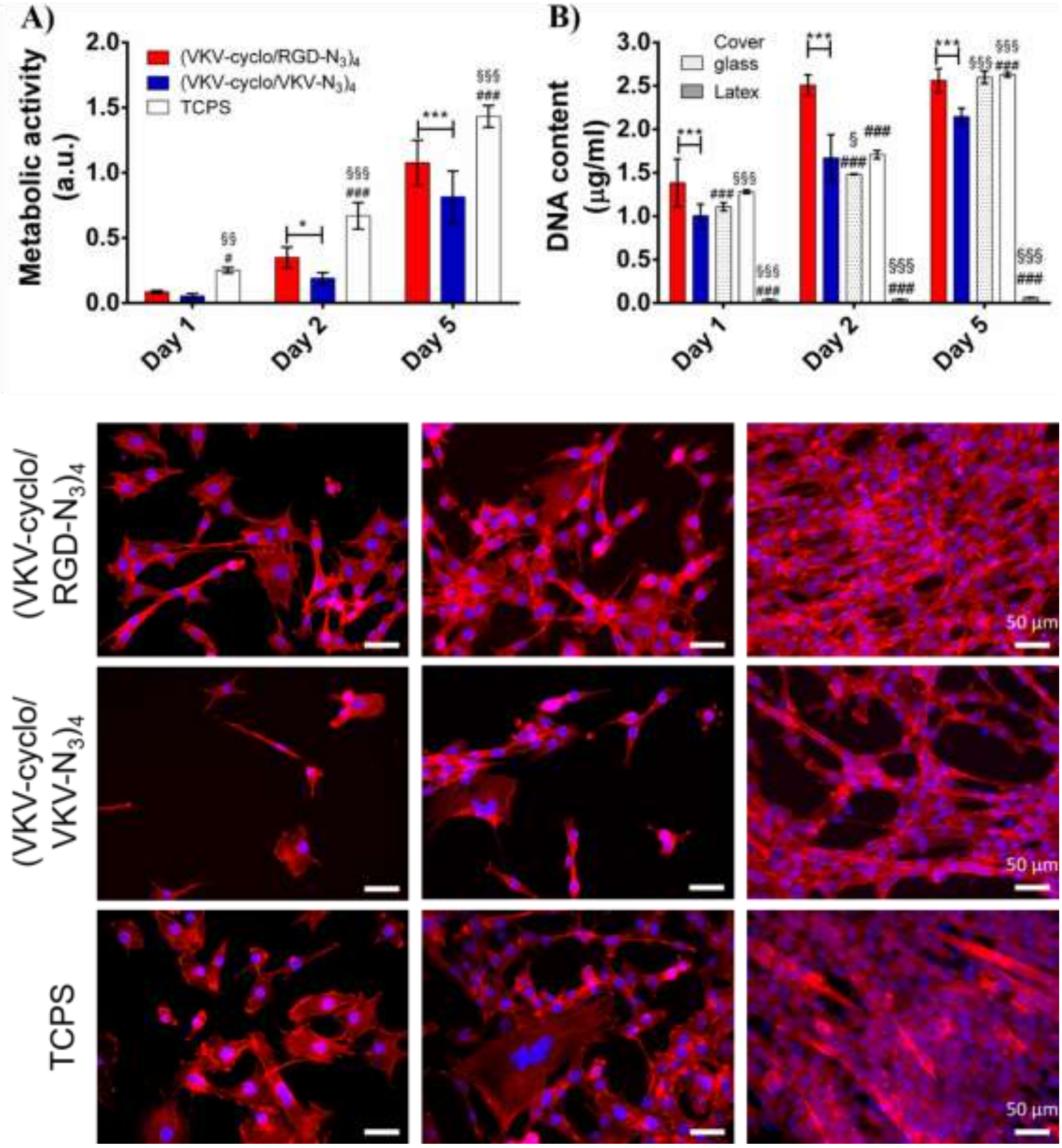

Figure IV-6. A) Metabolic activity results based on MTS test performed after 1, 2 and 5 days of culture with C2C12 cells. B) DNA content obtained from by DNA quantification of C2C12 seeded on ELR-based films and cultured for 5 days. Error bars represent means ± SD (n = 3). Differences on metabolic activity and DNA quantification between (VKV-cyclo/RGD-N$_3$)$_4$ and (VKV-cyclo/VKV-N$_3$)$_4$ were significant for $p < 0.05$ (*) and $p < 0.001$ (***). Statistically significant differences on metabolic activity and DNA quantification between (VKV-cyclo/RGD-N$_3$)$_4$ and TCPS, cover glass and latex were found for $p < 0.05$ (#) and $p < 0.001$ (###). Statistically significant differences on metabolic activity and DNA quantification between (VKV-cyclo/VKV-N$_3$)$_4$ and TCPS, cover glass and latex were found for $p < 0.05$ (§), $p < 0.01$ (§§) and $p < 0.001$ (§§§). C) Phalloidin labelled F-actin (red) and DAPI labelled nucleus (blue) merged fluorescent images for C2C12 cells seeded on (VKV-cyclo/RGD-N$_3$)$_4$ and (VKV-cyclo/VKV-N$_3$)$_4$ coatings and TCPS. The scale bar is representative for all images.

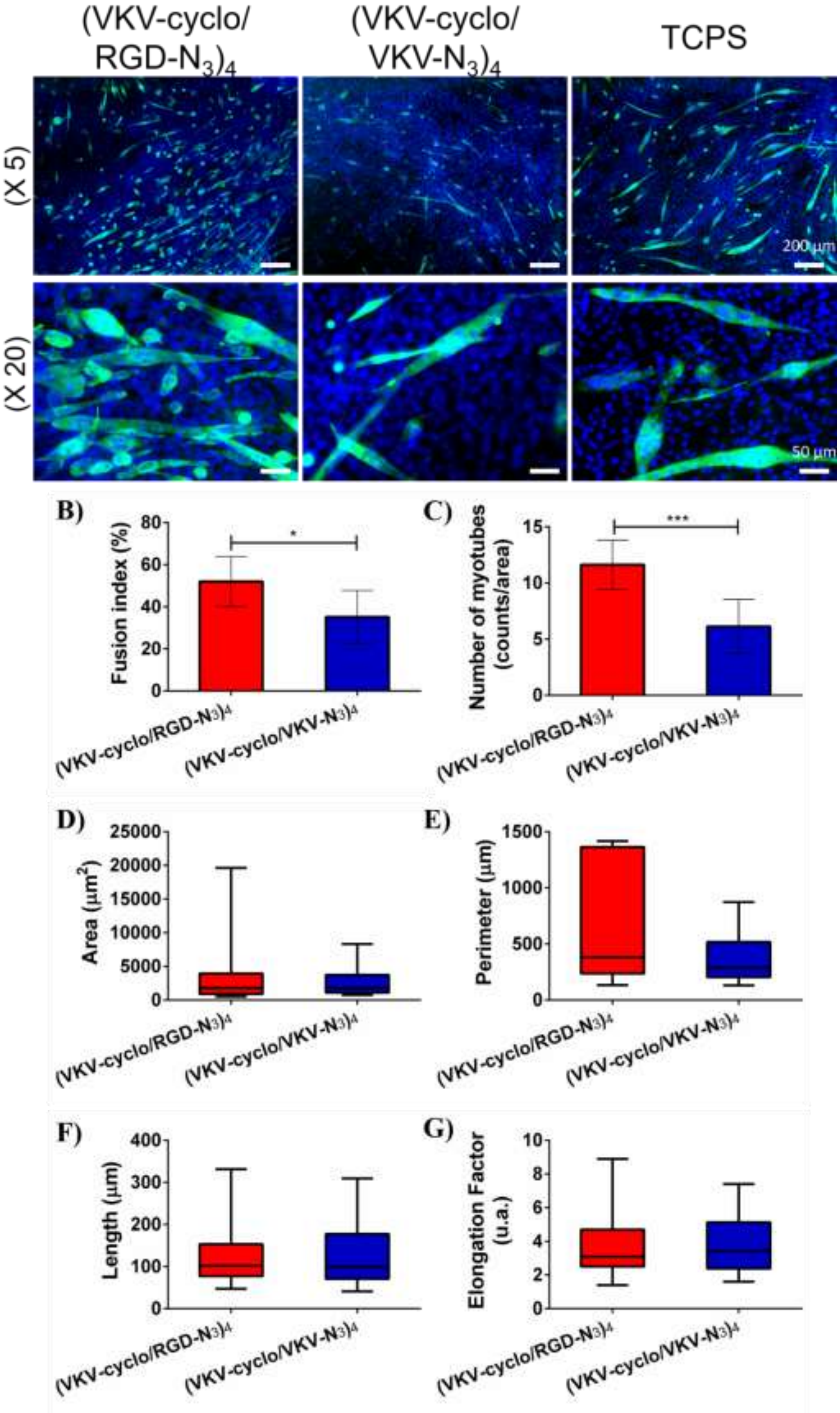

Figure IV-7. A) Myogenic differentiation at day 7 of culture of the cells seeded above the (VKV-cyclo/RGD-N_3)$_4$, (VKV-cyclo/VKV-N_3)$_4$ and TCPS. The images are the results of a fluorescence staining showing troponin T- positive cells (green) and cell nuclei (blue). Myogenic differentiation as determined by the B) fusion index (%) and the C) number of myotubes per area. Other parameters relatively to the formed myotubes were considered: D) area, E) perimeter, F) length and G) elongation factor. Statistically significant differences are indicated with $p < 0.05$ (*) and $p < 0.001$ (***).

4. Conclusions

We reported the development of stimuli-responsive polymer multilayer coatings, based on a click-chemistry system. We propose a simple click LbL methodology to fabricate these coatings, which consists in alternating cyclooctyne- and azide- modified ELRs, combined in a sequential multilayer mode. The build-up of the ELRs-based films was confirmed by QCM-D monitoring, following a non-linear growth. Herein, we show that both temperature and pH can act like stimuli to prompt independent responses by the developed ELRs-based films. Above LCST, ELRs formed folded and round structures. This phenomenon resulted in the increase of roughness of the coatings, and consequently in a more hydrophobic behavior, as compared to the ones found in the coating maintained at temperatures below LCST. Also, pH variations were responsible for changes in the coatings' WCA values; generally, the balance between charged amine and acid groups could determine the wetting behavior of the surfaces. The high stability of the films, conferred by the covalent bonding, was confirmed by QCM-D monitoring; in fact, the films withstood harsh conditions of pH, and only (VKV-cyclo/VKV-N_3)$_4$ coatings showed integrity loss while exposed to the most extreme pH value. The ability to introduce specific bioactive sequences like RGD motif on the ELRs structure was relevant for this investigation and central for tissue engineering and biomedical applications. Cell proliferation was increased on (VKV-cyclo/RGD-N_3)$_4$ films, and myogenic differentiation was also favored by the presence of the RGD bioactive sequence.

Overall, we were able to produce temperature and pH- responsive multilayer films composed exclusively by modified elastin-like polypeptides that can be easily used to as coatings. Besides glass, we hypothesize that these films may find application on coating implants with more complex shapes and compositions, nano/microstructures, gels and membranes. These systems show a great potential to develop structures for tissue engineering purposes or as platforms to culture cells in controlled conditions.

5. Acknowledgments

This research has received funding from the European Union's Horizon 2020 research and innovation programme under grant agreement No.646075. Maria P. Sousa and Mariana B. Oliveira acknowledge the Portuguese Foundation for Science and Technology (FCT) the grants SFRH/BD/97606/2013 and SFRH/BPD/111354/2015.

6. References

1. (a) Jeong, B.; Gutowska, A., Lessons from nature: stimuli-responsive polymers and their biomedical applications. *Trends in Biotechnology* **2002,** *20* (7), 305-311; (b) Stuart, M. A. C.; Huck, W. T. S.; Genzer, J.; Muller, M.; Ober, C.; Stamm, M.; Sukhorukov, G. B.; Szleifer, I.; Tsukruk, V. V.; Urban, M.; Winnik, F.; Zauscher, S.; Luzinov, I.; Minko, S., Emerging applications of stimuli-responsive polymer materials. *Nat Mater* **2010,** *9* (2), 101-113.

2. Nelson, A., Stimuli-responsive polymers: Engineering interactions. *Nat Mater* **2008,** *7* (7), 523-525.

3. (a) Alarcon, C. d. l. H.; Pennadam, S.; Alexander, C., Stimuli responsive polymers for biomedical applications. *Chemical Society Reviews* **2005,** *34* (3), 276-285; (b) Mano, J. F., Stimuli-Responsive Polymeric Systems for Biomedical Applications. *Advanced Engineering Materials* **2008,** *10* (6), 515-527.

4. (a) Tokarev, I.; Minko, S., Stimuli-responsive hydrogel thin films. *Soft Matter* **2009,** *5* (3), 511-524; (b) Costa, R. R.; Custódio, C. A.; Testera, A. M.; Arias, F. J.; Rodríguez-Cabello, J. C.; Alves, N. M.; Mano, J. F., Stimuli-Responsive Thin Coatings Using Elastin-Like Polymers for Biomedical Applications. *Advanced Functional Materials* **2009,** *19* (20), 3210-3218.

5. (a) Wandera, D.; Wickramasinghe, S. R.; Husson, S. M., Stimuli-responsive membranes. *Journal of Membrane Science* **2010,** *357* (1–2), 6-35; (b) Hu, X.; McIntosh, E.; Simon, M. G.; Staii, C.; Thomas, S. W., Stimuli-Responsive Free-Standing Layer-By-Layer Films. *Advanced Materials* **2016,** *28* (4), 715-721.

6. (a) Motornov, M.; Roiter, Y.; Tokarev, I.; Minko, S., Stimuli-responsive nanoparticles, nanogels and capsules for integrated multifunctional intelligent systems. *Progress in Polymer Science* **2010,** *35* (1–2), 174-211; (b) Sokolovskaya, E.; Rahmani, S.; Misra, A. C.; Bräse, S.; Lahann, J., Dual-Stimuli-Responsive Microparticles. *ACS Applied Materials & Interfaces* **2015,** *7* (18), 9744-9751.

7. Costa, R. R.; Mano, J. F., Polyelectrolyte multilayered assemblies in biomedical technologies. *Chemical Society Reviews* **2014,** *43* (10), 3453-3479.

8. (a) Richert, L.; Lavalle, P.; Payan, E.; Shu, X. Z.; Prestwich, G. D.; Stoltz, J.-F.; Schaaf, P.; Voegel, J.-C.; Picart, C., Layer by Layer Buildup of Polysaccharide Films: Physical Chemistry and Cellular Adhesion Aspects. *Langmuir* **2004,** *20* (2), 448-458; (b) Quinn, J. F.; Caruso, F., Facile Tailoring of Film Morphology and Release Properties Using Layer-by-Layer Assembly of Thermoresponsive Materials. *Langmuir* **2004,** *20* (1), 20-22; (c) Silva, J. M.; Reis, R. L.; Mano, J. F., Biomimetic Extracellular Environment Based on Natural Origin Polyelectrolyte Multilayers. *Small* **2016,** *12* (32), 4308-4342.

9. Borges, J.; Mano, J. F., Molecular Interactions Driving the Layer-by-Layer Assembly of Multilayers. *Chemical Reviews* **2014,** *114* (18), 8883-8942.

10. Borges, J.; Mano, J. F., Molecular interactions driving the layer-by-layer assembly of multilayers. *Chem. Rev.* **2014,** *114*, 8883-8942.

11. (a) Quinn, J. F.; Johnston, A. P. R.; Such, G. K.; Zelikin, A. N.; Caruso, F., Next generation, sequentially assembled ultrathin films: beyond electrostatics. *Chemical Society Reviews* **2007,** *36* (5), 707-718; (b) Bergbreiter, D. E.; Liao, K.-S., Covalent layer-by-layer assembly-an effective, forgiving way to construct functional robust ultrathin films and nanocomposites. *Soft Matter* **2009,** *5* (1), 23-28.

12. Seo, J.; Schattling, P.; Lang, T.; Jochum, F.; Nilles, K.; Theato, P.; Char, K., Covalently Bonded Layer-by-Layer Assembly of Multifunctional Thin Films Based on Activated Esters. *Langmuir* **2010,** *26* (3), 1830-1836.

13. Such, G. K.; Tjipto, E.; Postma, A.; Johnston, A. P. R.; Caruso, F., Ultrathin, Responsive Polymer Click Capsules. *Nano Letters* **2007,** *7* (6), 1706-1710.

14. (a) Rostovtsev, V. V.; Green, L. G.; Fokin, V. V.; Sharpless, K. B., A stepwise Huisgen cycloaddition process: Copper(I)-catalyzed regioselective "ligation" of azides and terminal alkynes. *Angew. Chem.-Int. Edit.* **2002,** *41* (14), 2596-+; (b) Meldal, M.; Tornøe, C. W., Cu-Catalyzed Azide−Alkyne Cycloaddition. *Chemical Reviews* **2008,** *108* (8), 2952-3015.

15. (a) Crouzier, T.; Boudou, T.; Picart, C., Polysaccharide-based polyelectrolyte multilayers. *Current Opinion in Colloid & Interface Science* **2010,** *15* (6), 417-426; (b) Silva, J. M.; Duarte, A. R. C.; Caridade, S. G.; Picart, C.; Reis, R. L.; Mano, J. F., Tailored freestanding multilayered membranes based on chitosan and alginate. *Biomacromolecules* **2014,** *15* (10), 3817-3826.

16. (a) Costa, R. R.; Custódio, C. A.; Arias, F. J.; Rodríguez-Cabello, J. C.; Mano, J. F., Layer-by-Layer Assembly of Chitosan and Recombinant Biopolymers into Biomimetic Coatings with Multiple

Stimuli-Responsive Properties. *Small* **2011,** *7* (18), 2640-2649; (b) Matsuzawa, A.; Matsusaki, M.; Akashi, M., Effectiveness of Nanometer-Sized Extracellular Matrix Layer-by-Layer Assembled Films for a Cell Membrane Coating Protecting Cells from Physical Stress. *Langmuir* **2013,** *29* (24), 7362-7368; (c) Oliveira, S. M.; Santo, V. E.; Gomes, M. E.; Reis, R. L.; Mano, J. F., Layer-by-layer assembled cell instructive nanocoatings containing platelet lysate. *Biomaterials* **2015,** *48*, 56-65.
17. He, P.; Bayachou, M., Layer-by-Layer Fabrication and Characterization of DNA-Wrapped Single-Walled Carbon Nanotube Particles. *Langmuir* **2005,** *21* (13), 6086-6092.
18. (a) Rodríguez-Cabello, J. C.; Martín, L.; Girotti, A.; García-Arévalo, C.; Arias, F. J.; Alonso, M., Emerging applications of multifunctional elastin-like recombinamers. *Nanomedicine* **2010,** *6* (1), 111-122; (b) Girotti, A.; Fernández-Colino, A.; López, I. M.; Rodríguez-Cabello, J. C.; Arias, F. J., Elastin-like recombinamers: Biosynthetic strategies and biotechnological applications. *Biotechnology Journal* **2011,** *6* (10), 1174-1186.
19. (a) D'Souza, S. E.; Ginsberg, M. H.; Plow, E. F., Arginyl-glycyl-aspartic acid (RGD): a cell adhesion motif. *Trends in Biochemical Sciences* **1991,** *16*, 246-250; (b) Hersel, U.; Dahmen, C.; Kessler, H., RGD modified polymers: biomaterials for stimulated cell adhesion and beyond. *Biomaterials* **2003,** *24* (24), 4385-4415.
20. González de Torre, I.; Santos, M.; Quintanilla, L.; Testera, A.; Alonso, M.; Rodríguez Cabello, J. C., Elastin-like recombinamer catalyst-free click gels: Characterization of poroelastic and intrinsic viscoelastic properties. *Acta Biomaterialia* **2014,** *10* (6), 2495-2505.
21. Alves, N. M.; Picart, C.; Mano, J. F., Self Assembling and Crosslinking of Polyelectrolyte Multilayer Films of Chitosan and Alginate Studied by QCM and IR Spectroscopy. *Macromolecular Bioscience* **2009,** *9* (8), 776-785.
22. Burattini, S.; Ferri, P.; Battistelli, M.; Curci, R.; Luchetti, E.; Falcieri, E., C2C12 murine myoblasts as a model of skeletal muscle development: morpho-functional characterization. *Eur. J. Histochem.* **2004,** *48* (3), 223-233.
23. Chang, S.; Song, S.; Lee, J.; Yoon, J.; Park, J.; Choi, S.; Park, J.-K.; Choi, K.; Choi, C., Phenotypic Modulation of Primary Vascular Smooth Muscle Cells by Short-Term Culture on Micropatterned Substrate. *PLoS ONE* **2014,** *9* (2), e88089.
24. (a) Oliveira, M. B.; Song, W.; Martin, L.; Oliveira, S. M.; Caridade, S. G.; Alonso, M.; Rodriguez-Cabello, J. C.; Mano, J. F., Development of an injectable system based on elastin-like recombinamer particles for tissue engineering applications. *Soft Matter* **2011,** *7* (14), 6426-6434; (b) Kinikoglu, B.; Rodríguez-Cabello, J. C.; Damour, O.; Hasirci, V., A smart bilayer scaffold of elastin-like recombinamer and collagen for soft tissue engineering. *Journal of Materials Science: Materials in Medicine* **2011,** *22* (6), 1541-1554; (c) Gonzalez de Torre, I.; Weber, M.; Quintanilla, L.; Alonso, M.; Jockenhoevel, S.; Rodriguez Cabello, J. C.; Mela, P., Hybrid elastin-like recombinamer-fibrin gels: physical characterization and *in vitro* evaluation for cardiovascular tissue engineering applications. *Biomaterials Science* **2016,** *4* (9), 1361-1370.
25. Girotti, A.; Reguera, J.; Arias, F. J.; Alonso, M.; Testera, A. M.; Rodríguez-Cabello, J. C., Influence of the Molecular Weight on the Inverse Temperature Transition of a Model Genetically Engineered Elastin-like pH-Responsive Polymer. *Macromolecules* **2004,** *37* (9), 3396-3400.
26. González de Torre, I.; Quintanilla, L.; Pinedo-Martín, G.; Alonso, M.; Rodríguez-Cabello, J. C., Nanogel Formation from Dilute Solutions of Clickable Elastin-like Recombinamers and its Dependence on Temperature: Two Fractal Gelation Modes. *ACS Applied Materials & Interfaces* **2014,** *6* (16), 14509-14515.
27. Glebe, U.; Santos de Miranda, B.; van Rijn, P.; Boker, A., Synthetic Modifications of Proteins. In *Bio-Synthetic Hybrid Materials and Bionanoparticles: A Biological Chemical Approach Towards Material Science*, The Royal Society of Chemistry: 2015; pp 1-29.
28. Marx, K. A., Quartz Crystal Microbalance: A Useful Tool for Studying Thin Polymer Films and Complex Biomolecular Systems at the Solution−Surface Interface. *Biomacromolecules* **2003,** *4* (5), 1099-1120.
29. Such, G. K.; Quinn, J. F.; Quinn, A.; Tjipto, E.; Caruso, F., Assembly of Ultrathin Polymer Multilayer Films by Click Chemistry. *Journal of the American Chemical Society* **2006,** *128* (29), 9318-9319.
30. Kinnane, C. R.; Wark, K.; Such, G. K.; Johnston, A. P. R.; Caruso, F., Peptide-Functionalized, Low-Biofouling Click Multilayers for Promoting Cell Adhesion and Growth. *Small* **2009,** *5* (4), 444-448.
31. Xiang, T.; Wang, R.; Zhao, W.-F.; Sun, S.-D.; Zhao, C.-S., Covalent Deposition of Zwitterionic Polymer and Citric Acid by Click Chemistry-Enabled Layer-by-Layer Assembly for Improving the Blood Compatibility of Polysulfone Membrane. *Langmuir* **2014,** *30* (18), 5115-5125.

32. (a) Golonka, M.; Bulwan, M.; Nowakowska, M.; Testera, A. M.; Rodriguez-Cabello, J. C.; Zapotoczny, S., Thermoresponsive multilayer films based on ionic elastin-like recombinamers. *Soft Matter* **2011,** *7* (19), 9402-9409; (b) Yang, W. J.; Pranantyo, D.; Neoh, K.-G.; Kang, E.-T.; Teo, S. L.-M.; Rittschof, D., Layer-by-Layer Click Deposition of Functional Polymer Coatings for Combating Marine Biofouling. *Biomacromolecules* **2012,** *13* (9), 2769-2780.

33. (a) El Haitami, A. E.; Thomann, J.-S.; Jierry, L.; Parat, A.; Voegel, J.-C.; Schaaf, P.; Senger, B.; Boulmedais, F.; Frisch, B., Covalent Layer-by-Layer Assemblies of Polyelectrolytes and Homobifunctional Spacers. *Langmuir* **2010,** *26* (14), 12351-12357; (b) Elosua, C.; Lopez-Torres, D.; Hernaez, M.; Matias, I. R.; Arregui, F. J., Comparative study of layer-by-layer deposition techniques for poly(sodium phosphate) and poly(allylamine hydrochloride). *Nanoscale Research Letters* **2013,** *8* (1), 539-539.

34. Norde, W.; MacRitchie, F.; Nowicka, G.; Lyklema, J., Protein adsorption at solid-liquid interfaces: Reversibility and conformation aspects. *Journal of Colloid and Interface Science* **1986,** *112* (2), 447-456.

35. da Silva, R. M. P.; Mano, J. F.; Reis, R. L., Smart thermoresponsive coatings and surfaces for tissue engineering: switching cell-material boundaries. *Trends in Biotechnology* **2007,** *25* (12), 577-583.

36. Parlak, O.; Ashaduzzaman, M.; Kollipara, S. B.; Tiwari, A.; Turner, A. P. F., Switchable Bioelectrocatalysis Controlled by Dual Stimuli-Responsive Polymeric Interface. *ACS Applied Materials & Interfaces* **2015,** *7* (43), 23837-23847.

37. Vihola, H.; Laukkanen, A.; Tenhu, H.; Hirvonen, J., Drug release characteristics of physically cross-linked thermosensitive poly(N-vinylcaprolactam) hydrogel particles. *Journal of Pharmaceutical Sciences* **2008,** *97* (11), 4783-4793.

38. Testera, A. M.; Girotti, A.; de Torre, I. G.; Quintanilla, L.; Santos, M.; Alonso, M.; Rodríguez-Cabello, J. C., Biocompatible elastin-like click gels: design, synthesis and characterization. *Journal of Materials Science: Materials in Medicine* **2015,** *26* (2), 1-13.

39. Wenzel, R. N., Resistance of solid surfaces to wetting by water. *Industrial & Engineering Chemistry* **1936,** *28* (8), 988-994.

40. Kowalczyk, T.; Hnatuszko-Konka, K.; Gerszberg, A.; Kononowicz, A. K., Elastin-like polypeptides as a promising family of genetically-engineered protein based polymers. *World journal of microbiology & biotechnology* **2014,** *30* (8), 2141-2152.

41. Shimizu, T.; Yamato, M.; Kikuchi, A.; Okano, T., Cell sheet engineering for myocardial tissue reconstruction. *Biomaterials* **2003,** *24* (13), 2309-2316.

42. (a) Li, B.; Daggett, V., The molecular basis of the temperature- and pH-induced conformational transitions in elastin-based peptides. *Biopolymers* **2003,** *68* (1), 121-129; (b) Carlos Rodríguez-Cabello, J.; Reguera, J.; Girotti, A.; Alonso, M.; Testera, A. M., Developing functionality in elastin-like polymers by increasing their molecular complexity: the power of the genetic engineering approach. *Progress in Polymer Science* **2005,** *30* (11), 1119-1145.

43. (a) Xia, F.; Feng, L.; Wang, S.; Sun, T.; Song, W.; Jiang, W.; Jiang, L., Dual-Responsive Surfaces That Switch between Superhydrophilicity and Superhydrophobicity. *Advanced Materials* **2006,** *18* (4), 432-436; (b) Zhang, Q.; Xia, F.; Sun, T.; Song, W.; Zhao, T.; Liu, M.; Jiang, L., Wettability switching between high hydrophilicity at low pH and high hydrophobicity at high pH on surface based on pH-responsive polymer. *Chemical Communications* **2008,** (10), 1199-1201.

44. Srokowski, E. M.; Woodhouse, K. A., Surface and adsorption characteristics of three elastin-like polypeptide coatings with varying sequence lengths. *Journal of materials science. Materials in medicine* **2013,** *24* (1), 71-84.

45. Ribeiro, A.; Arias, F. J.; Reguera, J.; Alonso, M.; Rodríguez-Cabello, J. C., Influence of the Amino-Acid Sequence on the Inverse Temperature Transition of Elastin-Like Polymers. *Biophysical Journal* **2009,** *97* (1), 312-320.

46. Silva, J. M.; Caridade, S. G.; Costa, R. R.; Alves, N. M.; Groth, T.; Picart, C.; Reis, R. L.; Mano, J. F., pH Responsiveness of Multilayered Films and Membranes Made of Polysaccharides. *Langmuir* **2015,** *31* (41), 11318-11328.

47. (a) Liu, W. F.; Chen, C. S., Engineering biomaterials to control cell function. *Materials Today* **2005,** *8* (12), 28-35; (b) García, A. J., Get a grip: integrins in cell–biomaterial interactions. *Biomaterials* **2005,** *26* (36), 7525-7529; (c) Oliveira, S. M.; Alves, N. M.; Mano, J. F., Cell interactions with superhydrophilic and superhydrophobic surfaces. *Journal of Adhesion Science and Technology* **2014,** *28* (8-9), 843-863.

48. Picart, C.; Elkaim, R.; Richert, L.; Audoin, F.; Arntz, Y.; Da Silva Cardoso, M.; Schaaf, P.; Voegel, J. C.; Frisch, B., Primary Cell Adhesion on RGD-Functionalized and Covalently Crosslinked Thin Polyelectrolyte Multilayer Films. *Advanced Functional Materials* **2005,** *15* (1), 83-94.

49. Rochlin, K.; Yu, S.; Roy, S.; Baylies, M. K., Myoblast fusion: When it takes more to make one. *Developmental Biology* **2010,** *341* (1), 66-83.

50. (a) Osses, N.; Brandan, E., ECM is required for skeletal muscle differentiation independently of muscle regulatory factor expression. *American Journal of Physiology - Cell Physiology* **2002,** *282* (2), C383-C394; (b) Wang, P.-Y.; Thissen, H.; Tsai, W.-B., The roles of RGD and grooved topography in the adhesion, morphology, and differentiation of C2C12 skeletal myoblasts. *Biotechnology and Bioengineering* **2012,** *109* (8), 2104-2115.

V. Elastic chitosan/ chondroitin sulphate multilayer membranes*

Abstract

Freestanding multilayered films were obtained using the layer-by-layer (LbL) technology from the assembly of natural polyelectrolytes, namely chitosan (CHT) and chondroitin sulphate (CS). The morphology and the transparency of the membranes were evaluated. The influence of genipin (1 and 2 mg/mL), a natural-derived crosslinker agent, was also investigated in the control of the mechanical properties of the CHT/CS membranes. The water uptake ability can be tailored by changing the crosslinker concentration that also control the young modulus and ultimate tensile strength. The maximum extension tends to decrease upon crosslinking with the highest genipin concentration, compromising the elastic properties of CHT/CS membranes: nevertheless, using the lower genipin concentration the ultimate tensile stress is similar to the no crosslinked one, but exhibiting a significant higher modulus. Moreover, the crosslinked multilayer membranes exhibited shape memory properties, through a simple hydration action. The *in vitro* biological assays showed better L929 cell adhesion and proliferation when using the crosslinked membranes and confirmed the non-cytotoxicity of the developed CHT/CS membranes. Within this research work, we were able to construct freestanding biomimetic multilayer structures with tailored swelling, mechanical and biological properties that could find applicability in a variety of biomedical applications.

Keywords: chondroitin sulphate; chitosan; layer-by-layer; polyelectrolyte multilayers; elasticity; stretchable films; shape memory

---

[*] This chapter is based on the following publication: Sousa, M. P.; Cleymand, F.; Mano, J. F., Elastic chitosan/chondroitin sulfate multilayer membranes. *Biomedical materials (Bristol, England)* **2016,** *11* (3), 035008.

1. Introduction

Biomimetic systems play an important role in biomedical sciences. Native tissues follow a hierarchical conformation and organization, from the nano to macroscales, which are difficult to mimic using conventional methodologies, such as solvent casting, freeze-drying or melt-based technologies. The use of non-physiological processing conditions and also the inability to control spatial distribution over the material triggered the urgent investigation for multiscale-based devices for biomedical applications [1], based on both bottom-up and top-down methodologies. Layer-by-layer (LbL) has been exploited to produce such type of controllable sized-architectures and has been growing faster [2]. This technique was firstly suggested by Decher and their co-workers [3], and follows a very simple foundation of consecutive and alternative deposition of oppositely charged polyelectrolyte solutions being usually described as an user-friendly way to prepare thin coatings. LbL promises the control over the architecture at both nano and microscales, mainly due to the possibility to use different adsorption conditions such as pH, ionic strength, charge density, polymer nature, functionality and concentration [4]. Another advantages are the abilities to incorporate different biomolecules, from synthetic [4b] to natural polymers [5] and different bioactive agents like growth factors [6], polypeptides [7] and nuclei acids [8], to repeat the process of assembly a hundreds of times and to extend from planar substrates [9] to three dimensional (3D) ones [10] .

LbL approaches have been mostly applied for surface modification of different substrates; for example, Cai and his co-workers [11] improved the biocompatibility of titanium films by modifying its surface with the alternate deposition of chitosan and gelatin. The possibility of producing structural 3D systems using such technology has permitted to extend its applicability in the biomedical field [2a]. In particular, efforts have been made to develop freestanding films from polyelectrolyte multilayers [11-12] those are obtained by removing the multilayer assembly from a solid substrate, where they were absorbed, using different strategies like neutralization of charged layers, sacrificial layers, dissolution of initial layers or even by applying mechanical forces [9]. Jiang *et al* [13] took advantage of a sacrificial layer of cellulose acetate to fabricate freely suspended nanocomposite polyelectrolyte membranes. Even so, the use of solvents or even mechanical forces can compromise the morphology and respective integrity of the membrane [9, 14]. To overcome this drawback, the production of easily detachable freestanding membranes was obtained via spontaneous detachment from an underlying low surface energy substrate [15]. The studied membranes were based on the combination of chitosan and alginate. Upon crosslinking the biological properties of the membranes were improved, but their maximum tensile strain decreased significantly [16]. For many biomedical applications it is required the use of more stretchable membranes, being elastic stretchability an important characteristic of the living tissues; thus other polyelectrolyte combinations should be explored.

Chitosan (CHT) has been broadly studied with LbL approaches, with many prospective works revealing its high potential for biomedical and tissue engineering applications [17]. Furthermore, CHT is a positively charged biopolymer, widely available from natural resources, biodegradable and is also a nontoxic compound [18]. Besides alginate, other natural polymers have been combined with chitosan;

Schneider and her group [19] combined chitosan with hyaluronic acid to observe the improvements on cell viability, elasticity and biodegradability and Neto *et al* [20] functionalized hyaluronic acid with dopamine to obtain a bioactive LbL coating, with more adhesive properties. Chondroitin sulphate (CS) is a naturally-derived polyanion and constituent of extracellular matrix, with an important role in the elasticity and function of cartilage and connective tissues [21] : we combined CHT and CS to produce reservoirs for calcium phosphate biomineralization [22] and to fabricate 3D highly porous scaffolds [23].

Herein, we propose the production of freestanding and easily detachable chitosan/chondroitin sulphate CHT/CS polyelectrolyte multilayer (PEM) membranes, from a planar substrate, without damaging it. We hypothesized that such polysaccharides combination could exhibit characteristics to make the final multilayer membranes suitable for biomedical applications. Moreover, another main objective of this work is to investigate the possibility to crosslink the CHT/CS freestanding membranes using a natural crosslinking agent and evaluate the effect of crosslinking over elasticity, water uptake, shape memory ability and cytotoxicity.

2. Materials and Methods

2.1. Materials

Chondroitin sulphate (CS) (Mw= 50-100kDa) and medium molecular weight Chitosan (CHT) (Mw=190-310 kDa, 75-85% degree of deacetylation) were purchased as a powder from Sigma Aldrich. This last one was subjected to a purification process, described elsewhere [24]. The polypropylene (PP) substrates, using as supports for the film growth were purchased from Firmo- Papéis e Papelarias S.A as A4 sheets and cut into small rectangles (10x4cm^2). Genipin was supplied by Waco Chemicals GmbH in Germany. Ethanol was supplied by Fisher Chemical, dimethyl sulfoxide (DMSO), sodium chloride (NaCl) and phosphate buffered saline (PBS) were purchased from Sigma Aldrich.

2.2. Methods for production and characterization of the membranes

2.2.1. QCM-D analysis and zeta potential measurements

Quartz crystal microbalance with dissipation monitoring (QCM-Dissipation, Q-Sense, Sweden) was used to monitor *in situ* the build-up process of CHT/CS multilayers and is based on the excitation of a gold coated crystal sensor, at a fundamental frequency of 5 MHz and eleventh overtone (55 MHz). Adsorption was accessed with a constant flow rate of 50 µl/min and, before using, the crystals were cleaned in an ultrasound bath with sequential acetone, ethanol and isopropanol baths, at 30°C. The CHT (0.2% (w/v) in 1% acetic acid/ 0.15 M NaCl, pH = 5.5, room temperature (RT)) solution was pumped into the system for 10 min to allow the adsorption equilibrium at the crystal surface. After rinsing with 0.15 M NaCl (10 min), the same procedure was followed for the deposition of CS (0.2% (w/v) in 1% acetic acid/ 0.15 M NaCl, pH = 5.5, RT). The frequency and dissipation were monitored in real time until the number of desired layers was achieved.

To access the charge density of the solutions, their zeta potentials were measured using a Zetasizer (Malvern, United Kingdom). A disposable cell was filled with the CHT and CS solutions, in the same conditions, and the zeta potential was determined for each solution. The mean values were presented, considering triplicated measurements of 3 samples.

2.2.2. Freestanding membranes production

CHT and CS solutions were adsorbed onto PP substrates, which were previously cleaned with water and ethanol and dried with nitrogen air. The substrates were placed in a dipping robot, a home-made equipment [25] automatically programmed for consecutive and alternately 6 minutes immersions on CHT and CS solutions, between 4 minutes of rinsing immersions in 0.15 M NaCl. The process was repeated until 250 bilayers were accomplished. Finishing this time, the substrates were dried at RT until the $(CHT/CS)_{250}$ membranes were detached and ready to use.

2.2.3. Chemical crosslinking

To reinforce the mechanical properties, genipin was chemically incorporated in $(CHT/CS)_{250}$ PEM membranes and compared with the original ones. Genipin solutions (1 and 2 mg/mL) were prepared in an optimized mixture of 1:4 DMSO/0.15 M NaCl. The $(CHT/CS)_{250}$ membranes were immersed in those solutions for 12 hours at RT [16]. In the end, the reaction was stopped using absolute ethanol a couple of times to remove the excess of genipin of the samples, and then dried at RT.

2.2.4. Scanning Electron Microscopy (SEM)

The morphology of the membranes was assessed by SEM (JSM-6010LV, JEOL, Japan). All the samples were previously sputtered with a conductive gold layer, using a sputter coater. Besides morphology, also the thickness of the resulting membranes was evaluated. Three samples were considered, taken triplicated thickness values for each one.

2.2.5. Fourier transform infrared spectroscopy (FTIR)

FTIR analysis of the different membranes (with and without crosslinking), and the respective natural polysaccharides was performed, using an IRPrestige-21 spectrophotometer. The samples were accessed using a membrane holder instrument, by the averaging 34 individual scans over the range 4400 cm^{-1} to 400 cm^{-1}. Using the same parameters but preparing in potassium bromide (KBr) discs, we obtained the FTIR spectrums for pure CHT and CS.

2.2.6. Water uptake ability

Water uptake ability of the membranes was determined by swelling film squares of 1 cm^2 (with known weights) in phosphate buffered saline (PBS, Sigma) at pH=7.4 up to 3 days and 37°C. The swollen membranes were removed at predetermined time points (10, 15, 30 minutes, 1, 2, 4, 6, 8 hours and 1, 2 and 3 days) and instantly weighted with an analytical balance (Scaltec, Germany), always after the removal of the water excess using filter paper (Whatman Pengamyn Paper). The water uptake was calculated using Equation V.1, where w_d and w_w represents the weights of dried and wetted membranes, respectively. For each condition, 5 samples were considered.

$$Water\ uptake\ (\%) = \frac{w_w - w_d}{w_d} \times 100 \qquad \text{Equation V.1}$$

2.2.7. Mechanical tests

Tensile tests were performed using a universal mechanical testing machine (Instron 5540, USA). 40×5mm^2 rectangles of $(CHT/CS)_{250}$ PEM membranes were tested in wet condition. A micrometer was used to measure both the thickness and the width of the samples. Before starting the test, the samples were immersed in PBS until equilibrium was reached, about 3 hours later. The tensile assays were made at a crosshead speed of 1mm.min^{-1} and room temperature, with a gauge length of 10 mm. The presented results are representative of at least five specimens and the Young's Modulus values were determined from the initial slope of the stress-strain curves.

2.2.8. Shape-memory properties

All the produced freestanding films presented a flat shape, but due to the elastic behavior associated to $(CHT/CS)_{250}$ membranes and their ability to uptake water, the initial shape can be deformed, through an external action. This can be described as a shape-memory phenomenon, triggered by hydration [26]. The 1 mg/mL crosslinked $(CHT/CS)_{250}$ membranes were cut in 40 mm x 8 mm rectangles and were then hydrated in PBS, until equilibrium was reached, about 3 hours after. With the help of a rod, the wetted membrane was rolled around, dehydrated with ethanol 100% to fix the shape, to induce the extraction of water molecules, and then allowed to dry. The membrane was carefully removed from the rod, to verify the maintenance of the resulting temporary shape. Rehydration was the next step, and the samples were again immersed in PBS to recover the initial and permanent flat shape. These transformations were observed and recorded by photography (Canon, G11 model, Japan). This test was repeated for different samples and all of them reveal the same tendency.

2.3. *In vitro* cell culture studies

A murine fibroblast cell line (L929, European Collection of Cell Cultures) was cultured in Dulbecco's modified eagle medium (DMEM, Sigma Aldrich) supplemented with 10% of fetal bovine serum (FBS, Biochrom AG, Germany) and 1% of antibiotics/antimycotic (Gibco, USA). The cells were maintained in culture in a 5% CO_2 atmosphere at 37°C until confluence. L929 cell suspensions were obtained from passages between 17 and 20. Previous to cell culture, the samples were immersed in ethanol 70% solution, for 2 hours.

In order to evaluate the biological performance and the cytotoxicity effects of the different $(CHT/CS)_{250}$ freestanding films we decided to use direct methods. After reaching 90% of confluence, the cells were detached using TrypLE Express (1x) (Alfagene) and seeded above the 1 cm^2 films at 5×10^4 cells/well. After 3 hours we nourished the culture and incubated again at 37 °C, for specific time points.

2.3.1. MTS assay – Cellular viability

Cellular viability and proliferation were evaluated using the colorimetric assay MTS [3-(4,5-dimethylthiazol-2-yl)-5-(3-carboxymethoxyphenyl)-2-(4-sulfophenyl)-2H-tetrazolium)] (Cell Titer 96 Aqueous One, Promega, USA). Briefly, the MTS reagent is biologically reduced into a brown formazan product by dehydrogenase enzymes presented in metabolically active cells. After 1, 3 and 7 days the culture medium was removed, and the cultured samples were incubated with MTS solution prepared in DMEM without phenol red and FBS in a 5:1 ratio, during 3 hours at 37 °C. Then the solution of each well was transferred to 96 well plates, in triplicate, and the absorbance was immediately recorded at 490 nm (BIO-TEK – Synergy HT). The results were expressed by the absorbance obtained for each condition as a function of the culturing time.

2.3.2. Morphological observation

To obtain fluorescence images, L929 fibroblasts were fixed in a solution of 10% of formalin (Termo Fisher Scientific), for 30 min at RT, after 1, 3 and 7 days. Then, the cells were permeabilized with 0.2% Triton X-100 (Sigma Aldrich) for 5 minutes and blocked with a 3% bovine serum albumin (BSA) (Sigma Aldrich) solution in PBS during 30 min. After this time, the cells were ready to be incubated with the phalloidin tetramethylrhodamine B (phalloidin, 50 µg/mL, Sigma Aldrich) solution in PBS (1:200), for 45 minutes, for actin-staining. For nucleus observation, the cells were incubated with 4',6-diamidino-2-phenylindole (DAPI, 20mg.mL^{-1}, Sigma Aldrich) in PBS (1:1000) for 15 minutes. Between each step, intensive washing steps were needed. Finishing this process, the membranes were observed with a transmitted and reflected light microscope with apotome 2 (Axio Imager Z1m, Zeiss). The chosen images were representative for each condition and time point.

2.4. Statistical analysis

All experiments were performed in triplicate unless the mechanical tensile tests (5 samples for condition at least). The results are always presented as mean ± standard deviation. Statistical significance between the different formulations was assessed using the two-way analysis of variance (ANOVA) test with Bonferroni post-test and was signed as $p<0.05$, $p<0.01$ and $p< 0.001$, using the software GraphPad Prism 5.0 for Windows.

3. Results and Discussion

3.1. Build-up CHT/CS multilayers

As already reported in literature, LbL approaches are mainly based on electrostatic interactions [4e]. Having this in mind, we measured the zeta potential of our polyelectrolytes: CHT and CS solutions presented a zeta potential of + 22.9 ± 1.6 mV and – 31.9 ± 2.3 mV, respectively. These results confirmed the cationic nature of chitosan solution and the anionic nature of chondroitin sulphate solution, at RT and at pH=5.5. This allowed our extrapolation, where the balance between the charges can reflect the similar deposition of CHT and CS.

The construction of the multilayer film was monitored *in situ*, using QCM-D. The results from QCM-D are represented in Figure V-1, representing the variations on normalized frequency (Δf_n, where n is the frequency overtone) and dissipation (ΔD) with time of deposition. We followed the growth of 8 bilayers of CHT/CS and as predictable, every time we introduced either CHT or CS the normalized frequency decreased while dissipation increased. The decrease on normalized frequency is related with the increasing mass over the gold crystal and the increase of dissipation evidences the non-rigid and viscoelastic nature of the adsorbed polyelectrolytes. Another assumption taken from QCM-D results is the strong interaction between the polyelectrolyte layers: during the washing steps the changes on frequency and dissipation was clearly shorter than during the polyelectrolyte solution steps [27]. During the 8 bilayers we assisted at a kind of plateau on the frequency variations, suggesting the formation of a homogeneous film. We assumed that this happens for the other 242 bilayers deposition.

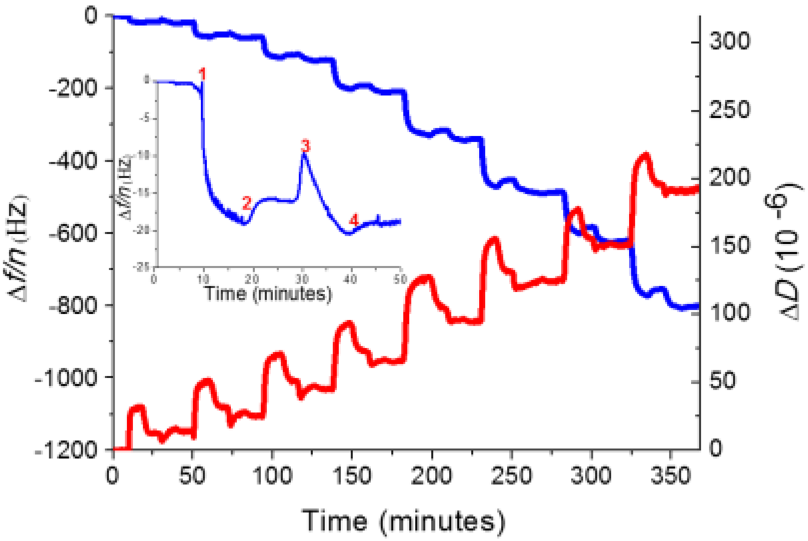

Figure V-1. Build-up monitoring of the $(CHT/CS)_{250}$ PEM construction, using QCM-D equipment: normalized frequency $\Delta f/3$ (blue) and dissipation ΔD (red) changes correspondent to the (1) CHT deposition, (2) and (4) the washing steps and (3) the CS deposition, obtained at third overtone.

3.2. Production of freestanding films and physico-chemical characterization

$(CHT/CS)_{250}$ freestanding PEMs films were constructed over low surface free energy PP substrates, through consecutive and sequential adsorption of CHT and CS, by immersing them in the respective polyelectrolyte solutions. Different number of bilayers could be tested and, in the end of the cycles, after drying at RT, the $(CHT/CS)_{250}$ PEMs membranes were easily detached from the underlying PP substrates (see Figure V-2). The facility of the detachment should be a consequence of the weak nature of the interactions between the first layers of the film and the PP substrate. Even though 50 bilayers were enough to obtain a consistent PEM membrane, with 250 bilayers we obtain more robust structures.

The morphology of the constructed freestanding PEM films was visualized using SEM. The surface of the $(CHT/CS)_{250}$ freestanding membrane, in the CS side (Figure V-3A), was homogeneous with rough structures with sizes of the order of 1-2 µm. Despite being the sacrificial layer, the other side of the membrane (Figure V-3B), corresponding to CHT, presented itself rougher than the top layer. This morphology is characteristic for CHT based membranes, as already reported in literature [16], and can be seen as an evidence that any defect resulted from the detachment step. From the cross-section SEM image (Figure V-3C) of the $(CHT/CS)_{250}$ PEM membranes we were able to conclude on their internal homogeneous morphology and to measure the averaged thickness. After 250 bilayers of $(CHT/CS)_{250}$ the thickness of the resulting freestanding membrane was about 48.7 ± 7.92 µm. Microscopic (Figure V-3B) and macroscopic (figure 2) observations did not reveal any defects or fractures derived from the detachment step. Another characteristic to note was the transparency of the PEM membranes, demonstrated in Figure V-2 and V-3D *(i)*.

To increase the stability of the membranes in the wet state, we evaluated the possibility to fabricate more robust PEM membranes by crosslinking with genipin. Two different concentrations (1mg/mL and 2mg/mL) were tested. Figure V-3D shows the image of 1 cm^2 squares of *(i)* unmodified $(CHT/CS)_{250}$ PEM, *(ii)* $(CHT/CS)_{250}$ PEM crosslinked with 1mg/mL and *(iii)* $(CHT/CS)_{250}$ PEM crosslinked with 2mg/mL membranes. Genipin is a natural crosslinking agent extracted from *Gardenia*, that when reacts with amino groups forms blue pigments [28]. As expected, the higher the concentration of genipin, the more blue pigmentation was acquired by the membrane – see Figure V-3D. This qualitative colorimetric test proved that the crosslinking took place.

Figure V-2. Detachment of the $(CHT/CS)_{250}$ multilayer assembled onto a low surface energy PP substrate: just by pushing through the dry membrane using tweezers, we obtain the freestanding film.

We performed FTIR tests on $(CHT/CS)_{250}$ PEM membranes and on the respective individual polysaccharides, CHT and CS powders, so that we could detect the presence of the two polymers in the final sample. The results are illustrated in Figure V-4. As expected by its closeness in terms of chemical structure, the spectra of CHT and CS were alike, sharing some characteristic peaks: the peak represents the bond stretching vibrations corresponding to -OH and N-H at about 3400 cm^{-1},at about 2900 cm^{-1} the band is assigned to the stretching of C-H, the peak of stretching of amide groups appears around 1648 cm^{-1} and between 1080 and 1020 cm^{-1} the peaks match the stretching of C-O functional bounds.

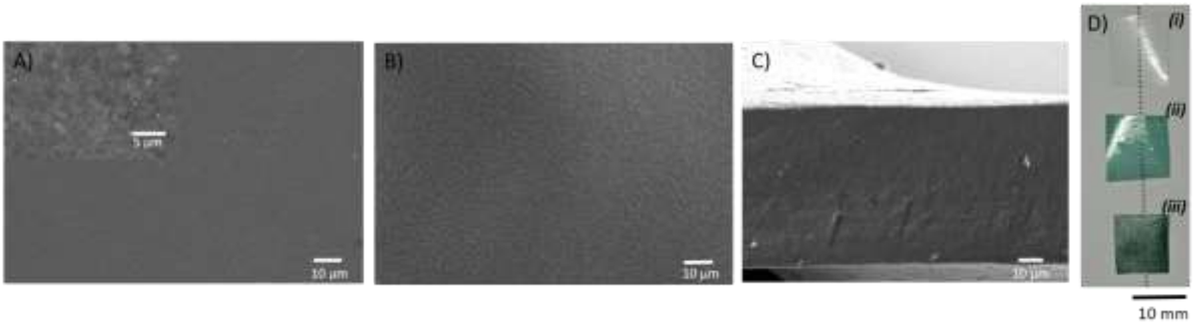

Figure V-3. SEM micrograph of the (CHT/CS)$_{250}$ PEM membranes (A) on the CS side, at different magnifications, (B) on the CHT side and (C) the cross-section; (D) Photographs of the membranes over a paper sheet printed with a dotted line: (i) unmodified (CHT/CS)$_{250}$ PEM, (ii) (CHT/CS)$_{250}$ PEM crosslinked with 1mg/mL of genipin and (iii) (CHT/CS)$_{250}$ PEM crosslinked with 2mg/mL of genipin membranes.

Despite their similarities, CHT and CS have unique fingerprint regions: around 1570 cm^{-1} [29] we observed the peak corresponding to amine groups of CHT and for CS there is a representative peak of the stretching of the S=O bond at 1250 cm^{-1} [30]. The spectrum of the (CHT/CS)$_{250}$ film revealed the absorption peaks of both CHT and CS, pinpointing the presence of both polysaccharides. When genipin were incorporated to the (CHT/CS)$_{250}$ PEM membrane, some differences were noted on the FTIR spectra. As already reported elsewhere [31], genipin reacts with the amino groups of chitosan, establishing amide linkage. Their C=O stretching band overlapped with the amide I adsorption band characteristic of chitosan, at 1650 cm^{-1}, making this one broader [31b]. Moreover, the C-N linkage of the amide III, characteristic of chitosan at 1233cm^{-1} was shifted to 1260 cm^{-1}, after the crosslinking with genipin [31a]. Any significant difference was noted on the FTIR spectra of both crosslinked membranes (with 1 or 2 mg/mL of genipin).

Figure V-5 displays the water uptake ability of the developed membranes. This phenomenon has particular interest since the nutrients and gas diffusion processes as well as both the mechanical and biological behavior depend on it [16, 32]. Polysaccharides present hydrophilic groups in their backbone, making them capable of being highly hydrated [33]. We immersed the samples in PBS and measured the changes on weight, up to 3 days: for all conditions, the trend of the water uptake profile was similar. Most of the water was uptake in the first hour: the presence of hydrophilic functional groups like carboxyl, hydroxyl, amino and sulphate is the main reason for its water uptake ability. When comparing the crosslinked membranes with the original one, we observed a discrepancy in the water uptake percentages, with statistical differences (*** meaning $p<0.001$): genipin acted at coupling chitosan free amines in the membrane network reducing the available space in hydrophilic chains and preventing the membranes to uptake large quantity of water [16, 32, 34].On the other hand, the 2 mg/mL crosslinked membrane was the one with the lowest values of water uptake, with statistical differences up to 10 minutes and then after 3 hours (## meaning $p<0.01$ and # meaning $p<0.05$). This behavior can be explained by the fact that the membrane with lower amount of genipin had naturally more hydrophilic groups not crosslinked, presenting higher water uptake ability.

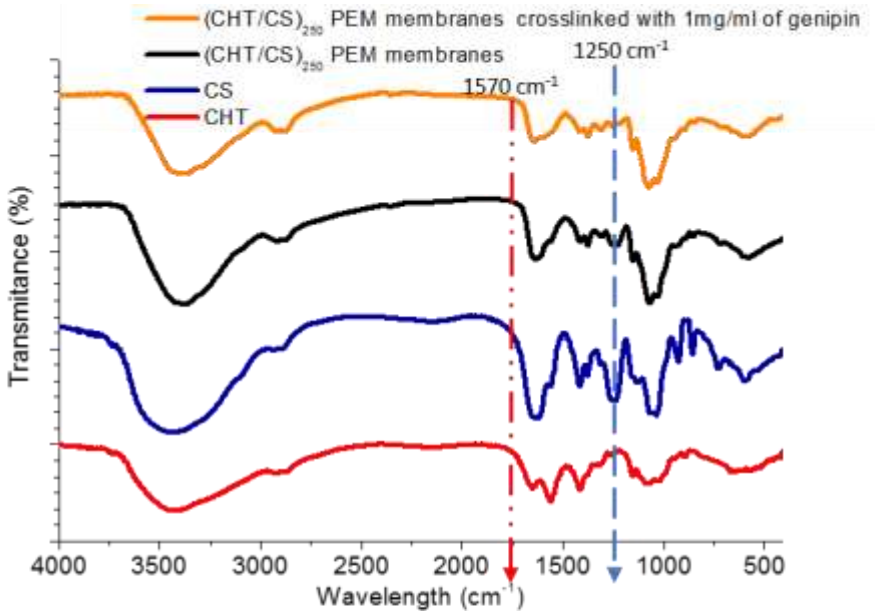

Figure V-4. FTIR spectra of the unmodified and crosslinked (with 1mg/ml of genipin) $(CHT/CS)_{250}$ PEM membranes and the pure polysaccharides, CHT and CS.

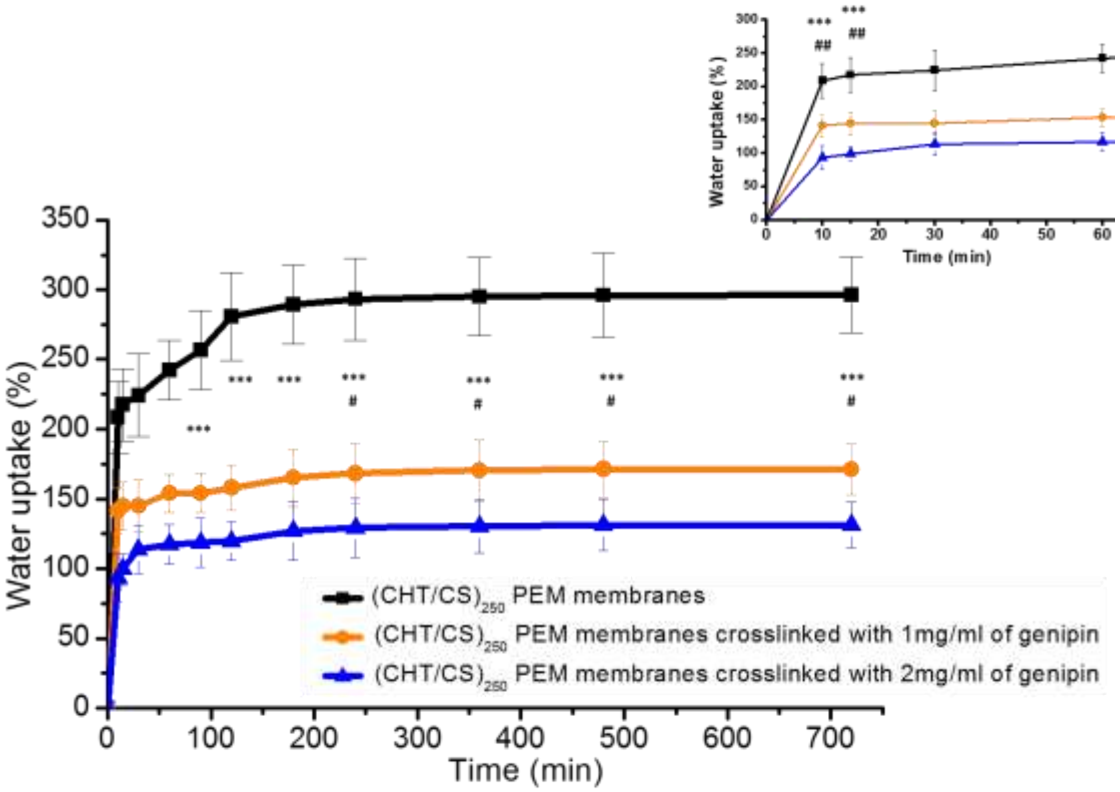

Figure V-5. Water uptake profile of the unmodified and crosslinked $(CHT/CS)_{250}$ PEM membranes, up to 3 days. The inset represents the water uptake for the first hour of immersion in PBS. Statistical differences were marked in the figure, with *** meaning $p<0.001$ between the unmodified membrane and both crosslinked and with # and ## meaning $p<0.01$ and $p<0.05$, respectively, between the crosslinked membranes.

3.3. Mechanical tests

Differences in the mechanical performance can be found between the dry and the wet state of the $(CHT/CS)_{250}$ PEM membranes. Following the physiological environment, we performed tensile tests in a hydrated environment, immersing the samples in PBS until equilibrium. The representative conventional stress-strain curves for each type of membrane are presented in Figure V-6A, and the respective values of Young's modulus (*E*), ultimate tensile strength ($\sigma_{\text{máx}}$) and maximum extension ($\varepsilon_{\text{máx}}$) are shown in figure 6B. An increase in the Young's modulus was observed within the crosslinked membranes. Otherwise, the maximum extension decreased with the increase of the crosslinker concentration. This is in accordance with the results of water uptake, where unmodified $(CHT/CS)_{250}$ membranes presented more ability to retain water molecules and be highly hydrated: literature [16, 24, 32, 35] already reported a kind of plasticization effect of water molecules in natural polymers that makes molecular mobility increases and stiffness decreases. Furthermore, ultimate strength presented a non-monotonic trend: with 1mg/ mL crosslinked membranes, the ultimate strength increased but above this concentration the value of this parameter decreased. We assumed that using higher genipin concentration than 1mg/mL, the film became too brittle and the yield point is much faster to achieve. Accordingly, with these results we can overtake the handling difficulty of the $(CHT/CS)_{250}$ PEMs membranes using the 1 mg/mL of genipin condition; the maximum extension is not far from the non-crosslinked one. Comparing with related literature [16], we are able to produce more extensible membranes; for 1 mg/mL crosslinked condition, the membrane extended up to the double of its original size, with an Young's modulus of 6.8± 0.80 MPa. Therefore, we fabricated more stretchable and elastic membranes than, for example, using alginate instead of CS; for the same concentration of genipin, crosslinked CHT/alginate membranes presented an Young's modulus of 12.8± 2 MPa with a maximum extension around 10 % of its original size [16]. The maximum strain of the obtained membranes are also higher than other chitosan-based membranes reported in literature [36].

3.4. Shape memory properties

Many biomedical applications can benefit with the possibility of flat and flexible substrates acquiring temporary shapes, under some external action [37]. In the case of our product, it could be interesting that the original flat membrane can be maintained in a temporary shape until inserted in the targeted body location. This can be important, for example, to maintain minimal the invasive surgery. Different stimuli have been reported in literature [38] but at our point of view the hydration action seemed to be an interesting option, with some good examples previously reported [26, 39]. The shape memory effect of the developed membranes, triggered by hydration/dehydration action is shown in Figure V-7, with a scheme of the process and a sequence of optical photographs representing each step. Crosslinked $(CHT/CS)_{250}$ membranes, at 1mg/mL, were immersed in a PBS solution, increasing the hydration level of the film; this stage was maintained until the temporary deformation of the film was requested. Then, a helicoidal shape was achieved by twisting the hydrated film around a rod: a dehydration step was fundamental to fix this geometry, upon which the membrane became rigid and undeformable. When the material is implantable, the membranes have to return for the original flat shape: through the action of a rehydration, the crosslinked $(CHT/CS)_{250}$ membranes deformed and easily recovered the flat configuration. The hydration action strongly influences the molecular motility and the glass transition dynamics of the polysaccharides, promoting this phenomenon [24, 26, 39c].

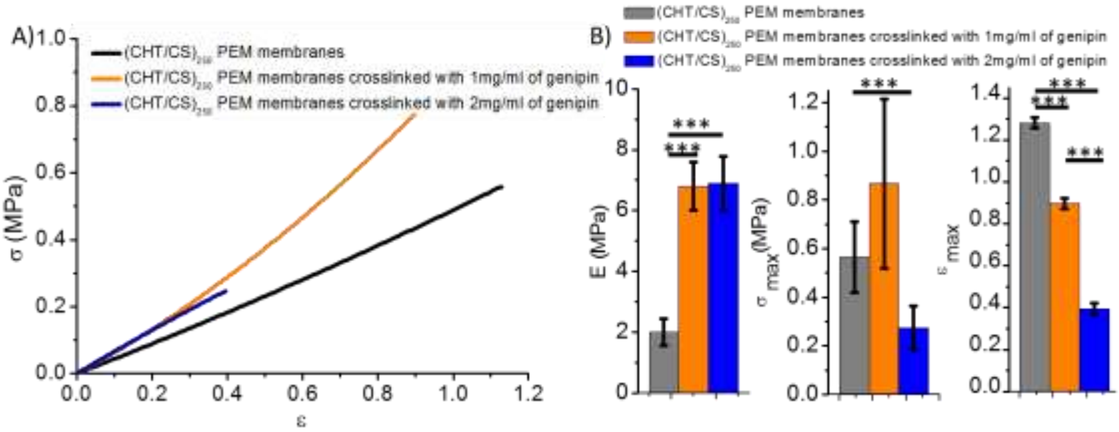

Figure V-6. (A) Representative conventional tensile strain-stress curves for the freestanding films with and without crosslinking, taken in the wet state. (B) Young's Modulus (E), ultimate tensile strength (σ max) and maximum extension (ε max) for each condition. Differences in data were considered statistically significant, with $p < 0.001$: (***) indicates significant differences.

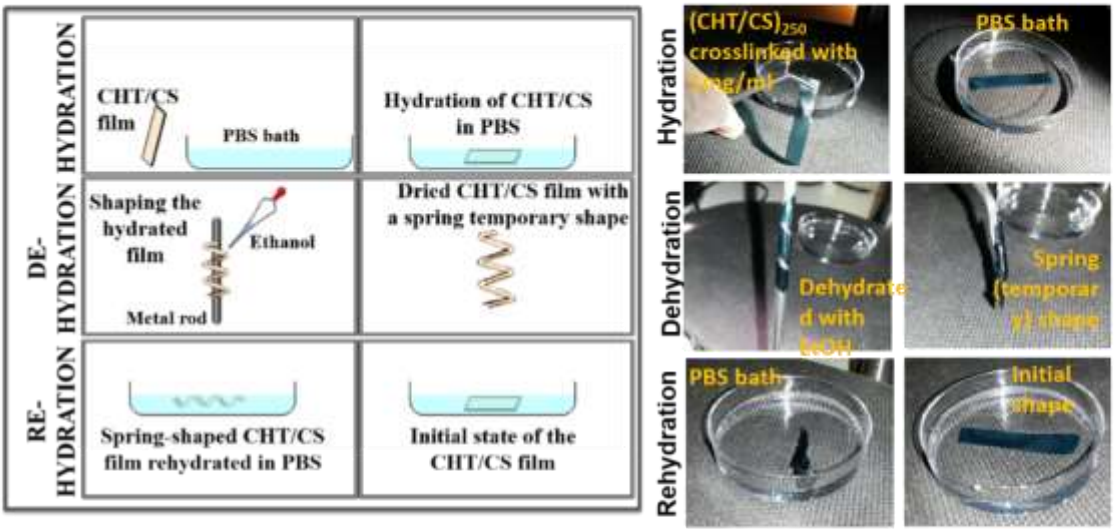

Figure V-7. Schematic representation of the methodology to monitor the shape-memory capability of CHI/CS membranes crosslinked with 1mg/mL of genipin (H_2O – ultrapure water; EtOH – 100% ethanol) (left image). Optical photographs that demonstrate the shape memory capability of $(CHT/CS)_{250}$ crosslinked with 1mg/mL of genipin freestanding multilayered films, induced by hydration (right image). These are the real images relative to the scheme.

3.5. *In vitro* cell culture

L929 were seeded on unmodified and crosslinked $(CHT/CS)_{250}$ membranes. Differences were observed between cellular adherence, proliferation and morphology - see Figure V-8. In literature there are several studies reporting the genipin effect on cellular behavior, from adherence to proliferation, morphology and differentiation for different cell types [28, 40]. Previous to this study, we already showed a trend on chitosan/ alginate multilayer membranes, where genipin has a positive effect on cell adhesion [16]. Beyond 3 days of cell culture, MTS assay results revealed significant statistical differences between the three conditions, with better cellular viability and proliferation in the crosslinked $(CHT/CS)_{250}$ membranes than in the unmodified ones. MTS absorbance increased along the time, for all formulations, which means that cells are alive and proliferating. Furthermore, there was clearly an indication that when modified with genipin the membranes shown better cellular performance, at least using up to 2 mg/mL of genipin (see Figure V-8). The cells seeded on unmodified $(CHT/CS)_{250}$ membranes shown a round morphology, creating weak anchors with the surface; this can be related with the higher water content of these films [16, 41]- see Figure V-9. On the other hand, when the membranes were crosslinked, they retained less volume of water molecules and created stronger bounds with cells, which evidenced a stretched morphology [16, 34, 41-42]. At day 7 of culture, the area of the membranes was almost covered by adhered cells on the modified membranes L929 proliferated in a dense layer but the same was not clearly observed for unmodified one. In this case, cells tended to form clusters.

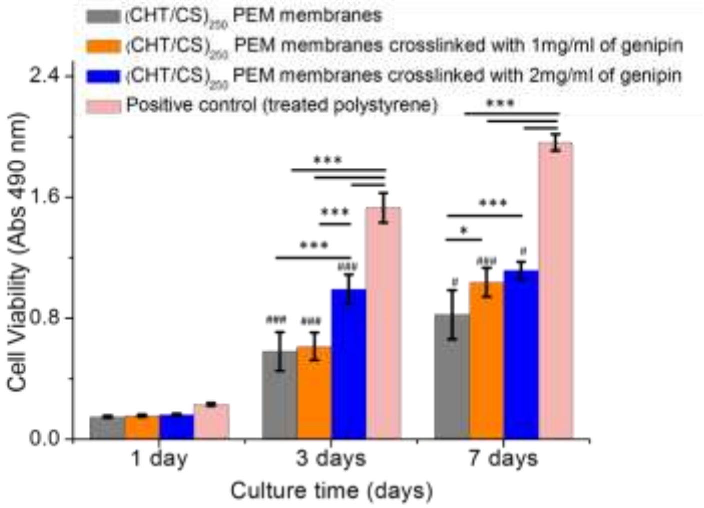

Figure V-8. Cell viability at 1, 3 and 7 days of culture on $(CHT/CS)_{250}$ PEM films with and without crosslinking with genipin, using the MTS assay. Statistical analysis between each time point were performed and the data relative to proliferation was considered statistical different, with (###) p< 0.001 and (#) p <0.05. Also, the differences between conditions were considered, having statistical differences with (***) p< 0.001 and (*) p <0.05.

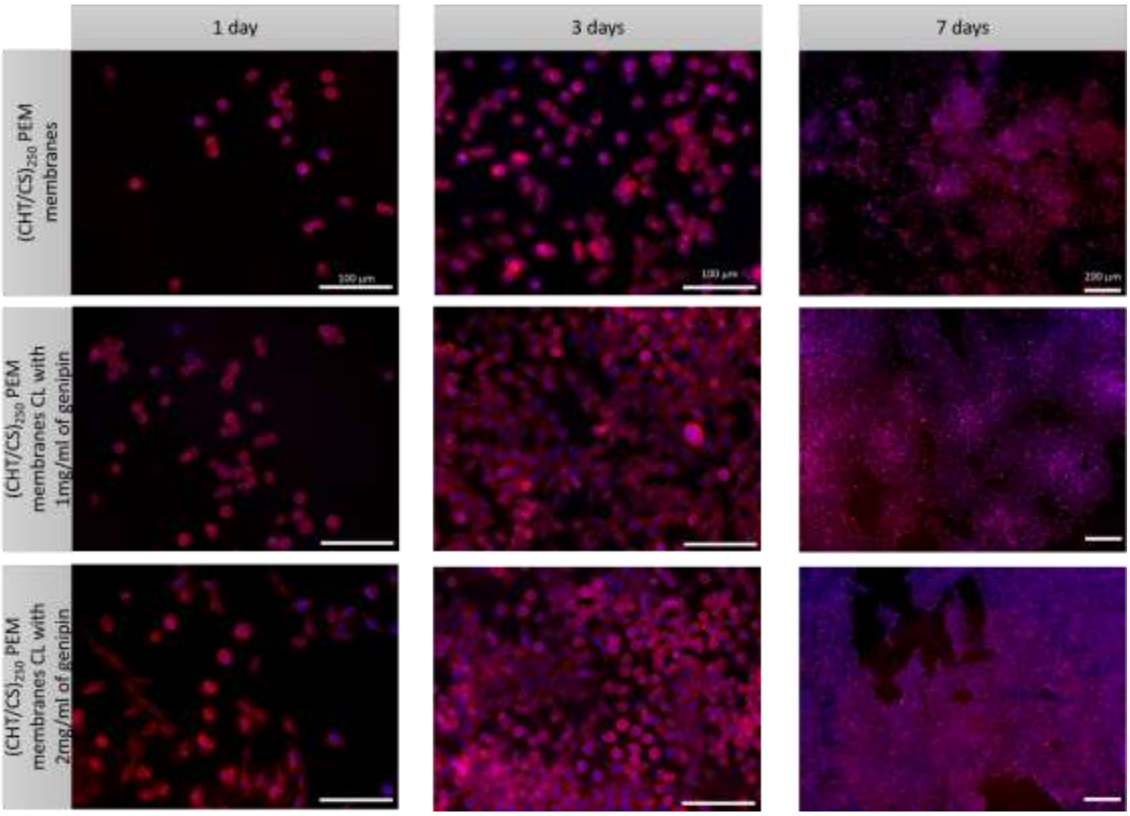

Figure V-9. DAPI-phalloidin fluorescence assay of L929 cells seeded on the unmodified and crosslinked $(CHT/CS)_{250}$ PEM membranes: at day 1, day 3 and day 7. Cells nuclei were stained blue using DAPI and the F-actin filaments (cytoskeleton) in red using phalloidin. Scale bar for day 1 and 3 represents 100 µm and for day 7 represents 200 µm.

Overall, we confirmed the positive genipin effect in the biological performance of $(CHT/CS)_{250}$ membranes. In conclusion, better viability and proliferation evidences and a stretched morphology was observed for crosslinked films.

Having in mind the combination of the physicochemical, mechanical and biological performance, the $(CHT/CS)_{250}$ freestanding PEM membranes crosslinked with 1 mg/mL of genipin seem to present the best result for the possible applicability in the biomedical field.

4. Conclusions

Easily detachable membranes made of CHT and CS were successfully obtained by LbL technology, in combination with the use of a low surface energy material as underlying substrate. The multilayers were crosslinked with genipin with the objective of enhancing the handling of the freestanding films. The results confirmed the ability of tailoring important properties of PEMs membranes, including water uptake, Young's modulus, ultimate tensile strength, maximum extension and biological performance, just playing with genipin concentration. It was possible to conclude that the crosslinking step was relevant to achieve better mechanical and biological performances: an interesting balance was achieved when we used the lowest genipin concentration. Such membranes could have promising applications as skin, cartilage, cardiac, bone, nerve, guided and for other soft tissue regeneration, as platforms for drug or growth factors delivery or even as substrates for biosensors integration.

5. Acknowledgments

FC and JFM would like to thank Region Lorraine, FEDER and Mines Nancy for their financial supports. Maria Sousa wants to acknowledge the Portuguese Foundation for Science and Technology (FCT) for financial support through SFRH/BD/97606/2013 grant.

6. References

1. Oliveira, S. M.; Reis, R. L.; Mano, J. F., Towards the design of 3D multiscale instructive tissue engineering constructs: Current approaches and trends. *Biotechnology Advances* **2015,** *33* (6, Part 1), 842-855.
2. (a) Costa, R. R.; Mano, J. F., Polyelectrolyte multilayered assemblies in biomedical technologies. *Chemical Society Reviews* **2014,** *43* (10), 3453-3479; (b) Monge, C.; Almodovar, J.; Boudou, T.; Picart, C., Spatio-Temporal Control of LbL Films for Biomedical Applications: From 2D to 3D. *Adv Healthc Mater* **2015,** *4* (6), 811-30.
3. Decher, G.; Hong, J. D.; Schmitt, J., Buildup of ultrathin multilayer films by a self-assembly process: III. Consecutively alternating adsorption of anionic and cationic polyelectrolytes on charged surfaces. *Thin Solid Films* **1992,** *210–211, Part 2* (0), 831-835.
4. (a) Ariga, K.; Hill, J. P.; Ji, Q., Layer-by-layer assembly as a versatile bottom-up nanofabrication technique for exploratory research and realistic application. *Physical Chemistry Chemical Physics* **2007,** *9* (19), 2319-2340; (b) Boudou, T.; Crouzier, T.; Ren, K.; Blin, G.; Picart, C., Multiple Functionalities of Polyelectrolyte Multilayer Films: New Biomedical Applications. *Advanced Materials* **2010,** *22* (4), 441-467; (c) Detzel, C. J.; Larkin, A. L.; Rajagopalan, P., Polyelectrolyte multilayers in tissue engineering. *Tissue Eng Part B Rev* **2011,** *17* (2), 101-113; (d) Matsusaki, M.; Ajiro, H.; Kida, T.; Serizawa, T.; Akashi, M., Layer-by-Layer Assembly Through Weak Interactions and Their Biomedical Applications. *Advanced Materials* **2012,** *24* (4), 454-474; (e) Borges, J.; Mano, J. F., Molecular Interactions Driving the Layer-by-Layer Assembly of Multilayers. *Chemical Reviews* **2014,** *114* (18), 8883-8942.
5. (a) Zhang, J.; Senger, B.; Vautier, D.; Picart, C.; Schaaf, P.; Voegel, J. C.; Lavalle, P., Natural polyelectrolyte films based on layer-by layer deposition of collagen and hyaluronic acid. *Biomaterials* **2005,** *26* (16), 3353-3361; (b) Alves, N. M.; Picart, C.; Mano, J. F., Self Assembling and Crosslinking of Polyelectrolyte Multilayer Films of Chitosan and Alginate Studied by QCM and IR Spectroscopy. *Macromol Biosci* **2009,** *9* (8), 776-785.
6. Ma, L.; Zhou, J.; Gao, C.; Shen, J., Incorporation of basic fibroblast growth factor by a layer-by-layer assembly technique to produce bioactive substrates. *Journal of Biomedical Materials Research Part B: Applied Biomaterials* **2007,** *83B* (1), 285-292.
7. Costa, R. R.; Testera, A. M.; Arias, F. J.; Rodríguez-Cabello, J. C.; Mano, J. F., Layer-by-Layer Film Growth Using Polysaccharides and Recombinant Polypeptides: A Combinatorial Approach. *The Journal of Physical Chemistry B* **2013,** *117* (22), 6839-6848.
8. Koyfman, A. Y.; Braun, G. B.; Reich, N. O., Cell-Targeted Self-Assembled DNA Nanostructures. *Journal of the American Chemical Society* **2009,** *131* (40), 14237-14239.
9. Larkin, A. L.; Davis, R. M.; Rajagopalan, P., Biocompatible, Detachable, and Free-Standing Polyelectrolyte Multilayer Films. *Biomacromolecules* **2010,** *11* (10), 2788-2796.
10. (a) Mueller, R.; Daehne, L.; Fery, A., Hollow Polyelectrolyte Multilayer Tubes: Mechanical Properties and Shape Changes. *The Journal of Physical Chemistry B* **2007,** *111* (29), 8547-8553; (b) Correia, C. R.; Reis, R. L.; Mano, J. F., Multilayered Hierarchical Capsules Providing Cell Adhesion Sites. *Biomacromolecules* **2013,** *14* (3), 743-751.
11. Cai, K.; Rechtenbach, A.; Hao, J.; Bossert, J.; Jandt, K. D., Polysaccharide-protein surface modification of titanium via a layer-by-layer technique: Characterization and cell behaviour aspects. *Biomaterials* **2005,** *26* (30), 5960-5971.
12. Mhamdi, L.; Picart, C.; Lagneau, C.; Othmane, A.; Grosgogeat, B.; Jaffrezic-Renault, N.; Ponsonnet, L., Study of the polyelectrolyte multilayer thin films' properties and correlation with the behavior of the human gingival fibroblasts. *Mat Sci Eng C-Bio S* **2006,** *26* (2-3), 273-281.
13. Jiang, C.; Markutsya, S.; Pikus, Y.; Tsukruk, V. V., Freely suspended nanocomposite membranes as highly sensitive sensors. *Nat Mater* **2004,** *3* (10), 721-728.
14. Lutkenhaus, J. L.; Hrabak, K. D.; McEnnis, K.; Hammond, P. T., Elastomeric Flexible Free-Standing Hydrogen-Bonded Nanoscale Assemblies. *Journal of the American Chemical Society* **2005,** *127* (49), 17228-17234.
15. Nolte, M.; Fery, A., Freestanding polyelectrolyte multilayers as functional and construction elements. *IEE Proceedings -- Nanobiotechnology* **2006,** *153* (4), 112-120.

16. Silva, J. M.; Duarte, A. R. C.; Caridade, S. G.; Picart, C.; Reis, R. L.; Mano, J. F., Tailored freestanding multilayered membranes based on chitosan and alginate. *Biomacromolecules* **2014,** *15* (10), 3817-3826.
17. (a) Alves, N. M.; Mano, J. F., Chitosan derivatives obtained by chemical modifications for biomedical and environmental applications. *International Journal of Biological Macromolecules* **2008,** *43* (5), 401-414; (b) Croisier, F.; Jérôme, C., Chitosan-based biomaterials for tissue engineering. *European Polymer Journal* **2013,** *49* (4), 780-792.
18. Mano, J. F.; Silva, G. A.; Azevedo, H. S.; Malafaya, P. B.; Sousa, R. A.; Silva, S. S.; Boesel, L. F.; Oliveira, J. M.; Santos, T. C.; Marques, A. P.; Neves, N. M.; Reis, R. L., Natural origin biodegradable systems in tissue engineering and regenerative medicine: present status and some moving trends. *Journal of the Royal Society Interface* **2007,** *4* (17), 999-1030.
19. Aurore, S.; Ludovic, R.; Gregory, F.; Jean-Claude, V.; Catherine, P., Elasticity, biodegradability and cell adhesive properties of chitosan/hyaluronan multilayer films. *Biomedical Materials* **2007,** *2* (1), S45.
20. Neto, A. I.; Cibrão, A. C.; Correia, C. R.; Carvalho, R. R.; Luz, G. M.; Ferrer, G. G.; Botelho, G.; Picart, C.; Alves, N. M.; Mano, J. F., Nanostructured Polymeric Coatings Based on Chitosan and Dopamine-Modified Hyaluronic Acid for Biomedical Applications. *Small* **2014,** *10* (12), 2459-2469.
21. (a) Schiraldi, C.; Cimini, D.; De Rosa, M., Production of chondroitin sulfate and chondroitin. *Appl Microbiol Biotechnol* **2010,** *87* (4), 1209-1220; (b) Vázquez, J.; Rodríguez-Amado, I.; Montemayor, M.; Fraguas, J.; González, M.; Murado, M., Chondroitin Sulfate, Hyaluronic Acid and Chitin/Chitosan Production Using Marine Waste Sources: Characteristics, Applications and Eco-Friendly Processes: A Review. *Marine Drugs* **2013,** *11* (3), 747-774.
22. Leite, Á. J.; Sher, P.; Mano, J. F., Chitosan/chondroitin sulfate multilayers as supports for calcium phosphate biomineralization. *Materials Letters* **2014,** *121* (0), 62-65.
23. Silva, J. M.; Georgi, N.; Costa, R.; Sher, P.; Reis, R. L.; Van Blitterswijk, C. A.; Karperien, M.; Mano, J. F., Nanostructured 3D Constructs Based on Chitosan and Chondroitin Sulphate Multilayers for Cartilage Tissue Engineering. *PLOS ONE* **2013,** *8* (2), e55451.
24. Mano, J. F., Viscoelastic Properties of Chitosan with Different Hydration Degrees as Studied by Dynamic Mechanical Analysis. *Macromol Biosci* **2008,** *8* (1), 69-76.
25. Silva, J. M.; Duarte, A. R. C.; Custódio, C. A.; Sher, P.; Neto, A. I.; Pinho, A. C. M.; Fonseca, J.; Reis, R. L.; Mano, J. F., Nanostructured Hollow Tubes Based on Chitosan and Alginate Multilayers. *Advanced Healthcare Materials* **2014,** *3* (3), 433-440.
26. Borges, J.; Caridade, S. G.; Silva, J. M.; Mano, J. F., Unraveling the Effect of the Hydration Level on the Molecular Mobility of Nanolayered Polymeric Systems. *Macromolecular Rapid Communications* **2015,** *36* (4), 405-412.
27. Silva, J. M.; Georgi, N.; Costa, R.; Sher, P.; Reis, R. L.; Van Blitterswijk, C. A.; Karperien, M.; Mano, J. F., Nanostructured 3D Constructs Based on Chitosan and Chondroitin Sulphate Multilayers for Cartilage Tissue Engineering. *Plos One* **2013,** *8* (2).
28. Gaudière, F.; Morin-Grognet, S.; Bidault, L.; Lembré, P.; Pauthe, E.; Vannier, J.-P.; Atmani, H.; Ladam, G.; Labat, B., Genipin-Cross-Linked Layer-by-Layer Assemblies: Biocompatible Microenvironments To Direct Bone Cell Fate. *Biomacromolecules* **2014,** *15* (5), 1602-1611.
29. Neves, S. C.; Moreira Teixeira, L. S.; Moroni, L.; Reis, R. L.; Van Blitterswijk, C. A.; Alves, N. M.; Karperien, M.; Mano, J. F., Chitosan/poly(epsilon-caprolactone) blend scaffolds for cartilage repair. *Biomaterials* **2011,** *32* (4), 1068-79.
30. Sui, W.; Huang, L.; Wang, J.; Bo, Q., Preparation and properties of chitosan chondroitin sulfate complex microcapsules. *Colloids and surfaces. B, Biointerfaces* **2008,** *65* (1), 69-73.
31. (a) Silva, S. S.; Motta, A.; Rodrigues, M. T.; Pinheiro, A. F. M.; Gomes, M. E.; Mano, J. F.; Reis, R. L.; Migliaresi, C., Novel Genipin-Cross-Linked Chitosan/Silk Fibroin Sponges for Cartilage Engineering Strategies. *Biomacromolecules* **2008,** *9* (10), 2764-2774; (b) Mi, F.-L.; Sung, H.-W.; Shyu, S.-S., Synthesis and characterization of a novel chitosan-based network prepared using naturally occurring crosslinker. *Journal of Polymer Science Part A: Polymer Chemistry* **2000,** *38* (15), 2804-2814.
32. Picart, C., Polyelectrolyte multilayer films: from physico-chemical properties to the control of cellular processes. *Current medicinal chemistry* **2008,** *15* (7), 685-97.
33. Picart, C.; Senger, B.; Sengupta, K.; Dubreuil, F.; Fery, A., Measuring mechanical properties of polyelectrolyte multilayer thin films: Novel methods based on AFM and optical techniques. *Colloids and Surfaces A: Physicochemical and Engineering Aspects* **2007,** *303* (1–2), 30-36.
34. Silva, S. S.; Caridade, S. G.; Mano, J. F.; Reis, R. L., Effect of crosslinking in chitosan/aloe vera-based membranes for biomedical applications. *Carbohydrate Polymers* **2013,** *98* (1), 581-588.

35. Schneider, A.; Francius, G.; Obeid, R.; Schwinte, P.; Hemmerle, J.; Frisch, B.; Schaaf, P.; Voegel, J. C.; Senger, B.; Picart, C., Polyelectrolyte multilayers with a tunable Young's modulus: influence of film stiffness on cell adhesion. *Langmuir* **2006,** *22* (3), 1193-200.
36. (a) Bellini, M. Z.; Pires, A. L. R.; Vasconcelos, M. O.; Moraes, Â. M., Comparison of the properties of compacted and porous lamellar chitosan–xanthan membranes as dressings and scaffolds for the treatment of skin lesions. *Journal of Applied Polymer Science* **2012,** *125* (S2), E421-E431; (b) De Silva, R. T.; Pasbakhsh, P.; Goh, K. L.; Chai, S.-P.; Ismail, H., Physico-chemical characterisation of chitosan/halloysite composite membranes. *Polymer Testing* **2013,** *32* (2), 265-271; (c) Ma, B.; Qin, A.; Li, X.; Zhao, X.; He, C., Structure and properties of chitin whisker reinforced chitosan membranes. *International journal of biological macromolecules* **2014,** *64*, 341-346; (d) Costa, R. R.; Costa, A. M. S.; Caridade, S. G.; Mano, J. F., Compact Saloplastic Membranes of Natural Polysaccharides for Soft Tissue Engineering. *Chem Mater* **2015,** *27* (21), 7490-7502.
37. Behl, M.; Lendlein, A., Shape-memory polymers. *Materials Today* **2007,** *10* (4), 20-28.
38. (a) Mohr, R.; Kratz, K.; Weigel, T.; Lucka-Gabor, M.; Moneke, M.; Lendlein, A., Initiation of shape-memory effect by inductive heating of magnetic nanoparticles in thermoplastic polymers. *P Natl Acad Sci USA* **2006,** *103* (10), 3540-3545; (b) Lendlein, A.; Jiang, H.; Junger, O.; Langer, R., Light-induced shape-memory polymers. *Nature* **2005,** *434* (7035), 879-882; (c) Lendlein, A.; Langer, R., Biodegradable, Elastic Shape-Memory Polymers for Potential Biomedical Applications. *Science* **2002,** *296* (5573), 1673-1676.
39. (a) Silva, J. M.; Caridade, S. G.; Reis, R. L.; Mano, J. o. F., Polysaccharide-based freestanding multilayered membranes exhibiting reversible switchable properties. *Soft Matter* **2016,** *12* (4), 1200-09; (b) Gil, S.; Silva, J. M.; Mano, J. F., Magnetically Multilayer Polysaccharide Membranes for Biomedical Applications. *ACS Biomaterials Science & Engineering* **2015,** *1* (10), 1016-1025; (c) Correia, C. O.; Caridade, S. G.; Mano, J. F., Chitosan membranes exhibiting shape memory capability by the action of controlled hydration. *Polymers* **2014,** *6* (4), 1178-1186.
40. (a) Hillberg, A. L.; Holmes, C. A.; Tabrizian, M., Effect of genipin cross-linking on the cellular adhesion properties of layer-by-layer assembled polyelectrolyte films. *Biomaterials* **2009,** *30* (27), 4463-4470; (b) Chen, Y.-S.; Chang, J.-Y.; Cheng, C.-Y.; Tsai, F.-J.; Yao, C.-H.; Liu, B.-S., An in vivo evaluation of a biodegradable genipin-cross-linked gelatin peripheral nerve guide conduit material. *Biomaterials* **2005,** *26* (18), 3911-3918.
41. Silva, J. M.; Caridade, S. G.; Oliveira, N. M.; Reis, R. L.; Mano, J. o. F., Chitosan?alginate multilayered films with gradients of physicochemical cues. *Journal of Materials Chemistry B* **2015,** *3* (22), 4555-4568.
42. Chiono, V.; Pulieri, E.; Vozzi, G.; Ciardelli, G.; Ahluwalia, A.; Giusti, P., Genipin-crosslinked chitosan/gelatin blends for biomedical applications. *J Mater Sci: Mater Med* **2008,** *19* (2), 889-898.

VI. Control of Cell Alignment and Morphology by Redesigning ECM-mimetic Nanotopography on Multilayer Membranes[*]

Abstract

Inspired by native extracellular matrix (ECM) together with the multilevel architecture observed in nature, we engineer a material which topography recapitulates topographic features of the ECM and the internal architecture mimics the biological materials organization. The nanopatterned design along the XY plane is combined with a nanostructured organization along the Z axis on freestanding membranes prepared by layer-by-layer deposition of chitosan and chondroitin sulfate. Cellular behavior is monitored using two different mammalian cell lines, fibroblasts (L929) and myoblasts (C2C12), to perceive the response to topography. Viability, proliferation and morphology of L929 are sensitively controlled by topography; also, differentiation of C2C12 into myotubes is influenced by the presence of nanogrooves. This kind of nanopatterned structure has been also associated with strong cellular alignment. To the best of our knowledge, it is the first time that such a straightforward and inexpensive strategy is proposed to produce nanopatterned freestanding multilayer membranes. Controlling cellular alignment plays a critical role in many human tissues, such as muscles, nerves or blood vessels, so these membranes can be potentially useful in specific tissue regeneration strategies.

Keywords: layer-by-layer, polysaccharides, nanogrooved freestanding membranes, cell alignment, C2C12 differentiation

---

[*] This chapter is based on the following publication: Sousa, M. P.; Caridade, S. G.; Mano, J. F., Control of Cell Alignment and Morphology by Redesigning ECM-Mimetic Nanotopography on Multilayer Membranes. *Advanced Healthcare Materials* **2017,** *6* (15), 1601462.

1. Introduction

Directing cellular behavior is essential for different physiological processes and a very important stage of tissue-material interactions. The design of a surface capable of recapitulating features occurring *in vivo* may benefit the development of promising tissue engineering strategies.[1] Native extracellular matrix (ECM) has a unique and complex structure, displaying well-defined features on its topography such as protein fibers, pores, ridges, grooves that can be found at both micro and nanoscale levels.[1b, 2] Tissues like bone or muscle present highly aligned multiscale structures that have inspired the development of nanoengineered material for tissue regeneration applications;[2a] for instance, well-aligned, long and parallel cylinders of collagen type-I are part of the cortical bone structure, being important for its mechanical properties.[3]

Both chemical and topographical surface patterning play a recognized role in the regulation of the cellular behavior, at both micro and nanoscale levels.[4] The mechanisms behind cell response to nanotopographical features are more complex than the ones behind cellular response to microtopography, where cells are of comparable size to the features. In fact, the connection established between each cell and their environment is even observed at the nanoscale length.[1b] The cell surface receptors, particularly integrins, bind to the extracellular ligands and react to extracellular stimuli, including pattern motifs on the material's surface, inducing an intracellular cascade of physical and chemical events, conditioning cell response.[5] In particular, the geometry of topographical nanofeatures direct cells to react in terms of adhesion [6], formation of focal adhesions (FAs) [7], proliferation [8], migration [9], alignment [4a, 10] and differentiation [11]. For example, the surface topography of human cornea basement membrane was reproduced using lithography, inducing elongation and alignment of cells along the grooves.[12] Curiously when changing cell environment parameters like the growth medium, the cells reacted totally differently, suggesting that the patterning effect is also dependent of other environmental factors.[13] It was also found that both shape and alignment of mesenchymal stem cells is dependent on the nanotopographical density of the surface, regulating their function and even osteo- or neurogenesis.[14]

Distinct technologies have permitted the introduction of nanofeatures over the surface of biomaterials, allowing an additional cellular control in medical devices and substrates for cell culturing. Among conventional techniques are colloidal lithography [15], polymer demixing [16] or even phase separation [17], which are usually easier, faster and cheaper than other technologies, but with less control over the geometry.[18] In order to increase this control, techniques such as electron-bean and photolithography [4c, 19] have been extensively reported; however, the high costs associated with the limitation in the chosen raw materials prompt the need of finding alternative nanofabrication technologies.

There exists a present need for a single step process that could surpass some of the drawbacks of the existing technologies. We propose a simple layer-by-layer (LbL) methodology that presents high versatility, precise control over the film construction and ability to process under physiological and ambient conditions.[20] Lithographic techniques were already combined with LbL strategies to generate patterned surfaces [21]; however, the inability to detach the LbL film from the anchored substrate and to create asymmetric membranes increased the need of substrate-free LbL patterned films. Immersing a low-surface free energy substrate sequentially and continuously into polyelectrolytes of opposite charges is possible to obtain a multilayer film that can be easily detached from the underlying substrate. This method was employed before to produce smooth freestanding (FS) membranes.[22]

Unlike other nanofabrication methodologies, LbL allows the incorporation of a wide range of materials, since synthetic to natural polymers [22-23], proteins [24], or even other bioactive molecules [25]. We hypothesize that the sequential deposition of nanolayers of polyelectrolytes during the LbL buildup could adapt to the nanoscale the geometrical features of textured templates, generating multilayer membranes with the replica of the patterns upon detachment. As polysaccharides present structural similarities with natural ECM, have biodegradable properties and are biocompatible [26], chitosan (CHT) and chondroitin sulfate (CS) were chosen in this work as polycation and polyanion, respectively, to produce natural-based nanopatterned FS membranes.

The effect of the nanogrooves on cellular function was investigated by assessing the morphology, elongation, alignment of fibroblasts and myoblasts and differentiation in the case of myoblasts.

2. Materials and Methods

2.1. Materials

Medium molecular weight CHT (*Mw* = 190-310 kDa; degree of deacetylation between 75% and 85%; viscosity between 200 and 800 cps) and CS were purchased as powder from Sigma Aldrich (St Louis, MO, USA). A purification process was applied to CHT, following a recrystallization approach already described elsewhere.[27] Flat FS membranes were obtained using an underlying PP substrate obtained as A4 sheets, at Firmo Papéis e Papelarias S.A. (Portugal), and were used as controls. Compact disks (CDs) were used as the underlying polycarbonate substrate for the nanopatterned FS membranes and were supplied from MITSAI®. Genipin was supplied from Waco Chemicals GmbH (Germany), ethanol from Fisher Chemical (USA) and sodium chloride (NaCl), PBS and dimethyl sulfoxide (DMSO) were purchased from Sigma Aldrich. Lysozyme from chicken egg white (dialyzed, lyophilized, powder, ≈100000 units.mg^{-1}), hyaluronidase from bovine tests (isoelectric point ≈ 5.4), (Type I−S, lyophilized powder, 400− 1000 units.mg^{-1} solid) and sodium azide (NaN_3) were purchased from Sigma-Aldrich. The suppliers of the missing materials and reagents were further indicated.

2.2. Construction of the CHT/CS polyelectrolyte multilayer

QCM-D monitoring (Q-Sense E4 system, Q-Sense AB, Sweden) was used to follow up the formation of the polyelectrolyte multilayer, composed of CHT and CS. Through the excitation of a piezoelectric quartz crystal, the variations of frequency (Δf) and dissipation (ΔD) were monitored during the multilayer construction.[28] The gold coated crystals were used as received, just rinsed several times with distilled water, acetone and ethanol and then dried prior to the experiments. Firstly, a sodium acetate buffer was injected to construct the baseline. Then, the CHT and CS solutions (0.2% (w.v^{-1}) in a sodium acetate buffer, pH=5.5, RT) were introduced into the measurement cell during 10 minutes at a constant flow of 50 mL.min^{-1}. A washing step of 10 minutes was performed between the adsorptions of polyelectrolyte solution, to remove the excess of polymer. Five bilayers composed of CHT and CS were assembled, at room temperature (RT). Besides allowing the measurement of frequency and dissipation changes in hydrated environments, the QCM-D data also enable the estimation of the viscoelastic properties. The Voight-based model was used to assess the thickness estimation.[28] The QTools software (version 3.0.6.213, Q-Sense AB) was chosen to analyze the data. The thickness, the viscosity and the shear modulus of the films were calculated by the best fitting of the QCM-D data regarding the 7th overtone. We assumed a fluid density of 1000 kg.m^{-3}, a fluid viscosity of 0.001 kg.m^{-1}.s^{-1} and a layer density of 1200 kg.m^{-3}.

2.3. Fabrication of the nanopatterned CHT/CS FS membranes

Nanopatterned CHT/CS FS membranes were produced using the LbL methodology. Different underlying substrates were used; flat FS membranes were made using PP substrates and nanopatterned FS membranes using optical media (CDs). The underlying substrate was immersed sequentially in CHT and CS solutions (0.2% (w.v^{-1}) in a sodium acetate buffer, pH=5.5, RT), with 2 washing steps (using sodium acetate buffer, pH=5.5, RT) between each deposition on polymers solution. These immersions were repeated 300 times with the time of immersions of 6 minutes for natural-based polymers and 3 minutes for each washing step. This process was automatized using a home-made dipping robot. Previous to the immersions, these substrates were cleaned with sonication in ethanol and distilled water (5 minutes each). To enhance the mechanical and biological behavior of the FS membranes, the multilayers were subjected to a crosslinking process. Based on previous studies [29], genipin (0.1% (w.v^{-1}) in a 4:1 sodium acetate buffer/DMSO, pH=5.5) was chosen as the crosslinking agent and the FS membranes were immersed in this solution overnight at RT. Absolute ethanol was used to stop the crosslinking reaction. Then the membranes were washed with sodium acetate buffer to remove the excess of crosslinker and left to dry at RT. Finally, both crosslinked and no crosslinked FS membranes were easily detached from the respective underlying substrate, just by peeling off with the help of a tweezer.

2.4. Morphological and physical characterization techniques

2.4.1. SEM

The morphology of the FS membranes was characterized by SEM (NanoSEM, Nova200), at an accelerating voltage of 15kV. Prior to microscopy, the samples were sputter-coated (Cressington) with a conductive gold layer, for 40 seconds at 40 mA. Cross-sections of the FS membranes were obtained through immersion on liquid nitrogen followed by fracturing.

2.4.2. AFM

AFM (Dimension Icon, Bruker, France) equipped with Nanoscope imaging software was used to evaluate in detail the topography of the surface of the membranes. Prior to microscopic observation the samples were rinsed with distilled water and dried at RT. We used an AFM equipped with ScanAsystAir (Bruker, France) probes, with a resonance frequency of 320 kHz and a spring constant of 2 $N.m^{-1}$. The topography of the membranes surface was acquired with a 512 × 512 $pixel^2$ resolution at line rates of 1 Hz, analyzing areas of 5 × 5 μm^2 and 10 x 10 μm^2 at line rates of 1 Hz and used to calculate the arithmetic mean and the average height (R_a and H_{av}, respectively). At least three measurements were performed on replica specimens (n = 3), with different areas on each sample being scanned. Moreover, the topography of the hydrated membranes was also evaluated. In this case we used probes from ScanAsystFluid (Bruker, France).

2.4.3. WCA

Static WCA on the obtained membranes was assessed using an OCA 15+ goniometer (DataPhysics, Germany), under RT, using the sessile drop method. All experiments were carried out using triplicates, with nine areas on each sample being considered. The volume of each droplet was kept at 3 µl and the experiments were performed at RT. The pictures were taken after droplet stabilization.

2.4.4. Mechanical properties – DMA

The mechanical/viscoelastic properties of the FS membranes were evaluated by DMA. All measurements were performed using a Tritec2000B DMA (Triton Technology, UK), equipped with the tensile mode. The membranes were cut with ≈ 8 mm width. Prior to the DMA assays, samples were soaked overnight, in a PBS solution, to reach the swelling equilibrium. The geometry of the samples was then measured accurately for each sample where the thickness was determined in three different regions of each sample using a micrometer (Mitutoyo, Japan). The measurements were carried out at 37°C during which the membranes were immersed in a PBS solution placed in a Teflon® reservoir. Membranes were clamped in the DMA apparatus with a gauge length of 10 mm and immersed in the PBS bath. After equilibration at 37°C, the DMA spectra were obtained during a frequency scan between 0.2 and 20 Hz. The experiments were performed under constant strain amplitude (50 µm) and a static pre-load of 1 N was applied during the tests to keep the sample tight. At least three specimens were tested for each condition with the same experimental settings.

2.4.5. Degradation studies

$[CHT/CS]_{300}$ membranes were placed in PBS, at pH=7.4 (control), and in an enzymatic solution composed by 0.13 $mg.mL^{-1}$ of lysosome and 0.33 $mg.mL^{-1}$ of hyaluronidase in PBS with NaN_3, at pH=7.11; all experiments were put in a shaking water bath at 37 °C. The medium was replaced every 3 days and at predetermined time points (3, 7, 14 and 30 days), the membranes were removed from the solutions and washed with distilled water to remove the excess of salts. Then, the membranes were dried at constant temperature and weighted. The percentage of weight loss (WL) of the membranes for the different conditions was determined following Equation VI.1, with W_i being the initial dry weight of the membrane and W_f being the weight of the dry membrane after each predetermined time point. Thus, the percentage of weight retaining (WR) was calculated using Equation VI.2, with the values obtained in Equation VI.1.

$$WL\ (\%) = \frac{w_i - w_f}{w_i} \times 100 \qquad \text{Equation VI.1}$$

$$WR(\%) = 100 - WL \qquad \text{Equation VI.2}$$

2.5. Cell seeding preparation and cell culture

Two mammalian cell lines, L929 fibroblasts and C2C12 myoblasts (European Collection of Cell Cultures (ECCC), UK), were chosen to test the developed FS membranes, with and without patterning. Prior to cell culture, the membranes were subjected to a sterilization process with 70 % (v.v^{-1}) ethanol, for 2 hours, and then removed and washed with sterile PBS. Three experiments were conducted for each condition and assay, with triplicates.

2.5.1. L929 fibroblast line

Murine L929 fibroblasts were chosen to investigate the differences between the obtained FS membranes in terms of cellular viability and metabolic activity, proliferation, morphology and alignment. L929 cells were maintained in Dulbecco's modified Eagle's medium (DMEM, Sigma-Aldrich) supplemented with 10% fetal bovine serum (FBS, Biochrom AG, Germany) and 1% of antibiotic/antimycotic (Sigma-Aldrich), at 37°C and 5% CO_2. When the confluence was reached, the cells, at passage 15 to 18, were trypsinized, centrifuged and re-suspended in cell culture medium. Then the fibroblasts were seeded at 2.5 x 10^4 cells per cm^2 under static conditions in aliquots of 200 µl, on the top of the FS membranes. After 4 hours, 800 µl of growth culture medium were added to each well. The fibroblast seeded membranes were nourished with fresh growth medium every 2 days and maintained at 37°C and 5% CO_2 until the end of each experiment.

L929 viability and proliferation

The metabolic activity and viability of the fibroblasts seeded on the FS membranes were assessed via a MTS assay. At each time point (1, 3 and 7 days) the culture medium was removed and replaced with 500 µl of serum-free DMEM with 20% of MTS reagent (Promega, USA). Then the cell seeded samples were incubated during 3 hours, at 37°C and 5% CO_2. The absorbance was measured with a microplate reader (BioTek, USA), at a wavelength of 490 nm. The negative control was considered as the background absorbance of serum-free medium and MTS reagent incubated with the FS membranes without cells. Fibroblasts relative viability was considered comparing the FS membranes results with TCPS (3D Biomatrix, USA).

A fluorometric double strand DNA (dsDNA) quantification kit (PicoGreen®, Molecular Probes, Invitrogen, UK) was used to evaluate the proliferation of cells seeded on the FS membranes. After each predetermined time-point (1, 3 and 7 days) the samples were washed with sterile PBS, transferred into eppendorfs containing 1 mL of ultra-pure and put at 37 °C for 1 hour. Then, the samples were relocated in a -80 °C freezer until using; before testing, the membranes were thawed and sonicated during 15 minutes. DNA standards ranging from 0 to 1.5 mg.mL^{-1} were prepared. The PicoGreen® working solution was incubated with each sample and standard for 10 minutes, in the dark at RT. A microplate reader (BioTek, USA) was used to measure the fluorescence, with an excitation wavelength of 485/20 nm and an emission wavelength of 528/20 nm. The fluorescence values were corrected for the fluorescence of the reagent blanks. The concentration of DNA was calculated against a standard curve obtained by the prepared DNA standards.

L929 Morphology

Fluorescent microscopy was used to observe the morphology of the adherent cells on the FS membranes. For 1, 3 and 7 days the fibroblast seeded membranes were washed with PBS and fixed with 10% formalin (Termo Fisher Scientific, USA) in PBS solution; after 30 minutes the cells were permeabilized using 0.2 % (v.v^{-1}) of Triton 100x (Sigma Aldrich) in PBS, for 5 minutes, and the non-specific binding sites were blocked using 3%(w.v^{-1}) BSA (Sigma Aldrich) in PBS, for 30 minutes. After this time fluorescein phalloidin (Sigma-Aldrich) at 1:150 in PBS, pH=7.4, was used to stain the F-actin of the cells and DAPI (Sigma-Aldrich) at 1:1000 in PBS, pH=7.4 to stain the nucleus of the cells. Between each stage three washing steps were performed using sterile PBS. Fluorescence microscopy were imaged using a transmitted and reflected light microscope with apotome 2 (Axio Imager Z1m, Zeiss, Germany). The photos were acquired and processed with the AxioVision software version: Zeiss2012 (Zeiss). The chosen micrographs were representative for each time point and condition.

SEM was also used to observe the morphology of the fibroblasts cultured on the FS membranes. After being cultured for 1, 3 and 7 days the adherent cells on the FS membranes were washed with sterile PBS and then fixed with 2.5% glutaraldehyde (Sigma Aldrich) in PBS at 4°C. After 30 minutes, the fixation solution was removed, and the cells were washed with sterile PBS three times; a dehydration process was applied to cell seeded membranes, following a series of graded ethanol solutions (20, 50, 80, 90, 95, 100 % (v.v^{-1})). The samples were left to dry at constant temperature and then were gold sputter-coated in vacuum prior to observe at SEM (NanoSEM, Nova200); an accelerating voltage of 15kV was used.

Nuclei elongation and orientation

The orientation analysis of the nucleus of individual cells adhered on CL FS membranes was assessed from fluorescent images. We used an image processing software (Image J®, National Institutes of Health, Bethesda, MD, USA) to define the boundary of the nuclei, in order to determine the orientation of the nucleus of the individual cells relative to the preferential direction (assumed as the patterning direction). Nuclei included for analysis had to be fully contained within the border of the image. The nuclei EF was obtained by dividing the longest nucleus axis by the maximal length perpendicular to this long axis. The orientation of the nuclei was based on the angle between the major axis of the object and the long axis of the underlying topography (defined as 0°). Nuclei were considered aligned for an orientation angle between 10° and -10°. Five images were analyzed for each condition. Representative fluorescent images of the nuclei of the cells were presented for each condition.

Morphometric parameters

Cells area, perimeter and EF were parameters evaluated using the software Image J® and were determined after 3 days of culture. The cell EF corresponds to the longest cell axis divided by the maximal length perpendicular to this long axis. The alignment was determined using information obtained by SEM, where images shown both the cells adhered on the membranes and the nanopatterning; the patterning orientation was rotated to be equal to 0°. Additionally, also the cells angle distribution was determined using the Image J® software analyzing 5 images per condition, relatively to the day 3 of culture (where cells were suitably grown and dispersed to measure these parameters).

2.5.2. C2C12 myoblast line

Murine C2C12 myoblasts were chosen to investigate the influence of the patterning on cell differentiation. C2C12 cells were maintained in DMEM supplemented with 10% FBS and 1% of antibiotic/antimycotic (Sigma-Aldrich), at 37°C and 5% CO_2. When the confluence was reached, the cells, at passage 6 to 8, were trypsinized, centrifuged and re-suspended in cell culture medium. Then the myoblasts were seeded at 2.0 x 10^4 cells per cm^2 under static conditions in aliquots of 200 µl, on the top of the FS membranes. After 4 hours, 800 µl of growth culture medium were added to each well. The myoblasts seeded membranes were nourished with fresh growth medium every 2 days and maintained at 37°C and 5% CO_2 until the end of each experiment.

C2C12 Morphology

Fluorescent microscopy was used, as already described for the case of studies involving L929 cells, to observe the morphology of the myoblasts seeded on the FS membranes. For 1, 3, 5 and 10 days the cell seeded membranes were washed with sterile PBS and fixed with 10% formalin in PBS solution; the same procedure described for phalloidin/DAPI staining of L929 cells was employed for imaging both C2C12 cytoskeleton and nucleus. The chosen micrographs were representative for each time point and condition.

SEM was also used to observe the morphology of the myoblasts cultured on the FS membranes. Again, the protocol used for L929 cells observation was repeated, but for different time points (4 hours, 3 days and 7 days).

Additionally, after 5 days of culture adherent cells were labelled with an immunofluorescence antibody to vinculin (Abcam®, UK). Basically, cell seeded membranes were fixed with formalin 10%, permeabilized with 1% triton for 5 minutes and the non-specific binding sites were blocked with 3% of BSA for 1 hour. The samples were incubated at 4°C overnight with the primary antibody vinculin (1:400 in PBS) and then incubated with secondary donkey antibody anti-mouse Alexa Fluor 488 (Invitrogen™, USA) (1:1000 in PBS) during 1 hour at RT, in the dark. Finally, the cells were incubated with DAPI (1:1000 in PBS) at RT for 15 minutes. Prior to fluorescence microscopy, the samples were washed several times, and left in PBS overnight. Microscopic images were obtained using the transmitted and reflected light microscope with apotome 2.

Myogenic Differentiation

To induce differentiation, the growth medium was replaced by differentiation medium (DM), after achieving 60% to 80% of C2C12 confluence. This medium was composed by DMEM supplemented with 2% of horse serum (Invitrogen ™) and 1% of antibiotic/antimycotic and was replaced every two days. Differentiation was also evaluated without using differentiation medium; instead the culture was maintained with growth medium (GM). Differentiation was evaluated for both conditions, using DM and GM, for 7 and 10 days of culture. At these time points, the samples were washed with sterile PBS and fixed with 10% of formalin. After 30 minutes, cell seeded FS membranes were washed 3 times and then permeabilized with 1% of triton in PBS for 5 minutes and the non-specific binding was blocked with 3% of BSA in PBS for 1 hour. Between each step the samples were washed 3 times with PBS. For immunofluorescence imaging the cells were incubated with the primary antibody troponin T (Acris Antibodies, Inc®, Germany), overnight at 4 °C, and then with the secondary goat antibody anti-mouse Alexa Fluor 488 (Invitrogen ™) for 1 hour at RT and in the dark. Finally, to stain the nuclei, the cells were incubated with DAPI for 15 minutes at RT and in the dark. Between each step, samples were extensively washed with PBS, with the help of an orbital shaker plate.

Morphometric parameters

Different differentiation parameters were also quantified using Image J®. The fusion index (in percentage) is defined as the relation between the number of nuclei within troponin T-positive myotubes and the total number of nuclei in a pre-established area. To complete this information, the average number of troponin T-positive myotubes for the same pre-established area was calculated.[30] Also the averaged area of the troponin-myotubes were determined.[31] At least five images were used for quantitative analysis.

The alignment of the myotubes were quantified using Image J® software. We hypothesized that the visual and preferential orientation of the myotubes matched with the patterning direction; five images were analyzed for each condition at the third day of culture.

2.6. Statistical analysis

All values were expressed as mean ± standard deviation. Comparison between 2 groups were obtained using one-way analysis of variance (ANOVA). Multiple comparison of more than 2 groups were made using one-way ANOVA followed by Bonferroni's multiple comparison test. Any exception to this procedure was referred on the appropriated section. A level of $p \leq 0.05$ was considered as statistically significant, being the statistical analysis performed through GraphPad Prism 6.0 (GraphPad Software Inc.).

3. Results and discussion

3.1. Polyelectrolyte multilayers construction

Quartz Crystal Microbalance with Dissipation (QCM-D) was used to monitor the variations on the deposition of the polyelectrolytes and the thickness of the film along the time - see Figure S VI-1A. As expected, frequency variation (Δf) decreased with the injection of CHT and CS, and with the increasing number of layers; this confirmed that the polyelectrolytes mass was deposited on the surface of the gold piezoelectric crystal. A slight increase in Δf was observed for the washing steps, which corresponds to the desorption of the excess of polyelectrolyte mass. In the other hand, dissipation variation (ΔD) increased with the consecutive injections of CHT and CS, evidencing the viscoelastic nature of the deposited polymers. A Voigt model was used to fit the QCM-D data and to estimate the thickness variation as a function of the number of deposited layers - see Figure S VI-1B. The results showed a linear growth of the polyelectrolyte multilayer film ($R^2 = 0.974$), composed by CHT and CS layers, being an indication that the polymers were adsorb along the multilayer during the depositions, contrarily to other systems already described in literature.[32]

Based on the same model and parameters used to obtain the thickness, parameters like viscosity and shear modulus were also estimated - see Figure S VI-1C and S VI-1D, respectively. These two parameters increased along the buildup of the film, which can be related with the viscoelastic behavior of the film.[28, 33] Fitting parameters like shear modulus, viscosity and thickness gave important continuous data on multilayer film construction.

3.2. Fabrication of nanopatterned FS films

Flat and nanopatterned membranes were produced by repeating 300 times the cyclic depositions on CHT and CS solutions, using appropriate templates. The underlying substrates selected to produce flat and nanopatterned membranes were polypropylene (PP) sheets and optical media material, respectively. The membranes were further crosslinked with genipin, to improve their mechanical and biological performance. After drying, both crosslinked and non-crosslinked membranes were easily detached from the underlying substrates, with the help of a tweezer. In the end, four formulations were designed: flat FS ($[CHT/CS]_{300}$), flat crosslinked FS (CL $[CHT/CS]_{300}$), nanopatterned FS (PAT $[CHT/CS]_{300}$) and nanopatterned crosslinked FS (PAT CL $[CHT/CS]_{300}$).

3.3. Morphological, topographical and physical characterization of the FS membranes

3.3.1. Morphology

The FS $[CHT/CS]_{300}$ films were detachable, without visible damages, from the respective underlying substrates. Figures VI-1A and VI-1B represent Scanning Electron Microscopy (SEM) micrographs of uncrosslinked and crosslinked flat FS membranes. Prior the crosslinking step, the membranes presented a homogeneous morphology with visible rough structures in the order of 1-2 µm. Crosslinked membranes showed a non-homogeneous morphology, with large and lower roughness areas randomly dispersed along the surface. The recordable part of the optical media presents nanofeatures on their surface.[34] We investigated the presence of this kind of topography on commercial blank optical media. The polycarbonate template used to create the nanotopography showed regular nanostructured stripes (width around 637 ± 36.1 nm) - see Figure VI-1C. The depth of the nanogrooves presented on the surface of the polycarbonate template was also calculated through SEM imaging - see Figure VI-1D; just by tilting the surface at 60° we were able to estimate the depth of the grooves (depth around 244 ± 16.2 nm). The LbL methodology was applied above these substrates trying to mimic their topographical features. It was possible to confirm the presence of a nanogrooved topography on the surface of both uncrosslinked and crosslinked FS patterned CHT/CS membrane - see Figures VI-1E and VI-1F, respectively. The results prove that the geometrical features of the polycarbonate template were successfully replicated on the FS membranes. The existence of the groove in the Z axis was confirmed by leaning the samples to 60°; Figure VI-1G clearly shows a depth on the stripe structures. Therefore, by using daily-used objects, such as optical media, we propose a pioneering and unconventional nanofabrication strategy, by transposing the defined nanoscale geometries of such simple substrates onto FS membranes. Anene-Nzelu, C.G. [34] had previously described the use of optical media as substrates for cellular alignment, controlling cells morphology and differentiation through its ordered nanotopography; however, polycarbonate can promote some problems in bio-integration. So far, for the best of our knowledge is the first time that such multifaceted technology is used to fabricate, through the repetition of a single step, ordered nanopatterned membranes.

Differences were found in the cross-section between flat and nanopatterned FS membranes – see Figures VI-1H and VI-1I, respectively. Flat membranes were considerably thicker (40.4 ± 0.93 µm) than nanopatterned membranes (9.9 ± 0.21 µm), with the same number of bilayers. Such differences can be related with the established interactions between the underlying substrate and the polyelectrolytes. Estimated thickness obtained using QCM-D data shows a linear growth of the film, so if a 300-bilayer film was constructed, it should be obtained a FS membrane with the thickness around 7.6 µm. Comparing the estimated thickness with real thicknesses, we can conclude that polyelectrolytes interactions with polycarbonate template is closest to those with the gold piezoelectric crystal.

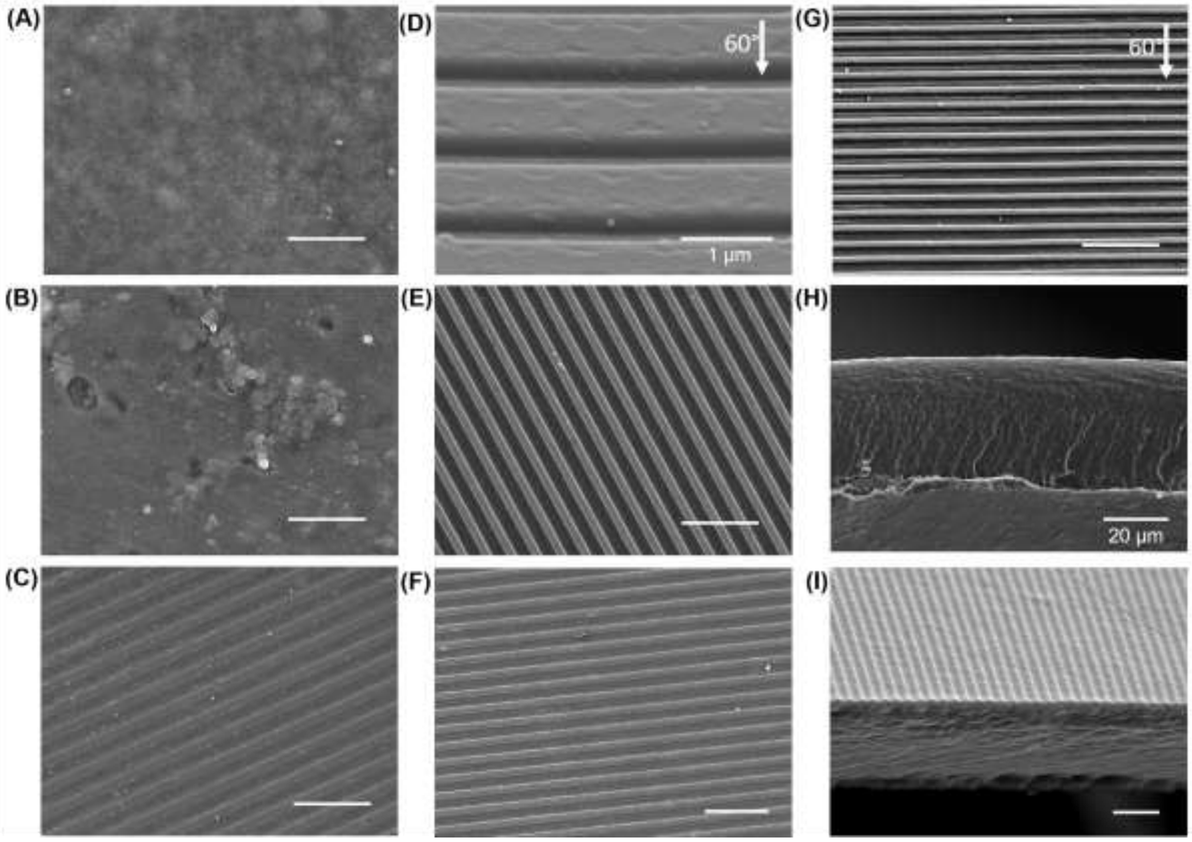

Figure VI-1. Representative SEM images of A) $[CHT/CS]_{300}$, B) CL $[CHT/CS]_{300}$, C) top-view and D) tilted view (60°) of optical media used as the patterned substrate used to produce the patterned (PAT) membranes, E) PAT $[CHT/CS]_{300}$, F) PAT CL $[CHT/CS]_{300}$ and G) PAT CL $[CHT/CS]_{300}$ tilted at 60°. SEM images of the cross-sections of H) $[CHT/CS]_{300}$ and I) PAT $[CHT/CS]_{300}$ membranes. The scale bars represent 5 µm unless for the image where it appears with the value.

3.3.2. Topography

The studies of the topography of different human tissues, like heart, nerve or muscle, have been useful for understanding the threshold of the patterns dimensions capable to influence the cellular response. For instance, materials nanoimprinted with depth of 200 nm and width of 500 nm were developed and the interactions between neuron cells and these nanograftings promoted both neurite alignment [35] and bipolarity [36]. Nanogrooved substrates with 450 nm in groove/ridge width; 100 or even 350 nm in depth regulated the orientation of cardiomyocytes and their contractile function.[37] As discussed below, our methodology provided such kind of dimensions, but using a quite simple methodology, providing the ability to use natural based polymers, employing wet based fabrication technologies.

Firstly, uncrosslinked and crosslinked flat FS membranes were analyzed with Atomic Force Microscopy (AFM) imaging - see Figure VI-2A and VI-2B respectively. Both presented some rough structures in the order of about 30 nm. Also, the topography of the uncrosslinked and crosslinked nanopatterned FS films was investigated. AFM imaging confirmed the good reproducibility of the nanopatterning, always with structures consistent with the patterning of the polycarbonate template - see Figure VI-2C and VI-2D, respectively. Besides the presence of the sub-micron patterning, the topography of these surfaces also presented rough areas, at the nanometer scale. AFM was also performed with wet samples, in order to conclude about the stability of the patterning in a hydrated environment. As observed in Figure VI-2E and VI-2F, even after the incubation in phosphate buffered saline (PBS) overnight, the uncrosslinked and crosslinked nanopatterned surfaces maintained the nanogrooved topography. To conclude about the stability of patterning, we also left the membranes immersed in the PBS solution for longer times and even after 14 days we verify the maintenance of the patterning. This information will be further supported by the SEM images of the cells above the patterned freestanding membranes.

Figure VI-2G shows the arithmetic roughness (R_a) and the average height (H_{av}) values for all type of developed FS membranes. No substantially changes were observed with the crosslinking step, but the R_a value was slightly lower for the PAT CL $[CHT/CS]_{300}$ when comparing with the unmodified nanopatterned ones; this can be related with the swelling and contraction of the upper layer. Naturally, crosslinked and non-crosslinked PAT $[CHT/CS]_{300}$ presented significantly higher values of H_{av} due to the presence of the nanogrooves on their surface; indeed, the uncrosslinked patterned membranes clearly exhibited the highest value and this fact also can be related with the swelling process.

Some differences were expected when hydrating the membranes, due to their ability to retain water.[38] Figure VI-2H shows distinct relevant dimensions of the pattern features calculated through the AFM image data. The averaged ridge width ($\mathrm{RW_{av}}$) in the FS films was similar between the different conditions, being around 500 nm. The averaged groove width ($\mathrm{GW_{av}}$) was different, following what happened with the averaged depth ($\mathrm{D_{av}}$) values: for PAT $[CHT/CS]_{300}$ membranes, the $\mathrm{GW_{av}}$ significantly decreased from 820.4 ± 40.7 nm (dry state) to 687.4 ± 64.1 nm (hydrated PAT $[CHT/CS]_{300}$). No significant differences in the $\mathrm{GW_{av}}$ were found between hydrated PAT CL $[CHT/CS]_{300}$ membranes and dried PAT CL $[CHT/CS]_{300}$; the crosslinking reaction allowed lower water contents in their composition and thus fewer differences were noticed in the $\mathrm{GW_{av}}$. The D_{av} of the crosslinked and uncrosslinked FS membranes significantly increased when the samples were hydrated; in the case of PAT CL $[CHT/CS]_{300}$ the D_{av} significantly increased from 208.3 ± 38.36 nm (dry state) to 449.4 ± 50.01 nm (wet state). Curiously, in the hydrated state, crosslinked membranes had higher values of depth than in the dry state. This is an indication that when hydrated, the topography of the PAT CL $[CHT/CS]_{300}$ membranes did not deform significantly along the XY plane, but this changing essentially happened in the Z plane.

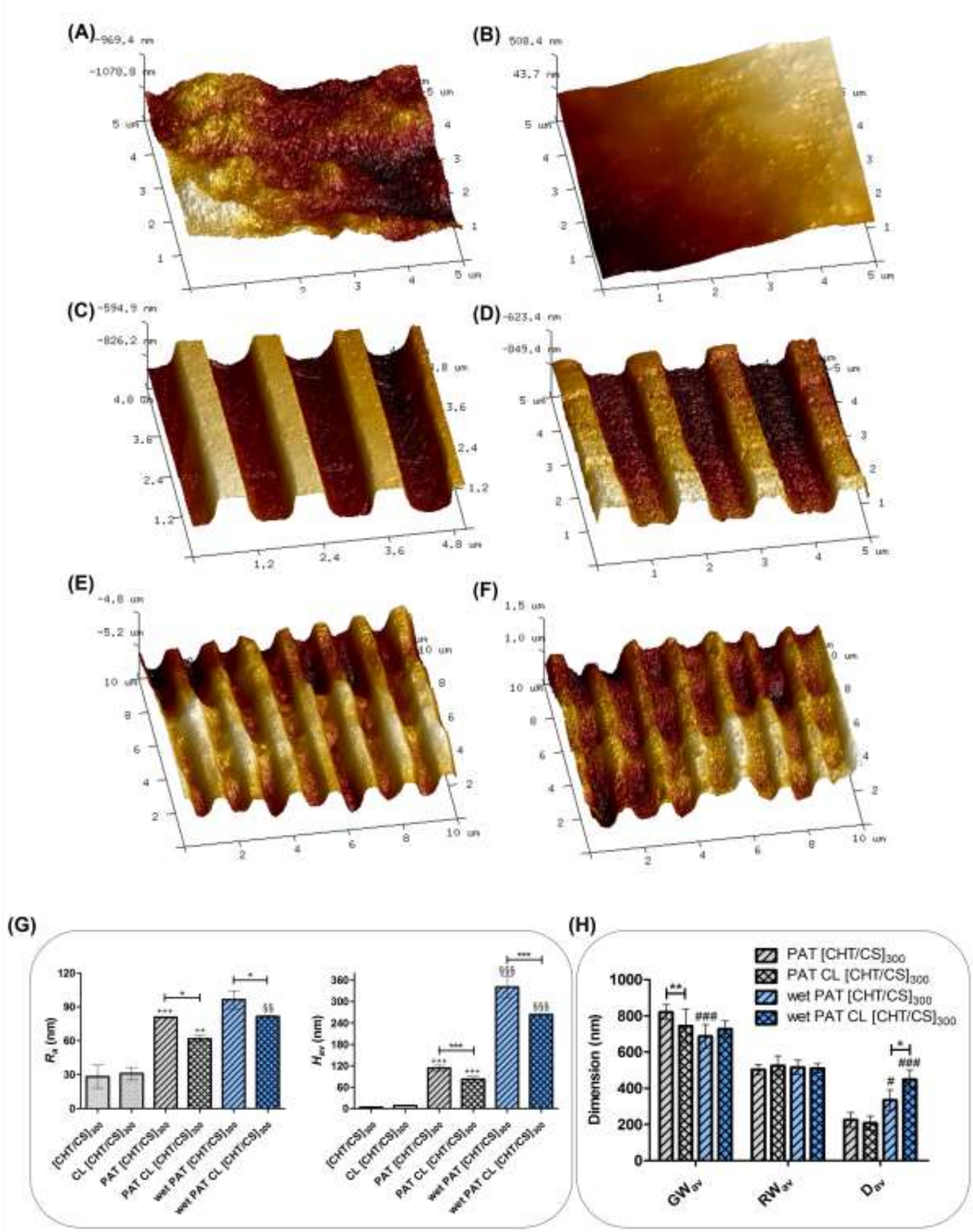

Figure VI-2. Representative AFM images of A) $[CHT/CS]_{300}$, B) CL $[CHT/CS]_{300}$, C) PAT $[CHT/CS]_{300}$, D) PAT CL $[CHT/CS]_{300}$ topographies in air, E) PAT $[CHT/CS]_{300}$ and F) PAT CL $[CHT/CS]_{300}$ in fluid. G) Arithmetic roughness (Ra) and average height value (Hav) for flat and patterned surfaces. H) Averaged dimensions of the nanofeatures, with the values for groove (GWav) and ridge (RWav) widths and the depth (Dav) for the different membranes in both dry (air) or wet (PBS) states. Significant differences for the patterning effect were found for (++) $p<0.01$ and (+++) $p<0.001$ and for the crosslink effect were found for (*) $p<0.01$ and (***) $p<0.001$. Significant differences between dry and wet states were found for (§§) $p<0.01$ and (§§§) $p<0.001$.

3.3.3. Water Contact Angle (WCA)

Wettability plays an important role in material-cell interactions;[39] it can depend on both chemical composition and topography of the surface. The WCA of the produced films are shown in Figure S VI-2A and VI-S2B. The crosslinking effect on the WCA was evident on flat CHT/CS membranes, with a significant increase on the hydrophilicity. The derivate of the crosslinking reaction is rich in hydrophilic groups, like amines, amides and hydroxyl groups;[40] indeed this result was consistent with some works in literature which reported the effect of genipin crosslinking in the decrease of the WCA, for hydrogels [41], capsules [40a] and also for multilayer films [42]. Significant differences were observed between flat and patterned membranes, for non-CL membranes (WCA = 107 ± 7.7°and WCA= 119 ± 3.1°, respectively) and for CL membranes (WCA = 74 ± 7.9°and WCA= 111 ± 1.3°, respectively). Therefore, the presence of a nanopatterned topography on the CHT/CS membranes enhanced the hydrophobicity of the surface, comparing with the flat ones. The explanation of this phenomenon is based on the Cassie-Baxter [43] regime that assumes that there is no penetration of the water droplets into the grooves, establishing a composite interface between the solid/air and the liquid droplet. In this case, if roughness increases, also the hydrophobicity of the surface will be higher, with higher WCA values. The effect of crosslinking was not significant in the case of patterned membranes, and we hypothesized that the crosslinking effect was masked by the patterning effect. Our results indicate that at this stage, surface topography prevented the decrease on WCA, that would be expectable by the introduction of hydrophilic groups. Similar competitive forces between hydrophilic surface groups and surface topography were already reported elsewhere. [44]

These results indicate that after an initial increase in hydrophobicity of glass surface with zeolite coverage, hydrophilic groups prevent the continuous increase in water contact angle with increasing zeolite density. In other words, the reason of the difference in the water contact angle values along the gradient surface can be attributed to the competitive effects between hydrophilic surface groups on zeolites and surface roughness.

3.3.4. Mechanical characterization of FS membranes

Dynamic Mechanical Analysis (DMA) experiments were performed to evaluate the mechanical/viscoelastic properties of the FS membranes. Mechanical studies are a vital part of the membranes characterization, as literature has been reported their determinant role on cellular phenotype and differentiation [45]. The variation of the storage (elastic) modulus (*E'*) along the frequency is presented in Figure S VI-3A. Overall, for all the studied FS membranes, *E'* slightly increases with frequency as already reported by other works.[46] Comparing the uncrosslinked membranes, it was observed that the curves of the graph were superimposed; thus, there are not significant differences in their *E'* values: 1.1 ± 0.40 MPa and 1.3 ± 0.32 MPa at 1 Hz, for unpatterned and patterned FS membranes, respectively. The same behavior was observed in the case of the crosslinked membranes where no significant differences could be found. However, significant differences were found between crosslinked and uncrosslinked membranes, with *E'* values of the crosslinked FS membranes (4.3 ± 0.84 MPa and 4.4 ± 0.67 MPa at 1 Hz, for unpatterned and patterned crosslinked FS membranes, respectively) being higher than *E'* values of the uncrosslinked ones. Such results are consistent with previous works that reported an increase in stiffness when membranes were submitted to a crosslinked reaction.[29, 42, 46a] These results also indicate that the presence of the patterning or the polymeric nature of the template on both uncrosslinked and crosslinked FS membranes have not influence on the stiffness of the samples.

The variation of the loss factor (tan δ) along the frequency is presented in Figure S VI-3B. The tan δ is the ratio of the amount of energy dissipated by viscous mechanisms relative to energy stored in the elastic component providing information about the damping properties of the membranes. For all membranes, it was observed that tan δ slightly increased with the frequency, but no signs of the presence of relaxation processes could be detected. Moreover, the uncrosslinked FS membranes presented higher dissipative properties, mainly at the higher frequencies.[47]

3.3.5. Degradation behaviour monitoring of FS membranes

Both degradability and stability are important parameters in implantable scaffolds. Among other components, human serum presents enzymes capable to degrade biopolymers;[48] thus our developed membranes composed by CHT and CS can have interesting biodegradable properties. To understand the degradability of flat and nanopatterned CHT/CS, non-crosslinked and crosslinked, their weight loss was investigated, by immersing them in suitable enzymatic solutions. Lysozyme [49] and hyaluronidase [50] are enzymes capable to degrade natural polymers as CHT and CS once they are presented in the human serum at different concentrations. The degradation phenomenon could be noted through the decrease in the film thickness, as already reported in literature for comparable systems.[51] No substantial differences were observed in the weight loss profile between flat and patterned membranes - see Figure S VI-4; nevertheless, the crosslink effect on the degradability and stability of the FS films was evident. The enzymatic degradation is retarded when the FS films were crosslinked. In fact, there are already some studies indicating the decrease of degradation rates for CL films and consequently the capability to use this strategy to control the material degradation.[51a, 52] Note that weight loss is also observed using just PBS solution, but it was accelerated with the presence of the enzymes. Looking deeper at Figure S VI-4, it is possible to observe that most degradation occurs within the first 3 days of immersion; water molecules diffused into the bulk of the FS membranes, weakening their structure and thus enhancing the degradation. After 7 days of immersion the rate of degradation decreases significantly for FS membranes. The crosslinking effect can be used to control the degradation and thus the FS membranes characteristics may be adapted to the therapeutic specifications.

3.4. L929 cellular response

3.4.1. L929 viability and proliferation

We investigated the influence of the crosslinking and patterning in the FS membranes on the behavior of L929 cells. Figure VI-3A shows the results of a (3-(4,5-dimethylthiazol-2-yl)-5-(3-carboxymethoxyphenyl)-2-(4-sulfophenyl)-2H-tetrazolium) (MTS) assay, used to assess the mitochondrial redox activity. One assumes that higher values of metabolic activity correspond to higher cellular viability. Differences between the non-crosslinked and crosslinked membranes became evident for day 3 and even more for day 7 of culture. In those time points, it was clearly observed higher values of cellular metabolic activity on crosslinked membranes. DNA quantification assay was used to complement these results and to have a measure of cell proliferation (see Figure VI-3B). Regarding the differences between non-crosslinked and crosslinked membranes, DNA quantification supported the results of MTS assay: in day 3 and day 7 of culture the crosslinked membranes induced significantly more proliferation. This fact matched with literature that has reported the positive effect of genipin on enhancing the cellular adhesion, viability and proliferation.[29, 38, 41] These works suggested that substrate stiffness increases when crosslinked with genipin, decreasing the water content and increasing the protein adsorption and resulting in improved cellular behavior. In fact, the mechanical properties of the membranes are also an important parameter to tailor the cellular behavior, and the crosslinking step with genipin seemed essential to increase the stiffness of the polysaccharide multilayer membranes and thus to enhance their biological performance, without compromising the non-cytotoxicity of the material. It can be said that the crosslinking effect on cell viability and proliferation followed the same trend along the days of culture but the same cannot be said for the effect of the topography. For day 7 of culture, the PAT CL $[CHT/CS]_{300}$ presented slightly higher DNA content and metabolic activity than flat CL $[CHT/CS]_{300}$ membranes while for uncrosslinked PAT $[CHT/CS]_{300}$ the DNA content and metabolic activity were slightly lower than for flat $[CHT/CS]_{300}$. We hypothesized that for CL membranes, the effect of genipin crosslinking overlapped the effect of topography. Literature [6, 53] reported the increasing number of filapodia and elongated cells when in presence of a nanogrooved surface, but this may not necessarily correspond to an increase in proliferation; other properties of the nanopatterned membranes can also play a role, such as surface chemistry, wettability or even stiffness. The influence of the presence of topography at nanoscale length on cellular proliferation can also depend on the cell type.[6, 54]

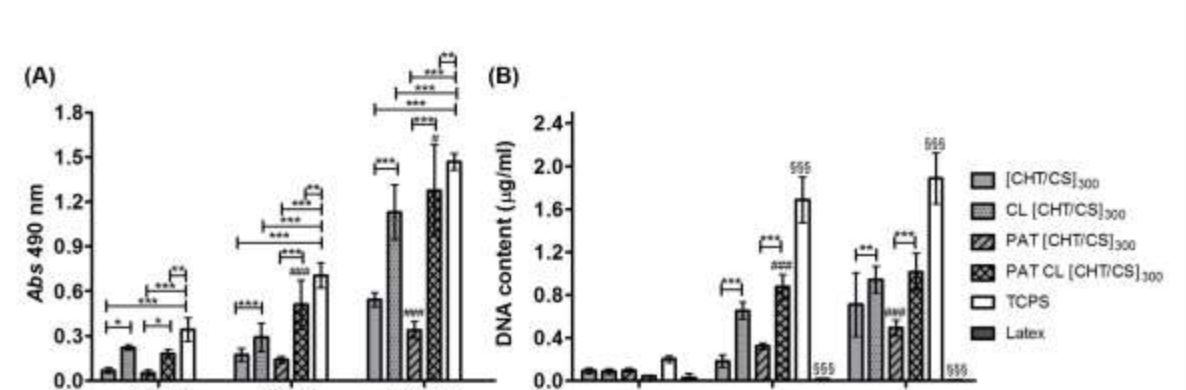

Figure VI-3. A) cellular viability through the absorbance of the metabolic activity of L929 cells (MTS assay) in function of culturing time and B) cellular proliferation through the determination of the DNA content (DNA quantification assay) in function of culturing time. Significant differences for the crosslink effect were found for (***) $p < 0.001$, (**) $p < 0.01$ and (*) $p < 0.05$. Significant differences for the patterning effect were found for (###) $p<0.001$ and (#) $p<0.05$. Significant differences were found for (***) $p < 0.001$ and (**) $p < 0.01$ with TCPS and for (§§§) $p < 0.001$ with latex.

3.4.2. L929 morphology

A sparser density was chosen to culture fibroblasts, to avoid cell-cell contacts and to evidence the effect of topography on the morphology of individual cells. Fibroblasts were fixed and then stained to observe their nucleus and cytoskeleton variances on fluorescence microscopy - see Figure VI-4A. Cell morphology differed between flat and nanogrooved substrates. Overall, F-actin structure was different between fibroblasts adhered on flat and nanopatterned $[CHT/CS]_{300}$ membranes and fibroblasts were more elongated on the patterned ones, even for the first day of culture. On the other hand, differences on L929 morphology between non-CL and CL was also noted, mostly from the third day of culture; well-spread fibroblasts were observed on CL FS membranes. The effect of crosslinking on cell morphology was previously investigated in multilayers using high-throughput approaches, where the area occupied by L929 or SaOs-2 cells increased, as compared with uncrosslinked membranes.[55] Nevertheless, the topography seemed to have more impact on morphology and cytoskeleton organization than crosslink and stiffness. These findings are in accordance with previous studies; Yim *et al*. [7] stated that while both material nanotopography and stiffness are crucial properties to modulate mechanical properties of cells, nanotopography is the main property involved in cytoskeletal organization and focal adhesions (FAs) formation. As observed for nanopatterned membranes, the cellular contact guidance followed a trend of orientation that was not observed for the flat ones. The first steps in the cellular contact guidance on nanogrooved surfaces is adhesion and guided spreading, with the cell usually assuming an elongated morphology parallel to the groove long axis;[56] the response changes according to parameters like geometry and respective dimensions of the nanotopographical features.

SEM analysis depicted the cells distribution over the flat and nanopatterned FS membranes - see representative images in Figure VI-4B for crosslinked membranes. The results obtained by fluorescence images (Figure VI-4A) were confirmed by SEM (Figure VI-4B); cell cultured over PAT CL $[CHT/CS]_{300}$ membranes presented predominantly a highly stretched morphology, aligned along the nanogrooves direction. As observed in Figure VI-4B, lamellipodia seemed to extend mostly towards the grooves and ridges direction (horizontally). However, when FAs were perpendicular to grooves direction, their limited width can be responsible for limiting the length of actin fibers and the random direction of lamellipodia. It was already reported that when lamellipodia are placed perpendicular to nanotopography direction, mesenchymal stem cells retract rapidly and become more round with dispersed filopodia.[57] Moreover, from Figure VI-4B we could also confirm the stability of the patterning on the surface of the membranes, even after 7 days of cell culture.

As already mentioned, there are different studies reporting the fabrication of nanopatterned materials and their respective topography-cells interactions but, for the best of our knowledge, this was the first time that nanopatterned FS membranes with ability to control cellular alignment, was fabricated by means of a single step process and using just natural-polymers.

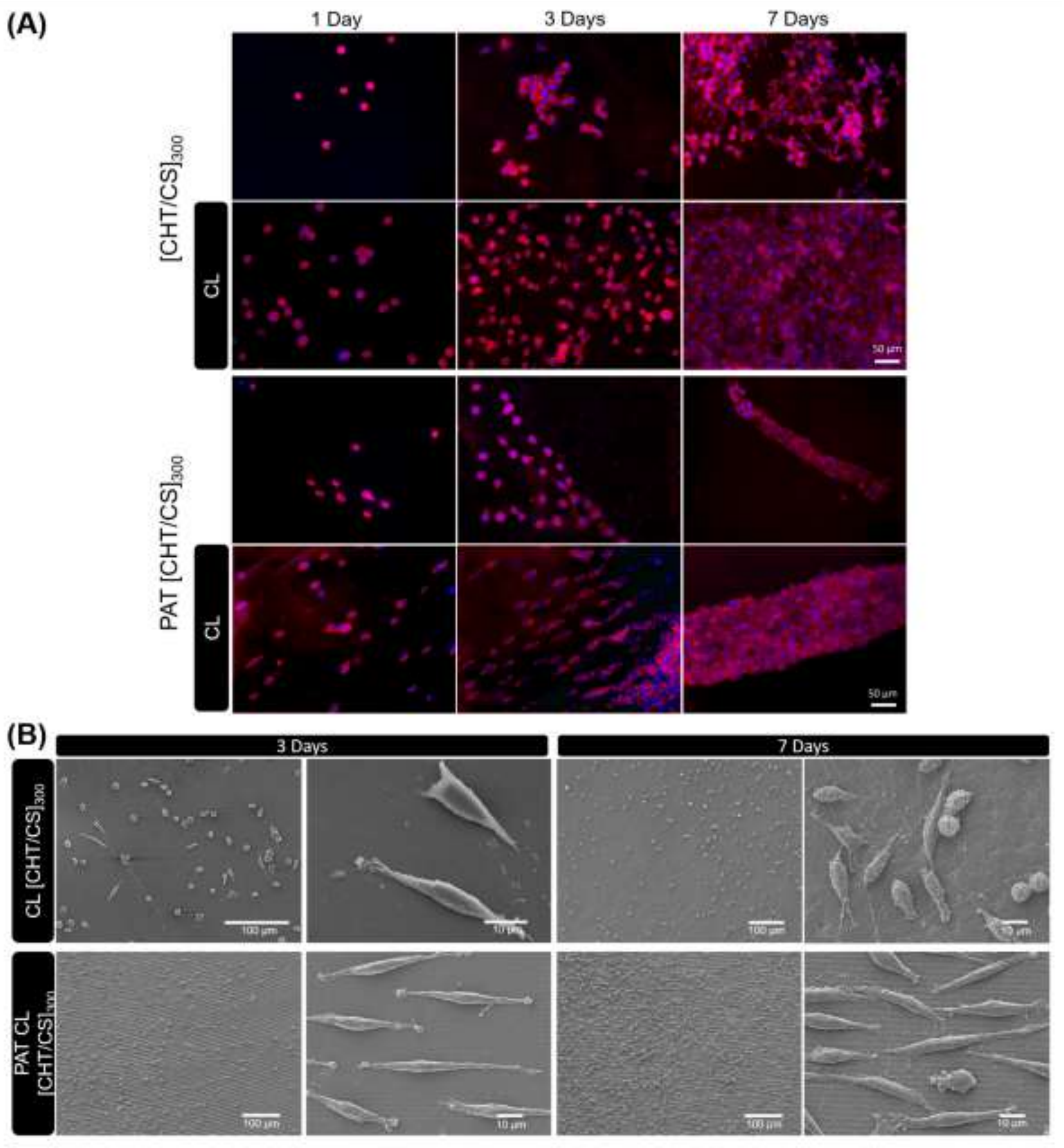

Figure VI-4. Representative images of L929 cells over the different membranes. (A) DAPI−phalloidin fluorescence assay at 1, 3 and 7 days of culture on flat and nanopatterned $[CHT/CS]_{300}$ membranes, with or without crosslinking. Cells nuclei are stained in blue by DAPI and F-actin filaments are stained in red by phalloidin. The scale bar is representative for all images. B) SEM observation at 3 and 7 days of culture above crosslinked flat and nanopatterned CL $[CHT/CS]_{300}$ membranes.

3.4.3. Nuclei morphology

Although different investigations have already reported changes in the cytoskeleton morphology as a result of using a nanostructured topography, few studies have explored the differences in nuclear shape. Comparing the nuclei of the fibroblasts adhered on CL $[CHT/CS]_{300}$ and PAT CL $[CHT/CS]_{300}$ membranes, significant differences were found in terms of the nuclei elongation factor (EF) - see graphics in Figure S VI-5A. When cultured on the patterned surface the nuclei of the cells predominantly showed an elliptical shape, while for unpatterned surfaces they preferred to display a circular shape, with no defined direction - see the representative images also presented in Figure S VI-5A. Graphical distributions of the nucleus orientation of the individual cells cultured on unpatterned and patterned membranes during 1, 3 and 7 days of culture days are presented on Figure S VI-5B. All the images were representative for each condition. On PAT CL $[CHT/CS]_{300}$ membranes, the larger part of nuclei was aligned in the same direction, with higher percentages of the cells between -10° and 10°, in opposite of what happened for CL $[CHT/CS]_{300}$ membranes. For unpatterned membranes, no significant differences were found in the range between -90° and 90°. These observations were according literature.[58]

3.4.4. Morphometric parameters

To have a quantitative idea of the nanotopography effect on cell (cytoskeleton) shape, we determined parameters like fibroblasts area, perimeter, circularity and alignment, regarding the third day of culture. Phalloidin-DAPI (4',6-diamidino-2-phenylindole) stained images provided the ability to calculate parameters like area and perimeter of the cells adhered on crosslinked flat and patterned $[CHT/CS]_{300}$ membranes - see Figure VI-5A. Flat surfaces exhibited a significantly larger cell area than patterned ones. If we assume that the volume of the cells will not change, differences in the cell area should be accompanied by opposite trends in their height. The same trend was obtained in terms of perimeter, yet with no significant differences.

Circularity and cell elongation factor (EF) were also calculated. Circularity is a quantitative parameter used to evaluate cell morphology, as well as cell EF. Significantly higher circularity values were obtained for flat CL $[CHT/CS]_{300}$, comparing with those obtained for PAT CL $[CHT/CS]_{300}$. These results indicate that fibroblasts grown on flat surfaces acquire more rounded morphologies than when grown in the nanopatterned surfaces, clearly consistent with the images of Figure VI5A. Cell EF is defined as the ratio between the longest axis of the cell (length) and the longest axis perpendicular to it. Contrarily to area, perimeter and circularity, the EF of cells cultured on nanopatterned substrates was significantly higher than for cell cultured above flat surfaces. As it was higher than 2 for PAT CL $[CHT/CS]_{300}$) it is possible to say that the majority of cells were elongated.[12]

Fibroblasts were cultured on substrates patterned with sub-micron wide stripes and, as already discussed, they elongated along the ridges and grooves direction. Flat substrates did not seem to have this ability. The angle between the topography direction and the longest axis of the cell was determined. Figure VI-5B shows the cell angle orientation distribution on flat CL $[CHT/CS]_{300}$ membranes, where the cell distribution seemed to be uniform in the range -90° to 90° and an indicative of a random orientation. On the other hand, as observed in Figure VI-5C, fibroblasts cultured on PAT CL $[CHT/CS]_{300}$ were distributed in the range -30° to 20° and approximately 71% of cells were aligned with the pattern direction (angle between -10° and 10°).[59] The phenomenon by which the matrix offers directional features to the cells and directs the motility response via anisotropy in the microenvironment has been designated as contact guidance.[4d, 60] This fact is based on the theory that cells make a projection in one direction depending on the shape and type of features it encountered; for nanopatterned surfaces, the alignment phenomenon will be expected in the direction with less topographic and mechanic obstruction.[61] The parameter that has been mostly correlated with cellular alignment are the groove depth, at sub-micro and nano-scales.[19, 62] The depth of the grooves should be smaller enough for cells run down into the grooves and form FAs and bigger enough for cells sense, with filapodia being able to adhere to the grooves and make cell aligning. Additionally, we also correlated the alignment of the cytoskeleton with the alignment of the nucleus and, in fact, they deformed in the same direction. This result is consistent with literature[63] that suggests that the cytoskeleton network mediates the nucleus deformation.

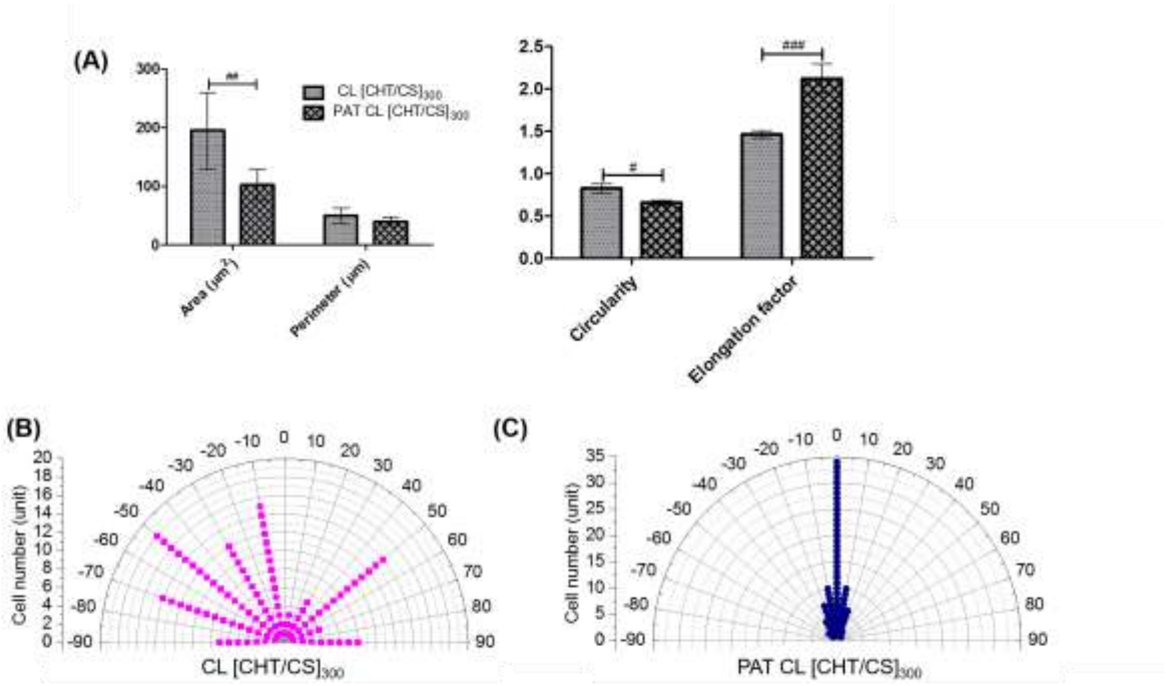

Figure VI-5. Morphometric parameters of L929 cell adhered on crosslinked flat and nanopatterned membranes: A) cell area, perimeter, circularity and elongation factor (EF). Polar graphical representation of cellular alignment for B) CL $[CHT/CS]_{300}$ and for C) PAT CL $[CHT/CS]_{300}$. For each parameter, significant differences were found for (#) $p < 0.05$, (##) $p < 0.01$ and for (###) $p < 0.001$.

3.5. C2C12 cellular response

3.5.1. C2C12 morphology and FAs formation

C2C12 myoblasts were chosen to study the influence of topography in cell differentiation, since it is a well-known and characterized model that has been reported in literature to study the influence of surface distinct properties.[64] Proliferating mononucleated myoblasts differentiate and fuse to multinucleated myotubes. Prior to evaluate the C2C12 differentiation towards myotubes, the morphology of the cells cultured above CL $[CHT/CS]_{300}$ and PAT CL $[CHT/CS]_{300}$ were investigated for 1, 3, 5 and 10 days of culture. Figure VI-6A shows the fluorescence microscopic images of C2C12 stained with phalloidin (cytoskeleton) and DAPI (nucleus). No significant differences in imaged cell density seem to exist between cells cultured above flat and nanopatterned surfaces. C2C12 adhered above CL $[CHT/CS]_{300}$ and PAT CL $[CHT/CS]_{300}$ presented well-organized F-actin on their cytoskeleton and spread on all over the surfaces with extended filapodia. The key of the influence of nanogrooved topography on myoblast morphology is related with the cellular alignment and the formed FAs. In the case of CL $[CHT/CS]_{300}$ membranes, the elongated myoblasts appeared to be random oriented on the surface, while, for the PAT CL $[CHT/CS]_{300}$ films, the elongated cells seemed to follow a specific orientation. In fact, the C2C12 cultured on nanopatterned surfaces seemed to be elongated within the nanotopography direction, starting from day one of culture. In day 3 and day 5 of culture, myoblasts were proliferative and started to form a C2C12 network; the cells extended their filapodia and started to communicate with neighboring cells. A higher cell density was imaged with 10 days of culture for both flat and patterned FS membranes.

SEM observations were also performed to follow up the morphology of C2C12 on the FS $[CHT/CS]_{300}$ membranes, during the first week of culture. Microscopic images reinforced the results of immunofluorescence with phalloidin and DAPI - see Figure VI-6B. Just with 4 hours of culture, myoblasts already started to elongate and acquired a spindle-shaped morphology, while for flat membranes they remained with a round morphology. In day 3 of culture, both patterned and unpatterned surfaces presented elongated cells with EF higher than 1.4. CL $[CHT/CS]_{300}$ films presented random distributed and oriented cells but PAT CL $[CHT/CS]_{300}$ exhibited a better control of cellular distribution and orientation, with the filapodia extended mainly along the groove’s direction. The patterned membranes induced cells fusion with a specific direction. Higher cellular densities were imaged for 7 days of culture and the alignment effect were maintained for the patterned surfaces. With increasing culture time, cells tended to elongate, with a decrease of the width and an increase of the length. These observations can be better understood by the formation of FA on the nanogrooved surface; as already reported in literature and discussed for L929, FAs were usually established on nanogrooved surfaces and they tend to extend protrusion in the direction without obstacles. The formation of FAs of the C2C12 adhered on flat and nanopatterned membranes were revealed using an immunofluorescent staining of vinculin after 3 and 5 days of culture - see Figure VI-6C. The influence of the patterning was also observed at the FAs level, in terms of orientation and morphology. For both time points the FAs seemed to be more distributed around the cells for flat CL $[CHT/CS]_{300}$, whereas for PAT CL $[CHT/CS]_{300}$ the FAs seemed confined in a preferential direction, supporting the idea of FAs are deeply involved in the mechanism of cellular alignment. Note that for 3 days of culture, the immunofluorescence with vinculin allowed to identify by staining the direction of the patterning and effectively a bigger part of FAs was constrained into the preferential direction of the topography.

3.5.2. Myogenic Differentiation

Troponin T was used as a marker for the expression of myogenic differentiation, to investigate the effect of the nanopatterns on differentiation. To perceive this effect, two different media were tested for cell differentiation: DMEM supplemented with horse serum (DM), typically used to trigger the differentiation of C2C12 into myotubes, and DMEM medium supplemented with FBS (GM), used routinely as a growth medium. Figure 7 shows the results of the immunocytochemistry studies for 7 and 10 days of culture. The process of VI-C2C12 differentiation comprises the fusion of myoblasts into multinucleated myotubes, expressing markers like troponin T.[65]

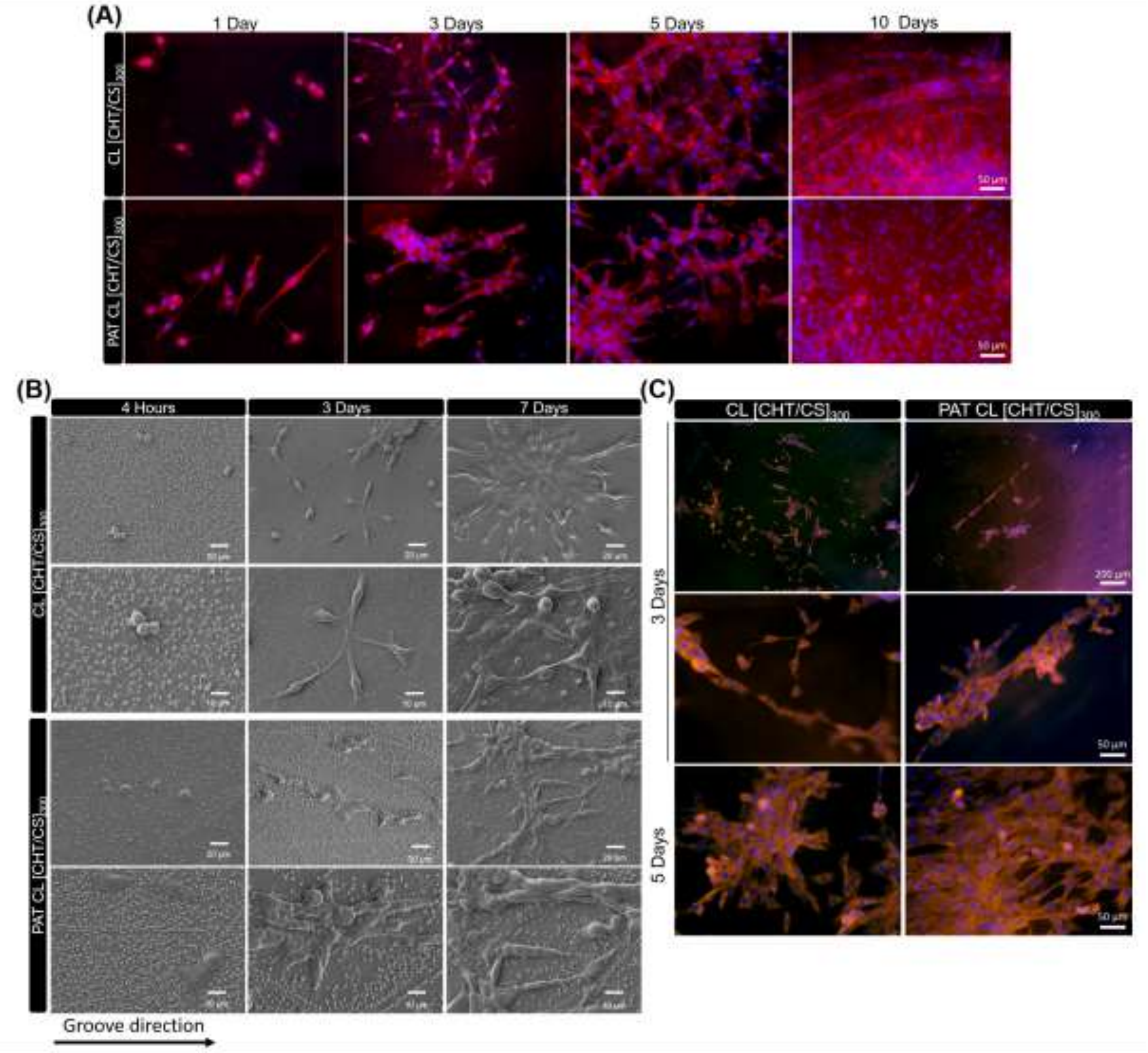

Figure VI--6. Representative images of C2C12 cells over the different CL membranes. (A) DAPI−phalloidin fluorescence assay at 1, 3, 5 and 10 days. Cells nuclei are stained in blue by DAPI and F-actin filaments are stained in red by phalloidin. The scale bar is representative for all images. B) SEM observation at 4 hours, 3 and 7 days, at different magnifications and C) Immunofluorescence with vinculin (orange focal adhesions) and DAPI (blue nuclei) at 3 and 5 days. The scale bar is representative for all images, at different magnifications. Images are representative of CL flat and nanopatterned $[CHT/CS]_{300}$ membranes.

In the case of using DM, no significant differences on troponin T expression were observed between CL $[CHT/CS]_{300}$ and PAT CL $[CHT/CS]_{300}$ membranes. For 7 days of culture, myoblasts started to fuse and formed small myotubes; tissue culture polystyrene surfaces (TCPS) presented larger myotubes and this could be due to a faster differentiation process for plastic-treated substrates. At the 10th day of culture, other myoblasts started to fuse with the small myotubes and longer and mature myotubes were formed. These observations are consistent with the basis of mammalian myoblast fusion, which occurs into two phases: an early phase of forming nascent myotubes and a later phase of forming mature myotubes.[66]

Contrarily, in the case of using GM, some differences were noted for unpatterned and patterned membranes. Visually, the amount of troponin T expression on the cells cultured on nanopatterned membranes using GM was considerably higher compared with flat membranes and TCPS; this can be a clear indication that when using a medium capable of inducing differentiation by itself, the pattern effect was almost masked. After 10 days of culture, myotubes were formed and presented a long and thin morphology; however, the cells reached a stage where they were overgrown. Myoblasts change their triangular shape to an elongated one during the early stages of differentiation;[67] this can support the results obtained in GM conditions. In the absence of DM, the presence of nanogrooved topography on PAT CL [CHT/CS]$_{300}$ prompted cells to acquired predominantly an elongated shape and could promote myoblast differentiation by itself with no need of special exogenous factors.

In Figure VI-7, it is also possible to perceive some indications of the effect of the nanogrooved topography, with myotubes oriented in a particular direction. The influence of topography on C2C12 differentiation was consistent with previous works.[64a, 68] In fact, the alignment step, which has been related with the cytoskeleton organization, has been suggested as a crucial process before cell fusion, and thus, an important step in differentiation;[68-69] actin filaments were randomly distributed in flat membranes while in nanopatterned ones a big part of actin filaments were aligned along the grooves. Moreover, by immunofluorescence images, morphological differences are perceived between flat CL [CHT/CS]$_{300}$ and PAT CL [CHT/CS]$_{300}$, using either DM or GM: for the flat ones myotubes presented an arc structure while for the nanogrooved surfaces they presented an aligned structure.

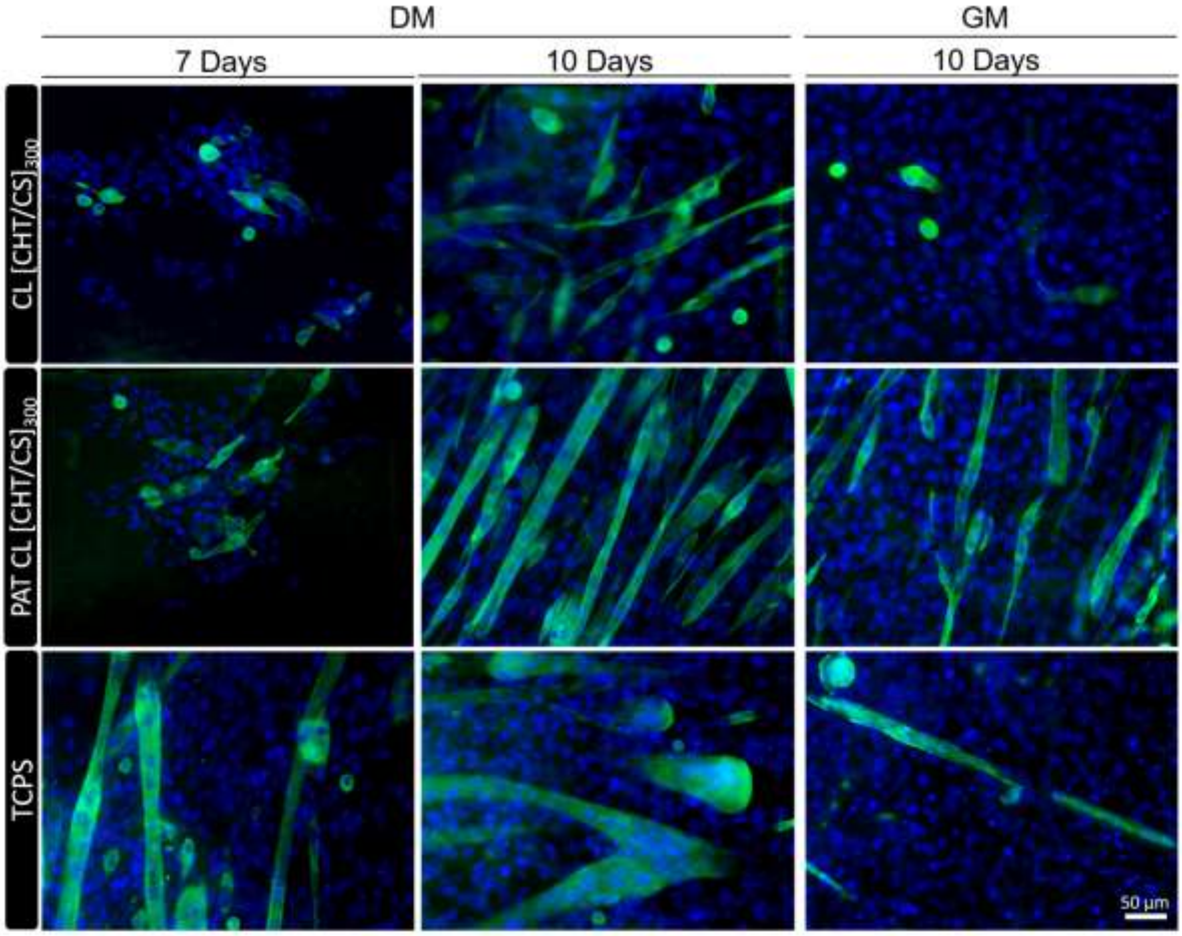

Figure VI-7. Immunofluorescence with troponin T (green myotubes) and DAPI (blue nuclei) at 7 and 10 days of culture. Images are representative of crosslinked flat and nanopatterned CHT/CS membranes and TCPS, using differentiation medium (DM) and normal growth medium (GM). The scale bar is representative for all images.

3.5.3. Morphometric parameters

The effect of the nanogrooves on myoblasts differentiation was also evaluated by exploring differentiation parameters: the fusion index, the number of troponin-positive myotubes, the area and the alignment of myotubes were determined for each condition after 10 days of culture.

Cells cultured on PAT CL $[CHT/CS]_{300}$ showed the highest percentage of fusion index, comparing with what happened with CL $[CHT/CS]_{300}$ - see Figure VI-8A. The fusion index percentage is significantly higher for PAT CL $[CHT/CS]_{300}$, either using DM or using GM. Otherwise, the number of troponin-positive myotubes is similar for flat CL $[CHT/CS]_{300}$ and PAT CL $[CHT/CS]_{300}$ when using DM, but significantly higher for PAT CL $[CHT/CS]_{300}$ in case of using GM. All these results together indicate that the myogenic differentiation into myotubes was boosted on PAT CL $[CHT/CS]_{300}$, mainly when using GM. Literature refers some different driving forces for myogenic differentiation but topography seemed to be one of the most significant.[70]

Either using DM or GM, significant differences in the myotubes area were found between flat and patterned FS films. The PAT CL $[CHT/CS]_{300}$ membranes presented myotubes with larger area than CL $[CHT/CS]_{300}$ - see Figure VI-8B. Regarding PAT CL $[CHT/CS]_{300}$ membranes, no significant differences were found in the myotubes area between DM or GM conditions.

Also, myotubes alignment was evaluated for the different conditions, after 10 days of culture. Figure VI-8C displays the distribution of the myotubes orientation on the different membranes. For CL $[CHT/CS]_{300}$, using DM or GM, the myotubes were distributed in a wide range of orientations. On the other hand, for PAT CL $[CHT/CS]_{300}$ myotubes were distributed in a short range of orientation, presenting for both cases (DM or GM) a preferential orientation. These data are supported by related literature that described alignment as a driven force for myogenic differentiation.[71] In the present study, it is possible to correlate these 3 important concepts: a nanogrooved topography seemed to have an interesting impact on cellular alignment, which in turn promote myogenic differentiation even in absence of some special culture media.

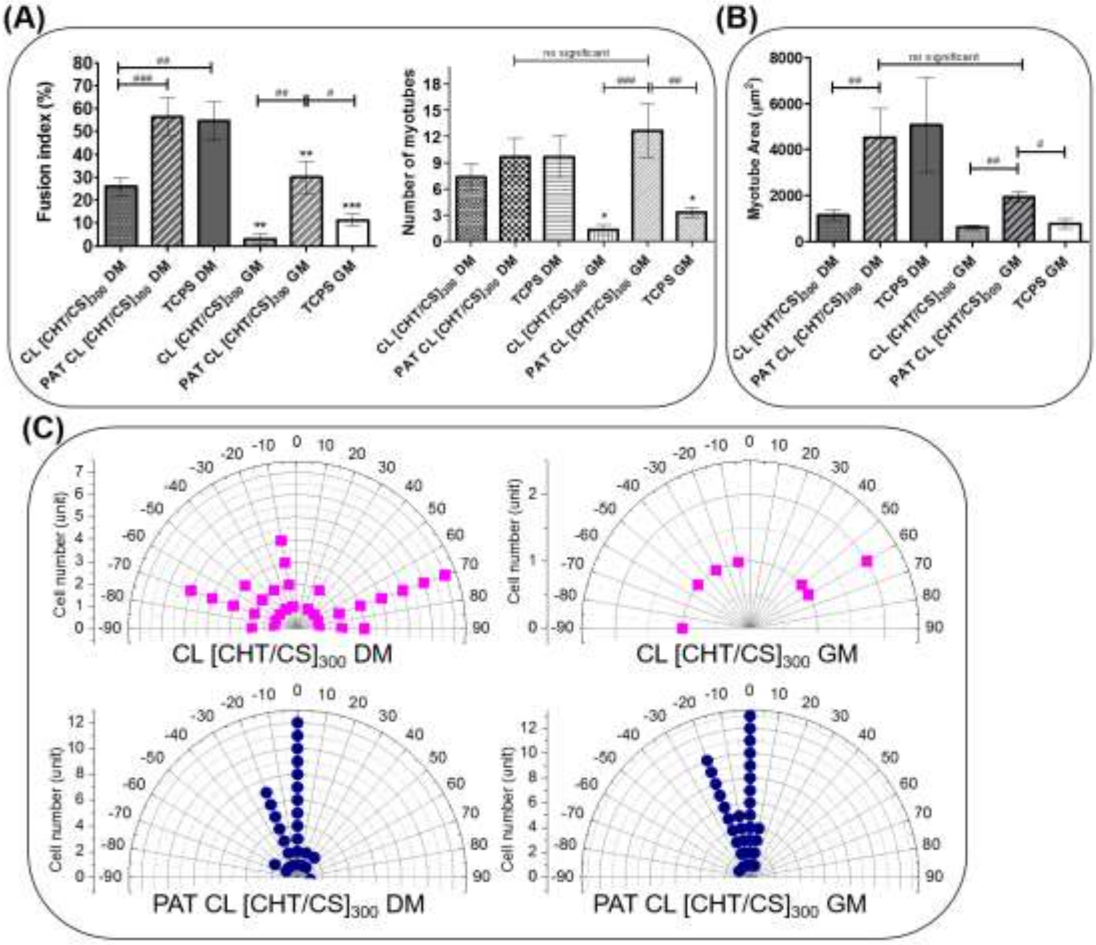

Figure VI-8. Morphometric parameters of C2C12 cell adhered on crosslinked flat and nanopatterned membranes: A) fusion index (%) and normalized number of myotubes and B) myotube area in an established area. For the effect of the culture medium, significant differences were found for (***) $p < 0.001$ and (**) $p < 0.01$ and for patterning effect the significant differences were found for (#) $p < 0.05$, (##) $p < 0.01$ and (###) $p < 0.001$. The statistical analysis for myotube area parameter was done using a nonparametric equivalent of one-way ANOVA (Kruskal–Wallis test) followed by Dunn's multiple comparison test. C) Polar graphical representation of cellular alignment for CL $[CHT/CS]_{300}$ and for PAT CL $[CHT/CS]_{300}$. It is assumed that the preferential alignment corresponds to the groove's orientation (arbitrary angle).

4. Conclusion

Nanoengineered materials for biomedical applications have been showing remarkable advances in the last years. However, the complexity of the used methodologies and materials, the inability to create hierarchically organized and layered scaffolds, the time required and the short incorporation of non-meltable natural-based polymers have been the major obstacles in such developments. In this study, we developed a pioneer strategy to produce nanogrooved freestanding multilayer biopolymer films capable to control the cellular behavior. Using LbL methodology it was possible to process polysaccharide-based films with well-defined patterned motifs engraved on the surface with a sub-micrometer resolution. Cellular behavior was investigated for two different type of mammalian cells. For mouse fibroblasts, parameters like viability and proliferation had generally higher values on flat membranes and the nanotopography could induce significantly cell orientation. Moreover, also the alignment and myogenic differentiation of C2C12 were observed on nanopatterned membranes, even in absence of special differentiation medium. We were able to develop freestanding membranes using wet and mild processing routes, that depending on the post-processing steps (crosslinking) and the presence of topographic motifs could control cellular behavior, including orientation and differentiation without any external stimuli or exogenous factors. Such kind of versatile multilayer membranes could be valuable bio-instructive substrates to be used in a variety of biomedical applications, such as in tissue engineering strategies.

5. Supporting Information

The supplementary information includes figures that complement the main figures presented in the main text.

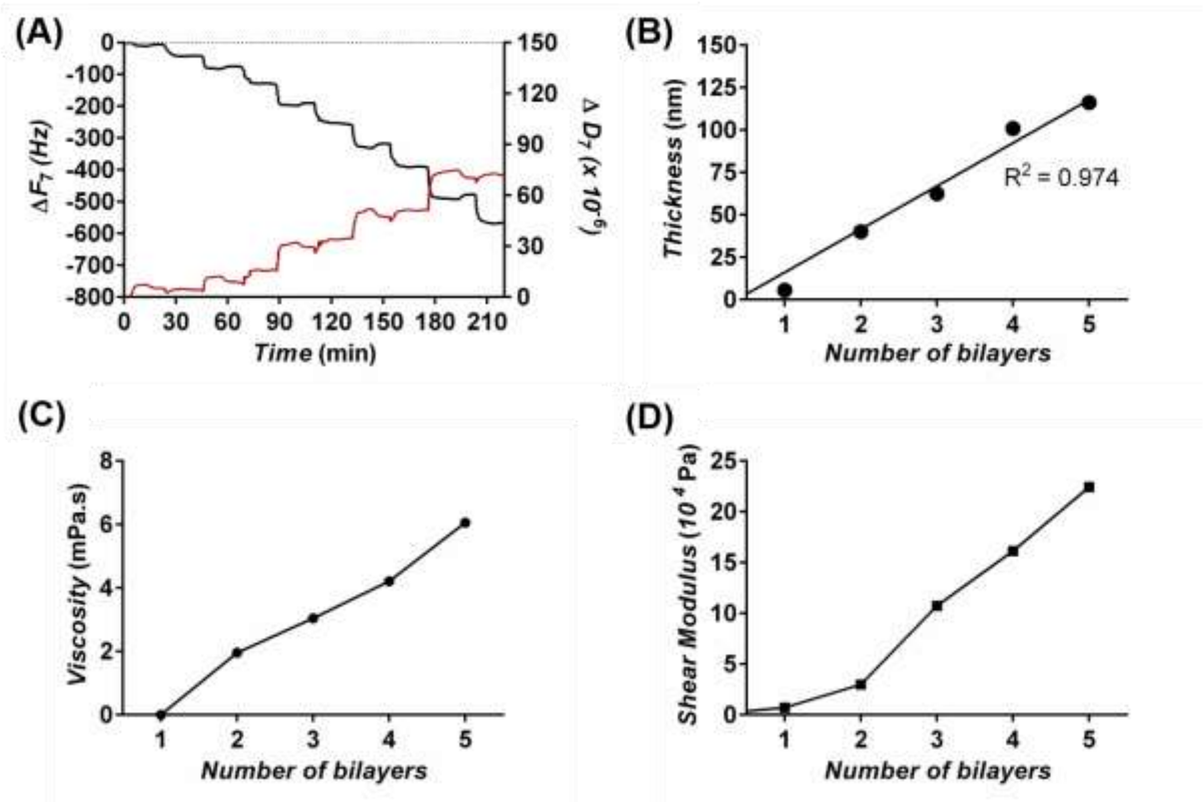

Figure S VI-1. A) Normalized frequency (Δ*f*7) and dissipation (Δ*D*7) changes measured by QCM-D during the construction of CHT/CS films, up to 5 bilayers. B) Thickness (the line represents a linear trend line with $R^2 = 0.974$), C) Viscosity and D) Shear Modulus of the growing CHT/CS film as a function of the number of bilayers, calculated using the Voigt model.

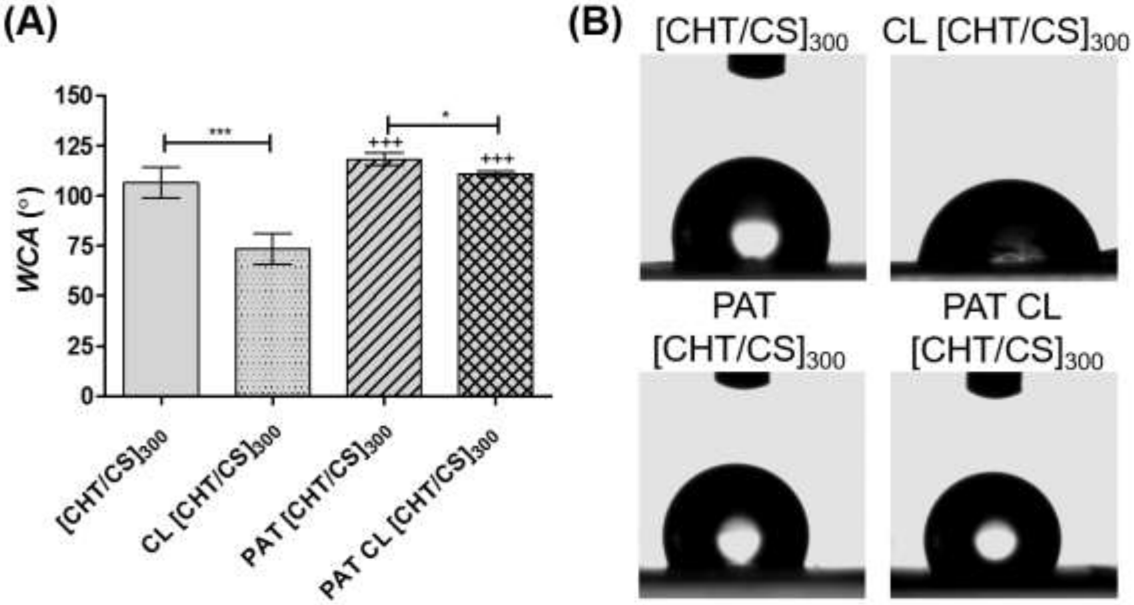

Figure S VI-2. A) Water contact angle (WCA) on different membranes, for the down side (the one that contacts with the underlying substrate). Significant differences for the crosslink effect were found for (*) p<0.05 and (***) p<0.001. Significant differences related with the patterning effect were observed as (+++) p<0.001. B) Representative images of the contour of the water droplets over the different membranes.

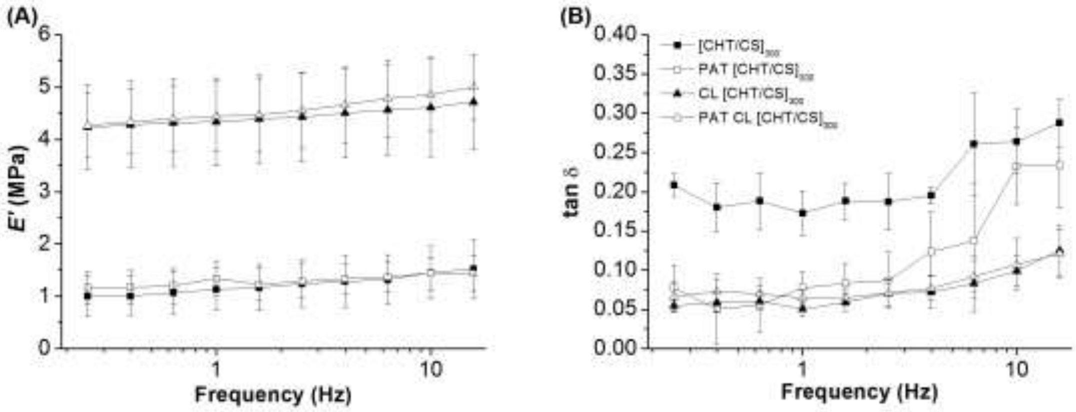

Figure S VI-3. Variation of the Storage modulus, E' (A) and the loss factor, tan δ (B) along a frequency scan ranging from 0.2-20 Hz, at 37ºC of the FS membranes while immersed in PBS.

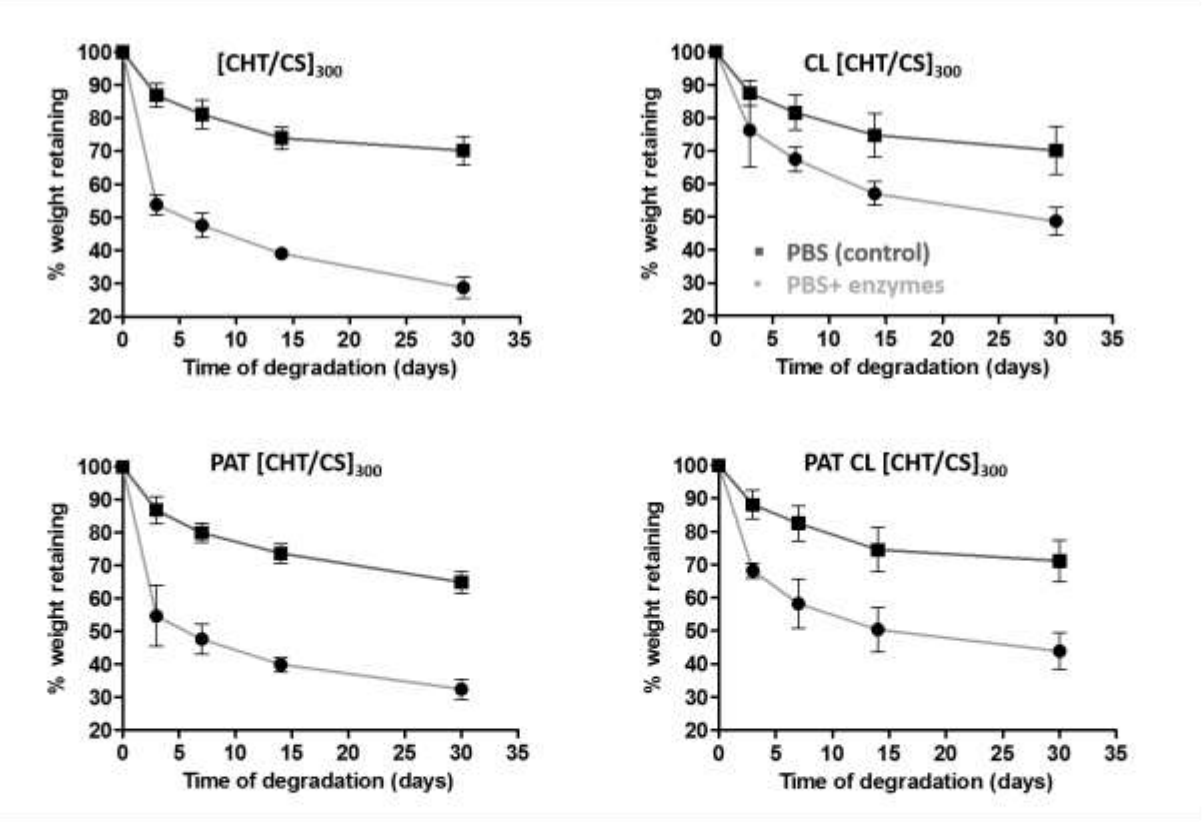

Figure S VI-4. Weight retaining (%) of the different membrane formulations up to 30 days of incubation in PBS used as a control (square) and PBS+ lysozyme + hyaluronidase (circle). Data are a means ± SD, for three independent experiments.

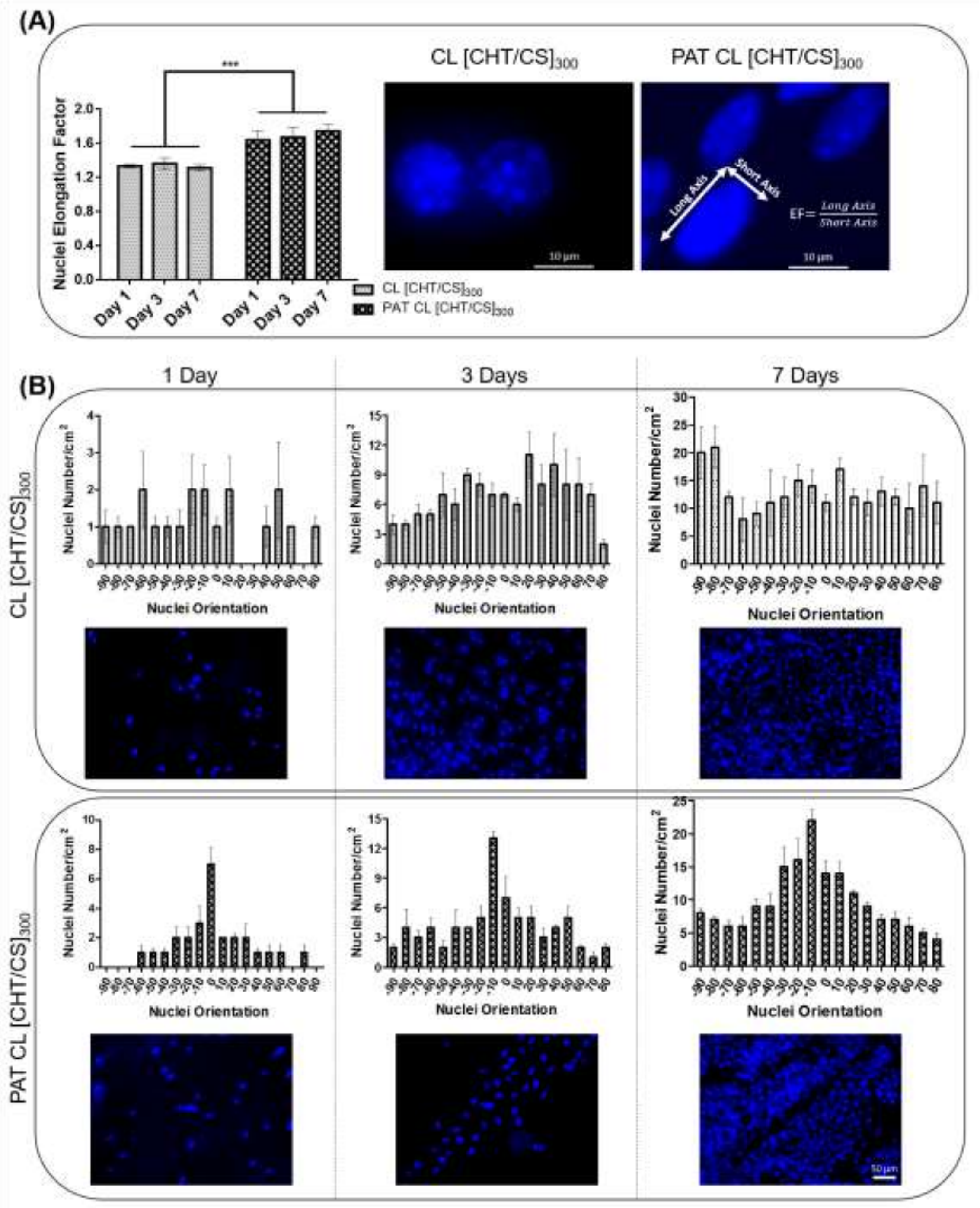

Figure S VI-5. Morphometric nuclei parameters of L929 cell adhered on crosslinked flat and nanopatterned membranes: A) nucleus elongation factor (EF) and respective representative images of the DAPI-labelled nuclei and B) nuclei number distribution over the different orientations for 1, 3 and 7 days. For each condition, one representative fluorescent image of nuclei was also presented. For each parameter, significant differences were found for (#) $p < 0.05$, (##) $p < 0.01$ and for (###) $p < 0.001$.

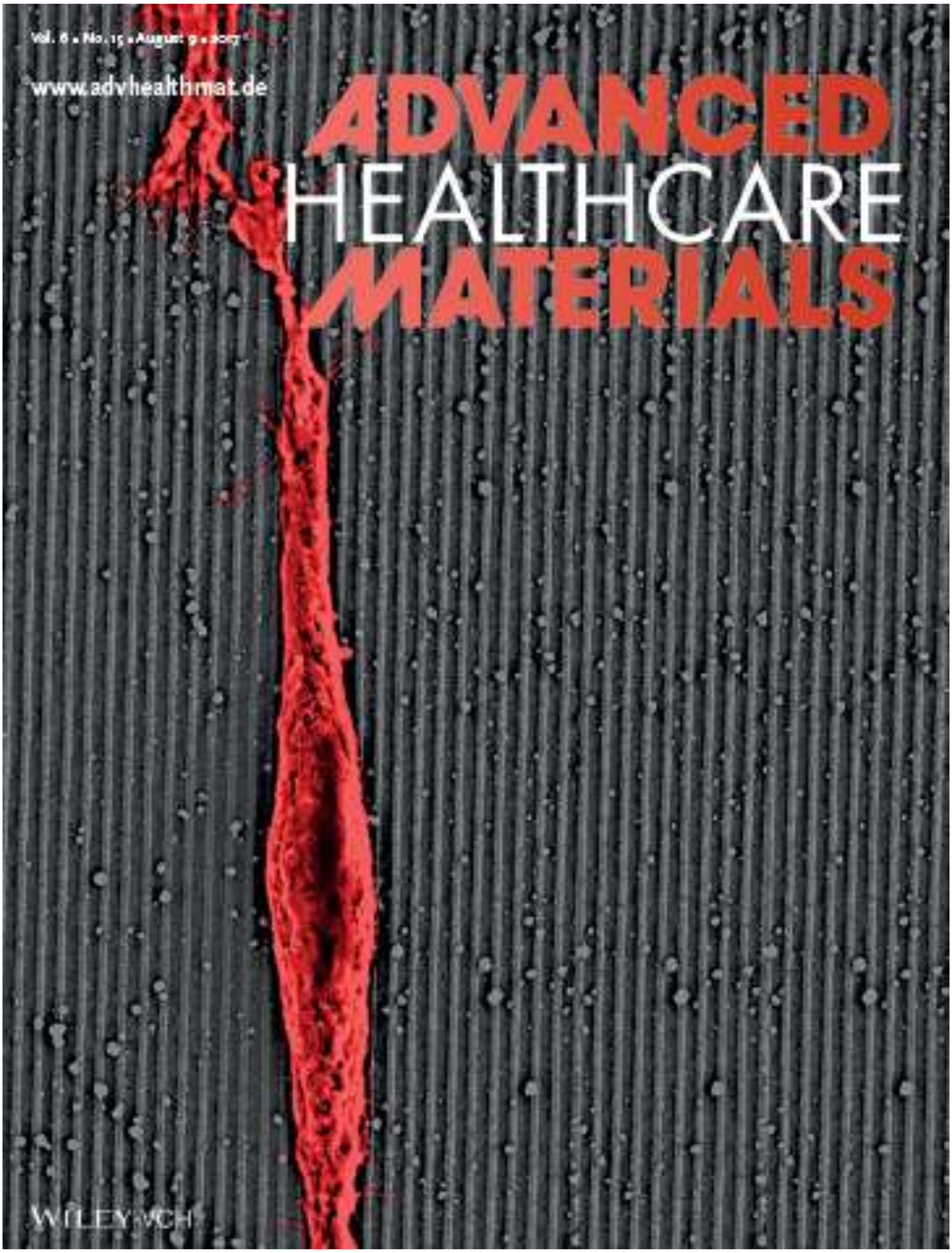

Figure S VI-6. Inside back cover of the Special Issue entitled Biomimetic Interfaces in Biomedical Devices, from Advanced healthcare Materials [72].

6. Acknowledgements

Maria P. Sousa acknowledges the Portuguese Foundation for Science and Technology (FCT) for financial support through SFRH/BD/97606/2013 grant and Sofia G. Caridade through SFRH/BPD/96797/2013 grant.

7. References

1. (a) Dalby, M. J.; Gadegaard, N.; Oreffo, R. O. C., Harnessing nanotopography and integrin-matrix interactions to influence stem cell fate. *Nature Materials* **2014,** *13* (6), 558-569; (b) Kim, D.-H.; Provenzano, P. P.; Smith, C. L.; Levchenko, A., Matrix nanotopography as a regulator of cell function. *The Journal of Cell Biology* **2012,** *197* (3), 351-360.
2. (a) Kim, H. N.; Jiao, A.; Hwang, N. S.; Kim, M. S.; Kang do, H.; Kim, D. H.; Suh, K. Y., Nanotopography-guided tissue engineering and regenerative medicine. *Adv Drug Deliv Rev* **2013,** *65* (4), 536-58; (b) von der Mark, K.; Park, J.; Bauer, S.; Schmuki, P., Nanoscale engineering of biomimetic surfaces: cues from the extracellular matrix. *Cell and Tissue Research* **2009,** *339* (1), 131.
3. Weiner, S.; Wagner, H. D., The material bone: Structure mechanical function relations. *Annual Review of Materials Science* **1998,** (28), 271-298.
4. (a) Ventre, M.; Natale, C. F.; Rianna, C.; Netti, P. A., Topographic cell instructive patterns to control cell adhesion, polarization and migration. *J. R. Soc. Interface* **2014,** *11* (100); (b) Kehr, N. S.; Riehemann, K.; El-Gindi, J.; Schäfer, A.; Fuchs, H.; Galla, H.-J.; De Cola, L., Cell Adhesion and Cellular Patterning on a Self-Assembled Monolayer of Zeolite L Crystals. *Advanced Functional Materials* **2010,** *20* (14), 2248-2254; (c) Bettinger, C. J.; Zhang, Z.; Gerecht, S.; Borenstein, J. T.; Langer, R., Enhancement of *In Vitro* Capillary Tube Formation by Substrate Nanotopography. *Advanced Materials* **2008,** *20* (1), 99-103; (d) Flemming, R. G.; Murphy, C. J.; Abrams, G. A.; Goodman, S. L.; Nealey, P. F., Effects of synthetic micro- and nano-structured surfaces on cell behavior. *Biomaterials* **1999,** *20* (6), 573-88.
5. (a) Khademhosseini, A.; Ling, Y.; Karp, J. M.; Langer, R., Micro- and Nanoscale Control of Cellular Environment for Tissue Engineering. In *Nanobiotechnology II*, Wiley-VCH Verlag GmbH & Co. KGaA: 2007; pp 347-364; (b) Even-Ram, S.; Artym, V.; Yamada, K. M., Matrix Control of Stem Cell Fate. *Cell* **2006,** *126* (4), 645-647; (c) Wang, D. A.; Williams, C. G.; Yang, F.; Elisseeff, J. H., Enhancing the Tissue-Biomaterial Interface: Tissue-Initiated Integration of Biomaterials. *Advanced Functional Materials* **2004,** *14* (12), 1152-1159.
6. Chen, W.; Villa-Diaz, L. G.; Sun, Y.; Weng, S.; Kim, J. K.; Lam, R. H. W.; Han, L.; Fan, R.; Krebsbach, P. H.; Fu, J., Nanotopography Influences Adhesion, Spreading, and Self-Renewal of Human Embryonic Stem Cells. *ACS Nano* **2012,** *6* (5), 4094-4103.
7. Yim, E. K. F.; Darling, E. M.; Kulangara, K.; Guilak, F.; Leong, K. W., Nanotopography-induced changes in focal adhesions, cytoskeletal organization, and mechanical properties of human mesenchymal stem cells. *Biomaterials* **2010,** *31* (6), 1299-1306.
8. Yim, E. K.; Reano, R. M.; Pang, S. W.; Yee, A. F.; Chen, C. S.; Leong, K. W., Nanopattern-induced changes in morphology and motility of smooth muscle cells. *Biomaterials* **2005,** *26* (26), 5405-13.
9. Kim, D. H.; Kshitiz; Smith, R. R.; Kim, P.; Ahn, E. H.; Kim, H. N.; Marban, E.; Suh, K. Y.; Levchenko, A., Nanopatterned cardiac cell patches promote stem cell niche formation and myocardial regeneration. *Integr Biol (Camb)* **2012,** *4* (9), 1019-33.
10. Lamers, E.; van Horssen, R.; te Riet, J.; van Delft, F. C.; Luttge, R.; Walboomers, X. F.; Jansen, J. A., The influence of nanoscale topographical cues on initial osteoblast morphology and migration. *European cells & materials* **2010,** *20*, 329-43.
11. Kulangara, K.; Yang, Y.; Yang, J.; Leong, K. W., Nanotopography as modulator of human mesenchymal stem cell function. *Biomaterials* **2012,** *33* (20), 4998-5003.
12. Teixeira, A. I.; Abrams, G. A.; Bertics, P. J.; Murphy, C. J.; Nealey, P. F., Epithelial contact guidance on well-defined micro- and nanostructured substrates. *J. Cell. Sci.* **2003,** *116* (Pt 10), 1881-92.
13. Teixeira, A. I.; McKie, G. A.; Foley, J. D.; Bertics, P. J.; Nealey, P. F.; Murphy, C. J., The effect of environmental factors on the response of human corneal epithelial cells to nanoscale substrate topography. *Biomaterials* **2006,** *27* (21), 3945-54.
14. Kim, J.; Kim, H. N.; Lim, K. T.; Kim, Y.; Seonwoo, H.; Park, S. H.; Lim, H. J.; Kim, D. H.; Suh, K. Y.; Choung, P. H.; Choung, Y. H.; Chung, J. H., Designing nanotopographical density of extracellular matrix for controlled morphology and function of human mesenchymal stem cells. *Sci Rep* **2013,** (3), 3552.
15. Dalby, M. J.; Riehle, M. O.; Sutherland, D. S.; Agheli, H.; Curtis, A. S., Changes in fibroblast morphology in response to nano-columns produced by colloidal lithography. *Biomaterials* **2004,** *25* (23), 5415-22.

16. Dalby, M. J.; Riehle, M. O.; Johnstone, H.; Affrossman, S.; Curtis, A. S. G., *In vitro* reaction of endothelial cells to polymer demixed nanotopography. *Biomaterials* **2002,** *23* (14), 2945-2954.
17. Smith, L. A.; Ma, P. X., Nano-fibrous scaffolds for tissue engineering. *Colloids and surfaces. B, Biointerfaces* **2004,** *39* (3), 125-31.
18. Norman, J. J.; Desai, T. A., Methods for fabrication of nanoscale topography for tissue engineering scaffolds. *Ann. Biomed. Eng.* **2006,** *34* (1), 89-101.
19. Loesberg, W. A.; te Riet, J.; van Delft, F. C. M. J. M.; Schön, P.; Figdor, C. G.; Speller, S.; van Loon, J. J. W. A.; Walboomers, X. F.; Jansen, J. A., The threshold at which substrate nanogroove dimensions may influence fibroblast alignment and adhesion. *Biomaterials* **2007,** *28* (27), 3944-3951.
20. (a) Costa, R. R.; Mano, J. F., Polyelectrolyte multilayered assemblies in biomedical technologies. *Chemical Society Reviews* **2014,** *43* (10), 3453-3479; (b) Decher, G., Fuzzy Nanoassemblies: Toward Layered Polymeric Multicomposites. *Science* **1997,** *277* (5330), 1232-1237.
21. (a) Niepel, M. S.; Mano, J. F.; Groth, T., Effect of Polyelectrolyte Multilayers Assembled on Ordered Nanostructures on Adhesion of Human Fibroblasts. *ACS Applied Materials & Interfaces* **2016,** *8* (38), 25142-25151; (b) Monge, C.; Saha, N.; Boudou, T.; Pózos-Vásquez, C.; Dulong, V.; Glinel, K.; Picart, C., Rigidity-Patterned Polyelectrolyte Films to Control Myoblast Cell Adhesion and Spatial Organization. *Advanced Functional Materials* **2013,** *23* (27), 3432-3442.
22. Caridade, S. G.; Monge, C.; Gilde, F.; Boudou, T.; Mano, J. F.; Picart, C., Free-standing polyelectrolyte membranes made of chitosan and alginate. *Biomacromolecules* **2013,** *14* (5), 1653-1660.
23. Zhang, J.; Senger, B.; Vautier, D.; Picart, C.; Schaaf, P.; Voegel, J.-C.; Lavalle, P., Natural polyelectrolyte films based on layer-by layer deposition of collagen and hyaluronic acid. *Biomaterials* **2005,** *26* (16), 3353-3361.
24. Wittmer, C. R.; Phelps, J. A.; Saltzman, W. M.; Van Tassel, P. R., Fibronectin Terminated Multilayer Films: Protein Adsorption and Cell Attachment Studies. *Biomaterials* **2007,** *28* (5), 851-860.
25. Ye, X.; Wang, H.; Zhou, J.; Li, H.; Liu, J.; Wang, Z.; Chen, A.; Zhao, Q., The Effect of Heparin-VEGF Multilayer on the Biocompatibility of Decellularized Aortic Valve with Platelet and Endothelial Progenitor Cells. *PLoS ONE* **2013,** *8* (1), e54622.
26. Boudou, T.; Crouzier, T.; Ren, K.; Blin, G.; Picart, C., Multiple functionalities of polyelectrolyte multilayer films: new biomedical applications. *Adv. Mater.* **2010,** *22* (4), 441-67.
27. Correia, C. R.; Moreira-Teixeira, L. S.; Moroni, L.; Reis, R. L.; van Blitterswijk, C. A.; Karperien, M.; Mano, J. F., Chitosan scaffolds containing hyaluronic acid for cartilage tissue engineering. *Tissue engineering. Part C, Methods* **2011,** *17* (7), 717-30.
28. Alves, N. M.; Picart, C.; Mano, J. F., Self Assembling and Crosslinking of Polyelectrolyte Multilayer Films of Chitosan and Alginate Studied by QCM and IR Spectroscopy. *Macromolecular Bioscience* **2009,** *9* (8), 776-785.
29. Silva, J. M.; Duarte, A. R. C.; Caridade, S. G.; Picart, C.; Reis, R. L.; Mano, J. F., Tailored freestanding multilayered membranes based on chitosan and alginate. *Biomacromolecules* **2014,** *15* (10), 3817-3826.
30. Wang, C.-Z.; Wang, G.-J.; Ho, M.-L.; Wang, Y.-H.; Yeh, M.-L.; Chen, C.-H., Low-magnitude vertical vibration enhances myotube formation in C2C12 myoblasts. *Journal of Applied Physiology* **2010,** *109* (3), 840-848.
31. Shin, Y. C.; Lee, J. H.; Kim, M. J.; Hong, S. W.; Kim, B.; Hyun, J. K.; Choi, Y. S.; Park, J.-C.; Han, D.-W., Stimulating effect of graphene oxide on myogenesis of C2C12 myoblasts on RGD peptide-decorated PLGA nanofiber matrices. *Journal of Biological Engineering* **2015,** *9* (1), 1-10.
32. Correia, C. R.; Reis, R. L.; Mano, J. F., Multilayered Hierarchical Capsules Providing Cell Adhesion Sites. *Biomacromolecules* **2013,** *14* (3), 743-751.
33. Höök, F.; Kasemo, B.; Nylander, T.; Fant, C.; Sott, K.; Elwing, H., Variations in Coupled Water, Viscoelastic Properties, and Film Thickness of a Mefp-1 Protein Film during Adsorption and Cross-Linking: A Quartz Crystal Microbalance with Dissipation Monitoring, Ellipsometry, and Surface Plasmon Resonance Study. *Analytical Chemistry* **2001,** *73* (24), 5796-5804.
34. Anene-Nzelu, C. G.; Choudhury, D.; Li, H.; Fraiszudeen, A.; Peh, K.-Y.; Toh, Y.-C.; Ng, S. H.; Leo, H. L.; Yu, H., Scalable cell alignment on optical media substrates. *Biomaterials* **2013,** *34* (21), 5078-5087.
35. Marco, C.; Giorgia, B.; Michela, S.; Fabio, B., PC12 differentiation on biopolymer nanostructures. *Nanotechnology* **2007,** *18* (50), 505103.
36. Cecchini, M.; Ferrari, A.; Beltram, F., PC12 polarity on biopolymer nanogratings. *Journal of Physics: Conference Series* **2008,** *100* (1), 012003.

37. Wang, P.-Y.; Yu, J.; Lin, J.-H.; Tsai, W.-B., Modulation of alignment, elongation and contraction of cardiomyocytes through a combination of nanotopography and rigidity of substrates. *Acta Biomaterialia* **2011,** *7* (9), 3285-3293.

38. Sousa, M. P.; Cleymand, F.; Mano, J. F., Elastic chitosan/chondroitin sulfate multilayer membranes. *Biomedical materials (Bristol, England)* **2016,** *11* (3), 035008.

39. Oliveira, S. M.; Alves, N. M.; Mano, J. F., Cell interactions with superhydrophilic and superhydrophobic surfaces. *Journal of Adhesion Science and Technology* **2014,** *28* (8-9), 843-863.

40. (a) Chen, H.; Ouyang, W.; Lawuyi, B.; Prakash, S., Genipin cross-linked alginate-chitosan microcapsules: membrane characterization and optimization of cross-linking reaction. *Biomacromolecules* **2006,** *7* (7), 2091-8; (b) Mi, F.-L.; Sung, H.-W.; Shyu, S.-S., Synthesis and characterization of a novel chitosan-based network prepared using naturally occurring crosslinker. *Journal of Polymer Science Part A: Polymer Chemistry* **2000,** *38* (15), 2804-2814.

41. Gao, L.; Gan, H.; Meng, Z.; Gu, R.; Wu, Z.; Zhang, L.; Zhu, X.; Sun, W.; Li, J.; Zheng, Y.; Dou, G., Effects of genipin cross-linking of chitosan hydrogels on cellular adhesion and viability. *Colloids and surfaces. B, Biointerfaces* **2014,** (117), 398-405.

42. Silva, J. M.; Caridade, S. G.; Oliveira, N. M.; Reis, R. L.; Mano, J. F., Chitosan-alginate multilayered films with gradients of physicochemical cues. *Journal of Materials Chemistry B* **2015,** *3* (22), 4555-4568.

43. Cassie, A. B. D.; Baxter, S., Wettability of porous surfaces. *Transactions of the Faraday Society* **1944,** (40), 546-551.

44. Kehr, N. S.; Motealleh, A.; Schäfer, A. H., Cell Growth on (“Janus”) Density Gradients of Bifunctional Zeolite L Crystals. *ACS Applied Materials & Interfaces* **2016,** *8* (51), 35081-35090.

45. (a) Engler, A. J.; Sen, S.; Sweeney, H. L.; Discher, D. E., Matrix Elasticity Directs Stem Cell Lineage Specification. *Cell* **2006,** *126* (4), 677-689; (b) Saha, K.; Keung, A. J.; Irwin, E. F.; Li, Y.; Little, L.; Schaffer, D. V.; Healy, K. E., Substrate Modulus Directs Neural Stem Cell Behavior. *Biophysical Journal* **2008,** *95* (9), 4426-4438.

46. (a) Caridade, S. G.; Monge, C.; Almodovar, J.; Guillot, R.; Lavaud, J.; Josserand, V.; Coll, J. L.; Mano, J. F.; Picart, C., Myoconductive and osteoinductive free-standing polysaccharide membranes. *Acta Biomaterialia* **2015,** *15*, 139-49; (b) Mano, J. F., Viscoelastic properties of chitosan with different hydration degrees as studied by dynamic mechanical analysis. *Macromol Biosci* **2008,** *8* (1), 69-76.

47. Alves, N. M.; Gómez, R.; Gómez, T.; Mano, J. F., Viscoelastic Behavior of Poly(methyl methacrylate) Networks with Different Cross-Linking Degrees. *Macromolecules* **2004,** *37* (10), 3735-3744.

48. Azevedo, H. S.; Reis, R. L., Understanding the enzymatic degradation of biodegradable polymers and strategies to control their degradation rate. In *Biodegradable systems in tissue engineering and regenerative medicine*, CRC Press: 2005; pp 177-201.

49. Nordtveit, R. J.; Vårum, K. M.; Smidsrød, O., Degradation of partially N-acetylated chitosans with hen egg white and human lysozyme. *Carbohydrate Polymers* **1996,** *29* (2), 163-167.

50. Honda, T.; Kaneiwa, T.; Mizumoto, S.; Sugahara, K.; Yamada, S., Hyaluronidases Have Strong Hydrolytic Activity toward Chondroitin 4-Sulfate Comparable to that for Hyaluronan. *Biomolecules* **2012,** *2* (4), 549-563.

51. (a) Cardoso, M. J.; Caridade, S. G.; Costa, R. R.; Mano, J. F., Enzymatic Degradation of Polysaccharide-Based Layer-by-Layer Structures. *Biomacromolecules* **2016,** *17* (4), 1347-1357; (b) Aurore, S.; Ludovic, R.; Gregory, F.; Jean-Claude, V.; Catherine, P., Elasticity, biodegradability and cell adhesive properties of chitosan/hyaluronan multilayer films. *Biomedical Materials* **2007,** *2* (1), S45.

52. (a) Yan, L. P.; Wang, Y. J.; Ren, L.; Wu, G.; Caridade, S. G.; Fan, J. B.; Wang, L. Y.; Ji, P. H.; Oliveira, J. M.; Oliveira, J. T.; Mano, J. F.; Reis, R. L., Genipin-cross-linked collagen/chitosan biomimetic scaffolds for articular cartilage tissue engineering applications. *Journal of biomedical materials research. Part A* **2010,** *95* (2), 465-75; (b) Etienne, O.; Schneider, A.; Taddei, C.; Richert, L.; Schaaf, P.; Voegel, J. C.; Egles, C.; Picart, C., Degradability of polysaccharides multilayer films in the oral environment: an *in vitro* and in vivo study. *Biomacromolecules* **2005,** *6* (2), 726-33.

53. (a) Kim, D.-H.; Han, K.; Gupta, K.; Kwon, K. W.; Suh, K.-Y.; Levchenko, A., Mechanosensitivity of fibroblast cell shape and movement to anisotropic substratum topography gradients. *Biomaterials* **2009,** *30* (29), 5433-5444; (b) Rebollar, E.; Frischauf, I.; Olbrich, M.; Peterbauer, T.; Hering, S.; Preiner, J.; Hinterdorfer, P.; Romanin, C.; Heitz, J., Proliferation of aligned mammalian cells on laser-nanostructured polystyrene. *Biomaterials* **2008,** *29* (12), 1796-1806.

54. Miller, D. C.; Thapa, A.; Haberstroh, K. M.; Webster, T. J., Endothelial and vascular smooth muscle cell function on poly(lactic-co-glycolic acid) with nano-structured surface features. *Biomaterials* **2004,** *25* (1), 53-61.

55. Neto, A. I.; Vasconcelos, N. L.; Oliveira, S. M.; Ruiz-Molina, D.; Mano, J. F., High-Throughput Topographic, Mechanical, and Biological Screening of Multilayer Films Containing Mussel-Inspired Biopolymers. *Advanced Functional Materials* **2016,** *26* (16), 2745-2755.

56. (a) Choi, C. H.; Hagvall, S. H.; Wu, B. M.; Dunn, J. C.; Beygui, R. E.; CJ, C. J. K., Cell interaction with three-dimensional sharp-tip nanotopography. *Biomaterials* **2007,** *28* (9), 1672-9; (b) Wood, M. A.; Wilkinson, C. D.; Curtis, A. S., The effects of colloidal nanotopography on initial fibroblast adhesion and morphology. *IEEE transactions on nanobioscience* **2006,** *5* (1), 20-31; (c) Berry, C. C.; Dalby, M. J.; McCloy, D.; Affrossman, S., The fibroblast response to tubes exhibiting internal nanotopography. *Biomaterials* **2005,** *26* (24), 4985-4992; (d) Dalby, M. J.; Riehle, M. O.; Sutherland, D. S.; Agheli, H.; Curtis, A. S. G., Changes in fibroblast morphology in response to nano-columns produced by colloidal lithography. *Biomaterials* **2004,** *25* (23), 5415-5422; (e) Dalby, M. J.; Riehle, M. O.; Johnstone, H. J.; Affrossman, S.; Curtis, A. S., Polymer-demixed nanotopography: control of fibroblast spreading and proliferation. *Tissue Eng* **2002,** *8* (6), 1099-108.

57. Fujita, S.; Ohshima, M.; Iwata, H., Time-lapse observation of cell alignment on nanogrooved patterns. *Journal of the Royal Society, Interface / the Royal Society* **2009,** *6* (Suppl 3), S269-77.

58. Versaevel, M.; Grevesse, T.; Gabriele, S., Spatial coordination between cell and nuclear shape within micropatterned endothelial cells. *Nature Communications* **2012,** *3* (671), 671.

59. Clark, P.; Connolly, P.; Curtis, A. S.; Dow, J. A.; Wilkinson, C. D., Topographical control of cell behaviour: II. Multiple grooved substrata. *Development* **1990,** *108* (4), 635-644.

60. Curtis, A.; Wilkinson, C., Topographical control of cells. *Biomaterials* **1997,** *18* (24), 1573-83.

61. Alapan, Y.; Younesi, M.; Akkus, O.; Gurkan, U. A., Anisotropically Stiff 3D Micropillar Niche Induces Extraordinary Cell Alignment and Elongation. *Advanced Healthcare Materials* **2016,** *5* (15), 1884-92.

62. (a) Fraser, S. A.; Ting, Y.-H.; Mallon, K. S.; Wendt, A. E.; Murphy, C. J.; Nealey, P. F., Sub-micron and nanoscale feature depth modulates alignment of stromal fibroblasts and corneal epithelial cells in serum-rich and serum-free media. *Journal of biomedical materials research. Part A* **2008,** *86* (3), 725-735; (b) Walboomers, X. F.; Croes, H. J. E.; Ginsel, L. A.; Jansen, J. A., Contact guidance of rat fibroblasts on various implant materials. *Journal of Biomedical Materials Research* **1999,** *47* (2), 204-212.

63. Nathan, A. S.; Baker, B. M.; Nerurkar, N. L.; Mauck, R. L., Mechano-topographic modulation of stem cell nuclear shape on nanofibrous scaffolds. *Acta biomaterialia* **2011,** *7* (1), 57-66.

64. (a) Padmanabhan, J.; Augelli, M. J.; Cheung, B.; Kinser, E. R.; Cleary, B.; Kumar, P.; Wang, R.; Sawyer, A. J.; Li, R.; Schwarz, U. D.; Schroers, J.; Kyriakides, T. R., Regulation of cell-cell fusion by nanotopography. *Scientific Reports* **2016,** *6* (33277), 33277; (b) Cantini, M.; Sousa, M.; Moratal, D.; Mano, J. F.; Salmeron-Sanchez, M., Non-monotonic cell differentiation pattern on extreme wettability gradients. *Biomaterials Science* **2013,** *1* (2), 202-212.

65. Cabane, C.; Englaro, W.; Yeow, K.; Ragno, M.; Dérijard, B., Regulation of C2C12 myogenic terminal differentiation by MKK3/p38α pathway. *American Journal of Physiology - Cell Physiology* **2003,** *284* (3), C658-C666.

66. Horsley, V.; Pavlath, G. K., Forming a multinucleated cell: molecules that regulate myoblast fusion. *Cells Tissues Organs* **2004,** *176* (1-3), 67-78.

67. (a) Ku, S. H.; Park, C. B., Myoblast differentiation on graphene oxide. *Biomaterials* **2013,** *34* (8), 2017-2023; (b) Swailes, N. T.; Colegrave, M.; Knight, P. J.; Peckham, M., Non-muscle myosins 2A and 2B drive changes in cell morphology that occur as myoblasts align and fuse. *Journal of cell science* **2006,** *119* (Pt 17), 3561-70.

68. (a) Yang, H. S.; Lee, B.; Tsui, J. H.; Macadangdang, J.; Jang, S. Y.; Im, S. G.; Kim, D. H., Electroconductive Nanopatterned Substrates for Enhanced Myogenic Differentiation and Maturation. *Adv Healthc Mater* **2016,** *5* (1), 137-45; (b) Cooper, A.; Jana, S.; Bhattarai, N.; Zhang, M., Aligned chitosan-based nanofibers for enhanced myogenesis. *Journal of Materials Chemistry* **2010,** *20* (40), 8904-8911.

69. Aubin, H.; Nichol, J. W.; Hutson, C. B.; Bae, H.; Sieminski, A. L.; Cropek, D. M.; Akhyari, P.; Khademhosseini, A., Directed 3D cell alignment and elongation in microengineered hydrogels. *Biomaterials* **2010,** *31* (27), 6941-6951.

70. Dang, J. M.; Leong, K. W., Myogenic Induction of Aligned Mesenchymal Stem Cell Sheets by Culture on Thermally Responsive Electrospun Nanofibers. *Advanced Materials* **2007,** *19* (19), 2775-2779.

71. Ostrovidov, S.; Hosseini, V.; Ahadian, S.; Fujie, T.; Parthiban, S. P.; Ramalingam, M.; Bae, H.; Kaji, H.; Khademhosseini, A., Skeletal Muscle Tissue Engineering: Methods to Form Skeletal Myotubes and Their Applications. *Tissue Engineering Part B: Reviews* **2013,** *20* (5), 403-436.

72. Sousa, M. P.; Caridade, S. G.; Mano, J. F., Cell Alignment: Control of Cell Alignment and Morphology by Redesigning ECM-Mimetic Nanotopography on Multilayer Membranes (Adv. Healthcare Mater. 15/2017). *Advanced Healthcare Materials* **2017,** *6* (15).

VII. Cell-Adhesive Bioinspired and Catechol-Based Multilayer Freestanding Membranes for Bone Tissue Engineering[*]

Abstract

Mussels are marine organisms that have been mimicked due to their exceptional adhesive properties to all kind of surfaces, including rocks, under wet conditions. The proteins present on the mussel's foot contain 3,4-dihydroxy-L-alanine (DOPA), an amino acid from the catechol family that has been reported by their adhesive character. Therefore, we synthesized a mussel-inspired conjugated polymer, modifying the backbone of hyaluronic acid with dopamine by carbodiimide chemistry. Ultraviolet–visible (UV–vis) spectroscopy and nuclear magnetic resonance (NMR) techniques confirmed the success of this modification. Different techniques have been reported to produce two-dimensional (2D) or three-dimensional (3D) systems capable to support cells and tissue regeneration; among others, multilayer systems allow the construction of hierarchical structures from nano- to macroscales. In this study, the layer-by-layer (LbL) technique was used to produce freestanding multilayer membranes made uniquely of chitosan and dopamine-modified hyaluronic acid (HA-DN). The electrostatic interactions were found to be the main forces involved in the film construction. The surface morphology, chemistry, and mechanical properties of the freestanding membranes were characterized, confirming the enhancement of the adhesive properties in the presence of HA-DN. The MC3T3-E1 cell line was cultured on the surface of the membranes, demonstrating the potential of these freestanding multilayer systems to be used for bone tissue engineering.

Keywords: mussel-inspired; biomimetic; dopamine; multilayer freestanding membranes; adhesiveness; osteogenic differentiation; bone tissue engineering

---

[*] This Chapter is based on the following publication: Sousa M. P.; Mano J. F., Cell adhesive bioinspired and catechol-based multilayer freestanding membranes for bone tissue engineering, Biomimetics, **2017**, 2 (4).

1. Introduction

Catechol-based materials have been investigated quite a bit in the last decade, presenting an interesting structural and chemical versatility capable of being applied in different fields such as food and agrochemical engineering, green technology, analytical, materials science, biomedicine, and biotechnology [1]. In fact, catechols are aromatic derivatives with two contiguous (ortho-)hydroxyl groups that occur ubiquitously in nature, being a part of different biochemical processes and functions as simple molecular units or even as macromolecules [2]. These interesting molecules occur in different systems such as fruits, tea, and insects, but it is on marine mussels that catechols were identified as being responsible for their extremely adhesive properties under wet conditions [2a, 3]. This adhesiveness is mediated by a class of protein, the mussel adhesive proteins (MAPs), known for containing a high amount of the noncationic amino acid 3,4-dihydroxy-L-alanine (DOPA) [4]. Intense research has been conducted in this field over the last few decades and it has been proven that the catechol element of DOPA is mainly responsible for the strong adhesion to different type of wet substrates, from inorganic to organic ones [4a, 5]. To develop MAPs-based materials, different strategies have been employed [6]. Recombinant DNA technology permits the engineering of MAPs precursors purified from *Escherichia coli* and converting into DOPA-containing mimetic by tyrosinase treatment [7]. Another strategy is the chemical modification of polymer backbones with adhesive moieties; for instance, DOPA-modified poly(ethylene glycol) macromers were synthetized through standard peptide chemistry and suggested to produce catechol-based hydrogels [8]. Also DOPA-modified poly(vinyl alcohol) hydrogels were produced with self-healing and pH-responsiveness properties [9]. The chemical modification with DOPA or its derivatives (like dopamine (DN)) of different natural polymers has also been investigated in recent years, from chitosan [10] to alginate [11], or even dextran [12] or hyaluronic acid [13]. For instance, DOPA-modified alginates with different substitution degrees were synthesized and used to produce membranes with enhanced adhesive and biocompatible properties [14].

Natural-based polymers are generally recognized by their high biocompatibility when compared with synthetic ones, exhibiting some recognition domains for cell-binding or cell-mediated processes and making them very interesting materials for tissue engineering and biomedical applications [15]. However, some challenges remain; mechanical properties and controlled biodegradability have been gaining increasing importance. Therefore, some strategies have been envisaged to enhance the potential of tissue engineering and biomedical products and their bioactivity, modifying the physico-chemistry or even the topography of the materials [16]. To improve the adhesive properties of materials, mainly in a hydrated environment such as the human body, researchers have been investigating the marine mussel system and taking advantage of the chemical reactivity of catechol moieties [3, 17].

In this study, a biomimetic approach was combined with the use of natural-based polymers to obtain a mussel-bioinspired system for tissue engineering purposes, focusing on bone tissue engineering. Nowadays, autologous or allogeneic bone transplantation are still the most employed strategies for bone defect treatment, but it entails some risks of causing secondary trauma or even immune system rejection [18]. To overcome these drawbacks, several efforts have been applied to find a bone substitute that is ideally composed of three elements: cells, support material, and bioactive agents. An ideal tissue substitute must mimic the extracellular matrix (ECM) and different material parameters should be taken into account, such as the chemical groups, the biochemical properties, and the topography at the material–cell interface [19]. To date, different processing methodologies have been suggested to produce bone substitutes where the support material mimics ECM; nano- and microscale control of different properties along with the deposition of hierarchical films have been suggested for this purpose [20].

Layer-by-layer (LbL) is a versatile and inexpensive technique that has been widely applied in this context, being based on the sequential of complementary multivalent molecules on a substrate via electrostatic and/or nonelectrostatic interactions [21]. Different authors have reported LbL strategies to mimic some aspect of ECM [22]; Mhanna *et al.* [23] coated polydimethylsiloxane substrates with specific ECM macromolecules using LbL technology; they used collagen type I, chondroitin sulfate, and heparin and, depending on the composition of the film, they studied specific ECM–cell interactions. Layer-by-Layer-based products have also been exploited for bone tissue engineering purposes, offering fine control over different parameters like film thickness, architecture, chemistry, and even mechanical and topographical properties [24]. Oliveira *et al.* [25] assembled 10 tetralayers of human platelet lysates and marine-origin polysaccharides by LbL technology and then shaped them into fibrils by freeze-drying; the resulting scaffolds could induce the differentiation of human adipose stem cells into mature osteoblasts. In turn, Crouzier *et al.* [26] showed that cross-linked poly(L-lysine)/hyaluronic acid (HA) can serve as a reservoir for recombinant human bone morphogenetic protein-2 (rhBMP-2) delivery to myoblasts and induce their differentiation into osteoblasts in a dose-dependent manner. Overall, the LbL technique allows us to produce bioinspired and tunable materials to local deliver immobilized growth factors or other bioactive agents and even to instruct stem cells towards osteogenic phenotypes. Moreover, these films can be deposited on an extensive range of substrates of different composition, size, and shape.

Herein, LbL methodology was used to produce bioinspired freestanding multilayer membranes containing catechol groups on the surface and the bulk to improve the adhesiveness properties of the material. In this sense, DN moieties were chemically grafted onto HA to develop multilayer membranes through electrostatic interactions with chitosan (CHT). The modification of HA was confirmed by nuclear magnetic resonance (NMR) and ultraviolet–visible (UV–vis) spectroscopy. The ability to construct multilayer films was monitored using quartz crystal microbalance with dissipation (QCM-D). Adhesion mechanical tests and *in vitro* adhesion assays assessed the effect of having DN on the performance of the freestanding multilayer membranes.

Overall, the combination of the versatility of LbL methodology with the protein mussels’ inspiration prompted us to exploit catechol-containing multilayer membranes to enhance the interfacial interaction between cells and materials, which takes advantage of the adhesive properties conferred by DN moieties. The potential to induce *in vitro* bone tissue regeneration was investigated, using a pre-differentiated MC3T3-E1 cell line.

2. Materials and Methods

2.1. Materials

Chitosan with a *N*-deacetylation degree of 80% and a molecular weight in the range of 190–310 kDa, HA as hyaluronic acid sodium salt from *Streptococcus equi* with a molecular weight in the range of 1500–1800 kDa, DN as dopamine hydrochloride with a molecular weight of 189.64 g.mol^{-1} and *N*-(3-dimethylaminopropyl)-*N′*-ethylcarbodiimide hydrochloride (EDC) (purum ≥ 98.0% (AT)) were purchased from Sigma (St. Louis, Missouri, United States of America). These materials were used as received, except CHT, which was purified afterwards, following a standard procedure reported elsewhere [27].

2.2. Synthesis of Dopamine-Modified Hyaluronic Acid

The conjugate of HA modified with DN was synthesized using EDC as an activation agent of the carboxyl groups on HA chains, based on the procedure proposed by Lee *et al.* [28]. Basically, 1 g of HA was dissolved in 100 mL of phosphate-buffered saline (PBS, Sigma) solution and the pH was adjusted to 5.5 with a hydrochloric acid (HCl, 37%, reagent grade, Sigma) aqueous solution. Then, this solution was purged with nitrogen for 30 min and mixed with EDC and DN and maintained in reaction at 4 °C for 3 h. The pH was maintained at 5.5. Extensive dialysis was performed to remove unreacted chemicals and urea byproducts. After this step, the resulting conjugate was lyophilized for one week and then stored at −20 °C, protected from the light, to avoid oxidation.

2.2.1. Ultraviolet–Visible Spectrophotometry

UV–Vis spectrophotometer (Jasco V-560 PC) was used to confirm the substitution of dopamine in the conjugate. A solution of 1 mg mL^{-1} in sodium acetate buffer (Scharlab, Barcelona, Spain) with 0.15 M sodium chloride (NaCl, LabChem, Pittsburgh, Pennsylvania, United States of America) at pH 5.5 was prepared for the UV–Vis analysis and placed in 1 cm quartz cells. The wavelength range used for this analysis was from 190 nm to 900 nm. Sodium acetate buffer with 0.15 M sodium chloride and at pH 5.5 was used as the reference solution.

2.2.2. Nuclear Magnetic Resonance

^{1}H-NMR analyses were made dissolving overnight the HA, DN and HA-DN in deuterated water (D_2O, Cambridge Isotope Laboratories, Inc., Andover, Massachusetts, United States of America) at a concentration of 1 mg mL^{-1} (^{1}H-NMR). The spectra were obtained using a spectrometer BioSpin 300 MHz (Bruker, Billerica, Massachusetts, United States of America). The spectra were recorded at 298 K and 300 MHz for ^{1}H.

2.3. Quartz Crystal Microbalance with Dissipation

The formation of the multilayers of CHT and HA-DN was followed in situ by QCM-D (Q-Sense, Biolin Scientific, Göteborg, Sweden). The mass change results from the variation of the normalized resonant frequency ($\Delta f/\upsilon$) of an oscillating quartz crystal when adsorption occurs on the surface and the dissipation factor (Δ*D*) provides a measure of the energy loss in the system. The measurements can be conducted at the fundamental frequency and at several overtones number (υ = 1, 3, 5, …, 11). Chitosan was used as the polycation while HA or HA-DN acted as the polyanion. Fresh polyelectrolyte solutions were prepared by dissolution of HA-DN, HA, and CHT in sodium acetate buffer containing 0.15 M of NaCl to yield a final concentration of 1 mg mL^{-1}, at pH 5.5. The sensor crystals used were AT-cut quartz (Q-Sense) with gold-plated polished electrodes. These crystals were excited at 5 MHz as well as at 15, 25, 35, 45, and 55 MHz corresponding to the 3rd, 5th, 7th, 9th, and 11th overtones. The crystals were previously cleaned with a pre-exposition to UV ozone (BioForce Nanosciences, Salt Lake City, Utah, EUA) irradiation during 10 min followed by an immersion on a 5:1:1-mixture of mQ-water, ammonia (25%, Sigma), and hydrogen peroxide (30%, Sigma) at 75 °C, during 5 min. Then the crystals were exposed to a sequential sonication for 3 min in acetone, ethanol, and isopropanol (all from Sigma) and then dried with flowing nitrogen gas avoiding contamination prior to use. To ensure that the crystals are perfectly clean and therefore show a null frequency, all the experiments started with a buffer/solvent baseline. Then, the polyelectrolyte solutions were injected into the cell during 10 min at a flow rate of 20 $\mu l.min^{-1}$, starting with CHT. A rinsing step of 10 min with the solvent was included between the adsorptions of each polyelectrolyte. The multilayer systems were assembled at pH 5.5. The pH was adjusted with HCl or sodium hydroxide (NaOH, pellets, Fine Chemicals, Akzo Nobel Chemicals S.A., Mons, Belgium). Chitosan/HA films were prepared for comparison, to conclude about the DN effect onto the multilayer system. Films with eight bilayers were produced. All experiments were conducted at 25 °C. During the entire process Δ*f*/υ and Δ*D* shifts were continuously recorded as a function of time. Thickness measurements were performed using the Voigt viscoelastic model implemented in the QTools software (Q-Sense, version 3.1.29.619). Changes in resonant frequency and dissipation of the fifth overtone were fitted. Based on the assumed growth models, the thickness of the multilayer films after 200 cycles was estimated for each system.

2.4. Freestanding Production and Characterization

Multilayer CHT/HA and CHT/HA-DN were built on polypropylene (PP) substrates (Auchan, Villeneuve-d'Ascq, France). Prior to the depositions, these surfaces were cleaned with ethanol and rinsed thoroughly with water before being dried with a stream of nitrogen. The polyelectrolyte solutions were freshly prepared at 1 mg. l^{-1} in a sodium acetate solution containing 0.15 M NaCl, being the pH adjusted to 5.5. The PP substrates were firstly dipped in CHT solution for 6 min and then rinsed twice in the washing solution (acetate buffer, pH 5.5) for 2 min each. Then, they were immersed in the polyanion solution (HA or HA-DN) for 6 min and again twice in the washing solution. This procedure was repeated 200 times with the help of a homemade dipping robot. After drying, the multilayer films were easily detached from the PP substrates without any damage resulting on the freestanding membranes $[CHT/HA]_{200}$ and $[CHT/HA\text{-}DN]_{200}$. After production, the membranes were characterized using different techniques and equipment.

2.4.1. Scanning Electron Microscopy and Energy-Dispersive X-ray Spectroscopy

The surface morphology of both sides of $[CHT/HA]_{200}$ and $[CHT/HA\text{-}DN]_{200}$ membranes was observed using a Hitachi SU-70 (Hitachi, Tokyo, Japan) scanning electron microscope. All samples were coated with a conductive layer of sputtered gold/palladium. The scanning electron microscopy (SEM) micrographs were taken at an accelerating voltage of 4 kV and at different magnifications. For the cross-section observation, the detached freestandings were immersed in liquid nitrogen until free fracture. After that, the free fracture was placed at 45° and observed by SEM. Energy-dispersive X-ray spectroscopy (EDS, Hitachi) was also used to determine the elemental components of the top surface and in the cross-section of the membranes. The samples were also sputtered with gold/palladium and the analysis was made at an accelerating voltage of 15 kV. The ratio between the oxygen (O) and the nitrogen (N) presented on the top surfaces was quantified in a representative area of the membrane ($A = 0.136\ mm^2$).

2.4.2. Adhesive Mechanical Tests

The adhesion properties of the multilayer were firstly evaluated using a universal mechanical testing machine (Instron model 5966, High Wycombe, Buckinghamshire, United Kingdom), following the standard test method for shear strength of single-lap-joint adhesively bonded metal specimens by tension loading ASTM D1002 (ASTM International, West Conshohocken, Pennsylvania, United States of America) with slightly modifications. All the adhesion experiments were conducted at 25 °C, at a cross-head speed of 5 $mm.min^{-1}$ and using a 1.0 kN static load cell. The lap shear adhesion specimens were squares (20 mm × 20 mm) of freestanding membranes that were incubated at 37 °C and equilibrated in a 50% humidity atmosphere prior to testing. Briefly, the samples were put between two glass slides and left in contact overnight. Then, the systems were stressed until enough force was applied to trigger their detachment and pull them apart, using the Instron apparatus. The lap shear bonding strength was then determined from the maximum of the force–deformation curve obtained. The average and standard deviations were determined using the results from five samples.

While lap shear strength gives a quantitative idea of the adhesive properties of the membranes, other nonconventional test was made to observe the bioadhesiveness potential of these systems. Briefly, the $[CHT/HA]_{200}$ and $[CHT/HA\text{-}DN]_{200}$ freestanding membranes were put in contact with a clean surface of porcine bone tissue in a 50% humidity-controlled environment at 37 °C. Then, the freestanding membranes were pulled out of the bone with tweezers. This process was recorded by a video camera (Canon EOS 1200D, Tokyo, Japan).

2.5. *In Vitro* Cellular Tests

The sub-clone 4 of MC3T3-E1 cell line was obtained from the American Type Culture Collection (ATCC)-*Laboratory of the Government Chemist (*LGC) standards (ATCC® CRL-2593™) [30]. The cells were cultured with Minimum Essential Medium (MEM) *Alpha* Modification (1X), (α-MEM, Gibco, Thermo Fisher Scientific, Waltham, Massachusetts, United States of America) supplemented with sodium bicarbonate suitable for cell culture (Sigma), 10% fetal bovine serum (FBS, Life Technologies™, Thermo Fisher Scientific, Waltham, Massachusetts, United States of America), and 1% antibiotic–antimycotic (Gibco) at pH 7.4. The cells were cultured in 75 cm^2 tissue culture flasks and incubated at 37 °C in a humidified air atmosphere of 5% CO_2. The medium was changed every three–four days. At 80–90% of confluence, cells grown in tissue culture flasks were washed with Dulbecco's phosphate-buffered saline (DPBS, Corning, New York, United States of America) and then detached by a chemical procedure with trypLE™ express solution (Life Technologies™) for 5 min at 37 °C in a humidified air atmosphere of 5% CO_2. To inactivate the trypLE™ express effect, cell culture medium was added. The cells were then centrifuged at 300 × g and 25 °C for 5 min and the medium was decanted. Cells between passage 12 and 13 were used for this study. Prior to cell seeding, the samples were cut in small squares of 25 mm^2 or 1 cm^2, treated with UV ozone for 10 min and immersed in ethanol for 2 h. Then, 150 µL or 300 µL (depending on the size of the sample) of supplemented α-MEM containing a cell suspension with a density of 2×10^4 $cells.cm^{-2}$ was dropped above the surfaces of the $[CHT/HA]_{200}$ and the $[CHT/HA\text{-}DN]_{200}$ freestanding membranes, and the positive control tissue culture polystyrene surface (TCPS, Sarstedt AG & Co., Nümbrecht, Germany) (in triplicate). Then, the samples were incubated at 37 °C in a humidified air atmosphere of 5% CO_2. After 4 h, cells already started to adhere, and fresh basal culture medium was added.

2.5.1. Metabolic Activity of MC3T3-E1 Cells

The samples were tested for cytotoxicity by analyzing their metabolic activity using the alamarBlue® reduction assay (Invitrogen™, Thermo Fisher Scientific, Waltham, Massachusetts, United States of America). Briefly, the samples (small squares of 25 mm^2) with adhered cells were placed in a nontreated surface 48-well cell culture plate (in triplicate) and incubated at 37 °C and 5% CO_2. At one, three and seven days of culture, the assay was performed, always protecting from light. Briefly, the culture medium was removed and 500 µL of supplemented α-MEM containing 10% (*v*/*v*) of alamarBlue solution was added to each well. The samples were then incubated in the dark, overnight, at 37 °C and 5% CO_2. After 12 h, 100 µL of each well (in triplicate) was transferred to a 96-well plate. The absorbance was monitored at 570 nm and 600 nm, using a microplate reader Synergy HTX (BioTek Instruments, Inc., Winooski, Vermont, United States of America).

2.5.2. DNA Quantification Assay

A DNA quantification assay (Quant-iT™ PicoGreen® dsDNA Assay Kit, Invitrogen™, Thermo Fisher Scientific, Waltham, Massachusetts, United States of America) was also performed to evaluate cell proliferation when cultured on the samples' surface. All seeding procedure was repeated for this assay. For each culture time, the samples were washed with DPBS, and then, transferred with 1 mL of ultrapure sterile water to an Eppendorf flask. These Eppendorf flasks were placed at 37 °C for 1 h and then immediately stored at −80 °C until use. The quantification of total DNA was determined after cell lysis, according with the manufacturer's description. After transferring each solution to a 96-well white opaque plate (in triplicate), the plate was incubated at 25 °C, protected from the light, for 10 min. The standard curve for DNA analysis was generated with provided DNA from the assay kit. Fluorescence was read at excitation of 485/20 nm and emission of 528/20 nm using a microplate reader Synergy HTX (BioTek Instruments, Inc.).

2.5.3. Morphological Observation of MC3T3-E1 Cells

MC3T3-E1 cell morphology was observed using a fluorescence microscope (Axio Imager 2, Zeiss, Oberkochen, Germany). Briefly, the cells were seeded above the samples (squares 1 cm^2) at a density of 2×10^4 $cells.cm^{-2}$ and cultured for three and seven days, using basal culture conditions. After each time-point, the samples were gently washed with sterile DPBS and fixed with 10% (*v*/*v*) of formalin (Sigma) in DPBS solution for 30 min. To obtain morphological fluorescence images, a rhodamine phalloidin (Thermo Fisher Scientific, Waltham, Massachusetts, United States of America) and 4',6-diamidino-2-phenylindole (DAPI, Thermo Fisher Scientific, Waltham, Massachusetts, United States of America) fluorescent assay was performed at each time culture period; DAPI stains preferentially nuclei and phalloidin the actin fibers of the cell cytoskeleton. Firstly, the fixed samples were permeabilized with 0.2% (*v*/*v*) of Triton X-100 (Sigma) in DPBS solution for 10 min and then blocked with 5% FBS (*v*/*v*) in DPBS solution for 30 min. Then, the samples were treated with rhodamine phalloidin for 45 min and consequently with DAPI for 15 min. Afterwards, the cell morphology was observed using the fluorescence microscope.

2.5.4. Osteogenic Potential of Dopamine-Modified Hyaluronic Acid Membranes and Differentiation of MC3T3-E1 Cells by Immunocytochemistry

To evaluate the osteogenic potential of these substrates, cells were cultured at 2×10^4 cells cm^{-2} in basal growth medium, at 37 °C and 5% of CO_2. After five days in basal conditions, the medium was changed for osteogenic medium (α-MEM containing 10% FBS, 10 mM β-glycerolphosphate disodium salt hydrate (Sigma), and 50 $\mu g.mL^{-1}$ L-ascorbic acid (Cayman Chemical, Ann Arbor, Michigan, United States of America)). The differentiation medium was changed every three days.

Intracellular osteopontin expression has been reported as a marker for osteogenic differentiation [30]. After 14 days in differentiation medium, the samples were fixed in 10% (*v*/*v*) formalin (Sigma) in DPBS. Following the fixation step, the fixed samples were permeabilized with 0.2% (*v*/*v*) of Triton X-100 in DPBS solution for 10 min and then blocked with 5% FBS (*v*/*v*) in DPBS solution for 60 min. Then, the samples were examined for protein expression visualization using a mouse antibody against osteopontin (BioLegend, San Diego, California, United States of America), by incubation overnight, at 4 °C. Subsequently, the samples were treated with the corresponding secondary antibody anti-mouse Alexa Fluor 647 (Invitrogen™) for 1 h at 25 °C and consequently with rhodamine phalloidin and DAPI for 45 min and 15 min, respectively. Between each step the samples were extensively washed. Afterwards, the cell morphology was observed using fluorescence microscopy.

2.6. Statistical Analysis

All the experiments were performed with at least three replicates and were independently performed three times. Results are expressed as mean ± standard deviation. Differences between the experimental results were analyzed using the one-factor or two-factor analysis of variance (ANOVA), with the Bonferroni's multiple comparison test, defined with a statistical significance of $p < 0.05$.

3. .Results

The HA was functionalized with DN and the resulting conjugate was combined with CHT to produce multilayer biomimetic membranes by LbL. The chemical structures of each compound, including the resulting chemical structure of HA-DN are represented in Figure VII-1. We hypothesize that the presence of DN moieties along the thickness of the films, especially on the last layer and top surface of the membrane, could enhance the interaction between cell and material and improve the osteogenic potential of MC3T3-E1 cells.

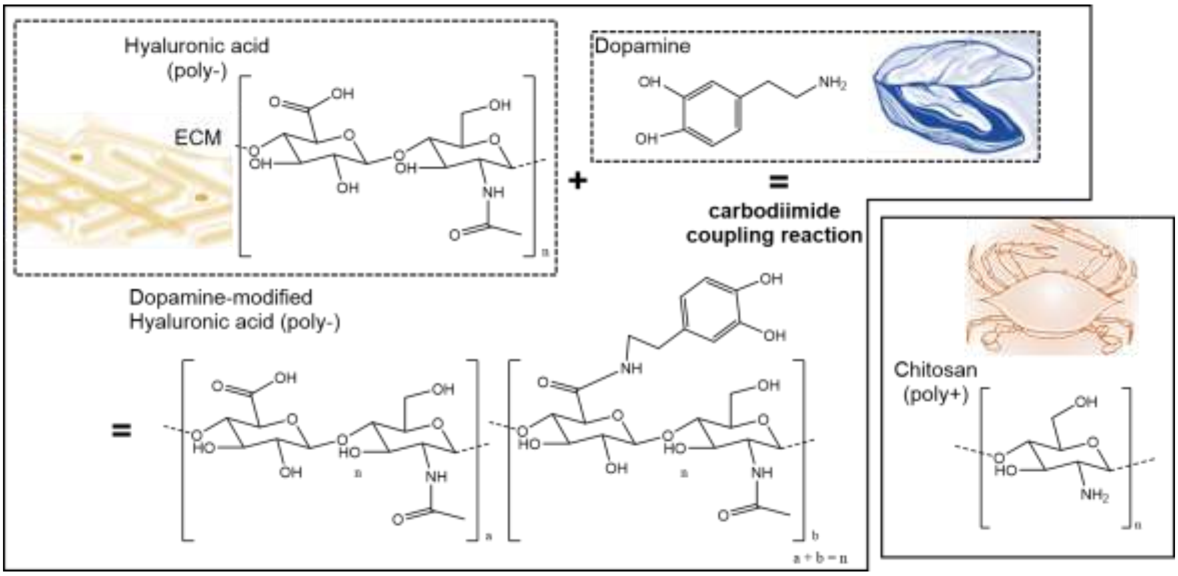

Figure VII-1. Chemical structure of hyaluronic acid (HA), dopamine (DN), and chitosan (CHT). Synthesis and chemical structure of dopamine-modified hyaluronic acid (HA-DN). ECM: extracellular matrix.

3.1. . Synthesis and Characterization of Conjugated Dopamine-Modified Hyaluronic Acid

The conjugation of DN on HA backbone was achieved by the standard carbodiimide coupling method. Using EDC chemistry, the carboxyl group of HA was activated to react with the amine group of DN. After lyophilizing, the resulting conjugated was characterized by UV–Vis and NMR for ^{1}H.

Figure VII-2A shows the UV–vis spectrum of each polymer solution, HA and HA-DN. The conjugation of DN onto the backbone of HA was confirmed by the presence of a typical peak around 280 nm, characteristic of dopamine. As expected, this peak did not appear for HA, confirming the presence of DN moieties on the final conjugated HA-DN [31].

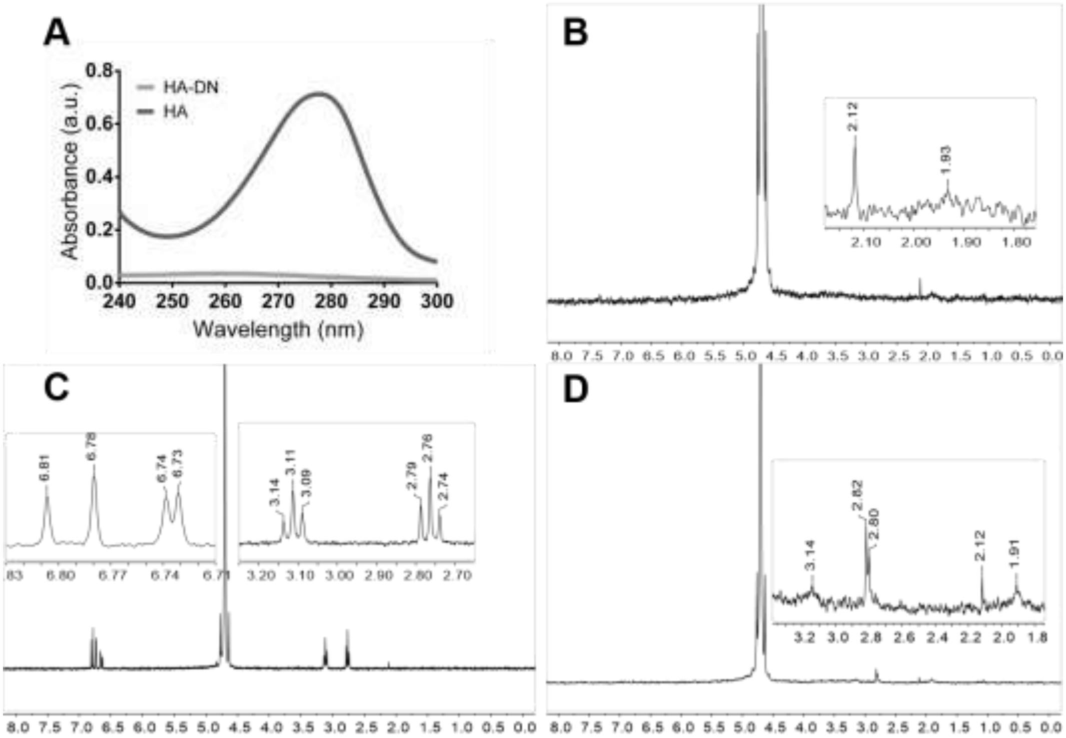

Figure VII-2. Characterization of conjugated dopamine-modified hyaluronic acid: (A) Ultraviolet–visible (UV–vis) spectra of the control (HA) and the catechol-based conjugate (HA-DN). ^{1}H-nuclear magnetic resonance (NMR) spectra of (B) HA; (C) DN and (D) the synthesized conjugate HA-DN, all with an expanded view. a.u.: Arbitrary units.

Figure VII-2B–D shows the NMR spectra of HA, DN, and HA-DN for ^{1}H. Regarding the spectrum of HA, the peak at $\delta = 1.93$ ppm is associated with the protons of the methyl group [32]. The spectrum of DN was characterized by the triplets centered at $\delta = 2.76$ ppm and at $\delta = 3.11$ ppm that are associated with the protons of the aliphatic group [33]. In turn, the multiplets between $\delta = 6.73$ ppm and $\delta = 6.81$ ppm are related with the protons in ortho- and meta-coupling position of the ring [13]. The spectrum of HA-DN was consistent with the HA and DN ^{1}H-NMR spectra, as observed in Figure VII-2D. Both the results of UV–vis spectroscopy and NMR confirmed that DN was successfully conjugated to HA.

3.2. Multilayer Construction and Thickness Estimation

The assembly of CHT and HA or HA-DN was first monitored on a gold quartz crystal by QCM-D. Figure VII-3A shows the LbL assembly of CHT and HA and Figure VII-3B shows the assembly of CHT and HA-DN. For both conditions, the first change in frequency happened when CHT was deposited on bare gold quartz. The second decrease in frequency corresponded to HA or HA-DN layers and this behavior was repeated during all the experiment (eight bilayers), indicating the successful of alternate adsorption of CHT and HA or HA-DN onto the quartz crystal surface. For both systems, the film seemed to have a stable growth for the first layers, but it appeared more unstable with the addition of further layers. We hypothesize that it could be due to the formation of soluble macromolecular complexes between the previous layer and the new polymer solution [34]. Besides monitoring frequency variation (Δf), QCM-D technology also detects dissipation variation (ΔD), allowing to take assumptions of the multilayer hydration state. When the film is rigid, the Δf and ΔD for the fundamental frequency superpose with the signals recorded in the higher harmonic [35]; in the case of CHT/HA and CHT/HA-DN systems the soft nature of the layers adhering on the crystal leads to the dispersion of the different overtones. A more swollen multilayer film was achieved for polysaccharide-based films when compared with other LbL systems [36]. The assembly of CHT and HA or HA-DN induced similar frequency changes but different dissipation variations, with a bigger dissipation shift when CHT was deposited. This could be related to the fact that more water molecules were entrapped in the CHT layer [29].

Using the modeling tool Q-Tools [29], other parameters could be estimated like the thickness of the films. The Voigt model was chosen to estimate the film thickness of each system, requiring three parameters to be fixed: solvent density, solvent viscosity, and layer density. The solvent viscosity was fixed at 1 mPa.s^{-1} (the same as water) and the film density at 1100 kg.m^{-3} (frequently assumed to return the lowest calculation error). The solvent density was changed by trial and error between 1000 and 1080 kg.m^{-3} until error was minimized. Figure VII-3C,D represents the thickness estimation along with the number of bilayers for CHT/HA and CHT/HA-DN systems, respectively. For the CHT/HA system, the thickness of the films seemed to increase exponentially with the number of bilayers. On the other hand, CHT/HA-DN seemed to increase linearly with the number of bilayers. These results are in accordance with the related literature [13]; CHT/HA multilayer films are uniquely composed of polysaccharides and naturally more water-rich than the other system. In turn, the presence of DN on the CHT/HA-DN system seemed to change the growth regime to a linear model; this could indicate that DN conferred less water content on the films. After eight bilayers, the estimated thickness for the CHT/HA system is 157 nm and for the CHT/HA-DN it is 137 nm. Using the resulting linear model, after 200 bilayers we expected a thickness of the CHT/HA-DN system of about 4.0 µm. As HA-DN presents bigger chains, we expected that the thickness of the CHT/HA-DN could be higher than for the CHT/HA system. However, for the first eight bilayers, we observed the opposite trend. We hypothesize that it could be the result of the re-arrangement of the polymer chains when LbL happens; the HA-DN chains seemed to compact more than HA chains, for the first layers of the film.

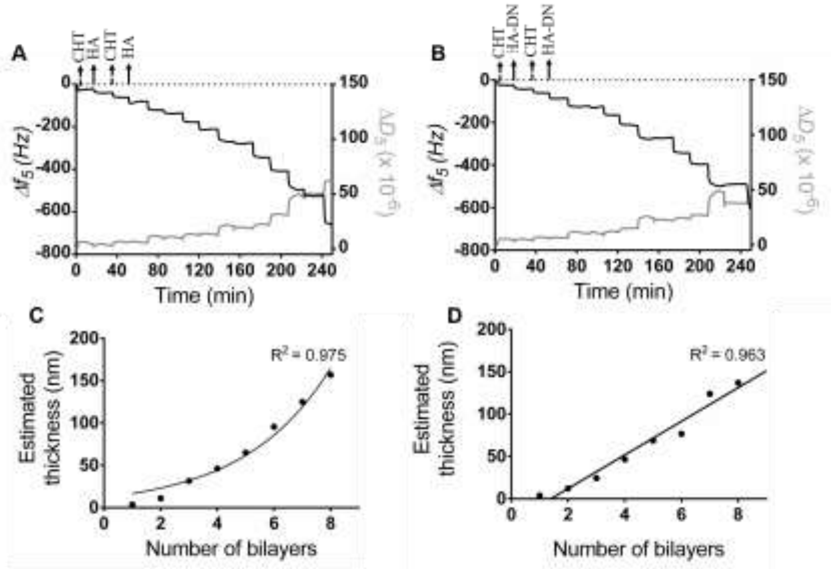

Figure VII-3. Build-up assemblies of (A) CHT and HA, and (B) CHT and HA-DN, monitored by quartz crystal microbalance with dissipation (QCM-D). Data shows the normalized frequency (Δf) and dissipation (ΔD) variations at the fifth overtone as a function of the time. Cumulative thickness evolution of the (C) CHT/HA and (D) CHT/HA-DN multilayer systems as a function of the number of deposition bilayers (Voigt model).

3.3. Production of the Freestanding Multilayer Membranes

From QCM-D monitoring results, CHT and HA or CHT and HA-DN could be combined to produce multilayer systems, with times of deposition of about 10 min; although from QCM-D data, using 6 min of deposition would be enough to construct such multilayer films. This observation was valuable to reduce the times of processing. Therefore, to produce freestanding polyelectrolyte multilayered membranes, we dipped an inert substrate successively on CHT and HA or on CHT and HA-DN solutions, for 6 min each immersion. The chosen underlying substrates were simple PP sheets that are widely available, inexpensive, and can be cut into a large range of shapes and sizes [37]. Between each dipping, we realized a washing step in the sodium acetate buffer (pH 5.5), to remove the excess of polymer. After 200 bilayers, the resulting multilayer films were dried at 25 °C and then easily detached from the underlying substrate, without requiring any post-treatment to dissolve the underlying substrate or any kind of mechanical force that could damage the membrane (see in Supplementary Figure S VII-1A images representing the sequence of actions to detach the membrane from the PP substrate). The number of cycles has a direct influence on the thickness of the membranes and, indirectly, on their robustness and easiness to handle [37]. These membranes were designed as a support material for cells to adhere and differentiate, allowing bone tissue regeneration; this means that we needed the smallest thickness possible, without compromising the stability in physiological medium and the handling. The LbL parameters were optimized, choosing for instance a different number of cycles, but 200 bilayers seemed to be the best compromise between thickness and stability/handling.

The build-up of such LbL-based freestanding membranes has been reported in the literature [37-38], and even with polymers with a potentially adhesive character it was possible to detach the membranes; this may be due to the first layer being CHT. The photograph of both $[CHT/HA]_{200}$ and $[CHT/HA\text{-}DN]_{200}$ membranes is presented in Figure S VII-1B, with some differences in color and transparency perceptible.

3.4. Surface Morphology and Thickness of the Freestanding Membranes

The morphologies of the surface of the freestanding membranes were investigated by SEM. Figure VII-4A shows the top view of upper side of the $[CHT/HA]_{200}$ membrane (HA-ending layer); a closed network pore configuration and a smooth surface was observed. In contrast, the top-view of the upper side of the $[CHT/HA\text{-}DN]_{200}$ membrane (HA-DN-ending layer) shows an interesting pore network, with bigger pore diameters and a rougher surface, as shown in Figure VII-4B. Therefore, some differences were noted between the morphologies of the upper layer of the two systems; we hypothesize that the presence of DN in the last layer of the freestanding membrane conferred a higher pore network system and rougher structures than HA alone. Figure VII-4C,D shows a SEM image of the down side of the $[CHT/HA]_{200}$ and $[CHT/HA\text{-}DN]_{200}$ membranes, respectively. Similar morphologies were observed on the CHT side of the membranes, highlighting the rough nature conferred by CHT. Figure VII-4E,F represents the cross-section of the $[CHT/HA]_{200}$ and $[CHT/HA\text{-}DN]_{200}$ freestanding membranes after free-fracture, respectively; $[CHT/HA]_{200}$ cross-section shows a more homogeneous distribution of the polyelectrolytes layers along with the thickness of the membrane, being possible to observe a kind of LbL stratification.

The thickness of the [CHT/HA]$_{200}$ membrane is around 5.5 ± 0.1 µm. A thickness of 7.7 ± 0.1 µm was achieved when DN is conjugated with HA and integrated in a multilayer system with CHT. The differences between the thickness of the membranes and the organization along the *z*-axis could be due to the arrangement of the polymer chains during the multilayer construction. Comparing the real thickness values with the ones estimated from QCM-D data, we obtained thicker [CHT/HA-DN]$_{200}$ films than expected. This fact could be due to some accumulation phenomenon and chain arrangement along with the thickness, which could happen after the construction of the initial layers of the multilayer. Curiously, the thickness of the [CHT/HA]$_{200}$ membranes was much lower than expected by the exponential growth. We hypothesize that for a higher number of bilayers, we cannot assume exponential growth but instead linear growth (R^2 = 0.969); therefore, the estimated thickness would be about 4.4 µm, which is approximated to be the real thickness of the freestanding [CHT/HA]$_{200}$ membrane.

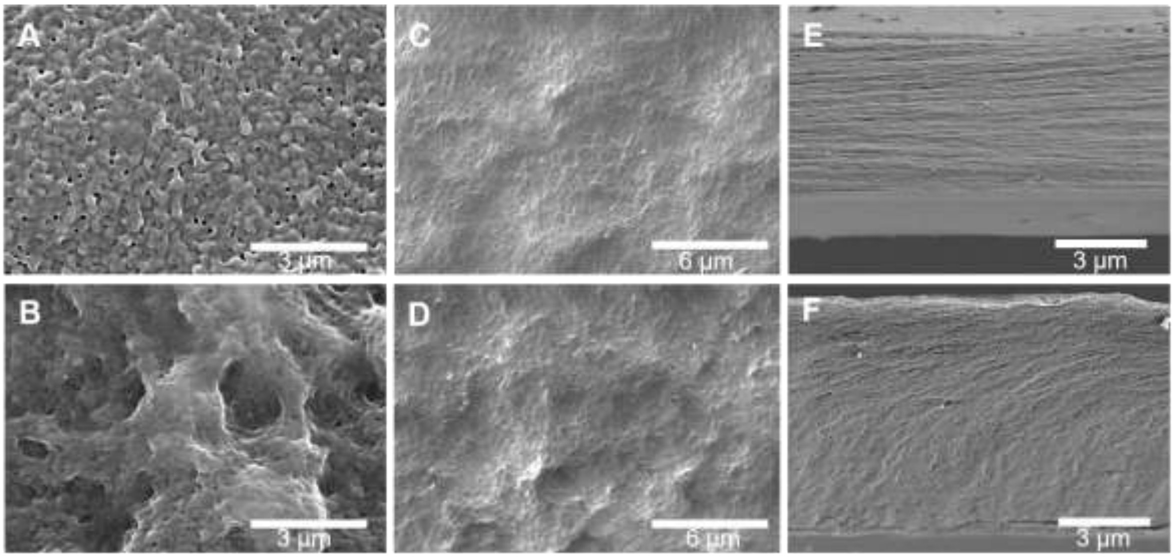

Figure VII-4. Representative scanning electron microscopy (SEM) images of the surfaces of (A) [CHT/HA]$_{200}$ (HA-ending side); (B) [CHT/HA-DN]$_{200}$ (HA-DN-ending side); (C) [CHT/HA]$_{200}$ (CHT-ending side); (D) [CHT/HA-DN]$_{200}$ (CHT-ending side). Representative SEM images of the cross-section of the (E) [CHT/HA]$_{200}$ and the (F) [CHT/HA-DN]$_{200}$ freestanding membranes.

3.5. Chemical Analysis of the Surface of the Freestanding Membranes

The surface chemical properties of the freestanding multilayer membranes were investigated by EDS analysis. Figure VII-5A,B shows EDS maps for [CHT/HA]$_{200}$ and [CHT/HA-DN]$_{200}$ membranes along the thickness (cross-section). Visually, both membranes revealed the presence of carbon, oxygen and nitrogen. All these elements are presented along with all the thickness of the membranes. In turn, Figure VII-5C,D shows EDS map images for the [CHT/HA]$_{200}$ and [CHT/HA-DN]$_{200}$ membranes' top surface and the respective quantification for the same area (Figure VII-5E and VII-5F, respectively). Both membranes revealed the presence of carbon, oxygen, sodium, and nitrogen. In fact, the ration between oxygen and nitrogen is significant higher for [CHT/HA-DN]$_{200}$ than for [CHT/HA]$_{200}$ membranes. We hypothesize that the nitrogen quantity could be higher for the [CHT/HA-DN]$_{200}$ due to the presence of DN in the last layer, which adds amine groups to the system.

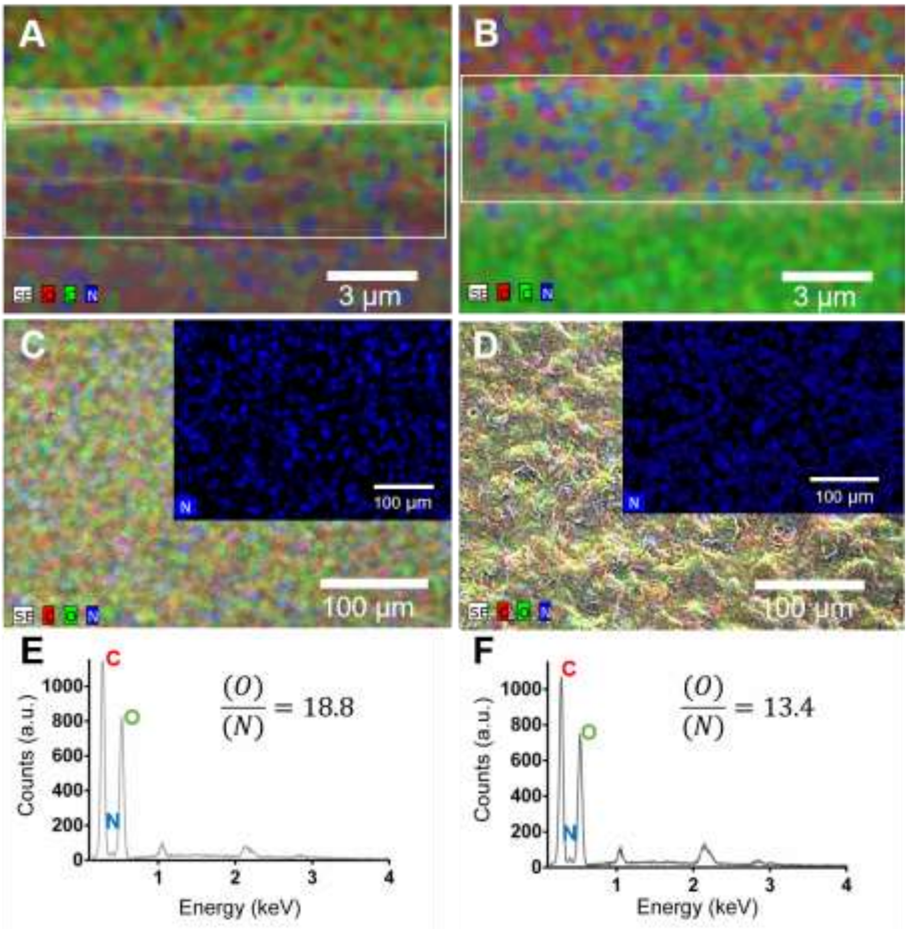

Figure VII-5. Mixed element map for carbon (C), oxygen (O) and nitrogen (N) of the cross-section of (A) $[CHT/HA]_{200}$ and (B) $[CHT/HA\text{-}DN]_{200}$ freestanding membranes. Mixed element map for carbon (C), oxygen (O), and nitrogen (N) of upper surface of (C) $[CHT/HA]_{200}$ and (D) $[CHT/HA\text{-}DN]_{200}$ freestanding membranes. Energy-dispersive X-ray spectra and ration quantification of O/N of (E) $[CHT/HA]_{200}$ and (F) $[CHT/HA\text{-}DN]_{200}$ freestanding membranes. a.u.: Arbitrary units.

3.6. Adhesive Properties of the Freestanding Membranes

In this work, freestanding membranes were used to glue two pieces of glass and this system was used as a proof of the concept for the adhesive strength of the $[CHT/HA]_{200}$ and $[CHT/HA\text{-}DN]_{200}$ membranes. The size of these membranes was around 20 mm × 20 mm, and the thickness was between 5 µm and 8 µm. Briefly, the freestanding membrane was sandwiched between two pieces of glass, in a controlled environment, trying to mimic the inner body conditions (37 °C in a moist environment), and incubated overnight. Most of the methods to determine the adhesive properties involve determination of the perpendicular force required to separate two surfaces. As biological tissues are more susceptible to shear stress than tensile stress, we decided to investigate the force that makes an adhesive slide on a surface in the direction parallel to the plane of contact [39]. The ability of $[CHT/HA]_{200}$ and $[CHT/HA\text{-}DN]_{200}$ to glue two glass substrates together was evaluated using a universal mechanical testing machine according to the standard procedure ASTM D1002, with subtle modifications. A heavy load (1.0 kN) could be held on a small joint area (20 mm × 20 mm) until it caused the detachment of the glass slides (see the mounting scheme in Figure VII-6A). Figure VII-6B presents the values of adhesive strength for each condition. From the lap shear adhesion tests, higher load values were obtained for the same displacement for $[CHT/HA\text{-}DN]_{200}$ membranes, indicating that more load is required to separate the glued glass slides. The calculation of lap shear adhesion strength was performed for each case; the $[CHT/HA]_{200}$ system presents an adhesion strength of 3.4 ± 0.6 MPa, while the $[CHT/HA\text{-}DN]_{200}$ system presents an adhesion strength of 8.6 ± 2.2 MPa. Such a difference highlights the adhesive strength of the membrane containing DN compared with the control. We hypothesize that the presence of the catechol moieties in the $[CHT/HA\text{-}DN]_{200}$ membranes increased the adhesion force between the two glass slides. The adhesive characteristics of catechol-based materials have been already investigated [13, 40]. For instance, Ninan *et al.* [41] studied the adhesive properties of marine mussel adhesive extracts to bond porcine skin in controlled dry and humid conditions; the tissue joint strength was about 1 MPa for mussel extract joints under humid conditions. Also, Kim *et al.* [42] reported the development of a water-immiscible mussel protein-based adhesive, composed of a complex coacervate of HA and DOPA with strong underwater adhesion; an adhesive strength of about 0.14 ± 0.03 MPa was obtained, using rat bladder tissue as the contact substrate. Even using a different contact substrate, the guidelines for adhesive tests were the same as for the previous examples. Even so, we obtained significantly higher values of strength adhesion with $[CHT/HA\text{-}DN]_{200}$ membranes. Well-known bioadhesiveness are fibrin and cyanoacrylate-based materials, which present a shear adhesive strength around 0.013 MPa and 0.068 MPa, respectively [43]. Bioadhesive hydrogels have been reported mainly for topical wound dressings and sealants as their adhesive strength is still considered to be weak [43]. For tissue engineering applications, bioadhesive films are of more interest. Layer-by-layer technology has been used for this purpose; Neto *et al.* [13, 44] already reported the ability to produce multilayer coatings composed of CHT and DOPA-modified HA with enhanced adhesive properties. The adhesive strength of the coating was about 2.3 ± 2.2 MPa, more than triple that of the control coating. Other LbL systems have been reported, but mostly in the form of coatings and not as freestanding membranes, which is more relevant for developing supports for tissue engineering purposes. To the best of our knowledge, there has already been one work on such adhesive freestanding multilayer membranes, but instead of dopamine they took advantage of the adhesive properties of levan derivatives [39]. Another strategy was envisaged to evaluate the bioadhesiveness of this membrane. After putting the $[CHT/HA]_{200}$ and $[CHT/HA\text{-}DN]_{200}$ membranes in contact with a clean surface of porcine bone at 37 °C, at 50% humidity overnight, it was possible to observe that more force is required to pull out the $[CHT/HA\text{-}DN]_{200}$ membrane (see representative images in Figure VII-6C (i) before and (ii) after applying a detachment force with tweezers, and the video recording in Supplementary Figure S VII.2). The $[CHT/HA]_{200}$ membrane was easier to detach from the surface of porcine bone than the $[CHT/HA\text{-}DN]_{200}$ membrane. This result is in accordance with the lap shear adhesion strength test, highlighting the adhesive potential of DN when incorporated in these multilayer freestanding systems.

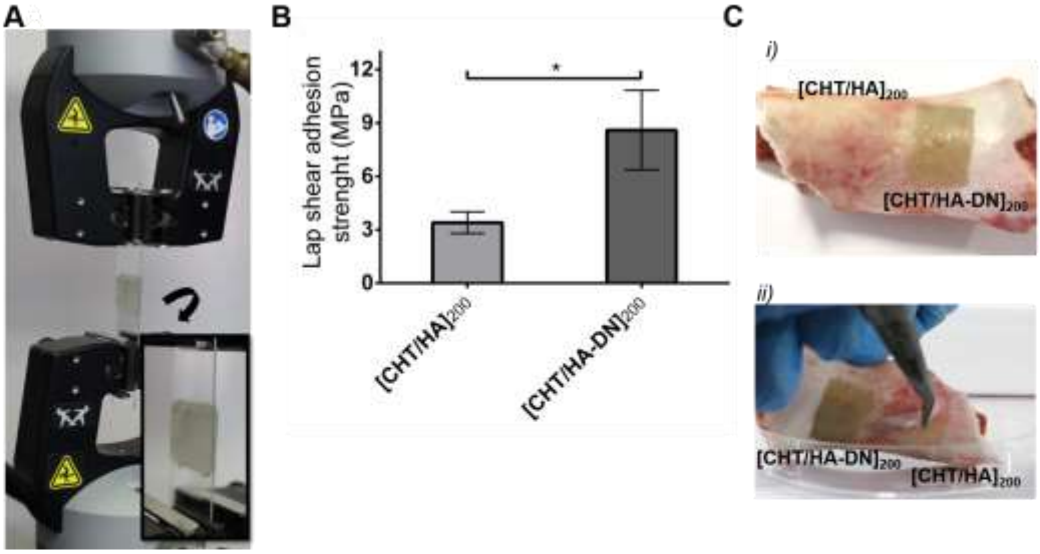

Figure VII-6. Adhesive properties of the freestanding membranes: (A) Mounting scheme for testing the lap shear adhesion strength on the Instron equipment; (B) lap shear adhesions strength values for each system. Significant differences were found for $p < 0.05$. (C) Representative images of the adhesiveness potential of $[CHT/HA]_{200}$ and $[CHT/HA\text{-}DN]_{200}$ freestanding membranes on a clean surface of porcine bone: (i) before and (ii) after applying a detachment force with tweezers.

3.7. *In Vitro* Cell Studies

MC3T3-E1 cells were seeded above $[CHT/HA]_{200}$ and $[CHT/HA\text{-}DN]_{200}$ freestanding membranes. The performance of such kind of adhesive substrates was evaluated for different cellular functions, namely the metabolic activity, cytotoxicity, proliferation, and morphology of MC3T3-E1. A preliminary immunofluorescent assay was performed to evaluate the osteogenic potential of these substrates. The MC3T3-E1 response for TCPS surfaces were used as reference and positive control.

3.7.1. Metabolic Activity, Cytotoxicity, Proliferation, and Morphology of MC3T3-E1 Cells

The metabolic activity of MC3T3-E1 cells and the cytotoxicity of $[CHT/HA]_{200}$ and $[CHT/HA\text{-}DN]_{200}$ membranes were evaluated by the Alamar blue colorimetric test. Figure VII-7A shows the results for the resulting Alamar blue absorbance. After one day of culture in basal growth medium, the cells seemed to adhere to the different substrates with no significant differences. Nevertheless, the values of absorbance of cells seeded above the freestanding membranes were comparable to the values for TCPS surfaces. This observation, combined with the increase in absorbance along with the days of culture for each condition, is an indication of the non-cytotoxicity of the materials. After three and seven days of culture, significant differences in metabolic activity were noted between $[CHT/HA]_{200}$ and $[CHT/HA\text{-}DN]_{200}$ freestanding membranes; higher absorbance values for cells seeded above $[CHT/HA\text{-}DN]_{200}$ freestanding membranes indicate enhanced metabolic activity and viability. Also, the proliferation of MC3T3-E1 was estimated using a standard DNA quantification assay. Figure VII-7B shows the content of DNA for each condition up to seven days of culture. After one day of culture the DNA content of MC3T3-E1 cells seeded above $[CHT/HA]_{200}$, $[CHT/HA\text{-}DN]_{200}$, and TCPS was quite similar, while for three and seven days of culture there were significant differences between these conditions. Following the same trend observed for Alamar blue results, the highest rates of proliferation were found for $[CHT/HA\text{-}DN]_{200}$ freestanding membranes, indicating a better cell response to the catechol-containing membranes. Additionally, the morphology of the cells was observed using a fluorescence assay (see Figure VII-7C). After three and seven days of culture in basal growth medium, the cells seeded above the different surfaces were fixed and stained with specific markers: phalloidin (in red) to label the actin cytoskeleton and DAPI (in blue) to label the nuclei of the cells. The representative images, presented in Figure VII-7C, corroborate the results of metabolic activity and DNA quantification: after three and seven days of culture, the density of cells adhered on the $[CHT/HA\text{-}DN]_{200}$ membranes was significantly higher than for the $[CHT/HA]_{200}$ membranes and close to the cell density on the TCPS surfaces. Moreover, the morphology of the MC3T3-E1 cells also differed; cells adhered above the $[CHT/HA\text{-}DN]_{200}$ started to establish cell–cell contact with each other after just one day of culture, while for cells seeded on $[CHT/HA]_{200}$ membranes this cell–cell contact was only perceptible after three days of culture; these observations reinforced the proliferation results as cell–cell contact promotes cell proliferation. We hypothesize that DN presence along the thickness of the multilayer membranes and concretely on the surface improved their biological performance at different stages: adhesion, viability, communication, and proliferation. These results could have potential applicability in the tissue engineering field, as adhesive and biocompatible substrates to support cells' functions. There are other works [11, 45] reporting the positive effect of catechol-based materials in promoting cellular adhesion and good function. Polycaprolactone scaffolds were modified using a mussel-inspired approach; polydopamine coating and hyaluronic acid immobilization seemed to be an effective way to improve cellular performance [46]. Zhang *et al.* [47] suggested LbL methodology to simply coat titanium implants with HA-DN and CHT, aiming to enhance the osteoblast proliferation. The greatest advantage of our system over the reported examples and the existing literature is related to the combination of a freestanding substrate composed of natural-based materials with enhanced adhesive strength and improved cell response. Moreover, this kind of flexible substrate could be produced, handled, and applied in quite a simple and adaptable way.

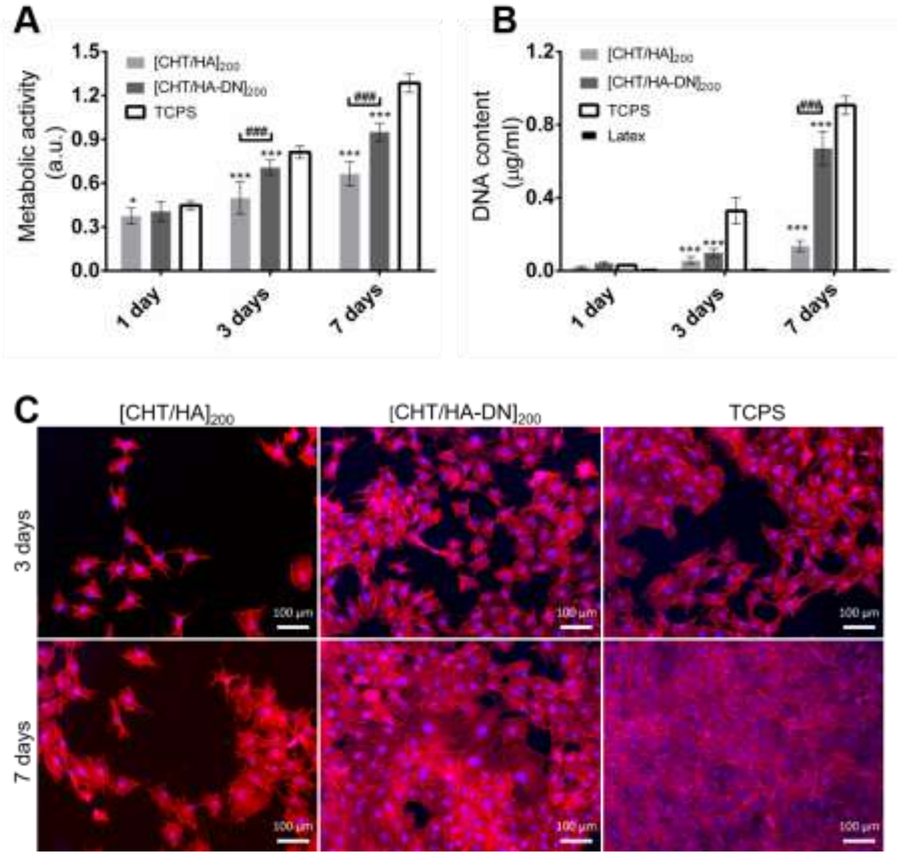

Figure VII-7. *In Vitro* Cell Studies: (A) Metabolic activity of MC3T3- E1 cells seeded on the membranes (Alamar Blue assay). Significant differences were found between membranes and TCPS conditions (for * $p < 0.05$; *** $p < 0.001$) and between the two kinds of systems (### $p < 0.001$); (B) DNA content of MC3T3- E1 seeded above the membranes (PicoGreen Kit). Significant differences were found between membranes and tissue culture polystyrene surface (TCPS) conditions (*** $p < 0.001$) and between the two kinds of systems (### $p< 0.001$). (C) Fluorescence images of MC3T3- E1 cells stained with phalloidin (red) and 4',6-diamidino-2-phenylindole (DAPI) (blue), at three and seven days of culture on the $[CHT/HA]_{200}$ and $[CHT/HA\text{-}DN]_{200}$ membranes and the TCPS (positive control). a.u.: Arbitrary units.

3.7.2. Differentiation of MC3T3-E1 Cells

The differentiation of mouse MC3T3-E1 pre-osteoblasts toward the formation of a mineralized extracellular matrix was also evaluated. This cell line was chosen as the model for our system due to its usually compressed level of differentiation and the ability to form a mineralized bone-like extracellular matrix [48]. Figure VII-8 shows the immunofluorescence images of cells seeded on the different materials, using osteopontin as the osteogenic marker. Typical osteogenic differentiation of MC3T3-E1 cells occurs in three phases: proliferation, extracellular matrix deposition and maturation, and finally mineralization. Each phase corresponds to higher expressions of certain genes; osteopontin is expressed near the later stages of osteogenic differentiation. Therefore, after 14 days in a differentiation medium containing ascorbic acid and β-glycerolphosphate, different behaviors could be observed for the freestanding systems. The cells cultured on $[CHT/HA\text{-}DN]_{200}$ showed stronger immunofluorescence for osteopontin protein staining than the cells cultured on $[CHT/HA]_{200}$ membranes, and very similar fluorescence to the TCPS positive control (see Figure VII-8A–C). We hypothesize that catechol-based moieties provided the multilayer films with important properties to improve their osteogenic potential. The characteristic chemical groups of $[CHT/HA]_{200}$ and $[CHT/HA\text{-}DN]_{200}$ membranes could be considered osteogenic differentiation promoters; besides CH_2 and CH_3 groups, these surfaces also present NH_2 and OH groups and for all of them a positive effect on endorsing osteogenic differentiation has been reported [49]. Few works have investigated the potential of mussel-inspired adhesive proteins for *in vitro* bone formation. For instance, Yu *et al.* [50] coated titanium substrates with polydopamine to facilitate the homogeneous covalent immobilization of collagen on their surface and promote the osteogenic differentiation of MC3T3-E1 cells. Another group [51] synthesized a conjugate of alginate and dopamine and produced alginate–dopamine gels, which seemed to promote the osteogenic differentiation of mesenchymal stem cells. The adhesive character of DN allowed the author to coat the gel with silver, providing antibacterial properties. Moreover, there are some studies reporting that the polydopamine coating could enhance hydroxyapatite nucleation and then promote mineralization; Lee *et al.* [52] coated 3D-printed polycaprolactone scaffolds with polydopamine to easily graft rhBMP-2. In addition, a higher amount of BMP-2 resulted in better bone tissue formation; even with small doses of this protein, they could induce osteogenic differentiation. In contrast, even in the absence of any other grafted protein or growth factor, our multilayer system based on mussel-inspired catechol groups could enhance the potential to differentiate MC3T3-E1 cells into osteoblasts. Figure VII-8D is a merged image of the MC3T3-E1 cells cultured on the $[CHT/HA\text{-}DN]_{200}$ membrane, overlaying osteopontin (green), phalloidin (red), and DAPI (blue) markers. As phalloidin stains the actin cytoskeleton of the cells and DAPI stains the nucleus, the appearance of osteopontin as an intracytoplasmic marker is clear from Figure VII-8D. We hypothesize that this positive intracellular activity could be related to the cellular calcification induced by the substrate and the culture conditions during the active stage of the differentiation of MC3T3-E1 cells in osteoblasts [53].

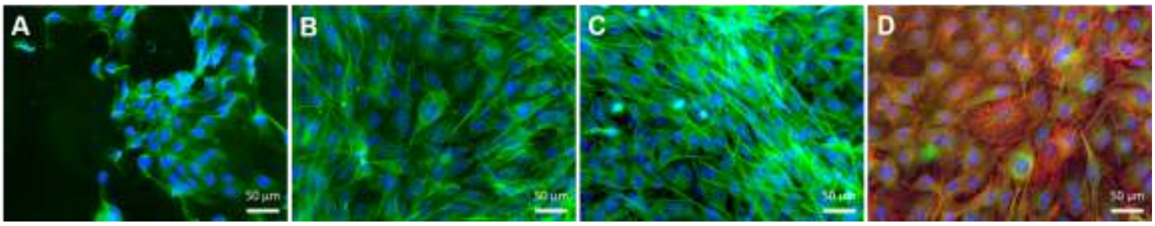

Figure VII-8. Osteopontin immunofluorescence images of MC3T3-E1 cells stained in green and with DAPI (in blue), after 14 days in osteogenic medium and cultured on the (A) $[CHT/HA]_{200}$ and (B) $[CHT/HA\text{-}DN]_{200}$ membranes and (C) TCPS (positive control); (D) Merged image of MC3T3-E1 cells cultured on the $[CHT/HA\text{-}DN]_{200}$ membrane is shown in the overlay with osteopontin (green), phalloidin (red) and DAPI (blue) markers.

Note that even after 21 days immersed in a physiological medium, the membranes seemed to be stable, but presented some signs of degradation.

Overall, the $[CHT/HA\text{-}DN]_{200}$ freestanding membranes showed enhanced adhesive strength properties, as well as improved cell adhesion, proliferation, and differentiation, making them a good candidate to regenerate bone tissue.

4. Conclusions

The notable ability of DOPA and its analogues to form strong interactions with both organic and inorganic surfaces was inspired by the process of wet adhesion in mussels and has been used to produce materials with unique adhesion properties. Bioadhesive materials have started to gain importance in bone tissue engineering strategies, which have been appearing to overcome some issues, often related to implant failure, by creating a system that directly promotes bone ingrowth into the material's structure and helps with tissue regeneration. Other features have been reported as significant for the success of the bone tissue engineering system. Using the LbL technique offers a unique vehicle to create a biomimetic environment due to the ability to incorporate materials that are presented in the ECM or have a bioactive role and assemble them into a functional tissue-like unit.

In conclusion, we covalently bonded DN on the backbone of HA with success, conferring important properties to this glycosaminoglycan. Taking advantage of the conjugate HA-DN and their negative nature at pH 5.5, we produced thin multilayer freestanding membranes composed only of CHT and HA-DN, using a simple LbL technology based on electrostatic interactions. Interestingly, when comparing membranes without DN with membranes where DN was conjugated with HA, we clearly enhanced the adhesive strength. MC3T3-E1 cell adhesion, viability, proliferation, and density were enhanced when cultured on $[CHT/HA\text{-}DN]_{200}$. We hypothesize that the mechanical and morphological differences between the different multilayer systems had a positive impact on cellular behavior. Additionally, our preliminary results for MC3T3-E1 differentiation studies suggest that the presence of HA-DN on the multilayer membranes provided better differentiation signals. We assume that enhanced differentiation of MC3T3-E1 cells is related to the morphology, chemistry, and mechanical properties conferred by this catechol-based material. Therefore, our investigation suggests a cheap, scalable, and versatile technology to produce biocompatible and osteophilic $[CHT/HA\text{-}DN]_{200}$ multilayer membranes with interesting adhesive properties that could potentially be applied in bone regeneration.

5. Supplementary Materials

The following are available online at www.mdpi.com/link, Figure S VII-1: Production of the Freestanding Multilayer Membranes: images showing (A) the detachment process of the freestanding membranes and (B) both resulting $[CHT/HA]_{200}$ and $[CHT/HA\text{-}DN]_{200}$ freestanding membranes; Figure S VII-2: QR-code for a video confirming the adhesiveness of the freestanding membranes to a clean surface of porcine bone.

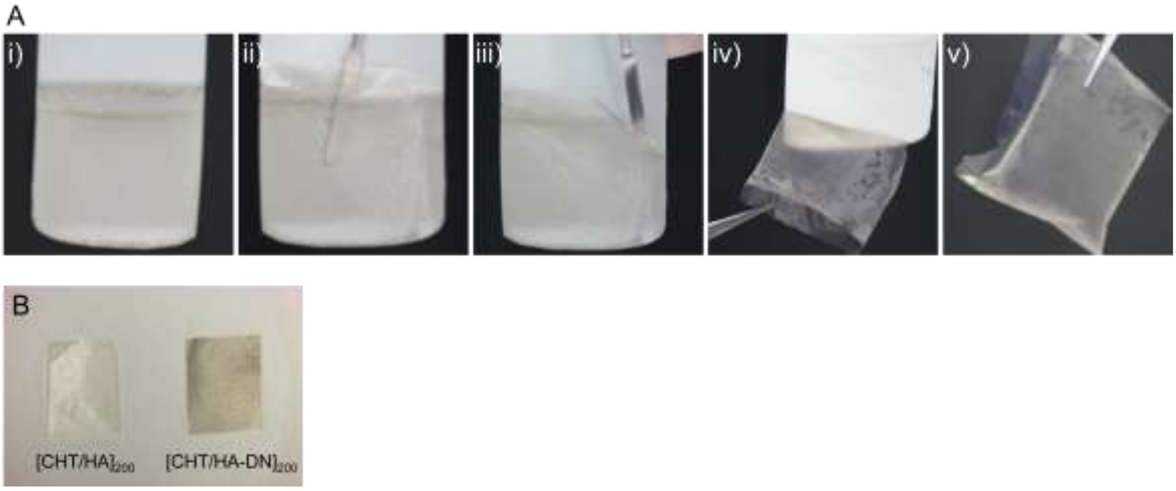

Figure S VII-1. Production of the freestanding multilayer membranes: images showing (A) the detachment process of the freestanding membranes and (B) both resulting $[CHT/HA]_{200}$ and $[CHT/HA\text{-}DN]_{200}$ freestanding membranes

Figure S VII-2. QR-code for a video of. confirming the adhesiveness of the freestanding membranes to a clean surface of porcine bone.

6. Acknowledgments

M.P.S. acknowledges the Portuguese Foundation for Science and Technology (FCT) for financial support through Grant No. SFRH/BD/97606/2013. This work was supported by the European Research Council grant agreement ERC-2014-ADG-669858 for the ATLAS project. The authors acknowledge Carmen Freire (CICECO, University of Aveiro, Aveiro, Portugal) for providing the Instron equipment to carry out the lap shear adhesion tests.

7. References

1. (a) Lee, H.; Dellatore, S. M.; Miller, W. M.; Messersmith, P. B., Mussel-Inspired Surface Chemistry for Multifunctional Coatings. *Science* **2007,** *318* (5849), 426-430; (b) Sedó, J.; Saiz-Poseu, J.; Busqué, F.; Ruiz-Molina, D., Catechol-Based Biomimetic Functional Materials. *Advanced Materials* **2013,** *25* (5), 653-701; (c) Liu, Y.; Ai, K.; Lu, L., Polydopamine and Its Derivative Materials: Synthesis and Promising Applications in Energy, Environmental, and Biomedical Fields. *Chemical Reviews* **2014,** *114* (9), 5057-5115.
2. (a) Faure, E.; Falentin-Daudré, C.; Jérôme, C.; Lyskawa, J.; Fournier, D.; Woisel, P.; Detrembleur, C., Catechols as versatile platforms in polymer chemistry. *Progress in Polymer Science* **2013,** *38* (1), 236-270; (b) Busqué, F.; Sedó, J.; Ruiz-Molina, D.; Saiz-Poseu, J., Catechol-Based Biomimetic Functional Materials and their Applications. In *Bio- and Bioinspired Nanomaterials*, Ruiz-Molina, D.; Novio, F.; Roscini, C., Eds. Wiley-VCH Verlag GmbH & Co. KGaA: Weinheim, Germany, 2014; pp 277-308.
3. Lee, B. P.; Messersmith, P. B.; Israelachvili, J. N.; Waite, J. H., Mussel-Inspired Adhesives and Coatings. *Annual Review of Materials Research* **2011,** *41* (1), 99-132.
4. (a) Lee, H.; Scherer, N. F.; Messersmith, P. B., Single-molecule mechanics of mussel adhesion. *Proceedings of the National Academy of Sciences of the United States of America* **2006,** *103* (35), 12999-13003; (b) Silverman, H. G.; Roberto, F. F., Understanding Marine Mussel Adhesion. *Marine Biotechnology (New York, N.y.)* **2007,** *9* (6), 661-681.
5. Lee, H.; Lee, B. P.; Messersmith, P. B., A reversible wet/dry adhesive inspired by mussels and geckos. *Nature* **2007,** *448* (7151), 338-341.
6. Cha, H. J.; Hwang, D. S.; Lim, S., Development of bioadhesives from marine mussels. *Biotechnology Journal* **2008,** *3* (5), 631-638.
7. Choi, Y. S.; Yang, Y. J.; Yang, B.; Cha, H. J., In vivo modification of tyrosine residues in recombinant mussel adhesive protein by tyrosinase co-expression in Escherichia coli. *Microbial Cell Factories* **2012,** *11*, 139-139.
8. Lee, B. P.; Dalsin, J. L.; Messersmith, P. B., Synthesis and Gelation of DOPA-Modified Poly(ethylene glycol) Hydrogels. *Biomacromolecules* **2002,** *3* (5), 1038-1047.
9. Shi, D.; Liu, R.; Dong, W.; Li, X.; Zhang, H.; Chen, M.; Akashi, M., pH-dependent and self-healing properties of mussel modified poly(vinyl alcohol) hydrogels in a metal-free environment. *RSC Advances* **2015,** *5* (100), 82252-82258.
10. Kim, K.; Ryu, J. H.; Lee, D. Y.; Lee, H., Bio-inspired catechol conjugation converts water-insoluble chitosan into a highly water-soluble, adhesive chitosan derivative for hydrogels and LbL assembly. *Biomaterials Science* **2013,** *1* (7), 783-790.
11. Lee, C.; Shin, J.; Lee, J. S.; Byun, E.; Ryu, J. H.; Um, S. H.; Kim, D.-I.; Lee, H.; Cho, S.-W., Bioinspired, Calcium-Free Alginate Hydrogels with Tunable Physical and Mechanical Properties and Improved Biocompatibility. *Biomacromolecules* **2013,** *14* (6), 2004-2013.
12. Park, J. Y.; Yeom, J.; Kim, J. S.; Lee, M.; Lee, H.; Nam, Y. S., Cell-repellant Dextran Coatings of Porous Titania Using Mussel Adhesion Chemistry. *Macromolecular Bioscience* **2013,** *13* (11), 1511-1519.
13. Neto, A. I.; Cibrão, A. C.; Correia, C. R.; Carvalho, R. R.; Luz, G. M.; Ferrer, G. G.; Botelho, G.; Picart, C.; Alves, N. M.; Mano, J. F., Nanostructured Polymeric Coatings Based on Chitosan and Dopamine-Modified Hyaluronic Acid for Biomedical Applications. *Small* **2014,** *10* (12), 2459-2469.
14. Scognamiglio, F.; Travan, A.; Borgogna, M.; Donati, I.; Marsich, E.; Bosmans, J. W. A. M.; Perge, L.; Foulc, M. P.; Bouvy, N. D.; Paoletti, S., Enhanced bioadhesivity of dopamine-functionalized polysaccharidic membranes for general surgery applications. *Acta Biomaterialia* **2016,** *44*, 232-242.
15. Mano, J. F.; Silva, G. A.; Azevedo, H. S.; Malafaya, P. B.; Sousa, R. A.; Silva, S. S.; Boesel, L. F.; Oliveira, J. M.; Santos, T. C.; Marques, A. P.; Neves, N. M.; Reis, R. L., Natural origin biodegradable systems in tissue engineering and regenerative medicine: present status and some moving trends. *Journal of the Royal Society Interface* **2007,** *4* (17), 999-1030.
16. (a) Cai, K.; Rechtenbach, A.; Hao, J.; Bossert, J.; Jandt, K. D., Polysaccharide-protein surface modification of titanium via a layer-by-layer technique: Characterization and cell behaviour aspects. *Biomaterials* **2005,** *26* (30), 5960-5971; (b) Alves, N. M.; Pashkuleva, I.; Reis, R. L.; Mano, J. F., Controlling Cell Behavior Through the Design of Polymer Surfaces. *Small* **2010,** *6* (20), 2208-2220.

17. (a) Moulay, S., Dopa/Catechol-Tethered Polymers: Bioadhesives and Biomimetic Adhesive Materials. *Polymer Reviews* **2014,** *54* (3), 436-513; (b) Kaushik, N. K.; Kaushik, N.; Pardeshi, S.; Sharma, J. G.; Lee, S. H.; Choi, E. H., Biomedical and Clinical Importance of Mussel-Inspired Polymers and Materials. *Marine Drugs* **2015,** *13* (11), 6792-6817.
18. Amini, A. R.; Laurencin, C. T.; Nukavarapu, S. P., Bone Tissue Engineering: Recent Advances and Challenges. *Critical reviews in biomedical engineering* **2012,** *40* (5), 363-408.
19. (a) Geckil, H.; Xu, F.; Zhang, X.; Moon, S.; Demirci, U., Engineering hydrogels as extracellular matrix mimics. *Nanomedicine (London, England)* **2010,** *5* (3), 469-484; (b) Gong, T.; Xie, J.; Liao, J.; Zhang, T.; Lin, S.; Lin, Y., Nanomaterials and bone regeneration. **2015,** *3*, 15029.
20. (a) Nassif, N.; Gobeaux, F.; Seto, J.; Belamie, E.; Davidson, P.; Panine, P.; Mosser, G.; Fratzl, P.; Giraud Guille, M.-M., Self-Assembled Collagen−Apatite Matrix with Bone-like Hierarchy. *Chemistry of Materials* **2010,** *22* (11), 3307-3309; (b) Yang, W.; Xi, X.; Si, Y.; Huang, S.; Wang, J.; Cai, K., Surface engineering of titanium alloy substrates with multilayered biomimetic hierarchical films to regulate the growth behaviors of osteoblasts. *Acta Biomaterialia* **2014,** *10* (10), 4525-4536.
21. (a) Decher, G., Fuzzy Nanoassemblies: Toward Layered Polymeric Multicomposites. *Science* **1997,** *277* (5330), 1232-1237; (b) Tang, Z.; Wang, Y.; Podsiadlo, P.; Kotov, N. A., Biomedical Applications of Layer-by-Layer Assembly: From Biomimetics to Tissue Engineering. *Advanced Materials* **2006,** *18* (24), 3203-3224; (c) Katsuhiko, A.; Yusuke, Y.; Gaulthier, R.; Qingmin, J.; Yusuke, Y.; C.-W., W. K.; P., H. J., Layer-by-layer Nanoarchitectonics: Invention, Innovation, and Evolution. *Chemistry Letters* **2014,** *43* (1), 36-68; (d) Gentile, P.; Carmagnola, I.; Nardo, T.; Chiono, V., Layer-by-layer assembly for biomedical applications in the last decade. *Nanotechnology* **2015,** *26* (42), 21.
22. Silva, J. M.; Reis, R. L.; Mano, J. F., Biomimetic Extracellular Environment Based on Natural Origin Polyelectrolyte Multilayers. *Small* **2016,** *12* (32), 4308-4342.
23. Mhanna, R. F.; Vörös, J.; Zenobi-Wong, M., Layer-by-Layer Films Made from Extracellular Matrix Macromolecules on Silicone Substrates. *Biomacromolecules* **2011,** *12* (3), 609-616.
24. (a) Gribova, V.; Auzely-Velty, R.; Picart, C., Polyelectrolyte Multilayer Assemblies on Materials Surfaces: From Cell Adhesion to Tissue Engineering. *Chemistry of Materials* **2012,** *24* (5), 854-869; (b) Shah, N. J.; Hyder, M. N.; Quadir, M. A.; Dorval Courchesne, N.-M.; Seeherman, H. J.; Nevins, M.; Spector, M.; Hammond, P. T., Adaptive growth factor delivery from a polyelectrolyte coating promotes synergistic bone tissue repair and reconstruction. *Proceedings of the National Academy of Sciences* **2014,** *111* (35), 12847-12852.
25. Oliveira, S. M.; Reis, R. L.; Mano, J. F., Assembling Human Platelet Lysate into Multiscale 3D Scaffolds for Bone Tissue Engineering. *ACS Biomater. Sci. Eng.* **2015,** *1* (1), 2-6.
26. Crouzier, T.; Ren, K.; Nicolas, C.; Roy, C.; Picart, C., Layer-By-Layer Films as a Biomimetic Reservoir for rhBMP-2 Delivery: Controlled Differentiation of Myoblasts to Osteoblasts. *Small* **2009,** *5* (5), 598-608.
27. Correia, C.; Caridade, S.; Mano, J., Chitosan Membranes Exhibiting Shape Memory Capability by the Action of Controlled Hydration. *Polymers* **2014,** *6* (4), 1178.
28. Lee, H.; Lee, Y.; Statz, A. R.; Rho, J.; Park, T. G.; Messersmith, P. B., Substrate-Independent Layer-by-Layer Assembly by Using Mussel-Adhesive-Inspired Polymers. *Advanced materials (Deerfield Beach, Fla.)* **2008,** *20* (9), 1619-1623.
29. Alves, N. M.; Picart, C.; Mano, J. F., Self Assembling and Crosslinking of Polyelectrolyte Multilayer Films of Chitosan and Alginate Studied by QCM and IR Spectroscopy. *Macromolecular Bioscience* **2009,** *9* (8), 776-785.
30. Baler, K.; Ball, J. P.; Cankova, Z.; Hoshi, R. A.; Ameer, G. A.; Allen, J. B., Advanced nanocomposites for bone regeneration. *Biomaterials Science* **2014,** *2* (10), 1355-1366.
31. Chen, S.-M.; Peng, K.-T., The electrochemical properties of dopamine, epinephrine, norepinephrine, and their electrocatalytic reactions on cobalt(II) hexacyanoferrate films. *Journal of Electroanalytical Chemistry* **2003,** *547* (2), 179-189.
32. Pomin, V. H., NMR Chemical Shifts in Structural Biology of Glycosaminoglycans. *Analytical Chemistry* **2014,** *86* (1), 65-94.
33. Mueller, D. D.; Morgan, T. D.; Wassenberg, J. D.; Hopkins, T. L.; Kramer, K. J., Proton and carbon-13 NMR of 3-O and 4-O conjugates of dopamine and other catecholamines. *Bioconjugate Chemistry* **1993,** *4* (1), 47-53.
34. Croll, T. I.; O'Connor, A. J.; Stevens, G. W.; Cooper-White, J. J., A Blank Slate? Layer-by-Layer Deposition of Hyaluronic Acid and Chitosan onto Various Surfaces. *Biomacromolecules* **2006,** *7* (5), 1610-1622.

35. Kujawa, P.; Schmauch, G.; Viitala, T.; Badia, A.; Winnik, F. M., Construction of Viscoelastic Biocompatible Films via the Layer-by-Layer Assembly of Hyaluronan and Phosphorylcholine-Modified Chitosan. *Biomacromolecules* **2007,** *8* (10), 3169-3176.
36. Picart, C., Polyelectrolyte multilayer films: from physico-chemical properties to the control of cellular processes. *Current medicinal chemistry* **2008,** *15* (7), 685-97.
37. Caridade, S. G.; Monge, C.; Gilde, F.; Boudou, T.; Mano, J. F.; Picart, C., Free-standing polyelectrolyte membranes made of chitosan and alginate. *Biomacromolecules* **2013,** *14* (5), 1653-1660.
38. Sousa, M. P.; Cleymand, F.; Mano, J. F., Elastic chitosan/chondroitin sulfate multilayer membranes. *Biomedical Materials* **2016,** *11* (3), 035008.
39. Costa, R. R.; Neto, A. I.; Calgeris, I.; Correia, C. R.; Pinho, A. C. M.; Fonseca, J.; Oner, E. T.; Mano, J. F., Adhesive nanostructured multilayer films using a bacterial exopolysaccharide for biomedical applications. *Journal of Materials Chemistry B* **2013,** *1* (18), 2367-2374.
40. (a) Yamada, K.; Chen, T.; Kumar, G.; Vesnovsky, O.; Topoleski, L. D.; Payne, G. F., Chitosan based water-resistant adhesive. Analogy to mussel glue. *Biomacromolecules* **2000,** *1* (2), 252-8; (b) Zhou, J.; Defante, A. P.; Lin, F.; Xu, Y.; Yu, J.; Gao, Y.; Childers, E.; Dhinojwala, A.; Becker, M. L., Adhesion Properties of Catechol-Based Biodegradable Amino Acid-Based Poly(ester urea) Copolymers Inspired from Mussel Proteins. *Biomacromolecules* **2015,** *16* (1), 266-274.
41. Ninan, L.; Monahan, J.; Stroshine, R. L.; Wilker, J. J.; Shi, R., Adhesive strength of marine mussel extracts on porcine skin. *Biomaterials* **2003,** *24* (22), 4091-4099.
42. Kim, H. J.; Hwang, B. H.; Lim, S.; Choi, B.-H.; Kang, S. H.; Cha, H. J., Mussel adhesion-employed water-immiscible fluid bioadhesive for urinary fistula sealing. *Biomaterials* **2015,** *72*, 104-111.
43. Lauto, A.; Mawad, D.; Foster, L. J. R., Adhesive biomaterials for tissue reconstruction. *Journal of Chemical Technology & Biotechnology* **2008,** *83* (4), 464-472.
44. Neto, A. I.; Vasconcelos, N. L.; Oliveira, S. M.; Ruiz-Molina, D.; Mano, J. F., High-Throughput Topographic, Mechanical, and Biological Screening of Multilayer Films Containing Mussel-Inspired Biopolymers. *Advanced Functional Materials* **2016,** *26* (16), 2745-2755.
45. (a) Lynge, M. E.; van der Westen, R.; Postma, A.; Stadler, B., Polydopamine--a nature-inspired polymer coating for biomedical science. *Nanoscale* **2011,** *3* (12), 4916-28; (b) Ryu, J. H.; Lee, Y.; Kong, W. H.; Kim, T. G.; Park, T. G.; Lee, H., Catechol-Functionalized Chitosan/Pluronic Hydrogels for Tissue Adhesives and Hemostatic Materials. *Biomacromolecules* **2011,** *12* (7), 2653-2659; (c) Madhurakkat Perikamana, S. K.; Lee, J.; Lee, Y. B.; Shin, Y. M.; Lee, E. J.; Mikos, A. G.; Shin, H., Materials from Mussel-Inspired Chemistry for Cell and Tissue Engineering Applications. *Biomacromolecules* **2015,** *16* (9), 2541-2555.
46. Jo, S.; Kang, S. M.; Park, S. A.; Kim, W. D.; Kwak, J.; Lee, H., Enhanced Adhesion of Preosteoblasts inside 3D PCL Scaffolds by Polydopamine Coating and Mineralization. *Macromolecular Bioscience* **2013,** *13* (10), 1389-1395.
47. Zhang, X.; Li, Z.; Yuan, X.; Cui, Z.; Yang, X., Fabrication of dopamine-modified hyaluronic acid/chitosan multilayers on titanium alloy by layer-by-layer self-assembly for promoting osteoblast growth. *Applied Surface Science* **2013,** *284*, 732-737.
48. Boskey, A. L.; Roy, R., Cell Culture Systems for Studies of Bone and Tooth Mineralization. *Chemical reviews* **2008,** *108* (11), 4716-4733.
49. Barradas, A. M.; Lachmann, K.; Hlawacek, G.; Frielink, C.; Truckenmoller, R.; Boerman, O. C.; van Gastel, R.; Garritsen, H.; Thomas, M.; Moroni, L.; van Blitterswijk, C.; de Boer, J., Surface modifications by gas plasma control osteogenic differentiation of MC3T3-E1 cells. *Acta Biomater* **2012,** *8* (8), 2969-77.
50. Yu, X.; Walsh, J.; Wei, M., Covalent Immobilization of Collagen on Titanium through Polydopamine Coating to Improve Cellular Performances of MC3T3-E1 Cells. *RSC advances* **2013,** *4* (14), 7185-7192.
51. Zhang, S.; Xu, K.; Darabi, M. A.; Yuan, Q.; Xing, M., Mussel-inspired alginate gel promoting the osteogenic differentiation of mesenchymal stem cells and anti-infection. *Materials Science and Engineering: C* **2016,** *69*, 496-504.
52. Lee, S. J.; Lee, D.; Yoon, T. R.; Kim, H. K.; Jo, H. H.; Park, J. S.; Lee, J. H.; Kim, W. D.; Kwon, I. K.; Park, S. A., Surface modification of 3D-printed porous scaffolds via mussel-inspired polydopamine and effective immobilization of rhBMP-2 to promote osteogenic differentiation for bone tissue engineering. *Acta Biomaterialia* **2016,** *40*, 182-191.
53. Tsutsumi, K.; Saito, N.; Kawazoe, Y.; Ooi, H.-K.; Shiba, T., Morphogenetic Study on the Maturation of Osteoblastic Cell as Induced by Inorganic Polyphosphate. *PLoS ONE* **2014,** *9* (2), e86834.

VIII. Bioinspired multilayer membranes as potential adhesive patch for skin wound healing[*]

Abstract

Bioinspired and adhesive multilayer membranes are produced using the layer-by-layer (LbL) assembly of chitosan (CHT), alginate (ALG) and hyaluronic acid modified with dopamine (HA-DN). Freestanding multilayer membranes without DN are also produced as a control. The success of the synthesis of HA-DN was confirmed using UV-visible spectroscopy. Scanning electron microscopy images indicate that the surface of the DN-containing membranes is quite more porous than the control ones; they also present a higher average thickness value for the same number of CHT/ALG/CHT/HA(-DN) tetralayers (n=100). Also, water uptake, mechanical strength and adhesion are enhanced with the introduction of DN moieties along the nano-layers. Besides, human dermal fibroblasts viability, enhanced adhesion and proliferation were confirmed by immunofluorescence assays and by measuring both metabolic activity and DNA content. Moreover, in vivo assays with such kind of DN-containing multilayer membranes were performed; the application of these membranes in the treatment of dermal wounds induced in Wistar rats results on the highest decreasing of inflammation of skin rat, compared with the control conditions. Overall, this investigation suggests that these mussel-inspired freestanding multilayer membranes may enhance either their mechanical performance as well as cellular adhesion and proliferation, leading to an improved wound healing process, being a promising material to restore the structural and functional properties of wounded skin.

Keywords: layer-by-layer; catechol; bioinspired; freestanding membranes; adhesive; human dermal fibroblasts; wound healing.

---

[*] This chapter is based on the following publication: Sousa, M. P.; Neto, A. I.; Correia, T. R.; Miguel, S. P.; Matsusaki, M.; Correia, I. J.; Mano, J. F., Bioinspired multilayer membranes as potential adhesive patches for skin wound healing. *Biomaterials Science* **2018,** *6* (7), 1962-1975.

1. Introduction

Skin is the largest and most exposed organ in humans, serving as a protective barrier to the remaining organs against pathogens, virus, microorganisms as wells as certain environmental conditions (chemical, mechanical or thermal constrains) [1]. Accordingly, skin can be always an open door to potentially harmful impairments or agents, resulting in non-healing wounds. Skin is a vascular tissue, with ability to regenerate; however, a skin's injury with a diameter higher than 4 centimeter will be incapable to heal without an external support [2]. For many years, donor skin grafting has been used as gold standard to treat such kind of skin defects, but the availability of donors is limited and restricted [1b]. Therefore, skin tissue engineering field has been growing during the last decades to create substitutes that mimic skin, towards clinical solutions that promote wound healing [3]. Ideally, tissue engineering combines the development of a support material with specific cells and bioactive agents to generate functional *in vitro* tissues that could be then transposed for the clinical practice [4].

For wound dressing, there are important specificities to meet; besides being non-toxic and non-allergic, these materials must be permeable to gas and provide a moist environment, protecting wounds from microbial action and absorbing resulting exudates[5]. Scientists have been pursuing materials that mimics the functional and structural features of the native extracellular matrix (ECM) of skin, serving as a barrier like epidermis and providing mechanical stability and elasticity like dermis [5b]. There are already some commercially available products; for instance, a hyaluronic acid (HA) ester bilayer scaffold (Hyalograft3D®) can be combined with an epidermal replacement autograft (Laserskin®) to permit wound closure [6]. However, commercially available products must overpass the high production costs, the need of an additional fixation strategy, the risk of infection as well as the surgical intervention times [7]. Therefore, to overcome such limitations other strategies have been investigated to design scaffolds for skin wound dressing, such as fibrous membranes[8], porous structures [9], hydrogels [10], composites [11] or microparticles [12]. However, these strategies usually encompass also some drawbacks as immune rejection for acellular scaffolds, poor cell adhesion for composite materials, limited mechanical strength in the case of hydrogels or the lack of interconnectivity in the case of porous scaffolds [13].

Layer-by-layer (LbL) technique is a quite simple technology to construct stable multilayer films by sequential adsorption of complementary multivalent molecules above a surface. The assembly of the different layers can be a result of covalent and/or noncovalent interactions, but, among the others, electrostatic driving forces have gained a key role [14]. LbL stands out from other methodologies by its versatility, cost-effectiveness, robustness, ability to integrate a wide range of organic and inorganic materials and finely control the multiscale architecture [14-15]. For instance, Guthrie K. M. *et al.* [16] incorporated silver nanoparticles within polyelectrolyte multilayers, constructed above elastomeric poly(dimethylsiloxane) (PDMS) sheets, to apply to the wounds beds of normal and diabetic mice and proved the feasibility of LbL-based substrates to improve wound healing. LBL films can be assembled in any type of substrate (regardless of size, shape or even surface geometry) and in certain occasions the template can be removed to generate a multilayer film that may retain the shape of the underlying substrate without the need of their physical support when implanted [17]. In this sense, more than coatings

LbL methodology can render free-template materials like capsules [18], compartmentalized [19] and tubular [20] structures or even freestanding membranes [21]. Mamedov A. A. *et al.* [22] suggested the LbL assembly of alternating layers of magnetite nanoparticles and poly(diallyldimethylammonium bromide) above a cellulose acetate substrate , that was further dissolved in acetone, to obtain freestanding multilayer films. Herein, LbL technique is used to fabricate a free-template multilayer patch to treat skin wounds, without the need of using any organic solvent or compromising the integrity, the composition and the mechanical properties of the membrane.

To better control the physicochemical cell-material interactions and improve the biocompatibility, different strategies have been suggested; for instance, one can modify the chemistry of the surface with specific motifs[23], increase the hydrophilicity of the surface [24] or even create a topography suitable to generate a cell response [25]. In the last decades, biomimetic materials have boosted tissue engineering and regenerative medicine field [26], with different suitable properties of materials being inspired in natural systems. In particular, friendly bioadhesive systems have been proposed based on natural phenomena chasing their effectiveness [27]. For instance, gecko's ability to adhere temporary to surfaces has been caught the attention of many scientists, which have been trying to reproduce the nanoscale topography of their foot pads; Lee H. *et al.* [28] developed a hybrid biologically-inspired adhesive material composed of an array of nanofabricated polymer pillars to mimic the nanoarchitecture organization of the gecko's foot pads. To improve the wet adhesion and durability, the authors coated the gecko-inspired pillars with a thin layer of a synthetic polymer, that mimics the wet adhesive proteins found in mussel holdfasts. In fact, mussels are other class of materials that has been nowadays very attracting to inspire bioadhesive systems. Mussels' ability to bond to any type of organic and inorganic substrate relies on their byssal threads' secretion of particular proteins, which amino acid content analysis showed the repetition of the 3,4-dihydroxyphenyl-alanine (DOPA) residue[29]. Molecules containing catechols groups, such as DOPA or dopamine have been used to functionalize polymers, such as chitosan (CHT) and HA; for instance, Ryu J. H. *et al.* [30] suggested a new thermo-sensitive and injectable DOPA modified CHT/pluronic hydrogels and showed that these hydrogels exhibit excellent tissue-adhesion properties with superior *in vivo* gel stability; Hong S. *et al.* [31] produced HA-dopamine hydrogels found to be highly compatible with neural stem cells, presenting better viability and cell adhesion compared to the existing HA hydrogels. We hypothesized that the development of adhesive materials could enhance the performance of our freestanding multilayer system, by adhering to the tissue with improved cell adhesive properties.

In this investigation, CHT, a polycation derived from marine crustaceans, as well as alginate (ALG), a polyanion derived from algae, and hyaluronic acid (HA), a polyanion that is also part of the native ECM and plays an important role on mechanical and structural support, were electrostatically combined to produce multilayer polyelectrolyte films. Moreover, getting inspiration from marine mussels, HA was modified with dopamine by carbodiimide chemistry and combined with CHT and ALG to produce self-supportive freestanding multilayer membrane, that could be readily applied for skin wound healing. Neto A. I. *et al.* [32] already developed a high-throughput screening platform to characterize arrays of multilayer films containing dopamine-modified HA in terms of mechanical adhesion and biological response. It was found that the introduction of the catechol groups in the multilayers clearly had a beneficial effect on adhesion and on cell adhesion and spreading. We hypothesize that such kind of multilayers could be transposed into multilayered membranes to be used as skin wound dressings. In this work both *in vitro* (morphology, mechanical properties, biofilm bacterial formation, adhesiveness, dermal cellular behavior) and *in vivo* (full thickness wounds in rats) characterization will be performed to assess the potential of such polysaccharide-based and biomimetic freestanding multilayer membranes.

2. Materials and Methods

2.1. Materials

CHT (Sigma, St. Louis, Missouri, United States of America(USA)) with a molecular weight in the range of 190–310 kDa, a N-deacetylation degree ranging from 75-85% and a viscosity of 0.2-0.8 Pa.s was purified following a standard procedure reported elsewhere [33]. Sodium alginate (ALG) with a viscosity of 0.005-0.04 Pa.s and obtained from brown algae, hyaluronic acid (HA) with a molecular weight of 595 kDa as hyaluronic acid sodium salt from Streptococcus equi, dopamine hydrochloride (DN) and N-(3-Dimethylaminopropyl)-N′-ethylcarbodiimide hydrochloride (EDC) (purum, ≥ 98.0% (AT)) were purchased from Sigma and used as received.

2.2. Synthesis of HA-DN

HA-DN conjugates were synthesized using EDC as an activation agent of the carboxyl groups on HA chains, based on an already reported procedure [32] (see Figure S VIII-1). To avoid oxidation, the conjugated was stored at -20 °C and protected from the light until using.

2.2.1. Ultraviolet-visible (UV) Spectrophotometry

The degree of substitution of dopamine in the conjugate was determined using a UV-vis spectrophotometer (JascoV560 PC, Easton, Maryland, USA) and 1 cm quartz cells. Polymer solutions of 0.5 mg. mL^{-1} in 0.15 M sodium chloride (NaCl, LabChem Inc, Zelienople, Pennsylvania, USA) were prepared for the UV-vis analyses.

2.2.2. ^{1}H-Nuclear Magnetic Resonance (NMR)

^{1}H-NMR analyses were performed dissolving overnight the HA and the conjugated HA-DN in deuterated water (D_2O, Cambridge Isotope Laboratories, Inc.) at a concentration of 1 mg. mL^{-1}. The spectra were obtained using a spectrometer BRUKER BioSpin - 300 MHz, at 298 K and 300 MHz for 1H.

2.3. Zeta (ζ)-potential measurements of polysaccharide solutions

Solutions of CHI (0.5 mg mL^{-1}), ALG (0.5 mg mL^{-1}), HA and HA-DN (0.25 mg mL^{-1}) containing NaCl (0.15 M) were prepared. The pH of the solutions was adjusted to 5.5. The ζ -potential of each solution was determined using a Nano range equipment from Malvern (United Kingdom), at 25 ° C.

2.4. Quartz Crystal Microbalance with dissipation (QCM-D) monitoring

The formation of the multilayers of CHT/ALG/CHT/HA-DN was followed *in situ* by QCM-D (Q-Sense, Biolin Scientific, Göteborg, Sweden). The mass change results from the variation of the normalized resonant frequency ($\Delta f/\upsilon$) of an oscillating quartz crystal when adsorption occurs on the surface and the dissipation factor (ΔD) provides a measure of the energy loss in the system. If a rigid mass is adsorbed onto the surface of the piezoelectric crystal, there will be a decrease in the oscillation frequency. For viscoelastic materials, the adsorbed mass does not fully couple to the oscillation of the crystal, damping the oscillation. QCM-D allows simultaneously measuring the changes in the resonant frequency and in the viscoelastic properties (dissipation) when a film is adsorbed at the crystal surface. The measurements can be conducted at the fundamental frequency and at several overtones number (υ = 1,3,5,7,9,11). CHT was used as the polycation while ALG and HA-DN acted as interspersed polyanions. Fresh polyelectrolyte solutions were prepared by dissolution of HA-DN, ALG and CHT in 0.15 M of NaCl to yield a final concentration of 0.25, 0.5 and 0.5 mg.mL^{-1}, respectively. The sensor crystals used were AT-cut quartz (Q-Sense) with gold plated polished electrodes. These crystals were excited at 5 MHz as well as at 15, 25, 35, 45 and 55 MHz corresponding to the 3rd, 5th, 7th, 9th and 11th overtones. The crystals were previously cleaned with sequential sonication for 3 min in acetone, ethanol and isopropanol and then dried with flowing nitrogen gas avoiding contamination prior to use. Firstly, the polyelectrolyte solutions were injected into the cell for 6 min, beginning with CHT. A rinsing step of 4 min with the solvent was included between the adsorptions of each polyelectrolyte. The multilayer systems were assembled at pH 5.5. The pH was adjusted with HCl or sodium hydroxide (NaOH, pellets, Fine Chemicals, Akzo Nobel Chemicals S.A., Mons, Belgium). CHT/ALG/CHT/HA films were also prepared for comparison. Films with 8 layers (2 tetralayers (TL)) were produced. All experiments were conducted at 25 ºC. During the entire process $\Delta f/\upsilon$ and ΔD shifts were continuously recorded as a function of time.

The films' viscoelastic properties were investigated using the Voigt viscoelastic model implemented in the QTools software from Q-Sense. According with this model, a Simplex algorithm was used to find the minimum of the sum of the squares of the scaled errors between the experimental and model Δf and ΔD values. Changes in resonant frequency and dissipation of the 5th, 7th and 9th overtone were fitted. The solvent viscosity selected was 1 mPa.s and a film density of 1 g.cm^{-3}. The solvent density was varied between values from 1000 to 1045 kg.m^{-3} to minimize the total error ($\chi 2$).

2.5. Freestanding Multilayer Membranes Production and Characterization

2.5.1. Production of the freestanding multilayer membranes

The production of the multilayer membranes was achieved using the LbL methodology with the help of a home-made dipping robot (see Figure S VIII-1). Polypropylene (PP) substrates were immersed in alternated polyelectrolyte solutions with a rinsing solution deposition between each polyelectrolyte. The rinsing solution used was a 0.15 M NaCl (pH = 5.5) and the polymer solutions were used at a concentration of 2 mg. mL^{-1} for CHT and ALG and 0.5 mg. mL^{-1} for the others. Deposition time of the polyelectrolytes was 6 min and 4 min for the rinsing solution.

In the end of 100 TL, two types of FS were produced (see Figure S VIII-1): multilayer membranes containing CHI, ALG and HA ($[CHT/ALG/CHT/HA]_{100}$) and multilayer membranes containing CHI, ALG and HA-DN with the same number of layers ($[CHT/ALG/CHT/HA\text{-}DN]_{100}$).

2.5.2. Scanning Electron Microscope (SEM)

The surface morphology of the samples was observed using a Hitachi S4100 (Tokyo, Japan) SEM. All samples were coated with a conductive layer of sputtered gold. The SEM micrographs were taken using an accelerating voltage of 15 kV and at different magnifications. For the cross-section observation, the freestanding membranes were immersed in liquid nitrogen and fractured. After that, the free fracture region was observed by SEM.

2.5.3. Water uptake

The water uptake ability of both type of freestanding multilayer membranes was studied by immersing previously weighed dry samples in a phosphate buffer saline (PBS, Sigma) solution. The FS samples were removed from immersion at pre-determined time points (t= 5 min,15 min, 30 min, 1 h, 2 h, 3 h, 6h, 12 h, and 24 h) in which the excess solution was removed using filter paper, and the membranes were then immediately weighed using an analytical balance (Radwag Balances and Scales, Radom, Poland). The water uptake was calculated using Equation VIII.1.

$$Water\ uptake\ (\%) = \frac{(m_x - m_i)}{m_i} \times 100 \qquad \text{Equation VIII.1}$$

Where, m_i is the dry mass of the sample and m_x is the hydrated mass of the sample at a given time point.

2.5.4. Mechanical tests: tensile behaviour

The tensile behavior of the freestanding multilayer membranes was evaluated using the mechanical testing machine Shimadzu MMT-101N (Shimadzu Scientific Instruments, Kyoto, Japan) with a load cell of 100 N. The produced FS were cut into rectangular samples (30 x 5 mm^2) and immersed in a PBS solution overnight at 37°C. Tensile tests were carried out with a gauge length of 10 mm and a loading speed of 1mm.min^{-1}. Resulting stress-strain curves allowed to determine the Young's Modulus, ultimate tensile strength and maximum extension at rupture of both $[CHT/ALG/CHT/HA]_{100}$ and $[CHT/ALG/CHT/HA\text{-}DN]_{100}$ freestanding membranes.

2.5.5. Mechanical tests: adhesive behaviour

The adhesive properties of the produced $[CHT/ALG/CHT/HA]_{100}$ and $[CHT/ALG/CHT/HA\text{-}DN]_{100}$ freestanding membranes were evaluated using a single lap shear adhesion strength test adapted from ASTM D1002 [34]. Rectangular samples (30 x 10 mm^2) were cut and overlapped in pairs with an overlapping area of 5 x 10 mm^2. Samples were then hydrated with a PBS solution and placed between firmly tight glass slides, overnight and at 37 °C. After that, the glass slides were removed and the samples were tested using the mechanical equipment Shimadzu MMT-101N, with each grip pulled the extremity of one of the overlapped samples. A tensile speed of 5 $mm.min^{-1}$ was used until sufficient stress was applied for membrane detachment. The resulting stress-strain curves allowed to determine the adhesion strength of the $[CHT/ALG/CHT/HA]_{100}$ and the $[CHT/ALG/CHT/HA\text{-}DN]_{100}$ freestanding membranes.

2.5.6. Biofilm formation analysis

To evaluate the bactericidal activity of the membranes, Staphylococcus aureus was used as model of a gram-positive bacterium, whereas Escherichia coli used as model of a gram-negative bacterium. To do that, both strains of bacteria (1×10^8 Colony-forming unit (CFU) mL^{-1}) were grown in sterilized LB (Lysogeny broth) and incubated for 4h at 37°C. 200 µL of the bacterial suspension were placed on the LB agar growth plates and spread uniformly using a sterile cotton swab. The different sides of the membranes were placed on the top of the inoculated agar plates and incubated overnight at 37°C. To determine the biofilm formation at the membranes surface' and the bacterial growth, SEM images were acquired.

2.6. *In vitro* biological assays

Human primary dermal fibroblasts (HDFs) were obtained from ATCC in partnership with LGC (USA) and used at passages between 8 and 11. The cells were cultured with DMEM (Gibco, ThermoFisher Scientific, Waltham, Massachusetts, United States of America) supplemented with 3.7 mg. mL^{-1} sodium bicarbonate (Sigma), 10% fetal bovine serum (FBS, ThermoFisher Scientific), and 1% penicillin−streptomycin (Gibco) at pH 7.4. The cells were grown in 75 cm^2 tissue culture flasks and incubated at 37 °C in a humidified air atmosphere of 5% CO_2. The medium was changed every 3−4 days. When confluents, cells grown in tissue culture flasks were washed with Dulbecco's phosphate-buffered saline (DPBS, Corning, New York, United States of America) and subsequently detached by a chemical procedure with trypLE™ express solution (Life Technologies™) for 5 min at 37 °C in a humidified air atmosphere of 5% CO_2. To inactivate the trypLE™ express solution effect, cell culture medium was added. The cells were then centrifuged at 300 g and 25 °C for 5 min and the medium was decanted. Prior to cell seeding, the samples were disinfected by immersion in ethanol for 2 hs and then washed with DPBS. 300 μL of supplemented DMEM containing a cell suspension with 1×10^4 cells was dropped above the surface of the samples: $[CHT/ALG/CHT/HA\text{-}DN]_{100}$ membranes, the respective control $[CHT/ALG/CHT/HA]_{100}$ membranes and the positive control (tissue culture polystyrene substrates, TCPS) (in triplicate). Then, the samples were incubated at 37 °C in a humidified air atmosphere of 5% CO_2. After 4 hs, fresh culture medium was added.

2.6.1. [3-(4,5-dimethylthiazol-2-yl)-5-(3-carboxymethoxyphenyl)-2-(4-sulfophenyl)-2H-tetrazolium, inner salt (MTS) assay

The samples were tested for cytotoxicity using MTS (CellTiter 96® AQueous One Solution Cell Proliferation Assay, Promega, Madison, Wisconsin, USA) colorimetric assay. Briefly, the samples with adhered cells were placed in a non-treated surface 24-well cell culture plate (in triplicate) and incubated at 37 °C and 5% CO_2. At 1, 3 and 7 days of culture, the assay was performed, protected from light. The culture medium was removed and 500 μL of supplemented DMEM containing MTS solution with a dilution ratio of 1:5 was added to each well. Samples were then incubated in the dark at 37 °C and 5% CO_2. After 3 hs, 100 μL of each well (in triplicate) was transferred to a 96-well plate. The absorbance was monitored at 490 nm using a microplate reader Synergy HTX (BioTek Instruments, Inc., Winooski, Vermont, USA).

2.6.2. DNA quantification assay

A DNA quantification assay (Quant-iT™ PicoGreen® dsDNA Assay Kit, Invitrogen™, Thermo Fisher Scientific, Waltham, Massachusetts, USA) was performed to evaluate cell proliferation in the samples. For each culture time, the wells of the plate (the same samples used in viability assay) were extensively washed with DPBS, and then, 1 mL of ultrapure sterile water was added to each well. The well plate was placed in a shaking water bath at 37 °C for 1 h and then the content of each well was transferred for eppendorfs. Ultimately, the eppendorfs were immediately stored at −80 °C until use. The quantification of total DNA was determined after cell lysis, according to the manufacturer's description. After transferring each solution to a 96-well white opaque plate (in triplicates), the plate was incubated at room temperature and protected from light for 10 min. The standard curve for DNA analysis was generated with provided DNA from the assay kit. Fluorescence was read at excitation of 485/20 nm and emission of 528/20 nm using a microplate reader Synergy HTX.

2.6.3. Morphological observation of HDFs adhered on the freestanding multilayer membranes

Primary HDFs cell morphology was observed using a fluorescence microscope (Axio Imager 2, Zeiss, Oberkochen, Germany). Briefly, the cells were seeded above the samples (squares 1 cm^2) at a density of 5×10^3 cells. cm^{-2} and cultured for three and seven days, using basal culture conditions. After each time-point, the samples were gently washed with sterile DPBS and fixed with 10% (*v*/*v*) of formalin (Sigma) in DPBS solution for 30 min. To obtain morphological fluorescence images, rhodamine phalloidin (ThermoFisher Scientific) and 4',6-diamidino-2-phenylindole (DAPI, ThermoFisher Scientific) were used as fluorochromes. Rhodamine phalloidin stains F-actin while DAPI binds to AT regions of DNA, staining the cell nucleus. In the fluorescent assay, the fixed samples were initially permeabilized with 0.2% (*v*/*v*) of Triton X-100 (Sigma) in DPBS solution for 10 min and then blocked with 5% FBS (*v*/*v*) in DPBS solution for 30 min. Then, the samples were treated with rhodamine phalloidin for 45 min and subsequently with DAPI for 15 min. After this procedure, the cell morphology was observed using the fluorescence microscope.

2.7. *In vivo* biological assays

All the animal experiments were performed according to the protocol approved by the Ethics Committee of Centro Hospitalar Cova da Beira (approval number 24/2009) and the guidelines set forth in the National Institute for the care and use of laboratory animals. To perform the *in vivo* assays, a total of 10 Wistar rats (4-6 weeks) weighing between 100- 150 g were used. The experimental setup was performed according to that previously used by Miguel S. *et al.* [35]. Animals were separated into three groups: group 1, wounds were treated with $[CHT/ALG/CHT/HA]_{100}$ membrane; group 2, wounds were covered $[CHT/ALG/CHT/HA\text{-}DN]_{100}$ membrane; whereas in the group 3, used as control, wounds were covered with serum physiologic solution. During the study, animals were kept in separate cages and were fed with commercial rat food and water ad libitum. Animals were sacrified after 10 and 21 days.

2.7.1. Hematoxilin and Eosin staining analysis

To evaluate the local and systemic immune response of different membranes, tissue specimens were obtained from each wound area by sharp dissection at days 10 and 21. Skin tissue samples were obtained by necropsy, formalin fixed and paraffin embedded for histological processing. Sections of 3 µm were obtained from each sample using a cryostat microtome (Leica CM1900) and then stained with hematoxylin and eosin (H&E) or with Toluidine blue. Subsequently, samples were visualized using a light microscope with a specific image analysis software from Zeiss. Skin fragments without membrane were used as control. Other tissue samples such as brain, lung, liver, spleen and kidney, were also obtained by necropsy and analyzed to check for any morphological.

2.8. Statistical Analysis

All quantitative data was represented as average value ± standard deviation with at least 5 replicates for each test subject, unless specifically mentioned. For tensile and lap shear strength adhesion data, an unpaired t test with Welch’s correction was used. For the cellular assays, two-way ANOVA was used. Statistical significance of all tests was accepted for $p<0.05$ (*). All statistical analysis was performed using the software GraphPad Prism 6.0.

3. Results

3.1. Synthesis and characterization of the conjugate HA-DN

HA is a component of the ECM, and may be combined with other polyelectrolytes to produce biocompatible and biodegradable materials to be applied as wound skin dressings[36]. To provide an adhesive character to this material, HA was conjugated with DN, taking advantage of carbodiimide chemistry. UV-vis spectroscopy standard spectra were obtained from solutions with different concentrations of free DN and are represented in the inset of Figure S VIII-2, where it is possible to confirm the characteristic UV-excitation band of DN, centered at 280 nm. For DN concentrations less than 1.0 mM, the relation between DN concentration and absorbance followed a linear regime - Figure S VIII-2. UV- vis spectra of the HA and the conjugate HA-DN solution are presented in Figure VIII-1. Besides confirming that the DN characteristic peak just appeared in the spectrum of the conjugate HA-DN, we also estimated the degree of DN substitution. Using the measured absorbance for the HA-DN, obtained at 280 nm, and the linear growth equation obtained from Figure VIII-1A, the degree of DN substitution in the conjugate is 24%. Furthermore, the ^{1}H-NMR spectra of HA and HA-DN were acquired, see Figure S VIII-3.

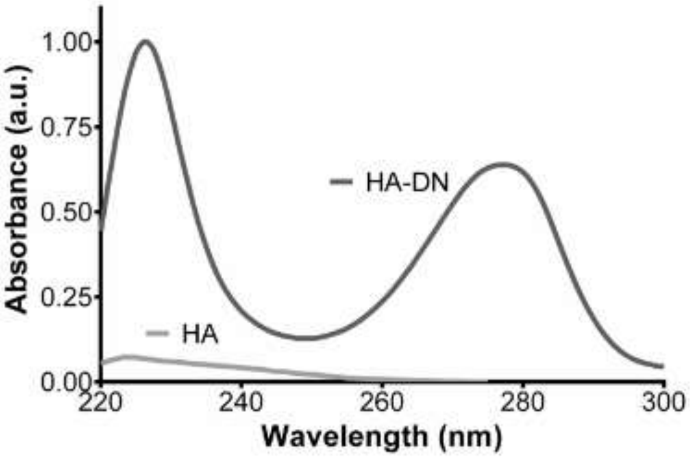

Figure VIII-1. UV-vis spectra of the conjugate the conjugate (HA-DN) and the control (HA), which is also shown for comparison.

3.2. Polyelectrolyte multilayers building-up

Prior to QCM-D monitoring, the ζ- potential of the different polyelectrolyte solutions was measured at working conditions (pH of 5.5 and ionic strength at 0.15 M). As expected, CHT presented a positive charge (+19.8±1.3 mV) while all the other polyelectrolyte solutions presented a negative charge. The ζ-potential values for ALG, HA and HA-DN solutions were -25.1±2.4 mV, -26.7±1.8 mV and -20.2±1.7 mV, respectively.

Once the conjugate was prepared, the ability to construct the polyelectrolyte multilayers was followed *in situ* by QCM-D monitoring. Figures VIII-2A and VIII-2B show the variation of the normalized frequency (Δf/v) and dissipation (ΔD) of the 5th overtone corresponding to the deposition of 2 CHT/ALG/CHT/HA-DN or CHT/ALG/CHT/HA tetralayers (TL) of polyelectrolytes; Figure 2A corresponds to the control system with HA and Figure VIII-2B corresponds to the system containing the conjugate HA-DN. The curves represent the state of frequency and dissipation after each material deposition which can be distinguished by the stepwise decrease in frequency and increase in dissipation. The decrease in frequency in each deposition step indicates that mass was adsorbed onto the gold-coated quartz crystals representing a successful deposition. The increase in dissipation values after each layer deposition indicates a non-rigid behavior of the materials adsorbed above the crystal's surface. The chemical nature of the used materials, the salt composition of the chosen solvent and washing buffer can have great influence on the viscoelastic nature of the resulting multilayer film [33]. Usually, lower increase of ΔD indicates that the film layer becomes denser than for higher increase of ΔD. VIII-Assuming a viscoelastic film, the polymer layers were modelled as an elastic component in parallel with a viscous part [37] – the Voigt Model. In result, both systems can be represented by a linear growth model during the construction of the first 8 layers. However, the overall estimated thickness for the [CHT/ALG/CHT/HA] system was smaller than for the [CHT/ALG/CHT/HA-DN].

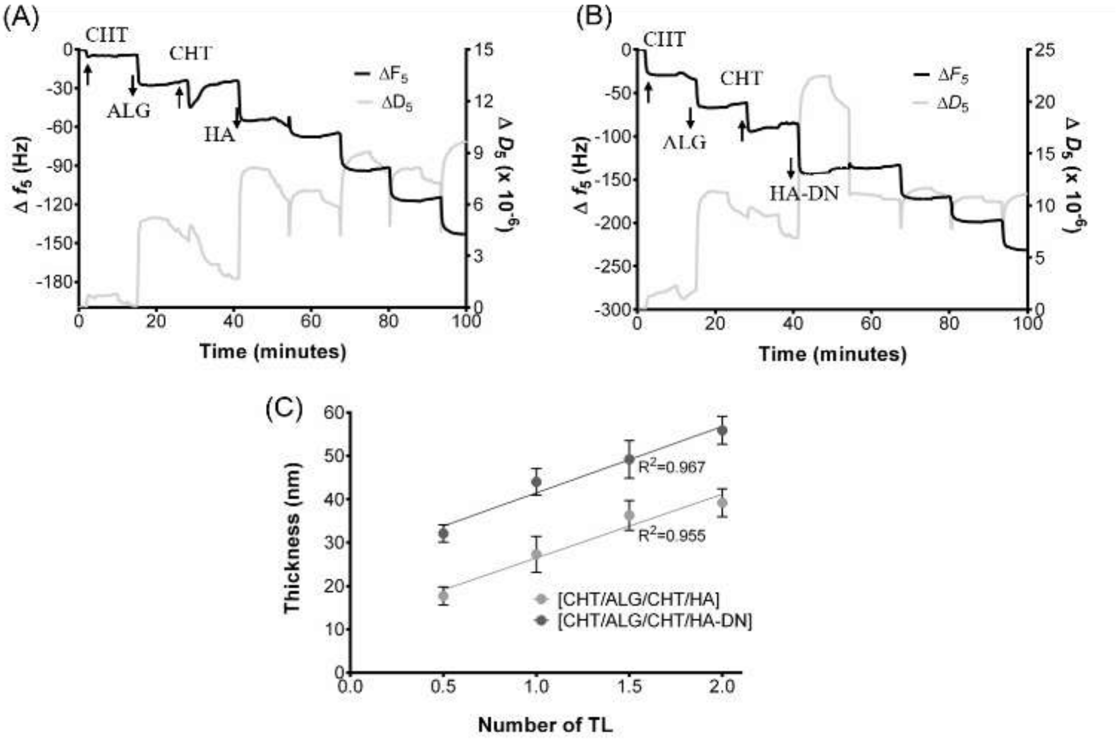

Figure VIII-2. Build-up assemblies of A) chitosan (CHT), alginate (ALG) and hyaluronic acid (HA) and B) chitosan (CHT), alginate (ALG) and conjugate (HA-DN) up to 8 deposition layers (2 tetralayers) in 0.15 M of NaCl, using QCM-D monitoring. C) Cumulative thickness evolution of CHT/ALG/CHT/HA and CHT/ALG/CHT/HA-DN polymeric films as a function of the number of deposited tetralayers. Thickness measurements were estimated using a Voigt viscoelastic model. Both systems followed a linear trend, which are also represented in the graph.

3.3. Production and characterization of the freestanding polyelectrolyte multilayer membranes

QCM-D experiments confirmed the ability to deposit the chosen polyelectrolytes above a quartz crystal. A homemade dipping robot was used to produce freestanding multilayer membranes, by repeating the process 100 times over low surface energy substrates. In the end two freestanding membranes were obtained from the simple detachment of the multilayers by drying:

$[CHT/ALG/CHT/HA]_{100}$ and $[CHT/ALG/CHT/HA\text{-}DN]_{100}$. All the necessary steps to produce the freestanding multilayer membranes are represented in Figure S VIII-1.

3.3.1. SEM

The morphology of the surface of the freestanding membranes was investigated by SEM. Figure VIII-3A and VIII-3B represent the morphology of the $[CHT/ALG/CHT/HA]_{100}$ surface's membrane at different magnifications; it was possible to observe a quite homogeneous morphology, presenting some micro features over the entire surface. The cross-section of the $[CHT/ALG/CHT/HA]_{100}$ – see Figure VIII-3C- also appeared homogeneous along with the thickness. Figure VIII-3D and VIII-3E show the morphology of the $[CHT/ALG/CHT/HA\text{-}DN]_{100}$ surface's membrane at different magnifications; it was possible to observe some nano to microfeatures randomly distributed over the entire surface, together with a very porous and interconnected structure. Moreover, the cross-section of the $[CHT/ALG/CHT/HA\text{-}DN]_{100}$ is presented in Figure VIII-3F, being less homogeneous than for the other system. Therefore, the thickness of both $[CHT/ALG/CHT/HA]_{100}$ and $[CHT/ALG/CHT/HA\text{-}DN]_{100}$ freestanding membranes was calculated from the cross-section images, being 18.7±1.22 µm for the control system and 25.3±1.10 µm for the DN-containing film.

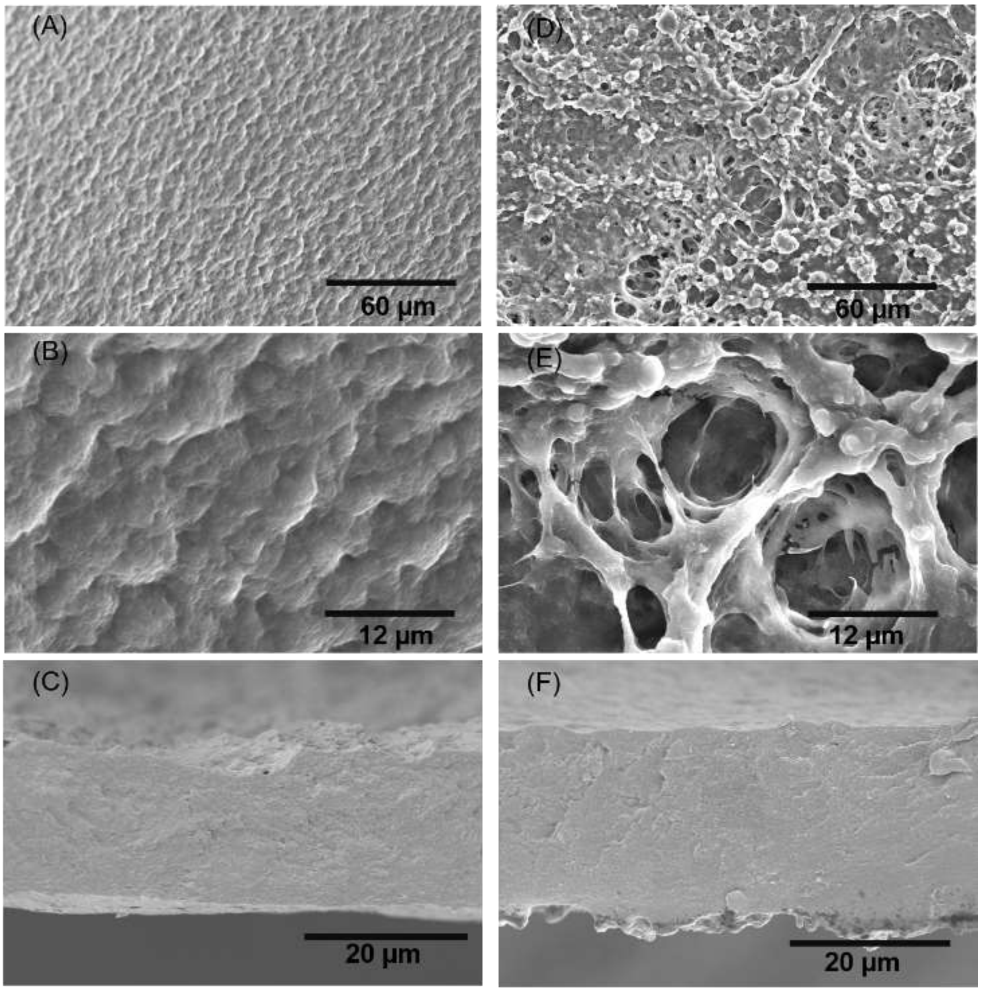

Figure VIII-3. SEM images of the morphology of the upper side of the $[CHI/ALG/CHI/HA]_{100}$ at A) lower and B) higher magnifications. The cross-section of the $[CHI/ALG/CHI/HA]_{100}$ membrane is presented in C). SEM images of the morphology of the upper side of the $[CHI/ALG/CHI/HA\text{-}DN]_{100}$ at D) lower and E) higher magnifications. The cross-section of the $[CHI/ALG/CHI/HA\text{-}DN]_{100}$ membrane is depicted in F).

3.3.2. Water uptake and tensile mechanical testing

The water uptake of the $[CHT/ALG/CHT/HA]_{100}$ and $[CHT/ALG/CHT/HA\text{-}DN]_{100}$ freestanding membranes was also evaluated for 1 day in PBS solution at 37 °C - see Figure VIII-4A. Both membranes showed ability to uptake water molecules; $[CHT/ALG/CHT/HA]_{100}$ and $[CHT/ALG/CHT/HA\text{-}DN]_{100}$ freestanding membranes seemed to reach the equilibrium after 1 h and 15 min in PBS, respectively. After these times, no significant changes occur in the system, in terms of water uptake. Comparing both systems, $[CHT/ALG/CHT/HA]_{100}$ freestanding membranes showed significant higher water content percentages than $CHT/ALG/CHT/HA\text{-}DN]_{100}$ membranes.

Tensile tests were also performed to study the mechanical properties of these materials – see Figure VIII-4B, which show the most representative stress-strain curves for the $[CHT/ALG/CHT/HA]_{100}$ and $[CHT/ALG/CHT/HA\text{-}DN]_{100}$ freestanding membranes, respectively. From these, it was possible to calculate important parameters like the Young’s modulus, the ultimate tensile strength and the maximum extension (Figure VIII-4C) for each type of membrane. All parameters are higher for the $[CHT/ALG/CHT/HA\text{-}DN]_{100}$ than for the $[CHT/ALG/CHT/HA]_{100}$ freestanding membranes, with significant differences in terms of Young’s modulus (8.3±1.47 MPa against 2.1±0.37 MPa) and ultimate tensile strength (1725.2±236.53 kPa against 654.3±125.19 kPa).

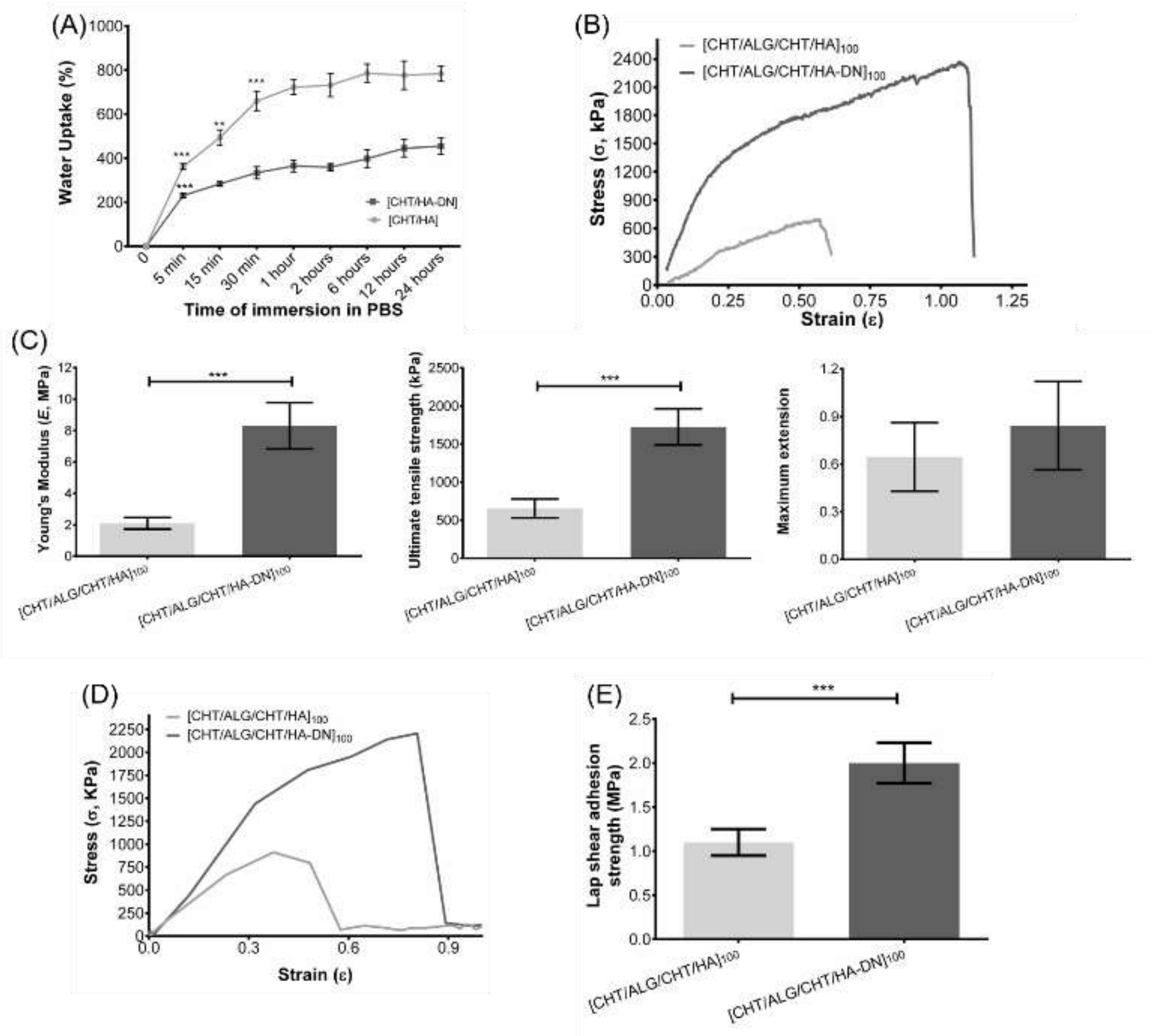

Figure VIII-4. A) Water uptake measurements of the [CHI/ALG/CHI/HA]$_{100}$ and [CHI/ALG/CHI/HA-DN]$_{100}$ freestanding multilayer membranes. B) Representation of a stress-strain curve, during the tensile tests, for [CHI/ALG/CHI/HA]$_{100}$ and [CHI/ALG/CHI/HA-DN]$_{100}$ hydrated membranes. Representation of the mechanical properties of the FS evaluated by tensile tests: C) Young's Modulus, ultimate tensile strength and maximum extension at rupture. D) Representative stress-strain curves, during the lap shear adhesion strength, for [CHI/ALG/CHI/HA]$_{100}$ and [CHI/ALG/CHI/HA-DN]$_{100}$ glued hydrated membranes. E) Lap shear strength tests for both [CHT/ALG/CHT/HA]$_{100}$ and [CHT/ALG/CHT/HA-DN]$_{100}$ membranes. Data is presented as average ± standard deviation where significant differences were found for $p < 0.001$(***) and $p < 0.01$(**).

3.3.3. "Bioactivity" properties: from adhesiveness to bacteriostatic

For the last years cathecols have been widely investigated to enhance adhesive [38] and also bacteriostatic properties [39] of different materials. Therefore the assessment of the lap shear adhesion strength and anti- bacterial tests were perfomed on the produced membranes.

Briefly, the HA-DN or HA side of a rectangle part of the membrane was put in contact with the CHT side of other rectangle part of the membrane and left under pressure stimuli overnight. Then, the samples were subbjected to adhesion tests where the required lap shear bonding strength necessary to detach the two parts of the systems was recorded– see Figure VIII-4D. Therefore, we found that [CHT/ALG/CHT/HA]$_{100}$ required a lap shear adhesion strength of 1.1±0.2 MPa while [CHT/ALG/CHTD/HA-DN]$_{100}$ ones involved higher lap shear strength of about 2.0±0.2 MPa, as show in the graph of Figure VIII-4E. It means that more strength was needed to detach the DN-containing freestanding membranes, allowing us to conclude that DN significantly contribute on enhancing the adhesive properties of the membranes.

Biofilm formation at the surface of the different materials was assessed by SEM. In Figure VIII-5, it is possible to observe some bacteria at the surface of HA layer without DN and CHT layer, although their number is not enough to be considered a biolfim, for both strains. On the other hand, HA-DN showed an increased bacterial adhesion at its surface when in contact with *S. aureus* but the inverse happenned for *E.coli*., where it is possible to observe that HA-DN and CHT layer did not present enough bacteria to be considered a biolfim.

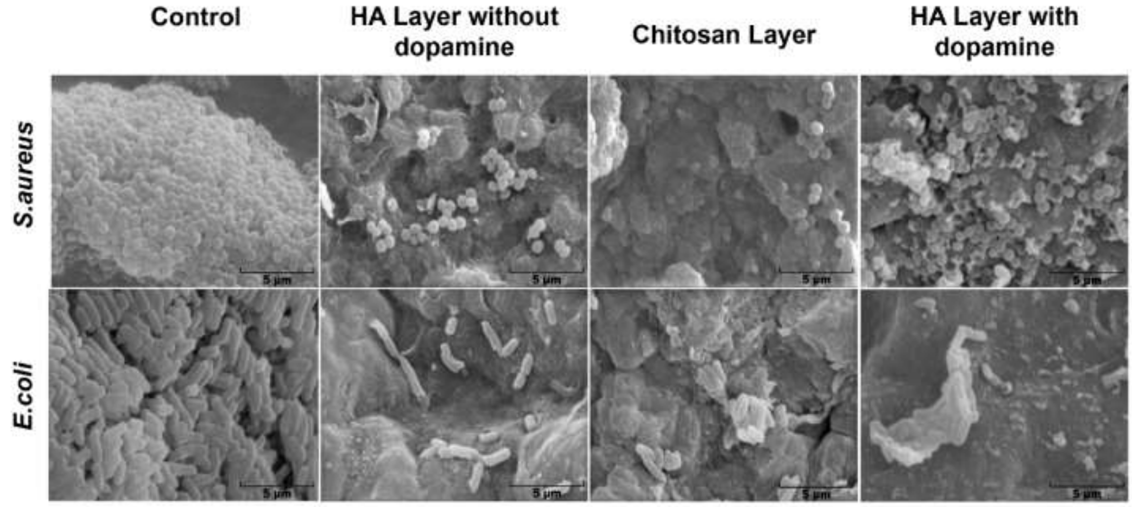

Figure VIII-5. SEM images of biofilm formation for *S. aureus* and *E. coli* at the surface of the HA layer, CHT layer and HA-DN layer.

3.4. *In vitro* cell culture with HDFs

HDF cells were cultured over both $[CHT/ALG/CHT/HA]_{100}$ and $[CHT/ALG/CHT/HA\text{-}DN]_{100}$ freestanding multilayers membranes for 7 days.

3.4.1. Cellular metabolic activity and cell content

The metabolic activity gave an indication about the cell viability and capability to proliferate – see Figure VIII-6A. From the first day of culture significant differences ($p < 0.01$) were found between cells cultured over $[CHT/ALG/CHT/HA]_{100}$ and $[CHT/ALG/CHT/HA\text{-}DN]_{100}$ freestanding multilayers, with the DN-containing membranes presenting higher values of metabolic activity. This trend was maintained at 3 and 7 days ($p<0.001$), suggesting good cell viability and activity on the surface of catechol-containing membrane. A more accurate measurement of proliferation was done by DNA quantification - see Figure VIII-6B. Overall, these results are in accordance with the ones obtained for the metabolic activity, with higher values of DNA content for $[CHT/ALG/CHT/HA\text{-}DN]_{100}$ freestanding multilayers. For the first day of culture, significant differences ($p<0.01$) were already found between the different formulations, suggesting that more cells attached to the surface. For the third and the seventh day of culture, these differences were even more pronounced ($p<0.001$).

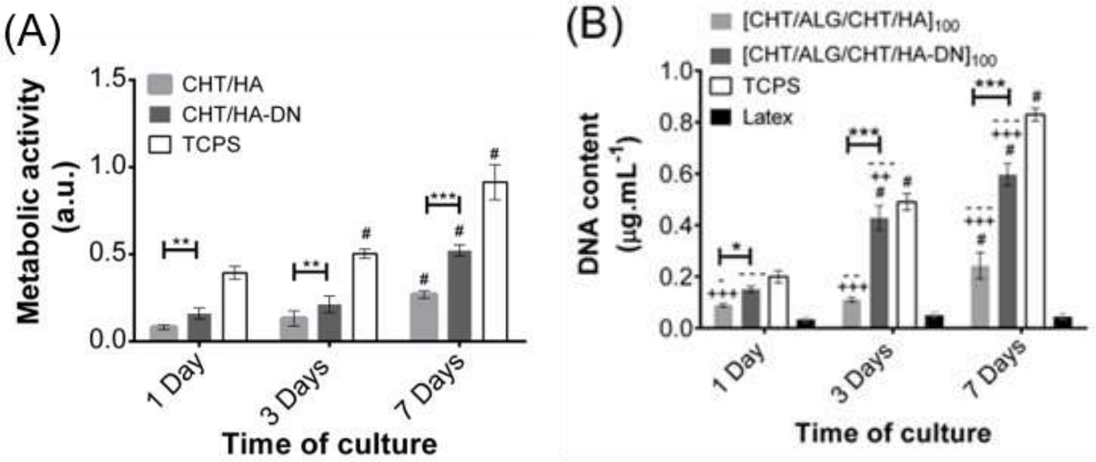

Figure VIII-6. A) Metabolic activity through the absorbance of HDFs seeded above the freestanding membranes (MTS assay) and B) cellular proliferation through the determination of the DNA content (DNA quantification assay), both for 1, 3 and 7 days. TCPS was used as positive control and latex as negative control. Significant differences were found for $p > 0.05$ (*); $p > 0.01$(**) and $p > 0.001$(***), between the membranes' systems. Moreover, significant differences with the positive control TCPS were found for $p > 0.01$(++) and $p > 0.001$(+++) and with negative control latex for $p > 0.05$ (-); $p > 0.01$(--) and $p > 0.001$(---). Significant differences with each previous time points were found for $p<0.001$(#).

3.4.2. Cell Morphology

The morphology of the HDFs when adhered above the freestanding membranes was also evaluated by phalloidin-DAPI staining – see Figure VIII-7. After 1 day of culture, the cells adhered above the freestanding membranes presented a more rounded shape than when adhered above TCPS. Nevertheless, this round morphology was altered along the days of culture; after 3 and 7 days, the cells present a spread morphology with well-defined actin filamentous and a spindle-like shape, either for both type of freestanding membranes or TCPS. Curiously, the cells adhered above the [CHT/ALGCHT/HA-DN]$_{100}$ freestanding multilayer membranes seemed to grow starting from an aggregated portion of cells that connect one with each other, resulting in an interconnected cell network. Even that, the cells seemed strongly adhered to the surface of the membrane unlike it happens with the cells adhered above the [CHT/ALG/CHT/HA]$_{100}$ freestanding membranes. After 7 days of culture, there are much less HDFs adhered above the surface and the ones that exist seemed poorly adhered to the surface. In terms of cell density, we observed again more cells adhered and distributed above the [CHT/ALG/CHT/HA-DN]$_{100}$ freestanding multilayer membranes than above the [CHT/ALG/CHT/HA]$_{100}$.

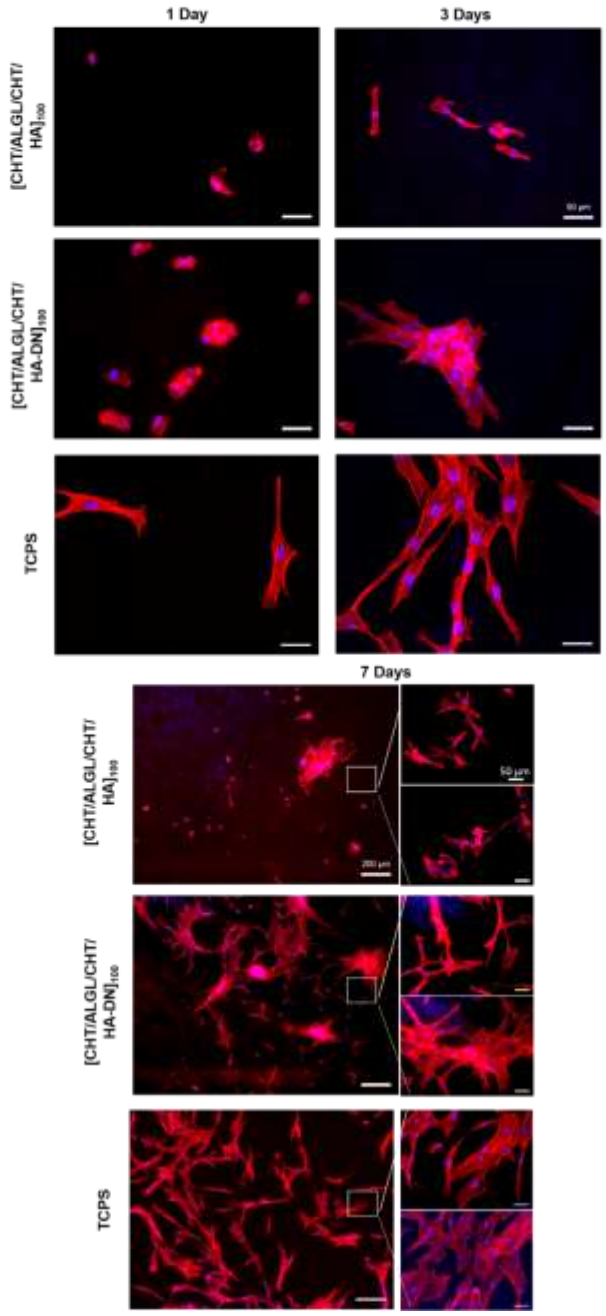

Figure VIII-7. Representative images of HDFs cells over the [CHT/ALG/CHT/HA]$_{100}$ and [CHT/ALG/CHT/HA-DN]$_{100}$ membranes, represented by DAPI−phalloidin fluorescence assay at 1, 3 and 7 days. Cells nuclei are stained in blue by DAPI and F-actin filaments are stained in red by phalloidin. The scale bar is representative for all images.

3.1. *In vivo* assay

A Hematoxylin-Eosin (H&E) staining of the skin wound tissues was performed during each timepoint of the assay – see Figure VIII-8A. A broad region of hyper-proliferative epithelial layer is a hallmark of the regenerating wound edge [40]. Typically, during wound maturation, the epidermal region narrows until it gets re-established to its original appearance, i.e., a very thin layer.

Clearly, for the wound area covered with the freestanding membrane, the inflammatory process was quite exuberant, i.e., the presence of inflammatory cells was more abundant. However, the wound healing process progresses to the next phases and the fibroblast proliferation and dermis production were evident, after 21 days.

In groups 1 and 3, we could see an epidermal region with an appearance of a thin layer without epidermal annexes formation. Unlike, group 2 showed a thin epidermal layer as well as the establishment of epidermal papillaes. Hence, we could observe that wounds treated with DN membranes were in an advanced stage of the healing process (please see table 1 for further information), after 21 days.

Table VIII-1. Histological Findings of H&E Stain

	Group 1	**Group 2**	**Group 3**
Granular Layer	+	+	-
Squamous Cell Layer	+	++	+/-
Basal Layer	+/-	+	-
Reticular Dermis	++	++	++

Note: -, low; +/-, moderate; +, much; ++, much more.

Additionally, a blue toluidine staining was used to highlight the presence of mastocyte cells, where their cytoplasm contains granules composed of heparin and histamine that become blue or violet stained- see Figure VIII-8B [41]. The results show that group 2 presented the higher level of inflammation compared to the other groups, as it displays a lot of mastocyte cells after 10 days. In fact, all groups, except the control, showed a lot of mastocyte cells, probably due to the presence of a foreign material in the organism. However, after 21 days, in group 2 the mastocytes population was significantly reduced, resulting on the highest decreasing of inflammation between the 10th and the 21st days, among the different samples (please see Figure VIII-8C for more data). Such results highlight the potential of using DN impregnated on HA membranes.

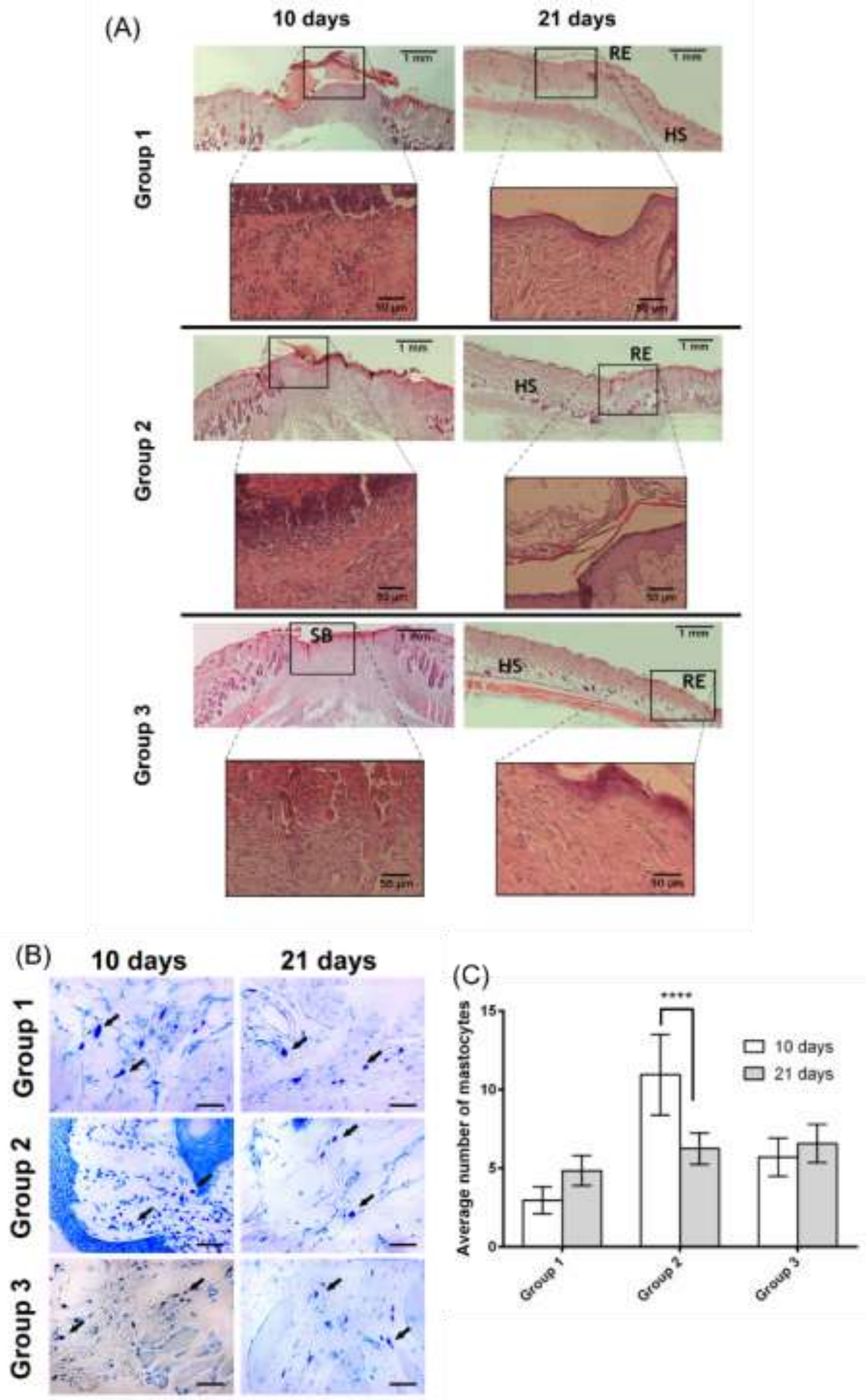

Figure VIII-8. Representative images of H&E-stained histological sections of explants at day 10 and 21, highlighting the wound healing progression along the time frame chosen. B) Micrographs of the different samples stained with blue toluidine after 10 and 21 days (magnification of 400x). C) Mastocyte cell number after 10 and 21 days in contact with the different materials. A p value lower than 0.001 (***) was considered statistically significant. HS: healthy skin; RE: re-epithelization; SB:scab. Group 1 – HA membrane; Group 2 – HA-DN membrane; Group 3 – Control.

4. Discussion

Being the biggest and most exposed tissue of the human body, skin is always on the light of defects, trauma or burns. Considerable efforts have been employed to develop ideal scaffolds for skin tissue engineering and medicine regenerative purposes, inclusive to promote skin wound healing [1a, 1b, 3a]. Nowadays, scientists are focused on mimicking the structure, composition, topography, mechanical properties and even the biological function of ECM to achieve better materials[1c]. Herein, we identified some criteria that must be taken into account in skin substitute production: besides being easy to handle and apply to the wound site, it should provide vital barrier function with appropriate water flux and be readily adherent, presenting suitable physical and mechanical properties[1c]. Therefore, we got inspiration on mussel's bonding abilities, to develop a conjugated polymer capable of adding adhesive properties to our material, modifying the HA backbones chains with the catecholamine DN, using a carbodiimide chemistry reaction. The UV-vis spectra for HA and HA-DN solutions showed that only the conjugate HA-DN presented the characteristic peak band of DN, at 280 nm (see Figure VIII-1). In fact, we could also determinate the degree of DN substitution by preparing a standard curve of known concentration of free DN and then following their UV excitation curve (Figure S VIII-2). The obtained substitution degree was 24%. This value is higher than some similar substitutions already reported in literature, indicating a better performance of our chemical conjugation reaction [42].

Both the results of UV–vis spectroscopy and ^{1}H-NMR confirmed that DN was presented in the conjugated HA-DN. Therefore, we believe that the chosen conditions were an adequate commitment between substitution and waste of material and would have a considerable impact on the adhesion properties of the resulting scaffold.

Additionally, this scaffold should undergo controlled degradation, be sterile, non-cytotoxic and evoke minimal inflammatory reactivity, while still being cost effective[1c]. The size of the skin wounds can be variable; therefore, it is highly recommendable to have a scaffold which acts like a patch on the skin wound and that we could cut according with the size of the defect. LbL is a cost-effective technique to produce multilayer structured membranes for tissue engineering[15a]. QCM-D monitoring confirmed the construction of a film composed by CHT, ALG and HA-DN or HA at the surface of the quartz sensor. Several QCM-D monitoring studies have been done with CHT and ALG[37a] and with CHT and HA[43], but it is the first time that all polymers were combined. This fact is mainly related with the desired degradation rate and offering more robustness for the developed material. When inside human body, HA is known by its fast degradation through the action of hyaluronidases [44]; however, we aimed a scaffold that undergo a controlled degradation, thus, adding an inherently non-degradable polysaccharide as ALG, we hypothesize that we could increase the time of degradation. For both cases of study, corresponding to Figure VIII-2A and VIII-2B, each decrease on the Δf corresponds to the adsorption of the corresponding polymers; indeed, similar Δf were obtained after each polymer deposition, suggesting that similar masses of the different polymers were deposited. This fact can be related with the charge of the polymers: measured zeta potential values for these polyelectrolytes, at pH 5.5, are close in terms of absolute value, being expected also similar changes of Δf. Note that it has been suggested [45] that electrostatic-based depositions require appropriate charge balance. Curiously, each decrease in Δf was followed by a subsequent increase, due to the desorption of a small fraction of free polyelectrolyte during the washing step. Each polymer deposition was also followed by the ΔD increase for both type of films. However, ΔD for CHT was lower than for the other polymers, meaning that when the polycation was adsorbed the film layer became denser than for the other polymers [46]. This observation can be associated with the highly water affinity of ALG and HA, which introduced softer layers to the system. In fact, HA is a hygroscopic material, having high ability of attracting water molecules from the surrounding environment [47]; combining hygroscopic polymers with non-hygroscopic ones could lead to detrimental effects. Analyzing the QCM-D data, we hypothesize that after the deposition of the first layer of either HA or HA-DN there were some re-arrangements of the film structure, which result in the weak detection of the subsequent CHT layer deposition. This effect disappeared after first TL was constructed, indicating that the construction films were already more stable. Comparing both CHT/ALG/CHT/HA and CHT/ALG/CHT/HA-DN systems, the catechol-containing one generated highest absolute values of Δf. In fact, when the modification of carboxylic acid groups in HA with carbodiimide chemistry happens, the surface charge of the conjugated decreased, as shown by the ζ-potential values. As follows, the absolute ζ-potential values of CHT and HA-DN solutions became more alike, allowing higher Δf. This observation goes according with thickness estimation results that revealed that after the construction of 2 TL, CHT/ALG/CHT/HA-DN was thicker than CHT/ALG/CHT/HA film (Figure VIII-2C). This goes oppositely to our previous results which revealed the formation of thinner films for CHT/HA-DN systems [42]. Such disagreement can be related by the incorporation of ALG in the multilayer system, as well as the different polymer concentrations and proportions.

Accordingly, biomimetic, polysaccharide-based and transparent membranes containing catechol domains were successfully produced following the same methodology already reported by Caridade S.G. *et al.*[21a]. The integrity of these membranes was maintained even after the detachment process, see Figure S VIII-1. SEM images of the upper layer of $[CHT/ALG/CHT/HA]_{100}$ (Figure VIII-3A and VIII-3B) and $[CHT/ALG/CHT/HA\text{-}DN]_{100}$ (Figure VIII-3D and VIII-3E) freestanding membranes showed singular rough morphologies, presenting micro to nanofeatures on their surface. Usually, rougher surfaces are preferred for cells adhesion and proliferation rather than smooth surfaces, mainly because roughness increases the contact area between cells and material [1c, 48]. Often, polysaccharide-based membranes' surface must be modified to increase their cellular performance. Therefore, using HA or HA-DN we could overcome the need of a surface treatment, being a time and money-saving strategy. Besides presenting a rough surface, $[CHT/ALG/CHT/HA\text{-}DN]_{100}$ freestanding membranes also exhibit a very porous structure. In fact, interconnected porous networks are benefic for cell nutrition, oxygen delivery, proliferation and migration processes, as well as to support and guide tissue vascularization[49].

Nonetheless, the increase on the porosity often compromises the mechanical properties of the scaffolds, diminishing their structural stability [50]. Therefore, it is important that the developed freestanding membranes have enough mechanical strength to maintain integrity until wound heals. The mechanical properties of native skin ECM vary according with different individual parameters like anatomic site, age or even genetics [51]. Uniaxial tensile tests revealed that both type of membranes exhibit strain-stiffening behavior (Figure VIII-4B), as well as happens for skin tissue where collagen fibers rotate, align, and straighten in the direction of stretch until the point of failure [51-52]. $[CHT/ALG/CHT/HA]_{100}$ freestanding membranes displayed a Young's modulus significantly lower than $[CHT/ALG/CHT/HA\text{-}DN]_{100}$ ones (Figure VIII-4C); Moreover, catechol-containing membranes presented significantly higher values of ultimate tensile strength (Figure VIII-4C). Also, maximum extension can be an important parameter, but no significant differences were found between the two systems (Figure VIII-4C); the introduction of the HA or of the conjugate HA-DN seems to increase the ability of the freestanding membranes to strain, comparing with unmodified CHT/ALG multilayer membranes [21b]. Mechanical properties can be correlated with the water uptake behavior of the $[CHT/ALG/CHT/HA]_{100}$ and $[CHT/ALG/CHT/HA\text{-}DN]_{100}$ membranes. Figure VIII-4A shows that $[CHT/ALG/CHT/HA]_{100}$ multilayer membranes presented higher ability to retain water molecules and become more hydrated than $[CHT/ALG/CHT/HA\text{-}DN]_{100}$ membranes. Previous studies reported that a kind of plasticization phenomenon of water molecules in polysaccharides can increase the molecular mobility and decrease the stiffness of the membrane [21b]. This fact can explain the lowest value of elastic modulus in the case of the control membranes.

The conjugate HA-DN was already reported in literature by conferring more adhesive behavior to materials [31-32]. In fact, $[CHT/ALG/CHT/HA\text{-}DN]_{100}$ multilayer membranes presented a significantly higher value of lap shear adhesion strength than their control $[CHT/ALG/CHT/HA]_{100}$ multilayer membranes (Figure VIII-4D and VIII-4E). We hypothesize that the increase in the bonding force is related with the strong adhesion force of catechol groups in the modified HA. Our results matched with previous investigations. Park H-J. *et al.* [53] developed a bioinspired hydrogel composed by HA modified with catechol moieties which presented better results in terms of biocompatibility and tissue adhesiveness compared with photopolymerized HA hydrogels; however, the adhesive strength of these hydrogels was about 47.61 ± 36.12 kPa, that is much less than the ones found in this investigation. Neto A. I. *et al.* [42] reported the development of adhesive CHT/HA-DN coatings above glass slides; even though, their system presented an adhesive shear strength about 2.32 ± 2.20 MPa, which is in accordance with the one achieved with our system. Note, that besides DN can oxidize spontaneously when exposed to the air, we believe that when coupled to HA, the conjugated became more stable than having just DN. In fact, Neto A. I.[42] et al. compared the adhesive strength obtained before and after exposing to sodium periodate oxidizing agent and conclude that no significant changes were found. Carvalho A. L. *et al.* [54] also produced mussel-inspired LbL coatings for orthopedic purposes, composed by CHT and HA-DN, but also including silver-doped bioactive glass nanoparticles. Besides authors confirmed the adhesive properties, they also performed microbiological assays, suggesting that coatings containing silver-doped nanoparticles displayed an antibacterial effect against *S. aureus* and *E. coli* cultures, two of the major causes of various human infections.

For skin wound healing, the evaluation of the biofilm formation at the surface of the scaffold is also highly recommended[5b]. While *S. aureus* is responsible by causing skin and soft tissue infections, *E.coli* is the most common cause of urinary tract infections. As observed by Figure VIII-5, *E.coli* and *S.aureus* were not able to form any biofilms at the surface of HA-DN films. Such preliminary result can be explained by the intrinsic bacteriostatic effect of catecholamines [55].

Once several desired properties were assembled in one material, *in vitro* and *in vivo* experiments comproved that $[CHT/ALG/CHT/HA\text{-}DN]_{100}$ multilayer membranes were effectively more suitable for skin wound healing than $[CHT/ALG/CHT/HA]_{100}$ ones. Parameters like HDFs viability, proliferation and infiltration (see Figure VIII-6A and VIII-6B and Figure VIII-7) were favored when cells were culture above the catechol-containing multilayer membranes, which imply that $[CHT/ALG/CHT/HA\text{-}DN]_{100}$ membranes were more functionally active than their control without DN. The main reasons for this improved behavior can be related with different aspects of the material. As above referred, rough and porous surfaces are usually described to enhance cellular behavior. Min B-M. *et al.* [56] produced silk fibroin nanofibers using electrospinning technology; the wide range of pore size distribution, the high porosity as well as the consequent high surface area to volume ratio of the nanofibers were suggested as favorable for cell adhesion, growth and proliferation. Also, Silva J. M. *et al.* [57] combined LbL with spherical template leaching to produce 3-dimensional nanostructures with high porosity and interconnectivity, just composed by self-assembled multilayers of CHT and chondroitin sulfate, to enhance cell adhesion and proliferation. Therefore, we hypothesized that it became easier for HDFs located on surface of the material to migrate into the pores network, due to the high porosity that $[CHT/ALG/CHT/HA\text{-}DN]_{100}$ multilayer membranes could offer for cell infiltration and growth. On the other hand, the stiffness of the material has been often referred as capable of modulating the cellular behavior above the material's surface. Ren K. *et al.* [58] produced poly(L-lysine)/hyaluronan multilayer films of controlled stiffness to evaluate the influence of this parameter on cellular behavior; they concluded that stiff films enhanced proliferation whereas soft films were not favorable for cell adhesion, spreading or proliferation. Our results are in agreement with this investigation: $[CHT/ALG/CHT/HA\text{-}DN]_{100}$ multilayer membranes were stiffer than the controls without DN, retaining less water volumes and increasing protein adsorption phenomena. Finally, the adhesive moieties conferred by DN have been also reported in literature to confer cell-adhesive properties. Yang X. *et al.* [59] conjugated recombinant human gelatin with DN to create biologically adhesive surfaces; they reported that the introduction of DN enhanced the binding of collagen-binding vascular endothelial growth factor and cell adhesion as compared with gelatin alone. Han L. *et al.* [60] developed adhesive and tough polydopamine-clay-polyacrylamide hydrogels that favored cell attachment and proliferation, owning to the high cell affinity of polydopamine. We believe that more than mechanical adhesion, the introduction of DN on our freestanding multilayer membranes' system conferred bioadhesive properties to the surface of the membrane unlike what happens to $[CHT/ALG/CHT/HA]_{100}$ multilayer membranes.

A complex *in vivo* wound healing process begins upon injury and includes different phases as blood clotting, inflammation, re-epithelialization, granulation tissue formation and tissue remodeling [61]. Among other cell types, mastocytes have been reported to usually migrate to the inflammation site. Moreover, mastocytes increased population is proportional to the degree of inflammation of the lesion [62]. In the inflammation phase, mastocyte cells accumulate at the wound site and release histamine, interleukins (IL-6 and IL-8), and growth factors such as vascular endothelial growth factor (VEGF) [63]. Posteriorly, mastocytes release serine proteases (chymase and tryptase), that breakdown the ECM inducing proliferation of fibroblasts and endothelial cells, initiating the following phase of wound healing process. Furthermore, the infiltration of neutrophils and other inflammatory mediators is enabled through vasodilatation and increased vascular permeability [64]. Reduction of inflammation process was more evident after 21 days for $[CHT/ALG/CHT/HA\text{-}DN]_{100}$ multilayer membranes. DN has been reported to reduce inflammation by inducing upregulation of cytokines, chemokines, adhesion molecules and by producing anti-inflammatory mediators [42, 64]. The control group (group 3) as well as

[CHT/ALG/CHT/HA]$_{100}$ multilayer membranes (group 1) were not able to reduce the mastocytes population. Hence, we hypothesize that the cells could populate the surface of the DN-containing membranes which is more porous, stiffer and adhesive than the CHT/ALG/CHT/HA]$_{100}$ membrane, building up a scaffold that enhances skin tissue engineering. Moreover, we believe that the porosity of the surface of the [CHT/ALG/CHT/HA-DN]$_{100}$ multilayer membranes could increase the cellular ingrowth, which could mimic even better the features of native ECM.

Overall, we could produce adhesive and biomimetic multilayer membranes, composed by natural-based materials, that could act as patch to replace the functions of native ECM until host cells can repopulate and resynthesize a new ECM for skin wound healing.

5. Conclusions

We constructed adhesive and bioinspired freestanding multilayer membranes, composed of polysaccharides, which morphology and composition recapitulate aspects presented by native ECM. The presence of DN, which contains catechol groups that were found as responsible for the adhesive behavior of mussels on wetted rocks, brought new advantages for this LbL system. The [CHT/ALG/CHT/HA-DN]$_{100}$ freestanding multilayer membranes supported better cell adhesion and proliferation and provided directional cues for cells communicate with each other and growth. These natural, biocompatible, highly porous and adhesive materials hold great potential in providing a support for skin wound healing, as shown by *in vitro* and *in vivo* assays.

6. Supplementary Information

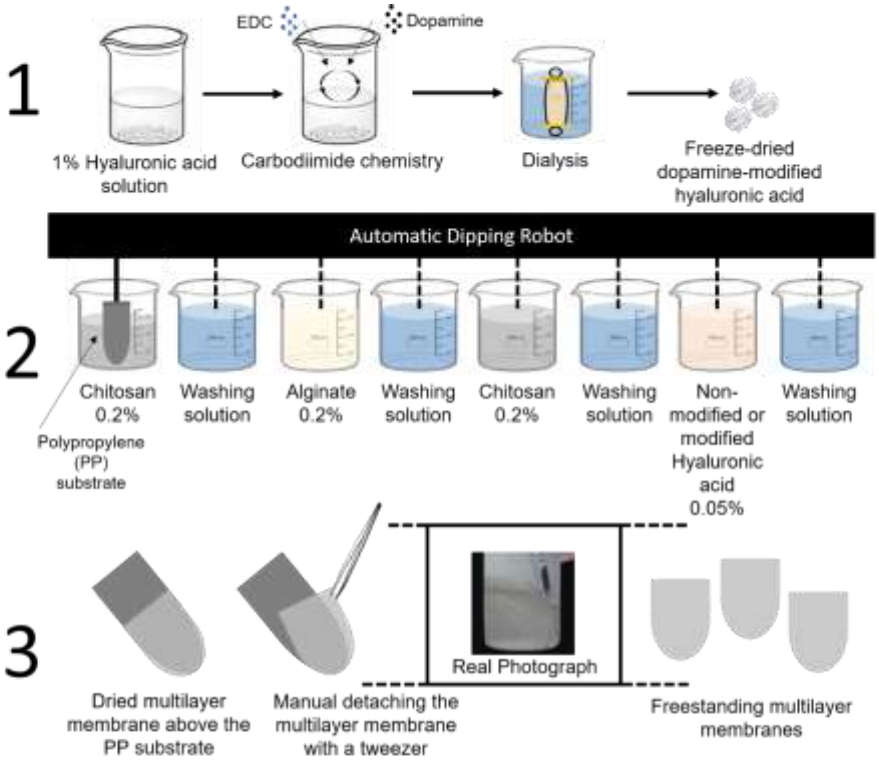

Figure S VIII-1. Schematic representation of the synthesis of the conjugated HA-DN (1), the layer-by-layer assembly using the dipping robot equipment (2) and finally the detachment method employed to obtain the freestanding multilayer membrane (3). A real photograph of the detachment step of the [CHT/ALG/CHT/HA-DN]$_{100}$ multilayer membrane is also presented.

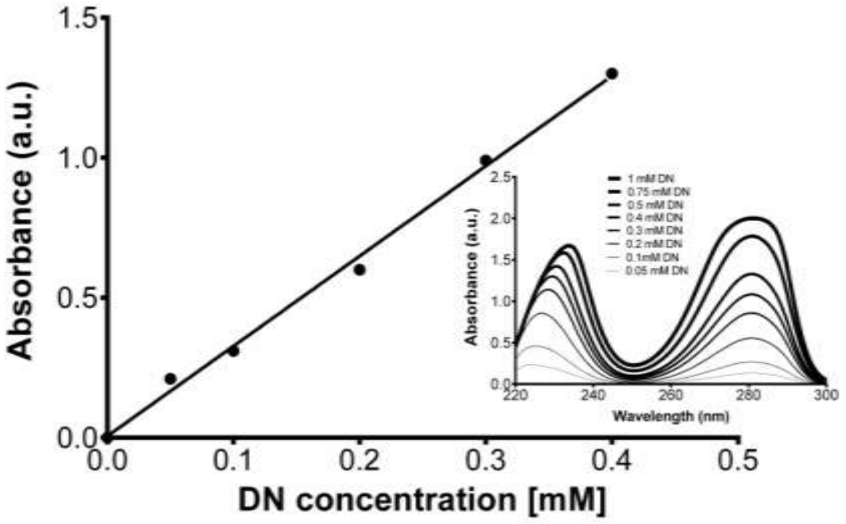

Figure S VIII-2. Inset shows the UV-Vis spectra of dopamine solutions with different concentrations and the figure represents the respective calibration curve that correlates DN concentration with measured absorbance.

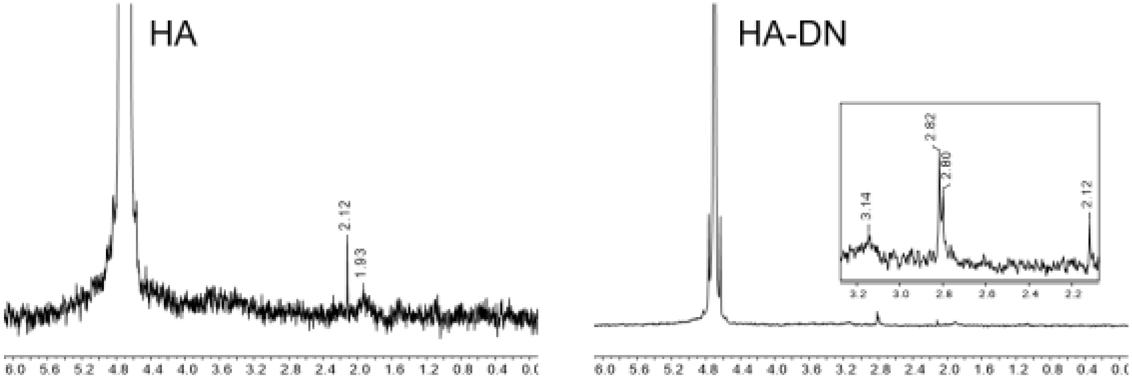

Figure S VIII-3. ^{1}H-NMR spectra of HA and the synthesized conjugate HA-DN.

7. Acknowledgements

M.P.S. acknowledges the Portuguese Foundation for Science and Technology (FCT) for financial support through Grant No. SFRH/BD/97606/2013. This work was supported by the European Research Council grant agreement ERC-2014-ADG-669858 for the ATLAS project. The authors acknowledge Paula Marques (Mechanical Engineering Department, University of Aveiro, Aveiro, Portugal) for providing the mechanical equipment to carry out the tensile tests and the lap shear adhesion tests.

8. References

1. (a) Metcalfe, A. D.; Ferguson, M. W. J., Tissue engineering of replacement skin: the crossroads of biomaterials, wound healing, embryonic development, stem cells and regeneration. *Journal of the Royal Society Interface* **2007,** *4* (14), 413-437; (b) Chen, M.; Przyborowski, M.; Berthiaume, F., Stem Cells for Skin Tissue Engineering and Wound Healing. *Critical reviews in biomedical engineering* **2009,** *37* (4-5), 399-421; (c) Zhong, S. P.; Zhang, Y. Z.; Lim, C. T., Tissue scaffolds for skin wound healing and dermal reconstruction. *Wiley Interdisciplinary Reviews: Nanomedicine and Nanobiotechnology* **2010,** *2* (5), 510-525.
2. Herndon, D. N.; Barrow, R. E.; Rutan, R. L.; Rutan, T. C.; Desai, M. H.; Abston, S., A comparison of conservative versus early excision. Therapies in severely burned patients. *Annals of surgery* **1989,** *209* (5), 547-52; discussion 552-3.
3. (a) Andersson, L. C.; Nettelblad, H. C.; Kratz, G., From Basic Wound Healing to Modern Skin Engineering. In *Artificial Organs*, Hakim, N. S., Ed. Springer London: London, 2009; pp 93-105; (b) Tenenhaus, M.; Rennekampff, H. O., Current Concepts in Tissue Engineering: Skin and Wound. *Plastic and reconstructive surgery* **2016,** *138* (3 Suppl), 42s-50s.
4. Langer, R.; Vacanti, J., Tissue engineering. *Science* **1993,** *260* (5110), 920-926.
5. (a) Skorkowska-Telichowska, K.; Czemplik, M.; Kulma, A.; Szopa, J., The local treatment and available dressings designed for chronic wounds. *Journal of the American Academy of Dermatology* **2013,** *68* (4), e117-26; (b) Sood, A.; Granick, M. S.; Tomaselli, N. L., Wound Dressings and Comparative Effectiveness Data. *Advances in Wound Care* **2014,** *3* (8), 511-529.
6. Caravaggi, C.; De Giglio, R.; Pritelli, C.; Sommaria, M.; Dalla Noce, S.; Faglia, E.; Mantero, M.; Clerici, G.; Fratino, P.; Dalla Paola, L.; Mariani, G.; Mingardi, R.; Morabito, A., HYAFF 11-Based Autologous Dermal and Epidermal Grafts in the Treatment of Noninfected Diabetic Plantar and Dorsal Foot Ulcers. *A prospective, multicenter, controlled, randomized clinical trial* **2003,** *26* (10), 2853-2859.
7. Dantzer, E.; Braye, F. M., Reconstructive surgery using an artificial dermis (Integra): results with 39 grafts. *British journal of plastic surgery* **2001,** *54* (8), 659-64.
8. Norouzi, M.; Boroujeni, S. M.; Omidvarkordshouli, N.; Soleimani, M., Advances in skin regeneration: application of electrospun scaffolds. *Adv Healthc Mater* **2015,** *4* (8), 1114-33.
9. Hou, Q.; Grijpma, D. W.; Feijen, J., Porous polymeric structures for tissue engineering prepared by a coagulation, compression moulding and salt leaching technique. *Biomaterials* **2003,** *24* (11), 1937-47.
10. (a) Sun, G.; Zhang, X.; Shen, Y. I.; Sebastian, R.; Dickinson, L. E.; Fox-Talbot, K.; Reinblatt, M.; Steenbergen, C.; Harmon, J. W.; Gerecht, S., Dextran hydrogel scaffolds enhance angiogenic responses and promote complete skin regeneration during burn wound healing. *Proc Natl Acad Sci U S A* **2011,** *108* (52), 20976-81; (b) Jaiswal, M.; Gupta, A.; Agrawal, A. K.; Jassal, M.; Dinda, A. K.; Koul, V., Bi-layer composite dressing of gelatin nanofibrous mat and poly vinyl alcohol hydrogel for drug delivery and wound healing application: in-vitro and in-vivo studies. *Journal of biomedical nanotechnology* **2013,** *9* (9), 1495-508.
11. Hong, Y.; Chen, X.; Jing, X.; Fan, H.; Gu, Z.; Zhang, X., Fabrication and Drug Delivery of Ultrathin Mesoporous Bioactive Glass Hollow Fibers. *Advanced Functional Materials* **2010,** *20* (9), 1503-1510.
12. Cao, H.; Chen, M. M.; Liu, Y.; Liu, Y. Y.; Huang, Y. Q.; Wang, J. H.; Chen, J. D.; Zhang, Q. Q., Fish collagen-based scaffold containing PLGA microspheres for controlled growth factor delivery in skin tissue engineering. *Colloids and surfaces. B, Biointerfaces* **2015,** *136*, 1098-106.
13. Chaudhari, A. A.; Vig, K.; Baganizi, D. R.; Sahu, R.; Dixit, S.; Dennis, V.; Singh, S. R.; Pillai, S. R., Future Prospects for Scaffolding Methods and Biomaterials in Skin Tissue Engineering: A Review. *International Journal of Molecular Sciences* **2016,** *17* (12), 1974.
14. Borges, J.; Mano, J. F., Molecular Interactions Driving the Layer-by-Layer Assembly of Multilayers. *Chemical Reviews* **2014,** *114* (18), 8883-8942.
15. (a) Costa, R. R.; Mano, J. F., Polyelectrolyte multilayered assemblies in biomedical technologies. *Chemical Society Reviews* **2014,** *43* (10), 3453-3479; (b) Richardson, J. J.; Cui, J.; Björnmalm, M.; Braunger, J. A.; Ejima, H.; Caruso, F., Innovation in Layer-by-Layer Assembly. *Chemical Reviews* **2016,** *116* (23), 14828-14867.

16. Guthrie, K. M.; Agarwal, A.; Teixeira, L. B. C.; Dubielzig, R. R.; Abbott, N. L.; Murphy, C. J.; Singh, H.; McAnulty, J. F.; Schurr, M. J., Integration of silver nanoparticle-impregnated polyelectrolyte multilayers into murine splinted cutaneous wound beds. *Journal of burn care & research : official publication of the American Burn Association* **2013,** *34* (6), e359-e367.
17. Picart, C.; Caruso, F.; Voegel, J. C.; Decher, G., *Layer-by-Layer Films for Biomedical Applications*. Wiley: 2014.
18. Correia, C. R.; Pirraco, R. P.; Cerqueira, M. T.; Marques, A. P.; Reis, R. L.; Mano, J. F., Semipermeable Capsules Wrapping a Multifunctional and Self-regulated Co-culture Microenvironment for Osteogenic Differentiation. *Scientific Reports* **2016,** *6*, 21883.
19. Kulygin, O.; Price, A. D.; Chong, S. F.; Stadler, B.; Zelikin, A. N.; Caruso, F., Subcompartmentalized polymer hydrogel capsules with selectively degradable carriers and subunits. *Small* **2010,** *6* (14), 1558-64.
20. Silva, J. M.; Duarte, A. R. C.; Custódio, C. A.; Sher, P.; Neto, A. I.; Pinho, A. C. M.; Fonseca, J.; Reis, R. L.; Mano, J. F., Nanostructured Hollow Tubes Based on Chitosan and Alginate Multilayers. *Advanced healthcare materials* **2014,** *3* (3), 433-440.
21. (a) Caridade, S. G.; Monge, C.; Gilde, F.; Boudou, T.; Mano, J. F.; Picart, C., Free-standing polyelectrolyte membranes made of chitosan and alginate. *Biomacromolecules* **2013,** *14* (5), 1653-1660; (b) Silva, J. M.; Duarte, A. R.; Caridade, S. G.; Picart, C.; Reis, R. L.; Mano, J. F., Tailored Freestanding Multilayered Membranes Based on Chitosan and Alginate. *Biomacromolecules* **2014,** *15* (10), 3817-3826.
22. Mamedov, A. A.; Kotov, N. A., Free-Standing Layer-by-Layer Assembled Films of Magnetite Nanoparticles. *Langmuir* **2000,** *16* (13), 5530-5533.
23. Picart, C.; Elkaim, R.; Richert, L.; Audoin, F.; Arntz, Y.; Da Silva Cardoso, M.; Schaaf, P.; Voegel, J. C.; Frisch, B., Primary Cell Adhesion on RGD-Functionalized and Covalently Crosslinked Thin Polyelectrolyte Multilayer Films. *Advanced Functional Materials* **2005,** *15* (1), 83-94.
24. Salloum, D. S.; Olenych, S. G.; Keller, T. C.; Schlenoff, J. B., Vascular smooth muscle cells on polyelectrolyte multilayers: hydrophobicity-directed adhesion and growth. *Biomacromolecules* **2005,** *6* (1), 161-7.
25. Sousa, M. P.; Caridade, S. G.; Mano, J. F., Control of Cell Alignment and Morphology by Redesigning ECM-Mimetic Nanotopography on Multilayer Membranes. *Advanced Healthcare Materials* **2017,** *6* (15), 1601462.
26. (a) Chrzanowski, W.; Khademhosseini, A., Biologically inspired 'smart' materials. *Adv Drug Deliv Rev* **2013,** *65* (4), 403-4; (b) Huang, R.; Li, W. Z.; Lv, X. X.; Lei, Z. J.; Bian, Y. Q.; Deng, H. B.; Wang, H. J.; Li, J. Q.; Li, X. Y., Biomimetic LBL structured nanofibrous matrices assembled by chitosan/collagen for promoting wound healing. *Biomaterials* **2015,** *53*, 58-75.
27. Flammang, P.; Santos, R., Biological adhesives: from biology to biomimetics. *Interface Focus* **2015,** *5* (1), 20140086.
28. Lee, H.; Lee, B. P.; Messersmith, P. B., A reversible wet/dry adhesive inspired by mussels and geckos. *Nature* **2007,** *448*, 338.
29. Lee, B. P.; Messersmith, P. B.; Israelachvili, J. N.; Waite, J. H., Mussel-Inspired Adhesives and Coatings. *Annual review of materials research* **2011,** *41*, 99-132.
30. Ryu, J. H.; Lee, Y.; Kong, W. H.; Kim, T. G.; Park, T. G.; Lee, H., Catechol-functionalized chitosan/pluronic hydrogels for tissue adhesives and hemostatic materials. *Biomacromolecules* **2011,** *12* (7), 2653-9.
31. Hong, S.; Yang, K.; Kang, B.; Lee, C.; Song, I. T.; Byun, E.; Park, K. I.; Cho, S.-W.; Lee, H., Hyaluronic Acid Catechol: A Biopolymer Exhibiting a pH-Dependent Adhesive or Cohesive Property for Human Neural Stem Cell Engineering. *Advanced Functional Materials* **2013,** *23* (14), 1774-1780.
32. Neto, A. I.; Vasconcelos, N. L.; Oliveira, S. M.; Ruiz-Molina, D.; Mano, J. F., High-Throughput Topographic, Mechanical, and Biological Screening of Multilayer Films Containing Mussel-Inspired Biopolymers. *Advanced Functional Materials* **2016,** *26* (16), 2745-2755.
33. Mano, J. F., Viscoelastic properties of chitosan with different hydration degrees as studied by dynamic mechanical analysis. *Macromol Biosci* **2008,** *8* (1), 69-76.
34. ASTM, Standard test method for: Apparent Shear Strenght of Single-Lap-Joint Adhesively Bonded Metal Specimens by Tension Loading (Metal - to - Metal). 1999.
35. Miguel, S. P.; Ribeiro, M. P.; Brancal, H.; Coutinho, P.; Correia, I. J., Thermoresponsive chitosan–agarose hydrogel for skin regeneration. *Carbohydrate polymers* **2014,** *111*, 366-373.
36. Croisier, F.; Atanasova, G.; Poumay, Y.; Jérôme, C., Polysaccharide-Coated PCL Nanofibers for Wound Dressing Applications. *Advanced Healthcare Materials* **2014,** *3* (12), 2032-2039.

37. (a) Alves, N. M.; Picart, C.; Mano, J. F., Self Assembling and Crosslinking of Polyelectrolyte Multilayer Films of Chitosan and Alginate Studied by QCM and IR Spectroscopy *Macromolecular bioscience* **2009,** *9* (8), 776-785; (b) Dunér, G.; Thormann, E.; Dėdinaitė, A., Quartz Crystal Microbalance with Dissipation (QCM-D) studies of the viscoelastic response from a continuously growing grafted polyelectrolyte layer. *Journal of Colloid and Interface Science* **2013,** *408*, 229-234.
38. Sedó, J.; Saiz-Poseu, J.; Busqué, F.; Ruiz-Molina, D., Catechol-Based Biomimetic Functional Materials. *Advanced Materials* **2013,** *25* (5), 653-701.
39. Iqbal, Z.; Lai, E. P. C.; Avis, T. J., Antimicrobial effect of polydopamine coating on Escherichia coli. *Journal of Materials Chemistry* **2012,** *22* (40), 21608-21612.
40. Silva, R. M.; Silva, G. A.; Coutinho, O. P.; Mano, J. F.; Reis, R. L., Preparation and characterisation in simulated body conditions of glutaraldehyde crosslinked chitosan membranes. *Journal of Materials Science-Materials in Medicine* **2004,** *15* (10), 1105-1112.
41. Donot, F.; Fontana, A.; Baccou, J. C.; Schorr-Galindo, S., Microbial exopolysaccharides: main examples of synthesis, excretion, genetics and extraction. *Carbohydrate Polymers* **2012,** *87*, 951.
42. Neto, A. I.; Cibrão, A.; Correia, C. R.; Carvalho, R. R.; Luz, G.; Ferrer, G. G.; Botelho, G.; Picart, C.; Alves, N. M.; Mano, J. F., Nanostructured polymeric coatings based on chitosan and dopamine-modified hyaluronic acid for biomedical applications. *Small* **2014,** *10* (12), 2459-2469.
43. Neto, A. I.; Cibrão, A. C.; Correia, C. R.; Carvalho, R. R.; Luz, G. M.; Ferrer, G. G.; Botelho, G.; Picart, C.; Alves, N. M.; Mano, J. F., Nanostructured Polymeric Coatings Based on Chitosan and Dopamine-Modified Hyaluronic Acid for Biomedical Applications. *Small* **2014,** *10* (12), 2459-2469.
44. Zhong, S. P.; Campoccia, D.; Doherty, P. J.; Williams, R. L.; Benedetti, L.; Williams, D. F., Biodegradation of hyaluronic acid derivatives by hyaluronidase. *Biomaterials* **1994,** *15* (5), 359-365.
45. Fischer, P.; Laschewsky, A.; Wischerhoff, E.; Arys, X.; Jonas, A.; Legras, R., Polyelectrolytes bearing azobenzenes for the functionalization of multilayers. *Macromolecular Symposia* **1999,** *137* (1), 1-24.
46. Slavin, S.; Soeriyadi, A. H.; Voorhaar, L.; Whittaker, M. R.; Becer, C. R.; Boyer, C.; Davis, T. P.; Haddleton, D. M., Adsorption behaviour of sulfur containing polymers to gold surfaces using QCM-D. *Soft Matter* **2012,** *8* (1), 118-128.
47. Hargittai, I.; Hargittai, M., Molecular structure of hyaluronan: an introduction. *Structural Chemistry* **2008,** *19* (5), 697-717.
48. (a) Chang, H.-I.; Wang, Y., Cell Responses to Surface and Architecture of Tissue Engineering Scaffolds. In *Regenerative Medicine and Tissue Engineering - Cells and Biomaterials*, Eberli, D., Ed. InTech: Rijeka, 2011; p Ch. 27; (b) Silva, S. S.; Popa, E. G.; Gomes, M. E.; Cerqueira, M.; Marques, A. P.; Caridade, S. G.; Teixeira, P.; Sousa, C.; Mano, J. F.; Reis, R. L., An investigation of the potential application of chitosan/aloe-based membranes for regenerative medicine. *Acta Biomaterialia* **2013,** *9* (6), 6790-6797.
49. (a) Hajicharalambous, C. S.; Lichter, J.; Hix, W. T.; Swierczewska, M.; Rubner, M. F.; Rajagopalan, P., Nano- and sub-micron porous polyelectrolyte multilayer assemblies: biomimetic surfaces for human corneal epithelial cells. *Biomaterials* **2009,** *30* (23-24), 4029-36; (b) Rnjak-Kovacina, J.; Wise, S. G.; Li, Z.; Maitz, P. K. M.; Young, C. J.; Wang, Y.; Weiss, A. S., Tailoring the porosity and pore size of electrospun synthetic human elastin scaffolds for dermal tissue engineering. *Biomaterials* **2011,** *32* (28), 6729-6736.
50. Loh, Q. L.; Choong, C., Three-Dimensional Scaffolds for Tissue Engineering Applications: Role of Porosity and Pore Size. *Tissue Engineering. Part B, Reviews* **2013,** *19* (6), 485-502.
51. Sander, E. A.; Lynch, K. A.; Boyce, S. T., Development of the mechanical properties of engineered skin substitutes after grafting to full-thickness wounds. *J Biomech Eng* **2014,** *136* (5), 051008.
52. Yang, W.; Sherman, V. R.; Gludovatz, B.; Schaible, E.; Stewart, P.; Ritchie, R. O.; Meyers, M. A., On the tear resistance of skin. *Nature Communications* **2015,** *6*, 6649.
53. Park, H.-J.; Jin, Y.; Shin, J.; Yang, K.; Lee, C.; Yang, H. S.; Cho, S.-W., Catechol-Functionalized Hyaluronic Acid Hydrogels Enhance Angiogenesis and Osteogenesis of Human Adipose-Derived Stem Cells in Critical Tissue Defects. *Biomacromolecules* **2016,** *17* (6), 1939-1948.
54. Carvalho, A. L.; Vale, A. C.; Sousa, M. P.; Barbosa, A. M.; Torrado, E.; Mano, J. F.; Alves, N. M., Antibacterial bioadhesive layer-by-layer coatings for orthopedic applications. *Journal of Materials Chemistry B* **2016,** *4* (32), 5385-5393.
55. Dhand, C.; Harini, S.; Venkatesh, M.; Dwivedi, N.; Ng, A.; Liu, S.; Verma, N. K.; Ramakrishna, S.; Beuerman, R. W.; Loh, X. J.; Lakshminarayanan, R., Multifunctional Polyphenols- and Catecholamines-

Based Self-Defensive Films for Health Care Applications. *ACS Applied Materials & Interfaces* **2016,** *8* (2), 1220-1232.
56. Min, B. M.; Lee, G.; Kim, S. H.; Nam, Y. S.; Lee, T. S.; Park, W. H., Electrospinning of silk fibroin nanofibers and its effect on the adhesion and spreading of normal human keratinocytes and fibroblasts *in vitro*. *Biomaterials* **2004,** *25* (7-8), 1289-97.
57. Silva, J. M.; Georgi, N.; Costa, R.; Sher, P.; Reis, R. L.; Van Blitterswijk, C. A.; Karperien, M.; Mano, J. F., Nanostructured 3D Constructs Based on Chitosan and Chondroitin Sulphate Multilayers for Cartilage Tissue Engineering. *PLOS ONE* **2013,** *8* (2), e55451.
58. Ren, K.; Crouzier, T.; Roy, C.; Picart, C., Polyelectrolyte multilayer films of controlled stiffness modulate myoblast cells differentiation. *Advanced functional materials* **2008,** *18* (9), 1378-1389.
59. Yang, X.; Zhu, L.; Tada, S.; Zhou, D.; Kitajima, T.; Isoshima, T.; Yoshida, Y.; Nakamura, M.; Yan, W.; Ito, Y., Mussel-inspired human gelatin nanocoating for creating biologically adhesive surfaces. *International Journal of Nanomedicine* **2014,** *9*, 2753-2765.
60. Han, L.; Lu, X.; Liu, K.; Wang, K.; Fang, L.; Weng, L.-T.; Zhang, H.; Tang, Y.; Ren, F.; Zhao, C.; Sun, G.; Liang, R.; Li, Z., Mussel-Inspired Adhesive and Tough Hydrogel Based on Nanoclay Confined Dopamine Polymerization. *ACS Nano* **2017,** *11* (3), 2561-2574.
61. Reinke, J. M.; Sorg, H., Wound repair and regeneration. *European surgical research. Europaische chirurgische Forschung. Recherches chirurgicales europeennes* **2012,** *49* (1), 35-43.
62. Alves, N. M.; Gómez Ribelles, J. L.; Gómez Tejedor, J. A.; Mano, J. F., Viscoelastic behaviour of polymethyl methacrylate networks with different crosslinking degrees. *Macromolecules* **2004,** (37), 3735-3744.
63. Sima, F.; Mutlu, E. C.; Eroglu, M. S.; Sima, L. E.; Serban, N.; Ristoscu, C.; Petrescu, S. M.; Oner, E. T.; Mihailescu, I. N., Levan Nanostructured Thin Films by MAPLE Assembling. *Biomacromolecules* **2011,** *12* (6), 2251-2256.
64. Costa, R. R.; Neto, A. I.; Calgeris, I.; Correia, C. R.; Pinho, A. C. M. d.; Fonseca, J. C.; Öner, E. T.; Mano, J. F., Adhesive nanostructured multilayer films using a bacterial exopolysaccharide for biomedical applications. *Journal of Materials Chemistry B* **2013,** *1*, 2367-2374.

IX. Dopamine-containing self-adhesive membranes as a delivery device of therapeutic stem cells for cartilage repair*

Abstract

Traumatic and degenerative cartilage damage cause serious clinical problems in millions of people, characterized by the progressive cartilage degradation, pain and loss of mobility. Due to the lack of vascularization and perichondrium, articular cartilage has a low capacity for spontaneous repair. Superficial defects are difficult to be treated with biomaterials, conceding space for cell therapies starting to be introduced in clinics. However, targeting cells to a virtually non-adhesive cartilage surface is a challenging task. In this work, we propose a biomaterial able to adhere and transfer cells directly to a cartilage surface. For that, self-adhesive freestanding multilayer membranes (FMM) consisting of chitosan, alginate, and hyaluronic acid were produced using a layer-by-layer (LbL) technique. Bioinspired adhesion was addressed through the modification of HA backbone with catechol groups of dopamine and their incorporation into the membranes. FMM with dissimilar nanotopographical structure were used as delivery devices for therapeutic cells (adipose derived stromal cells, ASCs). Fluorescence microscopy revealed that cells formed clusters on the membrane, but that the presence of nanotopographical features increased the spreading of ASCs. After application on human osteoarthritic cartilage discs, cells detached from the membrane and spread on the defects of the cartilage surface. Overall, the results showed that adhesive and functionalized LbL-engineered FMM membranes are promising materials for tissue engineering and reconstruction of superficial cartilage damage.

Keywords: layer-by-layer; catechol; freestanding membrane; adhesive; ASCs carrier; adhesive; migration; alignment; superficial cartilage damage; osteoarthritis

---

[*] This Chapter is based on the following publication: Sousa M. P.; Fürsatz M.; Lee H.; Mano J. F.; Nürnberger S., Dopamine-containing self-adhesive membranes as a delivery device of therapeutic stem cells for cartilage repair, **2019** (in submission process).

1. Introduction

Cartilage defects affect billions of people around the world generating cases of pain and functional limitations, restricting patients in their daily life. Damaged cartilage can be a result of trauma, age-related degeneration, malalignment of the joint . Already minor lesions can initiate degradation processes that bring dramatic consequences for the structure and function of articular cartilage or even chronic diseases such as osteoarthritis (OA) [1]. Superficial cartilage is the outer area of the tissue, composed of flattened ellipsoid cells parallel to the joint, covered by a thin film of synovial fluid [2]. When healthy, it presents a large content of water (~80%) provided by the high activity of chondrocytes in synthetizing collagen and the lower concentration of proteoglycans. Disruption of this zone makes cartilage vulnerable for degradation processes, since chondrocytes around the defect frequently react on the damage with further degradation and since deeper regions of cartilage, deprived from its superficial sealing and gliding layer, are exposed to the synovial fluid and shear forces, contributing for the development of OA [2]. This results from the fact that chondrocytes cannot escape themselves the dense matrix to refill sites of tissue loss and articular cartilage lacks on vascularization and perichondrium, as potential sources of regenerative cells [1a, 3]. Autologous chondrocyte transplantation (ACT) has been used as a strategy for deep traumatic cartilage repair, through the implantation of autologous patient's chondrocytes, obtained via cartilage biopsies and then injected into the cartilage area after expanded the cells *in vitro.* [4]. Besides this strategy has been already applied in clinics, some concerning limitations still exist: different studies concluded that chondrocytes when expanded in 2D systems can de-differentiate, stopping to produce indispensable matrix proteins like collagen type II, aggrecan and others or when they did not de-differentiate, the cells just presented short-term viability [5]. Furthermore, additional donor site morbidity can be a negative consequence of taking biopsies from healthy cartilage of the patient [5a]. While a lot of research has been applied to regenerate deep traumatic and usually locally restricted osteochondral defects, there are increasing number of investigations targeting cell therapy to treat superficial cartilage defects and early stages of OA.

Therefore, different strategies have been employed to treat cartilage defects, from simple pain-relieving drugs or techniques [6] to sophisticated tissue engineering and cell therapy approaches [6b, 7]. Different drugs [8] and hyaluronic acid (HA) injections [9] have been employed to reduce pain and control inflammation; their limited efficiency and fail to prevent damaging progression prompt the searching for new treatments. Cell therapies have been gaining increasingly importance to repair cartilage defect: adipose-derived stromal/stem cells (ASCs) have been investigated to treat cartilage damaging [10]; they are undifferentiated cells with the ability to self-renew and to be differentiate towards specific and multiple cell types including chondrocytes, under appropriate culture conditions [11]. Moreover, ASCs are generally easy to obtain by lipoaspiration of the fat tissue, involving minimal donor site morbidity with highly proliferative ability [12]. The ability of ASCs to form a cartilage-like matrix was reported by different authors [13]; they concluded that ASCs may hold greater potential for long-term cartilage function than differentiated chondrocytes. Phenotypically, ASCs are positive for markers as CD34+ and CD31−/CD45− but not for HLA-class II cell surface receptors, usually associated with transplant failure;

Lin *et. al.* [14] reported that the lack of HLA-class II antigen on the ASCs surface could be responsible for the no evidence of host rejection after transplanting ASCs allogenically or even xenogenically. Nowadays, ASCs are already used in clinics to treat osteoarthritic defects through intra-articular injections [15]. Toghraie *et. al.* [13b] investigated the possibility of restoring the matrix of arthritic knee joints in adult white New Zealand rabbits through the intra-articular injection of scaffold-free ASCs; they found significant differences comparing the quality of cartilage between ASCs-injected group and the control group 20 weeks after surgery. It seemed a valid approach for treating cartilage defects. In turn, ter Huurne *et. al.* [16] studied the effect of intra-articular injection of ASCs on synovial lining thickness in osteoarthritic C57BL/6 mice; they could inhibit synovial thickening, avoiding the destruction of the cartilage. Parallel to these results, Vilar *et. al.* [13c] suggested that injected ASCs may not integrate well with the OA-derived hip joint canine lameness. The author stated that even ASCs injections are an efficient method to treat cartilage defects for short time, the load-bearing improvements of osteoarthritic cartilage after this treatment can be progressively decreased till the starting point, after 3 months.

Nowadays, the treatment of early stages of OA and superficial cartilage defects has been based in the resurfacing of rough cartilage superficial layer with cells. Alternative strategies have been recently proposed to overcome the limitations of scaffold-free ASCs injections to repair superficial cartilage defects [17]: we hypothesize that the use of biomaterials can simplify the cellular delivery and consequently their adhesion, proliferation and differentiation. Cell carriers have been developed to provide a structured vehicle for delivery cells to the defect tissue [18]. In this field, synthetic polymers have been gradually replaced by natural ones, since polysaccharides are presented in native cartilage extracellular matrix (ECM) [19]. Particularly, positive results for the treatment of mild to intermediate OA were already obtained using viscosupplementation injections of polysaccharides with higher water retention behaviour as HA, improving the joint lubrification. Nevertheless, recent procedures failed to suggest this as a therapeutic modality, with inconsistent results that could be a consequence of the possibility of HA really vary in concentration, molecular weight, molecular organization, reticulation and protocol of injection [20].

However, problems related with the fixation and the mechanical loading and shear forces provided by the synovial environment [21]. Glue- and adhesive-based materials have been nowadays proposed to overcome these issues [22]. For instance, Kim *et. al.* [22b] used a fibrin glue to implant stem cells in patients with osteoarthritic knees; the authors found improved outcome with the International Cartilage Repair Society (ICRS) score when using cell-containing fibrin glue, suggesting a long-term stability. However, some limitations were also associated with this strategy: the weak mechanical properties, the shrinkage of the hydrogel, and the early degradation of fibrin must be solved [22b].

Therefore, in this investigation we suggest the use of adhesive based membranes to transport ASCs to osteoarthritic or superficial cartilage defects. To confer adhesive properties to the membrane, HA was modified with dopamine (DN), an analogue of the non-cationic amino acid 3,4-dihydroxy-L-alanine (DOPA), that is usually presented in high amounts in mussel adhesive proteins. The catechol component of DOPA is the main responsible for the strong adhesion of mussels to rocks, even in a wet environment [23]. Catechol chemistry has been intensively investigated in the last decades, exploiting the adhesion to different wet organic and inorganic substrates [24]. For that, different materials have been modified with catechols; for instance, Scognamiglioa *et. al.* [25] modified alginates with DOPA, at different substitution degrees, using these conjugates to produce membranes with enhanced adhesive and biocompatible properties. Lee *et. al.* [26] functionalized chitosan with catechols to use as a coating to hypodermic needles, helping to prevent bleeding after tissue puncture, by undergoing a solid-to-gel phase transition in situ to seal punctured tissues.

In the presented investigation, HA modified with DN (HA-DN) was combined with other polysaccharides, chitosan (CHT) and alginate (ALG) and the layer-by-layer (LbL) technology was employed to develop freestanding multilayer membranes (FMM). LbL assembly allows to produce nanostructured organized multilayered films, using a wide range of materials [27]. This versatile technology is based on the alternate and sequential deposition of materials, usually based on electrostatic interactions, that is self-organized in a specific substrate surface [27]. Particularly, LbL technique has been gaining interest as a hierarchal strategy to regenerate cartilage, in which smaller components are assembled in 3D constructs, mimicking the hierarchical organization of native cartilage [28]. Silva *et. al.* [29] combined LbL and template leaching to produce nanostructured 3-dimensional constructs for cartilage tissue engineering; they found that human MSCs could adhere and proliferate and differentiate in chondrocytes upon culture in chondrogenic differentiation medium. Moreover, with this bottom-up technology, it is possible to create biomaterials with unique properties that invoke the cartilaginous ECM characteristics, such as topography [28].

Topographical features on the surface of biomaterials are known to control cellular functions, such as adhesion, morphology or differentiation. The effect of introducing spatial topographical cues in the LbL membrane was also investigated, to confirm if it can potentially support the progress of ASCs integration. Our approach combined the advantages of using natural materials, with the versatile LbL methodology and the abilities to tailor the biochemical, mechanical, topographical and adhesive properties of the resulting product. Moreover, we emphasized the importance of having a very thin material that mainly serves as a temporary device to deliver ASCs capable of treating damage articular cartilage; even though, not less important as it is easy-to-handle, adhesive to the cartilage and can act as a gate between the synovial environment and the treatment of damaged cartilage.

2. Materials and Methods

2.1. Materials

Chitosan (CHT, Sigma, St. Louis, Missouri, United States of America (USA)) with a molecular weight in the range of 190–310 kDa, a N-deacetylation degree ranging from 75-85% and a viscosity of 0.2-0.8 Pa.s was purified following a standard procedure reported elsewhere [30]. Hyaluronic acid (HA) with a low molecular weight between 80-100 kDa was purchased as hyaluronic acid sodium salt was supplied by Carbosynth Limited (Compton, Berkshire, United Kingdom). Sodium alginate (ALG) with a viscosity of 0.005-0.04 Pa.s obtained from brown algae, and dopamine hydrochloride (DN) and N-(3-

Dimethylaminopropyl)-N′-ethylcarbodiimide hydrochloride (EDC) (purum, ≥ 98.0% (AT)) were purchased from Sigma and used as received.

2.2. Synthesis of HA-DN

HA-DN conjugates were synthesized using EDC as an activation agent of the carboxyl groups on HA chains, based on an already reported procedure [31]. To avoid oxidation, the conjugated material was stored at -20 °C and protected from the light until using.

2.2.1. Ultraviolet-visible (UV) Spectrophotometry.

The presence of dopamine in the conjugate was determined using a UV-vis spectrophotometer (JascoV560 PC, Easton, Maryland, USA) and 1 cm quartz cells. Polymer solutions of 0.5 mg. mL^{-1} in 0.15 M sodium chloride (NaCl, LabChem Inc, Zelienople, Pennsylvania, USA) were prepared for the UV-vis analysis.

2.2.2. ^{1}H-Nuclear Magnetic Resonance (NMR).

^{1}H-NMR analyses were performed dissolving overnight the HA, DN and the conjugated HA-DN in deuterated water (D_2O, Cambridge Isotope Laboratories, Inc.) at a concentration of 1 mg. mL^{-1}. The spectra were obtained using a spectrometer BRUKER BioSpin - 300 MHz, at 298 K and 300 MHz for ^{1}H.

2.3. Freestanding Multilayer Membranes Production and Characterization

2.3.1. Production of the freestanding multilayer membranes

The production of the multilayer membranes was achieved using the LbL methodology with the help of a home-made dipping robot, based on a methodology previously reported [32]. Polypropylene (PP) and patterned polycarbonate (PC) substrates were immersed in alternated polyelectrolyte solutions with a rinsing solution deposition between each polyelectrolyte. Patterned PC substrates was obtained from optical discs [33]. The rinsing solution used was a 0.15 M NaCl (pH = 5.5) and the polymer solutions were used at a concentration of 2 mg. mL^{-1} for CHT and ALG and 0.5 mg. mL^{-1} for the HA and HA-DN. Deposition time of the polyelectrolytes was 6 min and 4 min for the rinsing solution.

After 100 tetralayers (TL), multilayer membranes containing HA, CHT and ALG (HA film) and multilayer membranes containing HA-DN, CHT and ALG (HA-DN film) were detached from the underlying PP and PC substrates, with the help of a tweezer. Four types of freestanding multilayer membranes (FMM) were obtained: non-patterned HA and HA-DN membranes (detached from the PP substrate) and patterned (PAT) HA and HA-DN (detached from the PC substrates).

2.3.2. Scanning Electron Microscope (SEM)

The surface morphology of the samples was observed using a Hitachi S4100 (Tokyo, Japan) SEM. All samples were coated with a conductive layer of sputtered gold. The SEM micrographs were taken using an accelerating voltage of 15 kV and at different magnifications. The cross-section of cut membranes was also observed by SEM.

2.3.3. Degradation assays

The FMM were placed in PBS, at pH=7.4 (control), and in an enzymatic solution composed by 0.33 $mg.ml^{-1}$ of hyaluronidase in PBS with NaN_3, at pH=7.11; all FMM were put in a shaking water bath at 37 °C. The medium was replaced every 3 days and at predetermined time points (1, 3, 7, 14 and 30 days), the membranes were removed from the solutions and washed with distilled water to remove the excess of salts. Then, the membranes were dried at constant temperature and weighted. The percentage of weight loss (WL) of the membranes for the different conditions was determined following Equation 1, with W_i being the initial dry weight of the membrane and W_f being the weight of the dry membrane after each predetermined time point. Thus, the percentage of weight retaining (WR) was calculated using Equation 2, with the values obtained in Equation 1.

$$WL(\%) = \frac{w_i - w_f}{w_i} \times 100 \qquad \text{Equation IX.1}$$

$$WR(\%) = 100 - WL \qquad \text{Equation IX.2}$$

2.3.4. Mechanical tests: adhesive property

A simple visual test was used to determine the adhesive potential of the HA-DN membranes. Therefore, hydrated HA-DN membranes were cut in circles with a diameter of 8 mm and put in contact with human cartilage discs prepared with the same diameter. Then the system was incubated in cell medium at 37°C during at least 1 hour. An aluminium-pin was placed on the top of the membrane and the all system was again incubated for 30 minutes. The adhesive potential of the membranes was observed by the ability of handling all the system together, just holding one of the sides. This test was recorded using a photographic camera.

2.4. *In vitro* biological assays

Prior to cell seeding, the membranes were disinfected and sterilized by UV exposure for 20 minutes, followed by 1.5 hours immersion in ethanol in the end, the membranes were washed with sterile DPBS and immersed in a 10% FBS solution, during overnight (right before the seeding). In the day after, the membranes were washed with DPBS and maintained there until using. The well culture plates were also previously coated with poly-HEMA (poly 2-hydroxyethyl methacrylate, Sigma, St. Louis, Missouri, USA) to make low adhesive the bottom of the wells.

Telomerase Reverse Transcriptase immortalized Adipose-derived Stromal/Stem Cells (ASC/TERT1; Evercyte, Vienna, Austria) previously labelled with a red fluorescent protein (RFP) were used for all experiments. Cells were thawed and propagated in EGM™-2 medium from (Lonza, Basel, Switzerland) in T75 cell culture flasks at 37°C, 5% CO_2 and 95% air humidity and spitted at 60-70% of confluence. When reaching the required cell number for the experiments, they were transferred to the FMM membranes.

Cell adhesion, viability and proliferation. Cell adhesion, viability and proliferation was determined qualitatively, by imaging live cells after 5 days of culture, and quantitatively, by measuring the number of cells on the membranes after 1 and 3 days.

Briefly, the sterile membranes were cut in circles of 8 mm diameter (A superficial=0.5 cm^2) using a biopsy punch (Kai Europe, GMBH Solingen, Germany) and put inside each well of the poly-HEMA coated 48-well culture plates. A cell suspension of 100µl containing 2.5 x 10^4 cells was dropped gently and right above the membrane surface. The cells were incubated at 37°C for 4 hours. Live images of the RFP transfected ASC/TERT1 were taken for each condition, using a brightfield and fluorescence microscope (Olympus BX41). After that, 200µl of cell growth medium was added to each well and the cells were maintained in culture at 37°C for 5 days while the medium was changed every 2-3days. Live images were also taken at 5 days. Afterwards, samples were prepared for SEM imaging and fixed with 4% formalin (Sigma, St, Louis, Missouri, USA) for 1 hour and then washed with DPBS three times. Then the samples were dehydrated by an increasing series of ethanol (EtOH) and chemically dried with hexamethyldisilazane (HMDS, Sigma, St. Louis, Missouri, USA). When HDMS was totally evaporated, the samples were coated with gold and examined on a SEM (Zeiss MA 10) in the secondary electron mode.

The same cultivation procedure was used for quantitative assays, but with membrane samples with a larger area, A= 4 cm^2. The sterile membranes were placed in poly-HEMA coated 12-well culture plates and the same number of cells.mm^{-2} (5 x 10^4 cells.cm^{-2}) was dropped right above each membrane. After 1 and 5 days, three samples per condition were taken and the adherent cells detached with trypsin and counted using an automatic cell counter equipment (CASY1 cell counter, Schärfe Systems).

Morphometric cell parameters. Cells area, perimeter, circularity and elongation factor (EF) were parameters evaluated using the software Image J® (National Institutes of Health, Bethesda, MD, USA) and were determined after 5 days of culture. The cell EF corresponds to the longest cell axis divided by the maximal length perpendicular to this long axis [34]. This value serves to describe the elongation of the cells or their morphology in a group of aligned cells. whereas a higher EF means a more elongated cell morphology. The circularity is defined as the ratio of the area of the object to the area of a circle with the same perimeter as the object, serving as a measure of their roundness. A value of 1 indicated a perfect circle, whereas a value approaching zero indicates an increasingly longer and more protruded. The alignment was determined using information obtained by SEM images, from cells adhered on the membranes and the nanopatterning; the patterning orientation was rotated to be equal to 0°. Additionally, also the cells angle distribution was determined using the Image J® software analysing 5 images per condition, relatively to the day 3 of culture.

2.4.1. *In situ* biological assays

Preparation of human osteoarthritic cartilage discs. Human hip joints were used as the source for cartilage plug discs and were harvested with written consent of the patients and approval of the local ethic committee. Just hip joint samples with visible signs of damaging were considered for this study; therefore, parameters like colour and roughness were considered. Firstly, the cartilage areas of interest were cut from the hip joint with a scalper and 8 mm chips were prepared biopsy punch. Subsequently the discs were kept in a sterile solution of DPBS containing 10% of antibiotics at 4°C and used in the day after.

Cultivation of RFP-ASC/TERT1 seeded membranes on OA cartilage discs. To test the application of the cell-seeded membranes to the damaged human cartilage plug, the cell adhesion and proliferation on the cartilage and also the cellular differentiation capability, membranes were firstly prepared following the same procedure as above: briefly, the sterile membranes were cut in circles of 8 mm put inside each well of sterile poly-HEMA coated 48-well culture plates (d = 11 mm). Two cell density groups were formed: cell suspensions of 100 µl each containing 2.5 x 10^4 cells and 1.5 x 10^5 cells was dropped gently and right above the membrane surface. The cells were incubated at 37°C for 4 hours. After that, 100 µl of cell growth medium was added to each well and the cells were maintained in culture at 37°C, overnight.

The day after, RFP-ASC/TERT1 seeded-membranes were directly applied to the damaged surface of the human cartilage discs, with the RFP-ASC/TERT1 side facing the cartilage surface. Then this system was transferred in one-piece to the poly-HEMA coated 48-well culture plates, upside down (membrane in contact with the bottom and the chip right above).

To observe the interactions between cell-seeded membranes and damaged cartilage discs, each well/ system was cultured in basal ASC differentiation medium [Dulbecco's Modified Eagle's Medium (DMEM) high glucose, Insulin-Transferrin-Sodium Selenite (ITS), Acid Ascorbic, Sodium Piruvate, L-proline, bovine serum albumin (BSA), penicillin/streptomycin, L-glutamine], supplemented with 100 mM of dexamethasone. The medium was changed every 2-3 days and the culture was maintained for 3 weeks. All the reagents were supplied by Sigma (United States of America).

In turn, to investigate the ASCs differentiation potential with these systems, each well/system was cultured in ASC basal medium, supplemented with differentiation factors: 100 mM of dexamethasone and low-dose (1 ng.ml^{-1}) of transforming growth factor- beta 3 (TGF-β3) and bone morphogenetic protein 6 (BMP-6). The medium was changed every 2 days and the culture was maintained for 5 weeks.

Live cell imaging of the interaction between RFP-ASC/TERT1 seeded membranes and the damaged cartilage chip. The interaction between RFP-ASC/TERT1 seeded membranes and the damaged cartilage chip was recorded after 3 days, 1 week and 2 weeks of culture. Briefly the systems were maintained inside the well plates and placed above the plate support of the confocal microscope. Then, we started from the bottom top the top of the system until had found the interface between the membrane and the discs where the cells were located. Live images were imaged using confocal microscopy.

Cross-section observation of the RFP-ASCs /TERT1 seeded membranes and the damaged cartilage chip. After 2 weeks of culture, 3 samples of each condition were fixed with paraformaldehyde 4% solution during overnight, under automatic agitation. The day after, the samples were washed with DPBS three times, transversally cut in two halves and placed in a glass slide with the cross section turned down. The cross-sections were imaged with confocal microscopy.

Histological sections preparation: Immunohistochemistry (Azan staining analysis). After 3 weeks of culture, the other 3 samples of each condition were fixed with formalin 4% solution during overnight, under automatic agitation. Next day, the samples were washed under flowing tap water for 1 hour, transferred into 50% EtOH for another hour under automatic agitation and then into 70% EtOH were they were kept until further processing. Briefly, after EtOH incubation series, the samples were embedded in paraffin and sectioned with 3-4 µm thickness with a rotatory microtome. Then the samples were exposed to a deparaffination process. To evaluate the impact of the ASCs-seeded membranes on the cell distribution along the structure of the cartilage, the sections were stained with Azan trichrome and visualized using a light microscope with a specific image analysis software. This staining permits to distinguish cells from the extracellular matrix (cartilage matrix and collagen in blue and the nuclei in red). Cartilage fragments without membrane were used as control.

Histological sections preparation: Immunohistochemistry (Collagen-type II staining analysis). To evaluate the chondrogenic potential of these cells when in contact with the damaged cartilage discs and incubated in a TGF-β3/BMP-6 supplemented medium, immunohistochemistry and histological analysis were done as described above. Sections were immunolabelled against collagen type II (Neomarkers, CA, USA). Subsequently, samples were visualized using a light microscope with a specific image analysis software. Cartilage fragments without membrane were used as control.

2.5. Statistical Analysis

All quantitative data was represented as average value ± standard deviation with at least 5 replicates for each test subject, unless specifically mentioned. For the different quantification assays, multiple comparison of more than 2 groups were made using one-way ANOVA followed by Bonferroni's multiple comparison test. Any exception to this procedure was referred on the appropriated section. Statistical significance of all tests was accepted from $p<0.05$ (*). All statistical analysis was performed using the software GraphPad Prism 6.0.

3. Results

In this work, DN containing freestanding multilayered membranes were produced using a LbL technology, based on the sequential and alternated assembly of natural-based polyelectrolytes. These materials were developed to act as a vehicle to delivery ASCs to treat damaged cartilage. Firstly, these membranes were characterized in terms of morphology, chemistry and degradation and then tested *in vitro* and *in situ* for application on cartilage repair.

3.1. Synthesis and characterization of the conjugate hyaluronic acid modified with dopamine (HA-DN)

HA is a component of the ECM and may be combined with other polyelectrolytes to produce biocompatible and biodegradable materials. To provide an adhesive character to this material, HA was conjugated with DN. UV- vis spectra of the HA and the conjugate HA-DN water-based solutions are presented in Figure S1A, at wavelengths from 200 nm to 400 nm. Enhanced absorption of UV light at 280 nm wavelength was observed for the HA-DN solution, demonstrating the successful incorporation of catechol groups. These results permitted to determine the degree of DN substitution. For that, the UV-vis spectroscopy standard spectra were obtained from solutions with different concentrations of free DN and are represented in the inset of Figure S1B, where it is possible to confirm the characteristic UV-excitation band of DN, centered at 280 nm. For DN concentrations less than 0.75 mM, the relation between DN concentration and absorbance followed a linear regime - Figure S1B. Using the measured absorbance for the HA-DN, obtained at 280 nm, and the linear growth equation obtained from the DN spectra (Figure S1B), the estimated degree of DN substitution in the conjugate is 17.6%. The ^{1}H-NMR spectrum of the non-modified HA is shown in Figure S1C and is consistent with the one found in literature, where the multiplets located at δ =2.12 ppm is associated with the protons of N-$COCH_3$ groups. The peak at δ =1.91 ppm is associated with the proton in the methylene of the HA backbone. Figure S1D shows the ^{1}H-NMR spectrum of DN; the multiplets centered at δ = 2.876 ppm and δ = 3.227 ppm that can be observed are associated with the protons of the aliphatic group, according to the literature [35]. The region between δ = 6.6 ppm and δ = 7.0 ppm corresponds to the protons in the orto and meta coupling position of the ring. Figure S1E corresponds to the ^{1}H-NMR spectrum of the HA-DN conjugated; as observed all the peaks presented in the individual compounds are presented in the spectrum of the conjugated, confirming the presence of DN in the HA-DN conjugate. The catechol content (mol%) in HA-DN was determined from the quotient between the integral area of the peaks between δ = 6.6 ppm and δ = 7.0 ppm, corresponding to the amount of H in the aromatic rings of grafted catechol moieties, and the integral area of the peak at δ = 1.91, representing the amount of H in the methylene of polymeric backbone. The ratio of DN conjugated in the HA backbone was around 18%.

3.2. Production and characterization of the freestanding polyelectrolyte multilayer membranes

A homemade dipping robot was used to produce the respective freestanding multilayer membranes, by repeating the process 100 times over low surface energy substrates. In the end four types of freestanding membranes were obtained from the simple detachment of the multilayers by drying: non-patterned HA and HA-DN membranes and PAT HA and PAT HA-DN.

3.2.1. SEM

The morphology of the surface of the freestanding membranes was investigated by SEM (Figure 1). The HA-side and the ALG-side morphology of the HA membrane revealed a quite rough morphology, presenting some micro features over the entire surface. The morphology of the HA-DN-side and the ALG-side of the HA-DN membrane showed some nano- to microfeatures randomly distributed over the entire surface. In turn, for the HA or the HA-DN-side of PAT HA and PAT HA-DN membranes, the regular line pattern with grooves at the sub-micro scale were clearly visible. The cross-section of the HA membrane appeared homogeneous along the thickness while the cross-section of the HA-DN membrane is more heterogeneous along the thickness of the film. The cross-sections of the patterned membranes seemed homogenous like for non-patterned membrane (Figure 1).

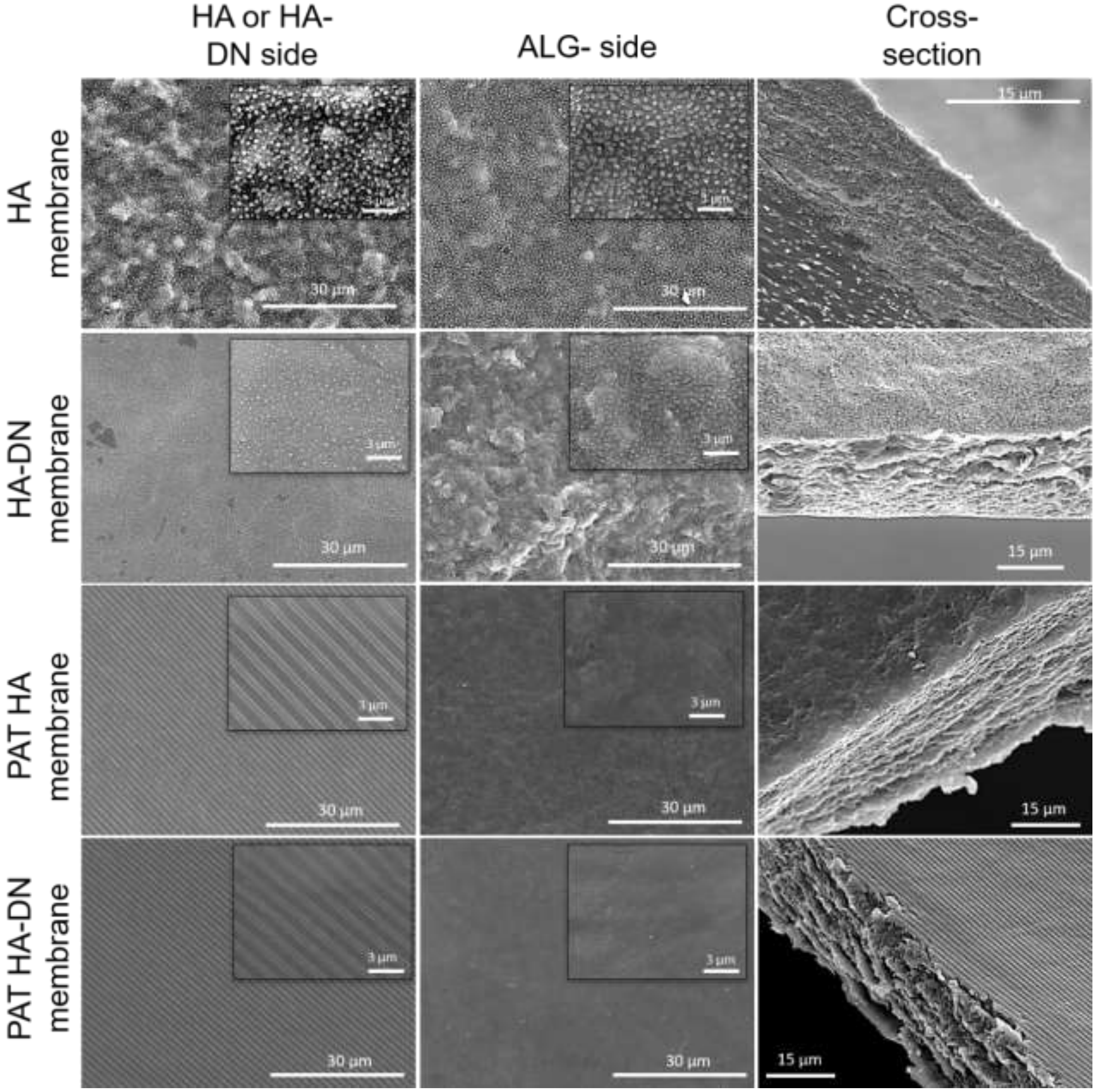

Figure IX-1. SEM images of the morphology of the upper and lower side and of the cross-section of the flat HA and HA-DN multilayer membranes and PAT HA and PAT HA-DN multilayer membranes (higher magnifications in the insets).

3.2.2. Degradation assays

The degradation profile of the HA, HA-DN, PAT HA and PAT HA-DN freestanding membranes was evaluated for 30 days in a hyaluronidase-based solution and in a PBS solution at 37 °C (Figure 2). After 1 week of immersion in hyaluronidase-based solution, HA membranes lost around 35%, PAT HA membranes lost around 28%. HA-DN and PAT HA-DN membranes lost significantly less weight (~17% of weight loss). The same trend was observed after 1 month of incubation in hyaluronidase-based solution, HA membranes lost around 73% while HA-DN membranes lost 52% of the initial weight. In the other hand, after 1 month of incubation in PBS solution, HA membranes lost around 40% while HA-DN membranes lost 30% of the initial weight. The percentage of weight retaining naturally decreased with the time, presenting the same trend for both hyaluronidase-based and PBS solutions. Nevertheless, the overall decreasing on the percentage of weight retaining was significantly higher in the case of using hyaluronidase-based solution.

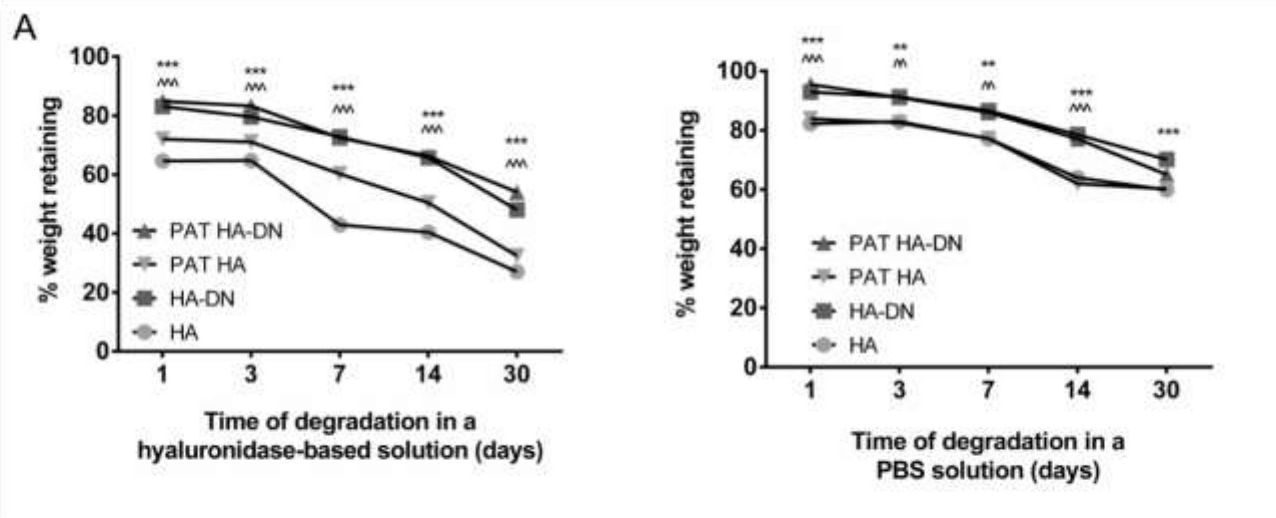

Figure IX-2. Degradation profile of the HA, HA-DN, PAT HA and PAT HA-DN multilayer membranes when immersed during 30 days in an enzymatic-based solution (composed of hyaluronidase) and in a PBS solution. Data are presented as average and standard deviation where significant differences between HA and HA-DN membranes were found for $p < 0.001$(***) and $p < 0.01$(**) and significant differences between PAT HA and PAT HA-DN were found for $p < 0.001$(^^^) and $p < 0.01$(^^).

3.2.3. Adhesion tests

The adhesion potential of the HA-DN membranes to the cartilage was demonstrated using a simple test: the video V1(presented as Figure S2, that corresponds to a QR-code image) shows the adhesive character of the HA-DN to cartilage and to aluminium, when incubated in a wet environment.

3.3. *In vitro* biological assays

The aim of this study was to evaluate the membrane as a temporay scaffold and a delivery device of ASCs to repair superficial defects of articular cartilage or early stages of OA. Therefore, biological assays were done to perceive how RFP-ASC/TERT1 interact with those membranes, varying cell number and times of cultivation. After five days of culture, fluorescence microscopy revealed that cells grown on non-patterned membranes formed clusters on both HA-DN membrane and the control membrane without the catechol modification. On the other hand, patterned membranes with the nanotopography on the surface increased the spreading capacity of ASC, being elongated and well distributed over the membrane (Figure 3 and Figure S3). The initial cell densities of $2.5\text{x}10^4$ and $1.5\text{x}10^5$ cells determined the size of cell clusters but also the number of cells attached to the membrane since day 1. Some individual cells seemed to attach the membranes' surface in the case of the lower initial cell density (Figure 3A) while cells had a stronger tendency to form clusters in the case of the higher initial cell density samples (Figure 3B). Nevertheless, the effect of having a nano-sized patterned surface was similar for both conditions.

After 5 days, cell-seeded membranes were visualized using SEM (Figure 3C and 3D); the images confirmed that RFP-ASC/TERT1 seeded above non-patterned membranes tended to aggregate in big clusters all over the sample while the same type of cells appeared to spread and strech along the grooves presented on the patterned membranes' surface. Lower initial cell density seemed to result in the decreased number of cells adhered on the membranes' surface (Figure 3C) than using a higher cell density (Figure 3D). Quantification of the cellular adhesion (Figure 4A), revealed more cells adhered to the HA-DN, PAT HA and PAT HA-DN membranes than HA membranes, either after 1 or 3 days of culture. Significant differences were found considering the number of cells adhered after 3 days on PAT HA-DN membrane in comparisson with the others – see Figure 4A. Morever, in the case of the patterned membranes, most RFP-ASCs/TERT1 appeared to spread and elongate within the directions of the nanogrooves (more evident in the magnifications presented in Figure S3) – see also the polar graphic representations (Figure 4B).

Cellular morphogenesis occurs in response to physical and topographical cues and offers insights into cytoskeletal organization, material- cell interaction and even signaling feedback that directs cellular fate. Therefore, morphometric characterization was done in this study, reflecting cellular proliferation and migration. The quantification of the averaged cell spreading area and perimeter are presented in Figure S4A. The average values of EF and circularity corresponding to HA, HA-DN, PAT HA and PAT HA-DN multilayer membranes are presented in Figure S4B. RFP-ASCs/TERT1 averaged area and perimeter were higher when cultured above the non-patterned surfaces than on the patterned ones. In terms of EF, patterned membranes enabled higher EF, while the circularity value was lower. Besides that, there are not significant differences between these parameters on both membranes. We concluded that cells adhered, spread and elongated very well above both membranes but with better performance for the catechol-containing membrane.

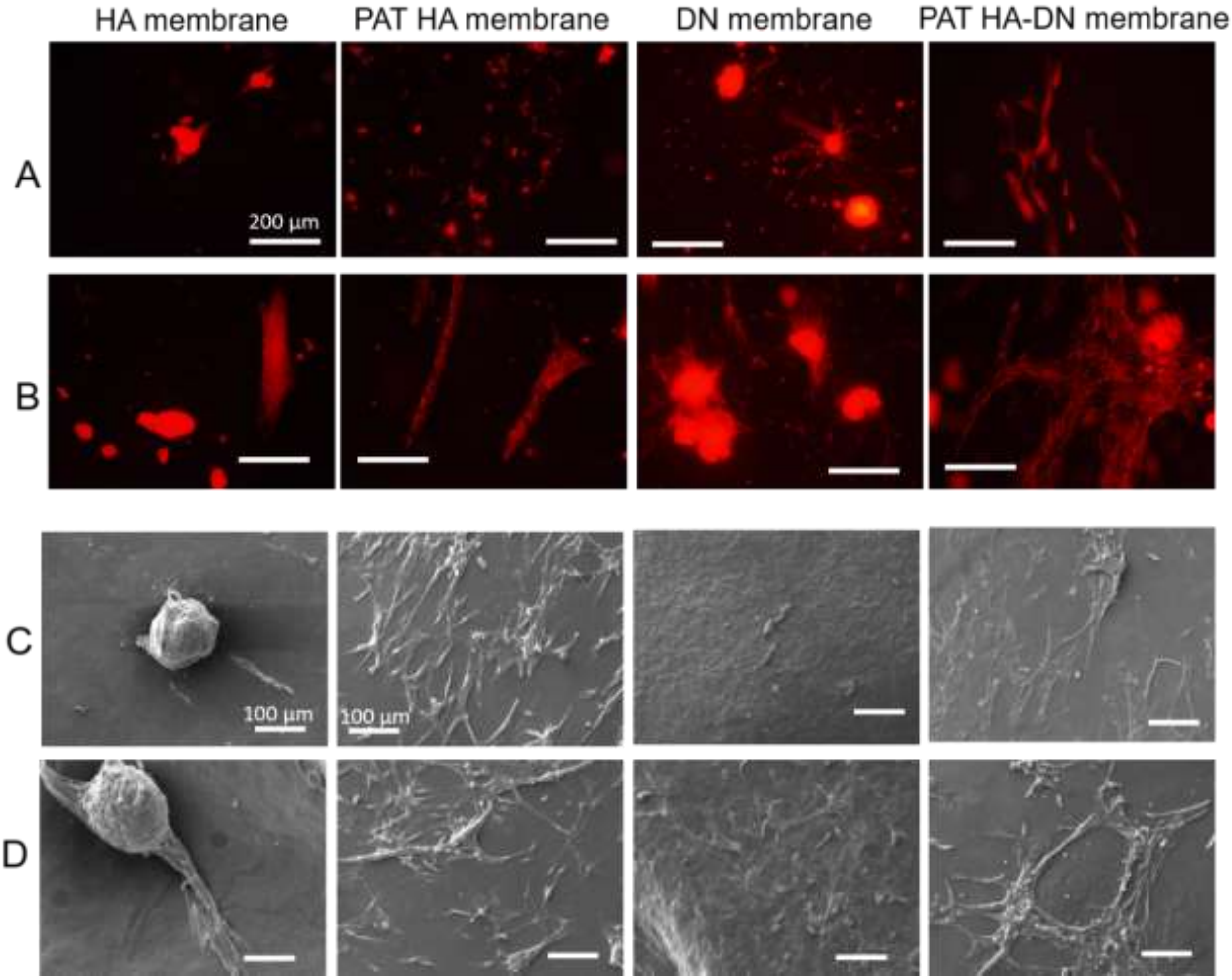

Figure IX-3. Fluorescence microscopy and SEM images of RFP-ASCs/TERT1 grown on the different freestanding multilayer membranes at different initial cell densities: A) 2.5x10^4 cells and B)1.5x10^5 cells correspond to fluorescence microscopy; C) 2.5x10^4 cells and D)1.5x10^5 cells correspond to SEM. The images were taken on day 5 of culture and correspond to a representative area of the membrane. A) and B) shared the same scale bar dimensions as well as C) and D).

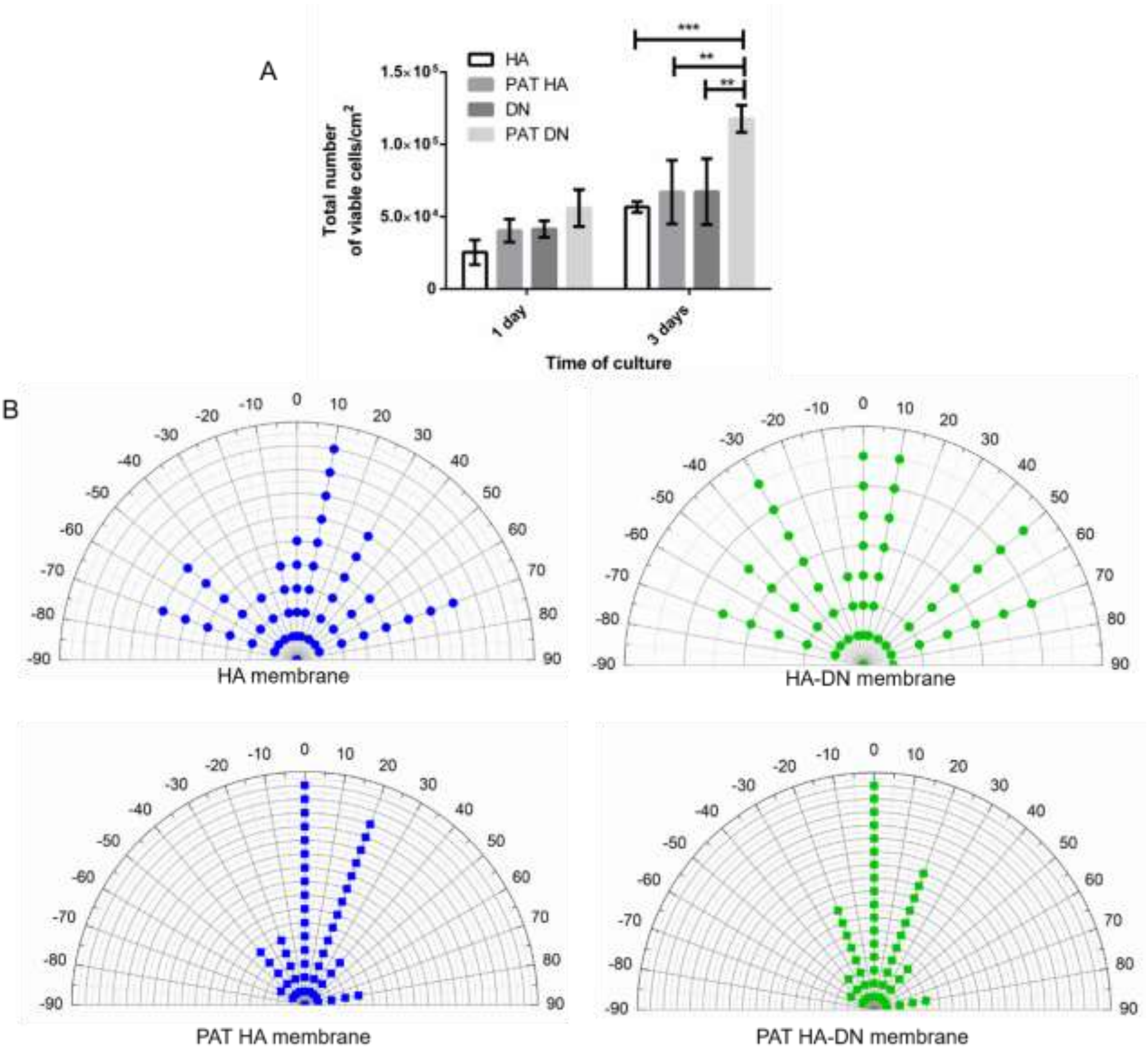

HA membrane

HA-DN membrane

PAT HA membrane

PAT HA-DN membrane

Figure IX-4. A) Bar graphic representing the total number of viable cells per area that adhered on the different types of membranes, after 1 and 3 days of culture. (seeded cell density=5.0 x10^{4}cell/ sample). The numbers are normalized by the superficial area of the membrane. Data are presented as average ± standard deviation, where significant differences are found for $p < 0.001$(***) and $p < 0.01$(**). B) Polar graphical representation of cellular orientation for the HA, HA-DN, PAT HA and PAT HA-DN membrane (n=50).

3.4. *In-situ* biological assays

After testing the RFP-ASCs/TERT1 behavior on the multilayer membranes surface, different *in-situ* biological assays were performed on cartilage tissue (Scheme S1). RFP-ASCs/TERT1 were seeded on the multilayer membranes and allowed to adhere overnight in basal growth ASCs medium. The day after, the cell-seeded membranes were transferred to the previously prepared human OA cartilages discs. Live cell imaging was performed from the bottom of the plugs, to observe the behaviour of the cells on the OA cartilage, by confocal microscopy at different time points (Figure 5 and Figure S5). The cells seemed to attach preferentially on the cartilage surface, suggesting a migration from the membrane to the tissue. Moreover, comparing the lower (Figure 5A) and higher (Figure 5B) initial cell density, some differences in cell density and distribution could be noted, but just for the first days of culture. After one week of culture no significant differences were observed and this was mantained for the remaining time of culture (Figure S5).

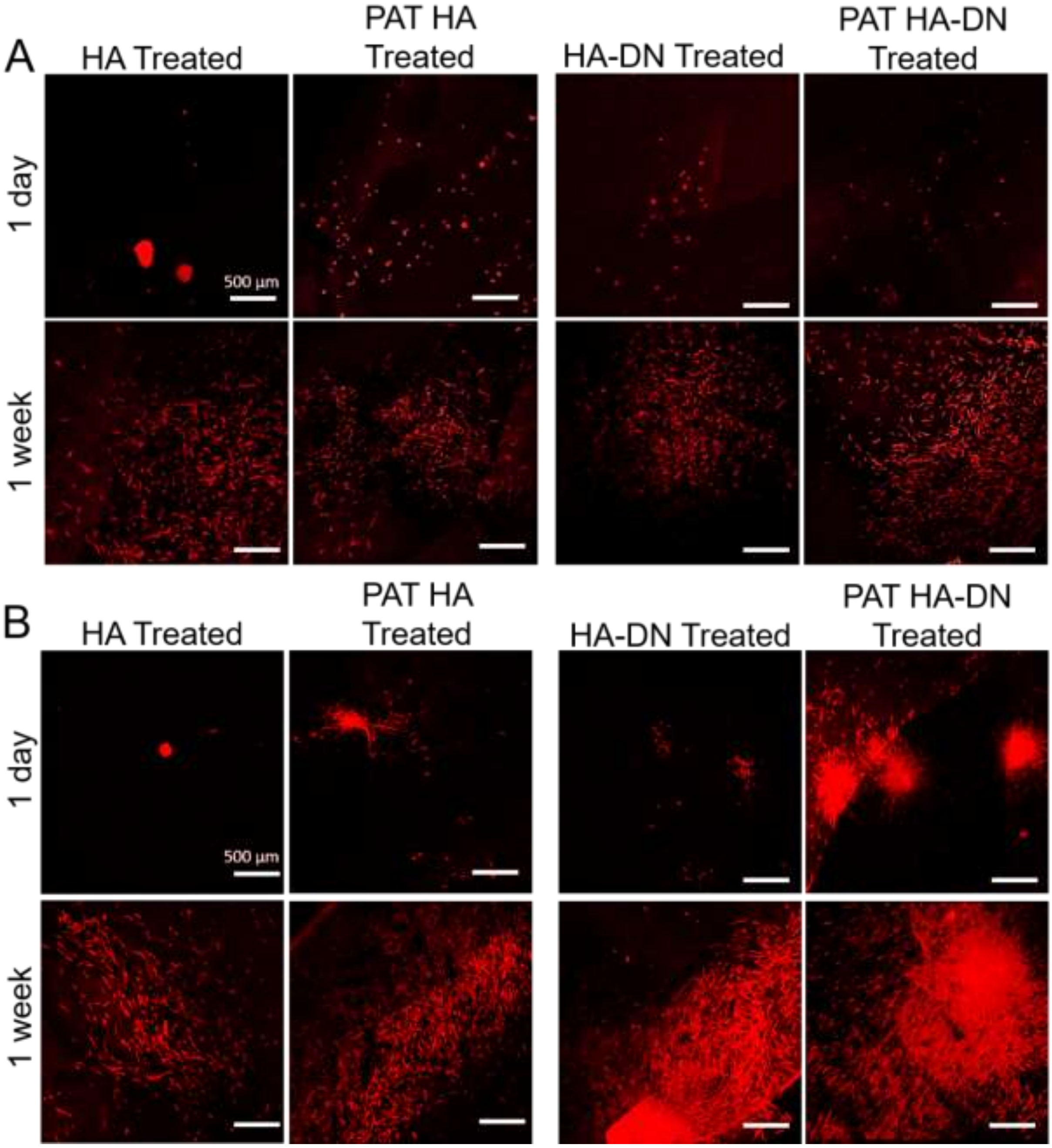

Figure IX-5. Fluorescence images of RFP-ASCs/TERT1 seeded at different cell densities A) 2.5x10^4 cell/ sample and B) 1.5x10^5 cell/ sample, growing in between different freestanding multilayer membranes and OA cartilage discs. The images represent vital cells growing in the interspace between the membrane and the damage cartilage disc, after 1 day and 1 week of culture.

In order to investigate the interaction of cells and damaged cartilage discs, samples were analyzed in cross-section, at the end point of cultivation. After 3 weeks of culture, confocal microscopy and histology (Figure S6A and S6B) showed that RFP-ASC/TERT1 tightly adhered to the damaged cartilage, and in samples with a rough surface they were colonizing the ridges and empty spaces, capable of interacting with the remaining cartilage matrix. According to the images, all the systems allowed cells to grow over from the membranes to the cartilage, adhering well and squeezing inside the small superficial ridges. Moreover, it seems that as cells adhered better in vitro on the surface of HA-DN and PAT HA-DN multilayer membranes, they also present more cells to migrate into the rough cartilage area. The same observations were made when RFP-ASC/TERT1-seeded HA-DN and PAT HA-DN membranes were applied to highly damaged cartilage discs (Figure 6A). The membranes could also be observed by confocal microscopy (Figure 6B).

Figure S6C presents confocal images that could elucidate about the influence of the roughness/damaging of the sample on the membrane/tissue interaction, the cell/ tissue interaction, as well as on the delivering process. In fact, when the articular tissue of the donor was too damaged, their surface appeared highly rough and the migration of the cells to the tissue was clearly noted the cells were delivered to the cartilage surface, adhering and proliferating. Meanwhile, they started to migrate into the defects interacting with the damage tissue. Additionally, it was easy to perceive with these cross-sections imaging analysis that the RFP-ASCs adhered temporarily to the membrane and, when in contact with the damaged cartilage, the cells started to bridge between the membrane and the damaged tissue.

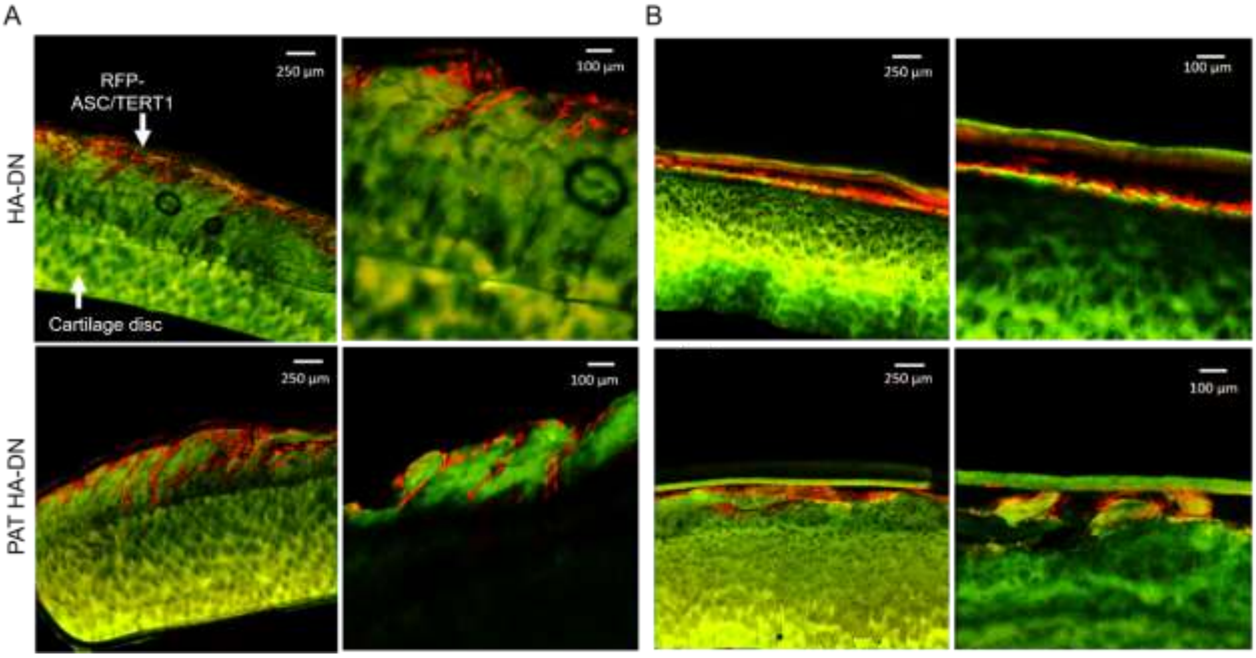

Figure IX-6. Fluorescence images of the paraformaldehyde fixed cross-section of the system RFP-ASCs/TERT1 –seeded (at the cell density of 2.5×10^4 cell) freestanding multilayer membranes, that were applied to treat A) very damaged cartilage chips, after 3 weeks of culture and B) cartilage chips, after 3 weeks of culture and where autofluorescence of the membranes allowed their visualization. The cells adhered to the cartilage, proliferated and spread on the surface and started to enter through the cartilage defects, colonizing the empty spaces and interacting with the remaining tissue. The membranes were tight to the cartilage surface.

Histological sections of each treatment system were also prepared after 3 weeks in culture (Figure 7 and Figure S7). To investigate the cell-matrix interaction ECM it was used the Heidenhain's Azan trichrome histological staining. Histological analysis supported the fluorescence images showing that the cells colonize the defects of the osteoarthritic cartilage and started to integrate the gaps between the cartilage matrix (Figure S7A). This tendency is shared when using an initial higher cell density (Figure S7B). However, increasing the initial cell density for DN and PAT DN-treated systems resulted in more adhered cells in the damaged cartilage, while for HA and PAT HA the quantity of RFP-ASCs/TERT1 adhered to the membrane surface is similar either using lower or higher initial number of cells seeding. The presence of the membrane could be observed (intense staining in red with AZAN staining), (Figure 7).

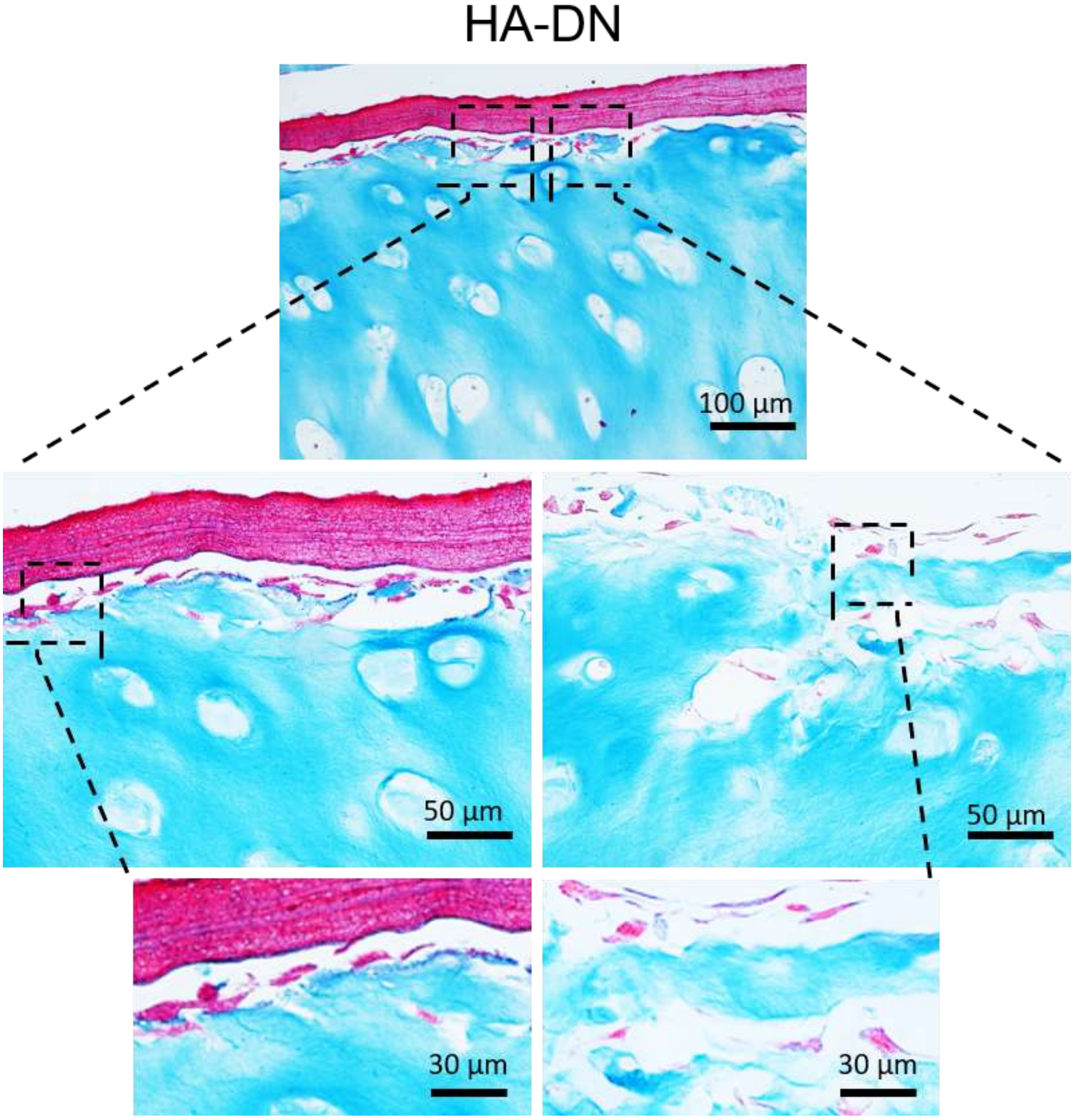

Figure IX-7. Histological images representative of the system RFP-ASC-seeded HA-DN membrane (at $2.5x10^4$ cells) sample plus damaged cartilage, fixed after 3 weeks in culture (Azan Staining). The cells invaded the ridges of the damaged cartilage surface. The irregularities presented on the lower part of the HA-DN membrane fit with the irregularities of the damaged cartilage surface.

3.4.1. *In-situ* biological assays-differentiation

Three groups were defined to study the chondrogenic potential of the RFP-ASC/TERT1 when delivered to the damaged cartilage discs: the osteoarthritic cartilage disc without treatment, the damaged discs treated with RFP-ASCs/TERT1-seeded HA-DN multilayer membranes and the damaged discs treated with RFP-ASCs/TERT1-seeded PAT HA-DN multilayer membranes. After 28 days cultured in medium supplemented with low dose of growth factors, the chondrogenic potential of the RFP-ASCs/TERT1 was investigated by immunohistochemical and histological analysis, specifically for newly synthesized collagen type II. This positive marker for chondrogenesis was found mainly on the middle and deeper zones of articular cartilage (Figure 8). However, different histological observations were noted for the RFP-ASCs/TERT1 treated samples: for both treated-systems, collagen type II staining was found more intensely on the superficial zone of articular cartilage (Figure 8). High magnification cells revealed rounded cells within the matrix localized between the middle and the superficial areas of cartilage: some of these cells appeared positive for newly synthesized collagen type II. Within the surface of these cartilage systems, more elongated cells were found, but negative for collagen type II.

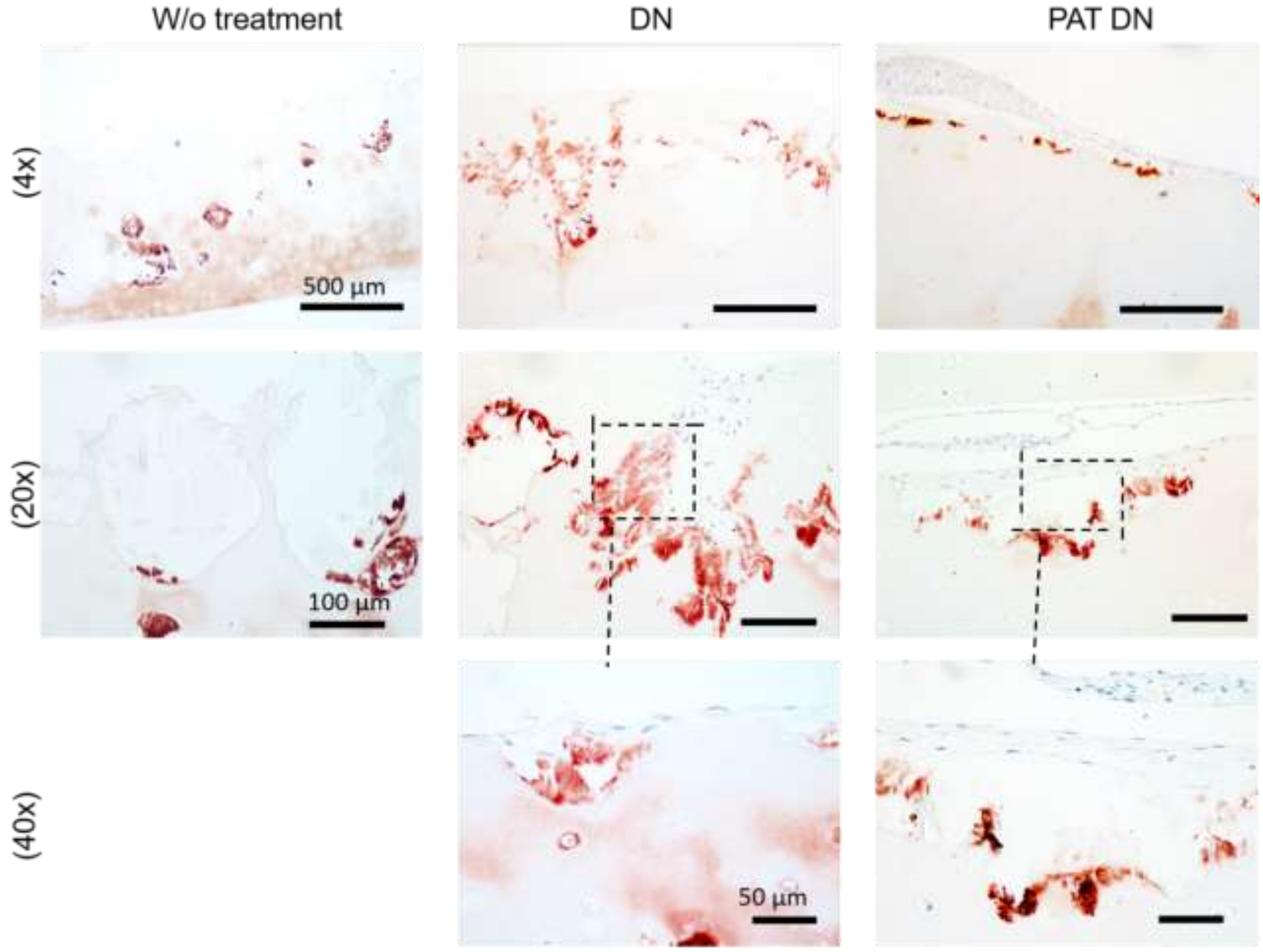

Figure IX-8. Immunohistochemistry/histology of the RFP-ASCs/TERT1- seeded FS membranes non-treated and treated damaged cartilage plugs, after 28 days of culture in chondrogenic supplemented medium. The samples were investigated for collagen type II. The scale bars are representative for each row.

4. Discussion

The current investigation was designed to evaluate the effectiveness of using an adhesive multilayer membrane as a delivery device for therapeutic cells to treat defects on superficial articular cartilage (Scheme 2). ASC/TERT1-were chosen cell source to avoid interdonor-viability.

In tissue engineering, different type of scaffolds have been designed to meet different tissue specifications; these materials usually act like a structural support for cells to attach, grow, migrate and differentiate *in vitro* and *in vivo* [36]. In our strategy, the transporting material was designed to follow specific requests: to be biocompatible, with an ideal rate of degradation and with adhesive properties strong enough to deliver and protect the cells from direct contact of the contralateral joint surface during the first days of treatment. Another important request for this biomaterial is to be adhesive to retain cells on their surface but still less adhesive than the surface of the native cartilage, and to temporary fix the material to the cartilage surface.

Therefore, we took advantage of the versatility of LbL assembly to produce freestanding multilayer membranes that could fit in the developed strategy. Neto *et. al.* [37] had already designed a high-throughput system platform that allow a fast and simple screening of multilayer arrays based on wettable and non-wettable spots. The functionalization of polyelectrolytes with different amounts of dopamine (DN) influenced the surface and mechanical properties, as well as cell adhesion. The authors reported that the presence of DN effectively enhanced their mechanical and cellular adhesion in comparison with the same membranes without DN. In our work, HA, ALG and CHT were chosen as raw materials, as they present generally some similarities with the cartilage ECM, being part of the biological environment. Especially, HA is prepared to recognize and deal with cells metabolically, They usually do not stimulate chronic inflammation or immunological reactions being non-toxic and they are highly available from natural resources [38]. Among them, HA has gained increasing attention for cartilage repair strategies, being in cartilage and in synovial fluid of articular cartilage joints, where maintains tissue hydration by immobilizing ions and water. HA has an important role in lubrication and shock absorption in joints and can control processes as cell migration and inflammatory processes [39]. In addition to these advantages, HA can also be chemically modified to achieve a specific and desired property like increasing the degradation rate or improving the mechanical stability [39b, 40]. Within this study, HA was successfully modified with DN to improve their adhesive properties, through a carbodiimide chemistry reaction, as shown by UV-vis spectroscopy and ^{1}H-NMR.

When analysing the SEM images of the HA side or the ALG side of the HA freestanding multilayer membranes showed similar rough morphologies, presenting micro to nanofeatures on their surface. On the other hand, SEM images of the HA-DN side or the ALG side of the HA-DN freestanding multilayer membranes showed different morphologies; the HA-DN side was smoother than the ALG side, but still presenting micro to nanofeatures on their surface. This could be related with the fact that the HA-DN first layer was directly in contact with the flat underlying substrate, acquiring its smooth texture unlike ALG side. The same principle is not valid in the case of the HA membrane, being the side in contact with the FMM still rough. In fact, we think that a kind of island-like growth started from the very first layer due to the hygroscopic property of HA [41]. Further, we hypothesize that when chemically modified with DN, the conjugate HA-DN seemed more stable avoiding the shrinking of the deposited layers.

For this investigation, it was important to keep the membrane not more adhesive than the cartilage matrix is. Therefore, we hypothesize that even having DN moieties on their surface, these membranes were not strongly cell-adhesive because of their smoother morphology. Cross-section observations showed that all membranes seemed to present a kind of a sheet-like stacking organization along the z axis, confirming the effectiveness of the LbL assembly, creating thin membrane composed of multi-ultrathin layers of HA or HA-DN, CHT and ALG.

Other important parameter is the biodegradation of the multilayer membrane. In fact, both degradable [42] and non-degradable materials [43] have been used for cartilage repair and regeneration strategies. Extreme slow-degradation rates can result in the lack of nutrient transport, physical space and higher chances of rejection, while very-fast degradation rate can allow the loss of cell products to the surrounding area before adequate tissue formation can happen [44]. Therefore, to investigate the biodegradability profile of the developed polyelectrolyte FMM we studied their enzymatic degradation by hyaluronidase, a plasmatic enzyme presented in the body fluids that catalyses the hydrolysis of HA and partially degrades the FMM [45]. HA membranes degraded more in the presence of hyaluronidase, losing about more 21% of weight than HA-DN membranes after 30 days of incubation. For the same time but patterned conditions, PAT HA membranes lost more 22% of weight than PAT HA-DN membranes. In fact, comparing patterning and non-patterning conditions, the same trend was maintained during all the time-points of the experiment, with HA-DN membranes retaining more weight than HA membranes. To chemically modify HA is one common strategy to prevent their fast degradation and diffusion out of the material [46]; herein, HA backbone was modified with DN moieties via a carbodiimide chemistry that could result indirectly on the decreasing of the degradation ratio, explaining the different mass loss profiles between HA and HA-DN membranes or PAT HA and PAT HA-DN membranes. The degradation rate of the membrane should not be too fast, to protect the ASCs treatment from the surrounding environment. We hypothesize that altering the conjugated HA-DN could be beneficial to improve the profile of degradation of the material and the presence of interspersed layers of ALG were important to avoid premature degradation of the membrane.

Adhesiveness was another major concern of this investigation, since it is required that the membrane areas not seeded by cells adheres to the cartilage surface. Improved adhesive properties have been achieved through different strategies, including the production and use of the conjugated HA-DN. For instance, Scognamiglioa, *et. al.* modified alginates with DN, at different substitution degrees, using these conjugates to produce membranes with enhanced adhesive and biocompatible properties [25] while Shin *et. al.* suggested the functionalization of HA with a catecholamine (CA) motif of mussel foot protein, producing an HA-CA hydrogel with a strong tissue adhesiveness [47]. Therefore, after modification of the HA backbone with DN moieties and their incorporation in the FMM, a simple adhesive test confirmed the adhesiveness of the membranes, particularly to the cartilage surface.

Intra-articular injections of ASCs have been reported for the treatment of low to mid damaging in the articular cartilage, usually with the cell density in the order of 10^6 to 10^7 cells; even though there is some controversy about the optimal cell concentration. For instance, Koga *et. al.*[48] compared the effect of intra-articular injection of different stem cells densities embedded in a collagen gel in a rabbit cartilage defect and concluded that higher cell density ($5x10^7$ cell. ml^{-1}) presented statistically better results in histological score than the low cell density group ($1x10^6$ cell. ml^{-1}) at 4 weeks post-transplantation. Park *et. al.* [49] compared the transplantation of different densities of MSCs embedded in a HA hydrogel: high cell concentration of MSCs (1.5×10^7 cell. ml^{-1}) showed the lowest cartilage repair score at 4, 8- and 16-weeks post transplantation, while the 0.5×10^7 cell. ml^{-1} condition resulted in better quality of cartilage repair. Fewer works reported the cell density effect of using particularly ASCs intra-articular injections as a treatment for damaged articular cartilage. Desando *et. al.* [50] investigated the influence of intra-articular ASCs injection in the healing process on cartilage, synovial membrane and menisci in an experimental rabbit model; overall, both cell densities ($2x10^6$ and $6\text{-}10^6$ cells) had similar impact, decreasing the progression of defect cartilage. In a clinical proof-of-concept, Jo *et. al.* [15a] tried to conclude about the safety and efficacy of intra-articular injection of autologous ACS for knee osteoarthritis: comparing high doses of ASCs ($1x10^8$ cells) with mid doses ($5x10^7$ cells) and with low doses ($1x10^8$ cells). Histological results showed that intra-articular injection of $1x10^8$ cells reduced pain of the knee joint and articular cartilage defects.

However, despite the good indications resulting from intra-articular injection of ASCs to repair cartilage, there are some concerns with the use of such an higher number of cells: the preparation of a sufficient number of cells for chondrogenic potential is not always possible and the injection of cell contain-hydrogel is not a very efficient process at long term, with the most cells being lost in the surrounding environment of the defect [13c, 51]. Moreover, independent of being in gel or in solution, it is important that the injected cells do not end up on the cartilage surface, not fulling up the superficial ridges. The strategy presented in this study is based on the transport of ASCs to repair superficial cartilage defects not by means of an injection but instead using a delivery material. Moreover, we envisaged to treat just special damaging and not deeper defects; thus, we hypothesized that less cells should be necessary.

Comparing both chosen cell densities ($2.5x10^4$ and $1.5\ x10^5$), it is possible to observe with SEM, fluorescence microscopy and cell quantification, that increasing the initial cell seeding number we could increase the number of cells attached to the membrane. More cells adhered on DN-containing membranes and PAT membranes, either after 1 or 3 days. The results suggest a synergy of the presence of DN and the existence of topographic nanofeatures, making these membranes the best carrier of ASCs. Nevertheless, in terms of cell adhesion and proliferation on the cartilage, all the systems presented good results, as after 1 week of transferring the cell-seeded membranes to the cartilage, no significant differences were found.

In vitro assays revealed that topographical nanofeatures influenced cell adhesion and morphology. ASCs attached all over the patterned membrane's surface, most of them acquiring a stretched morphology and spreading along the direction of the nanogrooves. For smoother membranes, cells acquired more rounded morphology, being randomly distributed on the material's surface. In fact, cartilage tissue is composed of four distinct zones, each one with a specific cell and ECM organization [1a]; our strategy is directed for the repairing of superficial cartilage damaging. The superficial zone of native articular cartilage consists of primarily flattened ellipsoidal-like chondrocytes and a very polarized dense organization of nanoscale collagen type II fibrils, which are oriented parallel to the plane of the articular surface [1c, 52]. The presence of the linear nanogrooved topography on the membranes 'surface allowed to mimic the fibrous effect of the cartilage surface, resulting in better cell adhesion of the cells on the nanogrooved membranes. In fact, as superficial articular cartilage, ECM in most part of natural tissues is not randomly organized, having specific special orientation. Wise *et. al.* [52] suggested that alignment and chondrogenic differentiation of human mesenchymal stem cells cultured on oriented electrospun polycaprolactone (PCL) scaffolds are possible; the chondrogenic differentiation was facilitated when cells were seeded on a nanofibrous scaffold (~500 nm diameter). Herein, SEM images were used to calculate morphometric parameters of the cells adhered on the FMM. Cells with higher area and perimeter are observed in patterned surfaces, as compared with flat ones; this could be related with the fact that major part of ASCs acquired a more rounded morphology on flat membranes and a spindle-like and well-stretched morphology in the other case. Other parameters were calculated as circularity index versus cell EF. Circularity is a quantitative parameter used to evaluate cell morphology, as well as cell EF [53]. Significantly higher circularity values were obtained for cells seeded on flat membranes, comparing with those obtained for PAT membranes. These results indicate that ASCs grown on flat surfaces acquire more rounded morphologies than when grown in the nanopatterned surfaces. Cell EF is defined as the ratio between the longest axis of the cell (length) and the longest axis perpendicular to it [33, 53]. Unlike circularity index, the EF of cells cultured on nanopatterned substrates was significantly higher than for cell cultured on flat surfaces. As it was higher than 2 for both type of patterned membranes (with and without DN) it is possible to conclude that most cells were well-elongated. RFP-ASC/TERT1 were cultured on substrates patterned with submicro- to nanometer wide stripes and they elongated along the ridges and grooves direction. Flat substrates did not induce this orientation. For PAT HA the cell distribution seemed to be in the range from -20° to 20° where ≈75% of cells were aligned with the pattern direction. For PAT HA-DN the cell distribution seemed to be distributed in the range from -20° to 20° where ≈78% of cells were aligned with the pattern direction. Contact guidance has been recognized as the phenomenon by which the matrix gives directional cues to the cells and guides the motility response in the microenvironment [54]. Briefly, we assume that cells project in one direction depending on the shape and type of structures it met; for nanopatterned surfaces, the cellular alignment is predictable in the direction with less topographic and mechanical obstacles [33, 55].

The poor self-regeneration capability of cartilage highlights the constant need of improving clinical therapies in problems related with tissue loss or degradation [56]. To allow an adequate environment to evaluate the effectiveness of these therapies, a simple *in situ* model was designed; vital but damaged cartilage plug discs were prepared from human femoral heads and used to replicate better what happens *in vivo*. This study was conceived to evaluate the feasibility of the successful delivering of therapeutic ASCs to damaged cartilage. Therefore, the first steps were established to understand how material and cells interact with the damaged cartilage. Resulting from their composition, the developed FMM were robust and hand able enough to provide enough strength to adapt the membrane to the defect geometry or location. The effectiveness of the cell delivery strategy was demonstrated in this investigation, showing the adherence of the cells to the cartilage, spreading on the surface and bridged between the multilayer membranes and the tissue. Because of their adhesive potential, HA-DN and PAT HA-DN membranes seemed to have a better performance than the HA membrane. These differences were not so perceptible for PAT HA membranes. We hypothesize that due to the presence of topographical features more cells adhered to the membrane allowing more cells bridged between the membrane and the tissue. Moreover, comparing the cell densities, some differences were naturally noted for the first day but after that these became almost undetectable; the rate of proliferation seemed higher for the lowest cell densities. With the increasing time of culture, the cells seemed to proliferate all over the cartilage surface, starting to migrate into the irregularities of the cartilage, perceptible because of the presence of RFP-ASCs/TERT1 in different layers.

The hypothesis of the RFP-ASCs/TERT1 starting to migrate into the irregularities of the cartilage surface raised the need of investigating what happens along the z axis of the system RFP-ASCs/TERT1-seeded membrane and damaged cartilage. Upon contact of the device, cells clearly bridged between the FMM membrane and the tissue adhered to the cartilage, proliferated and spread on the surface and started to enter through the cartilage defects, colonizing the empty spaces and interacting with the remaining tissue. We hypothesize that in these conditions, the ASCs could start to release biologically chondrogenic active, anti-fibrotic and anti-apoptotic growth factors, promoting the repair of articular cartilage without causing an immune response. These observations were essential to conclude about the success of the designed strategy, as cells when integrated with the remaining cartilage tissue are able to repair the superficial cartilage tissue [57]. The HA and HA-DN FMM seemed to be effective in the delivery process of the RFP-ASCs/TERT1, being really close to the cartilage surface. This observation can be an indication of the success of the membranes to protect the treatment from the surrounding environment. Increasing the initial cell seeding number, more RFP-ASCs/TERT1 were observed migrating into the defects of the cartilage. Nevertheless, even using a lower cell density, the deliver process was still possible. This can be understood as a positive aspect of our strategy, allowing to use smaller number of cells as compared with scaffold-free approaches. We hypothesize that alternative cell types can be further used, as nasal chondrocytes [58]. HA-DN and PAT HA-DN membranes seemed to be more effective in terms of cell delivering and protecting from the surrounding environment; the enhanced adhesive properties as well as the enhanced cell compatibility allowed better performance of the DN-containing multilayer membranes. HA-DN membranes were more moldable and adhered better to the cartilage surface; in this case, the defect site and the cells could be better protected from the synovial environment and less RFP-ASCs/TERT1 could be lost in this harsh scenery. The cells remained captive in area to treat. In fact, there are already some works reporting the use of fibrin as an adhesive material that could act like a carrier of therapeutic agents or a scaffold to repair and regenerate articular cartilage [22b, 59]; for instance, Kim *et. al.* [22b] suggested the implantation of MSCs loaded in fibrin glue in patients with osteoarthritic knees. However, there are some problems related with the use of fibrin gel like the non-durability and the lack of mechanical stability; we hypothesize that these limitations can be overcame using the HA-DN FMM.

The histological analysis of the treated cartilage defects emphasized the interaction between cells and cartilage matrix. After 3 weeks in culture, it is evident that cells colonized the defects of the damaged cartilage and started to interact with all the surrounding cartilage area: based on literature, there already some works reporting the positive effect of ASCs therapy to treat cartilage defects and their application already in clinics [15]. In fact, ASCs are well known by their ability to differentiate including in chondrocytes, responding to specific growth factors or environment cues. Even though, ASCs have been used as therapeutic for cartilage repair mainly because of their ability to release biologically chondrogenic active factors, such as transforming growth factor-β1 (TGF-β1) and bone morphogenetic protein 4 (BMP-4), anti-fibrotic and anti-apoptotic growth factors[50, 60].Other therapeutic features have been studied: Puissant *et. al.* [61] investigated the immunomodulatory effect of human ASCs finding immunosuppression properties for ASCs. For instance, Desando *et. al.* [50] found a positive effect of ASCs in promoting cartilage and opposing inflammatory processes in the synovial membrane.

In this investigation, we hypothesize that the use of DN or PAT DN membranes to deliver ASCs to human damaged cartilage can be extremely relevant: the ASCs-seeded membrane adhered on cartilage surface, delivering the cells, avoiding losing cells and protecting this therapy from the surrounding synovial environment. Thus, it can be possible to overcome some issues related with the injection of ASCs [21]. Although the membranes were fixed with formalin together with the respective cartilage plug, during the histological cutting procedure, the solvents affected the integrity of the membrane, denying their observation in some samples. However, it was still possible to observe the presence of HA-DN and PAT-DN membrane; some irregularities can be found on the surface of the membrane in contact with cartilage. Curiously these irregularities were coincident with some of the irregularities of the membrane, corroborating the close contact between membrane and cartilage and the adhesive potential. Moreover, some signs of membrane’s degradation were clearly observed in the images.

Immunohistochemical analysis for newly synthesized collagen type II was used to investigate the ability and the potential of using the treatment with RFP-ASCs/TERT1 to differentiate these cells into chondrocytes, producing a kind of a neo-cartilage matrix. While the damaged cartilage plugs present collagen type II positive staining mainly on the middle and deeper areas, more intense staining appeared on the superficial zone for the RFP-ASCs/TERT1 treated damaged cartilage discs. We postulate that the fact that the treated systems induced larger amounts of collagen type II on the superficial part of cartilage indicates that the RFP-ASCs/TERT1 responded to signals and stimuli from their surroundings to differentiate in a cartilage phenotype. The detection of type II collagen within the damaged area seems a very promising result, as the synthesis and assembly of collagen is often considered to be a limiting step in neocartilage matrix formation. In fact, Ng *et. al.* [62] reported that the limiting factor in synthesizing new collagen can be related to the lack of appropriate stimuli to induce rapid tissue remodelling. We believe that under appropriate stimulation combined with the treatment with the therapeutic RFP-ASCs/TERT1, collagen biosynthesis and accumulation was significant higher in a short culture period. Moreover, comparing both delivery systems, corresponding to the seeded HA-DN and the PAT HA-DN treated samples, it was possible to note some differences. The seeding of RFP-ASCs/TERT1 and their respective delivery by the PAT HA-DN membranes seemed to be more efficient than when using HA-DN membranes. The microenvironment around stem cells is critical for chondrogenic differentiation induction [63]. In fact, both systems represent promising materials to act as a delivery agent for therapeutic cells, as well as to integrate a suitable environment for chondrogenic differentiation. The differences on the shape and density between cells observed within the superficial layer of damage cartilage and the cells observed within the deeper regions of cartilage can be comparable with the organization of the normal and healthy cartilage. There, chondrocytes in the superficial zone are flatter and smaller and generally have a greater density than that of the cells deeper in the matrix [1c].

Taken all these results together, we suggest an adhesive and functional LbL-engineered freestanding membranes to repair superficial cartilage damaging: The freestanding multilayer membranes can adhere to cartilage tissue, delivering important therapeutic agents like ASCs as well as protecting the interaction between the therapeutic agent and the damaged cartilage from the synovial environment- see Scheme 1. One could envisage the entrapment of bioactive molecules in the membrane, as it has been shown that these kind of multilayered films could be used as a reservoir of therapeutic proteins [64].

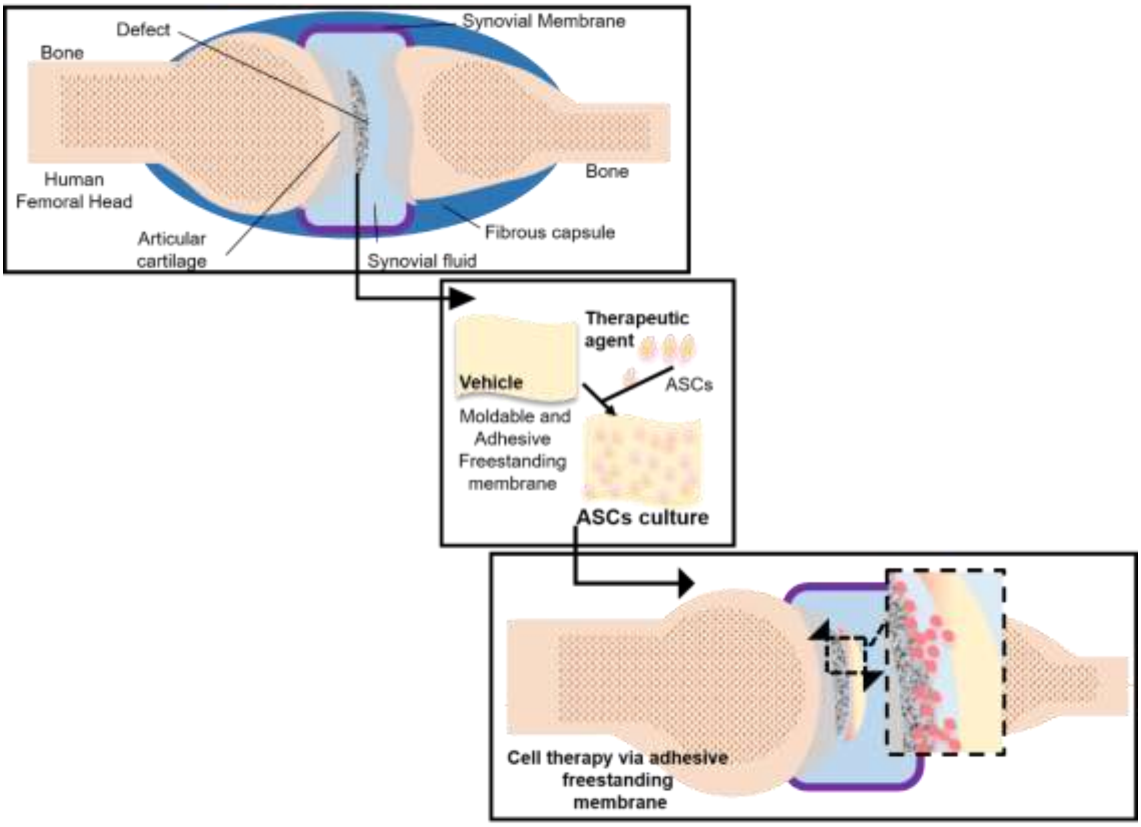

Scheme IX-1. Scheme representation of the developed concept: the material was developed to deliver ASCs directly to the defect place and protect the first days of treatment from the harsh synovial environment.

5. Conclusions

We proposed a novel tissue-engineering strategy based on a flexible bioinspired material for articular cartilage damaging or defect repair. The use of LbL strategy permits controlled insertion of multiple functional components, offering added flexibility, versatility and control to the resulting material. The developed engineered flexible freestanding multilayer membrane combined natural-based macromolecules (CHT, HA and ALG), specific catechol functionalities, and different topographies, to produce an adequate platform to successfully deliver therapeutic cells to repair defects of any lateral size and shape. MSCs and ASCs-based therapies have shown fruitful application in clinical trials for cartilage repair and pain relief, but the usual procedure to deliver the cells to the treated area must be improved: with the injection of the therapeutic agents, with or without a support material, a high number of therapeutic cells can be lost and the treatment can be quite exposed to the harsh surrounding environment inside the synovial membrane. The developed multilayer membranes showed great potential as delivery platforms of ASCs to damaged articular cartilage. Particularly, HA-DN and PAT HA-DN membranes exhibited improved properties compared with their controls in terms of degradation, mechanical adhesiveness and cellular viability. Therefore, we confirmed the potential of such kind of adhesive and functional LbL-engineered FMM to repair superficial cartilage damaging: FMM can adhere to cartilage tissue, delivering important therapeutic agents like ASCs as well as protecting the interaction between the therapeutic agent and the damaged cartilage from the synovial environment.

6. Supplementary Information

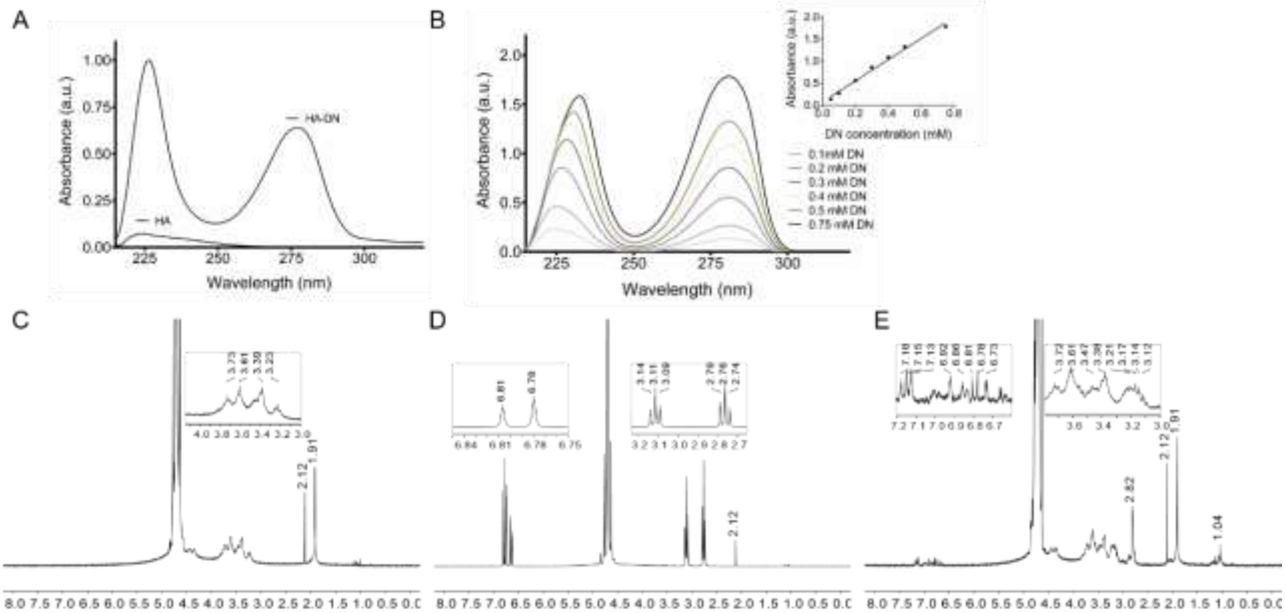

Figure S IX-1. A) UV-vis spectra of the conjugate the conjugate (HA-DN) and the control (HA), which is also shown for comparison. B) Inset shows the calibration curve that correlates DN concentration with measured absorbance and the main graph represents the UV-Vis spectra of dopamine solutions with different concentrations. ^{1}H-NMR spectra of the C) HA, D) the DN and E) the synthesized conjugate HA-DN.

Figure S IX-2. QR-code for a video of. confirming the adhesiveness of the freestanding membranes to a rough surface of a prepared human cartilage disc.

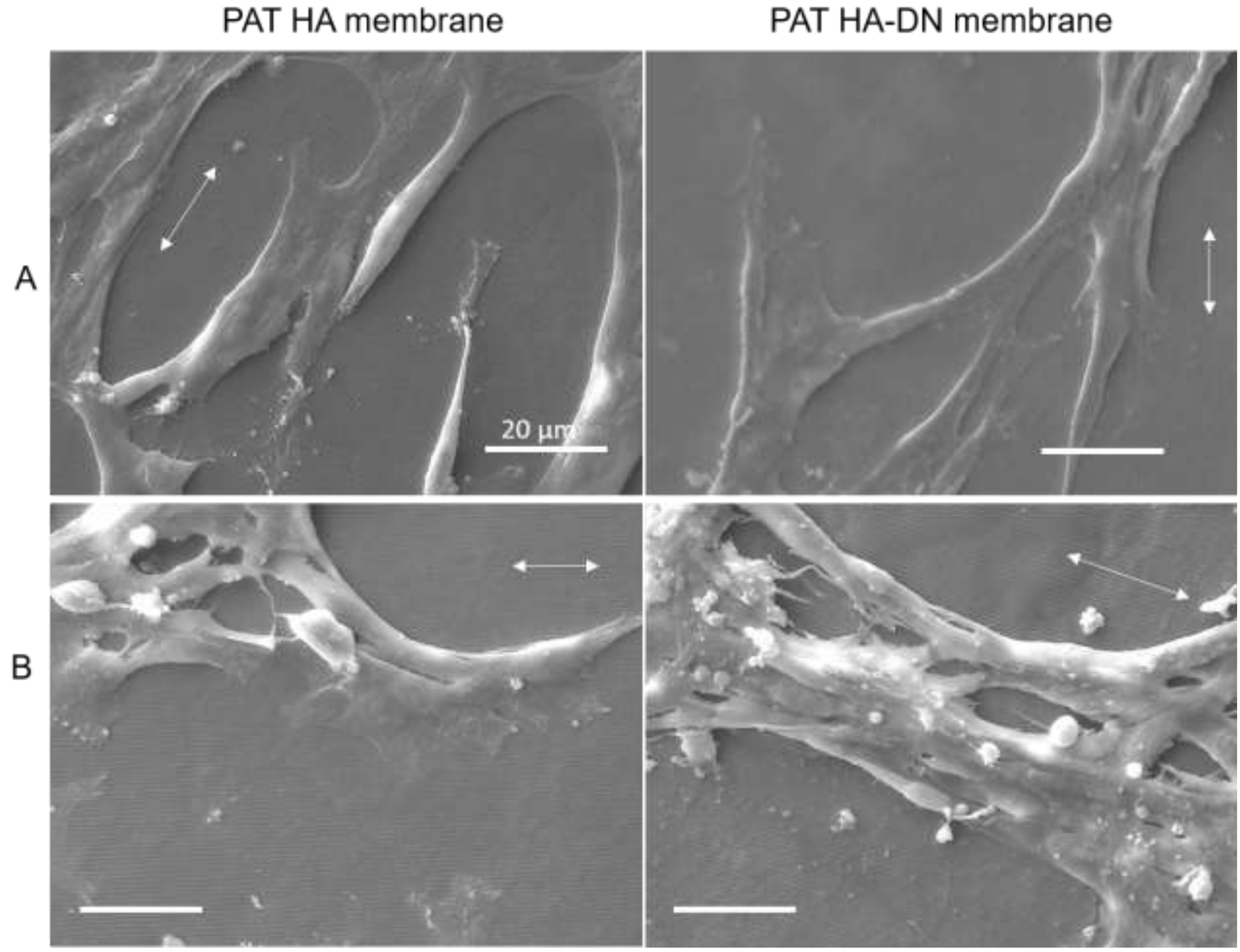

Figure S IX-3. Magnifications of the SEM images of RFP-ASCs/TERT1 grown on the patterned freestanding multilayer membranes at different initial cell densities: A) 2.5x10^4 cells and B)1.5x10^5 cells. The images were taken on day 5 of culture and correspond to a representative area of the membrane. The white arrows represent the pattern orientation.

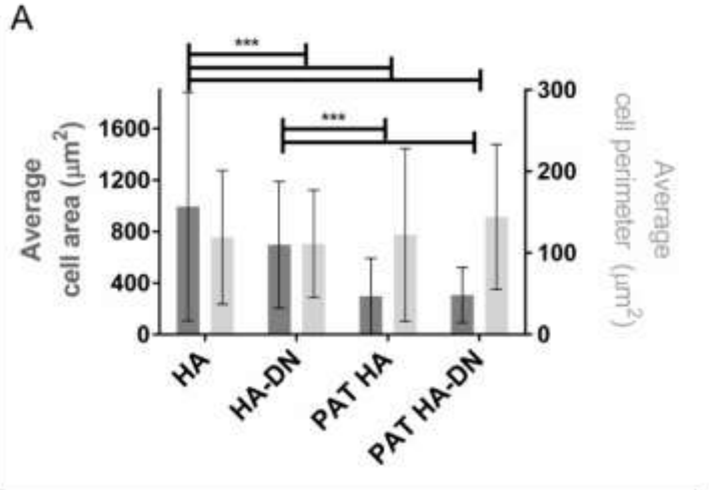

Figure S IX-4. Morphometric parameters of RFP-ASCs/TERT1 adhered on the different freestanding multilayer membranes: A) cell area, and perimeter and B) elongation factor (EF) and circularity.

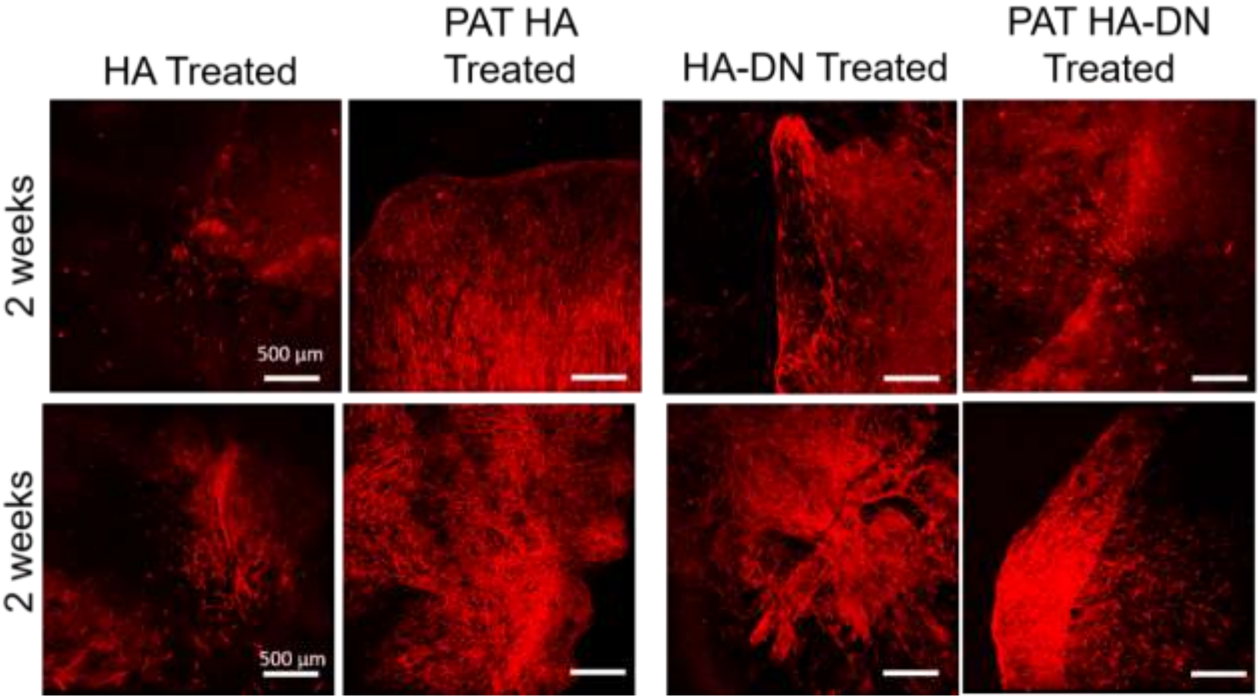

Figure S IX-5. Fluorescence images of RFP-ASCs/TERT1 seeded at different cell densities A) 2.5x10^4 cell/ sample and B) 1.5x10^5 cell/ sample, growing in between different freestanding multilayer membranes and OA cartilage discs. The images represent vital cells growing in the interspace between the membrane and the damage cartilage disc, after 2 weeks of culture.

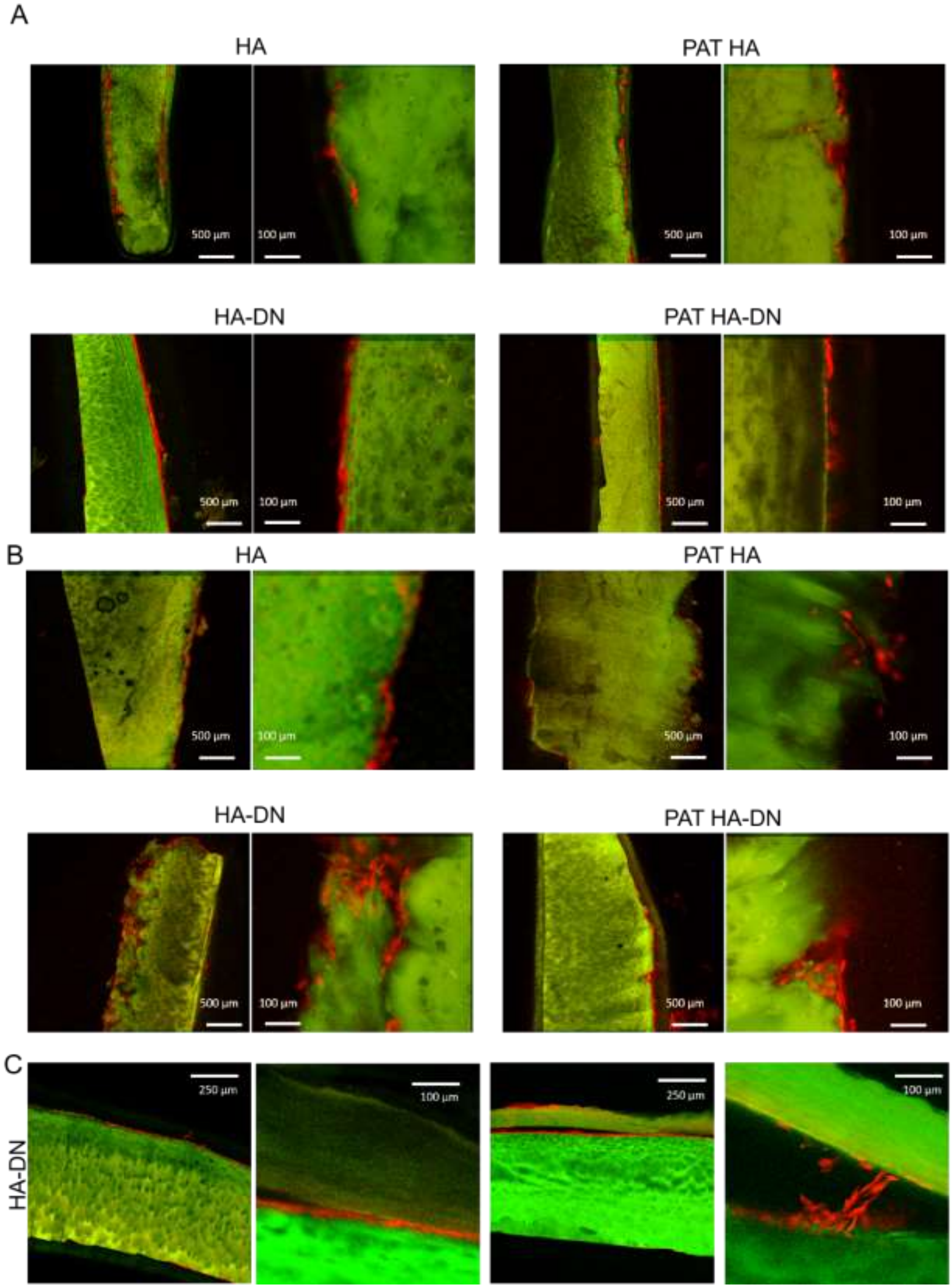

Figure S IX-6. Fluorescence images of the paraformaldehyde fixed cross-section of the system RFP-ASCs/TERT1 –seeded (at the different cell densities A) 2.5x10^4 cell/ sample and B) 1.5x10^5 cell/ sample. FMM that were applied to treat damaged cartilage discs and cultured for 3 weeks. The cells adhered to the cartilage, proliferated and spread on the surface and started to enter through the cartilage defects, colonizing the empty spaces and interacting with the remaining tissue. Fluorescence images of the paraformaldehyde fixed cross-section of the system RFP-ASCs/TERT1 –seeded (at the cell density of 2.5x10^4 cell) HA-DN freestanding multilayer membranes, that were applied to treat C) cartilage chips, after 3 weeks of culture and where autofluorescence of the membranes allowed their visualization. The cells bridged between membrane and cartilage surface, adhered to the cartilage, proliferated and spread on the surface and started to enter through the cartilage defects, colonizing the empty spaces and interacting with the remaining tissue. The membranes were tight to the cartilage surface.

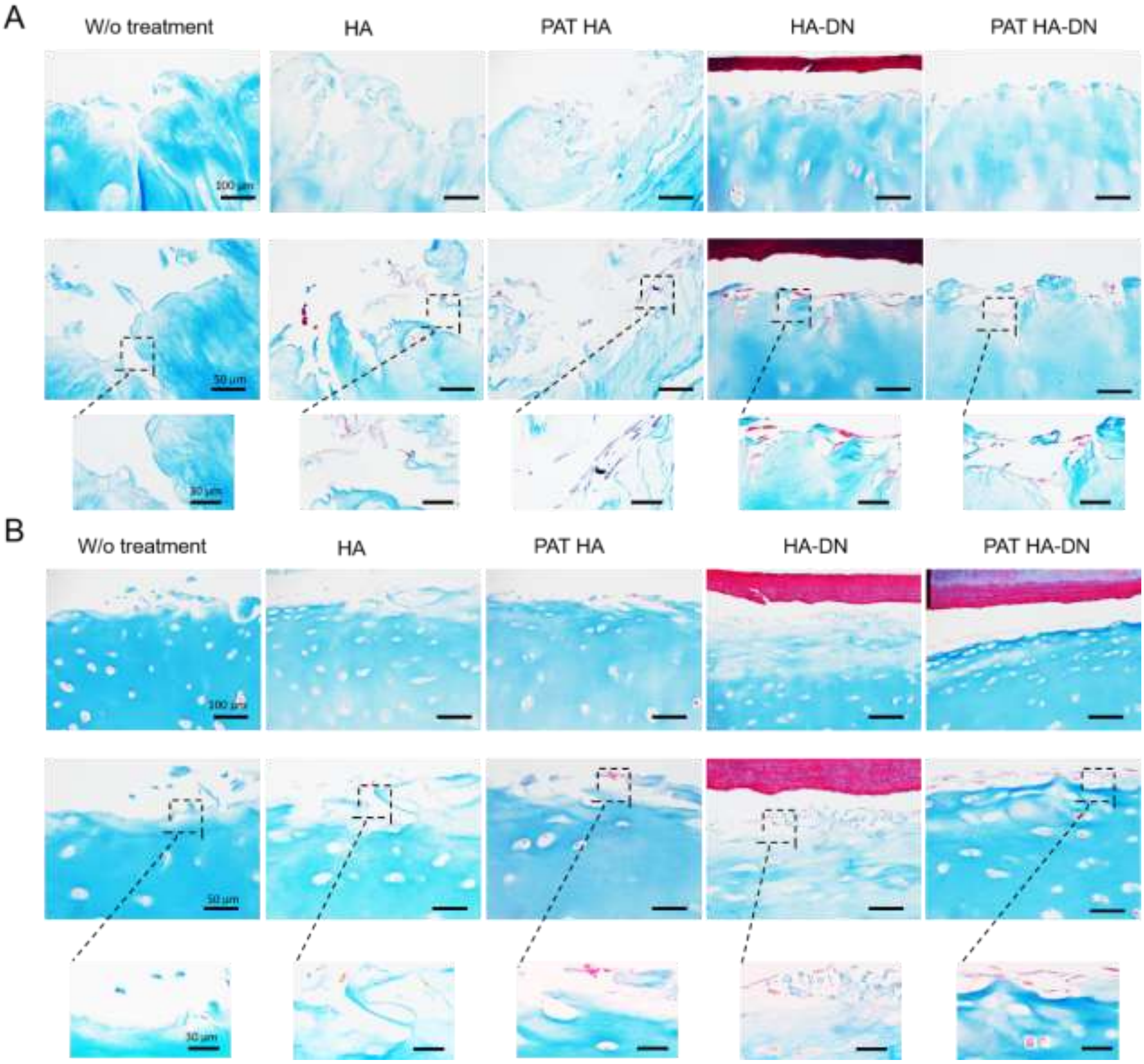

Figure S IX-7. Histological images, representative of the system RFP-ASC-seeded multilayer membrane plus damaged cartilage, fixed after 3 weeks in culture (Azan Staining), for initial cell densities of A) 2.5x10^4 cell/sample and B) 1.5x10^5 cell/ sample.

7. References

1. (a) Nürnberger, S.; Brand, G.; Jagersberger, T.; Vécsei, V.; Marlovits, S., Histological Aspects of Articular Cartilage. *Osteo trauma care* **2006,** *14* (03), 158-167; (b) Tatari, H., [The structure, physiology, and biomechanics of articular cartilage: injury and repair]. *Acta orthopaedica et traumatologica turcica* **2007,** *41 Suppl 2*, 1-5; (c) Sophia Fox, A. J.; Bedi, A.; Rodeo, S. A., The basic science of articular cartilage: structure, composition, and function. *Sports health* **2009,** *1* (6), 461-468.
2. Bhosale, A. M.; Richardson, J. B., Articular cartilage: structure, injuries and review of management. *British Medical Bulletin* **2008,** *87* (1), 77-95.
3. Vinatier, C.; Guicheux, J., Cartilage tissue engineering: From biomaterials and stem cells to osteoarthritis treatments. *Annals of Physical and Rehabilitation Medicine* **2016,** *59* (3), 139-144.
4. (a) Lee, C. R.; Grodzinsky, A. J.; Hsu, H. P.; Spector, M., Effects of a cultured autologous chondrocyte-seeded type II collagen scaffold on the healing of a chondral defect in a canine model. *Journal of Orthopaedic Research* **2003,** *21* (2), 272-281; (b) Frisbie, D. D.; Bowman, S. M.; Colhoun, H. A.; DiCarlo, E. F.; Kawcak, C. E.; McIlwraith, C. W., Evaluation of autologous chondrocyte transplantation via a collagen membrane in equine articular defects – results at 12 and 18 months. *Osteoarthritis and Cartilage* **2008,** *16* (6), 667-679.
5. (a) Hildner, F.; Albrecht, C.; Gabriel, C.; Redl, H.; van Griensven, M., State of the art and future perspectives of articular cartilage regeneration: a focus on adipose-derived stem cells and platelet-derived products. *Journal of Tissue Engineering and Regenerative Medicine* **2011,** *5* (4), e36-e51; (b) Diaz-Romero, J.; Gaillard, J. P.; Grogan, S. P.; Nesic, D.; Trub, T.; Mainil-Varlet, P., Immunophenotypic analysis of human articular chondrocytes: Changes in surface markers associated with cell expansion in monolayer culture. *Journal of Cellular Physiology* **2005,** *202* (3), 731-742.
6. (a) Hochberg, M. C.; Altman, R. D.; April, K. T.; Benkhalti, M.; Guyatt, G.; McGowan, J.; Towheed, T.; Welch, V.; Wells, G.; Tugwell, P., American College of Rheumatology 2012 recommendations for the use of nonpharmacologic and pharmacologic therapies in osteoarthritis of the hand, hip, and knee. *Arthritis care & research* **2012,** *64* (4), 465-474; (b) Zhang, W.; Ouyang, H.; Dass, C. R.; Xu, J., Current research on pharmacologic and regenerative therapies for osteoarthritis. *Bone Research* **2016,** *4*, 15040.
7. Mano, J. F.; Reis, R. L., Osteochondral defects: present situation and tissue engineering approaches. *J Tissue Eng Regen Med* **2007,** *1* (4), 261-73.
8. Dougados, M., The role of anti-inflammatory drugs in the treatment of osteoarthritis: a European viewpoint. *Clinical and experimental rheumatology* **2001,** *19* (6 Suppl 25), S9-14.
9. Eyigor, S.; Hepguler, S.; Sezak, M.; Oztop, F.; Capaci, K., Effects of intra-articular hyaluronic acid and corticosteroid therapies on articular cartilage in experimental severe osteoarthritis. *Clinical and experimental rheumatology* **2006,** *24* (6), 724.
10. (a) Awad, H. A.; Quinn Wickham, M.; Leddy, H. A.; Gimble, J. M.; Guilak, F., Chondrogenic differentiation of adipose-derived adult stem cells in agarose, alginate, and gelatin scaffolds. *Biomaterials* **2004,** *25* (16), 3211-3222; (b) Dragoo, J. L.; Carlson, G.; McCormick, F.; Khan-Farooqi, H.; Zhu, M.; Zuk, P. A.; Benhaim, P., Healing Full-Thickness Cartilage Defects Using Adipose-Derived Stem Cells. *Tissue Engineering* **2007,** *13* (7), 1615-1621; (c) Cheng, N.-C.; Estes, B. T.; Awad, H. A.; Guilak, F., Chondrogenic Differentiation of Adipose-Derived Adult Stem Cells by a Porous Scaffold Derived from Native Articular Cartilage Extracellular Matrix. *Tissue Engineering Part A* **2009,** *15* (2), 231-241; (d) Diekman, B. O.; Rowland, C. R.; Lennon, D. P.; Caplan, A. I.; Guilak, F., Chondrogenesis of Adult Stem Cells from Adipose Tissue and Bone Marrow: Induction by Growth Factors and Cartilage-Derived Matrix. *Tissue Engineering Part A* **2010,** *16* (2), 523-533; (e) Im, G. I., Regeneration of articular cartilage using adipose stem cells. *Journal of biomedical materials research. Part A* **2016,** *104* (7), 1830-44.
11. Weissman, I. L.; Anderson, D. J.; Gage, F., Stem and Progenitor Cells: Origins, Phenotypes, Lineage Commitments, and Transdifferentiations. *Annual Review of Cell and Developmental Biology* **2001,** *17* (1), 387-403.
12. Simonacci, F.; Bertozzi, N.; Raposio, E., Off-label use of adipose-derived stem cells. *Annals of Medicine and Surgery* **2017,** *24*, 44-51.
13. (a) Zuk, P. A.; Zhu, M.; Mizuno, H.; Huang, J.; Futrell, J. W.; Katz, A. J.; Benhaim, P.; Lorenz, H. P.; Hedrick, M. H., Multilineage cells from human adipose tissue: implications for cell-based therapies. *Tissue Eng* **2001,** *7* (2), 211-28; (b) Toghraie, F.; Razmkhah, M.; Gholipour, M. A.; Faghih, Z.; Chenari, N.; Torabi Nezhad, S.; Nazhvani Dehghani, S.; Ghaderi, A., Scaffold-free adipose-derived stem cells (ASCs) improve experimentally induced osteoarthritis in rabbits. *Archives of Iranian medicine* **2012,** *15*

(8), 495-9; (c) Vilar, J. M.; Batista, M.; Morales, M.; Santana, A.; Cuervo, B.; Rubio, M.; Cugat, R.; Sopena, J.; Carrillo, J. M., Assessment of the effect of intraarticular injection of autologous adipose-derived mesenchymal stem cells in osteoarthritic dogs using a double blinded force platform analysis. *BMC Veterinary Research* **2014,** *10* (1), 143.

14. Lin, C. S.; Lin, G.; Lue, T. F., Allogeneic and xenogeneic transplantation of adipose-derived stem cells in immunocompetent recipients without immunosuppressants. *Stem cells and development* **2012,** *21* (15), 2770-8.

15. (a) Jo, C. H.; Lee, Y. G.; Shin, W. H.; Kim, H.; Chai, J. W.; Jeong, E. C.; Kim, J. E.; Shim, H.; Shin, J. S.; Shin, I. S.; Ra, J. C.; Oh, S.; Yoon, K. S., Intra-articular injection of mesenchymal stem cells for the treatment of osteoarthritis of the knee: a proof-of-concept clinical trial. *Stem cells (Dayton, Ohio)* **2014,** *32* (5), 1254-66; (b) Perdisa, F.; Gostyńska, N.; Roffi, A.; Filardo, G.; Marcacci, M.; Kon, E., Adipose-Derived Mesenchymal Stem Cells for the Treatment of Articular Cartilage: A Systematic Review on Preclinical and Clinical Evidence. *Stem Cells International* **2015,** *2015*, 13; (c) Jo, C. H.; Chai, J. W.; Jeong, E. C.; Oh, S.; Shin, J. S.; Shim, H.; Yoon, K. S., Intra-articular Injection of Mesenchymal Stem Cells for the Treatment of Osteoarthritis of the Knee: A 2-Year Follow-up Study. *Am J Sports Med* **2017,** *45* (12), 2774-2783.

16. ter Huurne, M.; Schelbergen, R.; Blattes, R.; Blom, A.; de Munter, W.; Grevers, L. C.; Jeanson, J.; Noël, D.; Casteilla, L.; Jorgensen, C.; van den Berg, W.; van Lent, P. L. E. M., Antiinflammatory and chondroprotective effects of intraarticular injection of adipose-derived stem cells in experimental osteoarthritis. *Arthritis & Rheumatism* **2012,** *64* (11), 3604-3613.

17. (a) Grigolo, B.; Lisignoli, G.; Desando, G.; Cavallo, C.; Marconi, E.; Tschon, M.; Giavaresi, G.; Fini, M.; Giardino, R.; Facchini, A., Osteoarthritis Treated with Mesenchymal Stem Cells on Hyaluronan-Based Scaffold in Rabbit. *Tissue Engineering Part C: Methods* **2009,** *15* (4), 647-658; (b) Erickson, I. E.; Kestle, S. R.; Zellars, K. H.; Farrell, M. J.; Kim, M.; Burdick, J. A.; Mauck, R. L., High mesenchymal stem cell seeding densities in hyaluronic acid hydrogels produce engineered cartilage with native tissue properties. *Acta Biomaterialia* **2012,** *8* (8), 3027-3034.

18. (a) Garg, T.; Singh, O.; Arora, S.; Murthy, R., Scaffold: a novel carrier for cell and drug delivery. *Critical reviews in therapeutic drug carrier systems* **2012,** *29* (1), 1-63; (b) Liu, M.; Zeng, X.; Ma, C.; Yi, H.; Ali, Z.; Mou, X.; Li, S.; Deng, Y.; He, N., Injectable hydrogels for cartilage and bone tissue engineering. *Bone Research* **2017,** *5*, 17014.

19. Silva, J. M.; Reis, R. L.; Mano, J. F., Biomimetic Extracellular Environment Based on Natural Origin Polyelectrolyte Multilayers. *Small* **2016,** *12* (32), 4308-4342.

20. Henrotin, Y.; Raman, R.; Richette, P.; Bard, H.; Jerosch, J.; Conrozier, T.; Chevalier, X.; Migliore, A., Consensus statement on viscosupplementation with hyaluronic acid for the management of osteoarthritis. *Seminars in arthritis and rheumatism* **2015,** *45* (2), 140-9.

21. (a) Malda, J.; McIlwraith, C. W., Current Trends in Cartilage Science: An Impression from the ICRS World Conference 2012. *Cartilage* **2013,** *4* (4), 273-280; (b) Diekman, B. O.; Guilak, F., Stem cell-based therapies for osteoarthritis: Challenges and opportunities. *Current opinion in rheumatology* **2013,** *25* (1), 119-126.

22. (a) Ho, W.; Tawil, B.; Dunn, J. C.; Wu, B. M., The behavior of human mesenchymal stem cells in 3D fibrin clots: dependence on fibrinogen concentration and clot structure. *Tissue Eng* **2006,** *12* (6), 1587-95; (b) Kim, Y. S.; Choi, Y. J.; Suh, D. S.; Heo, D. B.; Kim, Y. I.; Ryu, J. S.; Koh, Y. G., Mesenchymal stem cell implantation in osteoarthritic knees: is fibrin glue effective as a scaffold? *Am J Sports Med* **2015,** *43* (1), 176-85.

23. Lee, H.; Scherer, N. F.; Messersmith, P. B., Single-molecule mechanics of mussel adhesion. *Proceedings of the National Academy of Sciences* **2006,** *103* (35), 12999-13003.

24. (a) Sedó, J.; Saiz-Poseu, J.; Busqué, F.; Ruiz-Molina, D., Catechol-Based Biomimetic Functional Materials. *Advanced Materials* **2013,** *25* (5), 653-701; (b) Lee, H.; Dellatore, S. M.; Miller, W. M.; Messersmith, P. B., Mussel-inspired surface chemistry for multifunctional coatings. *Science (New York, N.Y.)* **2007,** *318* (5849), 426-430.

25. Scognamiglio, F.; Travan, A.; Borgogna, M.; Donati, I.; Marsich, E.; Bosmans, J. W. A. M.; Perge, L.; Foulc, M. P.; Bouvy, N. D.; Paoletti, S., Enhanced bioadhesivity of dopamine-functionalized polysaccharidic membranes for general surgery applications. *Acta Biomaterialia* **2016,** *44*, 232-242.

26. Shin, M.; Park, S.-G.; Oh, B.-C.; Kim, K.; Jo, S.; Lee, M. S.; Oh, S. S.; Hong, S.-H.; Shin, E.-C.; Kim, K.-S.; Kang, S.-W.; Lee, H., Complete prevention of blood loss with self-sealing haemostatic needles. *Nature Materials* **2016,** *16*, 147.

27. Costa, R. R.; Mano, J. F., Polyelectrolyte multilayered assemblies in biomedical technologies. *Chemical Society Reviews* **2014,** *43* (10), 3453-3479.

28. Correia, C. R.; Reis, R. L.; Mano, J. F., Multiphasic, Multistructured and Hierarchical Strategies for Cartilage Regeneration. *Advances in experimental medicine and biology* **2015,** *881*, 143-60.
29. Silva, J. M.; Georgi, N.; Costa, R.; Sher, P.; Reis, R. L.; Van Blitterswijk, C. A.; Karperien, M.; Mano, J. F., Nanostructured 3D Constructs Based on Chitosan and Chondroitin Sulphate Multilayers for Cartilage Tissue Engineering. *PLOS ONE* **2013,** *8* (2), e55451.
30. Mano, J. F., Viscoelastic properties of chitosan with different hydration degrees as studied by dynamic mechanical analysis. *Macromol Biosci* **2008,** *8* (1), 69-76.
31. Neto, A. I.; Cibrão, A. C.; Correia, C. R.; Carvalho, R. R.; Luz, G. M.; Ferrer, G. G.; Botelho, G.; Picart, C.; Alves, N. M.; Mano, J. F., Nanostructured Polymeric Coatings Based on Chitosan and Dopamine-Modified Hyaluronic Acid for Biomedical Applications. *Small* **2014,** *10* (12), 2459-2469.
32. Silva, J. M.; Duarte, A. R. C.; Caridade, S. G.; Picart, C.; Reis, R. L.; Mano, J. F., Tailored freestanding multilayered membranes based on chitosan and alginate. *Biomacromolecules* **2014,** *15* (10), 3817-3826.
33. Sousa, M. P.; Caridade, S. G.; Mano, J. F., Control of Cell Alignment and Morphology by Redesigning ECM-Mimetic Nanotopography on Multilayer Membranes. *Advanced Healthcare Materials* **2017,** *6* (15), 1601462.
34. McWhorter, F. Y.; Wang, T.; Nguyen, P.; Chung, T.; Liu, W. F., Modulation of macrophage phenotype by cell shape. *Proceedings of the National Academy of Sciences of the United States of America* **2013,** *110* (43), 17253-17258.
35. Mueller, D. D.; Morgan, T. D.; Wassenberg, J. D.; Hopkins, T. L.; Kramer, K. J., Proton and carbon-13 NMR of 3-O and 4-O conjugates of dopamine and other catecholamines. *Bioconjugate Chemistry* **1993,** *4* (1), 47-53.
36. (a) Frenkel, S. R.; Di Cesare, P. E., Scaffolds for Articular Cartilage Repair. *Annals of Biomedical Engineering* **2004,** *32* (1), 26-34; (b) Nuernberger, S.; Cyran, N.; Albrecht, C.; Redl, H.; Vécsei, V.; Marlovits, S., The influence of scaffold architecture on chondrocyte distribution and behavior in matrix-associated chondrocyte transplantation grafts. *Biomaterials* **2011,** *32* (4), 1032-1040; (c) Rai, V.; Dilisio, M. F.; Dietz, N. E.; Agrawal, D. K., Recent strategies in cartilage repair: A systemic review of the scaffold development and tissue engineering. *Journal of Biomedical Materials Research Part A* **2017,** *105* (8), 2343-2354.
37. Neto, A. I.; Vasconcelos, N. L.; Oliveira, S. M.; Ruiz-Molina, D.; Mano, J. F., High-Throughput Topographic, Mechanical, and Biological Screening of Multilayer Films Containing Mussel-Inspired Biopolymers. *Advanced Functional Materials* **2016,** *26* (16), 2745-2755.
38. Mano, J. F.; Silva, G. A.; Azevedo, H. S.; Malafaya, P. B.; Sousa, R. A.; Silva, S. S.; Boesel, L. F.; Oliveira, J. M.; Santos, T. C.; Marques, A. P.; Neves, N. M.; Reis, R. L., Natural origin biodegradable systems in tissue engineering and regenerative medicine: present status and some moving trends. *Journal of The Royal Society Interface* **2007,** *4* (17), 999-1030.
39. (a) Almond, A., Hyaluronan. *Cellular and molecular life sciences : CMLS* **2007,** *64* (13), 1591-6; (b) Bauer, C.; Berger, M.; Baumgartner, R. R.; Höller, S.; Zwickl, H.; Niculescu-Morzsa, E.; Halbwirth, F.; Nehrer, S., A Novel Cross-Linked Hyaluronic Acid Porous Scaffold for Cartilage Repair:An *In Vitro* Study With Osteoarthritic Chondrocytes. *Cartilage* **2016,** *7* (3), 265-273.
40. (a) Kafedjiiski, K.; Jetti, R. K.; Foger, F.; Hoyer, H.; Werle, M.; Hoffer, M.; Bernkop-Schnurch, A., Synthesis and *in vitro* evaluation of thiolated hyaluronic acid for mucoadhesive drug delivery. *International journal of pharmaceutics* **2007,** *343* (1-2), 48-58; (b) Levett, P. A.; Hutmacher, D. W.; Malda, J.; Klein, T. J., Hyaluronic Acid Enhances the Mechanical Properties of Tissue-Engineered Cartilage Constructs. *PLOS ONE* **2014,** *9* (12), e113216.
41. Niepel, M. S.; Almouhanna, F.; Ekambaram, B. K.; Menzel, M.; Heilmann, A.; Groth, T., Cross-linking multilayers of poly-l-lysine and hyaluronic acid: Effect on mesenchymal stem cell behavior. *The International Journal of Artificial Organs* **2018,** *41* (4), 223-235.
42. (a) Duarte Campos, D. F.; Drescher, W.; Rath, B.; Tingart, M.; Fischer, H., Supporting Biomaterials for Articular Cartilage Repair. *Cartilage* **2012,** *3* (3), 205-221; (b) Zhao, W.; Jin, X.; Cong, Y.; Liu, Y.; Fu, J., Degradable natural polymer hydrogels for articular cartilage tissue engineering. *Journal of Chemical Technology & Biotechnology* **2013,** *88* (3), 327-339.
43. Stammen, J. A.; Williams, S.; Ku, D. N.; Guldberg, R. E., Mechanical properties of a novel PVA hydrogel in shear and unconfined compression. *Biomaterials* **2001,** *22* (8), 799-806.
44. Ng, K. W.; Kugler, L. E.; Doty, S. B.; Ateshian, G. A.; Hung, C. T., Scaffold degradation elevates the collagen content and dynamic compressive modulus in engineered articular cartilage. *Osteoarthritis and Cartilage* **2009,** *17* (2), 220-227.

45. Cardoso, M. J.; Caridade, S. G.; Costa, R. R.; Mano, J. F., Enzymatic Degradation of Polysaccharide-Based Layer-by-Layer Structures. *Biomacromolecules* **2016,** *17* (4), 1347-1357.
46. Santhanam, S.; Liang, J.; Baid, R.; Ravi, N., Investigating thiol-modification on hyaluronan via carbodiimide chemistry using response surface methodology. *Journal of Biomedical Materials Research Part A* **2015,** *103* (7), 2300-2308.
47. Shin, J.; Lee, J. S.; Lee, C.; Park, H.-J.; Yang, K.; Jin, Y.; Ryu, J. H.; Hong, K. S.; Moon, S.-H.; Chung, H.-M.; Yang, H. S.; Um, S. H.; Oh, J.-W.; Kim, D.-I.; Lee, H.; Cho, S.-W., Tissue Adhesive Catechol-Modified Hyaluronic Acid Hydrogel for Effective, Minimally Invasive Cell Therapy. *Advanced Functional Materials* **2015,** *25* (25), 3814-3824.
48. Koga, H.; Muneta, T.; Nagase, T.; Nimura, A.; Ju, Y.-J.; Mochizuki, T.; Sekiya, I., Comparison of mesenchymal tissues-derived stem cells for in vivo chondrogenesis: suitable conditions for cell therapy of cartilage defects in rabbit. *Cell and Tissue Research* **2008,** *333* (2), 207-215.
49. Park, Y.-B.; Ha, C.-W.; Kim, J.-A.; Rhim, J.-H.; Park, Y.-G.; Chung, J. Y.; Lee, H.-J., Effect of Transplanting Various Concentrations of a Composite of Human Umbilical Cord Blood-Derived Mesenchymal Stem Cells and Hyaluronic Acid Hydrogel on Articular Cartilage Repair in a Rabbit Model. *PLoS ONE* **2016,** *11* (11), e0165446.
50. Desando, G.; Cavallo, C.; Sartoni, F.; Martini, L.; Parrilli, A.; Veronesi, F.; Fini, M.; Giardino, R.; Facchini, A.; Grigolo, B., Intra-articular delivery of adipose derived stromal cells attenuates osteoarthritis progression in an experimental rabbit model. *Arthritis Research & Therapy* **2013,** *15* (1), R22-R22.
51. Kasir, R.; Vernekar, V. N.; Laurencin, C. T., Regenerative Engineering of Cartilage Using Adipose-Derived Stem Cells. *Regenerative Engineering and Translational Medicine* **2015,** *1* (1), 42-49.
52. Wise, J. K.; Yarin, A. L.; Megaridis, C. M.; Cho, M., Chondrogenic Differentiation of Human Mesenchymal Stem Cells on Oriented Nanofibrous Scaffolds: Engineering the Superficial Zone of Articular Cartilage. *Tissue Engineering. Part A* **2009,** *15* (4), 913-921.
53. Pincus, Z.; Theriot, J. A., Comparison of quantitative methods for cell-shape analysis. *Journal of Microscopy* **2007,** *227* (2), 140-156.
54. Guido, S.; Tranquillo, R. T., A methodology for the systematic and quantitative study of cell contact guidance in oriented collagen gels. Correlation of fibroblast orientation and gel birefringence. *Journal of cell science* **1993,** *105 (Pt 2)*, 317-31.
55. Curtis, A.; Wilkinson, C., Topographical control of cells. *Biomaterials* **1997,** *18* (24), 1573-83.
56. (a) Zhang, L.; Hu, J.; Athanasiou, K. A., The Role of Tissue Engineering in Articular Cartilage Repair and Regeneration. *Critical reviews in biomedical engineering* **2009,** *37* (1-2), 1-57; (b) Teuschl, A. H.; Nürnberger, S.; Redl, H.; Nau, T., Articular cartilage tissue regeneration—current research strategies and outlook for the future. *European Surgery* **2013,** *45* (3), 142-153.
57. Lee, W. Y.-w.; Wang, B., Cartilage repair by mesenchymal stem cells: Clinical trial update and perspectives. *Journal of Orthopaedic Translation* **2017,** *9*, 76-88.
58. Mumme, M.; Steinitz, A.; Nuss, K. M.; Klein, K.; Feliciano, S.; Kronen, P.; Jakob, M.; von Rechenberg, B.; Martin, I.; Barbero, A.; Pelttari, K., Regenerative Potential of Tissue-Engineered Nasal Chondrocytes in Goat Articular Cartilage Defects. *Tissue Eng Part A* **2016,** *22* (21-22), 1286-1295.
59. Peretti, G. M.; Randolph, M. A.; Zaporojan, V.; Bonassar, L. J.; Xu, J. W.; Fellers, J. C.; Yaremchuk, M. J., A biomechanical analysis of an engineered cell-scaffold implant for cartilage repair. *Annals of plastic surgery* **2001,** *46* (5), 533-7.
60. Maggini, J.; Mirkin, G.; Bognanni, I.; Holmberg, J.; Piazzón, I. M.; Nepomnaschy, I.; Costa, H.; Cañones, C.; Raiden, S.; Vermeulen, M.; Geffner, J. R., Mouse Bone Marrow-Derived Mesenchymal Stromal Cells Turn Activated Macrophages into a Regulatory-Like Profile. *PLOS ONE* **2010,** *5* (2), e9252.
61. Puissant, B.; Barreau, C.; Bourin, P.; Clavel, C.; Corre, J.; Bousquet, C.; Taureau, C.; Cousin, B.; Abbal, M.; Laharrague, P.; Penicaud, L.; Casteilla, L.; Blancher, A., Immunomodulatory effect of human adipose tissue-derived adult stem cells: comparison with bone marrow mesenchymal stem cells. *British Journal of Haematology* **2005,** *129* (1), 118-129.
62. Ng, K. W.; DeFrancis, J. G.; Kugler, L. E.; Kelly, T. A.; Ho, M. M.; O'Conor, C. J.; Ateshian, G. A.; Hung, C. T., Amino acids supply in culture media is not a limiting factor in the matrix synthesis of engineered cartilage tissue. *Amino acids* **2008,** *35* (2), 433-8.
63. Jang, Y.; Jung, H.; Ju, J. H., Chondrogenic Differentiation Induction of Adipose-derived Stem Cells by Centrifugal Gravity. *Journal of visualized experiments : JoVE* **2017,** (120).
64. Caridade, S. G.; Monge, C.; Almodóvar, J.; Guillot, R.; Lavaud, J.; Josserand, V.; Coll, J.-L.; Mano, J. F.; Picart, C., Myoconductive and osteoinductive free-standing polysaccharide membranes. *Acta Biomaterialia* **2015,** *15*, 139-149.

X. Conclusions and future perspectives

Abstract

The main conclusions of the developed work are described in this last chapter of the thesis. Furthermore, a reflection about the current limitations and the future perspectives of the employed strategies and techniques are also depicted.

Layer-by-layer (LbL) technique was successfully employed in accordance to the hypothesis of this thesis. 2D substrates were used as templates for films' growth with the purpose of coating or detaching. These multilayered films were composed of natural or biomimetic polymeric materials with distinct functionalities, that could result in different properties of the films. Moreover, changing different setting parameters of the LbL technique could tailor specific properties of the resulting films. The combination of these biomimetic strategies resulted in multilayered systems capable of being applied in a wide range of biomedical applications, namely coatings for biomaterials, drug delivery carriers, stimuli-responsive biomaterials, surfaces to study cells in a controlled environment, adhesive patches or tissue engineering applications. Therefore, throughout the chapters of this thesis, different biomimetic strategies were envisaged and combined with LbL technology, resulting in several bio-based systems.

Firstly, in Chapter IX it was demonstrated that elastin-like polypeptides (ELPs) can be used as the main constituent of multilayered films, conferring them the possibility of presenting bioactive functions. By using an ELP containing the bioactive sequence of arginine-glycine-aspartic acid (RGD), it was possible to construct nanostructured coatings with enhanced cell adhesion and higher evidences of supporting cell differentiation. These biomimetic peptides were designed to incorporate azide and alkyne groups, allowing their interaction by a click chemistry reaction. Unlike conventional LbL assembly which is usually driven by electrostatic forces, these multilayered biomimetic films were constructed by means of cycloaddition reactions between azides and alkynes. The high stability of these ELPs-films conferred by the covalent bonding, was monitored *in situ* using a QCM-D; the films withstood harsh conditions of pH. This confirmed the hypothesis of having more stable films than just with electrostatic interaction. The stimuli-responsive nature inherent of ELPs conferred these properties to the multilayered coatings. Jumping temperature and pH above and below a threshold triggered the transition of the ELP-based film, making it to present charged amino acids to the interface. Therefore, properties of the film's surface as the wettability and the surface roughness changed between these values of temperature and pH. Overall, it was possible to construct multilayer films that retained and exhibited the properties of their biomimetic elements. These stimuli-responsive films can find application on coating implants with more complex shapes and compositions, nano/microstructures, gels and membranes, or even on developing structures for tissue engineering purposes, such as platforms to culture cells in controlled conditions. Future developments of ELP-based multilayer films may include the presence of different bioactive sequences to modulate other cellular functions, for instance to direct cellular differentiation. It would be also interesting to evaluate the possibility of using this stimuli-responsive nature to create a kind of a cell-sheet system, promoting firstly the adhesion of the cells and then changing some parameter capable of detaching a cell monolayer.

LbL extrapolation from a multilayered coating to a real freestanding multilayered 2-dimensional structure was achieved by using other biomimetic strategy. In Chapter V, the biopolymers chitosan (CHT) and chondroitin sulfate (CS) were combined by LbL driven by electrostatic interactions, allowing the fabrication of multilayered films that exhibited superior biocompatibility, as they offer some similarities with the extracellular matrix (ECM) morphology and composition. Using an inert underlying substrate to construct the multilayer structure allowed their detachment after drying, obtaining a freestanding multilayered membrane; this methodology. Confirming the success of the detachment process was important to develop new freestanding systems. Further, the multilayered membranes were successfully crosslinked with genipin to improve their handling properties. This natural material offered the possibility to tailor the physico-chemical and the mechanical properties and enhance the *in vitro* biological performance of the membrane, being an interesting tool to adjust the material to different kind of biomedical and tissue engineering applications. Here, shape-memory ability may be important to implant this kind of freestanding multilayered systems *in vivo*.

Nowadays, more refined strategies have been envisaged to develop materials for tissue engineering applications. Among others, the presence of topographical features has been exploited to modulate the cellular behavior, being inspired by the topography of the ECM of different tissues. In Chapter V, it was possible to introduce specific physical cues on the surface of multilayered membranes, just by changing the underlying substrate. Using an optical disk as template resulted in freestanding multilayer membranes presenting grooved nanotopographical on their surface. As a result, it was possible to modulate the cellular behavior prompting the cellular elongation and alignment and favoring the cellular differentiation without the requirement of any exogenous factor. This work brought new perspectives for LbL technology, being able to easily produce micro- and nanoengineered substrates towards tissue engineering. Further developments on these methodologies may integrate the presence of topographical features but at different length scales and even transposing it from 2-dimensional to 3-dimensional multilayered systems. This can result in an adequate substrate to co-culture different type of cells, with different functions, allowing the construction of *in vitro* biomimetic tissue. Like real tissues, these systems can integrate different types of cells with different functions and behavior.

To create new functional multilayered systems, a new strategy involving freestanding LbL-based membranes and adhesiveness was exploited in the last chapters of this thesis. Inspired by the notable wet adhesion ability of mussels, the backbone of different molecular weight hyaluronic acid (HA) was successfully modified with dopamine (DN), a derivate of DOPA which contains catechol moieties nowadays reported as responsible for the mussels' adhesion. In chapters VII, VIII and IX, the conjugated HA-DN was combined with other biopolymers using the LbL technology, producing freestanding multilayered membranes. As a result, adhesive strength was clearly enhanced with the introduction of DN in the backbone of HA. Moreover, other properties were influenced by the presence of the conjugated HA-DN; more porous morphology, lower water uptake ability, increased Young's modulus and bactericidal activity were reported for these nanostructured membranes. The versatility of these LbL systems and, particularly, the adhesive properties conferred by the presence of dopamine allowed their application in a range of biomedical and tissue engineering applications In Chapter VII, it was possible to produce biomimetic, biocompatible and osteophilic freestanding multilayered membranes with interesting properties that can be potentially be applied in bone tissue engineering. Then, in Chapter VIII, these biocompatible, highly porous and adhesive materials showed great potential in providing a support for skin wound healing, confirmed by *in vitro* and *in vivo* assays. Lastly, in Chapter IX, a more complex strategy was envisaged to construct a flexible and bioinspired multilayered system, suitable to be applied for articular cartilage damaging or defect repair. Adhesive freestanding membranes were successfully produced, either presenting topographical features on their surface or not, to produce an adequate platform to successfully deliver therapeutic cells (adipose stem cells, ASCs) to repair defects of any lateral size and shape. Membranes containing DN showed improved properties compared with their controls in terms of degradation, mechanical adhesiveness and cellular viability, confirming their potential as adhesive and functional LbL-engineered membranes to repair superficial cartilage damaging. Unlike the ASCs-based therapies that are already used in clinic for this end, our strategy can allow the efficient delivery of a higher number of cells to the defect place, protecting the treatment from the harsh environment inside the synovial membrane.

Overall, combining natural polymers or biomimetic polymers which comprise similarities with the ECM or biorecognition moieties to interact with cells, with a versatile and bottom-up approach as LbL, capable of creating nano- and micro-organized structures, it was possible to produce biomimetic materials with a great potential towards biomedical and tissue engineering applications.

Future research comes with the urge of more complex engineered systems, that could mimic the intrinsic architecture and complexity of native tissues. Increasing the complexity of the developed LbL-based systems can comprise for instance the introduction of different cell-binding motifs or topographical features, the presence of functional microvasculature or the transition for 3-dimensional shapes. Moreover, LbL technique offers the opportunity of evolving on building modular microtissues to create complexity. Stimuli-responsive properties can be important to add functionality and dynamics to the multilayer system, being a different and interesting strategy to simply increase the complexity. Adhesive properties can be improved by for instance having adhesive moieties in each nanolayer of the system, being adhesive patch suitable for a wide range of biomedical and tissue engineering applications. Overall, great outcomes can be a result of more and deeper research using the strategies reported throughout the chapters of this thesis. The versatility of LbL assembly may be crucial to achieve even more adequate materials towards biomedical and tissue engineering ends.